Serpentine Ridge
Exploration Licence 45/2010

Annual Technical Report for the period 31/05/2015 to 30/05/2016

T Holmes
May 2016
Venture Minerals Ltd
288 Churchill Avenue, Subiaco WA 6008
PO Box 186, West Perth WA 6872

Contents

APPENDICES

Appendix 1: Holmes (2015) BSc. Hons Thesis. PDF
Appendix 2: Surface sampling data
Appendix 3: Assay methods
Appendix 4: BW003a structural data
Appendix 5: SEM results
Appendix 6: Laser Raman Results
Appendix 7: Tourmaline investigation results
Appendix 8: Sample photographs
Appendix 9: Geochronology results
Appendix 10: ID-TIMS method
Appendix 11: Hylogger
Appendix 12: Terraspec results
Appendix 13: Thin sections

Tables

Figures

1 Summary

Activities during the 2015-2016 tenement anniversary year were focused on developing paragenetic and geometric models for the Big Wilson Prospect (identified & tested by 13 DDC holes for 3572m by Venture in the 2012-2013 period) located in the northern part of EL45/2010. The analytical and research work was largely conducted by Travis Holmes as part of a BSc Honours project at the University of Tasmania and sponsored by Venture Minerals.

Four stages of alteration were identified and documented within the Big Wilson deposit. Direct dating of cassiterite from the Big Wilson skarn returned the same age (within analytical errors) as the adjacent Meredith Granite. The Meredith Granite contains two distinct tourmaline vein types, brown & green, with characteristic alteration envelopes dominated by white mica. Both tourmaline vein types strike dip steeply NE but only those with green tourmaline are typically also tin mineralised. Tourmaline major and trace element chemistry has potential to be used as a vector towards mineralisation. Tin mineralised veins were discovered in multiple locations in the granite adjacent to the Big Wilson skarn but drilling orientation to date has generally been suboptimal to test the NW striking cassiterite-tourmaline veins. Future drilling should focus on the NW striking cassiterite-tourmaline vein sets and where they intersect the skarn.

Further work on the use of tourmaline, white mica alteration and established calcsilicate vectors to mineralisation is recommended for the Big Wilson and Merton Hill prospects within EL45/2010 during the 2016-2017 tenement year.

2 Introduction

Exploration Licence 45/2010 is located within the tin-tungsten province of western Tasmania and includes part of the Meredith Granite's southern margin. The Meredith Granite is part of a suite of Devonian granites which is very important to tin-tungsten mineralization in Tasmania, and deposits associated with this suite include Renison Bell (26 Mt at 1.46% Sn), Mount Bischoff (10.54 Mt at 1.1% Sn), Cleveland (12.4 Mt at 0.62% Sn, 0.25% Cu) and King Island (17 Mt at 0.85% WO_3). EL45/2010 is situated immediately east of Venture's EL21/2005 which includes the Main and No.2 Sn-W-magnetite deposits at Mt Lindsay and the Livingstone and Reward Sn-W-Fe deposits in the Stanley River area. Exploration Licence 45/2010 includes the Big Wilson Sn skarn and veined greisen deposit, Merton Hill Sn+Cu+Pb+Zn+Ag vein and carbonate replacement deposit, and several Sn, W and/or Cu geochemical anomalies in the Little Wilson River, Keenan Creek, Harman River, and Limestone Creek areas.

EL45/2010 also includes part of the Wilson River Ultramafic Complex which is prospective for nickel and PGM mineralisation. Most of the streams draining the Wilson River Ultramafic Complex were prospected and mined for alluvial osmiridium in the early 1900s, with some alluvial deposits also yielding small amounts of gold. Much of the ultramafic complex is covered with a thin, residual lateritic soil, and at several locations, most notably Riley Creek, Keenan Creek and Limestone Creek areas, there are residual and colluvial deposits of ferruginous laterite to several metres thick. The ferruginous laterite deposits at Riley Creek

were previously evaluated by Callina NL for chromite and platinoids, and more recently Direct Shipping iron Ore (DSO) by Venture Minerals. The iron laterite deposits at Riley Creek have been excised from EL45/2010 into 5M/2012.

Exploration Licence 17/2012 covering 7 km^2 was amalgamated into the north eastern corner of EL45/2010 in February 2014. The amalgamated area includes Eldon Group rocks of the Huskisson syncline sediments located approx.1.5 km east of the Meredith Granite and c. 2 km from the Big Wilson Sn prospect. In 2015 c. 17 km^2 was relinquished from the northern, eastern and western margins of EL45/2010.

3 Location and Access

EL45/2010 currently covers c. 61 km^2 and is located c. 100-130 km by road southwest of the port of Burnie, and c. 20 km by road from the nearest town Tullah (Figure 3.1). The southern boundary of the licence is approximately 4 km north of the Renison Bell tin mine. The licence is covered by the Pieman 1:100,000 map sheet, and Parsons and Roseberry 1:25,000 map sheets. Topography is moderately rugged, the most notable topographic features comprising Serpentine Ridge and Websterite Hill. Average annual rainfall is approximately 2000 mm and vegetation is dominated by temperate rainforest, with dense scrub over ultramafic and granitic basement, and in areas of regenerating forest.

The bitumen HEC Pieman Road and Transend transmission lines traverse the southern half of EL45/2010, and a mixture of HEC, forestry and mineral exploration roads provide good access throughout much of the tenement south of the Wilson River. Access to the northern part of the licence is currently best obtained via a 4WD road from the Wilson River over Websterite Hill to the upper Harmen area, or by helicopter. Principal land uses include State Forest, Regional Reserve, and Forest Reserve. Parts of the State Forest area south of the Pieman Road are periodically being logged.

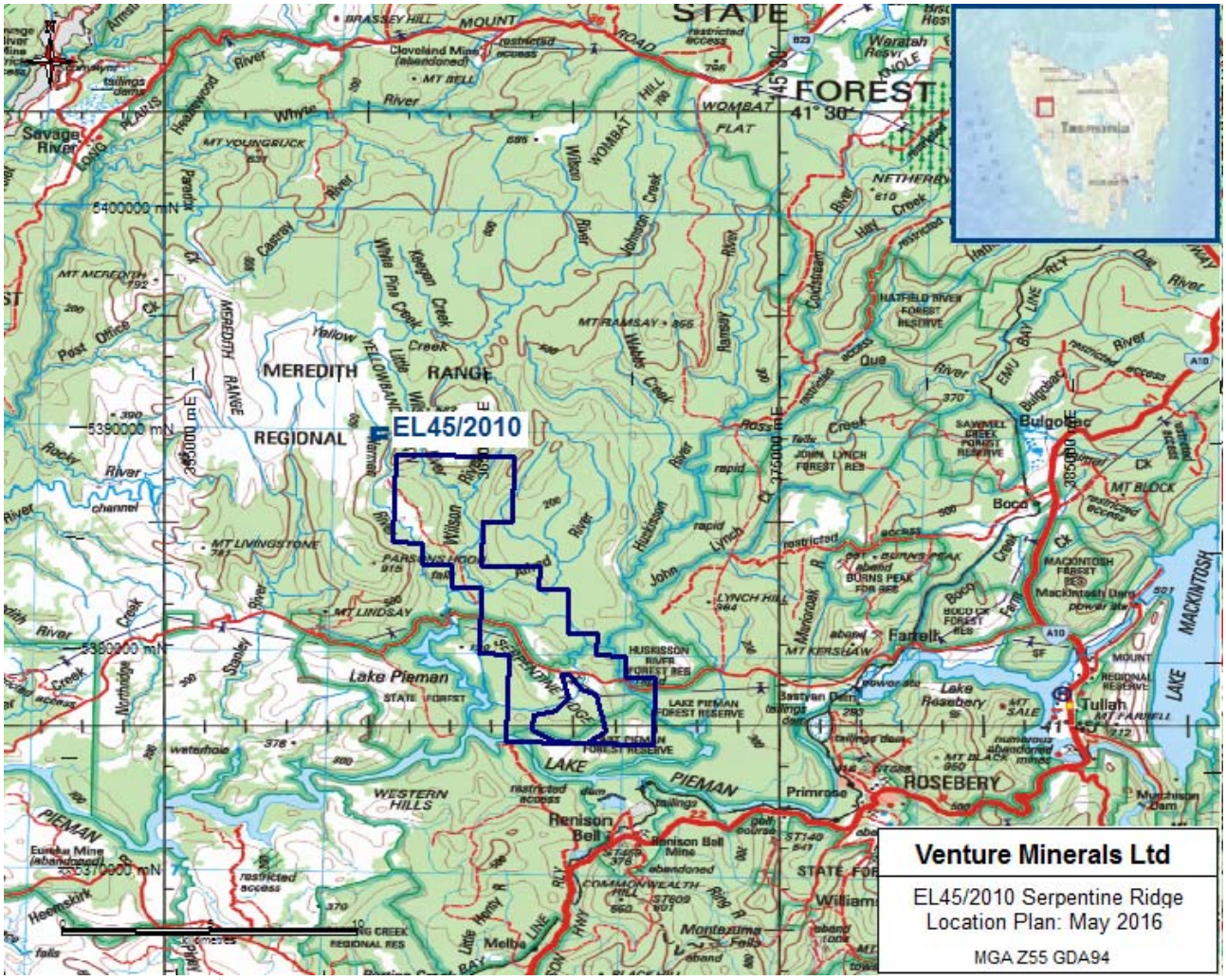

Figure 3.1: EL45/2010 Location Plan

4 Geological Setting

EL45/2010 is situated in the Dundas Trough of western Tasmania and underlain from west to east by the Crimson Creek Formation, the Wilson River Ultramafic Complex ("WRUC"), the Dundas and Gordon groups, and the Eldon Group (Figure 2). Sedimentary stratigraphy is moderately dipping to vertical. The Meredith Granite rims the northern extent of the licence and dips away at a modest angle beneath the sedimentary and ultramafic units, albeit complicated by numerous irregular granitic dykes, shelves and apophyses. Preliminary interpretation suggests several phases of granite intrusion culminating in late stage quartz-tourmaline veining and the localised development of quartz-tourmaline-topaz greisen and siderite-sericite greisen.

The Neoproterozoic - Early Cambrian Crimson Creek Formation comprises mainly of thin to thick bedded greenish grey lithic sandstones, siltstones and mudstones with scattered horizons of laminated to thin bedded light grey, green and pink felsic to mafic tuffites and thin to thick bedded calcareous sandstones, and rare tholeiitic basalt flows. Total thickness in the Mt Lindsay area is estimated at c. 5000 m, and EL45/2010 includes a narrow strip of the Crimson Creek Formation along its western edge (Figure 2).

The WRUC occupies the central NW-trending spine of the licence and general interpretation is that the WRUC is entirely fault bounded, the lower margin against Crimson Creek Formation, the upper margin against Devonian conglomerate, quartz arenite, siltstone and marl of the Eldon Group with localised slivers of the Ordovician Gordon Limestone. Radiometric dates are not available for the WRUC and a Neoproterozoic to Cambrian age has been estimated according to stratigraphic constraints (e.g. Brown 1986). A major episode of folding during the Devonian formed the northwest to north trending Huskisson Syncline, and contact metamorphism indicates emplacement of the WRUC into the current stratigraphic position prior to the intrusion of the Meredith Granite around 370 Ma. Vein and replacement-style tin and tungsten mineralization appears to be associated regionally with the intrusion of the Meredith Granite. The WRUC is part of a group of similar ultramafic bodies scattered along the Dundas and Adamsfield troughs in northwestern and western Tasmania. The WRUC is one of the largest exposed ultramafic bodies in the Dundas Trough at approx. 17 km long and up to 2 km wide, and was probably continuous with the Mt Stewart ultramafic body ca. 11 km to the north-northwest before intrusion of the Meredith Granite. Brown (1986) identified two petrogenetically distinct ultramafic successions within the WRUC, namely the Layered Dunite-Harzburgite succession (LDH) comprising dunite, orthopyroxene-bearing dunite, and harzburgite layered on a 10 mm to 400 mm scale, and the Layered Pyroxene-Dunite succession (LPD) consisting of thinly (<150 mm) layered orthopyroxenite, olivine orthopyroxenite, and dunite. Both units are partially serpentinised. Chromite is a ubiquitous accessory phase (1-5%) in the LDH, occurring as disseminated grains and locally in discontinuous laminations up to ca. 1-2 mm thick and 1-2 m long. The LPD has less chromite (1-2%) which is more common in the dunite layers. PGE-rich chromite nodules have been identified in the LDH of the Serpentine Ridge area (Brown 1986). The western 100-150 m of the LDH in the Harman River area consists of interlayered dunite and pyroxene-bearing dunite, and the eastern part layered harzburgite with minor thin dunite layers (Brown 1986). According to Brown (1986) serpentinite shears or faults separate the LDH and LPD everywhere and the original relationship of the two successions is unclear. The exposed WRUC is dominated by the LDH sequence. Two small, infaulted blocks of LPD have been mapped by Brown (1986) in the Websterite Hill area and the southern part of the complex comprises LPD. Work by Venture also suggests slivers of a third unit, the Layered Pyroxenite-Peridotite and associated Gabbro (LPG) succession recognised by Brown (1986) elsewhere in western Tasmania, may also be present on the eastern edge of the WRUC at Limestone Creek and Little Wilson River. The LPG as defined by Brown (1986) comprises disrupted blocks of layered orthopyroxenite in peridotite intruded by massive two-pyroxene gabbro.

Brown (1986) proposed intrusion of ultramafic bodies into the opening Dundas Trough during the Early Cambrian followed by tectonic re-emplacement prior to the Devonian. The presence of serpentinite pebbles and abundant detrital chromite within Huskisson Group sedimentary rocks at Merton Hill (Adamus observations) and Red Lead Conglomerate of the correlative Dundas Group in the Mt Razorback area (Brown 1986) suggests exposure and partial erosion of the ultramafic complexes prior to the Middle Cambrian.

Quaternary fluvioglacial sediments and Quaternary-Recent alluvial gravels cover minor parts of the WRUC. Osmiridium, gold, and chromite are locally concentrated in the Quaternary-Recent alluvial gravels. Patches of laterite and saprolite are locally present over the WRUC

representing a mixture of in situ relicts of a more extensive Tertiary lateritic blanket and Quaternary-Recent colluvial-alluvial deposits. Goethitic soils are widespread over Serpentine Ridge and the Websterite Hill area.

Significant deformation is recognised in the Crimson Creek Formation with narrow zones of bedding-parallel isoclinal folding with an associated S0-parallel cleavage (S1), and a later generation of metre-scale gentle to open folds with north to north northeast striking axial planes and crenulation cleavage (S2).

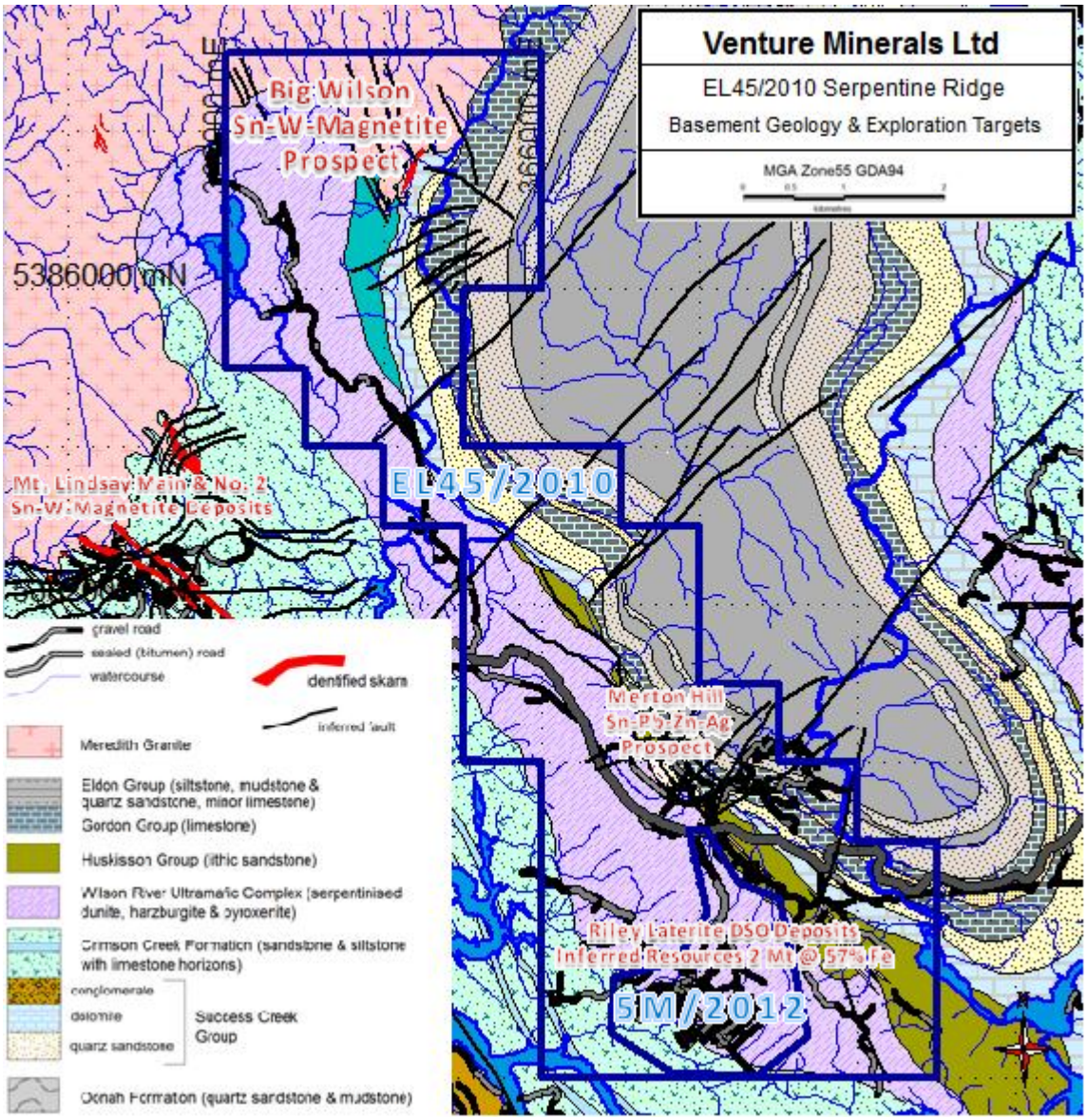

Figure 4.1: Project Geology and Exploration Prospects.

5 Exploration and Mining History

Osmiridium was first reported in Tasmania from the Wilson River valley in the 1876 by Surveyor-General Sprent, and the Riley, Trinder, Three Mile, Lippy Jane, Fowler, Sweeney, Osmiridium and Gold creeks were later extensively worked for detrital osmiridium. An exact osmiridium production figure for the Serpentine Ridge – Wilson River area is not available, but of the total 31,100 oz produced from Tasmania between 1910 and 1968 (first and last reported production) around half came from the Adamsfield area ca. 120 km to the southeast and much of the rest from the Heazlewood-Bald Hill area near Waratah approx. 30 km to the north. The detrital osmiridium typically occurs as flaky nuggets up to a few millimetres dimension, and petrographic work (Callina NL 1985-1990, Brown 1986) on material from the Riley Creek area also indicates occurrence as inclusions within chromite grains from the ultramafic basement. Numerous workers have identified small chromite lenses up to 20-30 mm thick and 1-2 m long within the ultramafics, and analyses of some primary chromitites indicate highly anomalous PGM levels (Brown 1986).

There was additionally minor alluvial tin and gold production from the Wilson and Huskisson valleys and during the 1970-1980s the area in the vicinity of the Meredith Granite was extensively explored for tin and tungsten mineralization. Tin-bearing alluvial gravels occur in many streams on the north eastern side of Serpentine Ridge, including Barnes, Sweeney and Tin creeks and Alfred River. Occurrences of primary tin mineralization were identified in the Harman River and Merton Hill areas, and Reid (1921) reported narrow dykes of tinstone-bearing quartz-feldspar porphyry cropping out in the vicinity of Tin Creek and Merton Hill.

Merton Hill was tested with 3 small adits by prospectors in the early 1900s. Exploration activities by Rension Ltd in the 1979-1983 period identified the presence of an irregular +100 ppm tin in soil anomaly centred around the three small adits at Merton Hill. Seven (7) diamond core holes were drilled by Renison and the best result obtained was c. 3 m of gossanous breccia assaying 0.19% Sn, 1.27% Pb, 3.68% Zn & 53g/t Ag from 52.9 m down hole in MH1 directly beneath the old workings. The identified mineralization was associated with veins and breccias within the Devonian Eldon Group (specifically, within the Crotty Quartzite and unnamed limestone member of the Amber Shale) associated with a northeast dipping fault zone adjacent to the contact with the Wilson River ultramafic body. MH2 appears to have intersected the same fault-hosted mineralisation but recoveries were very poor (<8%). Very thin veins with sphalerite, galena and silver and rarely cassiterite were encountered by most of the drill holes within the limestone and shale of the Crotty Quartzite. Narrow granitic dykes with disseminated pyrrhotite were encountered in some of the drill holes.

Mapping, geophysics and soil sampling by Renison in the early 1980s around the upper Harman and lower Little Wilson rivers in the early 1980s also identified Sn targets at Tadpole Hill within the Meredith Granite, and around the confluence of the Wilson and Little Wilson rivers within the granite and adjacent Gordon Limestone. Renison planned several drill holes to test the Wilson River target but terminated the project when the tin price collapsed in the mid-1980s.

The source of the alluvial gold was not thoroughly investigated and while most is probably reworked from glacial gravels, work by Callina NL in the 1980s suggested there could also be an ultramafic source. Significant gold mineralization has not been reported from any of the identified tin prospects within EL45/2010, although it was not commonly assayed. Adit samples and some of the Renison drill core from the Merton Hill tin prospect was subsequently re-assayed for gold (Black Horse Mining, 1986-1987 and Cyprus Gold Australia Corp, 1987-1989) with a best result of 2 m at 0.165 ppm Au obtained in a magnetite skarn.

Lateritic nickel and cobalt mineralization was identified in the southern Serpentine Ridge area by Aberfoyle in the late 1960s by a program that included hand auger drilling and man-portable coring (5 core holes) to a maximum depth of 30 ft. Grades of up to ca. 2% Ni and 1.5% Co were obtained from thin (<1-5 m) patches of laterite and in the underlying saprolitic serpentinite assays of >0.5% Ni were commonly obtained. There was no systematic investigation for Ni-sulphide mineralization beyond the Serpentine Ridge area (Camp 30 area of Aberfoyle). Variably serpentinised dunite from the Wilson River ultramafic complex typically assay c. 0.2-0.4% Ni although Brown (1986) could not detect nickel in the silicate phases. The nickel sulphide healzewoodite and Ni-Fe alloy awaruite were identified by Renison in serpentinite drill core from Merton Hill, and awaruite in serpentinised dunite samples from the Riley Creek area by Callina.

Callina NL (1985-1990) defined a detrital chromite resource in the Riley Creek area which was also the focus of the historic osmiridium workings. While the chromite is premium quality (>60% Cr_2O_3) the Callina resource was small (approx 1.7 Mt at 1.9% chromite) and at the time not considered economic. The associated detrital PGM (Os and Ir, lesser Pt) and gold content were not assigned any economic value by Callina.

Adamus Resources Ltd explored the area for nickel sulphides in the mid-2000s, conducting rock chip, stream sediment and soil sampling. Relict nickel-rich lateritic soils made it very difficult to interpret the results and clear primary nickel targets could not be delineated. The soil sampling does indicate some geochemical anomalism (mainly As and Cu) in the lower Harmen River area which could be associated with tin-tungsten metasomatism.

6 2015-2016 Anniversary Year Exploration Activities

This report includes the results of the BSc. Honours thesis investigation into the Big Wilson Prospect by Travis Holmes at the University of Tasmania. A combination of field observations and laboratory analyses of drill core and rock samples was used to investigate and document the geology and alteration paragenesis of the prospect, and was developed as a collaborative research project between Venture Minerals and the author, Travis Holmes, based at the University of Tasmania. A pdf of the thesis is attached to this report as Appendix 1.

The thesis aimed to map and model the spatial and temporal evolution of the Big Wilson Sn-W skarn focusing on the geometry, timing and controls on the high-grade cassiterite stage of

mineralisation. Understanding the mineralogical and geochemical zonation and the structural and lithological controls at Big Wilson is highly relevant to the exploration for extensions of the known mineralization and exploration for other skarn and greisen systems along the margin of the Meredith Granite. The specific project objectives were:

(1) To develop a mineralogical paragenesis of the skarn and ganite alteration-mineralisation system at Big Wilson
(2) To investigate the geometry of mineralised stages with a main focus on the high grade cassiterite veining in the granite
(3) To determine if the mineral chemistry of tourmaline associated with mineralised and barren veins can be a useful vector to high-grade mineralisation.
(4) To resolve the timing of tin mineralisation relative to the magmatic age of the Meredith Granite by directly dating the cassiterite.

6.1 Local Geology of the Big Wilson Prospect

The Big Wilson prospect is a Sn-W skarn hosted by Gordon Group limestones adjacent to the Meredith Granite (Figs. 6.1and 6.2). The north-northeast trending skarn was identified through soil geochemical surveys and geological, and drill tested by 13 DDC holes for 3572 m by Venture Minerals in the 2012-2013 period. The Big Wilson skarn strikes north-northeast approximately parallel to bedding in the limestone. A small gossanous subcrop occurs at the north end of the skarn, the remainder being covered with soil and/or alluvial gravels. The skarn is at least 800 m long and up to 50 m wide, with most of the high grade Sn mineralisation occurring in the northern part. The southern part of the skarn is not currently well known (no significant exposure and limited drilling) and is dominated by calcsilicate minerals and an increasing thickness of ultramafic rocks between the Gordon limestone and Meredith Granite.

6.1.1 Field mapping methods

The Big Wilson Prospect site was mapped during two field expeditions. The site was accessed via the walking track. All supplies were carried in and out on foot. The primary aim of the field mapping was to investigate the geometry of the quartz-tourmaline veins in the Meredith Granite to determine if the orientation and distribution of the high grade veins followed a regional pattern. Numerous granitic dykes were encountered and recorded. Time was also spent searching for evidence of topographically and stratigraphically inferred faults.

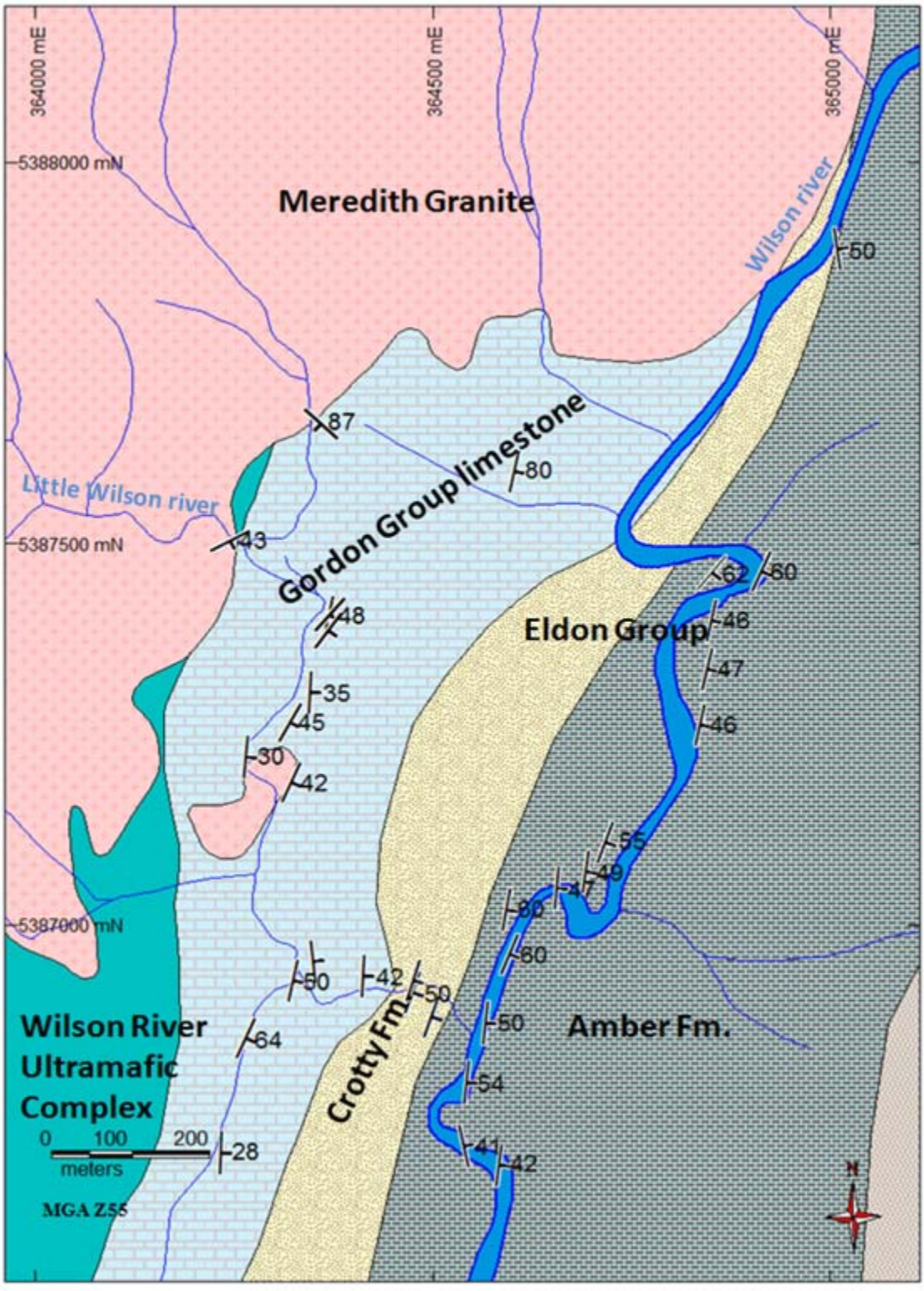

Figure 6.1 Basement geology of Big Wilson prospect area

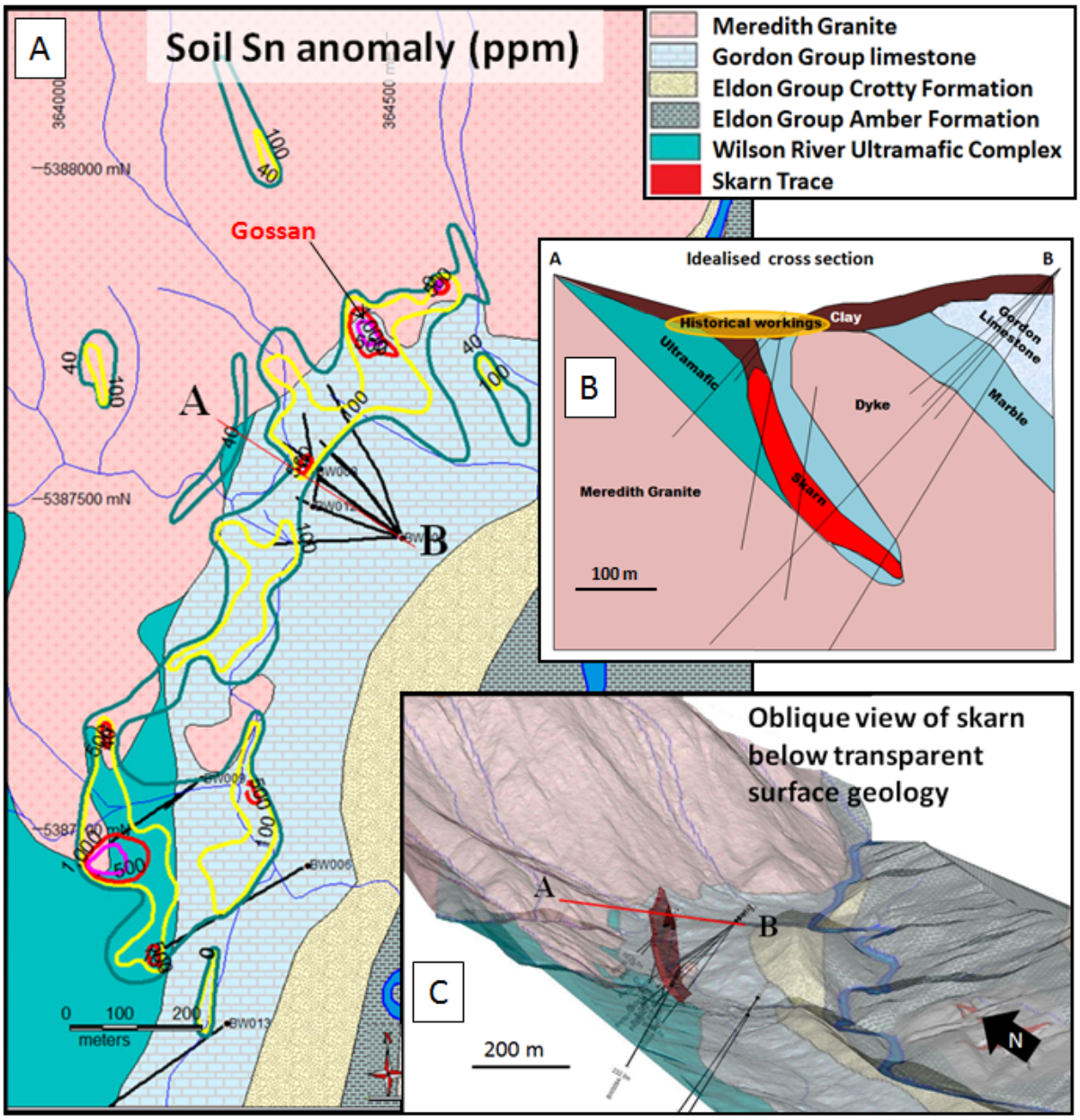

Figure 6.2 A) Soil Sn anomaly (ppm) B) Vertical cross section through the skarn C) Oblique 3-D view of the Big Wilson Skarn. Surface geology has been draped onto a LIDAR DEM and made 50% transparent so the skarn (outlined in red) is visible beneath the surface. The skarn most likely continues further south than shown.

Figure 6.3 The problem of lack of fresh outcrop in the temperate rainforest is illustrated by moss covering this potential rock exposure.

All locations were recorded using a Garmin 620x hand- held GPS and all structural measurements were made using a standard Sunto geological compass. A total of 35 rock chip samples of approximately 200 – 300g each were collected using a geological hammer or sledge hammer and chisel, and these were labeled and stored in geological sample bags. A list of samples, descriptions (Appendix 2), photographs (Appendix 8) and assay results (Appendix 3) are included the Appendices to this report.

Due to rainforest vegetation fresh outcrops of *in-situ* bedrock was best accessed in creek or river beds where periodic flooding has kept the exposures clean (Figs. 6.3 and 6.4). Sample dilution was a minor issue during sampling of many of the quartz-tourmaline veins. Hammering often produced chips, flakes and powder (Fig. 6.4) where the wall rock could not be separated from the target vein material. In cases where the vein could be separated it was difficult to separate all the wall rock without losing significant portions of the target vein minerals. Therefore all the samples sent for whole rock geochemistry contain some amount of wall rock dilution.

Figure 6.4 Collecting thin quartz-tourmaline veins on granite. Some samples come out intact and others are collected as powder.

Two-dimensional surface spatial modelling was undertaken using MapInfo software and used to create surface maps of the project area. Three-dimensional subsurface modelling was performed with Micromine software and used for the creation of vertical cross sections.

6.1.2 Stratigraphy

Tertiary alluvial deposits and swamps cover much of the valley floor in the vicinity of the Big Wilson prospect. The Meredith Granite and the quartzite units of the Eldon Group are highly resistant rocks that form major topographical features while the Gordon Limestone is recessive and underlies much of the Tertiary sedimentary deposits. The Wilson and Little Wilson Rivers tend to follow the strike of the Gordon Group.

Quaternary formations are localised to swamp, marsh and alluvial deposits confined to valley floors and the occasional patch of fluvioglacial conglomerates, gravel and sand.

6.1.2.1 Meredith Granite

The Meredith Granite is considered to be the source of the enriched hydrothermal fluids that created the mineralisation. In the prospect area the unaltered granite (Fig.6.5) tends to be equigranular with white to cream and occasionally pink feldspar crystals up to 15mm, quartz and biotite. A series of medium-grained granite dykes are observed in the bedrock of the Little Wilson River which contain an identical composition to the surrounding granite but a noticeably finer grain size (Table 6.1). The dominant quartz-tourmaline veining found in the granite is discussed in section 6.2.3.

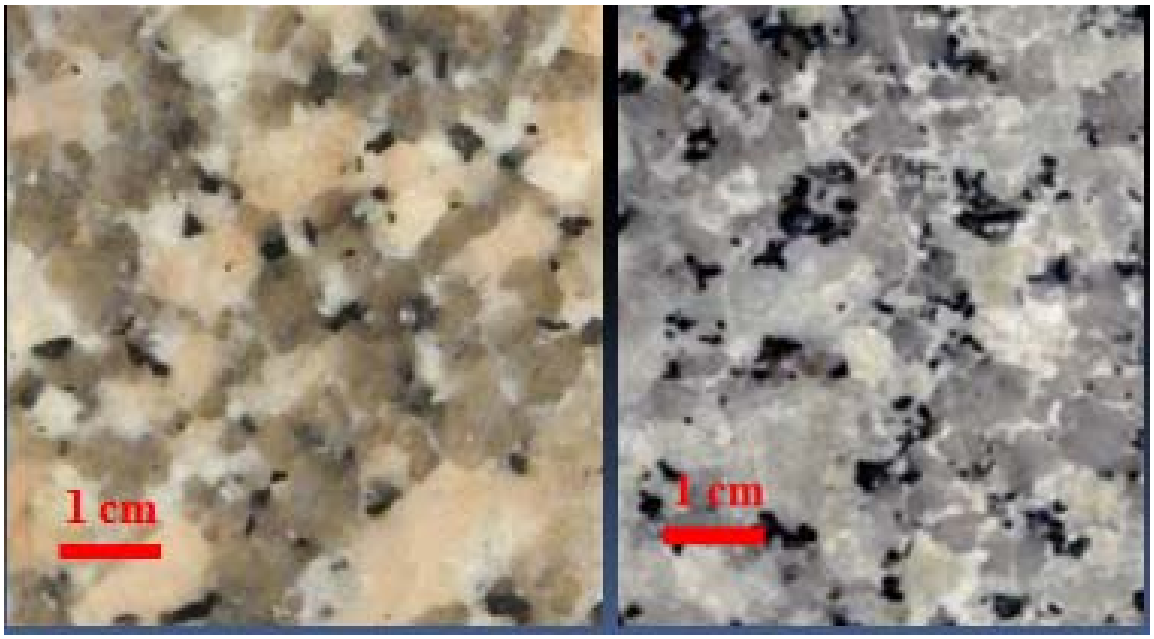

Figure 6.5 Various colours of the Meredith Granite observed at Big Wilson

Table 6.1 Dykes observed in the Meredith Granite

Site ID	E MGA55	N MGA55	Width m	Dip	Facing	Comments
THBW007	364246	5387484	2-3 2-3 2-3 2-3 2-3	70 70 70 62 75	235 050 110 233 118	Medium-grained igneous banding within a coarse-grained granite
THBW008	364224	5387530	2-5 2-5 4-5	62 50 84	252 255 030	Medium-grained igneous dykes in 10mm equigranular granite
THBW009	364175	5387500	2-3 2-3	47 24	208 038	2-3m fine-grained dykes with 10-20cm dyke swarms
THBW019b	364598	5387985	0.3	30	040	Manganese rich medium-grained igneous dyke. Only dyke found off the little Wilson River
THBW024	364053	5387560	5-8m	?	?	Unable to access – observed at a distance

6.1.2.2 Gordon Group Limestone

The Ordovician Gordon Group limestone is the host for the mineralised skarn system. In the vicinity of the Little Wilson River there is a well-bedded fossiliferous limestone unit up to 200m thick dipping steeply to the southeast. The limestone unit is mostly massive with occasional thinly bedded mudstone layers.

Most of the Gordon Group limestone has been recrystallised to a grey marble (Fig. 6.6) in the vicinity of the granite intrusion. The Gordon Group rocks are recessive and mostly under cover but a few outcrops can be found in creek beds where steep SE dipping bedding can be measured. Brown (1986) reports a 600m conformable succession of “grey pug” in the vicinity of the Little Wilson River that conformably connects the Gordon Group limestone with the Crotty Formation of the Eldon Group.

Figure 6.6 Drill core from the Gordon Limestone

6.1.2.3 Ultramafics

The Neoproterozoic-Cambrian Wilson River Ultramafics (Fig. 6.7) are a dark green pyroxene-rich medium to very fine-grained gabbro with plagioclase and clinopyroxene being the major constituents readily identifiable by eye. The exposed sections of the WRUC are dominated by the Layered Dunite-Harzburgite sequence. In drill core white carbonate veins are common. The WRUC is considered the source for the alluvial osmiridium that was mined in the area in the early 1900s.

6.1.2.4 Eldon Group

The Silurian Crotty Formation (Fig. 6.8) is a white to cream fine-grained quartzite with thin to medium beds (5-50cm) dipping steeply to the southeast. Brown (1986) reported sighting truncated cross-bedding in the area but none were identified during the fieldwork component of this project. This unit does not contain mineralisation. Bedding orientation is roughly the same as for the Gordon Group limestone and represents the locally steeply SE dipping western limb of the Huskisson Syncline.

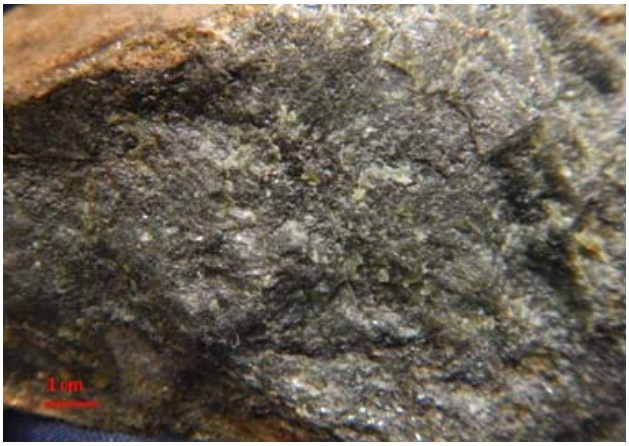

Figure 6.7 Pyroxenite from the Wilson River Ultramafic Complex

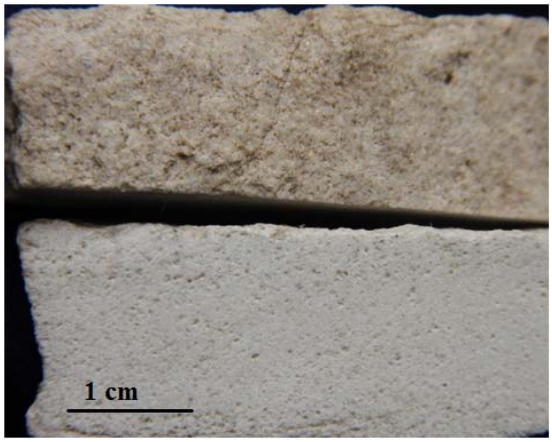

Figure 6.8 Quartzites of the Silurian Crotty Formation

6.1.3 Structure

Although the presence of faults in the Eldon Group that extend into the Gordon Limestone have been inferred through topographic interpretation no direct evidence of fault structures were found on the surface during local mapping. The medium grained granite dykes observed in a small stretch of the little Wilson River were not observed elsewhere in the prospect area. Although all contacts with the ultramafic units are assumed to be faulted, exposed contacts were difficult to find in the field and fault structures were not directly observed.

6.2 Alteration and mineralisation

This section describes the alteration and mineralisation assemblages observed in drill core and at surface around the Big Wilson prospect site. It includes a short summary of the different methods employed to document the observed alteration, followed by a description of the paragenesis and alteration mineral assemblages, and details of a proposed paragenesis model for the skarn and the granite alteration.

6.2.1 Analysis methods

6.2.1.1 Whole rock geochemistry

Seventeen rock chip samples were sent to ALS Chemex laboratories in South Australia for whole rock geochemical analysis. Major and minor elements including S, total Sn and W, from both drill hole and surface rock samples, were determined by X-Ray Fluorescence (XRF) spectroscopy (using ALS method XRF15b). Trace elements and acid-soluble Sn were measured by inductively coupled plasma atomic emission spectroscopy (ICP-AES) after dissolution using a four acid digestion method (ALS method ICP61). Soil samples from previous investigations by Venture Minerals were analysed for total Sn by a combination of ICP61 and MS62 and by XRF05. Technical details of the methods used by ALS Chemex are provided in Appendix 3, together with the full elemental results.

6.2.1.2 Short wave infrared (SWIR) spectroscopy

Short wave infrared (SWIR) data were collected from seven diamond drill holes, totalling 1,996 m of drill core and 332 rock chip samples. Data were obtained using an ASD TerraSpec instrument to measure the spectral reflectance at 1m intervals in drill core. TSG (The Spectral Geologist) software was used to process the SWIR data and to create scalars for specific spectral responses. In the context of this project, SWIR data were particularly useful for delimiting white mica alteration. Full results from the TerraSpec SWIR investigation are provided in Appendix 12.

6.2.1.3 CSIRO Hylogger™

Visible near infrared (VNIR), short-wave infrared (SWIR), and long-wave infrared (LWIR) spectral reflectance data was obtained at 8mm intervals from 513m of drill core, comprising subsets of five diamond drill holes (Table 6.2) using CSIRO's 3rd generation Hylogger™ instrument located at Mineral Resources Tasmania (MRT) core storage facility in Mornington, Tasmania. Core samples were shipped from Tullah to Mornington for spectral analysis and data processing at MRT. Visible near infared, SWIR and LWIR spectroscopy were used to identify alteration mineralogy based on the hyperspectral response of mineral groups. Hylogger data was processed using The Spectral Geologist (TSG) software with spectral libraries for minerals in both SWIR and LWIR. Core was prepared by the author and the Hylogger was operated by Mr. Peter Harding. Data processing and generation of spectral scalars was undertaken by Dr. David Green of Mineral Resources Tasmania. The raw data is publically available from Mineral Resources Tasmania and a full compilation of the spectral data scalars are provided in Appendix 11.

Table 6.2 Core intervals analysed by CSIRO Hylogger™

Hole	From (m)	To (m)	Metres of core
BW001	150	270	120
BW004	170	300	130
BW005	220	290	70
BW007	170	250	80
BW008	67	130	63
BW010	50	100	50

6.2.1.4 Scanning Electron Microscopy (SEM)

Petrographic analyses of polished thin sections and laser mounts were carried out using two different scanning electron microscopes (Hitachi SU-70 FE-SEM and FEI SEM) located at the Central Science Laboratory (CSL) at the University of Tasmania. Complete SEM results are provided in Appendix 5.

6.2.1.5 Optical microscopy and petrography

Twenty-five new polished thin sections and 17 1 inch round polishe mounts were prepared from representative samples of the skarn and granite alteration stages. Venture Minerals provided a further 40 thin sections to supplement this sample set. These samples were used to investigate the mineral assemblages and alteration associations to assist with the development of the paragenetic scheme, discussed in Section 4.3. Thin section logs and photographs are provided in Appendix 13.

6.2.1.6 Subsurface structural analysis

Subsurface structural measurements were made from selected intervals of diamond drill core were fully oriented oriented during drilling. Orientation of drill holes was made by lowering a red chinograph wax pencil mounted on the tip of a spear down the drill hole at irregular intervals determined by Venture Minerals to mark the downward facing segment of core before being drilled out. After drilling the core was reassembled by staff at the Venture Minerals core shed in Tullah and structural measurements were taken using a hand-held protractor and cylindrical sleeves to measure the alpha and beta angles of structural features. The true orientations of the structures were calculated on a spreadsheet using the geographic survey data from the drill hole. As a test of accuracy structural measurements made by Venture Minerals from hole BW003a were measured by the author to confirm consistency between measurements. The subsurface structural data is provided in Appendix 4.

6.2.1.7 Reviewing and sampling drill core

Sections of 13 diamond drill core holes were inspected and sampled for petrographic analysis and the original core logs were reviewed to assist with understanding the local geology and to establish logging accuracy. Petrographic samples were obtained from drill core using a diamond saw at the Venture Minerals core shed in Tullah. Logged mineral abundances were used in the creation of the spatial models.

6.2.1.8 Scanning Electron Microscopy (SEM)

Two different scanning electron microscopes (SEM) located at the central science laboratory at the University of Tasmania were used to aid in mineral identification and petrographical analysis. They were the FEI MLA650 environmental scanning electron microscope and the Hitachi SU-70 field emission scanning electron microscope. Full SEM results are provided in Appendix 5

6.2.1.9 Laser Raman

Laser Raman was used to identify the mineral vonsenite. A Renishaw inVia Raman microscope located at the central science laboratory at the University of Tasmania was used to analyse one polished thin section and two 1 inch polished round mounts containing vonsenite. Electron beam-based microscopes, such as the FESEM and EMPA are unable to positively identify light elements such a boron so the laser Raman was used to positively identify this borate mineral because it works by interacting with molecular vibrations of the crystal structure to provide light reflection patterns by which a specific mineral can be identified, rather than interacting with individual atoms the way the electron beam instruments do. This means that vonsenite can be identified by its crystal structure rather than by the ratio of its elemental constituents. Full results of the laser RAMAN investigation are provided in Appendix 6.

6.2.2 Skarn paragenesis

The skarn paragenetic scheme has been prepared as part of this study in order to describe the sequence of alteration in the Gordon Limestone unit located to the east of the Meredith Granite (Fig 6.2). Using the above analytical techniques, the skarn alteation has been divided into four parageneic stages (Table 6.3). The first two stages represent prograde alteration of the limestone unit. The third-stage is a series of retrograde skarn assemblages. The final stage consists of cross cutting late stage veins. The paragenetic model for the development of skarn alteration in the limestone is described separately from the alteration observed in the granite due to the absence of difiniative cross-cutting relationships observed between alteration assemblages developed in these two units. Although it is highly likely that the genesis of alteration in the limestone and the granite are linked, direct evidence from cross cutting relationships between alteration in the granite and the skarn are inconclusive. Speculation on these relationships are therefore deferred to the discussion section of the chapter.

Table 6.3 Skarn paragenesis stages

Skarn Stage	Type	Mineral association
1	Limestone recrystallisation	Marble
2	Prograde calc-silicate	Pyroxene ±garnet ± vesuvianite
3	Retrograde	Amphibole ± magnetite ± vonsenite ± vesuvianite ± pyrrhotite ± pyrite ± chalcopyrite ± biotite ± siderite ± cassiterite ± scheelite ± chlorite ± tourmaline
4	Hydrothermal veining	Quartz ± calcite ± siderite ± cassiterite ± chlorite

6.2.2.1 Skarn stage 1:

Skarn stage 1 alteration has caused recrystallization of the original limestone to a massive calcite (Fig. 6.9). Colour changes from light to dark grey are most likely caused by silt layers and organic impurities in the limestone protolith. Abundant styolites appear to preserve the original bedding in the limestone protolith. The most common vein mineral assemblages are consistent with the Stage 2 alteration assemblages described in the next section.

Figure 6.9 Stage 1 marble A) slab from diamond drill core highlighting styolites and common colour variations in marble (BW007 200.0)B)Photomicrograph of a pilished thin section highlighting massive calcite observed in transmitted cross-polarised light (BW001 56.1)

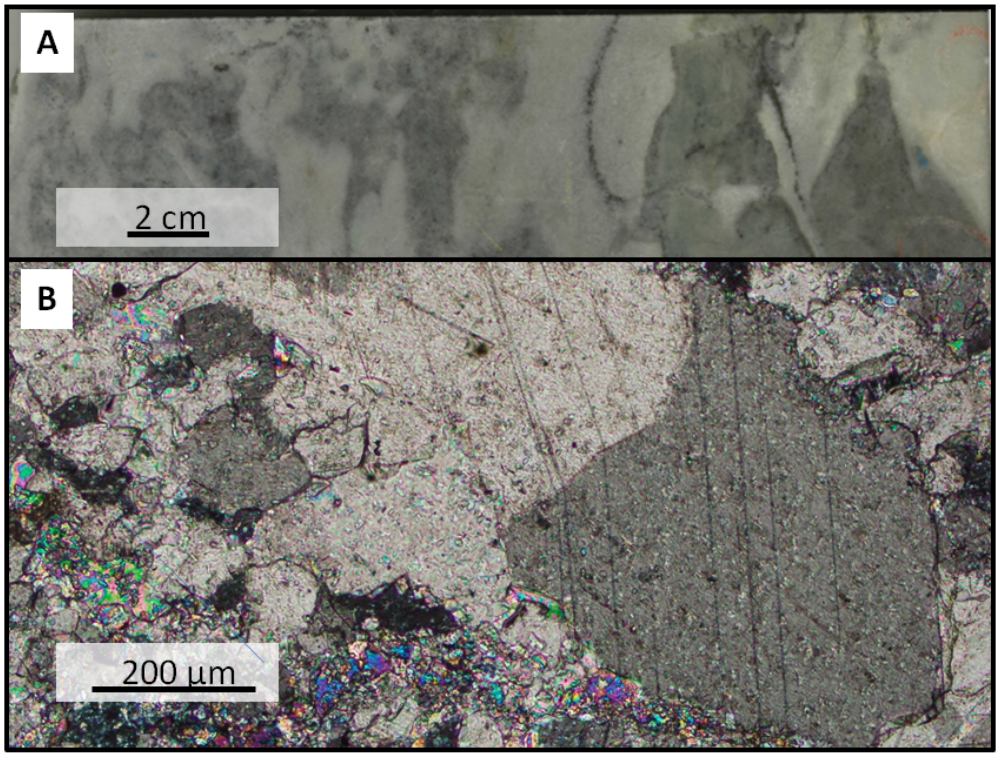

6.2.2.2 Skarn stage 2

Stage 2 skarn is dominated by calc-silicate minerals including garnet, vesuvianite and pyroxene (Fig. 6.10). Veins related to stage 2 are commonly comprised of calcite ± pyrite or pyroxene ± garnet ± vesuvianite with minor chlorite ± serpentinite. These calc-silicate minerals represent a high temperature prograde alteration of the limestone. The calc-silicate alteration is usually very fine-grained although garnet crystals may be up to 1mm in diameter locally. A significant characteristic of stage 2 is the lack of borates and oxide ore minerals.

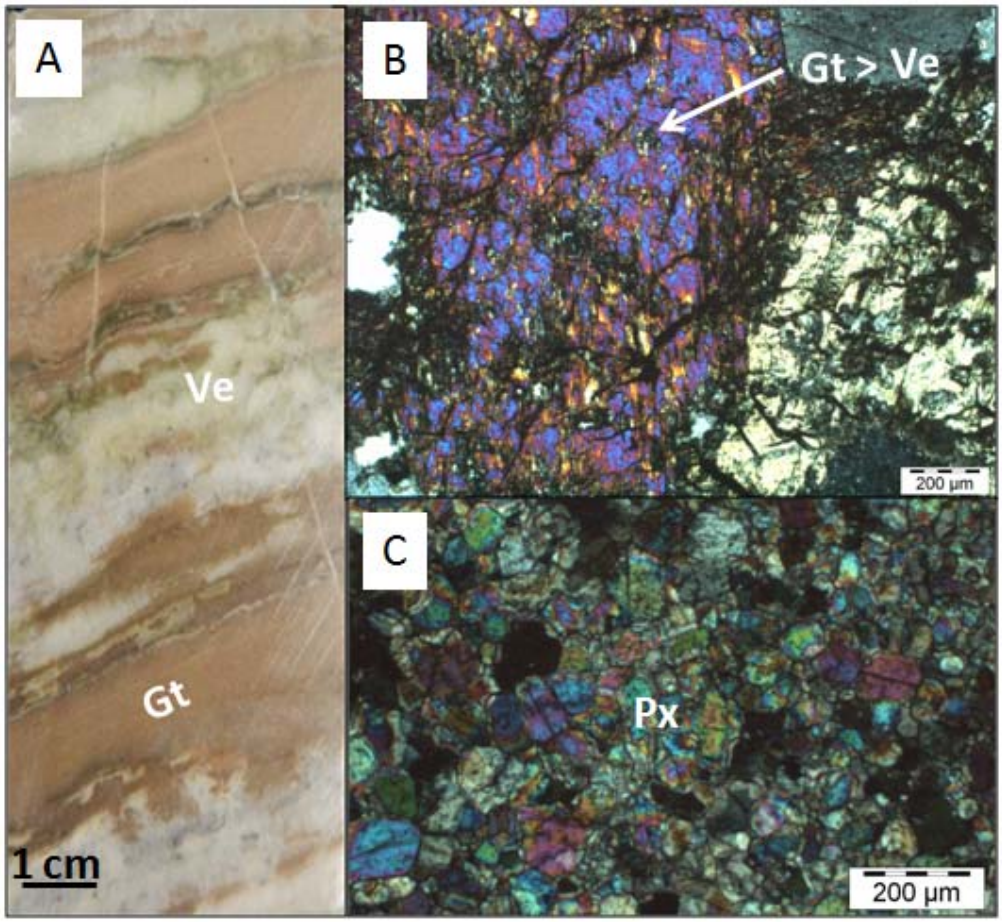

Figure 6.10 Prograde calc-silicate alteration. A) Slab sample of drill core dominated by stage 2 garnet with minor pyroxene and vesuvianite. (BW007 190.1) B) Vesuvianite replacing garnet under transmitted cross polarised light. Vesuvianite displays anomalous blue birefringence.(BW001 179.7) C) Pyroxene under transmitted cross polarised light.(BW001 120.9) Abbreviations: Gt = garnet, Ve= vesuvianite, Px = pyroxene

6.2.2.3 Skarn stage 3:

Stage 3 retrograde skarn alteration comprises a complex introgrowth of calc-silicate, borate, sulphide, carbonate, fluorite and chlorite-group minerals, together with hosting the three oxide ore minerals, cassiterite, scheelite and magnetite. Table 6.4 lists all of the major, minor and trace minerals identified in the Stage 3 assemblages through core logging, thin section microscopy, XRD, laser raman, Hylogger and SEM analysis.

Table 6.4 Alteration minerals identified in stage 3 retrograde skarn assemblages

Major rock forming minerals (>10%)	***Minor minerals (1-10%)***	***Trace minerals (<1%)***
Quartz	*Axinite*	*Sphene*
Vonsenite	*Dolomite*	*Hulsite*
Pyroxene – garnet – vesuvianite	*Scheelite*	*Serpentine*
Amphibole	*Hematite*	*Sphalerite*
Pyrrhotite - pyrite		*Arsenopyrite*
Biotite – phlogopite		*Chalcopyrite*
Chlorite – fluorite		*Muscovite - illite*
Calcite – siderite		*Xenotime*
Cassiterite		*Monazite*

The transition between the Stage 2 and 3 mineral assemblages typically occurs at an abrupt alteration front which cross cuts the styolites. Stage 3 alteration contains potentially economic deposits of cassiterite, scheelite and magnetite, however, Sn, W and Fe mineralisation is not distributed evenly throughout the skarn. Figure 6.11 illustrates a transition between Stage 2 and Stage 3 skarn alteration.

Stage 3 skarn mineralogy is highly variable in composition with apparently multiple complex mineral overprints and recrystallisation textures. The presence of acicular vonsenite, bladed actinolite (Fig. 6.11) and square prismatic quartz suggest open-space in fill by crystalising minerals. Table 6.5 summarises the overprinting relationships observed in Stage 3 retrograde skarn alteration.

Table 6.5 Mineral overprinting and recrystallisation textures observed in Stage 3 skarn alteration

Original mineral	**Replaced by:**
Garnet	Vesuvianite, amphibole, magnetite
Pyroxene	Garnet, vesuvianite, amphibole
Vonsenite	Magnetite, amphibole, siderite
Vesuvianite	Amphibole
Amphibole	Magnetite, serpentine
Calcite	Vonsenite

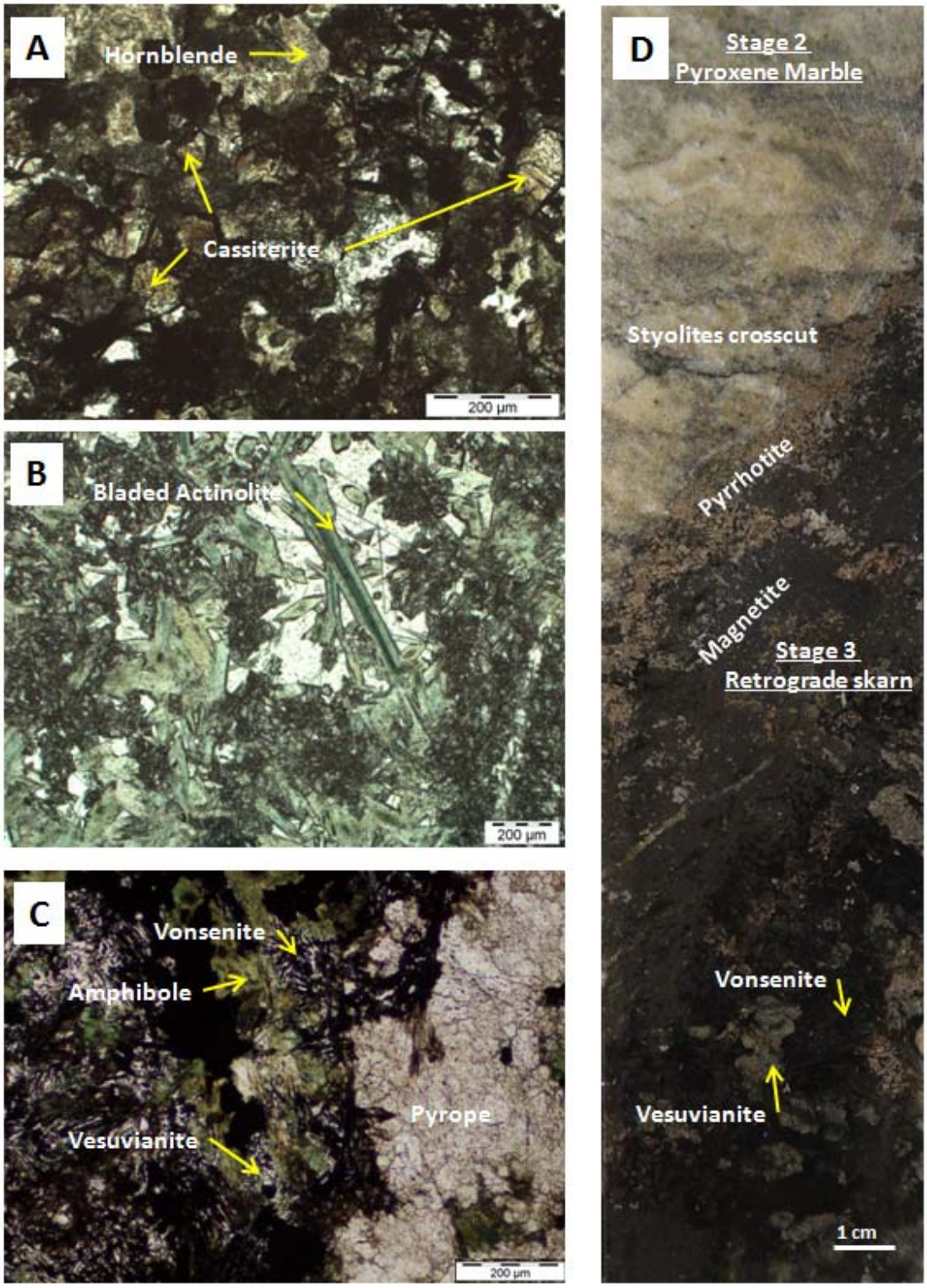

Figure 6.11 A selection of photomicrographs illustrating the complexity of mineral assemblages in stage 3 alteration A) High grade cassiterite zone in a hornblende rich skarn assemblage (BW001 215.7) B) Bladed and zoned actinolite suggesting crystals were infilling a void (BW001 204.5) C) Vonsenite amphibole(type undetermined) garnet(pyrope) skarn with minor vesuvianite (BW001 205.8). D) Transition between stage 2 and stage 3 alteration. Styolites crosscut by phrrhotitie, magnetite Vonsenite alteration. Porphyroblastic vesuvianite has replaced earlier garnet.(BW003A 211.3)

6.2.2.4 Stage 4: Late stage veining

Distinct white to cream-coloured veins crosscut the Stage 3 skarn at an angle nearly subparallel to drill core orientation (Fig. 6.12). Stage 4 veins are dominated by quartz ± calcite ± siderite ± fluorite but also contains zones enriched in cassiterite and scheelite. Zones of hydrothermal brecciation comprising siderite-amphibole altered clasts and fractured magnetite set in a siderite-quartz matrix also occur. Alteration is restricted to a small halo around the vein system and the vein system itself is restricted to a small band within the Stage 3 skarn. Concentrated cassiterite and scheelite mineralisation occur within these vein systems.

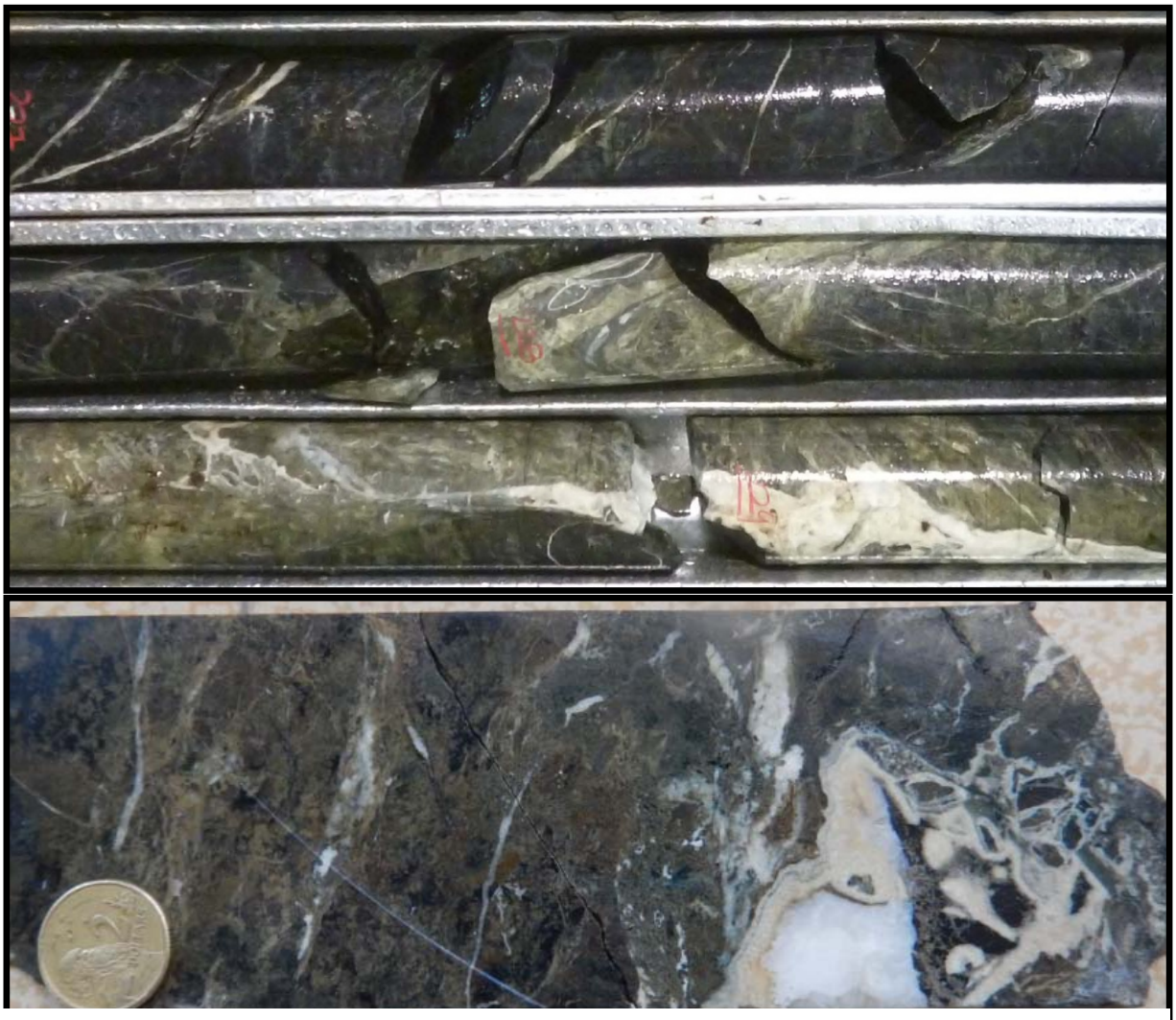

Figure 6.12 Stage 4 veining and hydrothermal breccia in drill core with veining orientation subparallel to the core axis (BW003A 226.0m)

6.2.3 Granite alteration and veining

The Meredith Granite in the vicinity of the Big Wilson prospect has been observed to host two distinct mineral alteration assemblages and two types of vein mineral assemblages (Table 6.6) that are distinct from alteration and vein mineral assemblages hosted in the limestone protolith.

The most common type of veins observed are black quartz tourmaline veins. These veins are often barren or contain only low grade Sn. They are often associated with a distal white mica alteration envelope.
The second type of vein is the quartz-carbonate-cassiterite vein which is associated with high grade cassiterite mineralisation and extensive siderite, fluorite, chlorite and tourmaline alteration in the granite. The following sections describe the vein and alteration mineral assemblages observed in the Meredith Granite

Table 6.6 Alteration mineral assemblages and vein mineral assemblages commonly found in the Meredith Granite

Mineral assemblage	**Alteration mineral association**
Barren veins	Quartz – tourmaline (black)
Mineralised veins	Quartz ± tourmaline (black and green) ± siderite ± cassiterite ±calcite ± fluorite ± chlorite ± scheelite
Mineralised alteration envelope	Quartz – tourmaline (black and green) ± siderite ± cassiterite ±calcite ± fluorite ± chlorite ± scheelite
White mical alteration envelope	Muscovite ± illite

6.2.3.1 Quartz –black tourmaline veins

Barren quartz tourmaline veins are the most abundant vein type that occurs in the Meredith Granite. They usually range in width from several millimetres to several centimetres and can occur as parallel swarms of veins (Fig. 6.13). The veins mostly consist of black to occasionally dark brown very fine grained to centimetre scale tourmaline crystals intergrown with clear to creamy quartz that ranges in size from very fine grained to several millimetres in diameter. These veins are typically surrounded by the muscovite - illite alteration halo described in section 6.2.4.

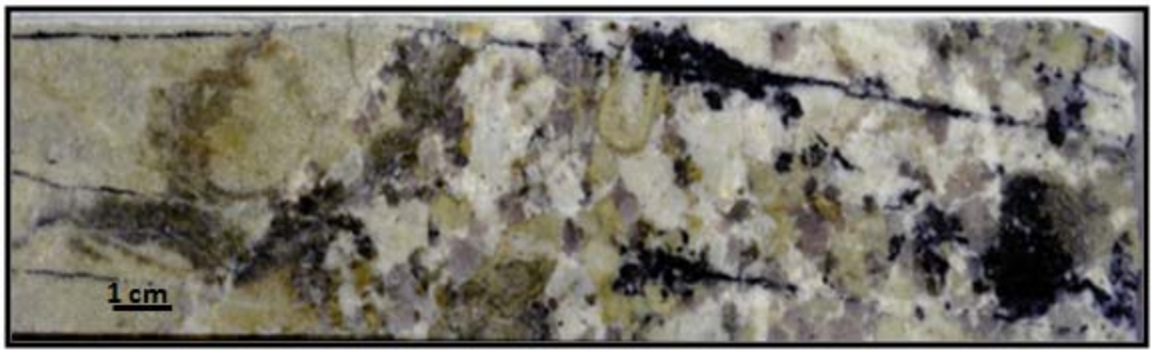

Fig. 6.13 Example of quartz – tourmaline veining in the Meredith Granite with white mica alteration of feldspar in the surrounding granite. Note veining is subparallel to drill core orientation

6.2.3.2 Quartz –green tourmaline - siderite – cassiterite veins

Mineralised veins within the granite are typically comprised of quartz ± tourmaline ± siderite ± calcite ± fluorite ± chlorite ± cassiterite ± scheelite. Cassiterite occurs as either massive veins or disseminations within veins where it is intergrown with quartz-tourmaline-siderite ± chlorite ± fluorite. These veins are surrounded by an alteration envelope with the same mineral alteration assemblages (Fig 6.14). Tourmaline is often green to dark green in colour and commonly replaces feldspar.

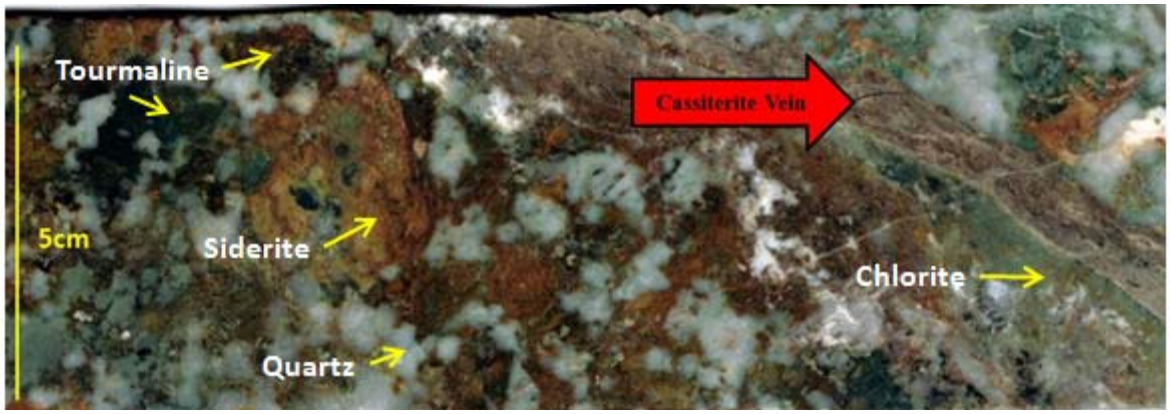

Figure 6.14 Cassiterite rich vein with quartz-siderite-chlorite-tourmaline alteration in the surrounding granite. Note the green tourmaline replacing feldspar and the sub-parallel vein orientation to core axis.

6.2.4 White mica alteration

A distinct halo of white mica alteration of feldspar is observed around most veins in the Meredith Granite (Fig. 6.13). This halo may be as small as a few millimetres around some of the barren veins or as large as tens of meters in the illite alteration zone that extends away from the contact between the granite and the mineralised skarn. Subtle white mica alteration is not always easy to detect by eye but shows up well in the short wave infrared spectrum. SWIR analysis, using both Terraspec and Hylogger instruments show a distinct white mica alteration halo extending from both sides of the granite contact with the mineralised skarn (Fig. 6.15D). Illite alteration occurs proximal to the skarn and muscovite occurs further away.

6.2.5 Surface distribution of granite alteration

Quartz-tourmaline veins that crop out at the surface of the Meredith Granite vary from a few millimetres to a few centimetres in width (Fig. 6.16). Most of the quartz-tourmaline veins sampled in the field returned geochemical assay values that were below the analytical detection limit for Sn (50ppm). Quartz-tourmaline veins which containined higher Sn assay grades occurred in four samples which were located in two surface locations separated by about 500m distance (Fig. 6.16). The highest whole rock Sn assay was 2340 ppm, however, this may be diluted by host granite material as it was not possible to completely separate the vein.

A distinct population of steeply dipping veins with a northwest strike was observed across the mapping area (Fig. 6.16A). Oriented drill core from BW003A was examined and the subsurface veining orientation displayed the same strike as the veining found on the surface, although with a slightly shallower dip angle (Fig. 6.16B).

Due to poor outcrop Sn grades found on the surface vary widely between sample locations over a scale of 10-20 m and soil Sn anomalies over the granite, which may be an indicator of potential high grade Sn zones near the surface, are separated by hundreds of meters in some places (Fig. 6.16C).

The high grade veins found in the drill core would not project to the surface at the same location as the high grade veins found on the surface. Veining measured in drill core projected to the surface should appear to the south of the Little Wilson River (Fig 6.1), however, this area was covered by dense vegetation and deep soils therefore it was not sampled. Likewise, the veins found and sampled at the surface would project too far north of the subsurface to intersect the area sampled by drill core.

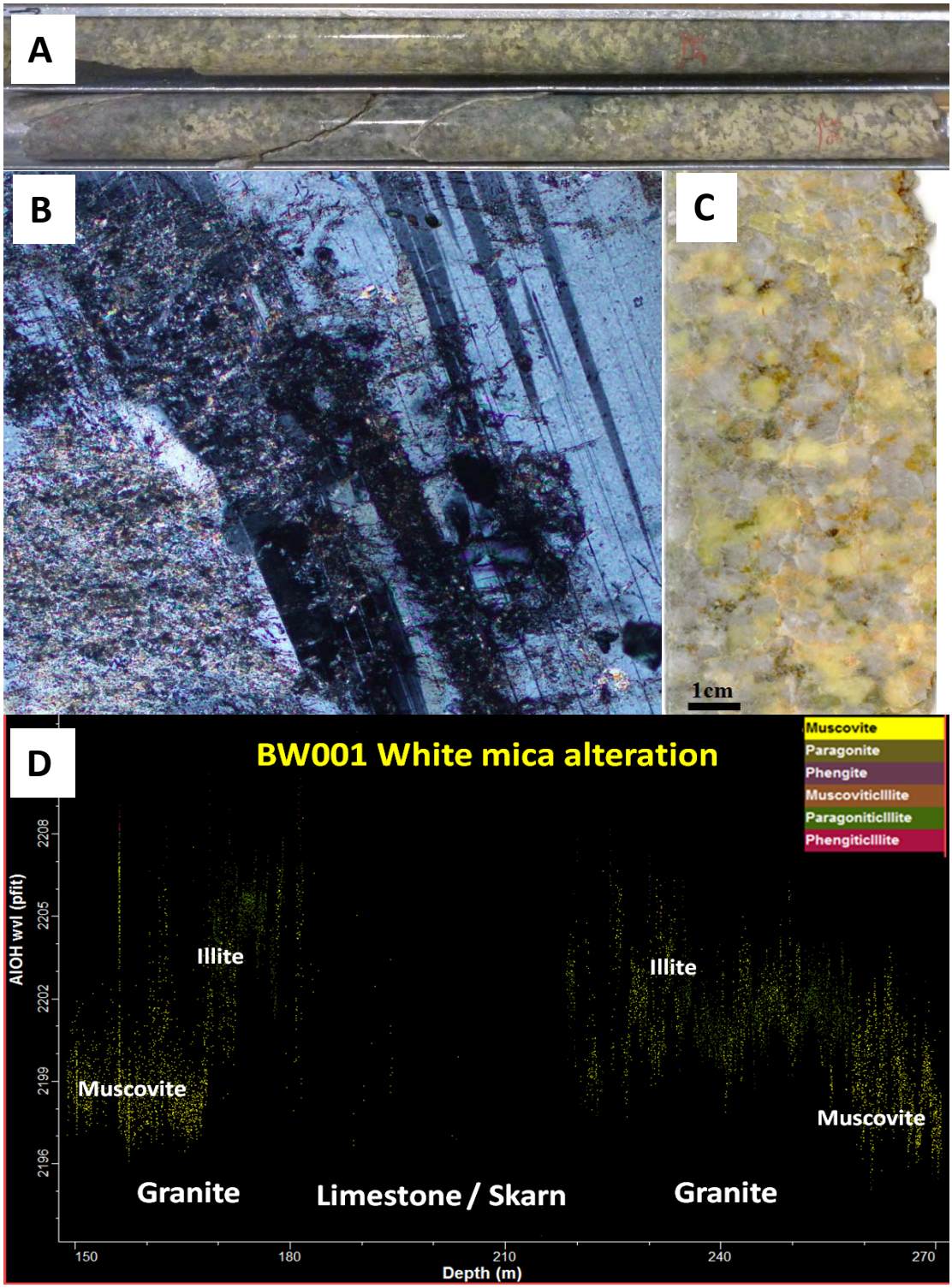

Figure 6.15 Muscovite-illite alteration in the Meredith Granite. A) Drillcore with alteration extending over several meters B) Thin section showing muscovite replacing feldspar in transmitted cross polarised light C) Rock slab showing extensive illite alteration of feldspar. D) Hylogger^{Tm} SWIR data highlighting variations in the 2200nm wavelength peak in hole BW001 showing downhole muscovite-illite alteration with elevated levels of illite on either side of the skarn and muscovite dominant further away from the skarn.

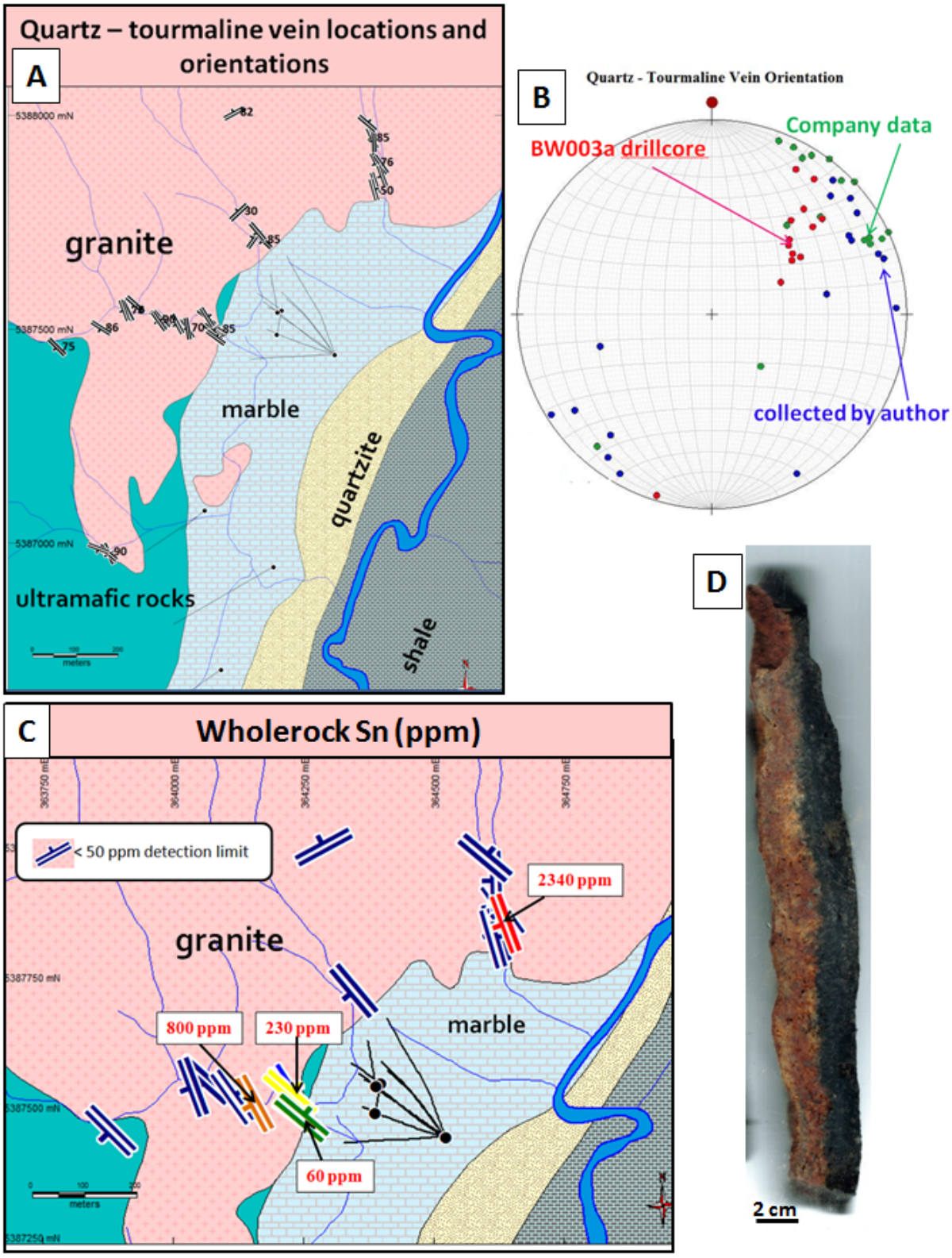

4.5 Ultramafic alteration

Figure 6.16 A) Orientation and location of quartz tourmaline veins B) Equal area lowe hemisphere stereographic projection showing Northwest strike of veins C) Wholerock Sn results for samples collected at surface D) Hand sample of a quartz-tourmaline vein (THBW024)

Alteration assemblages associated with hydrothermal interactions with the ultramafic rocks at Big Wilson currently have no defined economic mineralisation, and have therefore, not been investigated to the same extent as the limestone and granite-hosted alteration sequences.

Ultramafic rocks are commonly fractured and contain abundant carmbonate veins (Fig. 6.17). Dark green pyroxene and amphiboles minerals of the ultramafic host rock have been dominantly altered to serpentine with monor magnetite ± phyrrotite ± pyrite ± chlorite ± chromite ± spinel ± carbonates making up the minor phases. Veins are dominated by white to cream coloured carbonates intergrown with serpentine ± magnetite ± pyrite ± chlorite.

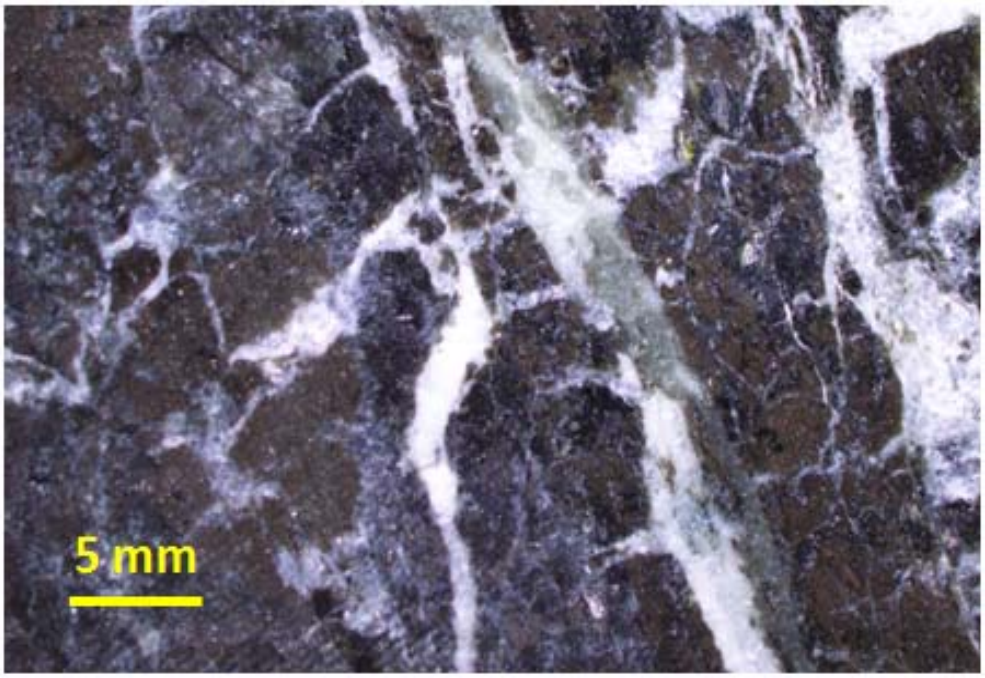

Figure 6.17 Intense carbonate veining in a dark green ultramafic sample

6.2.6 Weathering

At the extreme northern end of the skarn a small patch of gossanous subcrop was found (Fig. 6.2A) amongst some overturned tree root balls. It consisted of a variety of fist-sized samples containing tourmaline-rich granite and highly weathered and oxidised magnetite skarn (Fig. 6.18). It is possible this site was subject to historical mining activity.

Figure 6.18 Hand sample of weathered granite containing bladed tourmalinie in contact with weathered magnetite skarn.

6.2.7 Discussion

6.2.7.1 Skarn geometry

A representative cross-section of the skarn showing the spatial distribution of the alteration stages is shown in figure 6.19. Limestone within fifty to one hundred meters of the Meredith Granite is recrystallised to Stage 1 marble.

Stage 2 prograde calc-silicate alteration exists in a small zone around the edge of the Stage 3 retrograde alteration and in isolated spots near the contact with the granite where Stage 3 skarn is not present. Stage 2 calc-silicate alteration is rarely more than ten meters wide and can be patchy in places. The limited sulphides present in Stage 1 and 2 may have crystallised in the host limestone prior to the main hydrothermal stages

Stage 3 retrograde skarn is rich in borates and has more sulphides than Stage 2. Stage 3 also hosts the target economic minerals cassiterite, scheelite and magnetite. North of Big Wilson, where the majority of drilling has been performed, a Stage 3 skarn has been identified that is about fifty meters wide. In the south of Big Wilson the skarn appears more patchy and irregular and has probably been truncated by a fault which juxtaposed the ultramafic rocks (Figs. 6.1 and 6.2). The cross-section in Fig. 6.19 follows the trace of the discovery hole BW001 and shows the skarn nestled against a wedge of the ultramafic rock unit. However, if this cross-section were to be drawn further north, the skarn would be shown separated from the ultramafic rocks with marble found between these and the skarn. This truncation by the ultramafics in the south and separation from of the skarn and ultramafics in the north suggest that the skarn is following a fault. Potential structures bounding the skarn will be discussed in chapter 7.

There a few unusual aspects of the Stage 4 hydrothermal veins. One is that the veining seems to be confined to tight regions within the Stage 3 skarn. In Fig. 6.19 four drill holes constrain the position of this veining. Hydrothermal veining does not extend to the Stage 2 skarn and the carbonate veining in the ultramafics has a different character, different mineral associations and different vein orientations. Most of the sub-centimetre stage 4 veins are oriented at forty five degrees to the core. Although much of the core is not oriented it does suggest a veining angle parallel to the strike of the skarn. However, the larger veins which frequently contain zones of hydrothermal brecciation, are commonly subparallel to the drill core orientation (Fig. 6.12). This would suggest a veining orientation orthogonal to the skarn.

6.2.7.2 Borate mineralisation

Tourmaline is the main borate mineral found in the Meredith Granite at Big Wilson but rarely occurs outside the granite. A review of the drill core logs of 13 diamond drill holes found that tourmaline was observed and recorded in 121 drill core intervals with a granite protolith, and only five intervals where the protolith was other than granite. The five instances of tourmaline recorded in the core logs outside the granite occurred in five different drill holes and in various lithologies namely, marble, clay, skarn, fault breccia and ultramafic rocks (Table 6.7). Logged tourmaline abundances are estimated visually by Venture Minerals geologists and in each instance of tourmaline logged in an interval of core with a protolith other than granite

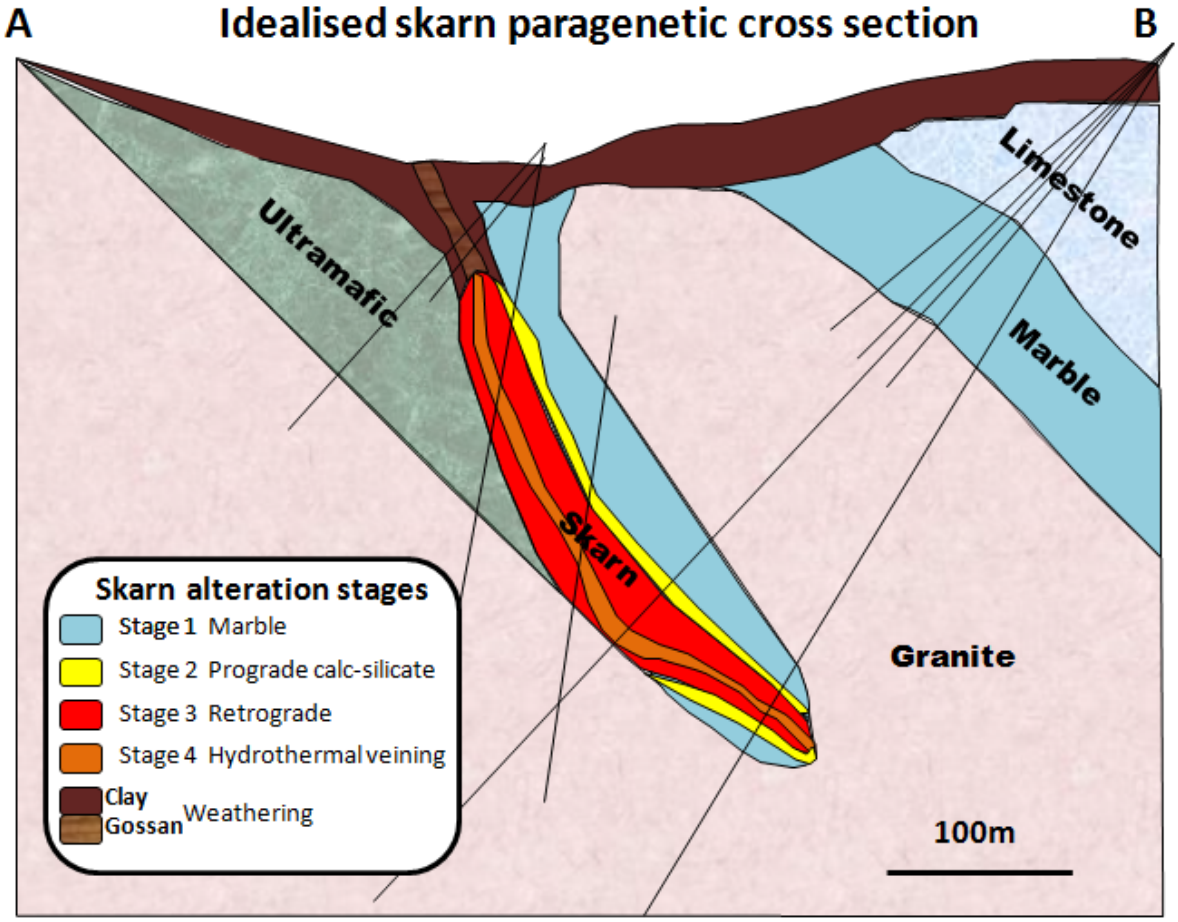

Figure 6.19 Cross section showing spatial distribution of skarn alteration stages

the abundance was estimated at 2.5% or less. Due to the fine-grained nature of tourmaline and the low logged abundances it is possible that some or all of these logged intervals of tourmaline outside the granite could be other dark fine-grained minerals misidentified as tourmaline. Tourmaline has a distinct spectral signature but was not identified by the Hylogger as occurring in the limestone or the skarn. Even if the logs are accurate and some trace amounts of tourmaline do exist outside the granite it shows that tourmaline outside the granite is very rare and does not follow a strong pattern or association with other protoliths or alteration minerals.

Vonsenite (Fe^{2+} Fe^{3+} BO5) occurs only in stage 3 skarn but can be a major rock forming mineral where it comprises over 40% by volume of the skarn. Much of the vonsenite in the skarn is likely original and not a replacement of specular hematite. Speculite has not been identified as a major rock forming mineral in the skarn and original vonsenite forms an acicular crystal habit (Swinnea and Steinfink, 1983) which is commonly observed (Fig. 6.20). Specular hematite has a bladed habit and if vonsenite were replacing earlier hematite then the crystals would have a much wider aspect ratio. Although it is possible there are isolated instances of vonsenite replacing early hematite it has never been definitively documented whereas the acicular crystal habit of original vonsenite is commonly observed throughout the skarn.

Vonsenite and hulsite $(Fe^{2+},Mg)_2(Fe^{3+},Sn)(BO_3)O_2$ has been identified by Venture Minerals using X-ray diffractometry. The presence of vonsenite was reconfirmed during this study using Laser Raman (Fig. 6.20C). energy dispersive techniques such as the SEM are not able to analyse elements with low atomic numbers and are prone to misidentify vonsenite as hematite. Like many other dark minerals it is very hard and does not give off a diagnostic electromagnetic signature easily detectable by SWIR and TIR detectors.
Techniques such as XRD and laser raman are sensitive to the crystallographic structure of the mineral rather than identifying elemental abundance. In hand sample vonsenite is recognisable by its jet black colour, acicular habit and black streak.
In many stage 3 skarn rocks in the Gordon Limestone at Big Wilson vonsenite is massive or a major component. The same style of vonsenite mineralisation is also observed at Mt. Lindsay in the skarn hosted by carbonate rich beds in the Crimson Creek Formation. The Stage 3 vonsenite rich skarn at Big Wilson must have experienced a massive flux of borate rich fluids from the Meredith Granite. The origin and relationship of these fluids to the rest of the system is discussed in chapter 7.

Table 6.7 Drill core intervals with logged tourmaline in 5 intervals outside the granite at Big Wilson. Tourmaline was recorded in 121 intervals inside the granite

Hole	Depth(m)	Lithology	Logged tourmaline abundance
BW002	16.2-19.5	Clay	0.1%
BW005	205.7-213.5	Marble	2.5%
BW007	201.5-204.3	Amphibole +/- vonsenite +/- garnet skarn	0.1%
BW009	74.3-85.0	Fault breccia	1.0%
BW010	66.2-70.4	Ultramafic	0.01%

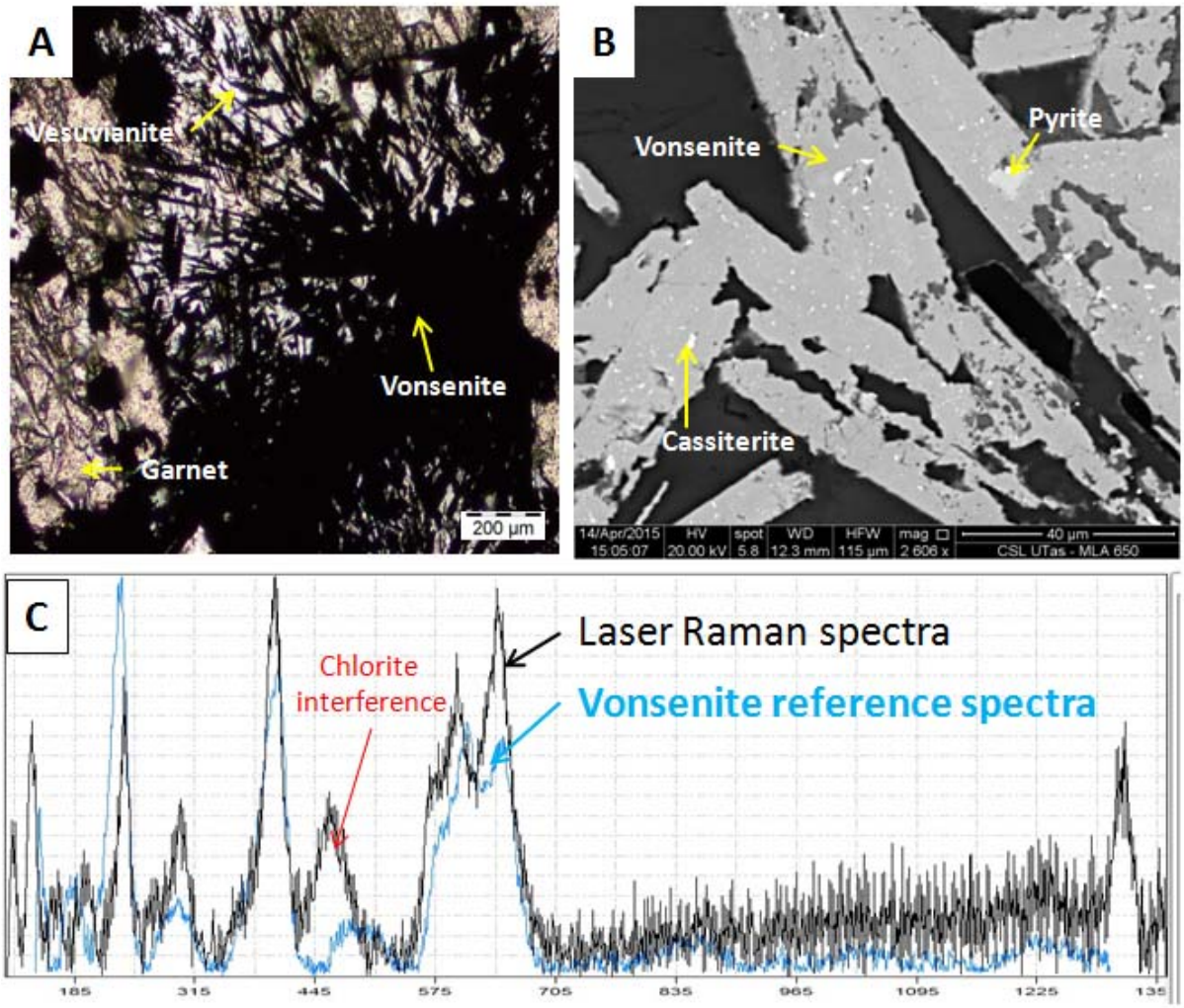

Figure 6.20 A) Thin section under plain polarised transmitted light showing opaque asicular vonsenite with garnet and vesuvianite B) SEM image of vonsenite containing disseminated cassiterite. C) Laser Raman spectrum of vonsenite sample from Big Wilson compared to a reference library spectrum.

6.3 Tourmaline mineral chemistry

Both black and green tourmaline has been observed at Big Wilson (Fig. 6.21). The green tourmaline usually occurs with, or very close to, zones of cassiterite. Field observations from other tin-bearing zones around the Meredith Granite by Venture Minerals geologists also note green tourmaline in close proximity to cassiterite. Although some black tourmaline has also been associated with tin mineralisation, around the Meredith Granite the vast majority of black tourmaline-bearing alteration is either barren or associated with low-grade Sn mineralisation. This chapter compares the physical and chemical characteristics of the black and green tourmaline at Big Wilson to determine whether tourmaline chemistry can be useful as an exploration tool for Sn mineralisation.

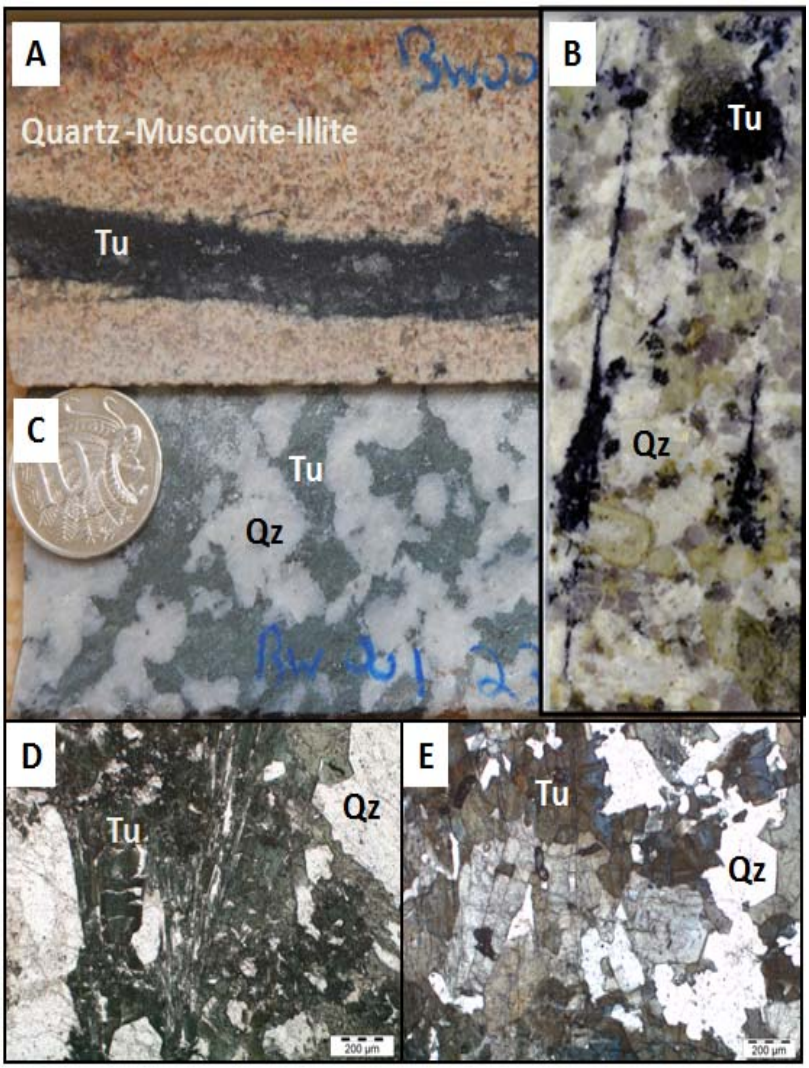

Figure 6.21 (A) Black tourmaline vein in muscovite-illite altered granite from BW001 286.3. (B) Black tourmaline clots and veins from altered granite BW007 211.3 (C) Core slab showing green tourmaline replacing feldsparBW001 231.0 (D) Thin section of green tourmaline in plain polarised light BW001 239.5 (E) Thin section of black tourmaline in plain polarised light BW001 257.9.

6.3.1 Methods

Twenty representative tourmaline-bearing samples containing green and black tourmalines were analysed for major and trace element chemistry. Subsurface tourmaline samples were collected from drill cores at the Venture Minerals core shed in Tullah and surface samples were collected during the field mapping for this project. Polished thin sections and polished 1-inch mounts were made at the University of Tasmania lapidary facility in Hobart.

Major element chemistry was obtained using a Cameca SX100 electron microprobe at the central science laboratory at the University of Tasmania. A 10µm diameter 15keV beam was used at a 40 degree takeoff angle and Schorl Harvard (E6) was used as a standard. Mineral abundances were normalised to 100% and boron weight percentages were calculated stochiometrically.

Trace element chemistry was determined using an Agilent 7900 quadrupole ICPMS with a 193nm Coherent Ar-F excimenr laser and the Resonetics S155 ablation cell at the University of Tasmania. Data was acquired using a 29µm laser spot size and NIST610, BCR-2, NIST612 and GSD-1g standards. A complete list of instrument conditions and settings is provided in Appendix 7.

6.3.2 General formula for tourmaline

Tourmaline is a complex borosilicate mineral which accommodates a wide variety of chemical substitutions. Variations in the major and trace element chemistry may be useful as a tool for exploration, based on their association with high-grade mineralisation. The general formula for tourmaline structure is $XY_3Z_6(T_6O_{18})(BO_3)_3V_3W$ where:

X site: usually occupied by Na but may include Ca, Mg or vacancy

Y site: tolerates extensive and diverse substitutions (Henry & Guidotti, 1985) and can accommodate monovalent, divalent, trivalent and quadrivalent cations (Frondel et al., 1966 in Henry and Guidotti, 1985). The most common elemental substitutions include Mg^{2+}, Fe^{2+}, Mn^{2+}, Al^{3+}, Cr^{3+}, V^{3+}, Fe^{3+} and Li^{+}. The two most common Sn cations (Sn^{2+} and Sn^{4+}) probably substitute at this site.

Z site: usually occupied by Al but may be replaced by Fe^{2+}, Fe^{3+}, Ti, Mg, Cr and V^{3+}

T site: usually dominated by Si^{4+} but may include substitutions of Al^{3+} and B^{3+}

B site: usually contains B^{3+} but may contain a vacancy

V site: usually contains OH- but may subsitiute for O^{2-}

W site: usually contains OH- but may substitute for F- or O^{2-}

Both the Y and Z are octahedral sites but the Y is slightly larger. Because of the large amount of substitution tourmaline is usually considered in terms of its common end-member components (Table 6.8).

6.3.3 Results

6.3.3.1 Tourmaline colour

Two distinct colours of tourmaline have been observed at the Big Wilson prospect (Fig. 6.21). Black is the most common colour and typically occurs in veins in the granite (Fig. 6.21A and 6.21B), although locally it can also be found disseminated in the granite, and regionally the Meredith Granite contains abundant tourmaline nodules (Kositcin and Everard, 2013). Some lower-grade tin mineralisation has been found associated with the black tourmaline veins at Big Wilson.

Table 6.8. Tourmaline end-members currently accepted by the International Mineralogical Association's (IMA) Commission on New Minerals, Nomenclature and Classification (from Fox, 2012)

	Structural site						
Species	**X**	**Y_3**	**Z_6**	**T_6O_{18}**	**B_3**	**V_3**	**W**
Alkali group							
Schorl	Na	Fe^{2+}_3	Al_6	Si_6O_{18}	$(BO_3)_3$	$(OH)_3$	(OH)
Oxy-schorl*	Na	Fe^{2+}_2Al	Al_6	Si_6O_{18}	$(BO_3)_3$	$(OH)_3$	(OH)
Fluor-schorl	Na	Fe^{2+}_3	Al_6	Si_6O_{18}	$(BO_3)_3$	$(OH)_3$	(F)
Dravite	Na	Mg_3	Al_6	Si_6O_{18}	$(BO_3)_3$	$(OH)_3$	(OH)
Oxy-dravite*	Na	Mg_2Al	Al_6	Si_6O_{18}	$(BO_3)_3$	$(OH)_3$	(OH)
Fluor-dravite	Na	Mg_3	Al_6	Si_6O_{18}	$(BO_3)_3$	$(OH)_3$	(F)
Chromium-dravite	Na	Mg_3	Cr_6	Si_6O_{18}	$(BO_3)_3$	$(OH)_3$	(OH)
Vanadium-dravite	Na	Mg_3	V_6	Si_6O_{18}	$(BO_3)_3$	$(OH)_3$	(OH)
Povondraite	Na	Fe^{3+}_3	$Fe^{3+}_4Mg_2$	Si_6O_{18}	$(BO_3)_3$	$(O)_3$	(OH)
Fluor-buergerite	Na	Fe^{3+}_3	Al_6	Si_6O_{18}	$(BO_3)_3$	$(O)_3$	(F)
Olenite	Na	Al_3	Al_6	Si_6O_{18}	$(BO_3)_3$	$(O)_3$	(OH)
Elbaite	Na	$Li_{1.5}Al_{1.5}$	Al_6	Si_6O_{18}	$(BO_3)_3$	$(OH)_3$	(OH)
Fluor-elbaite	Na	$Li_{1.5}Al_{1.5}$	Al_6	Si_6O_{18}	$(BO_3)_3$	$(OH)_3$	(OH)
Calcic group							
Uvite**	Ca	Mg_3	$MgAl_5$	Si_6O_{18}	$(BO_3)_3$	$(OH)_3$	(OH)
Fluor-uvite**	Ca	Mg_3	$MgAl_5$	Si_6O_{18}	$(BO_3)_3$	$(OH)_3$	(F)
Feruvite**	Ca	Fe^{2+}_3	$MgAl_5$	Si_6O_{18}	$(BO_3)_3$	$(OH)_3$	(OH)
Fluor-feruvite**	Ca	Fe^{2+}_3	$MgAl_5$	Si_6O_{18}	$(BO_3)_3$	$(OH)_3$	(F)
Liddicoatite**	Ca	Li_2Al	Al_6	Si_6O_{18}	$(BO_3)_3$	$(OH)_3$	(OH)
Fluor-liddicoatite**	Ca	Li_2Al	Al_6	Si_6O_{18}	$(BO_3)_3$	$(OH)_3$	(F)
Vacancy group							
Foitite	□	$Fe^{2+}_2(Al, Fe^{3+})$	Al_6	Si_6O_{18}	$(BO_3)_3$	$(OH)_3$	(OH)
Magnesio-foitite	□	Mg_2, Al	Al_6	Si_6O_{18}	$(BO_3)_3$	$(OH)_3$	(OH)

Species marked (*) are identified tourmaline compositions but are not currently accepted by the IMA. Species marked (**) represent end-member compositions modified from the initial tourmaline formula by Hawthorne and Henry (1999). Compositions and site occupancies are from Henry and Dutrow (1996), Novák et al. (2009) and Henry and Dutrow (2011). The structural sites V and W were previously referred to as the [O(3)]3 and O(1) sites respectively, by Henry and Dutrow (1996).

Green tourmaline is much less common but is usually observed in association with high grade tin mineralisation. Green tourmaline often replaces feldspar (Fig. 6.21C) in highly altered granites, and is associated with siderite, chlorite, fluorite and cassiterite (Fig. 6.13).

Black and green tourmaline can occur separately or together in the same sample. Black tourmaline has been observed growing on and layered with green tourmaline. The drill core samples used in this study appeared homogeneous but the samples obtained from the surface had a higher proportion of mixed colour tourmaline. For the purposes of this investigation if a sample contained both black and green tourmaline it was classified as being a green tourmaline. However, using this simple classification system for a mix of colour types means misclassification is a risk.

6.3.3.2 Tourmaline major element chemistry

The tourmaline crystals observed in this study were typically zoned with a large variation in major elements in individual crystals (Fig. 6.23). Electron microprobe analysis indicates that this variability is consistent for both black and green tourmaline, suggesting they have similar zonation although green tourmaline is generally more Fe-rich and has a wider range in Al concentration (Fig. 6.24). Fe-rich zones appear brighter in SEM images (Fig 6.22). EMPA data normalised on an atoms per formula unit basis shows that both black and green tourmaline samples are classified as schorl endmember compositions (Fig. 6.25).

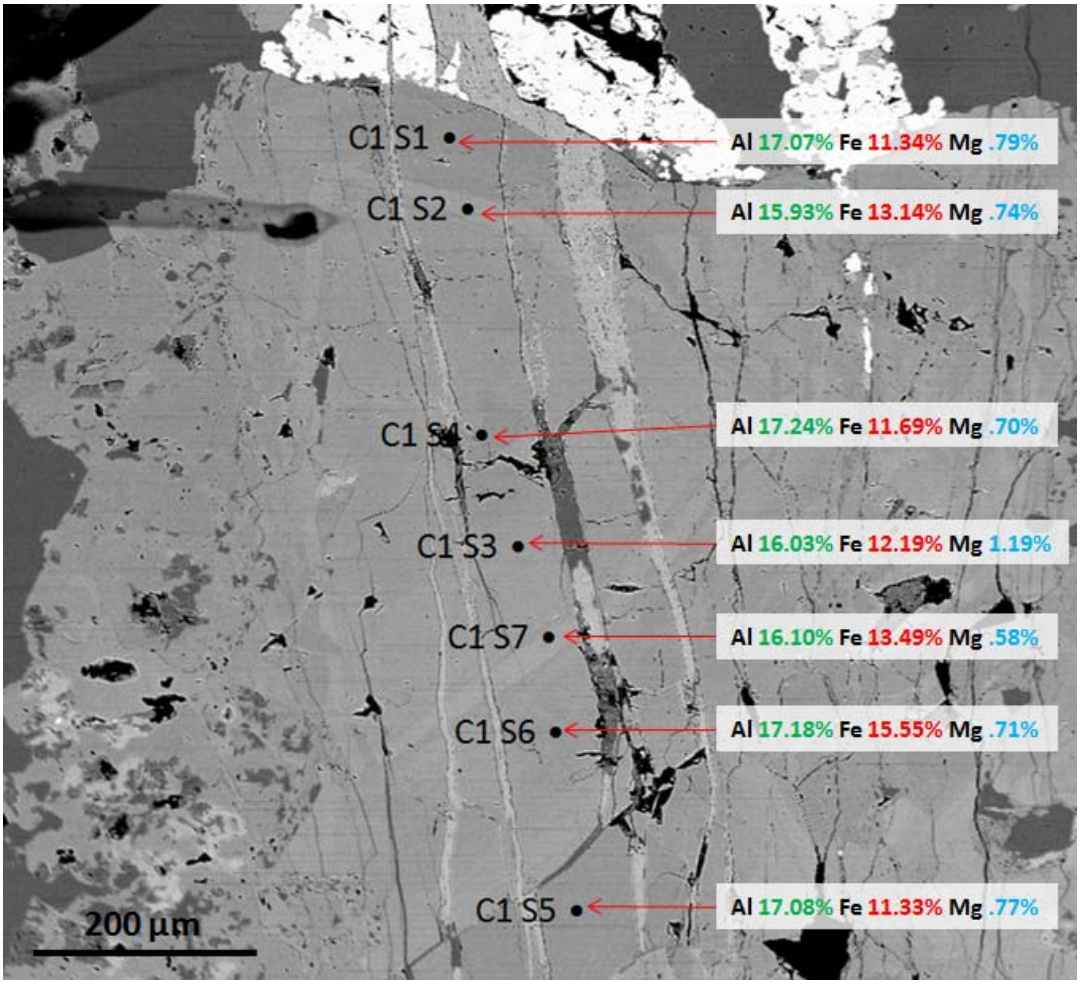

Figure 6.22 Microprobe image of a zoned black tourmaline (BW001 257.9) showing high degree of variation in major element chemistry between zones in a single crystal. Green tourmalines show similar variability.

All the black

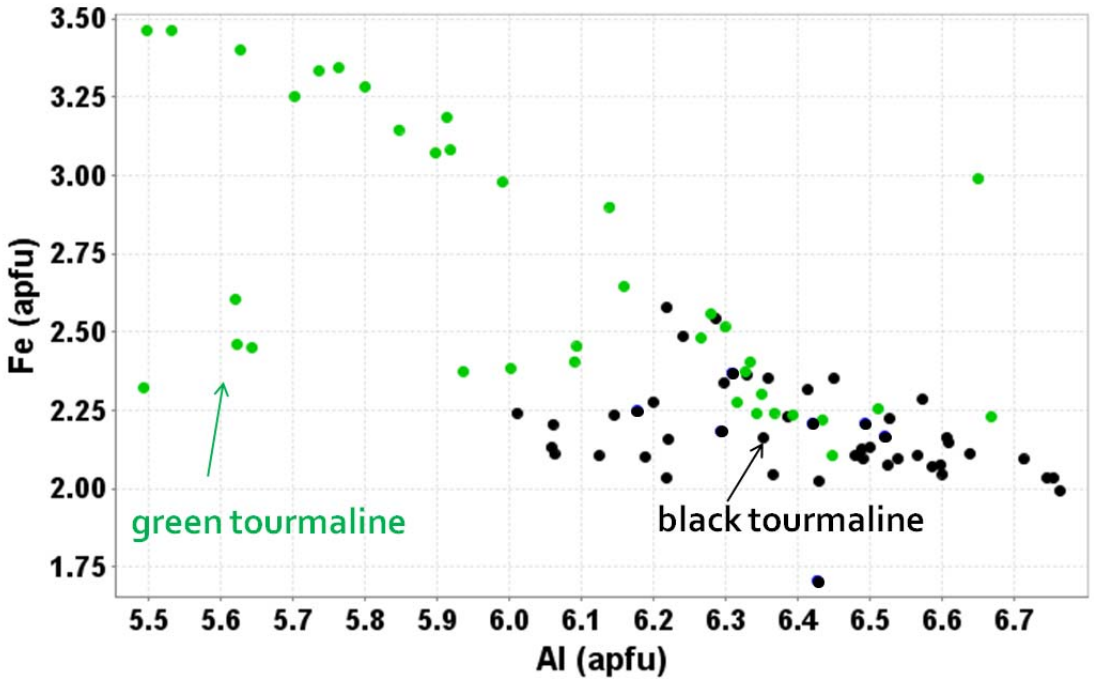

Figure 6.23 Tourmaline major element chemistry showing significant Al and Fe variability. Green tourmaline is higher in Fe and black tourmaline is higher in Al

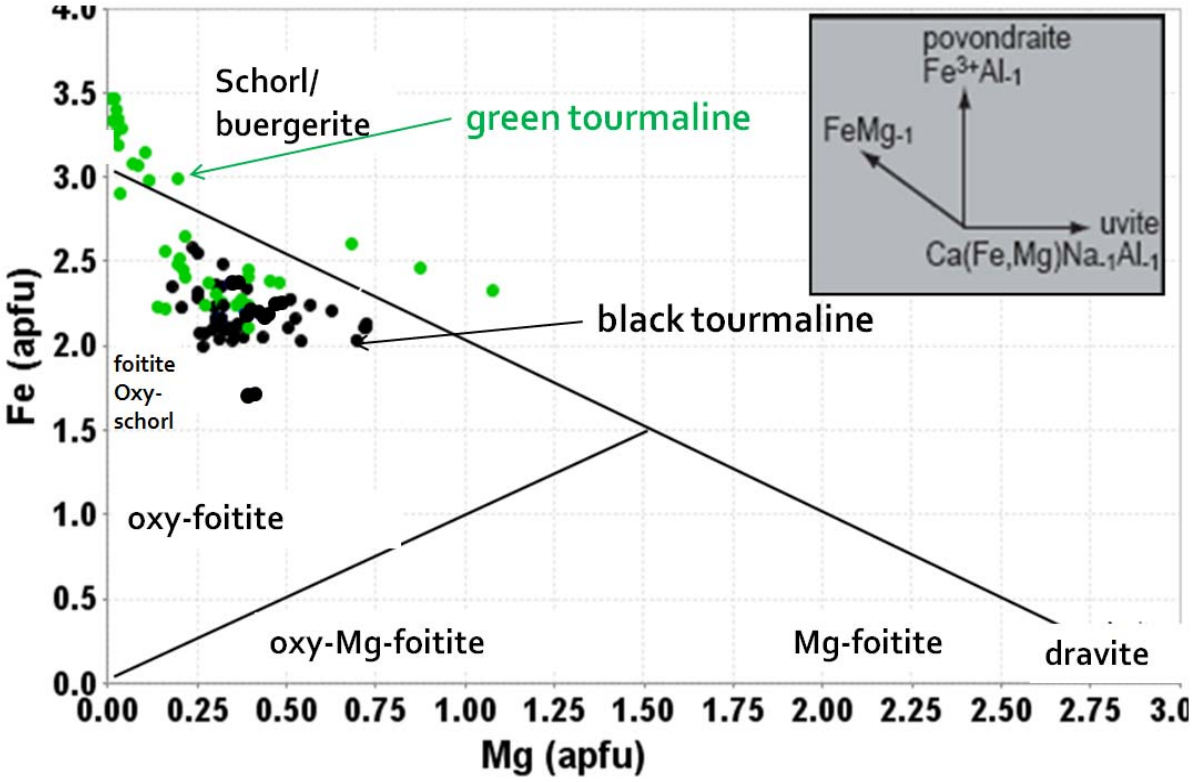

Figure 6.24 Compositional diagram showing Big Wilson tourmaline is near the schorl endmember

tourmaline analysed was >6.0 apfu Al (Fig 5.3). This means that the Z site is fully occupied by Al and excess Al is being incorporated into the Y site. The black tourmaline seems to follow the schorl dravite exchange (FeMg) while the green tourmaline with higher Fe is schorl/buegerite, which corresponds to the Fe^{3+} exchange up the Y axis, indicating green tourmaline is more oxidised than black tourmaline.

6.3.3.3 Tourmaline trace element chemistry

LA-ICP-MS analysis of tourmaline showed several strong trace element relationships. There is a general correlation between colour (green) and Sn concentration (Fig. 6.25). There are also correlations between tin concentration and zinc, lithium, rubidium and antimony (Fig. 6.26).

Tin and zinc show a strong inverse relationship with high Sn analysis. Green tourmaline has lower zinc concentration relative to high levels of Sn when compared to analysis of black tourmaline samples which have lower concentrations of Sn (Fig 6.26).

Tin and lithium also show a similar correlation to tin and zinc. Green tourmaline generally has high Sn concentrations and low concentration of lithium (Fig 6.26) whereas black tourmaline is low in Sn and higher in lithium.

The relationship between tin and strontium also shows a significant difference between green tourmaline and black tourmaline. Black tourmaline is consistently low in both Sn and strontium and green tourmaline contains more highly elevated and variable levels of Sn and strontium (Fig 6.26).

A similar pattern is observed between tin and antimony where black tourmaline is low in both and green tourmaline has much more elevated and variable levels. The five outlying black tourmaline data points with elevated antimony are all from the same sample (THBW024). This anomalous sample is the only one classified as black tourmaline and obtained from the surface. It is also the same sample that holds anomalously high Sn for a black tourmaline (Fig 6.25).

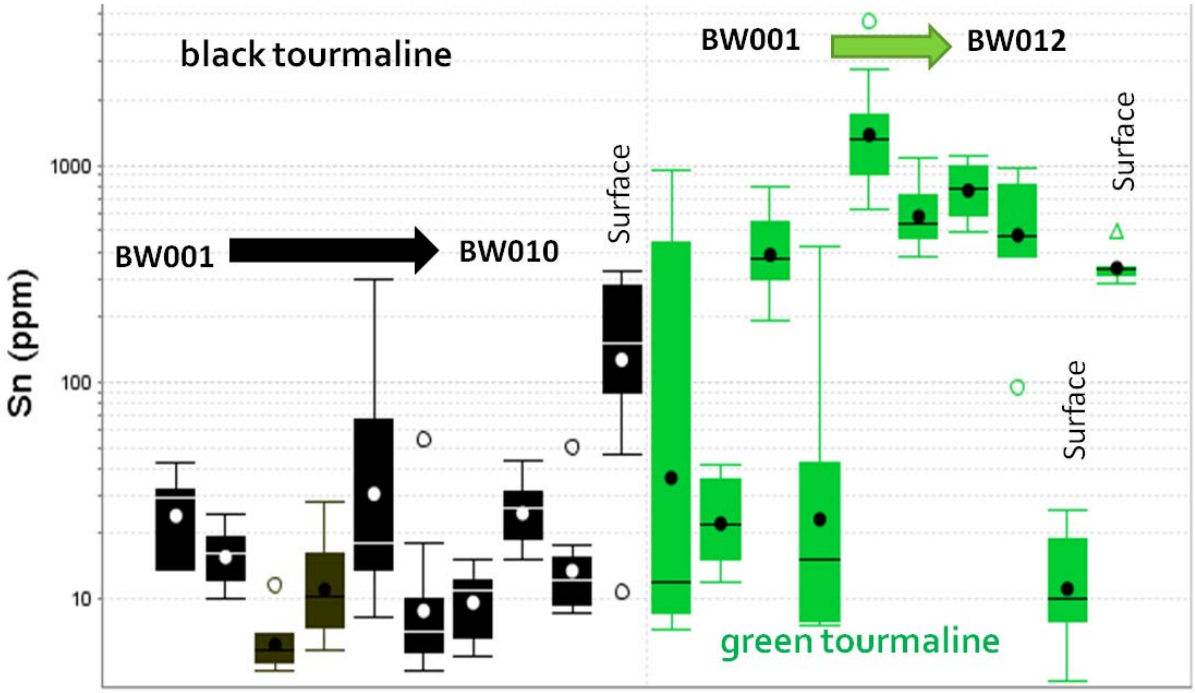

Figure 6.25 Sn (ppm) contained in green and black tourmaline samples, determined by LA-ICPMS analysis. Green generally higher in Sn.

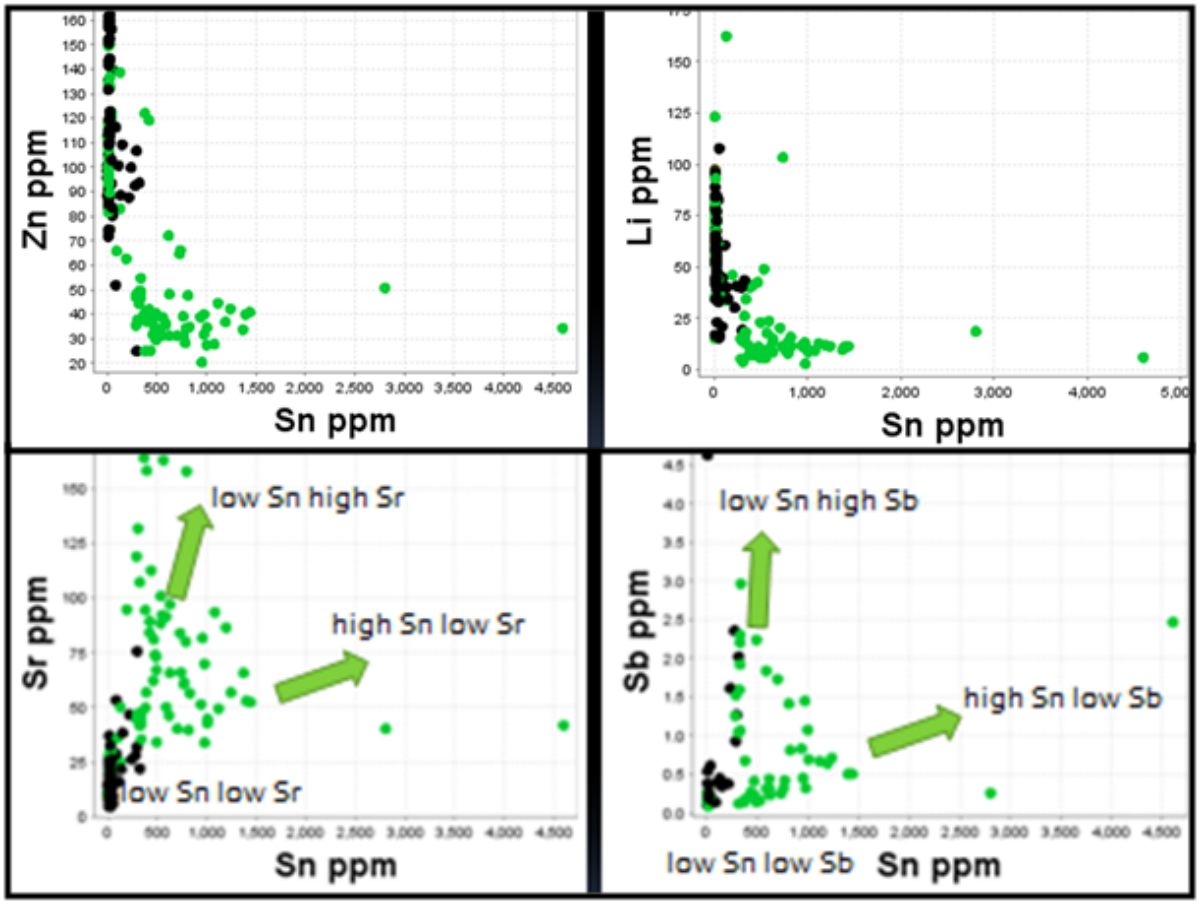

Figure 6.26 Trace element relationships between Sn and Zn, Li, Sr and Sb

6.3.4 Discussion

Determining the colour of tourmaline is a relatively subjective process and placing all samples into one of two categories simplifies what may be a more complex issue. In some circumstances determining colour is straightforward as the green colouration is distinctive in hand specimen, particularly where tourmaline has replaced feldspar. However, when samples are wet the green colour appears much darker and is difficult to distinguish in hand specimen. Green and black tourmaline may also occur in the same sample, as black tourmaline has been observed growing on, and layered with, green. Mineral chemistry shows a distinct difference between black and green tourmaline and the subjectivity of classifying colour by eye may explain some of the anomalous black tourmaline that has the mineral chemistry of green tourmaline and vice versa.

6.3.4.1 Spatial relationships

An attempt was made to place the data for each tourmaline sample in a spatial context to identify any spatial trends in the geochemical data. However, because tourmaline only occurs in abundance in the granite no chemical or spatial comparison between the granite-alteration and the skarn-alteration can be made using just tourmaline. In addition, samples collected from the surface cannot be incorporated onto a single planar cross section that includes samples collected in drill core because of the large offset distances between surface and subsurface samples.

Another issue was the fact that the drill core orientation was parallel to the orientation of the veining in the granite. Although it was possible to determine the tourmaline chemistry from the

middle of the high-grade ore zone and compare it to lower grade tourmaline above and below the high Sn tourmaline, however, given the near parallel orientation of the core to the veins, the true distance from mineralisation to the distal samples could not be established based on down-hole distance.

Despite these issues with generating a reliable spatial model it is clear that tourmaline containing high Sn is associated with high Sn in wholerock. Therefore the relationships also extend between high wholerock Sn and low Zn, Low Li, high Sr and high Sb in tourmaline. Conversely, distal low-grade tourmaline contains high Zn, high Li, low Sr and low Sb and is associated with low-grade or barren wholerock Sn. What is unclear is how these relationships change with increasing distance from high-grade mineralisation and, most importantly, over what scale do the most noticeable changes in tourmaline mineral chemistry occur.

6.3.4.2 Usefulness as a vector

A number of potentially useful relationships have been identified during this investigation. Significantly, it has been shown that the green tourmaline occurs both directly with cassiterite and in proximity to high-grade cassiterite veins in the granite. Green tourmaline also:

- Contains large amounts of Sn in its trace element structure.
- Is Fe-rich (schorl endmember).
- Is Zn and Li poor.
- Contains elevated levels of Sr and Sb.

A clear relationship between tourmaline colour, Sn content and the major and trace elements has been demonstrated, although the usefulness of tourmaline as a vector to tin mineralisation in a spatial context could not be established. However, tourmaline colour would be an excellent field indicator of proximity to mineralisation. The refractory nature of tourmaline and the granite it is hosted in means that it could survive in stream sediments, exposed resistant outcrops, sub-crops and within float material, and could therefore be observed in stream sediment and soil samples as well as through field mapping. It would be valuable for tin explorers around the granites of western Tasmania to be able to recognise green tourmaline and appreciate its significance as an indicator of mineralisation.

6.4 Geochronology

One possibility for the genesis of the high grade greisen is that Sn is concentrated during magma fractionation and partitions into hydrothermal fluids late in the granite crystallisation history so that it is deposited in late stage veins. If the age of the earliest-crystallised granite phases and the late-stage cassiterite-rich borate veins can be resolved using geochronological techniques, this will allow the duration of magmatic-hydrothermal activity to be constrained and may be helpful as an exploration tool, through potentially matching individual granite bodies with mineralisation. The technology to directly date minerals such as zircons, contained in the granite, is well developed (Black et al. 2004; Jackson et al. 2004; Chang et al. 2006; Harley and Kelly 2007), however, the science of directly dating cassiterite is just emerging.

6.4.1 Aims

The primary aim of the geochronogy is to determine if the age of the high-grade cassiterite greisen can be resolved from the magmatic age of the granite. A secondary aim is to confirm that cassiterite can be directly dated *in-situ* by LA-ICPMS using the U/Pb system.

6.4.2 Methods

Two samples of cassiterite were obtained for geochronological analysis. The first came from a small section of Big Wilson drill core (BW001 215.7). - It is Devonian in age (Figs. 6.27A and 6.28). The second, used for comparison and method development, was an Archaean sample from the University of Tasmania collections (Sample 12529) from Mt. Francisco, Western Australia (Fig. 6.27B). Both samples were initially analysed for their U-Pb isotopic composition using the University of Tasmania LA-ICPMS to determine if they were suitable for geochronology. The samples were then sent for analysis using ID-TIMS at the Pacific Centre for isotopic research at the University of British Columbia. The ID-TIMS method used by the UBC lab is detailed in Appendix 10. The LA-ICPMS method for analysing cassiterite is similar to that used for zircons. The sample preparation is described below and the University of Tasmania LA-ICP-MS methods for zircons are detailed in Appendix 9. Sample preparation was performed by the author with assistance from Dr Sebastien Meffre and the analysis and data reduction was undertaken by Dr Sebastien Meffre and Jay Thompson. Data reduction was carried out using Microsoft Excel in accordance with the methods described by Meffre (2008).

6.4.2.1 LA-ICP-MS

For the Achaean Mt. Francisco sample approximately 0.5g of coarse-grained cassiterite crystals

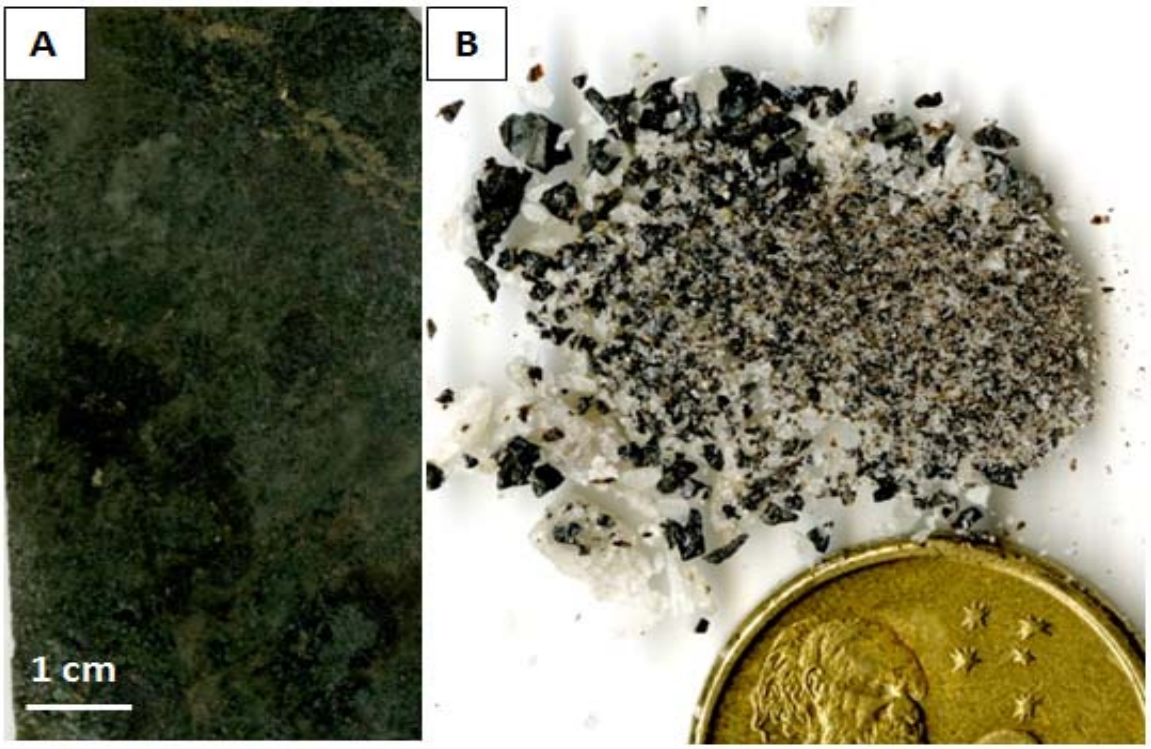

Figure 6.27 A: Sample of cassiterite-rich (12% Sn) core from BW001 215. B: Archaean cassiterite from Mt. Francisco W.A.

were flaked off by hand using a tungsten-tipped scribe into a watch glass. The fragments of cassiterite were handpicked under the microscope in cross-polarised transmitted light and placed on double-sided sticky tape. Epoxy glue was then poured into a 2.5 cm diameter mould on top of the cassiterite. The mount was dried for 12 hours and polished using clean sandpaper and a clean polishing lap.
The Big Wilson sample was cut out directly from the drill core and mounted *in-situ* on a 2.5cm round laser mount and polished. The samples were then washed in distilled water in an ultrasonic bath. The analyses for both samples were repeated twice on two different days to test whether the data could be reproduced. The results for both days were within error.

6.4.2.2 ID-TIMS methods and issues

Four samples were submitted to the Pacific Centre for Isotopic and Geochemical Research at the University of British Columbia, Canada for direct dating using the U-Pb system. The Isotope Dilution – Thermal Ionisation Mass Spectrometry (ID-TIMS) process involves dissolving individual grains of minerals to extract and measure the U-Pb content directly. This technique does not require matrix-matched standards and can give higher resolution age date results than using the sensitive high-resolution ion micro-probe (SHRIMP) or LA-ICPMS instruments (Gulson and Jones, 1992; Thirwall, 2000).
Samples were prepared by either directly flaking off large cassiterite crystals with a tungsten tipped scribe into a small envelope or by crushing a sample with a mortar and pestle, followed by gravity and magnetic separation in a pan with the final separate being placed in a watch glass and

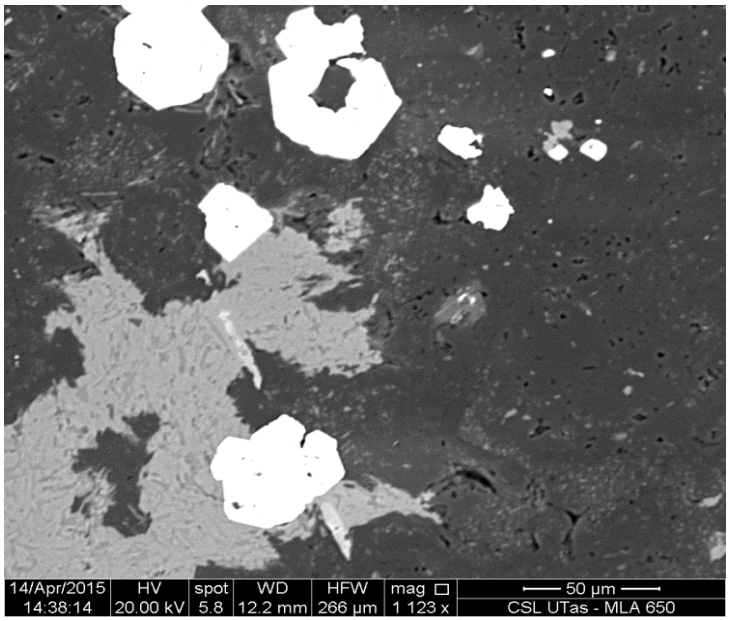

Figure 6.28 SEM image of BW001 215.7. Cassiterite is the white phase

checked under the microscope in cross polarised light. A detailed method used by the lab at the University of British Columbia is provided in Appendix 10.
The technique of dating cassiterite with the ID-TIMS process is still new and the laboratory initially tried to use their standard zircon technique directly on cassiterite. Unfortunately cassiterite is too refractory to dissolve in the HF normally used for zircons. An alternative technique was to dissolve the cassiterite in hydroiotic acid (HI). This approach encountered some issues due to recent increases in the regulation of HI. It is currently difficult to obtain reagent grade solutions, as HI is a

precursor to the production of methylamphetamine. This caused significant delay. Samples were submitted to the lab in August 2014. At the time the lab quoted a 4 month turn-around period with assurances that data would be provided by January 2015, however, at the time of writing (September 2015) the results are not yet available.

6.4.3 Results

The preliminary results using the 91500 zircons as a primary standard provided an age for the Big Wilson cassiterite of 357.9 ± 5.2 Ma using the $^{238}U/^{206}Pb$ system (Fig. 6.29). The Mt Francisco cassiterite gave an age of 2,736 ± 49 Ma using the $^{206}Pb/^{238}U$ system (Fig. 6.30). The full data tables of the LA-ICP-MS results are provided in Appendix 9. The results ^{207}Pb-^{206}Pb system using the NIST610 glass as primary standard were 2,862 ± 47 Ma for the Mt Francisco Cassiterite (Fig. 6.4) and the Big Wilson cassiterite contained a small amount of common Pb and were unable to be dated using this system. In the absence of a cassiterite standard the $^{238}U/^{206}Pb$ system is expected to be inaccurate due to differences in the ablation rate of cassiterite and zircons. The discrepancy between the two ages for the Mt Francisco cassiterites and the lack of common Pb in this sample (low^{204}Pb) allows a correction factor to be calculated for the differences in the $^{238}U/^{206}Pb$ ratio between cassiterite and zircons. When this is taken into account the Big Wilson cassiterites are dated at 373.6 ± 5.4 Ma using the $^{238}U/^{206}Pb$ system.

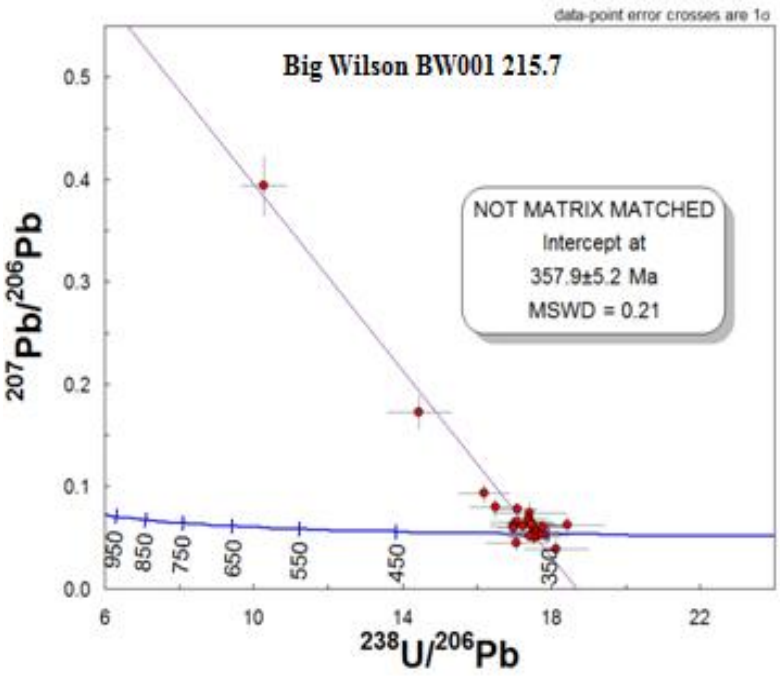

Figure 6.29 Tera-Wasserburg diagram for Big Wilson cassiterite with a non matrix matched uncorrected date of 357.9 +/-5.2Ma

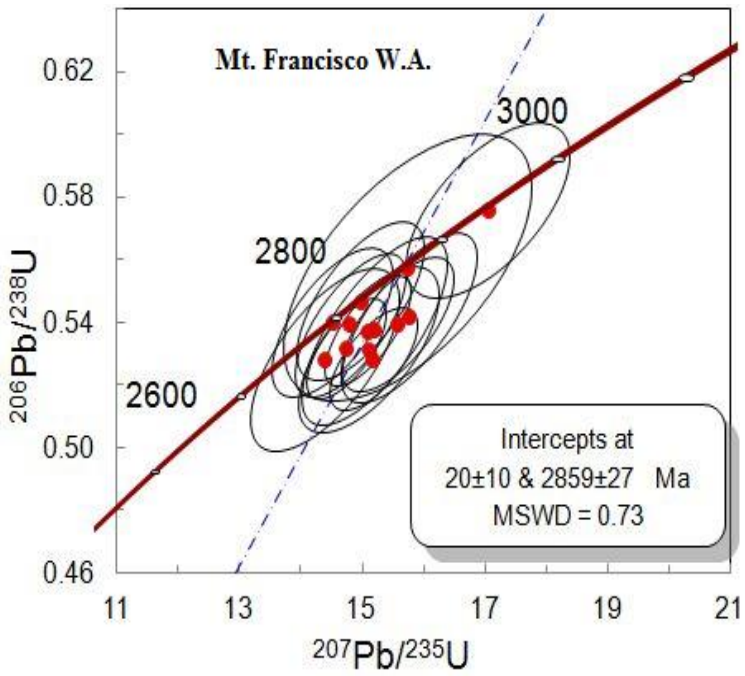

$^{206}Pb/^{238}U$ Age:
Mean = 2736±49 [1.8%]
95% conf.
Wtd by data-pt errs only, 0 of 14 rej.
MSWD = 0.42, probability = 0.96

$^{207}Pb/^{206}Pb$ age:
Mean = 2862±47 [1.6%]
95% conf.
Wtd by data-pt errs only, 0 of 14 rej.
MSWD = 0.36, probability = 0.98

Figure 6.30 Concordia diagram for Achaean cassiterite sample from Western Australia. Yellow boxes show the $^{207}Pb/^{206}Pb$ age and the non matrix matched uncorrected and $^{206}Pb/^{238}U$ age

6.4.4 Discussion

6.4.4.1 Correction for matrix effects

A zircon standard was used during analysis as a well characterised cassiterite U-Pb standard was not available, so the results will be affected by matrix effects due to variation in the rates of ablation between different minerals producing different U/Pb fractionation (Marillo-Sialer et al., 2014). The difference in the U/Pb fractionation was quantified using an Archaean cassiterite. This methodology relies on the fact that Archean crystals can be dated using either the $^{207}Pb/^{206}Pb$ system, which is unaffected by matrix effects, or the $^{206}Pb/^{238}U$ system, which is affected by matrix effects.

For the Mt. Francisco cassiterite sample, the difference between the $^{207}Pb/^{206}Pb$ age obtained of 2,862 ± 47 Ma and the 2,736 ± 49 Ma age obtained using the $^{206}Pb/^{238}U$ system is about 4.4%. The published dates for the Sn-bearing pegmatites in the Mt. Francisco area (Table 6.1) vary between 3,000 – 2,800 Ma (Sweetapple, 2000; Huston et al., 2002) which agree with the results of the $^{207}Pb/^{206}Pb$ date of 2,862 ± 47 Ma. As the Mt. Francisco sample was obtained from the University of Tasmania rock collection the precise locality was not recorded.

The 4.4% offset between the ^{207}Pb-^{206}Pb and ^{238}U-^{206}Pb ages for the Achaean cassiterites provides an estimate of the matrix effects between the U-Pb system on zircons and the U-Pb system on cassiterites. This can be used to correct the $^{238}U/^{206}Pb$ date obtained for the Devonian Big Wilson sample. The uncorrected date of 357.9 ± 5.2 Ma is then recalculated to 373.6 ± 5.4 Ma. This adjusted date is within error of the currently published age of the Meredith Granite of 372.2 ± 1.9 Ma (Fig 6.31) obtained from zircons at Big Wilson (Kositcin and Everard, 2013).

Table 6.9 Dates obtained from cassiterite at Mt. Francisco, Western Australia by Kinny (2000) in Sweetaple (2002)

Locality	Age (Ma)	Method
Tabba Tabba	2886 ± 21	$^{207}Pb/^{206}Pb$ SHRIMP
Tabba Tabba	2974 ± 59	Pb-Pb Isochron plot
Strelley	2836 ± 36	$^{207}Pb/^{206}Pb$ SHRIMP
Strelley	2924 ± 120	Pb-Pb Isochron plot
Moolyella	2839 ± 16	$^{207}Pb/^{206}Pb$ SHRIMP
Moolyella	2868 ± 63	Pb-Pb Isochron plot
Cooglegong	2839 ± 16	$^{207}Pb/^{206}Pb$ SHRIMP
Cooglegong	2901 ± 49	Pb-Pb Isochron plot
Hillside	2877 ± 20	$^{207}Pb/^{206}Pb$ SHRIMP
Hillside	2877 ± 62	Pb-Pb Isochron plot

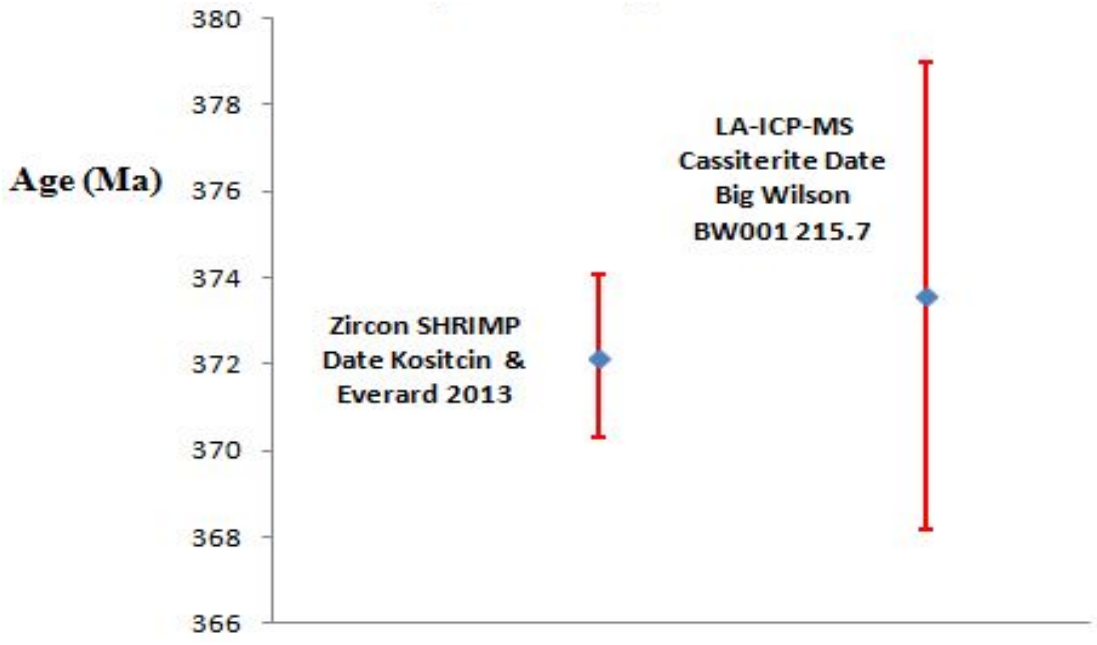

Figure 6.31 The age of cassiterite as determined by the LA-ICPMS after adjustment for the matrix effect is within error of the published zircon dates of the Meredith Granite.

6.4.4.2 Data precision and accuracy

Although a full precision and accuracy analysis of this methodology is beyond the scope of this project, the scatter in the ages and the isotopic ratio suggest that the method is accurate and precise.

The MSWD (mean square weighted deviation) is a measure of geochronological data precision that takes into account the relative importance of integral and external reproducibility of data. Where MSWD = 1, the data fit a gaussian normal distribution based on analytical uncertainty, MSWD < 1 if the observed scatter is less than predicted by analytical uncertainty and MSWD > 1 if the observed scatter is greater than predicted by analytical uncertainty (Brooks et al., 1972; McDougall and Harrison, 1988; Wendt and Carl, 1991). An example of typical MSWDs from an analysis of zircon and monazite standards by Halpin et. Al, (2014) is provided in table 6.10 showing MSWDs ranging from 0.91 to 1.5.

The most likely explanation for the higher than expected precision of the data (Fig 6.32) is that the analytical uncertainties expected from this method are based on previous experience with zircons. One of the biggest factors for data scatter in zircons is due to structural breakdown of the mineral and subsequent lead loss due to radiation damage (Jiang, et. al., 2004). Cassiterite is highly refractory and more resistant to radiation damage than zircons (Jiang et al., 2004; Gulson and Jones, 1992) so it is likely that it does not suffer lead loss to the same degree as zircons resulting in more precise data.

Table 6.10 MSWD's measured on zircon and monazite standards from Halpin et. al, (2014)

Standard Name		Standard Type	Age Obtained	MSWD
Gj-1		Zircon	604.3 ±2.6 Ma	0.91
TEMORA 1		Zircon	418.5 ± 3.1 Ma	1.3
91500		Zircon	1071.4 ± 9.5 Ma	1.00
MB35		Monazite	501.1 ± 3.3 Ma	1.5
N3364	Monazite	1585.1 ± 8.6 Ma	1.14	

6.4.4.3 Regional considerations

The age of granites in Tasmania becomes younger systematically from east to west with granites on the east coast ranging from 410 Ma to 380 Ma, granites in the central west coast ranging clustering around 370 Ma and granites in the far west coast ranging from 350-360 Ma (Fig. 6.33)(Black et al., 2005; Kositcin and Everard 2013). The age of Sn mineralisation seem to track the ages of the granites across Tasmania getting younger from east to west (Corbett, et al., 2014). The ages presented in this study support this age progression with the cassiterites dated at Big Wilson (373.6 ± 5.4 Ma) being intimately related to the nearby Meridith Granite dated at 372.2 ± 1.9 Ma; Kositcin and Everard 2013.

6.4.4.4 ID-TIMS

The highly refractory nature of cassiterite which resists radioactive breakdown and makes it ideal for retaining its original U and Pb also makes it very difficult for the ID-TIMS lab to dissolve it. As the ID-TIMS results are not available the aim of obtaining a high resolution date for the cassiterite to differentiate it from the magmatic age of the granite could not be achieved. However, this investigation has shown that cassiterite is suitable for dating *in-situ*

using the U/Pb system on the LA-ICP-MS. Samples submitted from this project are being used by Prof. Jim Mortensen at the University of British Columbia as part of a cassiterite dating project with the aim of developing an internationally recognised cassiterite standard.

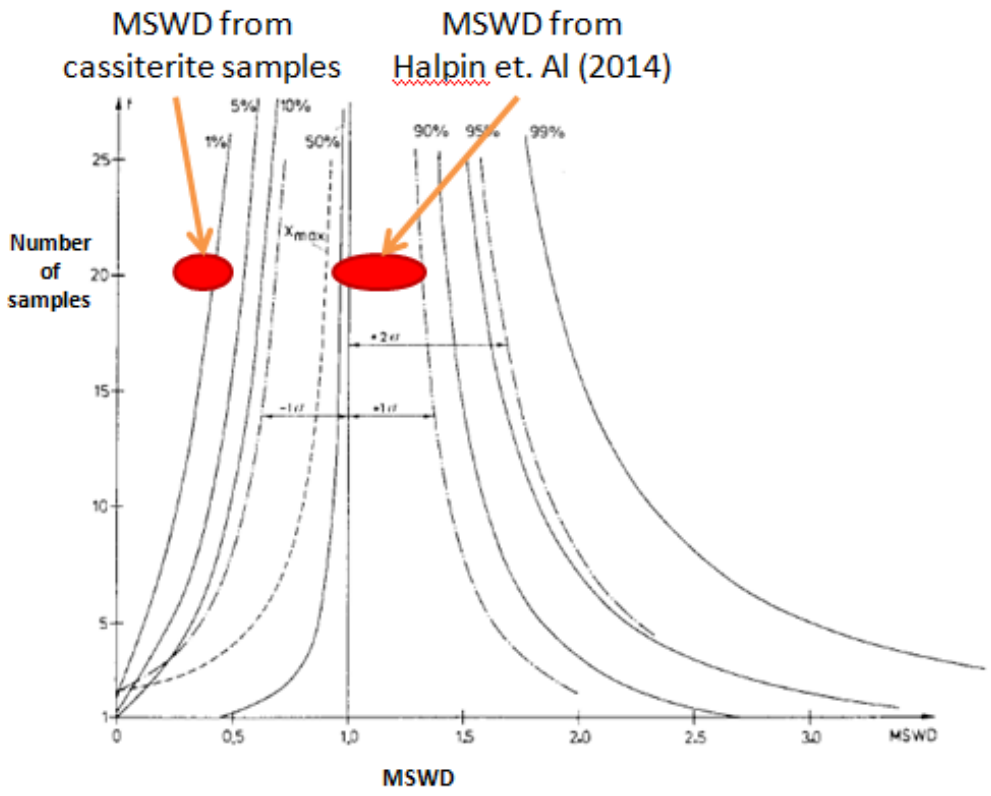

Figure 6.32 MSWD probability distribution (Wendt and Carl, 1991)

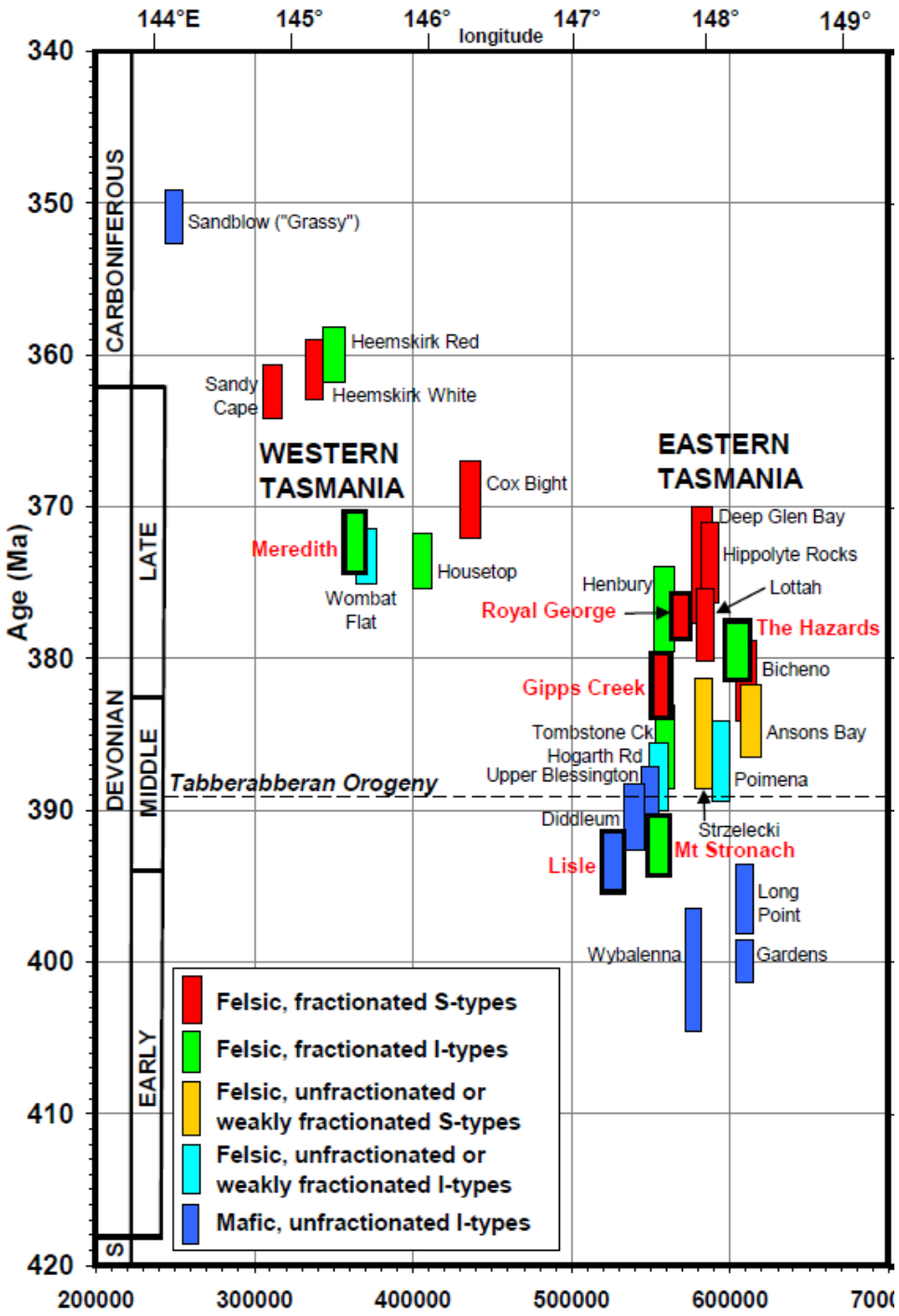

Figure 6.33 Summary time-space diagram plotting emplacement age vs. easting for Devonian-Carboniferous granites in Tasmania (from Kositchin and Everard 2013)

7 Genetic model and exploration implications

7.1 Introduction

Exploration by Venture Minerals at the Big Wilson prospect has targeted Sn and W mineralisation using a skarn-style carbonate replacement exploration model similar to that for other Sn-W deposits in western Tasmania, such as Mount Lindsay (Kwak, 1982) and Renison (Kitto, 1998; Fig 1.1). These models assume that the source of the Sn-W mineralisation was hydrothermal fluids exsolved from the Meredith Granite. Magmatic fluids become enriched in Sn and W during fractionation when the granites cool. These late-stage magmatic fluids were likely acidic (Kitto 1998) and migrated from the granite into the Gordon Limestone where interaction between the carbonate and the fluids caused progressive cooling and neutralisation of the ore fluid, forming the skarn-style alteration-mineralisation (Kwak, 1982; Kitto, 1998).

7.2 Relationship between the skarn and granite alteration assemblages

Four mineral alteration stages were identified in the skarn in a paragenetic sequence. The first two stages were early alteration, causing the recrystallisation of limestone to marble and the development of zones of calc-silicate alteration, probably as part of a high temperature prograde alteration of the calcareous protolith. This was followed by the third alteration stage which contains minerals stable over a range of temperatures and displays a complex history of recrystallisation and textural overprints. Significant cassiterite mineralisation occurred during this alteration stage coinciding with calc-silicate alteration and the formation of vonsenite at high temperatures (Bloise and Barrese, 2009; Mindat.org 2015). However, the presence of hydrous minerals including actinolite and biotite, along with lower temperature indicator minerals including chlorite, fluorite, sulphide and carbonate minerals, suggest a retrograde origin for Sn mineralisation. The hydrothermal veining that represents the fourth stage of skarn-like alteration are mineralised and support a late-stage origin for the mineralising fluids into the skarn. These veins may be genetically related to the high-grade cassiterite veins which occur in the granite.

Two different types of veins were identified in the granite. Both contain tourmaline but only one contains significant cassiterite. Although no direct cross-cutting relationships were found to be able to directly document a timing relationship between the vein types, it appears that the cassiterite-rich veins formed at a later-stage from a more evolved hydrothermal fluid which exploited a pre-existing vein network and consequently overprinted earlier alteration assemblages. The first stage hydrothermal fluid which is associated with low Sn grades may be correlated with black tourmaline veins in the granite and to vonsenite in Stage 3 skarn alteration.

Correlation between the late-stage cassiterite-rich veins in the granite with Stage 4 hydrothermal veining in the skarn can be inferred on the basis of similarity in the mineralogy and vein orientations.

The relationship between Sn mineralisation and mineral alteration stages is illustrated in Fig. 7., which shows the Sn content of hole BW001 correlated to the corresponding down hole TIR and SWIR results obtained using the Hylogger which show the calculated relative mineral abundances measured in each down hole spectral analysis. The highest Sn concentrations occur at the contact between high-grade cassiterite bearing quartz - carbonate - tourmaline veins in the granite and Stage 3 retrograde skarn alteration developed in the limestone at 215m depth. A secondary Sn spike at 225m is associated with a cassiterite-rich quartz-carbonate vein in the granite.

The rapid drop off in Sn grade of the Stage 3 skarn further away from the contact with the high-grade vein in the granite suggests the cassiterite was not transported far into the limestone before being deposited. Of the 13 drill holes at Big Wilson, one, BW001, returned the highest Sn grades in

the skarn. This may be because it intersected the skarn at the same location as a high grade cassiterite vein from the granite. If this hypothesis is correct, areas of high-grade Sn in parts of the skarn may be predicted from the position of high-grade veins in the granite.

7.3 Controls on mineralisation geometry

Structural controls may be important in understanding the genesis of mineralisation. The exact location and geometry of structures within the skarn is masked by extensive hydrothermal alteration. However, skarn formation was likely controlled by some combination of faulting and bedding parallel fluid flow. The orientation of the skarn is approximately parallel to local bedding in the limestone, suggesting fluids exploiting a permeable sedimentary horizon in the limestone protolith; however, the presence of hydrothermal breccias also suggest localised faulting. At high temperatures and pressures when pore fluid pressure approaches lithostatic pressure the permeability of marble may be increased by up to two orders of magnitude (Fischer and Paterson, 1992). Dissolution of carbonates by acidic hydrothermal fluids which exploited a permeable bed in the limestone may be one type of control.

The contact between the ultramafic unit and the Gordon Limestone is also considered to be faulted (Crawford and Berry 1992). The skarn occupies the space between the ultramafics and the marble in the southern half of the prospect area, suggesting that hydrothermal fluids may have exploited a faulted contact. However, in the north of the prospect area the skarn is bounded on both sides by marble and the skarn follows the strike of bedding rather than the profile of the ultramafic contact with the marble.

The steep dip of the skarn is also consistent with fluids escaping out of the granite by rising either vertically or propagating horizontally and following the weakest bedding plane in the original marble.

The skarn follows bedding with a northeast strike that is well-defined by the tin anomaly in soil geochemistry (Fig 3.2A). The skarn orientation is broadly orthogonal to the northwest-striking veins in the granite although both contain high-grade mineralisation. The high angle between the two high-grade mineralisation zones in the different protoliths means that any exploration drilling targeted in an orientation optimal for intersection of the skarn was also inadvertently oriented parallel to the veining in the granite (Fig. 7.2). If tin mineralisation in the skarn is highest where it is intersected by high-grade veins from the granite, as observed in BW001, (Fig. 7.1) then it is important to know more about the abundance and distribution of these high-grade veins. As a result of this investigation four samples of high-grade veins were discovered in two distinctly separate locations, suggesting that mineralisation discovered in BW001 may not simply represent an isolated vein but rather, that there is potential for multiple high-grade veins to occur elsewhere in the prospect area.

7.4 Ore deposit models revisited

During this project some features of mineralisation at Big Wilson have become apparent that are inconsistent with the ore deposit models outlined in section 7.1 above, as well as other regional Sn deposits. The Mt. Lindsay and Renison deposits both host all their target mineralisation outside the granite in the carbonate hosted skarn systems (Kwak, 1982; Kitto, 1998). Likewise the Cleveland tin mine (Fig 1.1) hosted its Sn mineralisation in sedimentary layers outside the granite (Collins, 1981) and Sn skarn mineralisation at Mount Bischoff (Fig 1.1) is hosted in a dolomite unit (Halley

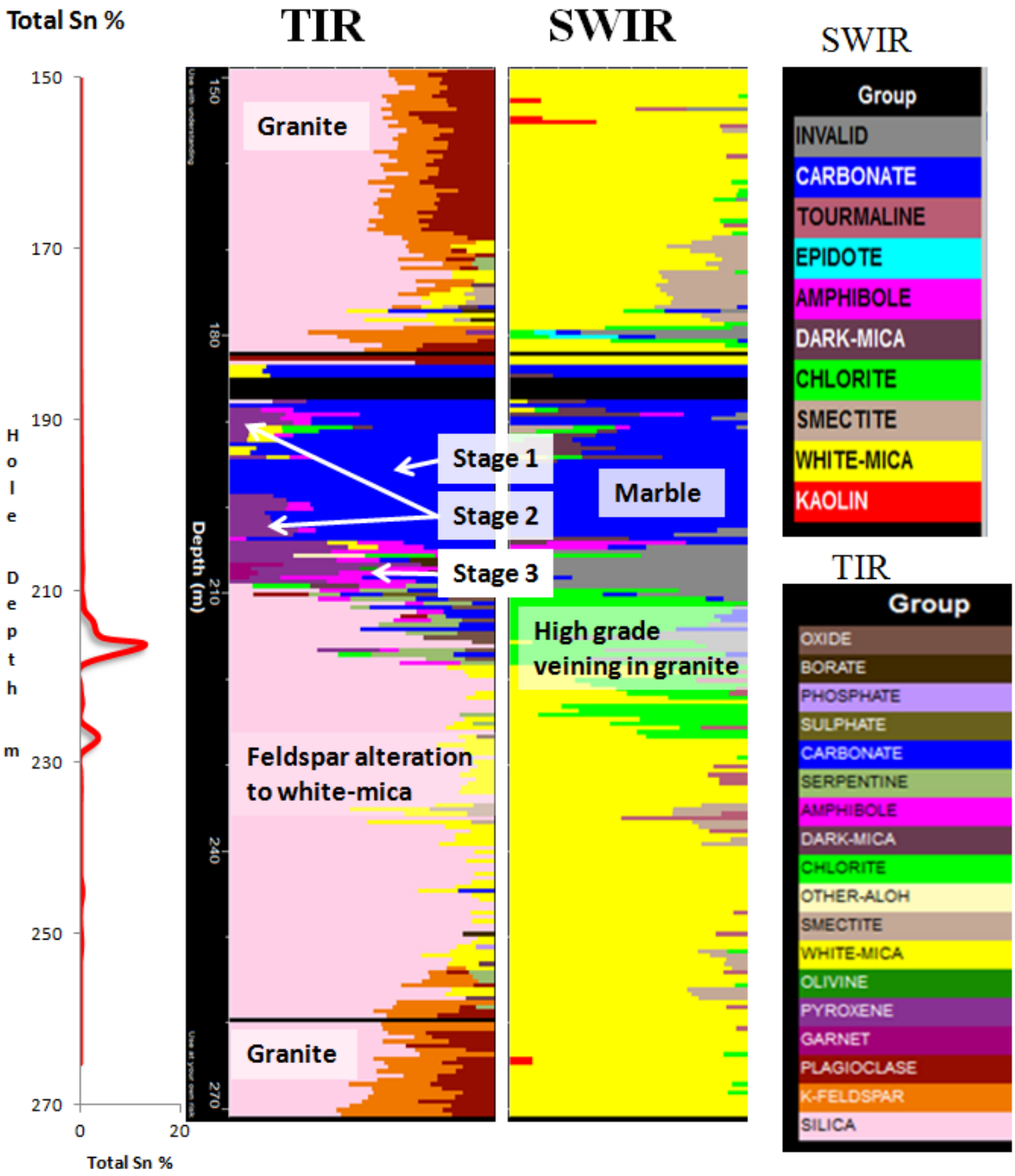

Figure 7.1 Total Sn shown beside SWIR and TIR Hylogger[tm] data from drill hole BW001 showing the highest Sn grades occur at the contact between high-grade veining in the granite and Stage 3 skarn mineralisation. Stage 4 hydrothermal veining in the skarn is likely a continuation of late stage high-grade veining in the granite.

and Walshe, 1995). Although in each of these deposits the granite was the source of the tin-rich hydrothermal fluids, none of these deposits have been shown to host economic Sn mineralisation in a granite protolith.

Wholerock Sn assay for BW001 (Fig 7.1) illustrates that much of the Sn mineralisation at Big Wilson is found in the granite protolith. Due to intense alteration the exact point where the protolith changes from granite to limestone in BW001 is unclear but is somewhere between a depth of 212m and 217m. The portion of this interval that is limestone protolith contains the highest grade Sn measured in the skarn. The highest grade Sn is in altered granite directly at the contact with the skarn. A secondary concentration of high-grade Sn is located further down hole in another quartz-siderite-cassiterite vein hosted in altered granite. If none of the regional ore deposits contain economic tin mineralisation in the granite in the same form as that observed at Big Wilson then perhaps a revised ore deposit model should be considered.

The San Rafael Sn-Cu deposit in southeastern Peru is the largest known tin deposit in the world (Kontak and Clark, 2002). Bonanza grade Sn mineralisation is controlled by brittle shear zones

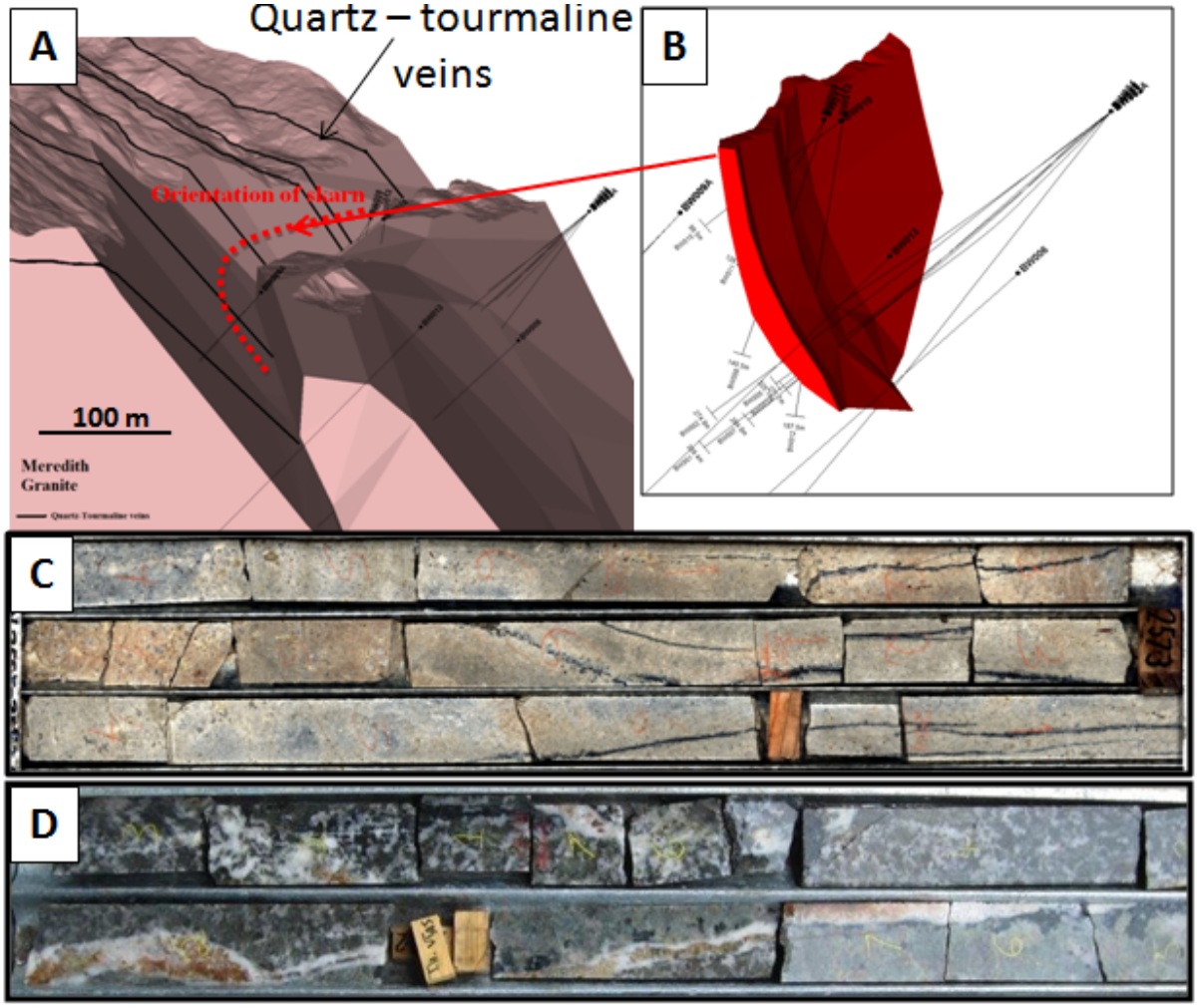

Figure 7.2 A) Block model of the Meredith Granite showing drill hole traces oriented parallel to quartz-tourmaline veins. The red dashed line shows the position of the skarn fitting between the dyke and the main body of the Meredith Granite. B) Block model of the skarn showing diamond drill hole traces oriented orthogonal to the skarn. C) Core from BW001 showing a low grade quartz – black tourmaline vein containing running parallel to core. D) Core from BW012 showing a high grade zone quartz – carbonate - cassiterite vein with a halo of green tourmaline replacing feldspar running parallel to core

hosted in granitoid rocks that have undergone intense metasomatization. Skarn and porphyry style Sn mineralisation has not been documented at San Rafiel (Kontak and Clark, 2002) although early alteration at San Rafael is characterised by abundant barren quartz-tourmaline veins. The majority of these veins were sealed prior to ore deposition, but a few remained open and these contain a second generation of Fe-rich green tourmaline which co-precipitated with abundant cassiterite and chlorite (Mlynarczyk and Williams-Jones, 2006).

Both the Big Wilson and San Rafael deposits contain multiple generations of tourmaline veining with a barren stage preceding an ore stage with Fe-rich green tourmaline. Future drilling at Big Wilson should target the high-grade Sn veins in the granite. This could be optimised by orienting drilling in a northeast direction, orthogonal to the northwest strike of the veins in the granite.

7.5 Tourmaline as a potential vector to mineralisation

This investigation demonstrated a significant correlation between the tin concentration of tourmaline and several major and trace elements in tourmaline that have the potential to be used as exploration vectors to tin mineralisation. Significantly, this study verifies that tourmaline colour, particularly the presence of green tourmaline and tourmaline replacing feldspar may be a very good field indicator of proximity to tin mineralisation. The refractory nature of tourmaline and the granite it is hosted in means it can survive in stream sediments, soil samples (gravels), and in outcrop, meaning it should be possible to observe during field surveys.

The relationships identified between Sn and Zn, Li, Sr and Sb also have potential to be useful as a vector to mineralisation, however, further work needs to be undertaken to examine these findings to determine how robust they are, and if they apply on a regional scale. The quantity and distribution of mineralised veins in the area is still unknown, and with the drilling orientation parallel to the veining, it is not possible to ascertain the distance to the nearest mineralisation.

7.6 Cassiterite geochronology

This study was successful in obtaining a new LA-ICP-MS age of mineralisation by direct, *in situ* analysis of cassiterite. Agreement between this age and the published age for the Meredith Granite provides support for the genetic link between the granite emplacement and mineralisation. A drawback to the LA-ICP-MS method is that no cassiterite standard yet exists so a non-matrix matched standard needed to be used, together with an untested matrix correction method based on the concordance of Archean cassiterite in the U-Pb and Pb-Pb systems. Dating the cassiterite at Big Wilson through the more precise ID-TIMS method would have provided a clearer indication of the timing of mineralisation based on the date of cooling of the granite . However, due to the highly refractory nature of cassiterite, the laboratory undertaking this work was unable to fully dissolve cassiterite for analysis in time for the completion of this thesis.

A by-product of the ID-TIMS analysis was the creation of a cassiterite standard for future microbeam geochronology work. Potential standards were identified but these were unable to be fully developed in time to be applied to this study. The science of directly dating cassiterite is just beginning to develop and attempts made in this project are important steps along the way to developing a suitable standard.

8 Conclusions and Recommendations

The main aims of the 2015-2016 analytical and research works on the Big Wilson Sn deposit were:

(1) To develop a mineralogical paragenesis for the skarn and granite alteration-mineralisation system at the Big Wilson prospect.
(2) To investigate the geometry of each of the major mineralised stages, focusing on. high-grade cassiterite bearing veins in the granite.
(3) To determine if the mineral chemistry of the tourmaline associated with both mineralised and barren veins could be a useful vector to high-grade mineralisation.
(4) To resolve the timing of tin mineralisation relative to the magmatic age of the Meredith Granite by direct dating of cassiterite.

The main findings were:

- The identification and documentation of four stages of alteration in the limestone-hosted skarn.
- That the Meredith Granite contains two distinct vein types with characteristic alteration envelopes dominated by white mica.
- Boron-rich fluids preferentially formed tourmaline-rich veins in the granite and vonsenite in the limestone-hosted skarn.
- Tourmaline-rich veins in the granite are generally steeply dipping with a northwest strike.
- High-grade mineralised veins in the granite were discovered in multiple locations.
- That tourmaline colour is a good field indicator of potential tin mineralisation.
- Tourmaline major and trace element chemistry has potential to be used as a vector towards mineralisation.
- Direct dating of cassiterite has returned the same age as the Meredith Granite, reinforcing the theory that the granite is the source of the mineralisation.
- The presence of cassiterite-rich veins in the granite oriented orthogonally to the skarn suggests fluid migration from the granite to the limestone.

Recommendations and proposed exploration activities for 2016-2017 Anniversary Year:

- Sampling and microprobe analysis of tourmaline veins and associated alteration zones within the margins of the Meredith Granite to investigate in particular spatial variation of tourmaline and white mica chemistry to vector towards high grade intersections with the Big Wilson skarn. Work on the major and trace element chemistry of tourmaline should focus on obtaining more samples around known mineralisation centres to develop a better understanding of the spatial variation in tourmaline chemistry (e.g. Al, Fe, Mg, Sn, Zn, Li, Sb, Sr) with distance from mineralisation. The distinctive green tourmaline associated with Sn mineralisation at Big Wilson should be studied relative to other tourmalines from around the greater Meredith Granite batholith
- Sampling and microprobe analysis of the Merton Hill prospect to test the use of established calcsilicate compositional vectors to mineralisation sources

9 Bibliography

Baker, J., Peate, D., Waight, T. and Meyzen, C., 2004. Pb isotopic analysis of standards and samples using a Pb-207-Pb-204 double spike and thallium to correct for mass bias with a double-focusing MC-ICP-MS. *Chemical Geology*, 211, pp. 275-303.

Black L. P., Gulson B. L. 1978. The age of the Mud tank Carbonatite, Strangways Range, Northern Territory. *BMR Journal of Australian Geology and Geophysics 3*, pp. 227-232.

Black, L. P., Kamos, L., Allen, C.M., Aleinikoff, J.N., Davis, D.W., Korsch, R.J., Foudoulis, C., 2003, TEMORA 1: a new zircon standard for Phanerozoic U–Pb geochronology. *Chemical Geology* 200, pp. 155–170.

Black, L.P., Kamo, S.L., Allen, C.M., Davis, D.W., Aleninikoff, J.N., Valley, J.W., Mundil, R., Campbell, I.H., Korsch, R.J., Williams, I.S., Foudoulis, C., 2004, Improved 206Pb/238U microprobe geochronology by the monitoring of a trace-element related matrix effect; SHRIMP, ID-TIMS, ELA-ICP-MS, and oxygen isotope documentation for a series of zircon standards. *Chemical Geology* 205, 115-140.

Bloise, A. & Barrese, E., 2009. Synthesis of isomorphic vonsenite-ludwigite series. *Journal of Mineralogy and geochemistry,* 186(3), pp. 345-350.

Brimhall, G. H., Dilles, J. H. and Proffett, J. M., 2006. The Role of Geological Mapping in Mineral Exploration. *Society of Economic Geologists Special Publication 12*, pp. 221-241.

Brooks, C., Hart, S. R. and Wendt, I., 1972. Realistic use of two-error regression treatments as applied to rubidium-strontium data. Rev. *Geophysics Space physics*, Volume 10, pp. 551-577.

Brown, A. V., 1980. *Some aspects of the geology of the Mt Lindsay - Dundas areas, western Tasmania*, Hobart: Tasmania Department of Mines.

Brown, A. V., 1986. *Geology of the Dundas - Mt. Lindsay - Mt. Younguck Region. Geological Survey Bulletin 62*, Rosny Park: Department of Mines.

Collins, P. L., 1981. The geology and genesis of the Cleveland tin deposit, Western Tasmania; fluid inclusion and stable isotope studies. *Economic Geology,* 76(2), pp. 365-392.

Chang, Z., Vervoort, J. D., McClelland, W. C., and Knaack, C., 2006, U-Pb dating of zircon by LA-ICP-MS: *Geochemistry, Geophysics, Geosystems*, v. 7.

Compston, W., 1999, Geological age by instrumental analysis: the 29th Hallimond Lecture. *Mineralogical Magazine* 63, pp.297-311.

Corbett, K. D., Quilty, P. G. and Calver, C. R., 2014. *Geological Evolution of Tasmania*. s.l.:Geological Society of Australia (Tasmania Division).

Crawford, A. J. and Berry, R. F., 1992. Tectonic implications of Late Proterozoic-Early Palaeozoic igneous rock association in western Tasmania. *Tectonophysics*, Volume 214, pp. 37-56.

Einaudi, M. T., 1997. *Mapping altered and mineralized rocks: An introduction to the "Anaconda Method".* s.l.:Stanford University.

Einaudi, M. T., Meinert, L. D. and Newberry, R. J., 1981. Skarn deposits. *Economic Geology*, Volume 75 ANN. Vol 77, pp. 317-391.

Everard, I. L. et al., 1991. *Current systematic regional mapping - new potential for mineral discovery*, Hobart: Bulletin of the Geological Survey of Tasmania.

Fischer, G. J. & Paterson, M. S., 1992. Measurement of Permeability and Storage Capacity in Rocks During Deformation at High Temperature and Pressure. *International Geophysics,* Volume 51, pp. 213-252.

Fox, N., 2012. *Controls on Alteration and Mineralsiation at the Cadia East Alkalic Porphyry Au-Cu Deposit, NSW,* Hobart: Univeristy of Tasmania.

Fryer, B.J., Jackson, S.E., Longerich, H.P., 1993, The Application of Laser Ablation Microprobe-Inductively Coupled Plasma-Mass Spectrometry (Lam-Icp-Ms) to in situ (U)-Pb Geochronology. *Chemical Geology* 109, pp.1-8.

Gulson, B. L. and Jones, M. T., 1992. Cassiterite: potential for direct dating of mineral deposits and a precise age for the Bushveld Complex granites. *Geology*, Volume 20, pp. 355-358.

Halley, S. W. and Walshe, J. L., 1993. A re-examination of the Mount Bischoff cassiterite sulfide skarn, Western Tasmania. *Economic geology*, Volume 90, pp. 1676-1693.

Halpin, J.A., Jensen, T., McGoldrick, P., Meffre, S., Berry, R.F., Everard, J.L., Calver, C.R., Thompson, J., Goemann, K., Whittaker, J.M. 2014. Authigenic monazite and detrital zircon dating from the Proterozoic Rocky Cape Group, Tasmania: Links to the Bel-Purcell Supergroup, North America. *Precambrian Research*.250, pp.50-67.

Harley, S.L. and Kelly, N.M., 2007. Zircon: Tiny but timely. *Elements*, 3(1): pp.13-18.

Haythornthwaite, J. R., 2011. *Spatial and Temporal Mineral Zonation of the Sn-W-Magnetite Main Skarn at Mt Lindsay, Tasmania*, s.l.: University of Exeter.

Henry, D. J. & Guidotti, C. V., 1985. Tourmaline as a petrogenetic indicator mineral: an example from the staurolite-grade metapelites of NW Maine. *American Mineralogist,* Volume 70, pp. 1-15.

Huston, D. L. et al., 2002. The Timing of Mineralization in the Archean North Pilbara Terrain, Western Australia. *Economic Geology*, Volume 97, pp. 733-755.

Jackson, P., Changkakoti, A., Krouse, H. R. and Gray, J., 2000. The origin of greisen fluids of the Foley's zone, Cleveland tin deposit, Tasmania, Australia. *Economic geology*, Volume 95, pp. 227-236.

Jackson, S.E., Pearson, N.J., Griffin, W.L., Belousova, E.A., 2004, The application of laser ablation-inductively coupled plasma-mass spectrometry to in situ U–Pb zircon geochronology. *Chemical Geology* 211, pp.47-69.

Jiang, S., Yu, J. & Lu, J., 2004. Trace and rare-earth element geochemistry in tourmaline and cassiterite from the Yunlong tin deposit, Yunan, China: implication for migmatitic hydrothermal fluid evolution and ore genesis. *Chemical Geology,* 20(209).

Kitto, P. A., 1994. *Structural and geochemical controls on mineralisation at Renison, Tasmania*. PhD thesis., Hobart: University of Tasmania.

Kitto, P. A., 1998. Renison-style carbonate-replacement Sn deposits. *Journal of Australian Geology & Geophysics,* 17(4), pp. 163-168.

Kontak, D. J. & Clark, A. H., 2002. Genesis of the Giant, Bonanza San Rafael Lode Tin Deposit, Peru: Origin and Significance of Pervasive Alteration. *Economic Geology,* 97(8), pp. 1741-1777.

Kositcin, N. and Everard, J. L., 2013. *New SHRIMP U-Pb zircon ages from Tasmania*, Canberra: Geoscience Australia record 2013/22.

Kosler, J., 2001, Laser-ablation ICPMS study of metamorphic minerals and processes. In: Sylvester P. J. ed. *Laser-ablation-ICPMS in the earth sciences; principles and applications* Mineralogical Association of Canada Short Course Handbook 29, pp.185-202.

Kosler J.and Sylvester P.J. ,2003 Present trends and the future of zircon in geochronology; laser ablation ICPMS. *Reviews in Mineralogy and Geochemistry 53*, pp.243-275.

Kwak, T. A., 1987. *W-Sn skarn deposits and related metamorphic skarns and granitoids*. Tokyo: Elsevier.

Kwak, T. A., 1982. *The geology and geochemistry of the zoned Sn-W-F-Be skarns at Mt. Lindsay, Tasmania, Australia,* Bundoora: La Trobe University.

Kwak, T. A. P., 1983. The Geology and Geochemistry of the Zoned, Sn-W-F-Be Skarns at Mt. Lindsay, Tasmania, Australia. *Economic Geology*, Volume 87, pp. 1440-1465.

Li, X., Long, W.G., Li, Q.L., Liu, Y., Zheng, Y.F., Yang, Y.H., Chamberlain, K.R., Wan, D.F., Guo, C.H., Wang, X.C., Tao, H., 2010. Penglai Zircon Megacrysts: A Potential New Working Reference Material for Microbeam Determination of Hf-O Isotopes and U-Pb Age. *Geostand Geoanal* Res 34, 117-134.

Marillo-Sialer, E. et al., 2014. The zircon "matrix effect": evidence for an ablation rate control on the accuracy of U-Pb age determinations by LA-ICP-MS. *Journal of analytical atomic spectrometry*, pp. 1-9.

McDougall, I. and Harrison, T. M., 1988. *Geochronology and Thermochronology by the 40Ar/39Ar Method*. s.l.:Oxford University Press.

Meffre, S., Large, R. R., Scott, R., Woodhead, J., Chang, Z., Gilbert, S. E., Danyushevsky, L. V., Maslennikov, V., and Hergt, J. M., 2008, Age and pyrite Pb-isotopic composition of the giant Sukhoi Log sediment-hosted gold deposit, Russia: *Geochimica et Cosmochimica Acta*, v. 72, pp. 2377-2391.

Meinert, L. D., Kipple, G. M. and Nicolescu, S., 2005. World Skarn Deposits. *Economic Geology,* Volume 100th Anniversary vol, pp. 299-336.

Meinert, L., 2008. *Workshop on Exploration for Skarn Deposits*. s.l.:s.n.

Mindat.org http://www.mindat.org/min-4207.html

Mlynarczyk, M. S. & Williams-Jones, A. E., 2006. Zoned Tourmaline Associated with Cassiterite: Implications for fluid evolution and tin mineralisatioin in the San Rafael Sn-Cu deposit, southeastern Peru. *The Canadian Mineralogist,* Volume 44, pp. 347-365.

Moore, D. H., Betts, P. G. and Hall, M., 2014. Fragmented Tasmania: the transition from Rodinia to Gondwana. *Australian Journal of Earth Sciences: An international Geoscience Journal of the Geological Society of Australia*.

Nicolescu, S. and Marza, I., 1989. On the history of ore deposit studies in Romania. *Geologia-Geographia*, Volume 34, pp. 94-99.

Owen, S. and Pfeifenberger, S., 2012. *Serpentine Ridge Explaration Licence 45/2010 Annual Technical Report for the period 30/05/2011 to 30/05/2012*, Perth: Venture Minerals Ltd.

Paton, C., Woodhead, J D., Hellstrom, J C. . Hergt, JM, Greig,A and Maas, R. 2010 Improved laser ablation U-Pb zircon geochronology through robust down-hole fractionation correction. *Geochemistry, Geophysics, Geosystems 11*, pp.1525-2027

Reid, A. M., 1921. *Tasmania Department of Mines Geological Survey Bulletin No. 32 Osmiridium in Tasmania*, Tasmania: Government printer.

Rice, P. J., 1985. *Environments and Diagenesis of the Gordon Group in the Zeehan area,* Hobart: University of Tasmania.

Sack, P.J., Berry, R.F., Meffre, S., Falloon, T.J., Gemmell, J.B., Friedman, R.M., 2011. In situ location and U-Pb dating of small zircon grains in igneous rocks using laser ablation-inductively coupled plasma-quadrupole mass spectrometry. *Geochemistry, Geophysics, Geosystems 12.*

Seymour, D. B., Green, G. R. and Calver, C. R., 2007. *Tasmanian Geological Survey Bulletin 72 The Geology and Mineral Deposits of Tasmania: a summary*, Rosny Park: Mineral Resources Tasmania.

Sweetapple, M. T., 2000. *Characteristics of Sn-Ta-Be-Li Industrial Mineral Deposits of the Arcaean Pilar Craton, Western Australia*, Canberra: Geoscience Australia.

Slama, J., Kosler, J., Condon, D.J., Crowley, J.L., Gerdes, A., Hanchar, J.M., Horstwood, M.S.A., Morris, G.A., Nasdala, L., Norberg, N., Schaltegger, U., Schoene, B., Tubrett, M.N., Whitehouse, M.J., 2008. Plesovice zircon - A new natural reference material for U-Pb and Hf isotopic microanalysis. *Chemical Geology* 249, pp.1-35.

Swinnea, J. S. & Steinfink, H., 1983. Crystal structure and Mossbauer spectrum of vonsenite,2FeO FeBO3. *American Mineralogist,* Volume 68, pp. 827-832.

Thirwall, M. F., 2000. Inter-laboratory and other errors in Pb isotope analyses investigated using a 207Pb-204Pb double spike:. *Chemical Geology*, Volume 163, pp. 299-322.

Tornebohm, A. E., 1875. Om lagerfoljden inom Norbergs malmfal. *Geol. Foren. Stockholm Forh*, Volume 2, pp. 329-335.

Venture Minerals, 2012. *Venture Minerals*. [Online]

Available at: http://www.ventureminerals.com.au/index.php/investor-resources/asx-announcements-page/asx-announcements/2012 [Accessed 10 07 2015].

Venture Minerals, 2013. *Venture Minerals*. [Online]

Available at: http://www.ventureminerals.com.au/index.php/investor-resources/asx-announcements-page/asx-announcements/annual-reports [Accessed 10 07 2015].

Wendt, I. & Carl, C., 1991. The statistical distribution of the mean squared weighted deviation. *Chemical Geology,* Volume 86, pp. 275-285.

Wiedenbeck, M., Alle, P., Corfu, F., Griffin W.L., Meier, M., Oberli, F., Vonquadt A., Roddick, J.C., Speigel W., 1995, 3 Natural Zircon Standards for U-Th-Pb, Lu-Hf, Trace-Element and REE Analyses. *Geostandards Newsletter* 19, pp.1-2

Appendix 1: Holmes (2015) BSc. Hons Thesis

Geometry, timing and controls on alteration and mineralization at the Big Wilson tin prospect, NW Tasmania

Travis E. Holmes BSc. BPE

A research thesis submitted in partial fulfilment of the requirements of the degree of Bachelor of Science with Honours (Economic Geology).

University of Tasmania: August 2015

Supervisors: Prof. David Cooke, Dr. Nathan Fox, Dr Lejun Zhang

Declaration

This thesis contains no material which has been accepted for a degree or diploma by the University of Tasmania or any other institution and to the best of my knowledge and belief, contains no material previously published or written by another except where due acknowledgment is made in the text of the thesis.

Travis E. Holmes
University of Tasmania
October 2015

Confidentiality

This thesis is subject to a confidentiality agreement between the University of Tasmania and Venture Minerals for a period of two years from the publication date. Publication of the results of this Honours study within the confidentiality period may only be made with the prior written consent of both Venture Minerals and the University of Tasmania.

Abstract

The Big Wilson prospect in northwest Tasmania is targeting a skarn-style Sn-W mineralisation in a two hundred-metre section of limestone beds that have been intruded by the Meredith Granite. A single steeply dipping northeast-striking mineralised skarn fifty metres wide has been identified through soil geochemistry and exploration drilling. Veining in the granite which represents pathways for the exolution of hydrothermal fluid from the granite to the skarn has a predominantly northwest strike, orthogonal to the skarn orientation.

Four stages of mineral alteration assemblages have been identified. Stage 1 is a recrystallisation of limestone into marble in the vicinity of the granite. Stage 2 is prograde calc-silicate alteration in the marble. Stage 3 is a complex borate and sulphide-rich retrograde assemblage containing significant cassiterite, scheelite and magnetite mineralisation. Stage 4 is a late stage carbonate-rich vein system with associated minor hydrothermal breccia which crosscuts earlier stages and contains significant cassiterite and scheelite mineralisation.

Two distinct vein mineral assemblages with associated mineral alteration envelopes have been identified in the granite; a barren quartz-tourmaline vein system and a cassiterite-rich quartz-siderite-fluorite-chlorite vein system with associated green tourmaline alteration. A halo of white mica alteration has been identified around veins and surrounding the contact with the skarn.

Tourmaline is mostly schorl endmember and there is a strong correlation between tourmaline colour and Sn content. Green tourmaline is associated with high-grade cassiterite veins and is higher in Fe than black tourmaline. There are strong trace element correlations in tourmaline between Sn and Li, Zn, Sr and Sb which may be useful as a vector towards mineralisation.

Cassiterite mineralisation at Big Wilson has been directly dated to 373.6 ± 5.4 Ma which is within error of the published age of the Meredith Granite.

Acknowledgements

There are many people who have helped make this project possible. I would especially like to thank the team at Venture Minerals for their support. This project was the brainchild of Dr. Stuart Owen to whom I am grateful for the time he has spent coaching me through the complexities of skarn geology under the west coast jungle. I would also like to thank Angelique Martin, Kristen Donahue and Will Dyott for their assistance with field work in Tullah.

Mineral Resources Tasmania provided use of the Hylogger and I would like to thank Peter Harding for operating the machine and Dr. David Green for assistance with processing the vast amounts of data it produces. Professor Jim Mortensen from the University of British Columbia gets an honourable mention for trying for over a year to date my cassiterite with ID-TIMS, thank you, and better luck next time Jim.

A number of UTAS and CODES staff also merit special mention for helping me with advice and specialised analytical tools. Dr Sandrin Feig at the Central Science Laboratory, Dr. Nicholas Jansen for training me to use the Terraspec, Dr. Sebastien Meffre for helping me with cassiterite geochronology and Jay Thompson for working me through the LA-ICP-MS.

I would also like to thank Ruth Painter, my proof reader extraordinaire who kept me focused when I needed it most.

Finally, I simply could not have completed this project without the support from my family that was above and beyond what I could have expected. During the second month of this study my wife Lelia Holmes gave birth to our second child. Since that time she has put aside her career ambitions and been the main caregiver for our children so I could have time to work on this project. Thank you Lelia.

TABLE OF CONTENTS

Appendices:

Contained in thesis:

Appendix 1. Literature review

Contained in electronic appendix:

Appendix 2. Surface sampling data

Appendix 3. Assay data for surface samples

Appendix 4. BW003a structural data

Appendix 5. SEM results

Appendix 6. Laser Raman Results

Appendix 7. Tourmaline investigation results

Appendix 8. Sample photographs

Appendix 9. Geochronology results

Appendix 10. ID-TIMS method

Appendix 11. Hylogger

Appendix 12. Terraspec results

Appendix 13. Thin sections

List of Figures

List of Tables

Chapter One Introduction

1.1 Project background

This thesis is an investigation of the geological origins of tin mineralisation at the Big Wilson prospect in north-west Tasmania. The study uses a combination of field observations and laboratory analyses of drill core and rock samples to investigate and document the geology and alteration paragenesis of the prospect, and was developed as a collaborative research project between Venture Minerals and the author, based at the University of Tasmania. Venture Minerals is a junior exploration company, based in Perth, Western Australia, who discovered mineralisation at Big Wilson in 2011 when exploration drilling successfully intercepted high grade Sn-W in a multi-phase skarn system. The characteristics and origin of this system is the subject of this thesis.

1.2 Aims

This project aims to map and model the spatial and temporal evolution of the Big Wilson Sn-W skarn focussing on the geometry, timing and controls on the high-grade cassiterite stage of mineralisation. Understanding the mineralogical and geochemical zonation and the structural and lithological controls at Big Wilson is critical for the advancement of mining works and has implications for exploration of other skarn and greisen systems along the margin of the Meredith Granite. The specific project objectives of this thesis are:

(1) To develop a mineralogical paragenesis for the skarn and granite alteration-mineralisation system at the Big Wilson prospect.
(2) To investigate the geometry of each of the major mineralised stages, focusing on. high-grade cassiterite bearing veins in the granite.
(3) To determine if the mineral chemistry of the tourmaline associated with both mineralised and barren veins could be a useful vector to high-grade mineralisation.
(4) To resolve the timing of tin mineralisation relative to the magmatic age of the Meredith Granite by direct dating of cassiterite.

1.3 Skarn definition

Mining of skarn deposits dates back at least 4000 years (Nicolescu and Marza, 1989; Meinert, 2005; Kipple and Nicolescu, 2005). The first published use of the term *skarn* is by

Tornebohm (1875) who was describing pyroxene-garnet rocks at a magnetite and chalcopyrite deposit in Sweden. Early uses of the term did not imply a genetic relationship to igneous intrusions but were simply descriptive (Tornebohm, 1875; Kwak, 1987). More modern definitions of the term *skarn* vary between sources. Meinert et al. (2005) state that a skarn is defined by having dominantly calc-silicate alteration mineralogy. Although skarns are primarily found in carbonate-bearing lithologies they can form in almost any rock type including shale, sandstone, granite, basalt and komatiite. This is in contrast to Kwak (1987) who describes skarns as rocks produced by the replacement of calcite or dolomite marble, regardless of whether calcic or magnesian silicates are abundant or even present (Einaudi et. al, 1981; Kwak T. A., 1987). Implicit in the strict use of the term skarn is that the rock is the product of metosomatism and exhibits a coarse grain size.

Exploration at the Big Wilson prospect is targeting Sn & W in a skarn style carbonate replacement model similar to the Mount Lindsay (Kwak, 1982) and Renison deposits (Kitto, 1998).

1.4 Thesis structure

This thesis is divided into eight chapters. The first three chapters provide an overview of the project, including the project aims, site location and a summary of the exploration and mining history of the area (Chapter 1), the regional geology (Chapter 2), and the local geology (Chapter 3).

Chapter 4 looks at the sequence of mineralising events in the Big Wilson prospect. It describes the alteration and mineralisation at the Big Wilson prospect and proposes a paragenetic model.

Chapter 5 discusses the findings of a geochemical investigation of tourmaline from the Big Wilson prospect, to determine if tourmaline could be useful as a vector towards high grade cassiterite zones.

Chapter 6 presents the results of the geochronological analysis. Chapter 7 discusses the main project findings. Chapter 8 provides a summary of conclusions and some suggestions for future research.

1.5 Project location

The Big Wilson prospect is located in the remote valley of the Wilson River at the confluence of the Wilson River and the Little Wilson River about 25km northwest of Tullah, north-west Tasmania (Fig. 1.1). Tin mineralisation at Big Wilson is related to a suite of Late Devonian granites which are associated with numerous significant Sn and W deposits in the region including the currently active Renison tin mine.

Access to the Big Wilson prospect site is by helicopter or via a 6 km walking track from the Pieman road. In good weather it takes about four hours to access the site on foot and all supplies must be either carried or flown in and out. As the walking track requires a major crossing of the Wilson River, which is impassable during periods of moderate to high rainfall, pedestrian access to the site is seldom used. Most exploration trips undertaken by Venture

Figure 3.1 Big Wilson prospect location and locations of significant nearby mines

Minerals are helicopter supported and very expensive, however, field visits for this research project were undertaken on foot. The site itself is located in temperate rainforest which also creates access difficulties due to thick vegetation and steep terrain. The limestone is recessive and almost entirely under cover and fresh outcrops of granite can usually only be found in creek beds.

1.6 Previous work

In 1876 Surveyor-General Sprent discovered osmiridium in the valley of the Big Wilson River. The deposits were originally thought to be palladium and there was little demand for osmiridium at the time, so economic extraction did not begin for another thirty years. By 1909 the growing market for osmiridium led to a period of intensive exploration and mining and by 1920 Tasmania was the world's largest producer of "free" osmiridium. The valleys of the Wilson River and the Little Wilson River were being worked primarily for alluvial osmiridium, although tin and minor amounts of gold were also recovered (Reid, 1921; Owen and Pfeifenberger, 2012). The remains of historic alluvial workings are abundant in the lower Little Wilson River area (Fig. 1.2) but official production figures are not available. Although historical operations in this area are mentioned in several sources (Reid, 1921; Brown, 1986; Owen and Pfeifenberger, 2012) but detailed records of development and production for the Little Wilson River area were not kept. The last reported production of osmiridium in Tasmania was in 1968 (Owen and Pfeifenberger, 2012) but the advanced state of regrowth noted during field visits would suggest most work in the area occurred during the early 1900s (Fig. 1.2).

The Reinson Mine is the largest currently operating tin mine in Australia and the only currently active tin mine in western Tasmania. However there are a number of other significant tin deposits near the Big Wilson prospect area (Table 1.1 and Fig. 1.1). The Mount Lindsay project is the closest of these deposits, is largely undeveloped and is 100% owned by venture minerals. If a tin processing plant is constructed at Mount Lindsay the discovery nearby tin deposits such as Big Wilson would add substantial value to that project.

Figure 1.2 Venture Minerals geologist Angelique Martin standing beside a trench from a network of alluvial workings from the early 1900s on a floodplain of the Little Wilson River. Note the extensive vegetation regrowth.

Table 1.1 Summary of significant tin deposits near the Big Wilson prospect. (Haythornthwaite, 2011; Venture Minerals, 2015)

Location	**Tonnage (Mt)**	**% Sn equivalent**	**Distance from Big Wilson**
Renison	26	1.46	10 km
Mt Bischoff	10.45	1.17	20 km
Cleveland	12.4	0.63	15 km
Mt Lindsay	13	0.7	5 km

In the early 1980s Renison Ltd. carried out a series of geological surveys around the lower Little Wilson River. Several Sn-W skarn targets were identified, however no exploration drilling was undertaken due to falling tin prices (Owen and Pfeifenberger, 2012). In 2011 the exploration lease was acquired by Venture Minerals. The first drilling program discovered high-grade tin (35.4m at 1% Sn including 4m at 4.56% Sn (Venture Minerals, 2012)). Venture Minerals named the project site "Big Wilson" and continued helicopter-supported drilling of a further 12 diamond drill holes, which delineated a steeply dipping Sn-W skarn system. However, by 2013 further exploration was suspended because the additional holes

encountered much lower Sn grades and the work was no longer considered economically viable (Venture Minerals, 2013). After the drilling program was suspended the company focused its resources on other projects and very little additional work was put into the Big Wilson prospect between mid-2013 and the start of this project in early 2014. This thesis represents a second look at the initial survey results.

Chapter Two Regional geology

2.1 Introduction

The Big Wilson prospect is part of an economically significant suite of tin deposits associated with the intrusion of granites across northern Tasmania during the Devonian (Fig. 1.1, Table 1.1). Three notable mines of this type are Renison (Kitto, 1994), which is currently the largest operating tin mine in Australia, located 10 km to the south-east of the Big Wilson prospect; Mt. Bischoff (Halley and Walshe, 1993), 20 km north-east of Big Wilson, which is currently in a care and maintenance phase, but was one of the largest tin mines in the world in the late 1800s, and the inactive Cleveland Mine, 15 km north of Big Wilson. This was the world's second largest tin-producing mine in the 1970s, and operated from 1968 to 1986 (Jackson et al., 2000).

2.2 Stratigraphy

The Big Wilson prospect is situated in the Dundas Trough of western Tasmania, close to the intersection of the western limb of the Huskisson syncline, the Meredith Granite and the Wilson River Ultramafic Complex (Fig. 2.1). The Big Wilson skarn is hosted by the calcareous Ordovician-Silurian Gordon Group where it is intruded by the Devonian Meredith Granite.

2.2.1 Oonah Formation

Western and central Tasmania is underlain by a multiply deformed continental basement, the eroded remnants (Rocky Cape and Tyennan Region) of the Penguin Orogeny (Corbett et al., 2014). The oldest rocks in the region are the clastic meta-turbidites of the Oonah Formation which consists of repeated packages of interbedded siltstone, quartz sandstone, greywacke and black siltstone (Brown, 1980). This highly deformed package has been interpreted to represent a series of shallow to deep sea turbidite sequences on a continental shelf during the Neoproterozoic (Corbett et al., 2014; Haythornthwaite, 2011).

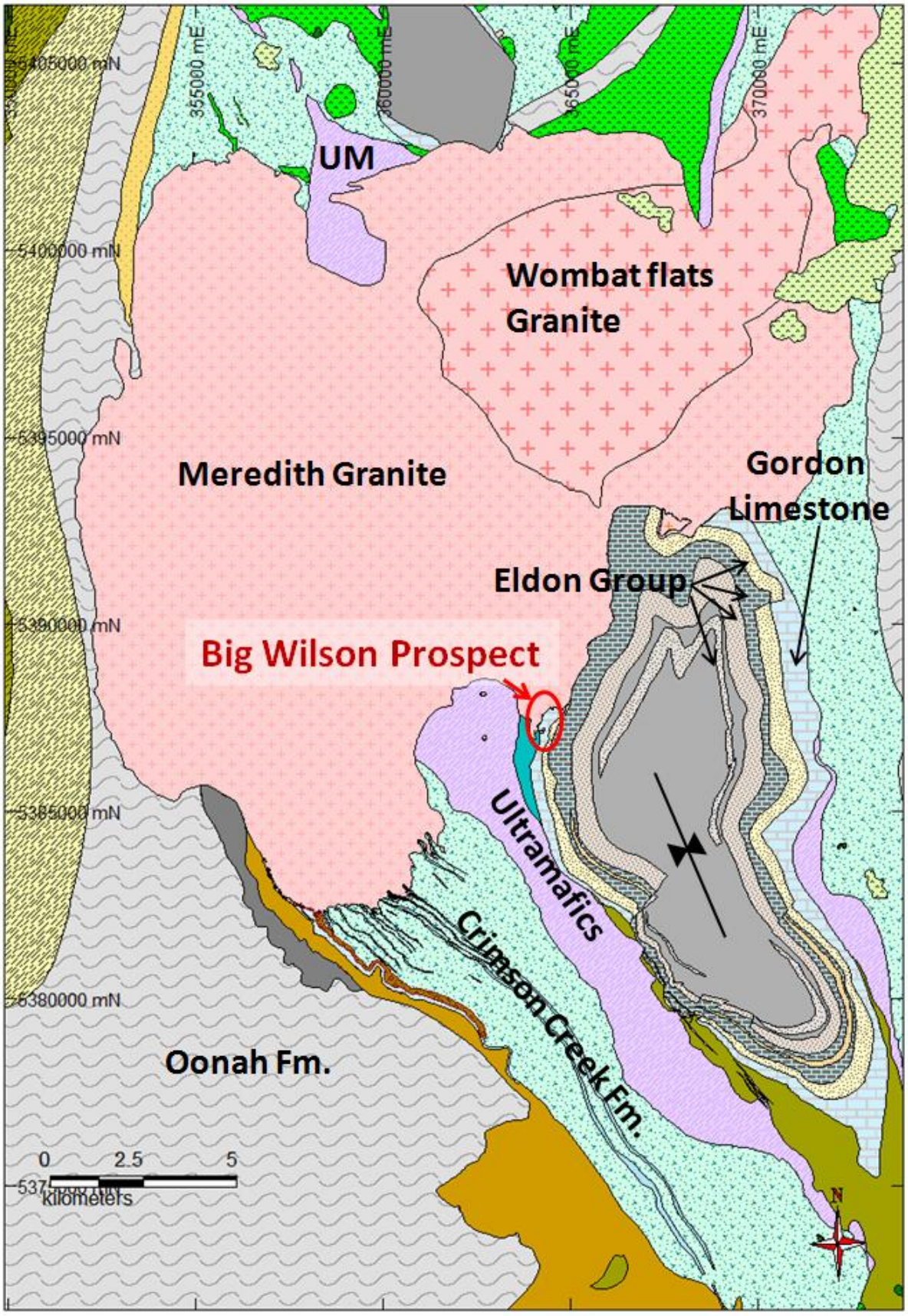

Figure 2.1 Regional geology of the Big Wilson prospect area. Datum MGA Z55

2.2.2 Success Creek Formation

During the Late Neoproterozoic – Early Cambrian, significant continental extension produced the Dundas Trough (Fig. 2.2). Three sedimentary and volcanic successions occur through the trough as separate belts. These are the Success Creek Group, Crimson Creek Formation and Dundas Group.

The Eocambrian Success Creek Group is a shallow water rift sequence which

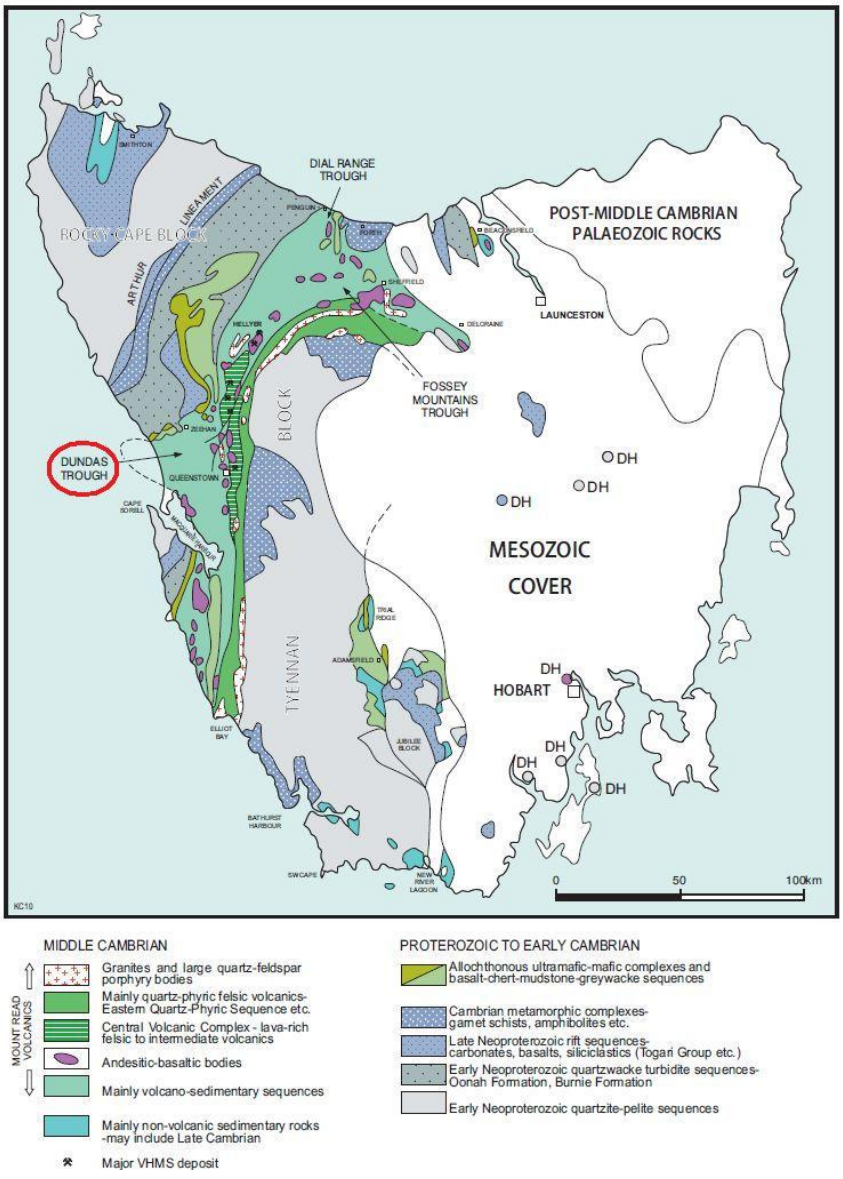

Figure 2.2 Location of the Dundas Trough in NW Tasmania (from Corbett et al., 2014).

unconformably overlies the Oonah Formation on the western margin of the Dundas Trough (Brown, 1986). A shallow marine sedimentary sequence with four distinct formations is described by Brown (1986) over a thickness of at least 950m (Fig. 2.1). The first of these is the basal formation, which contains poorly sorted, immature, polymict conglomerate with sandstone lenses. The Dalcoath Formation gradationally overlies the basal formation and is characterised by interbedded shallow-water quartz sandstones, siltstones, pebbly sandstone and conglomerates. The Dalcoath Formation is the host unit for most of the tin mineralisation at Renison (Kitto, 1994) and grades into the Renison-Bell Formation, which is characterised by laminated mudstone, siltstones, minor sandstone and conglomerate units. The final section is the "Red Rock" member, which is a hematitic chert-mudstone sequence and represents the top of the Success Creek Group (Brown, 1986).

2.2.3 Crimson Creek Formation

The deep-water early Cambrian Crimson Creek Formation conformably overlies the Success Creek Group (Fig. 2.1). Brown (1986) describes the Crimson Creek Formation as comprised of volcaniclastic lithic wacke and minor tuffaceous wacke horizons, monotonous, interbedded, laminated siltstone and mudstone, tholeiitic basalt flows and carbonate units. The clastic units show most of the characteristics of typical turbidite flows. The laminated siltstone and mudstone units may be calcareous, range in grainsize from clay to silt grade and commonly contain multiple truncated cross-laminations. There are no known fossils in the Crimson Creek Formation (Brown, 1986). At Mt. Lindsay the carbonate units of the Crimson Creek Formation host the skarn and the tin mineralisation. The conformable relationship between the Success Creek Group and the overlying turbiditic sequences of the Crimson Creek Formation indicates a gradual deepening of the depositional basin (Brown, 1986).

2.2.4 Dundas Group

The Dundas Group does not come to the surface in the immediate vicinity of the Big Wilson Project but does underlie the eastern part of the area. The Dundas Group is a marine sedimentary sequence that consists of two distinct successions that are presently juxtaposed by faults (Brown, 1986). The contact between the Early Cambrian Crimson Creek Formation and the Cambrian Dundas Group is also faulted. The basal sequence of the Dundas Group is sparsely fossiliferous and consists of laminated and thinly-bedded siliceous sandstones, siltstones and mudstones which are gradationally overlain by a sequence of mass-flow

conglomerate. The conglomerate sequence is conformably overlain by a laminated and thinly-bedded sandstone, siltstone and mudstone sequence followed by a turbiditic chert conglomerate and sandstone sequence. The upper succession is a fossiliferous turbidite sequence (Brown, 1986) (Corbett et al., 2014).

2.2.5 Wilson River Ultramafic Complex

Radiometric dates for the Wilson River Ultramafic Complex (WRUC) (Fig. 2.1) are not available but a Neoproterozoic to early Cambrian age has been estimated according to stratigraphic constraints (Brown, 1986; Corbett et al., 2014) . The WRUC is in fault contact to the west by the Neoproterozoic Crimson Creek Formation and to the east by late Cambrian-Early Devonian rocks which comprise the western limb of the Huskisson syncline (Fig. 2.1). The WRUC is truncated to the north by the Devonian Meredith Granite and locally slivers of the WRUC are present in the Ordovician Gordon Group near the margin of the Meredith Granite at the Big Wilson Project site. Brown (1986) described two distinct ultramafic successions within the WRUC:

1) The Layered Dunite-Harzburgite succession (LDH), which consists of well layered dunite, orthopyroxene-bearing dunite and harzburgite. The layering is 25-400mm averaging around 150mm and defined by sharp phase contacts, primary mineral alignment of orthopyroxene and spinel and a later foliation from tectonic flattening of olivine grains. Orthopyroxene and olivine appear as cumulate phases and chromite as an accessory phase is most abundant in the dunite layers. The alluvial osmiridium worked in the area is associated with the LDH ultramafic bodies (Brown, 1986) (Corbett et al., 2014).
2) The Layered Pyroxenite-Dunite (LPD) succession, which is dominated by orthopyroxene alternating with serpentinised dunite and occurs as fault bounded blocks with serpentinite sheaths. Its layering is thinner than the LDH succession ranging between a few millimetres up to 150 mm but generally < 20 mm. The most common layering sequences are dunite – orthopyroxenite – dunite - orthopyroxenite followed by dunite – orthopyroxenite - olivine and orthopyroxenite - orthopyroxenite (Owen and Pfeifenberger, 2012). The LPD has a smaller proportion of magnesian olivine and a higher proportion of clinopyroxene and chrome spinels are more aluminous (Brown, 1986; Corbett et al., 2014).

Brown (1986) observed that the LDH and LPD are separated by serpentinite faults and most of the exposed WRUC is the LDH sequence.

2.2.6 Gordon Group

The Ordovician Gordon Limestone Group is a well bedded and highly fossiliferous limestone succession with occasional interbedded laminated to thinly bedded mudstone units (Rice, 1985). The Gordon Limestone mostly crops out around the edges of the Huskisson Syncline as well as a few other locations in association with the basal Eldon Group (Fig. 2.1). Brown (1986) defines the Gordon Limestone Group as a sub-group of the Eldon Group. Although the original thickness of the Gordon Limestone group is not known due to Devonian deformation, it has been measured between 165-600m in various locations (Brown, 1986). The transition between the Ordovician Gordon Limestone Group and the Silurian-Devonian Eldon Group is structurally conformable, however, biostratigraphy implies a disconformity in sedimentation between the Middle Ordovician and Early Silurian indicating a period where sedimentation lapses (Brown 1986).

2.2.7 Eldon Group

The Silurian-Devonian Eldon Goup is broadly divided into four formations. The basal formation is the Crotty Formation which is dominated by white and pink quartz sandstone with minor granule and pebble conglomerate, siltstone and mudstone units. Bedding is typically 2-30cm but has been measured up to 6m (Brown, 1986). The Crotty quartzite (Fig. 2.8b) is highly resistant and often forms regional topographic highs. In the vicinity of the Big Wilson Prospect the Crotty formation of the Eldon Group is in conformable contact with the Gordon Group limestone.

The next formation in the Eldon Group sequence is the Amber Formation which is dominated by well bedded siltstones, mudstones and shale. This formation is interrupted in two places with a notable 75-100m limestone sequence and a 75-100m quartz sandstone sequence. The upper two formations in the Eldon Group are not observed in the Big Wilson prospect area but consist of a Quartz sandstone sequence and a sandstone – siltstone – mudstone sequence (Brown, 1986). The Gordon – Eldon Group successions are consistent with a prolonged period of shallow marine sedimentation.

2.2.8 Meredith Granite

The Meredith Granite is part of a suite of granitic intrusions across northern Tasmania during the Devonian. It is the largest (~225km^2) exposed granite body in western Tasmania and together with the Wombat Flat Granite comprise the Meredith Batholith (Kositcin and Everard, 2013). The Meredith Granite is a fractionated I-type alkali feldspar granite and has been dated to 372.2 ±1.9 Ma (Kositcin and Everard, 2013) which is within the margin of error for the date published for the age of the less felsic Wombat Flats Granite (Black, 2005). The Meredith Granite is a biotite-rich equigranular to porphyritic intrusive granite with roughly equal proportions of orthoclase and plagioclase feldspars and abundant tourmaline nodules.

2.3 Structural evolution

The two main deformation events responsible for shaping the surface geology of the Big Wilson prospect region are the Cambrian Tyennan Orogeny (Figs. 2.3 and 2.4) and the Devonian Tabberabberan Orogeny (Fig. 2.5).

2.3.1 Tyennan Orogeny

During the first stage of the Early Cambrian Tyennan Orogeny (c. 515-510 Ma) northwest Tasmania went through a period of collision and compression. Crawford and Berry (1991) suggested that there was a collision with an oceanic arc system (Fig. 2.4) but Moore et al. (2014) postulated a collision with multiple micro-continental fragments (Fig. 2.6). The second stage of the Tyennan Orogeny involved the collapse of the margin, development of a foreland basin and a rifting event that produced active subsidence and created the Dundas Trough. The present day Big Wilson prospect lies entirely within the Dundas Trough. Figure 2.4 shows the location of the Dundas Trough in NW Tasmania.

There is some uncertainty in the literature about the origin of the WRUC. Crawford and Berry (1992) state that the WRUC, along with other nearby mafic-ultramafc complexes were once part of an ophiolite sheet emplaced during the first stage of the Tyennan orogeny. However Corbett et. al (2014) state that all evidence supports Brown (1986) who postulated that the WRUC was not an ophiolitic emplacement during the first stage of the Tyennan Orogeny, but instead was a boninitic intrusion into the Dundas Trough during the second stage of the Tyennan Orogeny. This was followed by tectonic re-emplacement prior to the

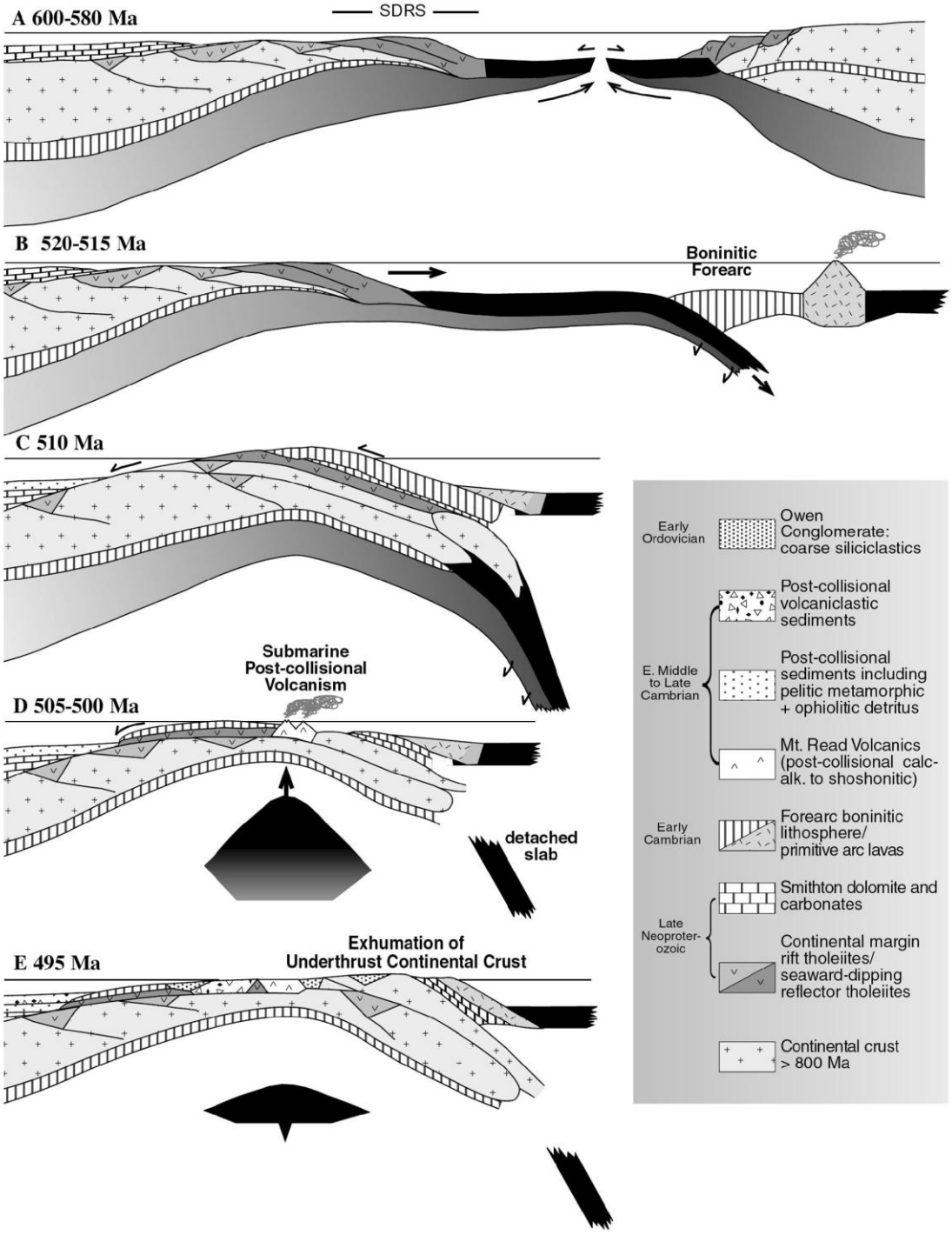

Figure 2. 3 Stages of the Tyennan Orogeny from Crawford et al., 2003)

Devonian. This theory is largely based on observations that the ultramafics were cumulates, orthopyroxene was prevalent over clinopyroxene and the units lacked protoclastic textures and stratigraphically associated sheeted dyke and pillow lava units typical of oceanic crust

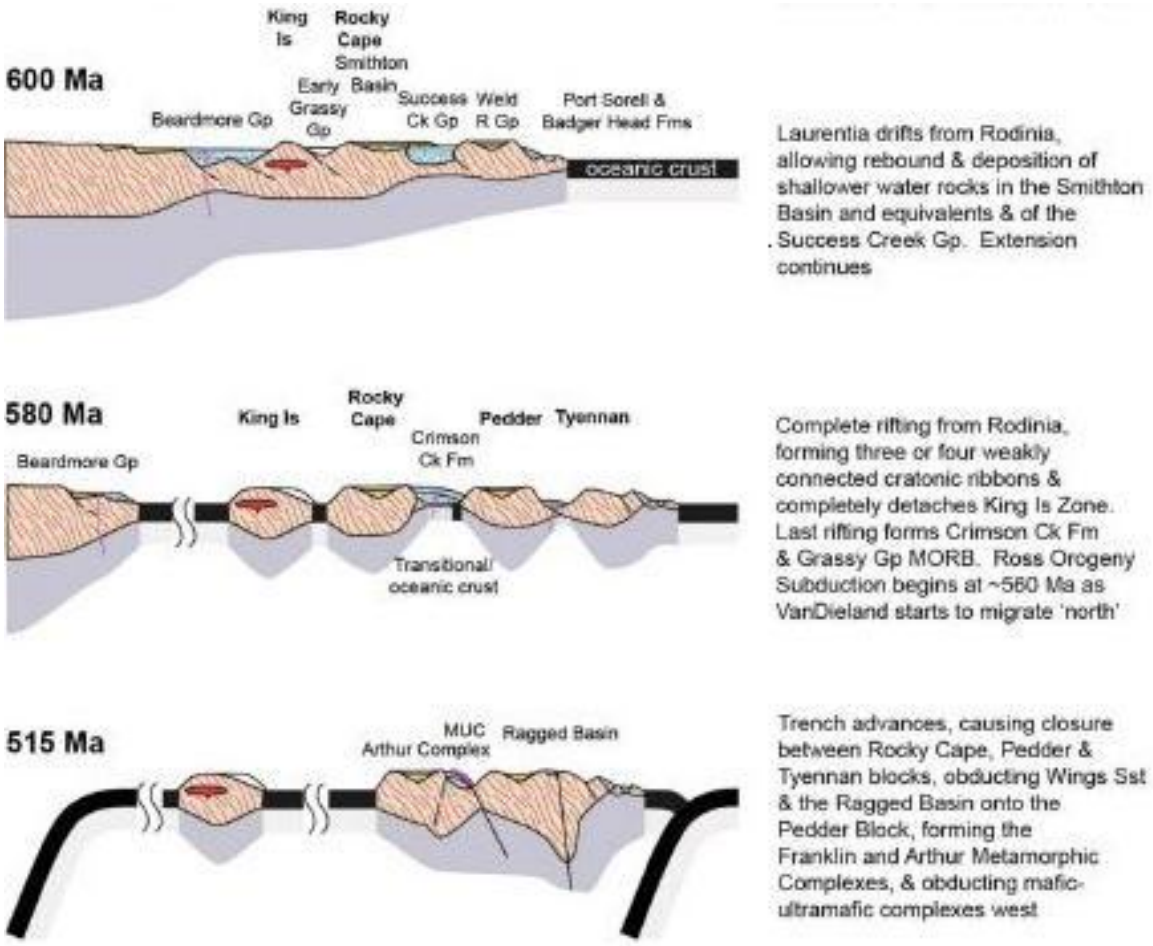

Figure 2.4 Moore (2014) model of the Tyennan Orogeny

which suggests an intra-oceanic forearc setting. Moore (2014) proposes a model (Fig. 2.4) that does not require the arc origin of Crawford and Berry (1992) but rather suggests that the mafic-ultramafic complexes with oceanic and transitional crust affinities were formed between micro-continental fragments that separated during Neoproterozoic extension and were then inverted during the Tyennan Orogeny, when individual ribbons of mafic-ultramafic units were amalgamated to their current geometries (Moore et al., 2014). This interpretation of the formation of the WRUC is significant in that it marks a change in tectonic environment from one of crustal extension to compression.

2.3.2 Tabberabberan Orogeny

In the Middle Devonian Orogenic folding associated with the Tabberabberan Orogeny created broad NW-SE and NNE-SSW trending fold structures (Fig. 2.4). The Huskisson syncline (Fig. 2.1) formed at this time. Late in the Tabberabberan Orogeny a series of granite

intrusions including the Meredith and Wombat Flat granites formed in these folded rocks over much of northern Tasmania (Everard et al., 1991). During magmatic cooling of the granite exsolution of hydrothermal fluids highly enriched in tin, tungsten, iron and sulphides is considered the primary source for the suite of economic Sn-W deposits in the area.

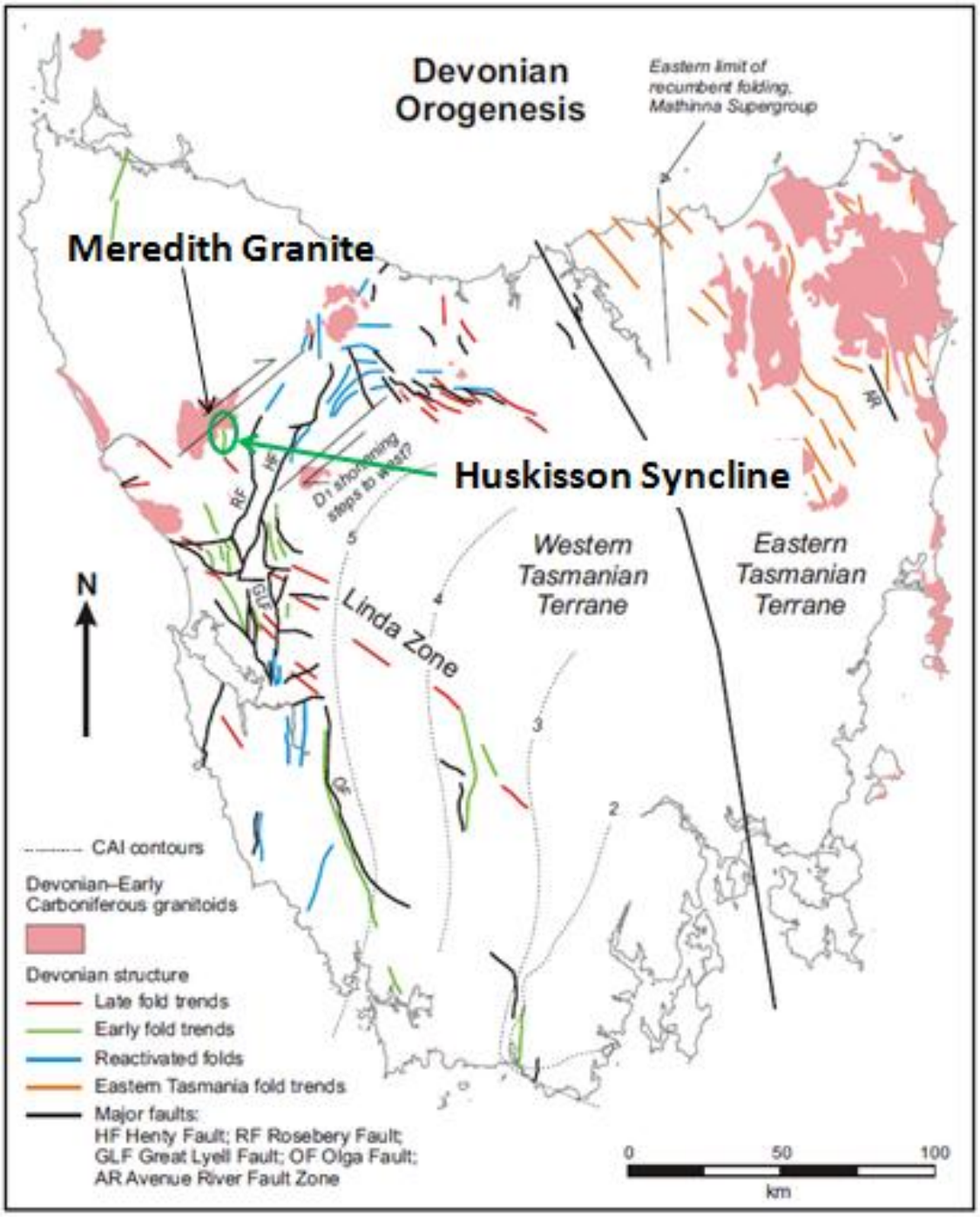

Figure 4.5 Devonian Tabberaberan deformation in Tasmania (Seymour et al, 2007)

Chapter Three Local geology

3.1 Overview

The Big Wilson prospect targets a Sn-W skarn hosted in a 800m N-S by 300m E-W section of limestone in the Gordon Group which has been intruded by Meredith Granite (Figs. 3.1 and 3.2). A Northeast trending skarn has been identified through soil geochemical surveys followed up by diamond core exploration drilling. To date only a single skarn has been identified but it may be discontinuous, or part of multiple skarns in the area. The skarn is oriented striking Northeast approximately parallel to bedding in the limestone. Almost all of the skarn is under cover but a small zone of gossinous subcrop can be found at the north end of the skarn. The bulk of the high grade mineralisation has been found in the northern region with an increased predominance of ultramafic units restricting skarn development in the south. The skarn is at least 800m long and up to 50m wide.

3.2 Field mapping methods

The Big Wilson Prospect site was mapped during two field expeditions. The site was accessed via the walking track as the costs associated with helicopter access were prohibitive. All supplies were carried in and out. The first field expedition involved three days of mapping in November 2014 followed by seven days in February 2015. On each expedition the author was accompanied by a staff member from Venture Minerals for safety and assistance. During the second expedition an additional team of two staff members from Venture Minerals was employed to help carry supplies in on the first day and samples out on the last day.

The primary aim of the field mapping was to investigate the geometry of the quartz-tourmaline veins in the Meredith Granite to determine if the orientation and distribution of the high grade veins followed a regional pattern. A number of dykes were encountered and recorded and some time was spent looking for evidence of suspected fault locations although none were discovered.

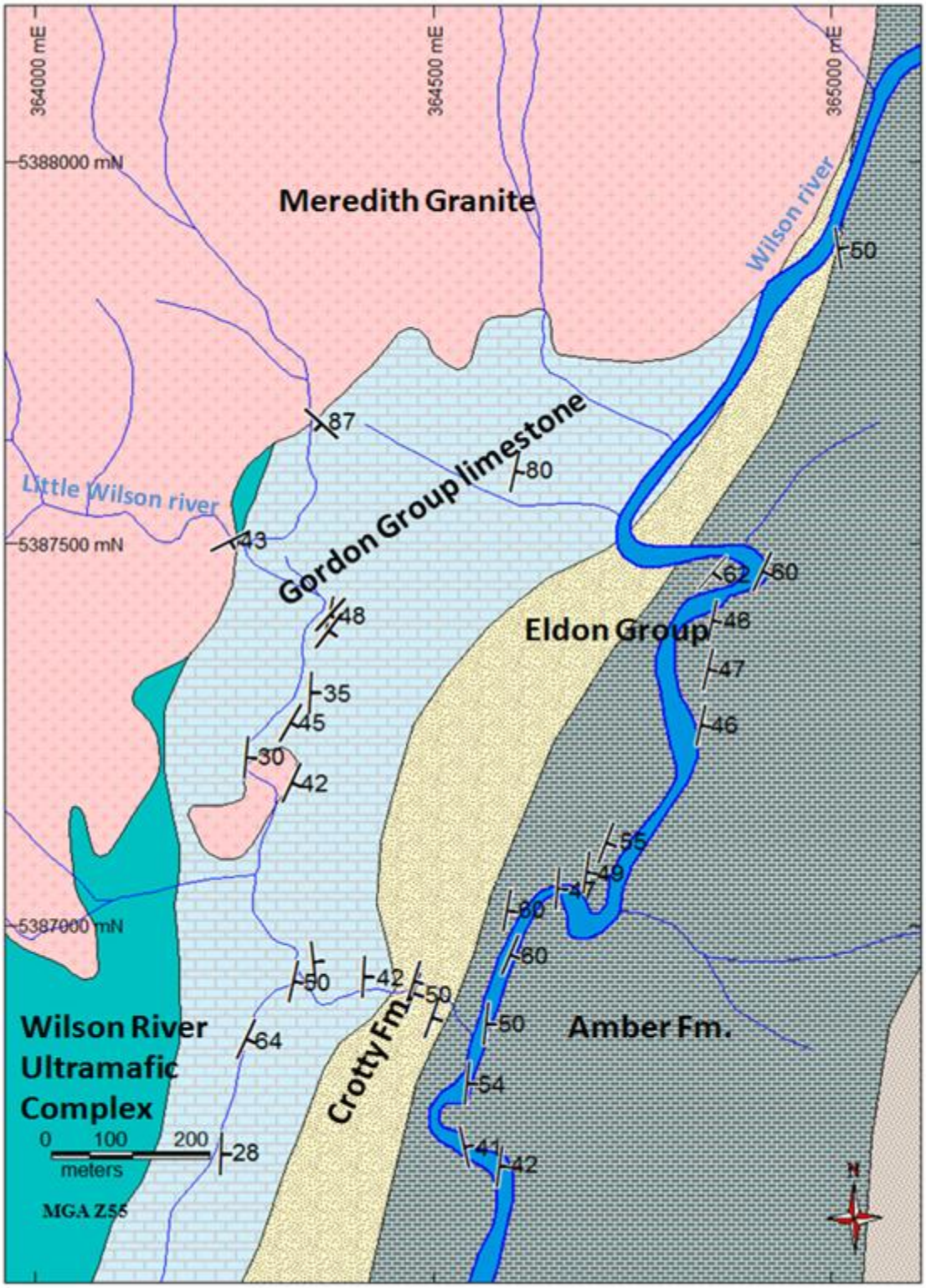

Figure 3.1 Geology of Big Wilson prospect area

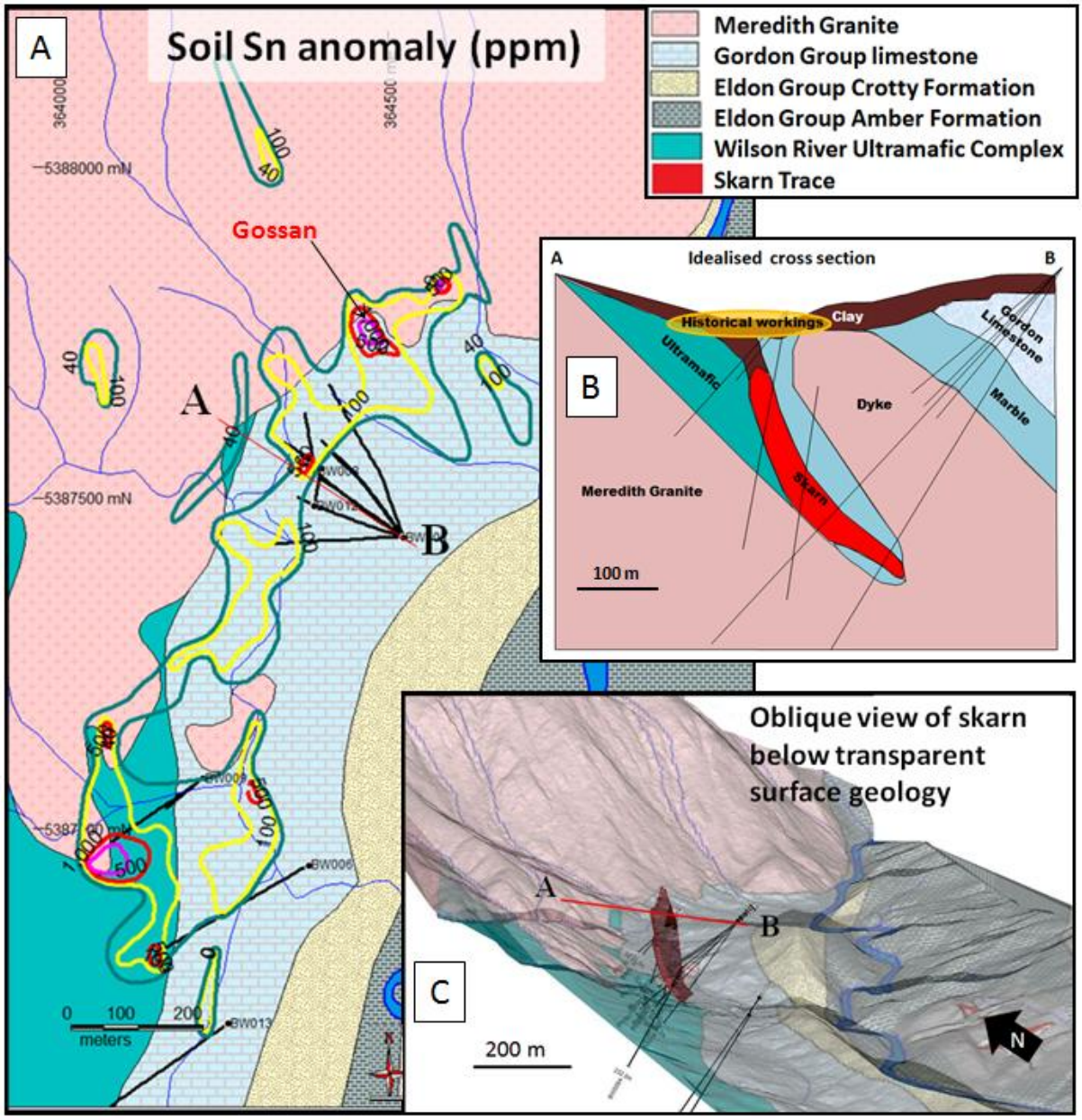

Figure 3.2 A) Soil Sn anomaly (ppm) B) Vertical cross section through the skarn C) Oblique 3-D view of the Big Wilson Skarn. Surface geology has been draped onto a LIDAR DEM and made 50% transparent so the skarn (outlined in red) is visible beneath the surface. The skarn most likely continues further south than shown.

Figure 3.3 The problem of lack of fresh outcrop in the temperate rainforest is illustrated by moss covering this potential rock exposure.

Initial field work was undertaken using the Anaconda mapping method (Einaudi, 1997; Brimhall et al., 2006), which was originally developed for mapping vertical pit walls. This method also works well in plan view if there are sufficient exposures to get a wide spatial data distribution. The Anaconda method works best when multiple types of data are recorded on different layers and all the layers can be plotted at the same scale. At Big Wilson the major lithological boundaries had already been documented by Venture Minerals and most contacts were under cover and interpreted through geophysics and topography, so a geological map, based on company data, was used as a base layer. With only one primary feature to map, (the quartz-tourmaline vein orientations) the multi-layered Anaconda approach was not practical for this purpose as the geochemical data from the samples could not be added in the field. The dykes that were encountered on a small stretch of the Little Wilson River could not be plotted on the same scale as the quartz – tourmaline veins. Therefore the Anaconda method was abandoned for practical reasons in favour of simply recording the data in a weatherproof notebook.

Figure 3.4 Collecting thin quartz-tourmaline veins on granite. Some samples come out intact and others are collected as powder.

All locations were recorded using a Garmin 620x hand- held GPS and all structural measurements were made using a standard Sunto geological compass. A total of 35 rock chip samples of approximately 200 – 300g each were collected using a geological hammer or sledge hammer and chisel, and these were labelled and stored in geological sample bags. A list of samples, descriptions (Appendix 2), photographs (Appendix 8) and assay results (Appendix 3) are contained in the electronic appendix.

Due to rainforest vegetation fresh outcrops of *in-situ* bedrock were best accessed in creek or river beds where periodic flooding has kept the exposures clean (Figs. 3.3 and 3.4). Sample dilution was a significant issue when obtaining of many of the quartz-tourmaline veins. Hammering often produced chips, flakes and powder (Fig. 3.4) where the wall rock could not

be separated from the target vein material. In cases where the vein could be separated it was difficult to separate all the wall rock without losing significant portions of the target vein minerals. Therefore all the samples sent for wholerock geochemistry contain some amount of wall rock dilution.

Two-dimensional surface spatial modelling was undertaken using MapInfo software and used to create surface maps of the project area. Three-dimensional subsurface modelling was performed with Micromine software and used for the creation of vertical cross sections.

3.3 Stratigraphy

Tertiary alluvial deposits and swamps cover much of the valley floor in the vicinity of the Big Wilson prospect. The Meredith Granite and the quartzite units of the Eldon Group are highly resistant rocks that form major topographical features while the Gordon Limestone is recessive and underlies much of the Tertiary sedimentary deposits. The Wilson and Little Wilson Rivers tend to follow the strike of the Gordon Group.

Quaternary formations are localised to swamp, marsh and alluvial deposits confined to valley floors and the occasional patch of fluvioglacial conglomerates, gravel and sand.

3.3.1 Meredith Granite

The Meredith Granite is considered to be the source of the enriched hydrothermal fluids that created the mineralisation. In the prospect area the unaltered granite (Fig. 3.5) tends to be equigranular with white to cream and occasionally pink feldspar crystals up to 15mm, quartz and biotite. A series of medium-grained granite dykes are observed in the bedrock of the Little Wilson River which contain an identical composition to the surrounding granite but a noticeably finer grain size (Table 3.1). The dominant quartz-tourmaline veining found in the granite is discussed in detail in chapters 4 and 5.

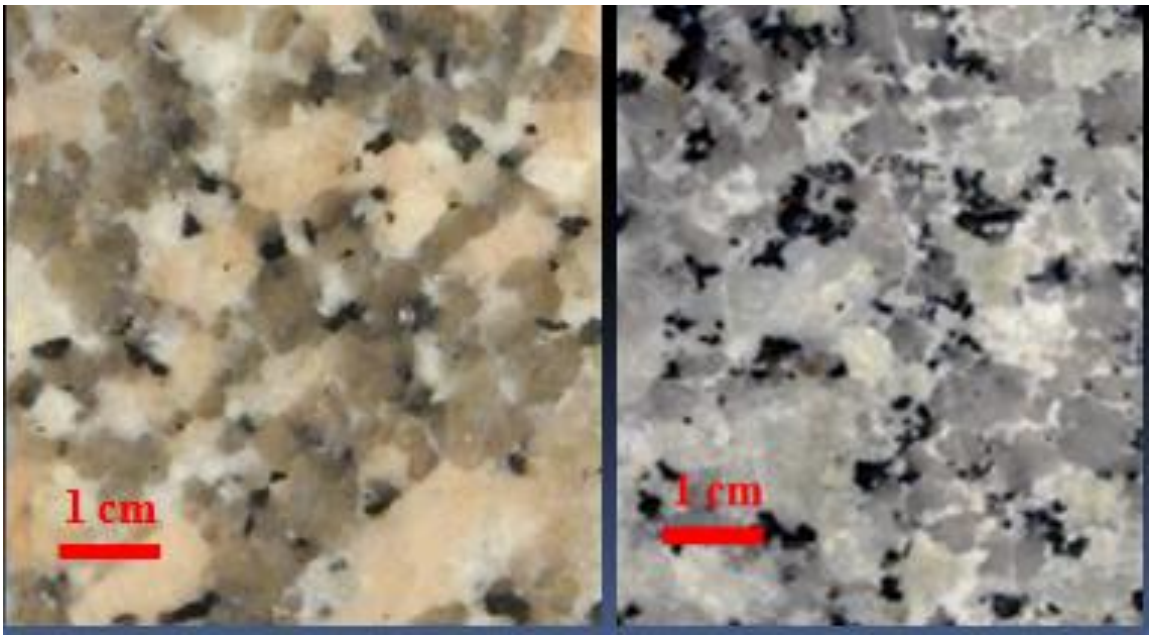

Figure 3.5 Various colours of the Meredith Granite observed at Big Wilson

Table 3.1 Dykes observed in the Meredith Granite

Site ID	Easting MGA Z55	Northing	Width (m)	Dip	Facing	Comments
THBW007	364246	5387484	2-3	70	235	Medium-grained igneous banding within a coarse-grained granite
			2-3	70	050	
			2-3	70	110	
			2-3	62	233	
			2-3	75	118	
THBW008	364224	5387530	2-5	62	252	Medium-grained igneous dykes in 10mm equigranular granite
			2-5	50	255	
			4-5	84	030	
THBW009	364175	5387500	2-3	47	208	2-3m fine-grained dykes with 10-20cm dyke swarms
			2-3	24	038	
THBW019b	364598	5387985	0.3	30	040	Manganese rich medium-grained igneous dyke. Only dyke found off the little Wilson River
THBW024	364053	5387560	5-8m	?	?	Unable to access – observed at a distance

3.3.2 Gordon Group Limestone

The Ordovician Gordon Group limestone is the host for the mineralised skarn system. In the vicinity of the Little Wilson River there is a well-bedded fossiliferous limestone unit up to 200m thick dipping steeply to the southeast (Fig 3.1). The limestone unit is mostly massive with occasional thinly bedded mudstone layers.

Most of the Gordon Group limestone has been recrystallised to a grey marble (Fig. 3.6) in the vicinity of the granite intrusion. The Gordon Group rocks are recessive and mostly under cover but a few outcrops can be found in creek beds where steep SE dipping bedding can be measured. Brown (1986) reports a 600mm conformable succession of "grey pug" in the vicinity of the Little Wilson River that conformably connects the Gordon Group limestone with the Crotty Formation of the Eldon Group.

Figure 3.6 Drill core from the Gordon Limestone

3.3.3 Ultramafics

The Neoproterozoic-Cambrian Wilson River Ultramafics (Fig. 3.7) are a dark green pyroxene-rich medium to very fine-grained gabbro with plagioclase and clinopyroxene being the major constituents readily identifiable by eye. The exposed sections of the WRUC are dominated by the Layered Dunite-Harzburgite sequence. In drill core white carbonate veins are common. The WRUC is considered the source for the alluvial osmiridium that was mined in the area in the early 1900s.

3.3.4 Eldon Group

The Silurian Crotty Formation (Fig. 3.8) is a white to cream fine-grained quartzite with thin to medium beds (5-50cm) dipping steeply to the southeast. Brown (1986) reported sighting

Figure 3.7 Pyroxenite from the Wilson River Ultramafic Complex

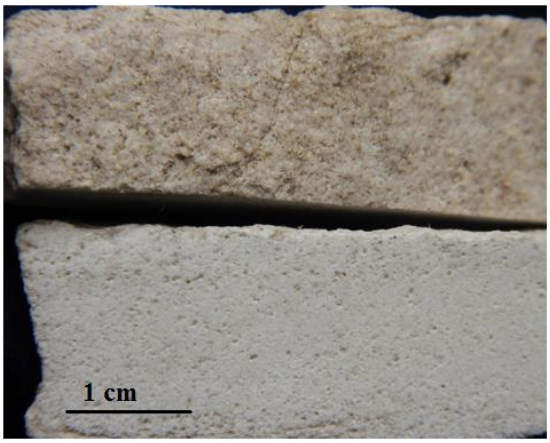

Figure 3.8 Quartzites of the Silurian Crotty Formation

truncated cross-bedding in the area but none were identified during the fieldwork component of this project. This unit does not contain mineralisation. Bedding orientation is roughly the same as for the Gordon Group limestone and represents the locally steeply SE dipping western limb of the Huskisson Syncline.

3.3 Structure

Although the presence of faults in the Eldon Group that extend into the Gordon Limestone have been inferred through topographic interpretation no direct evidence of fault structures were found on the surface during local mapping. The medium grained granite dykes observed in a small stretch of the little Wilson River and described in table 3.1 were not observed elsewhere in the prospect area. Although all contacts with the ultramafic units are assumed to be faulted, exposed contacts were difficult to find in the field and fault structures were not directly observed.

Chapter Four Alteration and mineralisation

4.1 Introduction

This chapter describes the alteration and mineralisation assemblages observed in drill core and at surface around the Big Wilson prospect site. It includes a short summary of the different methods employed to document the observed alteration, followed by a description of the paragenesis and alteration mineral assemblages, and details of a proposed paragenetic model for the skarn and the granite alteration.

4.2 Analysis methods

4.2.1 Whole rock geochemistry

Seventeen rock chip samples were sent to ALS Chemex laboratories in South Australia for whole rock geochemical analysis. Major and minor elements including S, total Sn and W, from both drill hole and surface rock samples, were determined by X-Ray Fluorescence (XRF) spectroscopy (using ALS method XRF15b). Trace elements and acid-soluble Sn were measured by inductively coupled plasma atomic emission spectroscopy (ICP-AES) after dissolution using a four acid digestion method (ALS method ICP61). Soil samples from previous investigations by Venture Minerals were analysed for total Sn by a combination of ICP61 and MS62 and by XRF05. Technical details of the methods used by ALS Chemex are provided in Appendix 3, together with the full elemental results.

4.2.2 Short wave infrared (SWIR) spectroscopy

Short wave infrared (SWIR) data were collected from seven diamond drill holes, totalling 1,996 m of drill core and 332 rock chip samples. Data were obtained using an ASD TerraSpec instrument to measure the spectral reflectance at 1m intervals in drill core. TSG (The Spectral Geologist) software was used to process the SWIR data and to create scalars for specific spectral responses. In the context of this project, SWIR data were particularly useful for delimiting white mica alteration. Full results from the TerraSpec SWIR investigation are provided in Appendix 12.

4.2.3 CSIRO Hylogger™

Visible near infrared (VNIR), short-wave infrared (SWIR), and long-wave infrared (LWIR) spectral reflectance data was obtained at 8mm intervals from 513m of drill core, comprising

subsets of five diamond drill holes (Table 4.1) using CSIRO's 3rd generation Hylogger™ instrument located at Mineral Resources Tasmania (MRT) core storage facility in Mornington, Tasmania. Core samples were shipped from Tullah to Mornington for spectral analysis and data processing at MRT. Visible near infared, SWIR and LWIR spectroscopy were used to identify alteration mineralogy based on the hyperspectral response of mineral groups. Hylogger data was processed using The Spectral Geologist (TSG) software with spectral libraries for minerals in both SWIR and LWIR. Core was prepared by the author and the Hylogger was operated by Mr. Peter Harding. Data processing and generation of spectral scalars was undertaken by Dr. David Green of Mineral Resources Tasmania. A full compilation of the spectral data and scalars are provided in Appendix 11.

Table 4.1 Core intervals analysed by CSIRO Hylogger™

Hole	From (m)	To (m)	Metres of core
BW001	150	270	120
BW004	170	300	130
BW005	220	290	70
BW007	170	250	80
BW008	67	130	63
BW010	50	100	50

4.2.4 Scanning Electron Microscopy (SEM)

Petrographic analyses of polished thin sections and laser mounts were carried out using two different scanning electron microscopes (Hitachi SU-70 FE-SEM and FEI SEM) located at the Central Science Laboratory (CSL) at the University of Tasmania. Complete SEM results are provided in Appendix 5.

4.2.5 Optical microscopy and petrography

Twenty-five new polished thin sections and 17 1 inch round polished mounts were prepared from representative samples of the skarn and granite alteration stages. Venture Minerals provided a further 40 thin sections to supplement this sample set. These samples were used to investigate the mineral assemblages and alteration associations to assist with the development

of the paragenetic scheme, discussed in Section 4.3. Thin section logs and photographs are provided in Appendix 13.

4.2.6 Subsurface structural analysis

Subsurface structural measurements were made from selected intervals of diamond drill core which were fully oriented oriented during drilling. Orientation of drill holes was made by lowering a red chinograph wax pencil mounted on the tip of a spear down the drill hole at irregular intervals determined by Venture Minerals to mark the downward facing segment of core before being drilled out. After drilling the core was reassembled by staff at the Venture Minerals core shed in Tullah and structural measurements were taken using a hand-held protractor and cylindrical sleeves to measure the alpha and beta angles of structural features. The true orientations of the structures were calculated on a spreadsheet using the geographic survey data from the drill hole. As a test of accuracy structural measurements made by Venture Minerals from hole BW003a were measured by the author to confirm consistency between measurements. The subsurface structural data is provided in Appendix 4.

4.2.7 Reviewing and sampling drill core

Sections of 13 diamond drill core holes were inspected and sampled for petrographic analysis and the original core logs were reviewed to assist with understanding the local geology and to establish logging accuracy. Petrographic samples were obtained from drill core using a diamond saw at the Venture Minerals core shed in Tullah. Logged mineral abundances were used in the creation of the spatial models.

4.2.8 Scanning Electron Microscopy (SEM)

Two different scanning electron microscopes (SEM) located at the central science laboratory at the University of Tasmania were used to aid in mineral identification and petrographical analysis. They were the FEI MLA650 environmental scanning electron microscope and the Hitachi SU-70 field emission scanning electron microscope. Full SEM results are provided in Appendix 5

4.2.9 Laser Raman

Laser Raman was used to identify the mineral vonsenite. A Renishaw inVia Raman microscope located at the central science laboratory at the University of Tasmania was used to analyse one polished thin section and two 1 inch polished round mounts containing

vonsenite. Electron beam-based microscopes, such as the FESEM and EMPA are unable to positively identify light elements such a boron so the laser Raman was used to positively identify this borate mineral because it works by interacting with molecular vibrations of the crystal structure to provide light reflection patterns by which a specific mineral can be identified, rather than interacting with individual atoms the way the electron beam instruments do. This means that vonsenite can be identified by its crystal structure rather than by the ratio of its elemental constituents. Full results of the laser raman investigation are provided in Appendix 6.

4.3 Skarn paragenesis

The skarn paragenetic scheme has been prepared as part of this study in order to describe the sequence of alteration in the Gordon Limestone unit located to the east of the Meredith Granite (Fig 3.2). Using the above analytical techniques, the skarn alteation has been divided into four parageneic stages (Table 4.2). The first two stages represent prograde alteration of the limestone unit. The third-stage is a series of retrograde skarn assemblages. The final stage consists of cross cutting late stage veins. The paragenetic model for the development of skarn alteration in the limestone is described separately from the alteration observed in the granite due to the absence of difiniative cross-cutting relationships observed between alteration assemblages developed in these two units. Although it is highly likely that the genesis of alteration in the limestone and the granite are linked, direct evidence from cross cutting relationships between alteration in the granite and the skarn are inconclusive. Speculation on these relationships are therefore deferred to the discussion section of the chapter.

Table 4.2 Skarn paragenesis stages

Skarn Stage	**Type**	**Mineral association**
1	Limestone recrystallisation	Marble
2	Prograde calc-silicate	Pyroxene ±garnet ± vesuvianite
3	Retrograde	Amphibole ± magnetite ± vonsenite ± vesuvianite ± pyrrhotite ± pyrite ± chalcopyrite ± biotite ± siderite ± cassiterite ± scheelite ± chlorite ± tourmaline
4	Hydrothermal veining	Quartz ± calcite ± siderite ± cassiterite ± chlorite

4.3.1 Skarn stage 1:

Skarn stage 1 alteration has caused recrystallization of the original limestone to a massive calcite (Fig. 4.1). Colour changes from light to dark grey are most likely caused by silt layers and organic impurities in the limestone protolith. Abundant styolites appear to preserve the original bedding in the limestone protolith. The most common vein mineral assemblages are consistent with the Stage 2 alteration assemblages described in the next section.

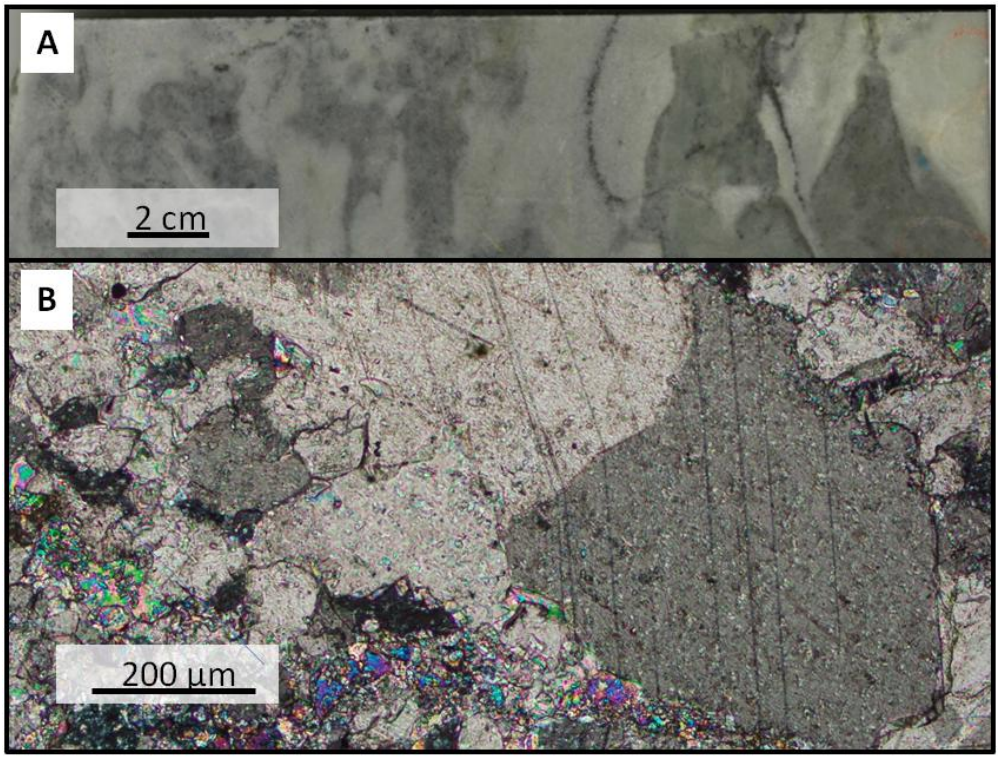

Figure 4.1 Stage 1 marble A) slab from diamond drill core highlighting styolites and common colour variations in marble (BW007 200.0)B)Photomicrograph of a pilished thin section highlighting massive calcite observed in transmitted cross-polarised light (BW001_56.1)

4.3.2 Skarn stage 2:

Stage 2 skarn is dominated by calc-silicate minerals including garnet, vesuvianite and pyroxene (Fig. 4.2). Veins related to stage 2 are commonly comprised of calcite ± pyrite or pyroxene ± garnet ± vesuvianite with minor chlorite ± serpentinite. These calc-silicate minerals represent a high temperature prograde alteration of the limestone. The calc-silicate alteration is usually very fine-grained although garnet crystals may be up to 1mm in diameter locally. A significant characteristic of stage 2 is the lack of borates and oxide ore minerals.

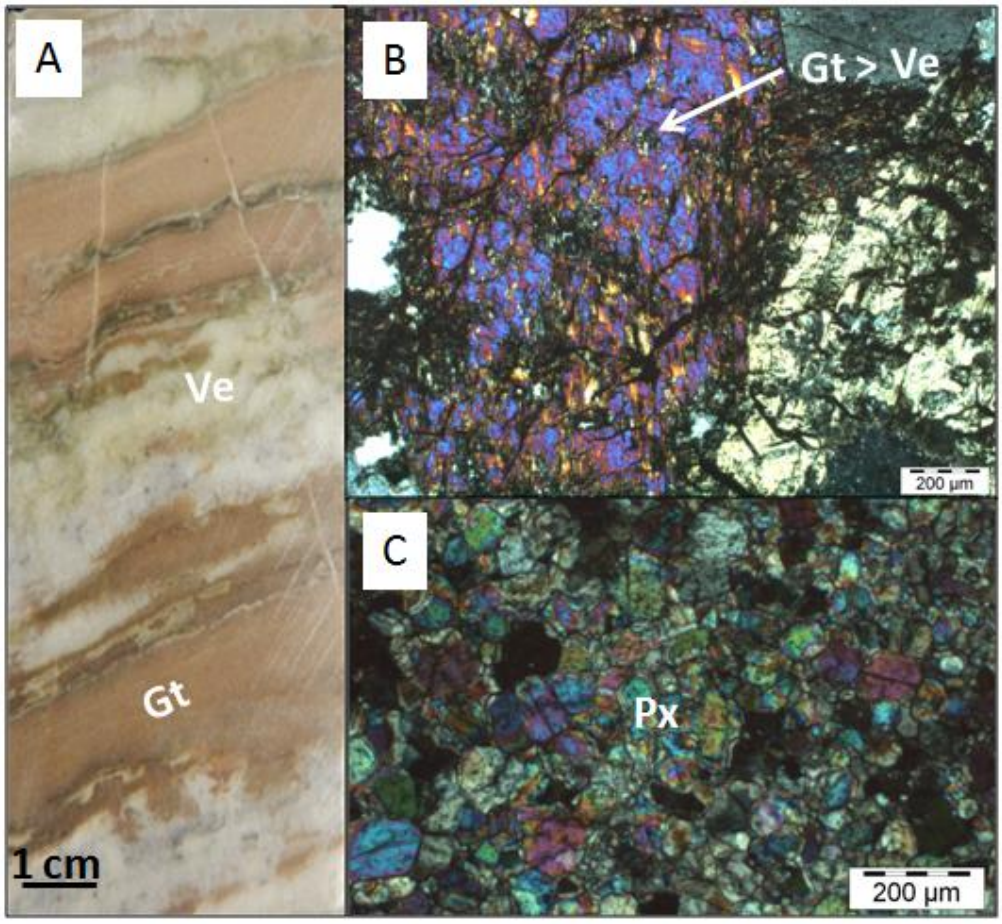

Figure 4.2 Prograde calc-silicate alteration. A) Slab sample of drill core dominated by stage 2 garnet with minor pyroxene and vesuvianite. (BW007 190.1) B) Vesuvianite replacing garnet under transmitted cross polarised light. Vesuvianite displays anomalous blue birefringence.(BW001 179.7) C) Pyroxene under transmitted cross polarised light.(BW001 120.9) Abbreviations: Gt = garnet, Ve= vesuvianite, Px = pyroxene

4.3.3 Skarn stage 3:

Stage 3 retrograde skarn alteration comprises a complex introgrowth of calc-silicate, borate, sulphide, carbonate, fluorite and chlorite-group minerals, together with hosting the three oxide ore minerals, cassiterite, scheelite and magnetite. Table 4.3 lists all of the major, minor and trace minerals identified in the Stage 3 assemblages through core logging, thin section microscopy, XRD, laser raman, Hylogger and SEM analysis.

Table 4.3 Alteration minerals identified in stage 3 retrograde skarn assemblages

Major rock forming minerals (>10%)	***Minor minerals (1-10%)***	***Trace minerals (<1%)***
Quartz	*Axinite*	*Sphene*
Vonsenite	*Dolomite*	*Hulsite*
Pyroxene – garnet – vesuvianite	*Scheelite*	*Serpentine*
Amphibole	*Hematite*	*Sphalerite*
Pyrrhotite - pyrite		*Arsenopyrite*
Biotite – phlogopite		*Chalcopyrite*
Chlorite - fluorite		*Muscovite - illite*
Calcite – siderite		*Xenotime*
Cassiterite		*Monazite*
Magnetite		*Danalite*

The transition between the Stage 2 and 3 mineral assemblages typically occurs at an abrupt alteration front which cross cuts the styolites. Stage 3 alteration contains potentially economic deposits of cassiterite, scheelite and magnetite, however, Sn, W and Fe mineralisation is not distributed evenly throughout the skarn. Figure 4.3 illustrates a transition between Stage 2 and Stage 3 skarn alteration.

Stage 3 skarn mineralogy is highly variable in composition with apparently multiple complex mineral overprints and recrystallisation textures. The presence of acicular vonsenite, bladed actinolite (Fig. 4.3) and square prismatic quartz suggest open-space in fill by crystalising minerals. Table 4.4 summarises the overprinting relationships observed in Stage 3 retrograde skarn alteration.

Table 4.4 Mineral overprinting and recrystalisation textures observed in Stage 3 skarn alteration

Original mineral	**Replaced by:**
Garnet	Vesuvianite, amphibole, magnetite
Pyroxene	Garnet, vesuvianite, amphibole
Vonsenite	Magnetite, amphibole, siderite
Vesuvianite	Amphibole
Amphibole	Magnetite, serpentine
Calcite	Vonsenite

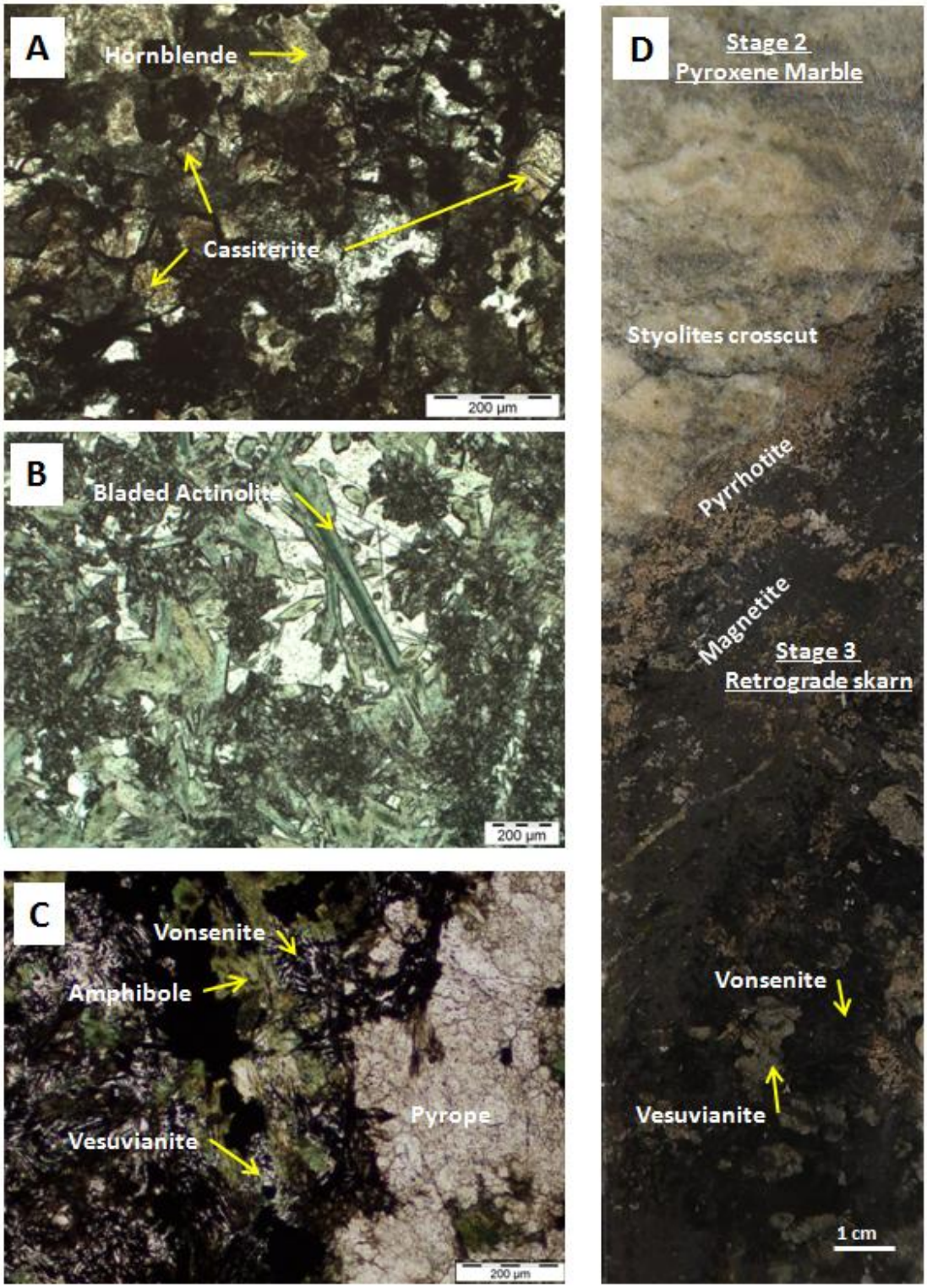

Figure 4.3 A selection of photomicrographs illustrating the complexity of mineral assemblages in stage 3 alteration A) High grade cassiterite zone in a hornblende rich skarn assemblage (BW001 215.7) B) Bladed and zoned actinolite suggesting crystals were infilling a void (BW001 204.5) C) Vonsenite amphibole(type undetermined) garnet(pyrope) skarn with minor vesuvianite (BW001 205.8). D) Transition between stage 2 and stage 3 alteration. Styolites crosscut by phrrhotitie, magnetite Vonsenite alteration. Porphyroblastic vesuvianite has replaced earlier garnet.(BW003A 211.3)

4.3.4 Stage 4: Late stage veining

Distinct white to cream-coloured veins crosscut the Stage 3 skarn at an angle nearly subparallel to drill core orientation (Fig. 4.4). Stage 4 veins are dominated by quartz ± calcite ± siderite ± fluorite but also contains zones enriched in cassiterite and scheelite. Zones of hydrothermal brecciation comprising siderite-amphibole altered clasts and fractured magnetite set in a siderite-quartz matrix also occur. Alteration is restricted to a small halo around the vein system and the vein system itself is restricted to a small band within the Stage 3 skarn. Concentrated cassiterite and scheelite mineralisation occur within these vein systems.

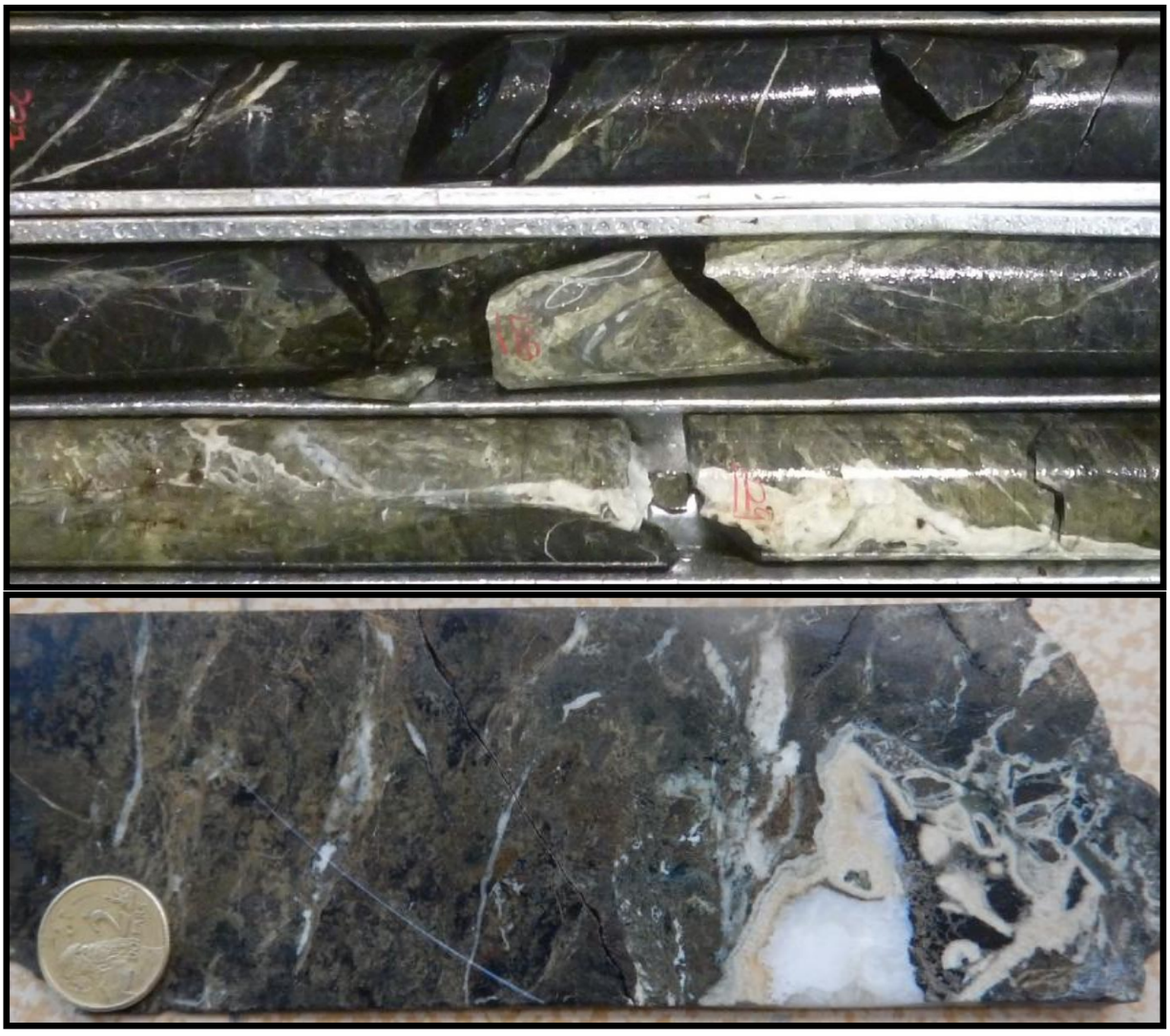

Figure 4.4 Stage 4 veining and hydrothermal breccia in drill core with veining orientation subparallel to the core axis (BW003A 226.0)

4.4 Granite alteration and veining

The Meredith Granite in the vicinity of the Big Wilson prospect has been observed to host two distinct mineral alteration assemblages and two types of vein mineral assemblages (Table 4.5) that are distinct from alteration and vein mineral assemblages hosted in the limestone protolith.

The most common type of veins observed are black quartz tourmaline veins. These veins are often barren or contain only low grade Sn. They are often associated with a distal white mica alteration envelope.

The second type of vein is the quartz-carbonate-cassiterite vein which is associated with high grade cassiterite mineralisation and extensive siderite, fluorite, chlorite and tourmaline alteration in the granite. The following sections describe the vein and alteration mineral assemblages observed in the Meredith Granite

Table 4.5 Alteration mineral assemblages and vein mineral assemblages commonly found in the Meredith Granite

Mineral assemblage	**Alteration mineral association**
Barren veins	Quartz – tourmaline (black)
Mineralised veins	Quartz ± tourmaline (black and green) ± siderite ± cassiterite ±calcite ± fluorite ± chlorite ± Scheelite
Mineralised alteration envelope	Quartz – tourmaline (black and green) ± siderite ± cassiterite ±calcite ± fluorite ± chlorite ± Scheelite
White mical alteration envelope	Muscovite ± illite

4.4.1 Quartz –black tourmaline veins

Barren quartz tourmaline veins are the most abundant vein type that occurs in the Meredith Granite. They usually range in width from several millimetres to several centimetres and can occur as parallel swarms of veins (Fig. 4.5). The veins mostly consist of black to occasionally dark brown very fine grained to centimetre scale tourmaline crystals intergrown with clear to creamy quartz that ranges in size from very fine grained to several millimetres in diameter. These veins are typically surrounded by the muscovite - illite alteration halo described in section 4.4.3.

4.4.2 Quartz –green tourmaline - siderite – cassiterite veins

Mineralised veins within the granite are typically comprised of quartz ± tourmaline ± siderite ± calcite ± fluorite ± chlorite ± cassiterite ± scheelite. Cassiterite occurs as either massive veins or disseminations within veins where it is intergrown with quartz-tourmaline-siderite ± chlorite ± fluorite. These veins are surrounded by an alteration envelope with the same mineral alteration assemblages (Fig 4.6). Tourmaline is often green to dark green in colour and commonly replaces feldspar .

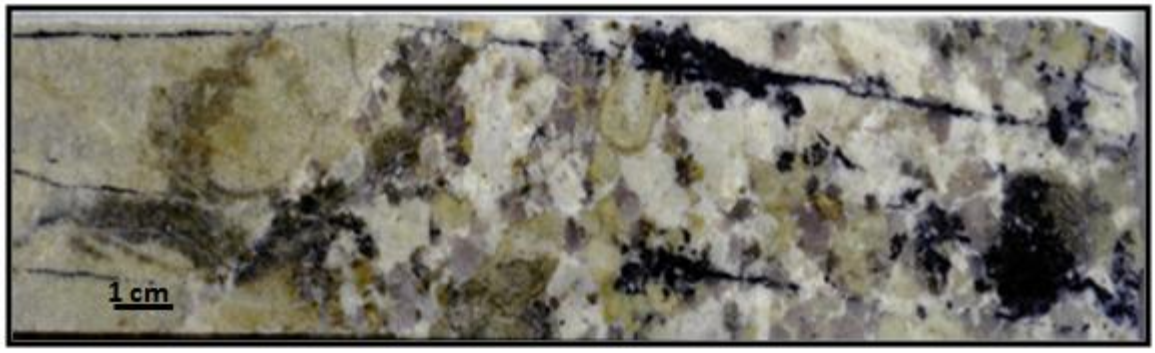

Fig. 4.5 Example of quartz – tourmaline veining in the Meredith Granite with white mica alteration of feldspar in the surrounding granite. Note veining is subparallel to drill core orientation

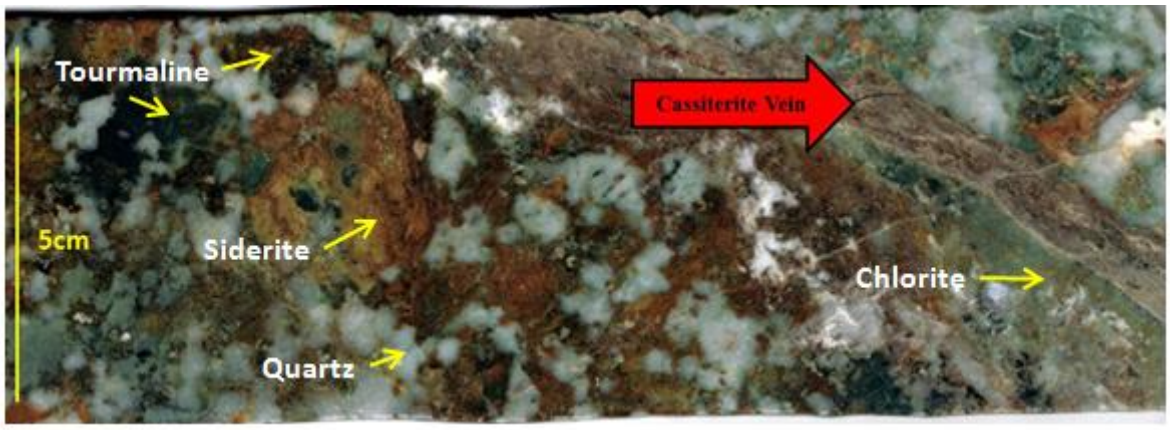

Figure 4.6 Cassiterite rich vein with quartz-siderite-chlorite-tourmaline alteration in the surrounding granite. Note the green tourmaline replacing feldspar and the sub-parallel vein orientation to core axis.

4.4.3 White mica alteration

A distinct halo of white mica alteration of feldspar is observed around most veins in the Meredith Granite (Fig. 4.7). This halo may be as small as a few millimetres around some of the barren veins or as large as tens of meters in the illite alteration zone that extends away

from the contact between the granite and the mineralised skarn. Subtle white mica alteration is not always easy to detect by eye but shows up well in the short wave infrared spectrum. SWIR analysis, using both Terraspec and Hylogger instruments show a distinct white mica alteration halo extending from both sides of the granite contact with the mineralised skarn (Fig. 4.7D). Illite alteration occurs proximal to the skarn and muscovite occurs further away.

4.4.4 Surface distribution of granite alteration

Quartz-tourmaline veins that crop out at the surface of the Meredith Granite vary from a few millimetres to a few centimetres in width (Fig. 4.8). Most of the quartz-tourmaline veins sampled in the field returned geochemical assay values that were below the analytical detection limit for Sn (50ppm). Quartz-tourmaline veins which containined higher Sn assay grades occurred in four samples which were located in two surface locations separated by about 500m distance (Fig. 4.8). The highest whole rock Sn assay was 2340 ppm, however, this may be diluted by host granite material as it was not possible to completely separate the vein from the wall rock.

A distinct population of steeply dipping veins with a northwest strike was observed across the mapping area (Fig. 4.8A). Oriented drill core from BW003A was examined and the subsurface veining orientation displayed the same strike as the veining found on the surface, although with a slightly shallower dip angle (Fig. 4.8B).

Due to poor outcrop Sn grades found on the surface vary widely between sample locations over a scale of 10-20 m and soil Sn anomalies over the granite, which may be an indicator of potential high grade Sn zones near the surface, are separated by hundreds of meters in some places (Fig. 4.8C).

The high grade veins found in the drill core do not project to the surface at the same location as the high grade veins found on the surface. Veining measured in drill core projected to the surface should appear to the south of the Little Wilson River (Fig 3.1), however, this area was covered by dense vegetation and deep soils therefore it was not sampled. Likewise, the veins found and sampled at the surface project down too far north to intersect the area sampled by drill core.

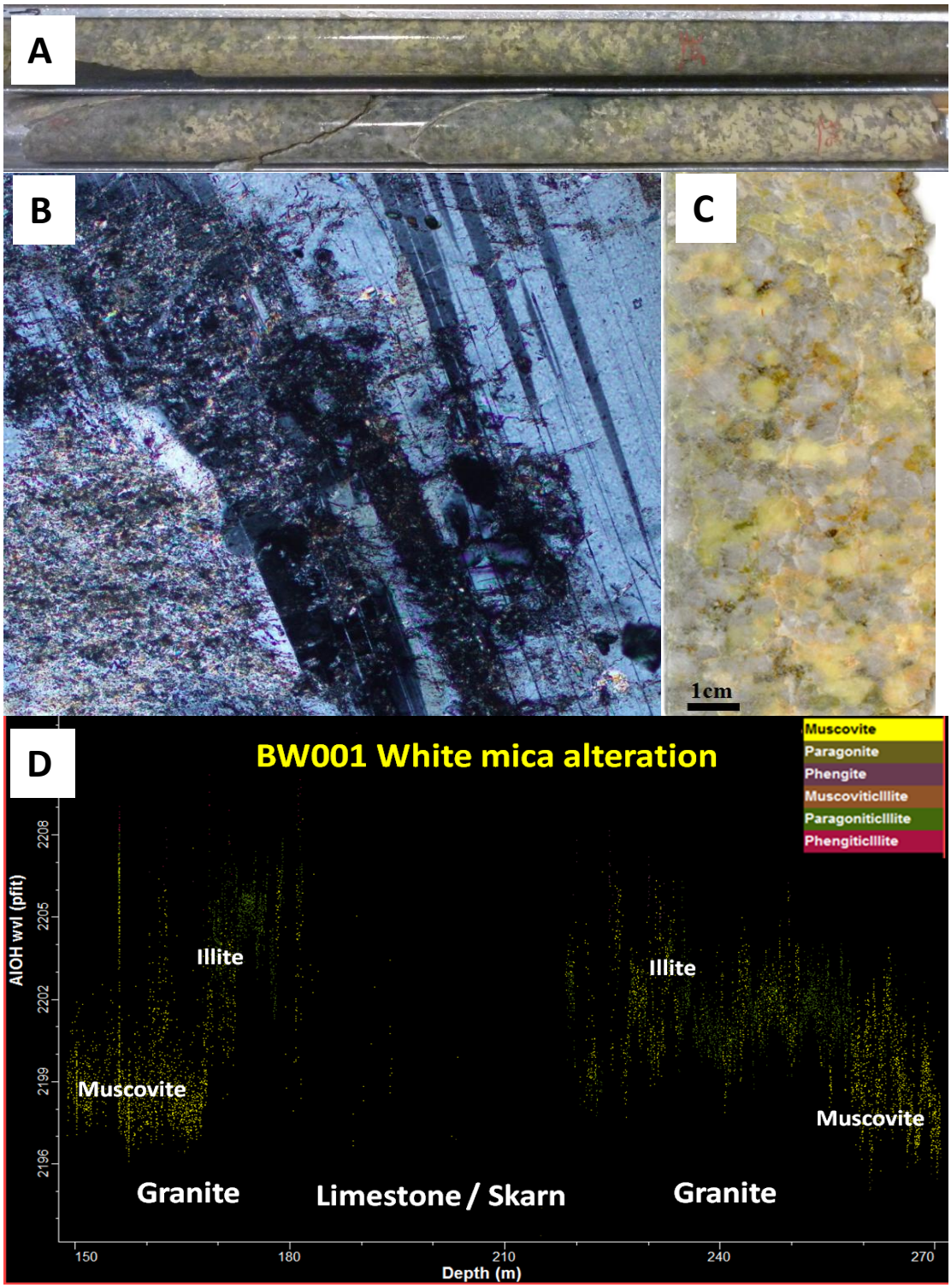

Figure 4.7 Muscovite-illite alteration in the Meredith Granite. A) Drillcore with alteration extending over several meters B) Thin section showing muscovite replacing feldspar in transmitted cross polarised light C) Rock slab showing extensive illite alteration of feldspar. D) Hylogger^{Tm} SWIR data highlighting variations in the 2200nm wavelength peak in hole BW001 showing downhole muscovite-illite alteration with elevated levels of illite on either side of the skarn and muscovite dominant further away from the skarn.

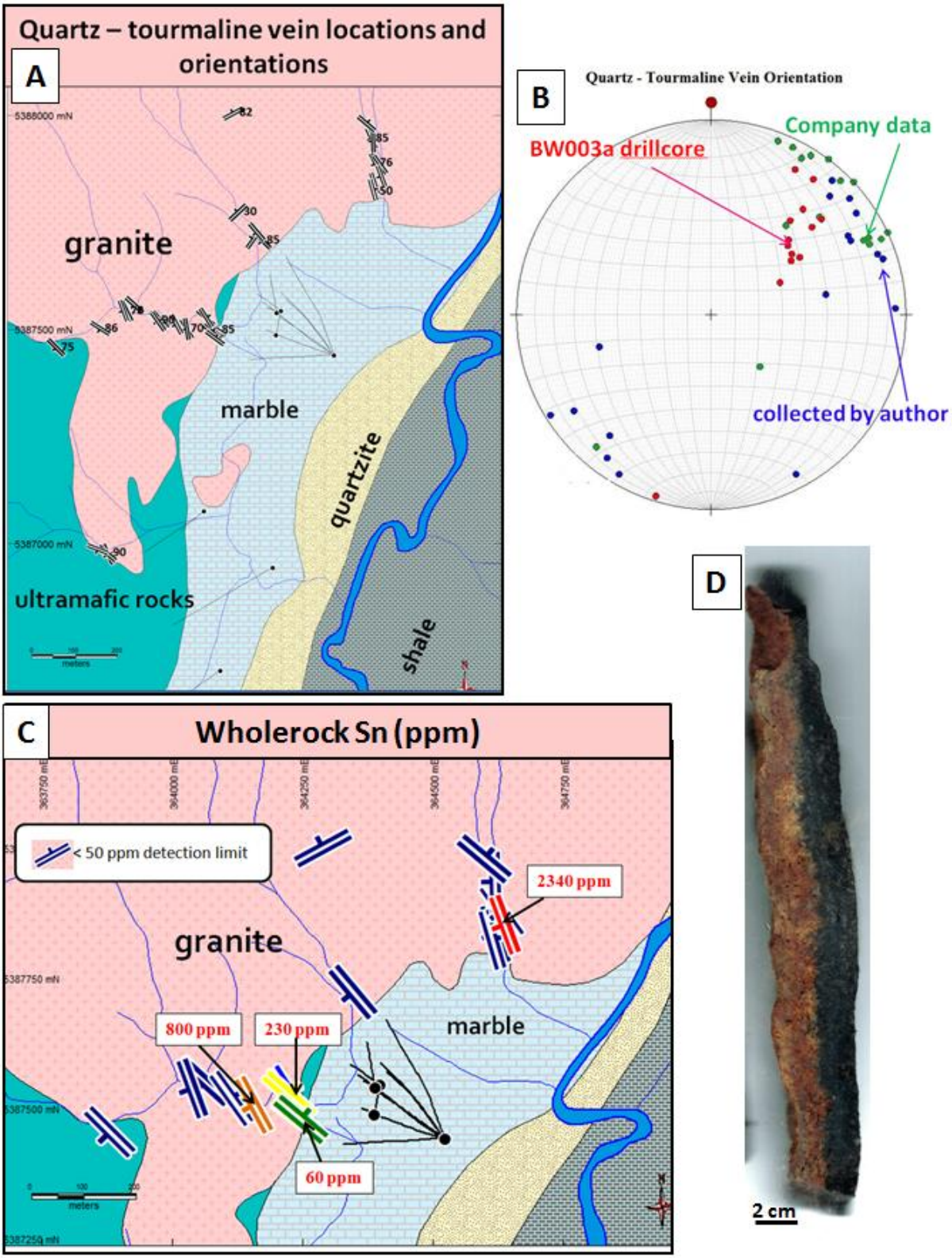

Figure 4.8 A) Orientation and location of quartz tourmaline veins B) Equal area lowe hemisphere stereographic projection showing Northwest strike of veins C) Wholerock Sn results for samples collected at surface D) Hand sample of a quartz-tourmaline vein (THBW024)

4.5 Ultramafic alteration

Alteration assemblages associated with hydrothermal interactions with the ultramafic rocks at Big Wilson currently have no defined economic mineralisation, and have therefore, not been investigated to the same extent as the limestone and granite-hosted alteration sequences.

Ultramafic rocks are commonly fractured and contain abundant carmbonate veins (Fig. 4.9). Dark green pyroxene and amphiboles minerals of the ultramafic host rock have been dominantly altered to serpentine with monor magnetite ± phyrrotite ± pyrite ± chlorite ± chromite ± spinel ± carbonates making up the minor phases. Veins are dominated by white to cream coloured carbonates intergrown with serpentine ± magnetite ± pyrite ± chlorite.

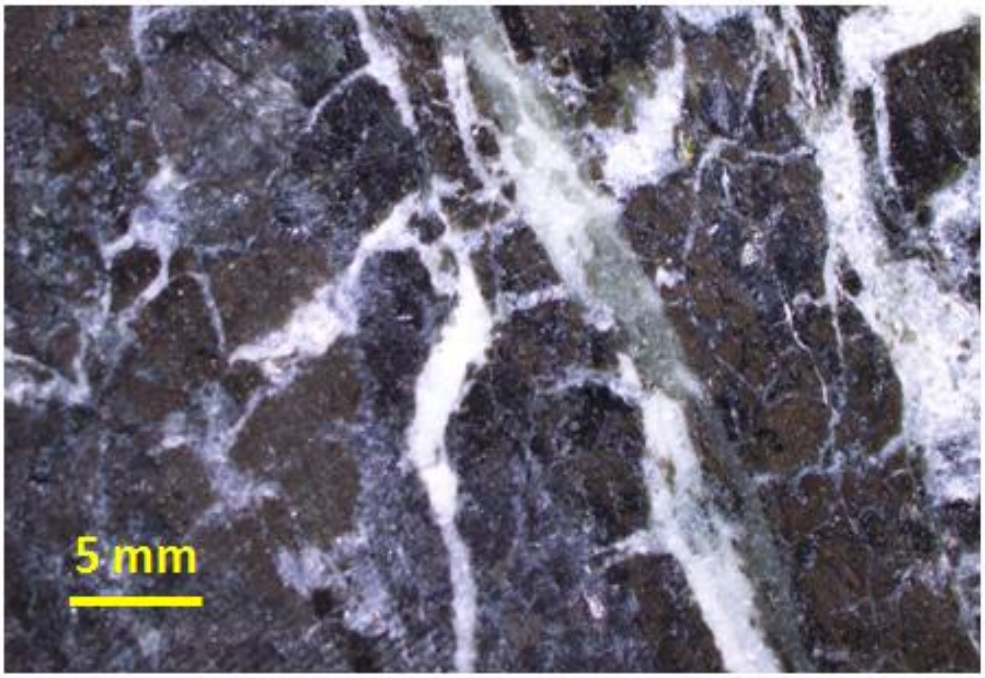

Figure 4.9 Intense carbonate veining in a dark green ultramafic sample

4.6 Weathering

At the extreme northern end of the skarn a small patch of gossanous subcrop was found (Fig. 3.2A) amongst some overturned tree root balls. It consisted of a variety of fist-sized samples containing tourmaline-rich granite and highly weathered and oxidised magnetite skarn (Fig. 4.10). It is possible this site was subject to historical mining activity.

Figure 4.10 Hand sample of weathered granite containing bladed tourmalinie in contact with weathered magnetite skarn.

4.7 Discussion

4.7.1 Skarn geometry

A representative cross-section of the skarn showing the spatial distribution of the alteration stages is shown in figure 4.11. Limestone within fifty to one hundred meters of the Meredith Granite is recrystallised to Stage 1 marble.

Stage 2 prograde calc-silicate alteration exists in a small zone around the edge of the Stage 3 retrograde alteration and in isolated spots near the contact with the granite where Stage 3 skarn is not present. Stage 2 calc-silicate alteration is rarely more than ten meters wide and can be patchy in places. The limited sulphides present in Stage 1 and 2 may have crystallised in the host limestone prior to the main hydrothermal stages

Stage 3 retrograde skarn is rich in borates and has more sulphides than Stage 2. Stage 3 also hosts the target economic minerals cassiterite, scheelite and magnetite. North of Big Wilson, where the majority of drilling has been performed, a Stage 3 skarn has been identified that is about fifty meters wide. In the south of Big Wilson the skarn appears more patchy and irregular and has probably been truncated by a fault which juxtaposed the ultramafic rocks (Figs. 3.1 and 3.2). The cross-section in Fig. 4.11 follows the trace of the discovery hole BW001 and shows the skarn nestled against a wedge of the ultramafic rock unit. However, if

this cross-section were to be drawn further north, the skarn would be shown separated from the ultramafic rocks with marble found between these and the skarn. This truncation by the ultramafics in the south and separation from of the skarn and ultramafics in the north suggest that the skarn is following a fault. Potential structures bounding the skarn will be discussed in chapter 7.

There are a few unusual aspects of the Stage 4 hydrothermal veins. One is that the veining seems to be confined to tight regions within the Stage 3 skarn. In Fig. 4.11 four drill holes constrain the position of this veining. Hydrothermal veining does not extend to the Stage 2 skarn and the carbonate veining in the ultramafics has a different character, different mineral associations and different vein orientations. Most of the sub-centimetre stage 4 veins are oriented at forty five degrees to the core. Although much of the core is not oriented it does suggest a veining angle parallel to the strike of the skarn. However, the larger veins which frequently contain zones of hydrothermal brecciation, are commonly subparallel to the drill

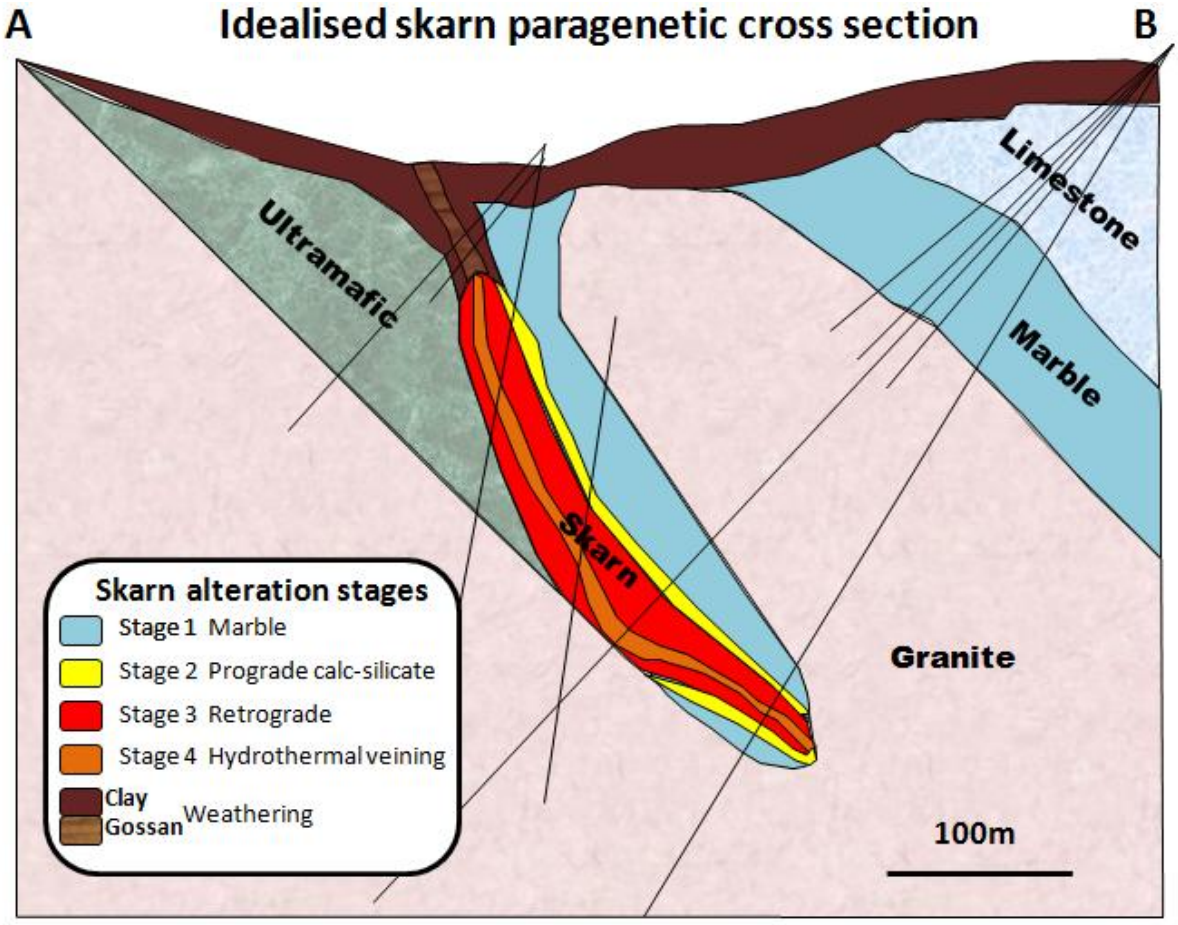

Figure 4.11 Cross section showing spatial distribution of skarn alteration stages

core orientation (Fig. 4.4). This would suggest a veining orientation orthogonal to the skarn.

4.7.2 Borate mineralisation

Tourmaline is the main borate mineral found in the Meredith Granite at Big Wilson but rarely occurs outside the granite. A review of the drill core logs of 13 diamond drill holes found that tourmaline was observed and recorded in 121 drill core intervals with a granite protolith, and only five intervals where the protolith was something other than granite. The five instances of tourmaline recorded in the core logs outside the granite occurred in five different drill holes and in various lithologies namely, marble, clay, skarn, fault breccia and ultramafic rocks (Table 4.6). Logged tourmaline abundances are estimated visually by Venture Minerals geologists and in each instance of tourmaline logged in an interval of core with a protolith other than granite the abundance was estimated at 2.5% or less. Due to the fine-grained nature of tourmaline and the low logged abundances it is possible that some or all of these logged intervals of tourmaline outside the granite could be other dark fine-grained minerals misidentified as tourmaline. Tourmaline has a distinct spectral signature but was not identified by the Hylogger as occurring in the limestone or the skarn. Even if the logs are accurate and some trace amounts of tourmaline do exist outside the granite it shows that tourmaline outside the granite is very rare and does not follow a strong pattern or association with other protoliths or alteration minerals.

Table 4.6 Drill core intervals with logged tourmaline in 5 intervals outside the granite at Big Wilson. Tourmaline was recorded in 121 intervals inside the granite

Hole	**Depth(m)**	**Lithology**	**Logged tourmaline abundance**
BW002	16.2-19.5	Clay	0.1%
BW005	205.7-213.5	Marble	2.5%
BW007	201.5-204.3	Amphibole +/- vonsenite +/- garnet skarn	0.1%
BW009	74.3-85.0	Fault breccia	1.0%
BW010	66.2-70.4	Ultramafic	0.01%

Vonsenite (Fe^{2+} Fe^{3+} BO5) occurs only in stage 3 skarn but can be a major rock forming mineral where it comprises over 40% by volume of the skarn. Much of the vonsenite in the skarn is likely original and not a replacement of specular hematite. Speculite has not been identified as a major rock forming mineral in the skarn and original vonsenite forms an acicular crystal habit (Swinnea and Steinfink, 1983) which is commonly observed (Fig. 4.12). Specular hematite has a bladed habit and if vonsenite were replacing earlier hematite then the crystals would have a much wider aspect ratio. Although it is possible there are isolated instances of vonsenite replacing early hematite it has never been definitively documented whereas the acicular crystal habit of original vonsenite is commonly observed throughout the skarn.

Vonsenite and hulsite $(Fe^{2+},Mg)_2(Fe^{3+},Sn)(BO_3)O_2$ has been identified by Venture Minerals using X-ray diffractometry. The presence of vonsenite was reconfirmed during this study using Laser Raman (Fig. 4.12C). energy dispersive techniques such as the SEM are not able to analyse elements with low atomic numbers and are prone to misidentify vonsenite as hematite. Like many other dark minerals it is very hard and does not give off a diagnostic electromagnetic signature easily detectable by SWIR and TIR detectors.

Techniques such as XRD and laser raman are sensitive to the crystallographic structure of the mineral rather than identifying elemental abundance. In hand sample vonsenite is recognisable by its jet black colour, acicular habit and black streak.

In many stage 3 skarn rocks in the Gordon Limestone at Big Wilson vonsenite is massive or a major component. The same style of vonsenite mineralisation is also observed at Mt. Lindsay (Fig 1.1) in the skarn hosted by carbonate rich beds in the Crimson Creek Formation (Fig 2.1). The Stage 3 vonsenite rich skarn at Big Wilson must have experienced a massive flux of borate rich fluids from the Meredith Granite. The origin and relationship of these fluids to the rest of the system is discussed in chapter 7.

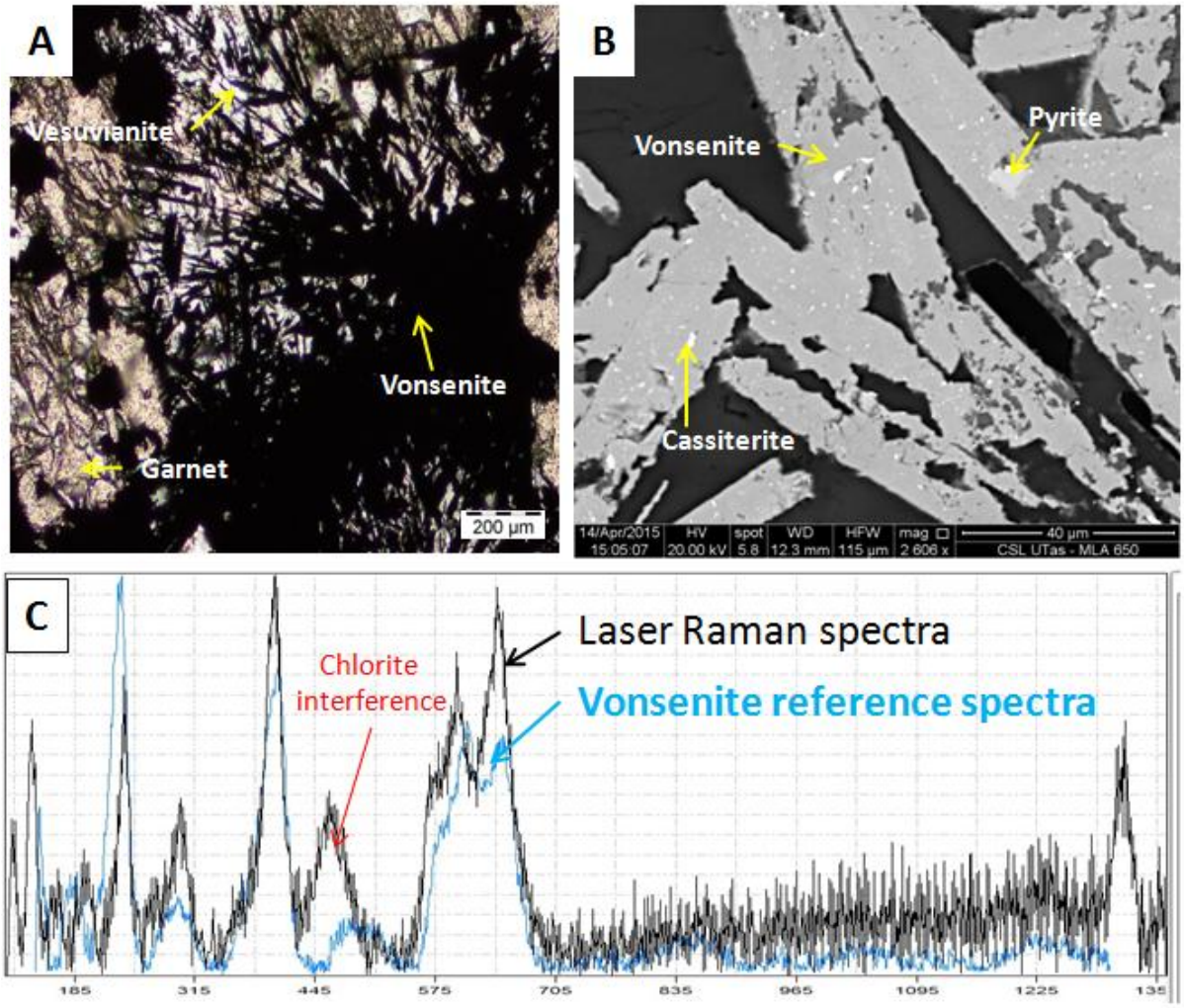

Figure 4.12 A) Thin section under plain polarised transmitted light showing opaque asicular vonsenite with garnet and vesuvianite B) SEM image of vonsenite containing disseminated cassiterite. C) Laser Raman spectrum of vonsenite sample from Big Wilson compared to a reference library spectrum.

Chapter Five Tourmaline mineral chemistry

5.1 Introduction

Both black and green tourmaline has been observed at Big Wilson (Fig. 5.1). The green tourmaline usually occurs with, or very close to, zones of cassiterite. Field observations from other tin-bearing zones around the Meredith Granite by Venture Minerals geologists also note green tourmaline in close proximity to cassiterite. Although some black tourmaline has also

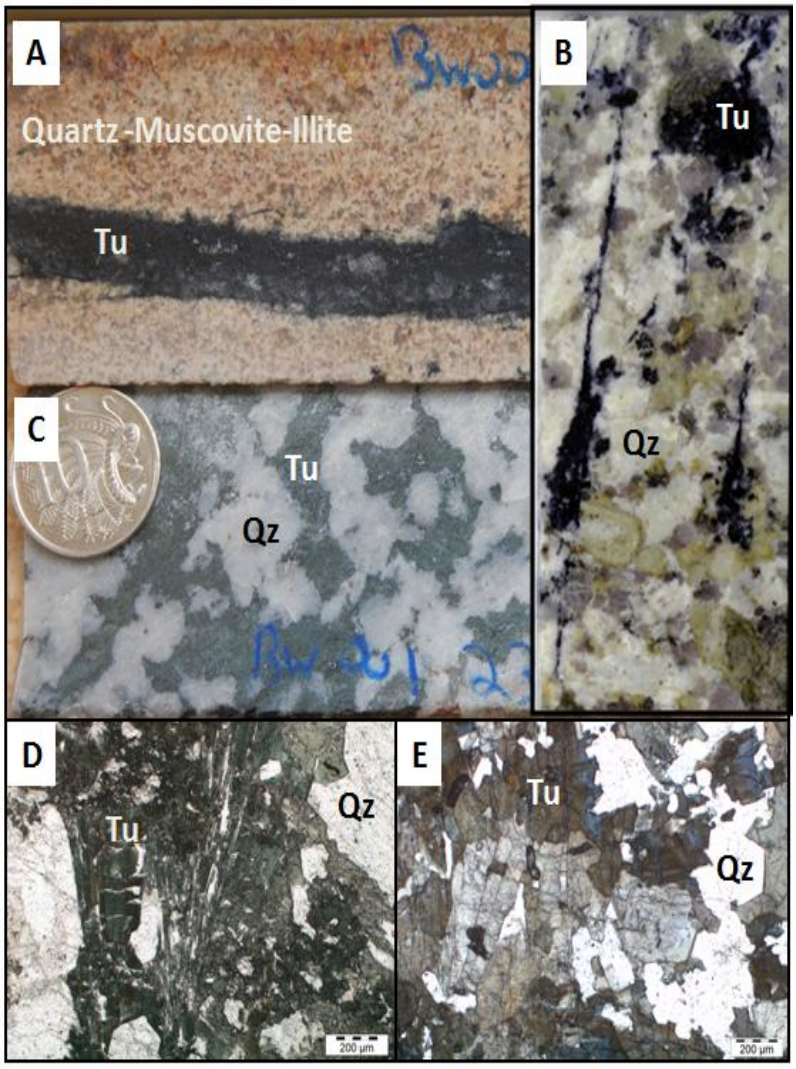

Figure 5.1 (A) Black tourmaline vein in muscovite-illite altered granite from BW001 286.3. (B) Black tourmaline clots and veins from altered granite BW007 211.3 (C) Core slab showing green tourmaline replacing feldsparBW001 231.0 (D) Thin section of green tourmaline in plain polarised light BW001 239.5 (E) Thin section of black tourmaline in plain polarised light BW001 257.9.

been associated with tin mineralisation, around the Meredith Granite the vast majority of black tourmaline-bearing alteration is either barren or associated with low-grade Sn mineralisation. This chapter compares the physical and chemical characteristics of the black and green tourmaline at Big Wilson to determine whether tourmaline chemistry can be useful as an exploration tool for Sn mineralisation.

5.2 Methods

Twenty representative tourmaline-bearing samples containing green and black tourmalines were analysed for major and trace element chemistry. Subsurface tourmaline samples were collected from drill cores at the Venture Minerals core shed in Tullah and surface samples were collected during the field mapping for this project. Polished thin sections and polished 1-inch mounts were made at the University of Tasmania lapidary facility in Hobart.

Major element chemistry was obtained using a Cameca SX100 electron microprobe at the central science laboratory at the University of Tasmania. A 10μm diameter 15keV beam was used at a 40 degree takeoff angle and Schorl Harvard (E6) was used as a standard. Mineral abundances were normalised to 100% and boron weight percentages were calculated stochiometrically.

Trace element chemistry was determined using an Agilent 7900 quadrupole ICPMS with a 193nm Coherent Ar-F excimenr laser and the Resonetics S155 ablation cell at the University of Tasmania. Data was acquired using a 29μm laser spot size and NIST610, BCR-2, NIST612 and GSD-1g standards. A complete list of instrument conditions and settings is provided in Appendix 7.

5.3 General formula for tourmaline

Tourmaline is a complex borosilicate mineral which accommodates a wide variety of chemical substitutions. Variations in the major and trace element chemistry may be useful as a tool for exploration, based on their association with high-grade mineralisation. The general formula for tourmaline structure is $XY_3Z_6(T_6O_{18})(BO_3)_3V_3W$ where:

X site: usually occupied by Na but may include Ca, Mg or vacancy

Y site: tolerates extensive and diverse substitutions (Henry & Guidotti, 1985) and can accommodate monovalent, divalent, trivalent and quadrivalent cations (Frondel et al., 1966 in Henry and Guidotti, 1985). The most common elemental substitutions include Mg^{2+}, Fe^{2+},

Mn^{2+}, Al^{3+}, Cr^{3+}, V^{3+}, Fe^{3+} and Li^{+}. The two most common Sn cations (Sn^{2+} and Sn^{4+}) probably substitute at this site.

Z site: usually occupied by Al but may be replaced by Fe^{2+}, Fe^{3+}, Ti, Mg, Cr and V^{3+}

T site: usually dominated by Si^{4+} but may include substitutions of Al^{3+} and B^{3+}

B site: usually contains B^{3+} but may contain a vacancy

V site: usually contains OH- but may subsitiute for O^{2-}

W site: usually contains OH- but may substitute for F- or O^{2-}

Both the Y and Z are octahedral sites but the Y is slightly larger. Because of the large amount of substitution tourmaline is usually considered in terms of its common end-member components (Table 5.1).

5.4 Results

5.4.1 Tourmaline colour

Two distinct colours of tourmaline have been observed at the Big Wilson prospect (Fig. 5.1). Black is the most common colour and typically occurs in veins in the granite (Fig. 5.1A and 5.1B), although locally it can also be found disseminated in the granite, and regionally the Meredith Granite contains abundant tourmaline nodules (Kositcin and Everard, 2013). Some lower-grade tin mineralisation has been found associated with the black tourmaline veins at Big Wilson.

Green tourmaline is much less common but is usually observed in association with high grade tin mineralisation. Green tourmaline often replaces feldspar (Fig. 5.1C) in highly altered granites, and is associated with siderite, chlorite, fluorite and cassiterite (Fig. 4.7).

Black and green tourmaline can occur separately or together in the same sample. Black tourmaline has been observed growing on and layered with green tourmaline. The drill core samples used in this study appeared homogeneous but the samples obtained from the surface had a higher proportion of mixed colour tourmaline. For the purposes of this investigation if a sample contained both black and green tourmaline it was classified as being a green tourmaline. However, using this simple classification system for a mix of colour types means misclassification is a risk.

Table 5.1. Tourmaline end-members currently accepted by the International Mineralogical Association's (IMA) Commission on New Minerals, Nomenclature and Classification (from Fox, 2012)

		Structural site					
Species	**X**	**Y_3**	**Z_6**	**T_6O_{18}**	**B_3**	**V_3**	**W**
Alkali group							
Schorl	Na	$Fe^{2+}{}_3$	Al_6	Si_6O_{18}	$(BO_3)_3$	$(OH)_3$	(OH)
Oxy-schorl*	Na	$Fe^{2+}{}_2Al$	Al_6	Si_6O_{18}	$(BO_3)_3$	$(OH)_3$	(OH)
Fluor-schorl	Na	$Fe^{2+}{}_3$	Al_6	Si_6O_{18}	$(BO_3)_3$	$(OH)_3$	(F)
Dravite	Na	Mg_3	Al_6	Si_6O_{18}	$(BO_3)_3$	$(OH)_3$	(OH)
Oxy-dravite*	Na	Mg_2Al	Al_6	Si_6O_{18}	$(BO_3)_3$	$(OH)_3$	(OH)
Fluor-dravite	Na	Mg_3	Al_6	Si_6O_{18}	$(BO_3)_3$	$(OH)_3$	(F)
Chromium-dravite	Na	Mg_3	Cr_6	Si_6O_{18}	$(BO_3)_3$	$(OH)_3$	(OH)
Vanadium-dravite	Na	Mg_3	V_6	Si_6O_{18}	$(BO_3)_3$	$(OH)_3$	(OH)
Povondraite	Na	$Fe^{3+}{}_3$	$Fe^{3+}{}_4Mg_2$	Si_6O_{18}	$(BO_3)_3$	$(O)_3$	(OH)
Fluor-buergerite	Na	$Fe^{3+}{}_3$	Al_6	Si_6O_{18}	$(BO_3)_3$	$(O)_3$	(F)
Olenite	Na	Al_3	Al_6	Si_6O_{18}	$(BO_3)_3$	$(O)_3$	(OH)
Elbaite	Na	$Li_{1.5}\,Al_{1.5}$	Al_6	Si_6O_{18}	$(BO_3)_3$	$(OH)_3$	(OH)
Fluor-elbaite	Na	$Li_{1.5}\,Al_{1.5}$	Al_6	Si_6O_{18}	$(BO_3)_3$	$(OH)_3$	(OH)
Calcic group							
Uvite**	Ca	Mg_3	$MgAl_5$	Si_6O_{18}	$(BO_3)_3$	$(OH)_3$	(OH)
Fluor-uvite**	Ca	Mg_3	$MgAl_5$	Si_6O_{18}	$(BO_3)_3$	$(OH)_3$	(F)
Feruvite**	Ca	$Fe^{2+}{}_3$	$MgAl_5$	Si_6O_{18}	$(BO_3)_3$	$(OH)_3$	(OH)
Fluor-feruvite**	Ca	$Fe^{2+}{}_3$	$MgAl_5$	Si_6O_{18}	$(BO_3)_3$	$(OH)_3$	(F)
Liddicoatite**	Ca	Li_2Al	Al_6	Si_6O_{18}	$(BO_3)_3$	$(OH)_3$	(OH)
Fluor-liddicoatite**	Ca	Li_2Al	Al_6	Si_6O_{18}	$(BO_3)_3$	$(OH)_3$	(F)
Vacancy group							
Foitite	□	$Fe^{2+}{}_2(Al, Fe^{3+})$	Al_6	Si_6O_{18}	$(BO_3)_3$	$(OH)_3$	(OH)
Magnesio-foitite	□	Mg_2, Al	Al_6	Si_6O_{18}	$(BO_3)_3$	$(OH)_3$	(OH)

Species marked (*) are identified tourmaline compositions but are not currently accepted by the IMA. Species marked (**) represent end-member compositions modified from the initial tourmaline formula by Hawthorne and Henry (1999). Compositions and site occupancies are from Henry and Dutrow (1996), Novák et al. (2009) and Henry and Dutrow (2011). The structural sites V and W were previously referred to as the [O(3)]3 and O(1) sites respectively, by Henry and Dutrow (1996).

5.4.2 Tourmaline major element chemistry

The tourmaline crystals observed in this study were typically zoned with a large variation in major elements in individual crystals (Fig. 5.3). Electron microprobe analysis indicates that this variability is consistent for both black and green tourmaline, suggesting they have similar

zonation although green tourmaline is generally more Fe-rich and has a wider range in Al concentration (Fig. 5.4). Fe-rich zones appear brighter in SEM images (Fig 5.2). EMPA data normalised on an atoms per formula unit basis using the method described by Fox, (2012 ch.5) shows that both black and green tourmaline samples are classified as schorl endmember compositions (Fig. 5.5).

All the black tourmaline analysed was >6.0 apfu Al (Fig 5.3). This means that the Z site is fully occupied by Al and excess Al is being incorporated into the Y site. The black tourmaline seems to follow the schorl dravite exchange (FeMg) while the green tourmaline with higher Fe is schorl/buegerite, which corresponds to the Fe^{3+} exchange up the Y axis, indicating green tourmaline is more oxidised than black tourmaline.

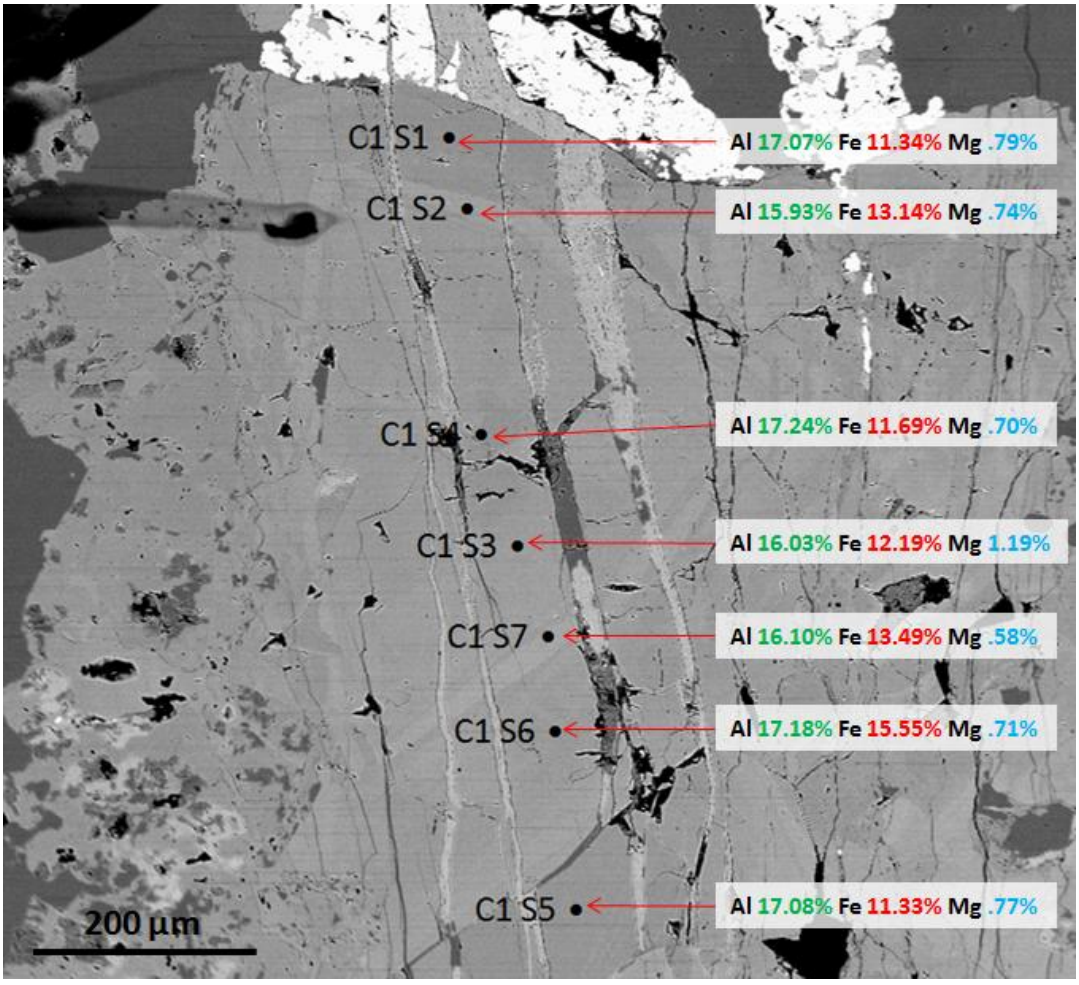

Figure 5.2 Microprobe image of a zoned black tourmaline (BW001 257.9) showing high degree of variation in major element chemistry between zones in a single crystal. Green tourmalines show similar variability.

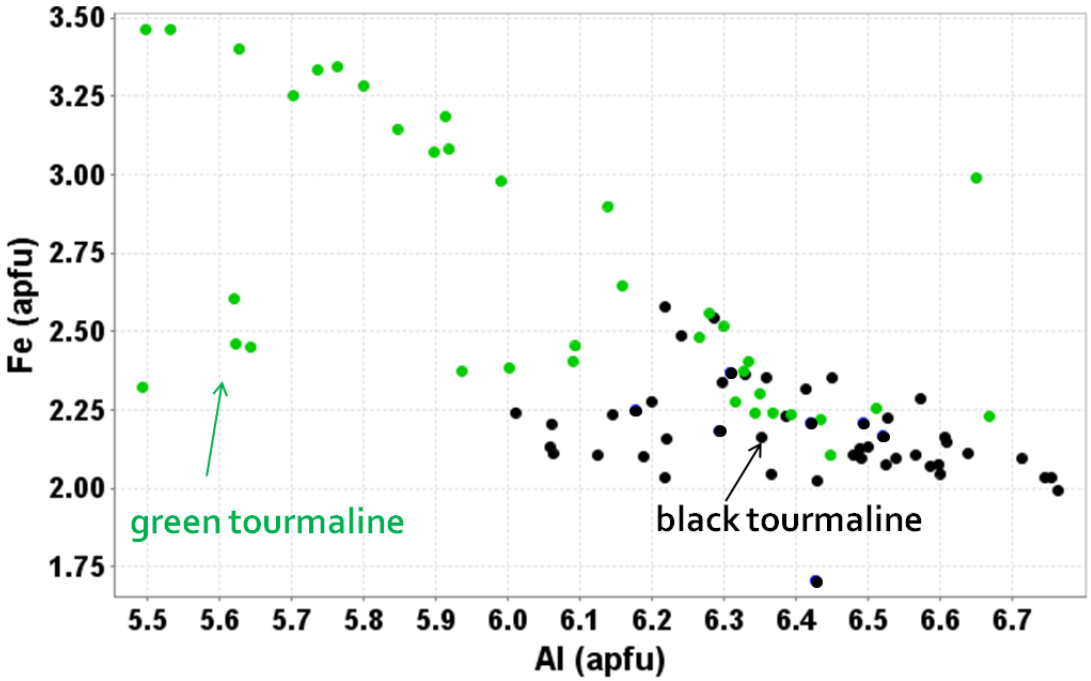

Figure 5.3 Tourmaline major element chemistry showing significant Al and Fe variability. Green tourmaline is higher in Fe and black tourmaline is higher in Al

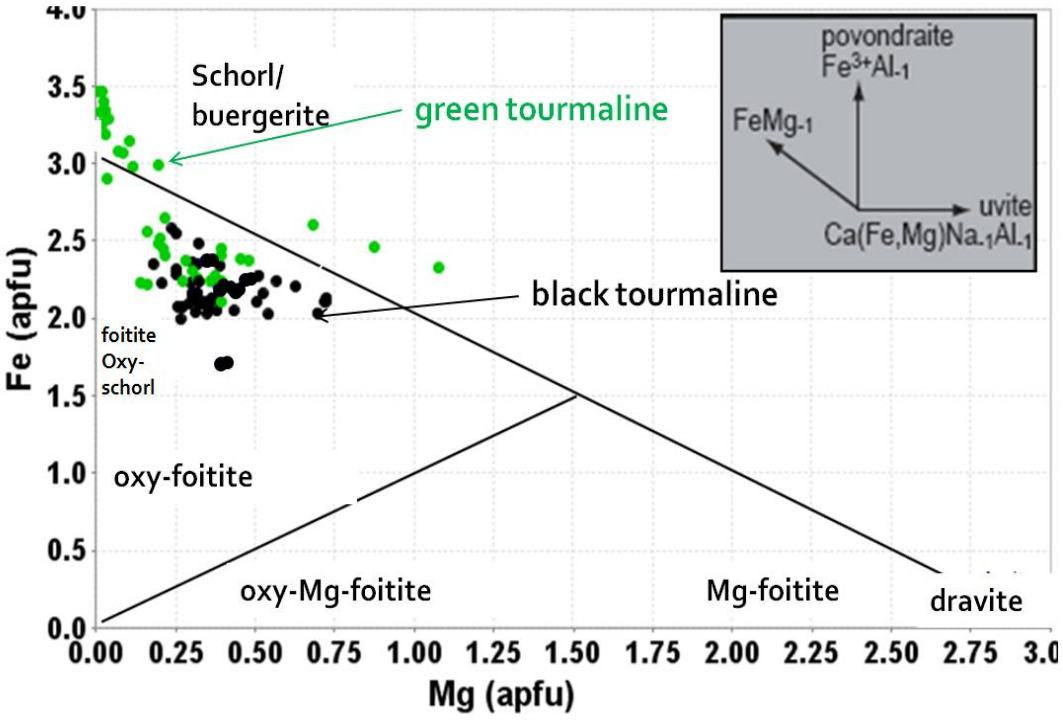

Figure 5.4 Compositional diagram showing Big Wilson tourmaline is near the schorl endmember

5.4.3 Tourmaline trace element chemistry

LA-ICP-MS analysis of tourmaline showed several strong trace element relationships. There is a general correlation between colour (green) and Sn concentration (Fig. 5.5). There are also correlations between tin concentration and zinc, lithium, rubidium and antimony (Fig. 5.6).

Tin and zinc show a strong inverse relationship with high Sn analysis. Green tourmaline has lower zinc concentration relative to high levels of Sn when compared to analysis of black tourmaline samples which have lower concentrations of Sn (Fig 5.6).

Tin and lithium also show a similar correlation to tin and zinc. Green tourmaline generally has high Sn concentrations and low concentration of lithium (Fig 5.6) whereas black tourmaline is low in Sn and higher in lithium.

The relationship between tin and strontium also shows a significant difference between green tourmaline and black tourmaline. Black tourmaline is consistently low in both Sn and strontium and green tourmaline contains more highly elevated and variable levels of Sn and strontium (Fig 5.6). A similar pattern is observed between tin and antimony where black tourmaline is low in both and green tourmaline has much more elevated and variable levels. The five outlying black tourmaline data points with elevated antimony are all from the same

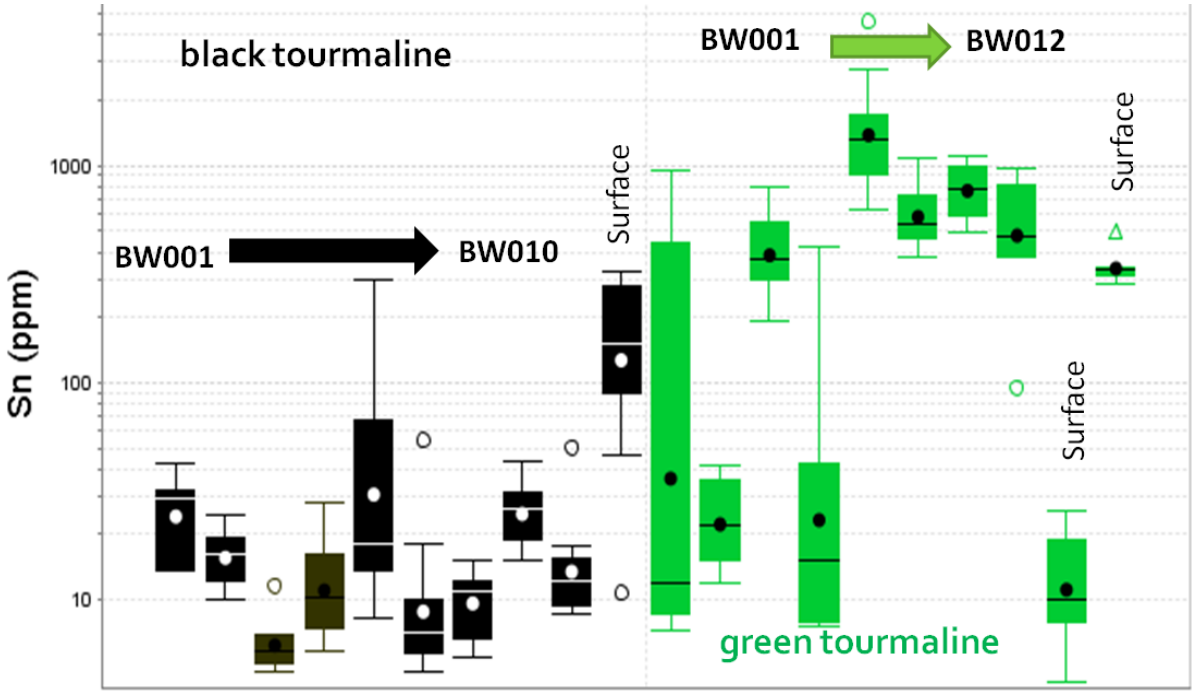

Figure 5.5 Sn (ppm) contained in green and black tourmaline samples, determined by LA-ICPMS analysis. Green generally higher in Sn.

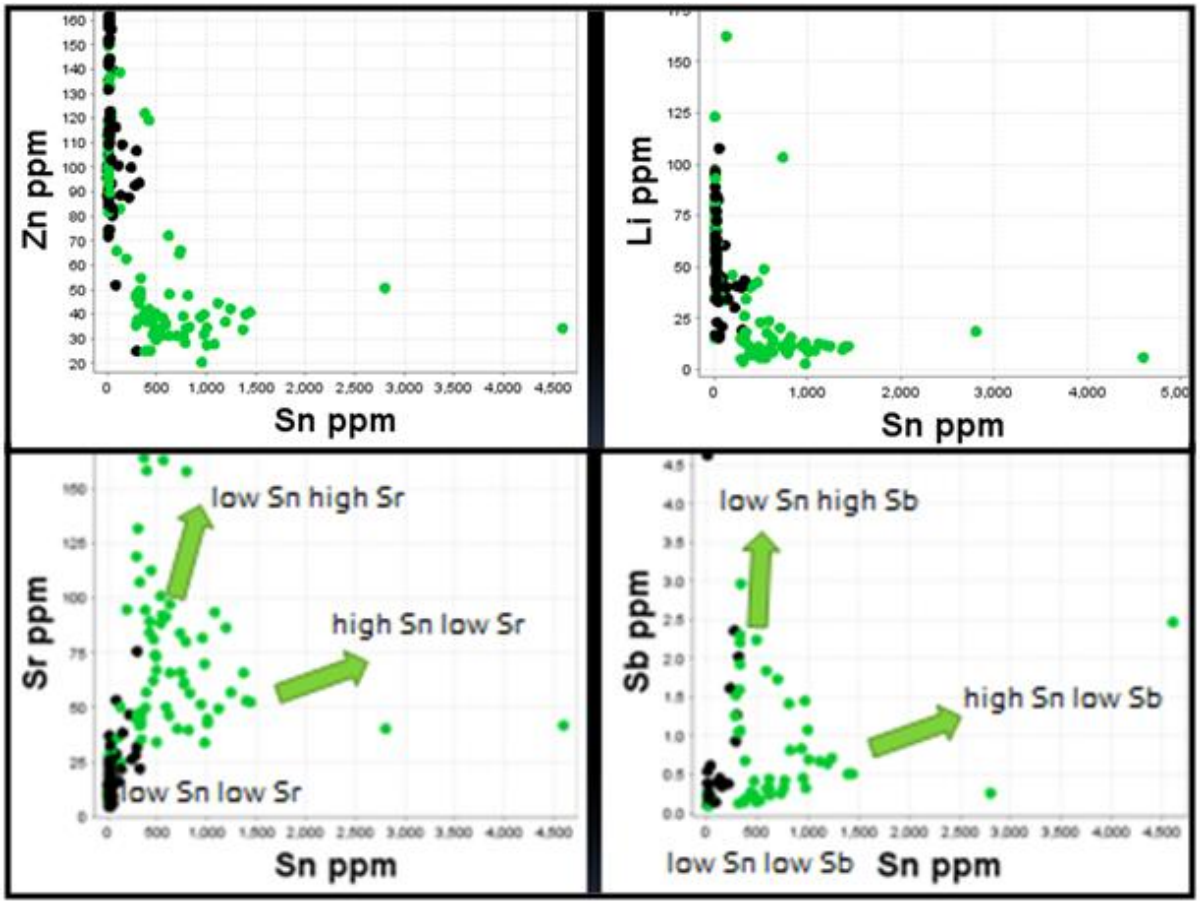

Figure 5.6 Trace element relationships between Sn and Zn, Li, Sr and Sb

sample (THBW024). This anomalous sample is the only one classified as black tourmaline and obtained from the surface. It is also the same sample that holds anomalously high Sn for a black tourmaline (Fig 5.5).

5.5 Discussion

Determining the colour of tourmaline is a relatively subjective process and placing all samples into one of two categories simplifies what may be a more complex issue. In some circumstances determining colour is straightforward as the green colouration is distinctive in hand specimen, particularly where tourmaline has replaced feldspar. However, when samples are wet the green colour appears much darker and is difficult to distinguish in hand specimen. Green and black tourmaline may also occur in the same sample, as black tourmaline has been observed growing on, and layered with, green. Mineral chemistry shows a distinct difference between black and green tourmaline and the subjectivity of classifying colour by eye may

explain some of the anomalous black tourmaline that has the mineral chemistry of green tourmaline and vice versa.

5.5.1 Spatial relationships

An attempt was made to place the data for each tourmaline sample in a spatial context to identify any spatial trends in the geochemical data. However, because tourmaline only occurs in abundance in the granite no chemical or spatial comparison between the granite-alteration and the skarn-alteration can be made using just tourmaline. In addition, samples collected from the surface cannot be incorporated onto a single planar cross section that includes samples collected in drill core because of the large offset distances between surface and subsurface samples.

Another issue was the fact that the drill core orientation was parallel to the orientation of the veining in the granite. Although it was possible to determine the tourmaline chemistry from the middle of the high-grade ore zone and compare it to lower grade tourmaline above and below the high Sn tourmaline, however, given the near parallel orientation of the core to the veins, the true distance from mineralisation to the distal samples could not be established based on down-hole distance.

Despite these issues with generating a reliable spatial model it is clear that tourmaline containing high Sn is associated with high Sn in wholerock. Therefore the relationships also extend between high wholerock Sn and low Zn, Low Li, high Sr and high Sb in tourmaline. Conversely, distal low-grade tourmaline contains high Zn, high Li, low Sr and low Sb and is associated with low-grade or barren wholerock Sn. What is unclear is how these relationships change with increasing distance from high-grade mineralisation and, most importantly, over what scale do the most noticeable changes in tourmaline mineral chemistry occur.

5.5.3 Usefulness as a vector

A number of potentially useful relationships have been identified during this investigation. Significantly, it has been shown that the green tourmaline occurs both directly with cassiterite and in proximity to high-grade cassiterite veins in the granite. Green tourmaline also:

- Contains large amounts of Sn in its trace element structure.
- Is Fe-rich (schorl endmember).
- Is Zn and Li poor.

- Contains elevated levels of Sr and Sb.

A clear relationship between tourmaline colour, Sn content and the major and trace elements has been demonstrated, although the usefulness of tourmaline as a vector to tin mineralisation in a spatial context could not be established. However, tourmaline colour would be an excellent field indicator of proximity to mineralisation. The refractory nature of tourmaline and the granite it is hosted in means that it could survive in stream sediments, exposed resistant outcrops, sub-crops and within float material, and could therefore be observed in stream sediment and soil samples as well as through field mapping. It would be valuable for tin explorers around the granites of western Tasmania to be able to recognise green tourmaline and appreciate its significance as an indicator of mineralisation.

Chapter Six Geochronology

6.1 Introduction

One possibility for the genesis of the high grade tin veining is that Sn is concentrated during magma fractionation and partitions into hydrothermal fluids late in the granite crystallisation history so that it is deposited in late stage veins. If the age of the earliest-crystallised granite phases and the late-stage cassiterite-rich borate veins can be resolved using geochronological techniques, this will allow the duration of magmatic-hydrothermal activity to be constrained and may be helpful as an exploration tool, through potentially matching individual granite bodies with mineralisation. The technology to directly date minerals such as zircons, contained in the granite, is well developed (Black et al. 2004; Jackson et al. 2004; Chang et al. 2006; Harley and Kelly 2007), however, the science of directly dating cassiterite is just emerging (see Literature Review, Appendix 1).

6.2 Aims

The primary aim of the geochronogy is to determine if the age of the high-grade cassiterite greisen can be resolved from the magmatic age of the granite. A secondary aim is to confirm that cassiterite can be directly dated *in-situ* by LA-ICPMS using the U/Pb system.

6.3 Methods

Two samples of cassiterite were obtained for geochronological analysis. The first came from a small section of Big Wilson drill core (BW001 215.7). - It is Devonian in age (Figs. 6.1A and 6.2). The second, used for comparison and method development, was an Archaean sample from the University of Tasmania collections (Sample 12529) from Mt. Francisco, Western Australia (Fig. 6.1B). Both samples were initially analysed for their U-Pb isotopic composition using the University of Tasmania LA-ICPMS to determine if they were suitable

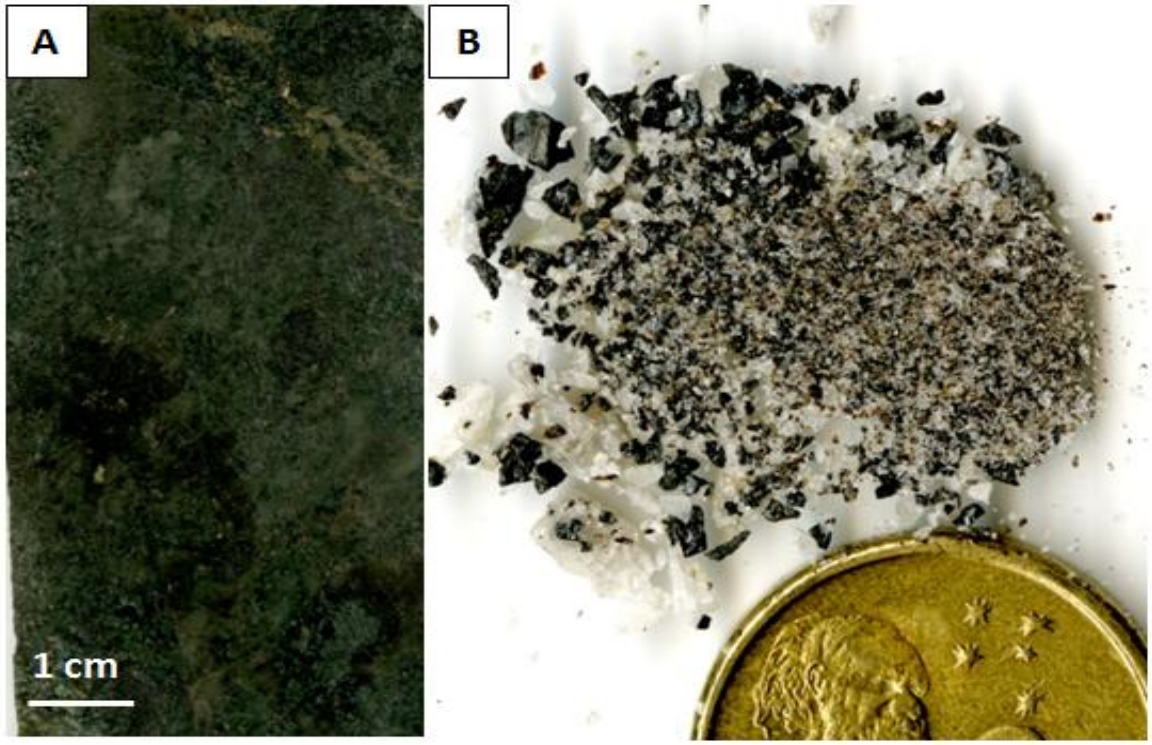

Figure 6.1 A: Sample of cassiterite-rich (12% Sn) core from BW001 215. B: Archaean cassiterite from Mt. Francisco W.A.

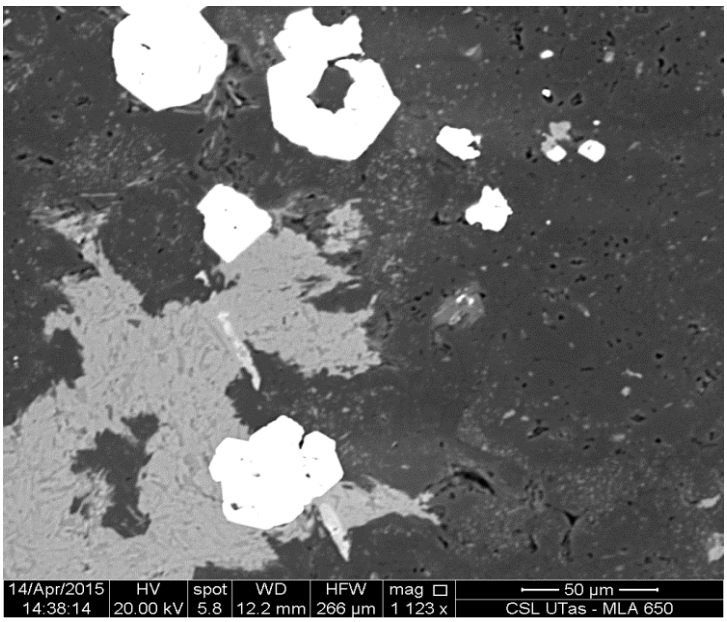

Figure 6.2 SEM image of BW001 215.7. Cassiterite is the white phase

for geochronology. The samples were then sent for analysis using ID-TIMS at the Pacific Centre for isotopic research at the University of British Columbia. The ID-TIMS method used by the UBC lab is detailed in Appendix 10. The LA-ICPMS method for analysing

cassiterite is similar to that used for zircons. The sample preparation is described below and the University of Tasmania LA-ICP-MS methods for zircons are detailed in Appendix 9. Sample preparation was performed by the author with assistance from Dr Sebastien Meffre and the analysis and data reduction was undertaken by Dr Sebastien Meffre and Jay Thompson. Data reduction was carried out using Microsoft Excel in accordance with the methods described by Meffre (2008).

6.3.1 LA-ICP-MS

For the Achaean Mt. Francisco sample approximately 0.5g of coarse-grained cassiterite crystals were flaked off by hand using a tungsten-tipped scribe into a watch glass. The fragments of cassiterite were handpicked under the microscope in cross-polarised transmitted light and placed on double-sided sticky tape. Epoxy glue was then poured into a 2.5 cm diameter mould on top of the cassiterite. The mount was dried for 12 hours and polished using clean sandpaper and a clean polishing lap.

The Big Wilson sample was cut out directly from the drill core and mounted *in-situ* on a 2.5cm round laser mount and polished. The samples were then washed in distilled water in an ultrasonic bath. The analyses for both samples were repeated twice on two different days to test whether the data could be reproduced. The results for both days were within error.

6.3.2 ID-TIMS methods and issues

Four samples were submitted to the Pacific Centre for Isotopic and Geochemical Research at the University of British Columbia, Canada for direct dating using the U-Pb system. The Isotope Dilution – Thermal Ionisation Mass Spectrometry (ID-TIMS) process involves dissolving individual grains of minerals to extract and measure the U-Pb content directly. This technique does not require matrix-matched standards and can give higher resolution age date results than using the sensitive high-resolution ion micro-probe (SHRIMP) or LA-ICPMS instruments (Gulson and Jones, 1992; Thirwall, 2000).

Samples were prepared by either directly flaking off large cassiterite crystals with a tungsten tipped scribe into a small envelope or by crushing a sample with a mortar and pestle, followed by gravity and magnetic separation in a pan with the final separate being placed in a watch glass and checked under the microscope in cross polarised light. A detailed method used by the lab at the University of British Columbia is provided in Appendix 10.

The technique of dating cassiterite with the ID-TIMS process is still new and the laboratory initially tried to use their standard zircon technique directly on cassiterite. Unfortunately cassiterite is too refractory to dissolve in the HF normally used for zircons. An alternative technique was to dissolve the cassiterite in hydroiotic acid (HI). This approach encountered some issues due to recent increases in the regulation of HI. It is currently difficult to obtain reagent grade solutions, as HI is a precursor to the production of methylamphetamine. This caused significant delay. Samples were submitted to the lab in August 2014. At the time the lab quoted a 4 month turn-around period with assurances that data would be provided by January 2015, however, at the time of writing (September 2015) the results are not yet available.

6.4 Results

The preliminary results using the 91500 zircons as a primary standard provided an age for the Big Wilson cassiterite of 357.9 ± 5.2 Ma using the $^{238}U/^{206}Pb$ system (Fig. 6.3). The Mt Francisco cassiterite gave an age of 2,736 ± 49 Ma using the $^{206}Pb/^{238}U$ system (Fig. 6.4). The full data tables of the LA-ICP-MS results are provided in Appendix 9. The results ^{207}Pb-^{206}Pb system using the NIST610 glass as primary standard were 2,862 ± 47 Ma for the Mt Francisco Cassiterite (Fig. 6.4) and the Big Wilson cassiterite contained a small amount of common Pb and were unable to be dated using this system. In the absence of a cassiterite standard the $^{238}U/^{206}Pb$ system is expected to be inaccurate due to differences in the ablation rate of cassiterite and zircons. The discrepancy between the two ages for the Mt Francisco cassiterites and the lack of common Pb in this sample (low^{204}Pb) allows a correction factor to be calculated for the differences in the $^{238}U/^{206}Pb$ ratio between cassiterite and zircons. When this is taken into account the Big Wilson cassiterites are dated at 373.6 ± 5.4 Ma using the $^{238}U/^{206}Pb$ system.

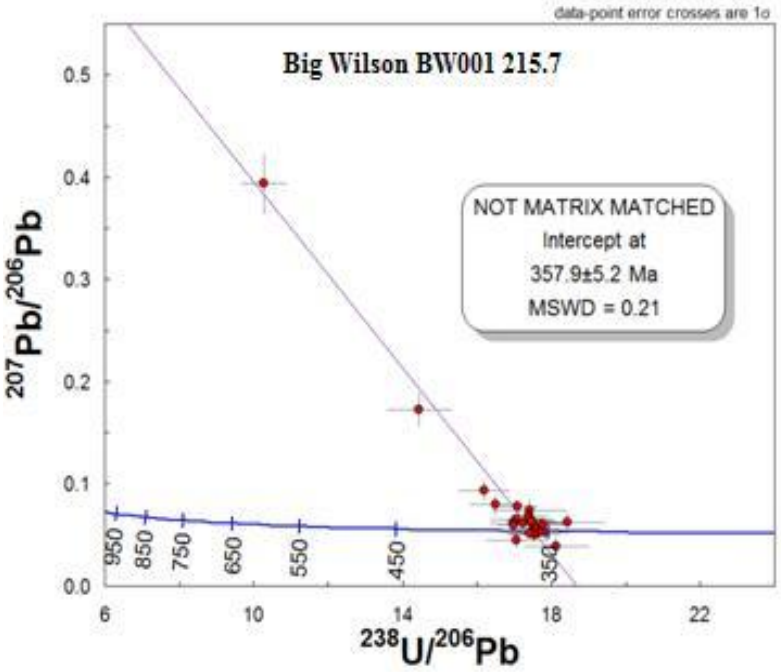

Figure 6.3 Tera-Wasserburg diagram for Big Wilson cassiterite with a non matrix matched uncorrected date of 357.9 +/-5.2Ma

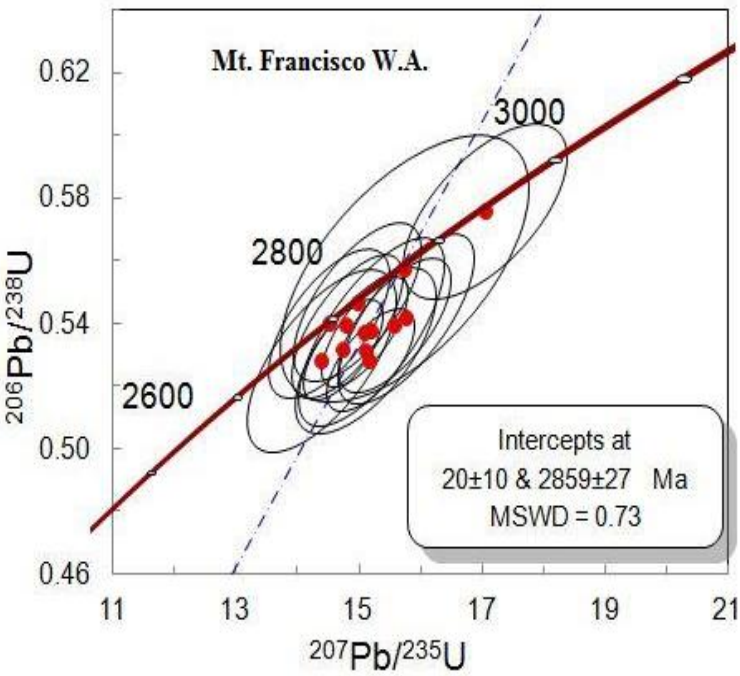

$^{207}Pb/^{206}Pb$ age:
Mean = 2862±47 [1.6%]
95% conf.
Wtd by data-pt errs only, 0 of 14 rej.
MSWD = 0.36, probability = 0.98

$^{206}Pb/^{238}U$ Age:
Mean = 2736±49 [1.8%]
95% conf.
Wtd by data-pt errs only, 0 of 14 rej.
MSWD = 0.42, probability = 0.96

Figure 6.4 Concordia diagram for Achaean cassiterite sample from Western Australia. Yellow boxes show the $^{207}Pb/^{206}Pb$ age and the non matrix matched uncorrected and $^{206}Pb/^{238}U$ age

6.5 Discussion

6.5.1 Correction for matrix effects

A zircon standard was used during analysis as a well characterised cassiterite U-Pb standard was not available, so the results will be affected by matrix effects due to variation in the rates of ablation between different minerals producing different U/Pb fractionation (Marillo-Sialer et al., 2014). The difference in the U/Pb fractionation was quantified using an Archaean cassiterite. This methodology relies on the fact that Archean crystals can be dated using either the $^{207}Pb/^{206}Pb$ system, which is unaffected by matrix effects, or the $^{206}Pb/^{238}U$ system, which is affected by matrix effects.

For the Mt. Francisco cassiterite sample, the difference between the $^{207}Pb/^{206}Pb$ age obtained of 2,862 ± 47 Ma and the 2,736 ± 49 Ma age obtained using the $^{206}Pb/^{238}U$ system is about 4.4%. The published dates for the Sn-bearing pegmatites in the Mt. Francisco area (Table 6.1) vary between 3,000 – 2,800 Ma (Sweetapple, 2000; Huston et al., 2002) which agree with the results of the $^{207}Pb/^{206}Pb$ date of 2,862 ± 47 Ma. As the Mt. Francisco sample was obtained from the University of Tasmania rock collection the precise locality was not recorded.

The 4.4% offset between the ^{207}Pb-^{206}Pb and ^{238}U-^{206}Pb ages for the Achaean cassiterites provides an estimate of the matrix effects between the U-Pb system on zircons and the U-Pb system on cassiterites. This can be used to correct the $^{238}U/^{206}Pb$ date obtained for the Devonian Big Wilson sample. The uncorrected date of 357.9 ± 5.2 Ma is then recalculated to 373.6 ± 5.4 Ma. This adjusted date is within error of the currently published age of the Meredith Granite of 372.2 ± 1.9 Ma (Fig 6.5) obtained from zircons at Big Wilson (Kositcin and Everard, 2013).

Table 6.1 Dates obtained from cassiterite at Mt. Francisco, Western Australia by Kinny (2000) in Sweetaple (2002)

Locality	Age (Ma)	Method
Tabba Tabba	2886 ± 21	$^{207}Pb/^{206}Pb$ SHRIMP
Tabba Tabba	2974 ± 59	Pb-Pb Isochron plot
Strelley	2836 ± 36	$^{207}Pb/^{206}Pb$ SHRIMP
Strelley	2924 ± 120	Pb-Pb Isochron plot
Moolyella	2839 ± 16	$^{207}Pb/^{206}Pb$ SHRIMP
Moolyella	2868 ± 63	Pb-Pb Isochron plot
Cooglegong	2839 ± 16	$^{207}Pb/^{206}Pb$ SHRIMP
Cooglegong	2901 ± 49	Pb-Pb Isochron plot
Hillside	2877 ± 20	$^{207}Pb/^{206}Pb$ SHRIMP
Hillside	2877 ± 62	Pb-Pb Isochron plot

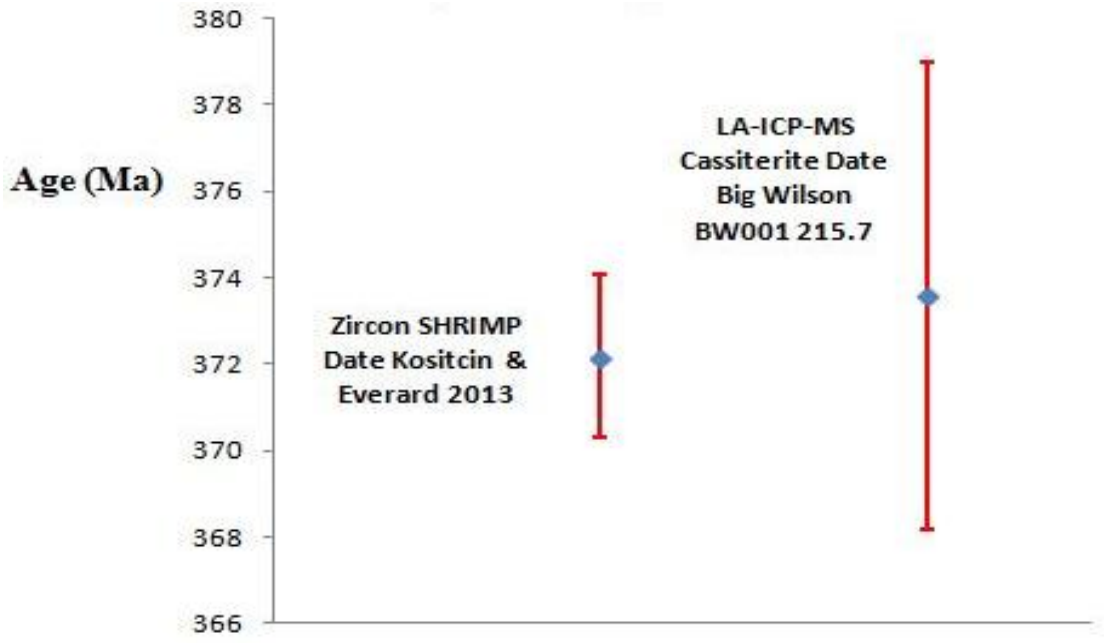

Figure 6.6 The age of cassiterite as determined by the LA-ICPMS after adjustment for the matrix effect is within error of the published zircon dates of the Meredith Granite.

6.5.2 Data precision and accuracy

Although a full precision and accuracy analysis of this methodology is beyond the scope of this project, the scatter in the ages and the isotopic ratio suggest that the method is accurate and precise.

The MSWD (mean square weighted deviation) is a measure of geochronological data precision that takes into account the relative importance of integral and external reproducibility of data. Where MSWD = 1, the data fit a gaussian normal distribution based on analytical uncertainty, MSWD < 1 if the observed scatter is less than predicted by analytical uncertainty and MSWD > 1 if the observed scatter is greater than predicted by analytical uncertainty (Brooks et al., 1972; McDougall and Harrison, 1988; Wendt and Carl, 1991). An example of typical MSWDs from an analysis of zircon and monazite standards by Halpin et. Al, (2014) is provided in table 6.2 showing MSWDs ranging from 0.91 to 1.5.

Table 6.2 MSWD's measured on zircon and monazite standards from Halpin et. al, (2014)

Standard Name	Standard Type	Age Obtained	MSWD
Gj-1	Zircon	604.3 ±2.6 Ma	0.91
TEMORA 1	Zircon	418.5 ± 3.1 Ma	1.3
91500	Zircon	1071.4 ± 9.5 Ma	1.00
MB35	Monazite	501.1 ± 3.3 Ma	1.5
N3364	Monazite	1585.1 ± 8.6 Ma	1.14

The most likely explanation for the higher than expected precision of the data is that the analytical uncertainties expected from this method are based on previous experience with zircons. One of the biggest factors for data scatter in zircons is due to structural breakdown of the mineral and subsequent lead loss due to radiation damage (Jiang, et. al., 2004). Cassiterite is highly refractory and more resistant to radiation damage than zircons (Jiang et al., 2004; Gulson and Jones, 1992) so it is likely that it does not suffer lead loss to the same degree as zircons resulting in more precise data.

6.5.3 Regional considerations

The age of granites in Tasmania becomes younger systematically from east to west with granites on the east coast ranging from 410 Ma to 380 Ma, granites in the central west coast ranging clustering around 370 Ma and granites in the far west coast ranging from 350-360 Ma (Fig. 6.7)(Black et al., 2005; Kositcin and Everard 2013). The age of Sn mineralisation seem to track the ages of the granites across Tasmania getting younger from east to west (Corbett, et al., 2014). The ages presented in this study support this age progression with the cassiterites dated at Big Wilson (373.6 ± 5.4 Ma) being intimately related to the nearby Meridith Granite dated at 372.2 ± 1.9 Ma; Kositcin and Everard 2013.

6.5.4 ID-TIMS

The highly refractory nature of cassiterite which resists radioactive breakdown and makes it ideal for retaining its original U and Pb also makes it very difficult for the ID-TIMS lab to dissolve it. As the ID-TIMS results are not available the aim of obtaining a high resolution date for the cassiterite to differentiate it from the magmatic age of the granite could not be achieved. However, this investigation has shown that cassiterite is suitable for dating *in-situ*

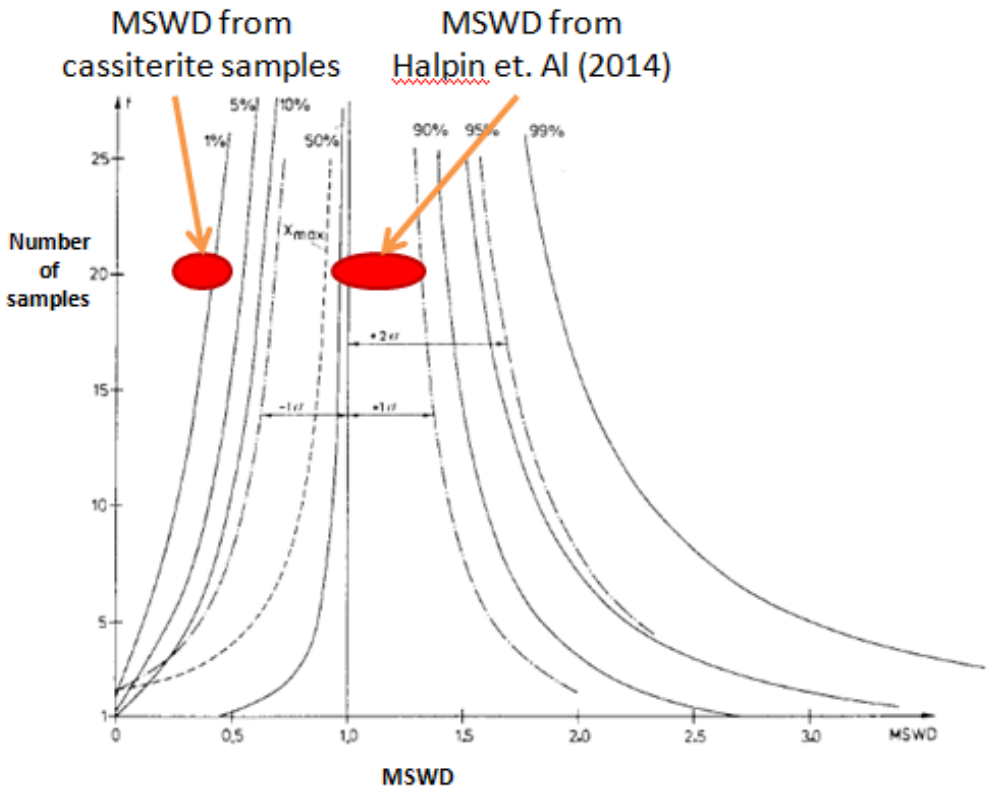

Figure 6.6 MSWD probability distribution (Wendt and Carl, 1991)

using the U/Pb system on the LA-ICP-MS. Samples submitted from this project are being used by Prof. Jim Mortensen at the University of British Columbia as part of a cassiterite dating project with the aim of developing an internationally recognised cassiterite standard.

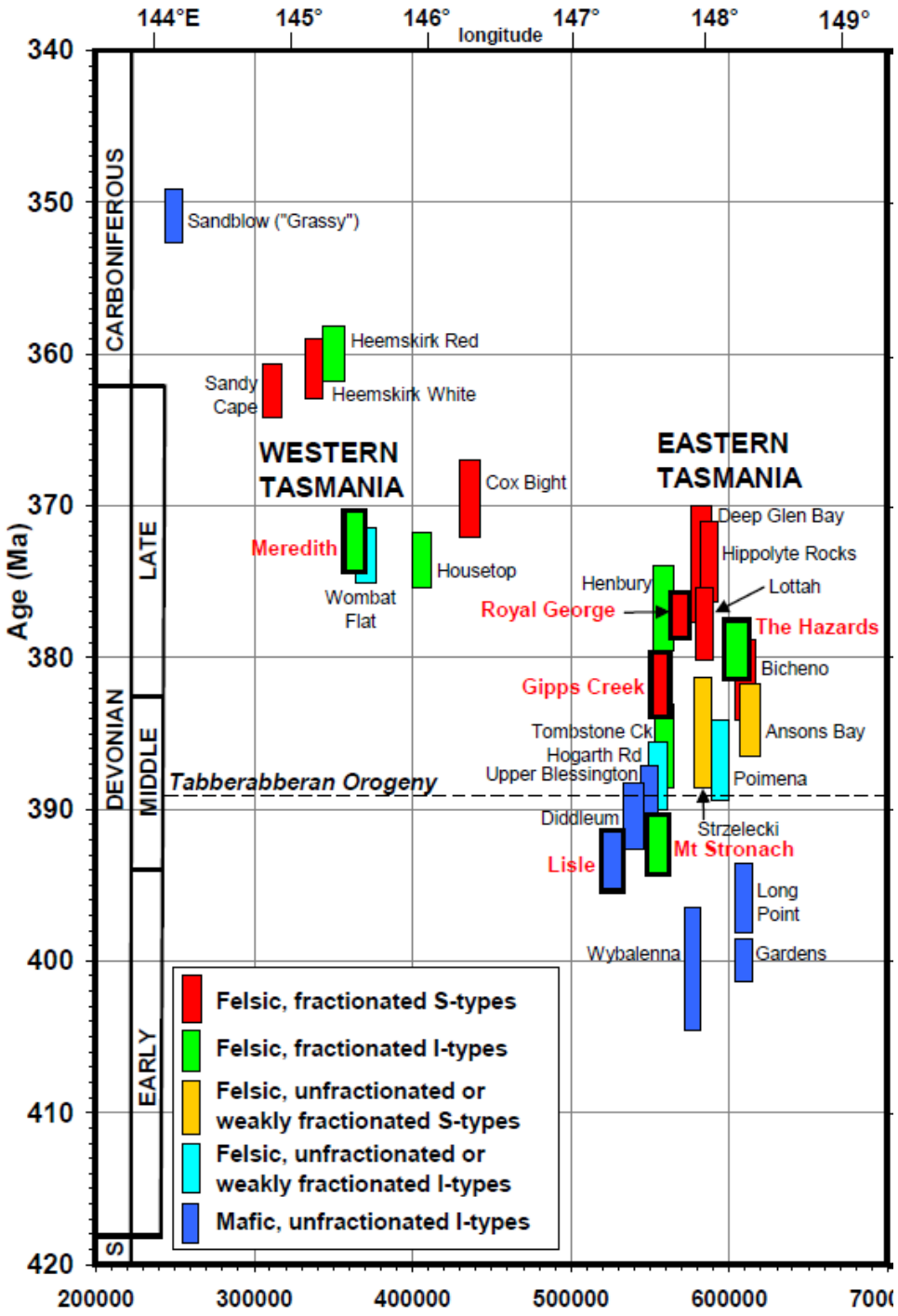

Figure 6.7 Summary time-space diagram plotting emplacement age vs. easting for Devonian-Carboniferous granites in Tasmania (from Kositchin and Everard 2013)

Chapter Seven Genetic model and exploration implications

7.1 Introduction

Exploration by Venture Minerals at the Big Wilson prospect has targeted Sn and W mineralisation using a skarn-style carbonate replacement exploration model similar to that for other Sn-W deposits in western Tasmania, such as Mount Lindsay (Kwak, 1982) and Renison (Kitto, 1998; Fig 1.1). These models assume that the source of the Sn-W mineralisation was hydrothermal fluids exolved from the Meredith Granite. Magmatic fluids become enriched in Sn and W during fractionation when the granites cool. These late-stage magmatic fluids were likely acidic (Kitto 1998) and migrated from the granite into the Gordon Limestone where interaction between the carbonate and the fluids caused progressive cooling and neutralisation of the ore fluid, forming the skarn-style alteration-mineralisation (Kwak, 1982; Kitto, 1998).

This chapter discusses the results of this investigation in the context of this exploration model and makes suggestions for future exploration and research.

7.2 Relationship between the skarn and granite alteration assemblages

Four mineral alteration stages were identified in the skarn in a paragenetic sequence. The first two stages were early alteration, causing the recrystallisation of limestone to marble and the development of zones of calc-silicate alteration, probably as part of a high temperature prograde alteration of the calcareous protolith. This was followed by the third alteration stage which contains minerals stable over a range of temperatures and displays a complex history of recrystallisation and textural overprints. Significant cassiterite mineralisation occurred during this alteration stage coinciding with calc-silicate alteration and the formation of vonsenite at high temperatures (Bloise and Barrese, 2009; Mindat.org 2015). However, the presence of hydrous minerals including actinolite and biotite, along with lower temperature indicator minerals including chlorite, fluorite, sulphide and carbonate minerals, suggest a retrograde origin for Sn mineralisation. The hydrothermal veining that represents the fourth stage of skarn-like alteration are mineralised and support a late-stage origin for the mineralising fluids into the skarn. These veins may be genetically related to the high-grade cassiterite veins which occur in the granite.

Two different types of veins were identified in the granite. Both contain tourmaline but only one contains significant cassiterite. Although no direct cross-cutting relationships were found to be able to directly document a timing relationship between the vein types, it appears that the cassiterite-rich veins formed at a later-stage from a more evolved hydrothermal fluid which exploited a pre-existing vein network and consequently overprinted earlier alteration assemblages. The first stage hydrothermal fluid which is associated with low Sn grades may be correlated with black tourmaline veins in the granite and to vonsenite in Stage 3 skarn alteration.

Correlation between the late-stage cassiterite-rich veins in the granite with Stage 4 hydrothermal veining in the skarn can be inferred on the basis of similarity in the mineralogy and vein orientations.

The relationship between Sn mineralisation and mineral alteration stages is illustrated in Fig. 7.1, which shows the Sn content of hole BW001 correlated to the corresponding down hole TIR and SWIR results obtained using the Hylogger which show the calculated relative mineral abundances measured in each down hole spectral analysis. The highest Sn concentrations occur at the contact between high-grade cassiterite bearing quartz - carbonate - tourmaline veins in the granite and Stage 3 retrograde skarn alteration developed in the limestone at 215m depth. A secondary Sn spike at 225m is associated with a cassiterite-rich quartz-carbonate vein in the granite.

The rapid drop off in Sn grade of the Stage 3 skarn further away from the contact with the high-grade vein in the granite suggests the cassiterite was not transported far into the limestone before being deposited. Of the 13 drill holes at Big Wilson, one, BW001, returned the highest Sn grades in the skarn. This may be because it intersected the skarn at the same location as a high grade cassiterite vein from the granite. If this hypothesis is correct, areas of high-grade Sn in parts of the skarn may be predicted from the position of high-grade veins in the granite.

7.3 Controls on mineralisation geometry

Structural controls may be important in understanding the genesis of mineralisation. The exact location and geometry of structures within the skarn is masked by extensive hydrothermal alteration. However, skarn formation was likely controlled by some combination of faulting and bedding parallel fluid flow. The orientation of the skarn is

approximately parallel to local bedding in the limestone, suggesting fluids exploiting a permeable sedimentary horizon in the limestone protolith; however, the presence of hydrothermal breccias also suggest localised faulting. At high temperatures and pressures when pore fluid pressure approaches lithostatic pressure the permeability of marble may be increased by up to two orders of magnitude (Fischer and Paterson, 1992). Dissolution of carbonates by acidic hydrothermal fluids which exploited a permeable bed in the limestone may be one type of control.

The contact between the ultramafic unit and the Gordon Limestone is also considered to be faulted (Crawford and Berry 1992). The skarn occupies the space between the ultramafics and the marble in the southern half of the prospect area, suggesting that hydrothermal fluids may have exploited a faulted contact. However, in the north of the prospect area the skarn is bounded on both sides by marble and the skarn follows the strike of bedding rather than the profile of the ultramafic contact with the marble.

The steep dip of the skarn is also consistent with fluids escaping out of the granite by rising either vertically or propagating horizontally and following the weakest bedding plane in the original marble.

The skarn follows bedding with a northeast strike that is well-defined by the tin anomaly in soil geochemistry (Fig 3.2A). The skarn orientation is broadly orthogonal to the northwest-striking veins in the granite although both contain high-grade mineralisation. The high angle between the two high-grade mineralisation zones in the different protoliths means that any exploration drilling targeted in an orientation optimal for intersection of the skarn was also inadvertently oriented parallel to the veining in the granite (Fig. 7.2). If tin mineralisation in the skarn is highest where it is intersected by high-grade veins from the granite, as observed in BW001, (Fig. 7.1) then it is important to know more about the abundance and distribution of these high-grade veins. As a result of this investigation four samples of high-grade veins were discovered in two distinctly separate locations, suggesting that mineralisation discovered in BW001 may not simply represent an isolated vein but rather, that there is potential for multiple high-grade veins to occur elsewhere in the prospect area.

7.3 Ore deposit models revisited

During this project some features of mineralisation at Big Wilson have become apparent that are inconsistent with the ore deposit models outlined in section 7.1 above, as well as other regional Sn deposits. The Mt. Lindsay and Renison deposits both host all their target

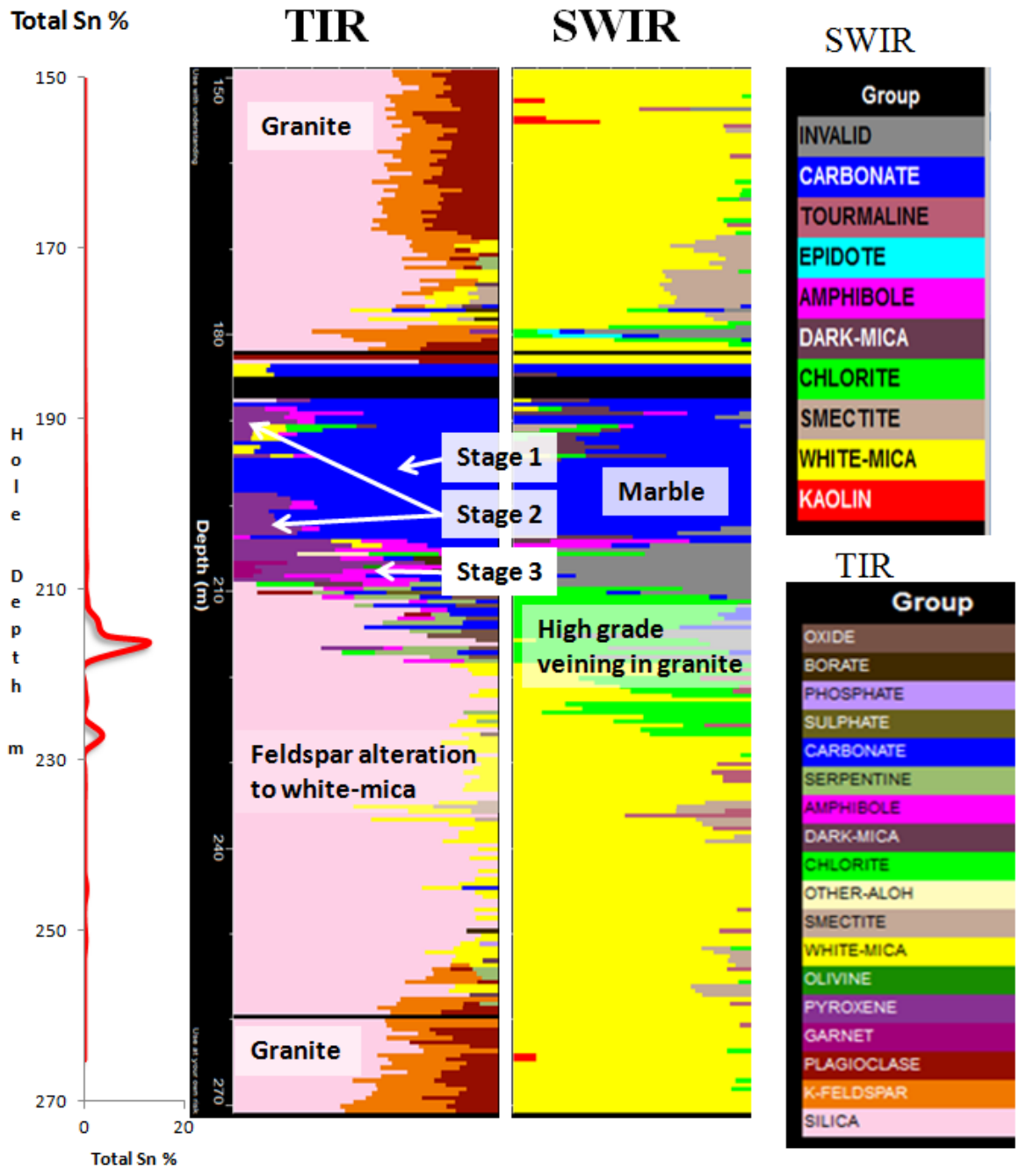

Figure 7.1 Total Sn shown beside SWIR and TIR Hylogger[tm] data from drill hole BW001 showing the highest Sn grades occur at the contact between high-grade veining in the granite and Stage 3 skarn mineralisation. Stage 4 hydrothermal veining in the skarn is likely a continuation of late stage high-grade veining in the granite.

mineralisation outside the granite in the carbonate hosted skarn systems (Kwak, 1982; Kitto, 1998). Likewise the Cleveland tin mine (Fig 1.1) hosted its Sn mineralisation in sedimentary layers outside the granite (Collins, 1981) and Sn skarn mineralisation at Mount Bischoff (Fig 1.1) is hosted in a dolomite unit (Halley and Walshe, 1995). Although in each of these deposits the granite was the source of the tin-rich hydrothermal fluids, none of these deposits have been shown to host economic Sn mineralisation in a granite protolith.

Wholerock Sn assay for BW001 (Fig 7.1) illustrates that much of the Sn mineralisation at Big Wilson is found in the granite protolith. Due to intense alteration the exact point where the

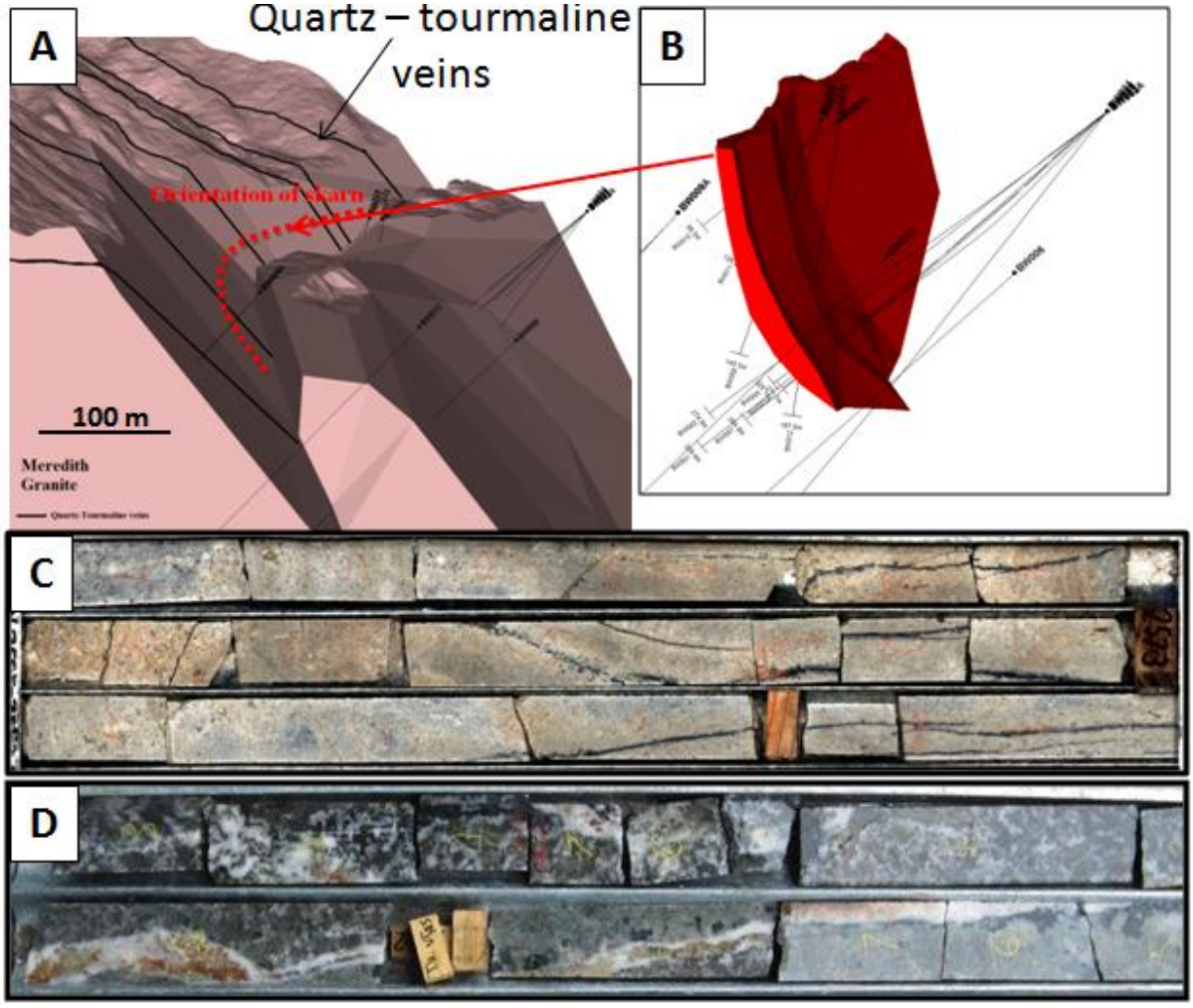

Figure 7.2 A) Block model of the Meredith Granite showing drill hole traces oriented parallel to quartz-tourmaline veins. The red dashed line shows the position of the skarn fitting between the dyke and the main body of the Meredith Granite. B) Block model of the skarn showing diamond drill hole traces oriented orthogonal to the skarn. C) Core from BW001 showing a low grade quartz – black tourmaline vein containing running parallel to core. D) Core from BW012 showing a high grade zone quartz – carbonate - cassiterite vein with a halo of green tourmaline replacing feldspar running parallel to core

protolith changes from granite to limestone in BW001 is unclear but is somewhere between a depth of 212m and 217m. The portion of this interval that is limestone protolith contains the highest grade Sn measured in the skarn. The highest grade Sn in the hole is in altered granite directly at the contact with the skarn. A secondary concentration of high-grade Sn is located further down hole in another quartz-siderite-cassiterite vein hosted in altered granite. If none of the regional ore deposits contain economic tin mineralisation in the granite in the same form as that observed at Big Wilson then perhaps a revised ore deposit model should be considered.

The San Rafael Sn-Cu deposit in southeastern Peru is the largest known tin deposit in the world (Kontak and Clark, 2002). Bonanza grade Sn mineralisation is controlled by brittle shear zones hosted in granitoid rocks that have undergone intense metasomatization. Skarn and porphyry style Sn mineralisation has not been documented at San Rafiel (Kontak and Clark, 2002). Early alteration at San Rafael is characterised by abundant barren quartz-tourmaline veins. The majority of these veins were sealed prior to ore deposition, but a few remained open and these contain a second generation of Fe-rich green tourmaline which co-precipitated with abundant cassiterite and chlorite (Mlynarczyk and Williams-Jones, 2006).

Both the Big Wilson and San Rafael deposits contain multiple generations of tourmaline veining with a barren stage preceding an ore stage with Fe-rich green tourmaline. Future drilling at Big Wilson should target the high-grade Sn veins in the granite. This could be optimised by orienting drilling in a northeast direction, orthogonal to the northwest strike of the veins in the granite.

7.4 Tourmaline as a potential vector to mineralisation

This investigation demonstrated a significant correlation between the tin concentration of tourmaline and several major and trace elements in tourmaline that have the potential to be used as exploration vectors to tin mineralisation. Significantly, this study verifies that tourmaline colour, particularly the presence of green tourmaline and tourmaline replacing feldspar may be a very good field indicator of proximity to tin mineralisation. The refractory nature of tourmaline and the granite it is hosted in means it can survive in stream sediments, soil samples (gravels), and in outcrop, meaning it should be possible to observe during field surveys.

The relationships identified between Sn and Zn, Li, Sr and Sb also have potential to be useful as a vector to mineralisation, however, further work needs to be undertaken to examine these findings to determine how robust they are and if they apply on a regional scale. The quantity and distribution of mineralised veins in the area is still unknown, and with the drilling orientation parallel to the veining, it is not possible to ascertain the distance to the nearest mineralisation.

7.5 Cassiterite geochronology

This study was successful in obtaining a new LA-ICP-MS age of mineralisation by direct, *in situ* analysis of cassiterite. Agreement between this age and the published age for the Meredith Granite provides support for the genetic link between the granite emplacement and mineralisation. A drawback to the LA-ICP-MS method is that no cassiterite standard yet exists so a non-matrix matched standard needed to be used, together with an untested matrix correction method based on the concordance of Archean cassiterite in the U-Pb and Pb-Pb systems. Dating the cassiterite at Big Wilson through the more precise ID-TIMS method would have provided a clearer indication of the timing of mineralisation based on the date of cooling of the granite . However, due to the highly refractory nature of cassiterite, the laboratory undertaking this work was unable to fully dissolve cassiterite for analysis in time for the completion of this thesis.

A by-product of the ID-TIMS analysis was the creation of a cassiterite standard for future microbeam geochronology work. Potential standards were identified but these were unable to be fully developed in time to be applied to this study. The science of directly dating cassiterite is just beginning to develop and attempts made in this project are important steps along the way to developing a suitable standard.

Chapter Eight Conclusions

The four main aims of this study were:

1 To develop a mineralogical paragenesis for the skarn and granite alteration-mineralisation system at the Big Wilson prospect.
2 To investigate the geometry of each of the major mineralised stages, focusing on. high-grade cassiterite bearing veins in the granite.
3 To determine if the mineral chemistry of the tourmaline associated with both mineralised and barren veins could be a useful vector to high-grade mineralisation.
4 To resolve the timing of tin mineralisation relative to the magmatic age of the Meredith Granite by direct dating of cassiterite.

The main findings of this study were:

- The identification and documentation of four stages of alteration in the limestone-hosted skarn.
- That the Meredith Granite contains two distinct vein types with characteristic alteration envelopes dominated by white mica.
- Boron-rich fluids preferentially formed tourmaline-rich veins in the granite and vonsenite in the limestone-hosted skarn.
- Tourmaline-rich veins in the granite are generally steeply dipping with a northwest strike.
- High-grade mineralised veins in the granite were discovered in multiple locations.
- That tourmaline colour is a good field indicator of potential tin mineralisation.
- Tourmaline major and trace element chemistry has potential to be used as a vector towards mineralisation.
- Direct dating of cassiterite has returned the same age as the Meredith Granite, reinforcing the theory that the granite is the source of the mineralisation.
- The presence of cassiterite-rich veins in the granite oriented orthogonally to the skarn suggests fluid migration from the granite to the limestone.

Further research:

- Future exploration drilling should target the mineralised veins in the granite.

- Work on the major and trace element chemistry of tourmaline should focus on obtaining more samples around known mineralisation centres to develop a better understanding of the spatial variation in tourmaline chemistry (e.g. Al, Fe, Mg, Sn, Zn, Li, Sb, Sr) with distance from mineralisation.
- The distinctive green tourmaline associated with Sn mineralisation at Big Wilson should be studied relative to other tourmalines from around the greater Meredith Granite batholith and other Tasmanian and international granites to see if the relationships observed at Big Wilson also occur on a regional or global scale.
- Cassiterite is a useful mineral for U-Pb geochronology but the development of cassiterite standards are required.

References

Baker, J., Peate, D., Waight, T. and Meyzen, C., 2004. Pb isotopic analysis of standards and samples using a Pb-207-Pb-204 double spike and thallium to correct for mass bias with a double-focusing MC-ICP-MS. *Chemical Geology*, 211, pp. 275-303.

Black L. P., Gulson B. L. 1978. The age of the Mud tank Carbonatite, Strangways Range, Northern Territory. *BMR Journal of Australian Geology and Geophysics 3*, pp. 227-232.

Black, L. P., Kamos, L., Allen, C.M., Aleinikoff, J.N., Davis, D.W., Korsch, R.J., Foudoulis, C., 2003, TEMORA 1: a new zircon standard for Phanerozoic U–Pb geochronology. *Chemical Geology* 200, pp. 155– 170.

Black, L.P., Kamo, S.L., Allen, C.M., Davis, D.W., Aleninikoff, J.N., Valley, J.W., Mundil, R., Campbell, I.H., Korsch, R.J., Williams, I.S., Foudoulis, C., 2004, Improved 206Pb/238U microprobe geochronology by the monitoring of a trace-element related matrix effect; SHRIMP, ID-TIMS, ELA-ICP-MS, and oxygen isotope documentation for a series of zircon standards. *Chemical Geology* 205, 115-140.

Bloise, A. & Barrese, E., 2009. Synthesis of isomorphic vonsenite-ludwigite series. *Journal of Mineralogy and geochemistry*, 186(3), pp. 345-350.

Brimhall, G. H., Dilles, J. H. and Proffett, J. M., 2006. The Role of Geological Mapping in Mineral Exploration. *Society of Economic Geologists Special Publication 12*, pp. 221-241.

Brooks, C., Hart, S. R. and Wendt, I., 1972. Realistic use of two-error regression treatments as applied to rubidium-strontium data. Rev. *Geophysics Space physics*, Volume 10, pp. 551-577.

Brown, A. V., 1980. *Some aspects of the geology of the Mt Lindsay - Dundas areas, western Tasmania*, Hobart: Tasmania Department of Mines.

Brown, A. V., 1986. *Geology of the Dundas - Mt. Lindsay - Mt. Younguck Region. Geological Survey Bulletin 62*, Rosny Park: Department of Mines.

Collins, P. L., 1981. The geology and genesis of the Cleveland tin deposit, Western Tasmania; fluid inclusion and stable isotope studies. *Economic Geology*, 76(2), pp. 365-392.

Chang, Z., Vervoort, J. D., McClelland, W. C., and Knaack, C., 2006, U-Pb dating of zircon by LA-ICP-MS: *Geochemistry, Geophysics, Geosystems*, v. 7.

Compston, W., 1999, Geological age by instrumental analysis: the 29th Hallimond Lecture. *Mineralogical Magazine* 63, pp.297-311.

Corbett, K. D., Quilty, P. G. and Calver, C. R., 2014. *Geological Evolution of Tasmania*. s.l.:Geological Society of Australia (Tasmania Division).

Crawford, A. J. and Berry, R. F., 1992. Tectonic implications of Late Proterozoic-Early Palaeozoic igneous rock association in western Tasmania. *Tectonophysics*, Volume 214, pp. 37-56.

Einaudi, M. T., 1997. *Mapping altered and mineralized rocks: An introduction to the "Anaconda Method"*. s.l.:Stanford University.

Einaudi, M. T., Meinert, L. D. and Newberry, R. J., 1981. Skarn deposits. *Economic Geology*, Volume 75 ANN. Vol 77, pp. 317-391.

Everard, I. L. et al., 1991. *Current systematic regional mapping - new potential for mineral discovery*, Hobart: Bulletin of the Geological Survey of Tasmania.

Fischer, G. J. & Paterson, M. S., 1992. Measurement of Permeability and Storage Capacity in Rocks During Deformation at High Temperature and Pressure. *International Geophysics*, Volume 51, pp. 213-252.

Fox, N., 2012. *Controls on Alteration and Mineralsiation at the Cadia East Alkalic Porphyry Au-Cu Deposit, NSW,* Hobart: Univeristy of Tasmania.

Fryer, B.J., Jackson, S.E., Longerich, H.P., 1993, The Application of Laser Ablation Microprobe-Inductively Coupled Plasma-Mass Spectrometry (Lam-Icp-Ms) to in situ (U)-Pb Geochronology. *Chemical Geology* 109, pp.1-8.

Gulson, B. L. and Jones, M. T., 1992. Cassiterite: potential for direct dating of mineral deposits and a precise age for the Bushveld Complex granites. *Geology*, Volume 20, pp. 355-358.

Halley, S. W. and Walshe, J. L., 1993. A re-examination of the Mount Bischoff cassiterite sulfide skarn, Western Tasmania. *Economic geology*, Volume 90, pp. 1676-1693.

Halpin, J.A., Jensen, T., McGoldrick, P., Meffre, S., Berry, R.F., Everard, J.L., Calver, C.R., Thompson, J., Goemann, K., Whittaker, J.M. 2014. Authigenic monazite and detrital zircon

dating from the Proterozoic Rocky Cape Group, Tasmania: Links to the Bel-Purcell Supergroup, North America. *Precambrian Research*.250, pp.50-67.

Harley, S.L. and Kelly, N.M., 2007. Zircon: Tiny but timely. *Elements*, 3(1): pp.13-18.

Haythornthwaite, J. R., 2011. *Spatial and Temporal Mineral Zonation of the Sn-W-Magnetite Main Skarn at Mt Lindsay, Tasmania*, s.l.: University of Exeter.

Henry, D. J. & Guidotti, C. V., 1985. Tourmaline as a petrogenetic indicator mineral: an example from the staurolite-grade metapelites of NW Maine. *American Mineralogist*, Volume 70, pp. 1-15.

Huston, D. L. et al., 2002. The Timing of Mineralization in the Archean North Pilbara Terrain, Western Australia. *Economic Geology*, Volume 97, pp. 733-755.

Jackson, P., Changkakoti, A., Krouse, H. R. and Gray, J., 2000. The origin of greisen fluids of the Foley's zone, Cleveland tin deposit, Tasmania, Australia. *Economic geology*, Volume 95, pp. 227-236.

Jackson, S.E., Pearson, N.J., Griffin, W.L., Belousova, E.A., 2004, The application of laser ablation-inductively coupled plasma-mass spectrometry to in situ U–Pb zircon geochronology. *Chemical Geology* 211, pp.47-69.

Jiang, S., Yu, J. & Lu, J., 2004. Trace and rare-earth element geochemistry in tourmaline and cassiterite from the Yunlong tin deposit, Yunan, China: implication for migmatitic hydrothermal fluid evolution and ore genesis. *Chemical Geology*, 20(209).

Kitto, P. A., 1994. *Structural and geochemical controls on mineralisation at Renison, Tasmania*. PhD thesis., Hobart: University of Tasmania.

Kitto, P. A., 1998. Renison-style carbonate-replacement Sn deposits. *Journal of Australian Geology & Geophysics*, 17(4), pp. 163-168.

Kontak, D. J. & Clark, A. H., 2002. Genesis of the Giant, Bonanza San Rafael Lode Tin Deposit, Peru: Origin and Significance of Pervasive Alteration. *Economic Geology*, 97(8), pp. 1741-1777.

Kositcin, N. and Everard, J. L., 2013. *New SHRIMP U-Pb zircon ages from Tasmania*, Canberra: Geoscience Australia record 2013/22.

Kosler, J., 2001, Laser-ablation ICPMS study of metamorphic minerals and processes. In: Sylvester P. J. ed. *Laser-ablation-ICPMS in the earth sciences; principles and applications* Mineralogical Association of Canada Short Course Handbook 29, pp.185-202.

Kosler J.and Sylvester P.J. ,2003 Present trends and the future of zircon in geochronology; laser ablation ICPMS. *Reviews in Mineralogy and Geochemistry 53*, pp.243-275.

Kwak, T. A., 1987. *W-Sn skarn deposits and related metamorphic skarns and granitoids*. Tokyo: Elsevier.

Kwak, T. A., 1982. *The geology and geochemistry of the zoned Sn-W-F-Be skarns at Mt. Lindsay, Tasmania, Australia*, Bundoora: La Trobe University.

Kwak, T. A. P., 1983. The Geology and Geochemistry of the Zoned, Sn-W-F-Be Skarns at Mt. Lindsay, Tasmania, Australia. *Economic Geology*, Volume 87, pp. 1440-1465.

Li, X., Long, W.G., Li, Q.L., Liu, Y., Zheng, Y.F., Yang, Y.H., Chamberlain, K.R., Wan, D.F., Guo, C.H., Wang, X.C., Tao, H., 2010. Penglai Zircon Megacrysts: A Potential New Working Reference Material for Microbeam Determination of Hf-O Isotopes and U-Pb Age. *Geostand Geoanal* Res 34, 117-134.

Marillo-Sialer, E. et al., 2014. The zircon "matrix effect": evidence for an ablation rate control on the accuracy of U-Pb age determinations by LA-ICP-MS. *Journal of analytical atomic spectrometry*, pp. 1-9.

McDougall, I. and Harrison, T. M., 1988. *Geochronology and Thermochronology by the 40Ar/39Ar Method*. s.l.:Oxford University Press.

Meffre, S., Large, R. R., Scott, R., Woodhead, J., Chang, Z., Gilbert, S. E., Danyushevsky, L. V., Maslennikov, V., and Hergt, J. M., 2008, Age and pyrite Pb-isotopic composition of the giant Sukhoi Log sediment-hosted gold deposit, Russia: *Geochimica et Cosmochimica Acta*, v. 72, pp. 2377-2391.

Meinert, L. D., Kipple, G. M. and Nicolescu, S., 2005. World Skarn Deposits. *Economic Geology*, Volume 100th Anniversary vol, pp. 299-336.

Meinert, L., 2008. *Workshop on Exploration for Skarn Deposits*. s.l.:s.n.

Mindat.org http://www.mindat.org/min-4207.html

Mlynarczyk, M. S. & Williams-Jones, A. E., 2006. Zoned Tourmaline Associated with Cassiterite: Implications for fluid evolution and tin mineralisatioin in the San Rafael Sn-Cu deposit, southeastern Peru. *The Canadian Mineralogist,* Volume 44, pp. 347-365.

Moore, D. H., Betts, P. G. and Hall, M., 2014. Fragmented Tasmania: the transition from Rodinia to Gondwana. *Australian Journal of Earth Sciences: An international Geoscience Journal of the Geological Society of Australia*.

Nicolescu, S. and Marza, I., 1989. On the history of ore deposit studies in Romania. *Geologia-Geographia*, Volume 34, pp. 94-99.

Owen, S. and Pfeifenberger, S., 2012. *Serpentine Ridge Explaration Licence 45/2010 Annual Technical Report for the period 30/05/2011 to 30/05/2012*, Perth: Venture Minerals Ltd.

Paton, C., Woodhead, J D., Hellstrom, J C. . Hergt, JM, Greig,A and Maas, R. 2010 Improved laser ablation U-Pb zircon geochronology through robust down-hole fractionation correction. *Geochemistry, Geophysics, Geosystems 11*, pp.1525-2027

Reid, A. M., 1921. *Tasmania Department of Mines Geological Survey Bulletin No. 32 Osmiridium in Tasmania,* Tasmania: Government printer.

Rice, P. J., 1985. *Environments and Diagenesis of the Gordon Group in the Zeehan area,* Hobart: University of Tasmania.

Sack, P.J., Berry, R.F., Meffre, S., Falloon, T.J., Gemmell, J.B., Friedman, R.M., 2011. In situ location and U-Pb dating of small zircon grains in igneous rocks using laser ablation-inductively coupled plasma-quadrupole mass spectrometry. *Geochemistry, Geophysics, Geosystems 12.*

Seymour, D. B., Green, G. R. and Calver, C. R., 2007. *Tasmanian Geological Survey Bulletin 72 The Geology and Mineral Deposits of Tasmania: a summary*, Rosny Park: Mineral Resources Tasmania.

Sweetapple, M. T., 2000. *Characteristics of Sn-Ta-Be-Li Industrial Mineral Deposits of the Arcaean Pilar Craton, Western Australia,* Canberra: Geoscience Australia.

Slama, J., Kosler, J., Condon, D.J., Crowley, J.L., Gerdes, A., Hanchar, J.M., Horstwood, M.S.A., Morris, G.A., Nasdala, L., Norberg, N., Schaltegger, U., Schoene, B., Tubrett, M.N., Whitehouse, M.J., 2008. Plesovice zircon - A new natural reference material for U-Pb and Hf isotopic microanalysis. *Chemical Geology* 249, pp.1-35.

Swinnea, J. S. & Steinfink, H., 1983. Crystal structure and Mossbauer spectrum of vonsenite,2FeO FeBO3. *American Mineralogist,* Volume 68, pp. 827-832.

Thirwall, M. F., 2000. Inter-laboratory and other errors in Pb isotope analyses investigated using a 207Pb-204Pb double spike:. *Chemical Geology,* Volume 163, pp. 299-322.

Tornebohm, A. E., 1875. Om lagerfoljden inom Norbergs malmfal. *Geol. Foren. Stockholm Forh,* Volume 2, pp. 329-335.

Venture Minerals, 2012. *Venture Minerals*. [Online]

Available at: http://www.ventureminerals.com.au/index.php/investor-resources/asx-announcements-page/asx-announcements/2012 [Accessed 10 07 2015].

Venture Minerals, 2013. *Venture Minerals*. [Online]

Available at: http://www.ventureminerals.com.au/index.php/investor-resources/asx-announcements-page/asx-announcements/annual-reports [Accessed 10 07 2015].

Wendt, I. & Carl, C., 1991. The statistical distribution of the mean squared weighted deviation. *Chemical Geology,* Volume 86, pp. 275-285.

Wiedenbeck, M., Alle, P., Corfu, F., Griffin W.L., Meier, M., Oberli, F., Vonquadt A., Roddick, J.C., Speigel W., 1995, 3 Natural Zircon Standards for U-Th-Pb, Lu-Hf, Trace-Element and REE Analyses. *Geostandards Newsletter* 19, pp.1-23.

Appendix 2: Surface sampling data

H0002	Version	3				
H0003	Date_generated	14/05/2016				
H0004	Reporting_period_end_date	28/05/2016				
H0005	State	TAS				
H0100	Tenement	EL45/2010				
H0101	Tenement_holder	Venture Minerals Ltd				
H0102	Project_name	Big Wilson				
H0106	Tenement_operator	Venture Minerals Ltd				
H0150	250K_map_sheet	SK5503 Burnie				
H0151	100K_map_sheet	7914 Pieman				
H0152	50K_map_sheet	na				
H0153	25K_map_sheet	3637 Rosebury, 3638 Parsons				
H0200	Start_date_of_data_acquisition	28/05/2015				
H0201	End_date_of_data_acquisition	28/05/2016				
H0202	Data_format	SG3				
H0203	Number_of_data_records	73				
H0204	Date_of_metadata_update	28/05/2016				
H0500	Feature_Located	geological mapping observation				
H0501	Geodetic_datum	GDA94				
H0502	Vertical_datum	na				
H0503	Projection	MGA				
H0531	Projection_zone	55				
H0532	Surveying_instrument	Garmin GPS60CSx & 62s				
H0533	Surveying_Company	Venture Minerals Ltd				
H0600	Sample_code	GEOLOC				
H0601	Sample_type	geological mapping location & structural observations				
H0900	Remarks:					
H1000	Location	Prospect	Lith1	Lith2	Lith3	Description
H1001						
D	MHAK001	Merton Hill	qzV			Angular cobble of wt qz vein with euhedral qz up to 30mm
D	MHAK002	Merton Hill	FG	ST		moderately weathered equigranular fine grained granite, 60% feldpsar & 30% quartz, sor sericite, contact with moderately weathered wt-gn sericitic siltstone, anastomosing qz-go vein at contact, outcrop on side of drill pad.
D	SWAK001	Sweeney Creek	SMUD			gy silty mud. Very swampy. Rare small qz grains seen.
D	SWAK002	Sweeney Creek	SMUD			gy silty mud with fragments of clean medium grained qz & ?tourmaline
D	SWAK003	Sweeney Creek	SMUD			Yabby mount in swamp with gy silty mud & qz grains
D	SWAK004	Sweeney Creek	USERP			mod weathered fol serpentinite with dgy-dbl fine fibrous veinlets
D	SWAK005	Sweeney Creek	FG	ST		moderately weathered medium to coarse grained sericitic qz-phyric granite dyke cutting siltstone, coarse grained (to 20mm) white euhedral qz vein in granite
D	SWAK006	Sweeney Creek	SMUD			muddy silty gy soil
D	SWAK007	Sweeney Creek	SM			Angular float in tree bowl of thin cobbles of weathered dgy mudstone, thick soil
D	SWAK008	Sweeney Creek	ST			gy silstone on powerline track. 3cm wt qz vein through, euh qz.
D	SWAK009	Sweeney Creek	ST			mw siltstone in Sweeney Ck, ang float cobbles of siltstone & ang fragment of prismatic qz vein
D	SWAK010	Sweeney Creek	ST ?			bedded gy sedimentary rock, beds rich in altered fsp, 5m upstream only gy siltstone without fsp

H1000	Location	Prospect	Lith1	Lith2	Lith3	Description
H1001						
D	SWAK011	Sweeney Creek	UM	RLC	qzST	Old workings with rounded cobbles of medium grained ultramafic & ?gabbro (50% fsp, fe mt grains), rounded laterite cobble, rounded qz siltstone cobble
D	SWAK012	Sweeney Creek	ST			lam gy siltstone
D	SWAK013	Sweeney Creek	ST			Outcrop on side of powerline track, lbn-og weathered siltstone, boulder of Red Rock Member conglomerate on the road.
D	SWAK014	Sweeney Creek	SCG	SS	ST	On powerline track, subrounded-subrangular boulders of Red Rock Member & cobbles of gy sandstone & siltstone.
D	SOKW01	Keenan-Wilson	SGVL			>1.5m thickness of clay supported alluvial gravels exposed in alluvial workings, clasts dominated by subrounded ultramafic boulders & lesser mt+am hornfels after laminated ?calcareous siltstone, no basement exposure
D	SOKW02	Keenan-Wilson	SGVL			extensive alluvial workings in creek dominated by granite fossiliferous qz sandstone, ultramafic & gabbro clasts, no basement exposure
D	SOKW03	Keenan-Wilson	gtZAMP			low rise in valley with subcrop of pale green medium grained amphibolite with c. 2% pyrrhotite & patchy magnetite, pk ?garnet patch
D	SOKW04	Big Wilson	SLST			planar & locally cross laminated marble with scattered cg (>5mm) calcite nodules after shells?
D	SOKW04A	Big Wilson	SLST	SGVL		1m tk alluvial gravel terrace on top of mdb gy limestone
D	SOKW05	Big Wilson	FG			medium grained to cg bt granite forming cataract in Little Wilson River
D	SOKW06	Big Wilson	ZXS	ZGRS		subcrop cobbles of granular magnetite skarn with minor weathered sulphides & silicates, light weight porous gossan after ?sx+calcsilicate skarn?, se-?sd altered granite, rare cg qz+tu vein (>10mm tk) cutting altered granite, rare weakly acicular & scaley mt skarn after borate skarn?
D	SOKW07	Big Wilson	tuV	FG		dk bn & locally gn bn qz+tu veins to 10mm tk spaced 10cm to several metres apart in cg equigranular granite, qz+tu veins comprise <1% of outcrop area
D	SOKW07	Big Wilson	tuV			dk bn & locally gn bn qz+tu veins to 10mm tk spaced 10cm to several metres apart in cg equigranular granite, qz+tu veins comprise <1% of outcrop area
D	SOKW07	Big Wilson	FG			subtle ?igneous banding in granite
D	SOKW08	Big Wilson	FGRS			orange ferruginous weathered se+?sd altered cg equigranular granite, weak foliation
D	SOML111	Salmons Creek	SDOL			ferruginous clay after ?dolomite with gy siliceous ?oolite rubble
D	THBW001	Big Wilson	mtZXS			Highly weathered 2-4cm banded granular magnetite float. Strongly magnetic, granite boulder nearby. Big wilson gossan site.
D	THBW002	Big Wilson	FG	mtZXS	qztuV	granite with quartz-tourmaline vein in contact with oxidised magnetite skarn (gossan), 1-2mm radiating qz-fsp-tu crystals, some possible historic diggings nearby
D	THBW003	Big Wilson	FG			se altered qz rich granite with fine grained ?tourmaline, fe-ox staining
D	THBW004	Big Wilson	feoZXS			rd-og porous gossan, magnetite poor
D	THBW005	Big Wilson	FG			Weathered sericitic granite-?greisen
D	THBW006	Big Wilson	ammtZXS			granular magnetite+amphibole skarn with acicular texture after ?vonsenite, oxides coating surface
D	THBW007	Big Wilson	tuV	FG		tourmaline vein in granite
D	THBW007	Big Wilson	tuV	FG		tourmaline vein in granite
D	THBW007	Big Wilson	FG			igneous banding in granite
D	THBW007	Big Wilson	FG			igneous banding in granite
D	THBW007	Big Wilson	FG			igneous banding in granite
D	THBW007	Big Wilson	FG			igneous banding in granite

H1000	Location	Prospect	Lith1	Lith2	Lith3	Description
H1001						
D	THBW007	Big Wilson	FG			igneous banding in granite
D	THBW008	Big Wilson	tuV	FG		tourmaline vein in granite
D	THBW008	Big Wilson	FG			4-5m thick med grained granite dyke in coarse grained granite
D	THBW008	Big Wilson	FG			4-5m thick med grained granite dyke in coarse grained granite
D	THBW008	Big Wilson	tuV			quartz+tourmaline+sericite vein 10-20cm thick in granite
D	THBW008	Big Wilson	FG			medium grained granite dyke
D	THBW009	Big Wilson	tuV	tuV		quartz+tourmaline vein in granite
D	THBW009	Big Wilson	tuV			quartz+tourmaline+chlorite vein in coarse grained granite
D	THBW009	Big Wilson	FG			2-3m thick medium grained granite dyke in coarse grained granite
D	THBW009	Big Wilson	FG			2-3m thick medium grained granite dyke in coarse grained granite
D	THBW010	Big Wilson	SLST			lam-tnb gy-wt limestone with pyroxene & ?axinite or ?garnet, silver magnetic pyroxene rimming rounded fossils
D	THBW011	Big Wilson	qzSS	SLST	qzSST	south side of river channel has bluffs of white thin-medium bedded fine grained quartz sandstone & siltstone, north bank of river has abundant rounded limestone & siltstone boulders to 1.5m size but no bedrock, limestone recessive
D	THBW012	Big Wilson	qzSS	qzSST		thin to medium bedded fine-medium grained quartz sandstone & siltstone, continuation of THBW011 further downstream in Wilson River
D	THBW013	Big Wilson	qzSST			laminated to medium bedded pale grey fine grained sandstone & siltstone outcrop in riverbed outcrop, extensive riverwide outcrop extending 100m downstream, cascades
D	THBW014	Big Wilson	tuV	FG		15-20mm thick qz-tourmaline vein with minor pyrite & ?manganese in coarse grained granite, highly weathered sample
D	THBW015	Big Wilson	tuV	FG		5-15mm tk tourmaline vein with sericite rims in coarse grained granite, group of veins in 3m exposure
D	THBW016	Big Wilson	tuV	FG		5cm tourmaline vein in coarse grained granite
D	THBW017	Big Wilson	tuV	FG		creek wall in pool at bottom of 8m cascade. 5-30mm subparallel qz-tourmaline vein set within 5cm
D	THBW018	Big Wilson	tuV	FG		1-5mm tourmaline vein within a 10 cm band of coarse grained granite
D	THBW019A	Big Wilson	tuV	FG		bk ?manganese-oxide vein with sulphides, 10-15mm vein in coarse grained granite
D	THBW019B	Big Wilson	FG			30cm black & white tourmaline rich granite dyke
D	THBW020	Big Wilson	tuV	FG		series of 1-5mm tourmaline vein in coarse grained granite. 2 veins 6cm apart sampled
D	THBW021	Big Wilson	tuV	FG		outcrop partly under water, very large boulder float upstream, 1-.5mm parallel tourmaline vein sets in coarse grained granite, vein sample diluted with abundant wall rock.
D	THBW022	Big Wilson	FG			1m rounded boulder of porphyroblastic granite, 20mm tabular qz crystals, cm 10-15mm rounded fsp crystals, clear-gy 10mm angular qz crystals & 5-8mm black angular ?tourmaline in a fine grained qz-fsp-tu matrix (10%tu, 60%fsp, 30% qz), ?dyke
D	THBW023	Big Wilson	FG	SLST		granite - siltstone contact, first appearance limestone float in creek
D	THBW024	Big Wilson	tuV	FG		Riverbed outcrop at cascade in Little Wilson River, 20-30mm tourmaline vein with 10-20mm bladed cystals, in coarse grained granite, fine grained granite dyke nearby
D	THBW025	Big Wilson	tuV	FG		thin (1-2mm) dgn tourmaline vein with 5-10mm bladed crystals, creek bed outcrop on 3m tiered cascade of coarse grained granite

H1000	Location	Prospect	Lith1	Lith2	Lith3	Description
H1001						
D	THBW026	Big Wilson	tuV	FG		10-20mm qz-tourmaline vein in coarse grained granite, more coarse grained granite outcrops upstream & downstream but barren - no tourmaline veins
D	THBW027	Big Wilson	UM			dgn ultramafic, pyroxene to 4mm weakly magnetic, outcrop on side of creek & subcrop in creek bed, very little granite float in creek above this point
D	THBW028	Big Wilson	FG			barren coarse grained granite outcrop on both banks of river, increasing ultramafic float upstream before ultramafic begins to outcrop, no tourmaline alteration observed numerous granite outcrops between THBW028 & THBW026
D	THBW029	Big Wilson	FG			FG float observed from this point onward down the drainage
D	THBW030	Big Wilson	tuV	FG		15-20mm qz-tourmaline vein in coarse grained granite
D	THBW031	Big Wilson	tuV	FG		bk-dgn tourmaline vein 1-2mm, sample diluted with wall rock granite, series of parallel veins in outcrop with dark green tourmaline in places
EOF						

Version						
Date_generated						
Reporting_period_end_date						
State						
Tenement						
Tenement_holder						
Project_name						
Tenement_operator						
250K_map_sheet						
100K_map_sheet						
50K_map_sheet						
25K_map_sheet						
Start_date_of_data_acquisition						
End_date_of_data_acquisition						
Data_format						
Number_of_data_records						
Date_of_metadata_update						
Feature_Located						
Geodetic_datum						
Vertical_datum						
Projection						
Projection_zone						
Surveying_instrument						
Surveying_Company						
Sample_code						
Sample_type						
Remarks:						
Location	Type	E_MGA55	N_MGA55	Structure	Dip	Dip_direction_MGA55
		metres	metres			
MHAK001	float	368241	5379317			
MHAK002	outcrop	368136	5379438			
SWAK001	float	368340	5379140			
SWAK002	float	368355	5379140			
SWAK003	float	368500	5379069			
SWAK004	outcrop	368257	5379170			
SWAK005	outcrop	368350	5378944			
SWAK006	float	368312	5378846			
SWAK007	subcrop	368236	5378913			
SWAK008	outcrop	368541	5378768			
SWAK009	outcrop	368599	5378687			
SWAK010	outcrop	368598	5378632			

Location	Type	E_MGA55	N_MGA55	Structure	Dip	Dip_direction_MGA55
		metres	metres			
SWAK011	float	368571	5378599			
SWAK012	outcrop	368550	5378572			
SWAK013	outcrop	369596	5378183			
SWAK014	float	369356	5377833			
SOKW01	outcrop	364289	5385085			
SOKW02	outcrop	364165	5385540			
SOKW03	float	364125	5385664			
SOKW04	outcrop	364377	5386900	bedding	32	128
SOKW04A	outcrop	364354	5386892	bedding	60	120
SOKW05	outcrop	364275	5387156			
SOKW06	subcrop	364470	5387769			
SOKW07	outcrop	364238	5387498	tourmaline vein	84	216
SOKW07	outcrop	364238	5387498	tourmaline vein	88	040
SOKW07	outcrop	364238	5387498	igneous banding	80	124
SOKW08	outcrop	364112	5387530	foliation	62	112
SOML111	outcrop	359423	5380938			
THBW001	float	364485	5387760			
THBW002	subcrop	364485	5387760			
THBW003	outcrop	364485	5387760			
THBW004	float	364485	5387760			
THBW005	outcrop	364485	5387760			
THBW006	subcrop	364485	5387760			
THBW007	outcrop	364246	5387484	tourmaline vein	70	040
THBW007	outcrop	364246	5387484	tourmaline vein	80	036
THBW007	outcrop	364246	5387484	igneous banding	70	235
THBW007	outcrop	364246	5387484	igneous banding	70	050
THBW007	outcrop	364246	5387484	igneous banding	70	110
THBW007	outcrop	364246	5387484	igneous banding	62	233

Location	Type	E_MGA55	N_MGA55	Structure	Dip	Dip_direction_MGA55
		metres	metres			
THBW007	outcrop	364246	5387484	igneous banding	75	118
THBW008	outcrop	364224	5387530	tourmaline vein	85	041
THBW008	outcrop	364224	5387530	dyke	62	252
THBW008	outcrop	364224	5387530	dyke	50	255
THBW008	outcrop	364224	5387530	quartz-tourmaline-sericite vein	87	058
THBW008	outcrop	364224	5387530	dyke	84	030
THBW009	outcrop	364175	5387505	quartz-tourmaline vein	70	240
THBW009	outcrop	364175	5387505	quartz-tourmaline-chlorite vein	50	260
THBW009	outcrop	364175	5387505	dyke	47	208
THBW009	outcrop	364175	5387505	dyke	24	038
THBW010	outcrop	364259	5387198	bedding	41	114
THBW011	outcrop	364778	5387493	bedding	54	103
THBW012	outcrop	364833	5387474	bedding	62	128
THBW013	outcrop	364879	5387452	bedding	48	120
THBW014	outcrop	364614	5387827	tourmaline vein	50	074
THBW015	outcrop	364625	5387888	tourmaline vein	80	235
THBW016	outcrop	364612	5387845	tourmaline vein	82	252
THBW017	outcrop	364628	5387862	tourmaline vein	80	250
THBW018	outcrop	364610	5387944	tourmaline vein	84	268
THBW019A	outcrop	364598	5387985	tourmaline vein	30	040
THBW019B	outcrop	364598	5387985	?bedding	30	040
THBW020	outcrop	364287	5388009	tourmaline vein	82	332
THBW021	outcrop	364338	5387731	tourmaline vein	82	230
THBW022	outcrop	364351	5387638			
THBW023	float	364336	5387829			
THBW024	outcrop	364058	5387560	tourmaline vein	82	222
THBW025	outcrop	364028	5387548	tourmaline vein	80	250

Location	Type	E_MGA55	N_MGA55	Structure	Dip	Dip_direction_MGA55
		metres	metres			
THBW026	outcrop	363872	5387461	tourmaline vein	75	225
THBW027	outcrop	363720	5387509			
THBW028	outcrop	363775	5387505			
THBW029	float	363909	5387237			
THBW030	outcrop	364115	5387521	tourmaline vein	75	055
THBW031	outcrop	364151	5387516	tourmaline vein	70	242

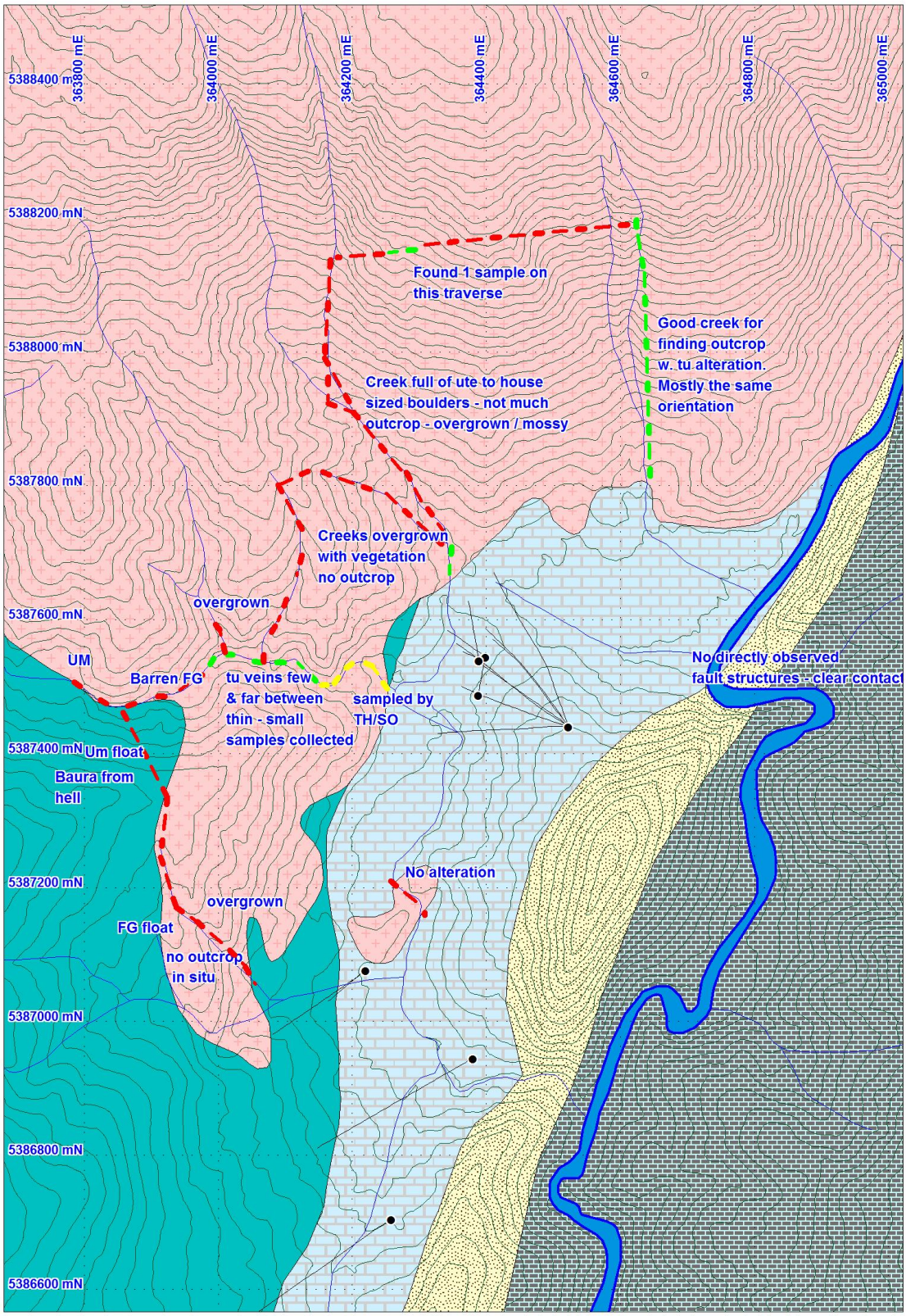
363800 mE
364000 mE
364200 mE
364400 mE
364600 mE
364800 mE
365000 mE
5388400 mN
5388200 mN
5388000 mN
5387800 mN
5387600 mN
5387400 mN
5387200 mN
5387000 mN
5386800 mN
5386600 mN
Found 1 sample on this traverse
Good creek for finding outcrop w. tu alteration. Mostly the same orientation
Creek full of ute to house sized boulders - not much outcrop - overgrown / mossy
Creeks overgrown with vegetation no outcrop
overgrown
UM
Barren FG
tu veins few & far between thin - small samples collected
sampled by TH/SO
Um float
Baura from hell
No directly observed fault structures - clear contact
No alteration
overgrown
FG float
no outcrop in situ

Venture Minerals Lithologic Codes

Code	Description	Code	Description	Code	Description
Regolith					
R	undifferentiated regolith	RL	undifferentiated laterite	RCLY	in situ clay
RCAC	calcrete	RLG	lateritic gravel	RSAP	undifferentiated saprolite
RSIC	silcrete	RLI	in situ laterite	RGOS	gossan ("iron cap"); textural or mineral prefix as appropriate
RFEC	ferricrete	RLT	transported laterite		
Unconsolidated Sediments		**Breccias, Faults and Shear Rocks**		**No Recovery & Cavities**	
S	undifferentiated sediment	XHB	hydrothermal breccia	NCAV	cavity
SLG	lateritic gravel	XMYL	mylonite	NREC	no sample recovery
SGVL	unconsolidated gravel	XFB	Fault breccia - incohesive >30% clastic	NSAV	sample no longer available
SPCS	unconsolidated pebbly/cobbly sand			NCTM	contaminationed interval
SAND	unconsolidated sand	XFG	Fault gouge - incohesive <30% clastic		
SILT	unconsolidated silt			**Veins**	
SMUD	unconsolidated mud	XFC	Fault cataclasite - cohesive more than >30% clastic		
SCLY	unconsolidated clay (transported)			*V	Veins, ≤2 mineral prefixes
cyRB	regolith breccia with clay matrix			*VB	Vein breccia, ≤2 cement prefixes
Sedimentary Rocks (S*)					
SS qzSS volcSS lithSS ccSS	>75% sandstone (undifferentiated) over minimum 5m logging interval, prefixes qz = quartz, lith = lithic, volc = volcanogenic, cc = calcareous	SMP	phyllite	SCB, ooSCB, stSCB,	undifferentiated carbonate, prefixes oo=oolitic, st=stromatolitic, bc=bioclastic
		SGRT	grit		
		SSPC	pebbly or cobbly sandstone		
		SSIC	intraclastic SS & SCG	SLST	limestone
SM	>75% mudstone over ≥5m	SCG	conglomerate	SDOL	dolomite
ST	>75% siltstone over ≥5m	SCGR	mud chip conglomerate (rip-ups)	SCHT	chert
SSM	25-75% SS & SM over ≥5m	SCGM	monomict conglomerate	SBIF	banded iron formation
SST	25-75% SS & ST over ≥5m	SCGP	polymict conglomerate	SLIG	lignite
SMH	shale	SBRM	monomict breccia	STIL	tillite
SML	slate	SBRP	polymict breccia	STUF	tuffite (redeposited)
SMA	argillite			SLAP	redeposited lapilli-stone
Igneous Rocks (U* for Ultramafic, M* for Mafic, I* for Intermediate, F* for Felsic)					
UM	undifferentiated ultramafic	UKoMC	olivine mesocumulate; komatiite flow	ID	diorite
UDUN	dunite			F	undifferentiated felsic rock
UHAR	harzburgite	MG	gabbro	FG	undifferentiated granitoid
UPX	pyroxenite	MGL	leucogabbro	FGRA	granite
USERP	serpentinite	MD	dolerite	FGRD	granodiorite
UKIM	kimberlite	MB	basalt	FDIO	diorite
ULAP	lamproite	MBHM	high-magnesium basalt	FMOZ	monzonite
ULAY	ultramafic lamprophyre	MBP	pillow-basalt	FSYE	syenite
UK	komatiite (undifferentiated)	MBHY	basaltic hyaloclastite	FTUF	felsic tuff
UKSTX	spinifex textured; komatiite flow	MLAP	mafic lapilli-stone	FV	undifferentiated felsic volcanic rock
UKoOC	olivine orthocumulate; komatiite flow	MTUF	mafic tuff		
		IA	andesite	FRHY	rhyolite
				FDAC	dacite
Metamorphic & Metasomatic Rocks (Z*)					
ZSCH	undifferentiated schist	ZMRB doMRB	marble, >50% cb; ≤1 key mineral prefix	mtZXS	>50%) magnetite; matrix replacement to massive bands. <am, po & cb. Grn, or aci after vo.
mZSCH	undifferentiated mafic schist; >am, cl &/or bt; <fp, qz, lx etc...	gtZXS	pbl gt in px+cc matrix (<10% px = gtZMRB) ± minor matrix am, mt, po etc. gt→ve; gradational with veZXS	voZXS	>50% vonsenite; aci, radiating
fZSCH	undifferentiated felsic schist; >qz, fp, mu; <mafic minerals			poZXS	>50% pyrrhotite; bnd, semi-mas to mas
btZSCH	use mineral code prefixes for only the	veZXS	tab, pbl, & orb ve in px-cc matrix.		
ZGNS	undifferentiated gneiss	olZXS	>50% grn ol; ± ol→sr, hrn, dis mt, patches wt-lgn px.	pyZXS	>50% pyrite; semi-mas to mas
btZGNS ksp-ZGNS	bt-gneiss, K-fp-gneiss, etc… using mineral code prefixes for only the distinguishing minerals	lpZXS	leopard skarn = olZXS w/ irregular granitic blobs/dyklets→px, rimmed by pk gt, lgn px, gn ph.	sdZXS	>25% siderite; includes sqp & s+p, <cs + ksp
ZAMP	undifferentiated amphibolite			btZXS	>50% biotite; bn-bk, "books" common ± fl
ZHF	hornfels, ifg; ≤2 mineral prefixes as appropriate (eg. muZHF, andZHF)	amZXS	>50% amphibole; mas felted bands &/or pseudomorphs of pbl gt. <cb, mt, po, vo.	srZXS	>50% serpentine; mas translucent to flakey lgn-dgn, after olZXS.
amZHF	amphibole (>20%) hornfels			ZGRS	Undifferentiated greisen; saccharoidal qz-mu aggregate. Ppy fp→po.
btZHF	biotite (>20%) hornfels; brownish, brown streak	am-voZXS	amphibole (25-50%) + vonsenite (25-50%); vo often radiating aci between am &/or ve after pbl gt.		
pxZHF	pyroxene (>20%) hornfels; whitish to whitish-green			ZQT	tourmaline "greisen" = FGRA w/ ppy fp→tu, saccharoidal qz groundmass ± ifg mu.
axZHF	axinite (>20%) hornfels; purplish	ammt-ZXS	amphibole (25-50%) + magnetite (25-50%); typically matrix around ex-gt pbl		
qzZHF	quartz (>20%) hornfels; hard, bronze-grey, microcrystalline qz w/ po, black streak				
		ampo-ZXS	amphibole (25-50%) + pyrrhotite (25-50%); pbl		

Venture Minerals Mineral and Textural Codes

Code	Description	Code	Description	Code	Description	Code	Description	Code	Description
Minerals									
ac	actinolite	cdp	chrome diopside	gt	garnet	mz	monazite	sd	siderite
ak	ankerite	cl	chlorite	he	hematite	nac	nacrite	sh	scheelite
ab	albite	cpy	chalcopyrite	hb	hornblende	ol	olivine	si	siliceous
al	almandine	cpx	clinopyroxene	ilt	illite	or	orthoclase	sr	serpentine
and	andalusite	cr	chromite	il	ilmenite	ops	opaline silica	sph	sphalerite
ano	anorthite	crp	chrysoprase	ka	kaolin	ph	phlogopite	sp	spinel
am	amphibole	crt	chrysotile	ksp	misc. k-feldspar	pl	plagioclase	sb	stilbite
ana	anatase	cs	cassiterite	ky	kyanite	po	pyrrhotite	st	stannite
atg	antigorite	cv	chenevixite	lau	laumontite	pp	pyrope	sx	sulphide
asp	arsenopyrite	cy	misc. clay	lm	limonite/misc.	prh	prehnite	sxo	oxidised sulphide
as	arsenates	da	danalite	lo	lollingite	pv	perovskite	tc	talc
aug	augite	dd	diamond	lw	ludwigite	px	pyroxene	ti	titanite (sphene)
ax	axinite	di	diopside	lx	leucoxene	py	pyrite	tr	tremolite
az	azurite	do	dolomite	mc	malachite	qz	quartz	tu	tourmaline
ba	baryte	ep	epidote	mi	misc. mica	rd	rhodochrosite	tz	topaz
Bi	native bismuth	fe	feO or FeOH	mg	magnesite	rf	rock fragments	vo	vonsenite
bt	biotite	fl	flourite	mn	mn-oxides	ru	rutile	ve	vesuvianite (idocrase)
cb	misc. carbonate	fsp	feldspar	mon	montmorillonite	sa	saponite	zin	zinnwaldite
cc	calcite	ga	galena	ms	moissanite	sc	scorodite	ze	zeolites
ch	chalcedony	go	goethite	mt	magnetite	se	sericite	zr	zircon
cd	cordierite	gr	graphitic	mu	muscovite				
Pseudomorphs		**Sedimentary Bedding**		**Sedimentary Grain size**				**Igneous/Metamorphic Grain Size**	
gt→ve	gt replaced by ve	lam	laminated (<1cm)	svfg	very fine grained <64 um (mud, silt & clay)				
gt→am	gt replaced by am	tnb	thin (1-10cm)	sfg	fine grained 64 um to 0.25 mm (fine sand)			ifg	fine, <1mm
fp→tu	fp replaced by tu	mdb	medium (10-30cm)	smg	medium grained 0.25 to 0.5mm (medium sand)			img	medium, 1-5mm
fp→se	fp replaced by se	tkb	thick (>30cm)	scg	coarse grained 0.5 to 2 mm (coarse sand)			icg	coarse, 5-30mm
fp→po	fp replaced by po	vtkb	very thick (>1m)	svcg	very coarse grain >2mm (2 - 4mm granules, 4 - 16mm pebbles, 16-256 mm cobbles, >256 mm			ipg	pegamatitic, >30mm
vo→mt	vo replaced by mt								
Textures								**Sample Recovery**	
aci	acicular	gph	graphic	pbl	porphyroblastic	spt	spotted	e	excessive
amg	amygdaloidal	grn	granular	pcl	porphyroclastic	sqp	qz prisms in sd	g	good
anh	anhedral	gtp	(ex)garnet pbl	ppy	porphyritic	stwk	stockwork	m	moderate
bdn	boudins	lam	laminated	psm	prismatic	sub	subhedral	p	poor
bnd	banded	mas	massive	rcz	recrystalised	tab	tabular	n	none
bxw	boxwork	mot	mottled	ruc	rip-up clasts	tad	am±po tailed spots		
col	cauliflower texture	mta	acicular magnetite	sch	schistose	tuf	tuffaceous	**Moisture**	
den	dendritic	mtg	granular magnetite	scl	cleaved	ves	vesicular	S	Sloppy
dis	disseminated	mzn	mineral zoning	shz	shear/shearzone	vet	tabular ve	M	Moist
euh	euhedral	oph	ophitic	spk	speckled	wrg	wrigglite	D	Dry
fol	foliated	orb	orbicules	s+p	salt+pepper; mt-sd				
Colours		**Structures**		**Weathering**					
l-	light (eg. lgn)	bkn	broken by drilling	vw	very weathered, BOTH PRIMARY TEXTURE & MINERALOGY DESTROYED; no sulphide, dominant Fe & Al oxides &/or silica (eg. Laterite)				
d-	dark (eg. dgn)	brc	brecciated						
bk	black	flt	fault	mw	moderately weathered, PRIMARY TEXTURE REMAINS but MINERALOGY SECONDARY clays (eg. saprolite)				
bl	blue	frc	fracture zone						
bn	brown	ftz	fault or fault zone	ww	weakly weathered, MAINLY PRIMARY TEXTURE & MINERALOGY; minor clay, partly oxidised sulphide (eg. saprock & fresh rock with iron staining)				
bz	bronze (sulphides)	hbr	healed-breccia						
cm	cream	mcf	microfaults, <1cm	fr	fresh (compeletely primary texture & mineralogy without significant iron staining on				
gn	green	slk	slickensides						
gy	grey	ssf	small-scale faults, 1-10cm offset			**Description Shorthand**			
kk	khaki					SOI	"start of interval"		
og	orange	BCA	acute angle: core axis & bedding			EOI	"end of interval"		
ov	olive					TCA	"to core axis"		
pk	pink	SCA	acute angle: core axis & foliation			PDW	post-drilling weathering (used during relogging)		
pl	purple					RCON	interval has redrilled fragments and/or contamination		
rd	red	FCA	acute angle: core axis & fault			HCl-	HCl non-reactive		
wt	white					HCl+	HCl reactive		

Appendix 3: Assay methods

Analytical Methodology

U-Pb dating of cassiterite by thermal ionization mass spectrometry (TIMS) methods was first reported by Gulson and Jones (1992). More recently, several groups in China (e.g., Yuan et al., 2008; 2011; Zhang et al., 2014, 2015) have also reported U-Pb TIMS ages for cassiterites from several tin-bearing deposits (together with LA-ICP U-Pb ages, Re-Os molybenite ages, and $^{40}Ar/^{39}Ar$ muscovite ages).

Cassiterite is extremely difficult to dissolve, and this has greatly hampered previous attempts to date the mineral using U-Pb TIMS methods. It is critical that the individual sample aliquots be fully dissolved prior to the separation and purification of U and Pb for isotopic analysis. The current study is being carried out at the Pacific Centre for Isotopic and Geochemical Research at the University of British Columbia. Our initial attempts to dissolve cassiterite using concentrated HCl encountered the same problems with dissolution that had been encountered by previous workers. We are currently investigating the use of concentrated hydroiodic acid (HI) instead of HCl for cassiterite dissolution, a method described by Yamazaki et al. (2013) in a tin isotope study. Initial results look very favorable, indicating a significantly more rapid dissolution rate than that obtained using concentrate HCl. The HI has been purified by sub-boiling distillation of commercially available concentrated HI stock.

The methodology that will be employed for separation and purification of U and Pb after dissolution of the individual cassiterite aliquots will generally follow that described for U-Pb TIMS dating of rutiles by Scoates and Friedman (2008), with the following modifications. Clean, hand-picked cassiterite grains are first ground in an agate mortar and sieved to separate the 50-100 micron size fraction, which were first cleaned in an ultrasonic bath in 1N HNO_3 for ten minutes, then washed in warm 1N HNO_3 for ten minutes to remove any possible surface contamination, and finally rinsed in ultra-pure acetone and dried. Individual sample aliquots (5-15 individual grains per aliquot) are weighed into a series of PFA mini-crucibles together with a few drops of concentrated HI together with a carefully weighed drop of $^{233–235}U$-^{205}Pb isotopic tracer. A number of these mini-crucibles are then placed inside a high-pressure dissolution bomb and several milliliters of concentrated HI are added. Dissolution is done at 210° for approximate 72 hours. Each sample is carefully examined to ensure that the samples have been completely dissolved. Any sample in which undissolved cassiterite remains is dried down on a hotplate and the bomb dissolution step is repeated until complete dissolution has been achieved.

The dissolved samples are dried down, re-dissolved in 3.1 HCL, and loaded onto pre-cleaned anion exchange columns. U and Pb are separated and purified using first 0.5N HBr and then 7N HNO_3, as described by Scoates and Friedman (2008).

Purified Pb and U from each sample aliquot are loaded onto single zone-refined Re filaments with 5 μL of silicic acid activator (Gerstenberger and Haase, 1997). Isotopic ratios are measured using a modified single collector VG-54R thermal ionization mass spectrometer equipped with a Daly photomultiplier. Measurements are done in peak-switching mode on the Daly detector. U fractionation is determined directly on individual runs using the $^{233–235}U$ tracer. Pb isotope ratios are corrected for a fractionation of 0.23 to 0.32%/amu based on replicate analyses of the NBS-981 and NBS-982 Pb reference materials and the values recommended by Thirwall (2000). All analytical errors

are numerically propagated through the entire age calculation using the technique of Roddick (1987). Final plotting and regression of the final isotopic compositions are calculated with Isoplot 3.00 (Ludwig, 2000); all errors are quoted at the 2σ level.

References

Gerstenberger, H., and Haase, G., 1997, A highly effective emitter substance for mass spectrometric Pb isotope ratio determinations: Chemical Geology, v. 136, p. 309–312.

Gulson, B.L. and Jones, M.T., 1992, Cassiterite: Potential for direct dating of mineral deposits and a precise age for the Bushveld Complex granites; Geology, v. 20, p. 355-358.

Ludwig, K.R., 2000, Isoplot/Ex 3.00, a geochronological toolkit for Microsoft Excel: Berkeley Geochronology Center.

Roddick, J.C., 1987, Generalized numerical error analysis with application to geochronology and thermodynamics: Geochimica et Cosmochimica Acta, v. 51, p. 2129–2135.

Scoates, J.S. and Friedman, R.M., 2008, Precise age of the Platiniferous Merensky Reef, Bushveld Complex, South Africa, by the U-Pb zircon chemical abrasion ID-TIMS technique – digital supplement; Economic Geology, v. 103, pp. 465-471.

Thirwall, M.F., 2000, Inter-laboratory and other errors in Pb isotope analyses investigated using a 207Pb-204Pb double spike: Chemical Geology, v. 163, p. 299–322.

Yamazaki, E., Nakai, S., Yokoyama, T., Ishihara, S and Tang, H., 2013, Tin isotope analysis of cassiterites from Southeastern and Eastern Asia; Geochemical Journal, v. 47, pp. 21-35.

Yuan, S., Peng, J., Hu, R., Li, H., Shen, N. and Zhang, D., 2008, A precise U–Pb age on cassiterite from the Xianghualing tin-polymetallic deposit (Hunan, South China); Mineralium Deposita, v. 43, pp. 375-382.

Yuan, S., Peng, J., Hao, S., Li, H., Geng, J. and Zhang, D., 2011, *In situ* LA-MC-ICP-MS and ID-TIMS U–Pb geochronology of cassiterite in the giant Furong tin deposit, Hunan Province, South China: New constraints on the timing of tin–polymetallic mineralization; Ore Geology Reviews, v. 43, pp. 235-242.

Zhang, R.-Q., Lua, J.-J., Wang, R.-C., Yang, P., Zhu, J.-C., Yao, Y., Gao, J.-F., Li, C., Lei, Z.-H., Zhang, W.-L. and Guo, W.-M., 2015, Constraints of *in situ* zircon and cassiterite U–Pb, molybdenite Re–Os and muscovite ^{40}Ar–^{39}Ar ages on multiple generations of granitic magmatism and related W–Sn mineralization in the Wangxianling area, Nanling Range, South China; Ore Geology Reviews, v. 65, pp. 1021-1042.

ALS Chemex

Geochemical Procedure – ME-ICP61
Trace Level Methods Using Conventional ICP-AES Analysis

Sample Decomposition: HNO_3-$HClO_4$-HF-HCl digestion, HCl Leach (GEO-4ACID)

Analytical Method: Inductively Coupled Plasma - Atomic Emission Spectroscopy (ICP - AES)

A prepared sample (0.25 g) is digested with perchloric, nitric, hydrofluoric and hydrochloric acids. The residue is topped up with dilute hydrochloric acid and the resulting solution is analyzed by inductively coupled plasma-atomic emission spectrometry. Results are corrected for spectral interelement interferences.

NOTE: Four acid digestions are able to dissolve most minerals; however, although the term "*near-total*" is used, depending on the sample matrix, not all elements are quantitatively extracted.

Element	Symbol	Units	Lower Limit	Upper Limit	Default Overlimit Method
Silver	Ag	ppm	0.5	100	Ag-OG62
Aluminum	Al	%	0.01	50	
Arsenic	As	ppm	5	10000	
Barium	Ba	ppm	10	10000	
Beryllium	Be	ppm	0.5	1000	
Bismuth	Bi	ppm	2	10000	
Calcium	Ca	%	0.01	50	
Cadmium	Cd	ppm	0.5	500	
Cobalt	Co	ppm	1	10000	Co-OG62
Chromium	Cr	ppm	1	10000	
Copper	Cu	ppm	1	10000	Cu-OG62

ALS Chemex

Geochemical Procedure – ME-MS62s
Single Element Trace Level Method Using ICP-MS

Sample Decomposition: $HF-HNO_3-HClO_4$ acid digestion, HCl leach (GEO-4ACID)

Analytical Methods: Inductively Coupled Plasma - Mass Spectrometry (ICP-MS)

This method is an effective option when analytical results for one or only a few elements are required. With this method you can create your own package of elements specific to your exploration program.

A prepared sample (0.25 g) is digested with perchloric, nitric, and hydrofluoric acids to near dryness. The sample is then further digested in a small amount of hydrochloric acid. The solution is made up to a final volume of 12.5 mL with 11 % hydrochloric acid, homogenized, and analysed by inductively coupled plasma-atomic emission spectrometry.

NOTE: Four acid digestions are able to dissolve most minerals; however, although the term "*near-total*" is used, depending on the sample matrix, not all elements are quantitatively extracted.

Element	Symbol	Units	Lower Limit	Upper Limit
Silver	Ag	ppm	0.02	100
Arsenic	As	ppm	0.2	500
Barium	Ba	ppm	10	500
Beryllium	Be	ppm	0.05	50
Bismuth	Bi	ppm	0.01	500
Cadmium	Cd	ppm	0.02	500
Cerium	Ce	ppm	0.01	500
Cobalt	Co	ppm	0.1	500
Cesium	Cs	ppm	0.05	500
Copper	Cu	ppm	0.2	500

ALS Chemex

Pressed Pellet Geochemical Procedure – ME-XRF05

Sample Decomposition: Pressed Powder Pellet (XRF-PPP)
Analytical Method: X-Ray Fluorescence Spectroscopy (XRF)

A finely ground sample powder (10 g minimum) is mixed with a few drops of liquid binder (Polyvinyl Alcohol) and then transferred into an aluminum cap. The sample is subsequently compressed under approximately 30 ton/in^2 in a pellet press. After pressing, the pellet is dried to remove the solvent and analyzed by WDXRF spectrometry for the following elements.

Element	Symbol	Units	Lower Limit	Upper Limit
Arsenic	As	ppm	5	5 000
Barium	Ba	ppm	10	10 000
Bismuth	Bi	ppm	4	10 000
Chromium	Cr	ppm	5	10 000
Gallium	Ga	ppm	4	10 000
Molybdenum	Mo	ppm	4	10 000
Niobium	Nb	ppm	2	10 000
Rubidium	Rb	ppm	2	10 000
Antimony	Sb	ppm	4	10 000
Selenium	Se	ppm	2	10 000
Tin	Sn	ppm	5	10 000
Strontium	Sr	ppm	2	10 000
Tantalum	Ta	ppm	10	10 000
Thorium	Th	ppm	4	10 000
Titanium	Ti	ppm	5	10 000
Uranium	U	ppm	4	10 000

Geochemical Procedure

ME-XRF15b
Base Metal Ores by Fusion / XRF

Sample Decomposition:

Lithium Metaborate, Lithium Tetraborate and Sodium Nitrate Fusion (WEI-GRA10b)

Analytical Method:

X-Ray Fluorescence Spectroscopy (XRF)

This method is intended for a variety of ore samples.

Finely pulverized sample is oven dried before pre-oxidation and decomposition by fusion with 12:22 lithium borate flux containing 20% sodium nitrate as an oxidizing agent. The resulting melt is manually poured to form a fused disk. Sodium Nitrate enables the fusion of material containing sulphides. During fusion with a standard lithium metaborate and tetraborate flux, sulphides only partially oxidize forming gaseous compounds; hence sulphur is lost to the atmosphere. With the use of this strongly oxidizing flux, sulphur is oxidized beyond the gaseous form and retained in the fused disk, allowing it to be quantitatively measured.

This disk is then analyzed using a wavelength dispersive X-Ray fluorescence spectrometer.

A loss-on-ignition at 1000°C may be undertaken in conjunction with the elemental analysis by either TGA or manual gravimetric method, but is not used to normalize results.

Appendix 4: BW003A structural data

H0002	Version	3					
H0003	Date_generated	14/05/2016					
H0004	Reporting_period_end_date	28/05/2016					
H0005	State	TAS					
H0100	Tenement	EL45/2010					
H0101	Tenement_holder	Venture Minerals Ltd					
H0102	Project_name	Big Wilson					
H0106	Tenement_operator	Venture Minerals Ltd					
H0150	250K_map_sheet	SK5503 Burnie					
H0151	100K_map_sheet	7914 Pieman					
H0152	50K_map_sheet	na					
H0153	25K_map_sheet	3637 Rosebury, 3638 Parsons					
H0200	Start_date_of_data_acquisition	28/05/2015					
H0201	End_date_of_data_acquisition	28/05/2016					
H0202	Data_format	SG3					
H0203	Number_of_data_records	34					
H0204	Date_of_metadata_update	28/05/2016					
H0500	Feature_Located	vein orientation					
H0501	Geodetic_datum	GDA94					
H0502	Vertical_datum	AHD83					
H0503	Projection	MGA					
H0531	Projection_zone	55					
H0532	Surveying_instrument	Garmin GPS60CSx & 62s					
H0533	Surveying_Company	Venture Minerals Ltd					
H0600	Sample_code	GEOLOB					
H0601	Sample_type	vein orientation					
H0900	Remarks:						
H1000	Location	E_MGA55	N_MGA55	RL_AHD	Dip	Dip Direction MGA	Description
H1001		metres	metres	metres			
D	BW003A_241.7m	364414.39	5387571.92	18.79	55	225	Fg tu-qz vein
D	BW003A_242m	364414.24	5387572.07	18.58	44	251	Fg tu-qz vein
D	BW003A_242.17m	364414.15	5387572.15	18.46	43	231	Fg tu-qz vein
D	**BW003A_242.26m**	364414.11	5387572.19	**18.40**	**44**	**228**	**Coarser-grained tu-qz-se**
D	BW003A_242.47m	364414	5387572.3	18.25	43	233	Fg tu-qz vein
D	BW003A_242.63m	364413.92	5387572.37	18.13	41	236	Fg tu-qz vein
D	BW003A_242.85m	364413.81	5387572.48	17.98	45	237	Fg tu-qz vein
D	**BW003A_243.6m**	364413.43	**5387572.85**	**17.45**	**43**	**233**	**Coarser-grained tu-qz-se**
D	BW003A_244.14m	364413.15	5387573.12	17.07	32	245	Fg tu-qz vein
D	BW003A_244.37m	364413.03	5387573.23	16.90	58	229	Fg tu-qz vein
D	BW003A_244.47m	364412.98	5387573.28	16.83	46	226	Fg tu-qz vein
D	BW003A_244.6m	364412.92	5387573.34	16.74	53	220	Fg tu-qz vein
D	BW003A_244.74m	364412.85	5387573.41	16.64	61	221	Fg tu-qz vein
D	**BW003A_245.6m**	**364412.41**	**5387573.83**	**16.03**	**75**	**210**	**Cs-cl(tu)-qz vein**
D	**BW003A_246.2m**	**364412.1**	**5387574.13**	**15.61**	**64**	**229**	**Cs vein**
D	**BW003A_246.25m**	**364412.08**	**5387574.15**	**15.57**	**76**	**217**	**Cs vein**
D	**BW003A_246.7m**	**364411.85**	**5387574.37**	**15.26**	**87**	**17**	**Cs vein**
D	BWAS002	364615	5387891	na	76	244	qz-tu vein
D	BWAS003	364607	5387950	na	85	246	qz-tu vein
D	BWAS008	364108	5387524	na	90	227	tu veins
D	BWAS009	364113	5387526	na	64	228	qz-tu vein
D	BWAS009	364113	5387526	na	90	217	qz-tu vein
D	BWAS010	364035	5387546	na	79	244	tu vein
D	BWAS010	364035	5387546	na	78	246	tu vein
D	BWAS011	363974	5387505	na	86	212	tu vein
D	BWAS020	363991	5386979	na	90	245	tu vein
D	BWAS020	363991	5386979	na	50	220	qz-tu vein
D	BWAS021	363968	5386989	na	85	201	tu vein
D	BWAS030	364245	5387503	na	85	206	qtz vein
D	BWAS030	364245	5387503	na	79	41	tu vein
D	BWAS036	364297	5387777	na	30	317	Qtz vein
D	BWAS037	364351	5387711	na	85	224	tu vein
D	BWAS038	364333	5387716	na	52	305	Ferruginous vein
D	BWSJ024	364245	5387503	na	82	210	thin tu veins in granite
EOF							

Appendix 5: SEM results

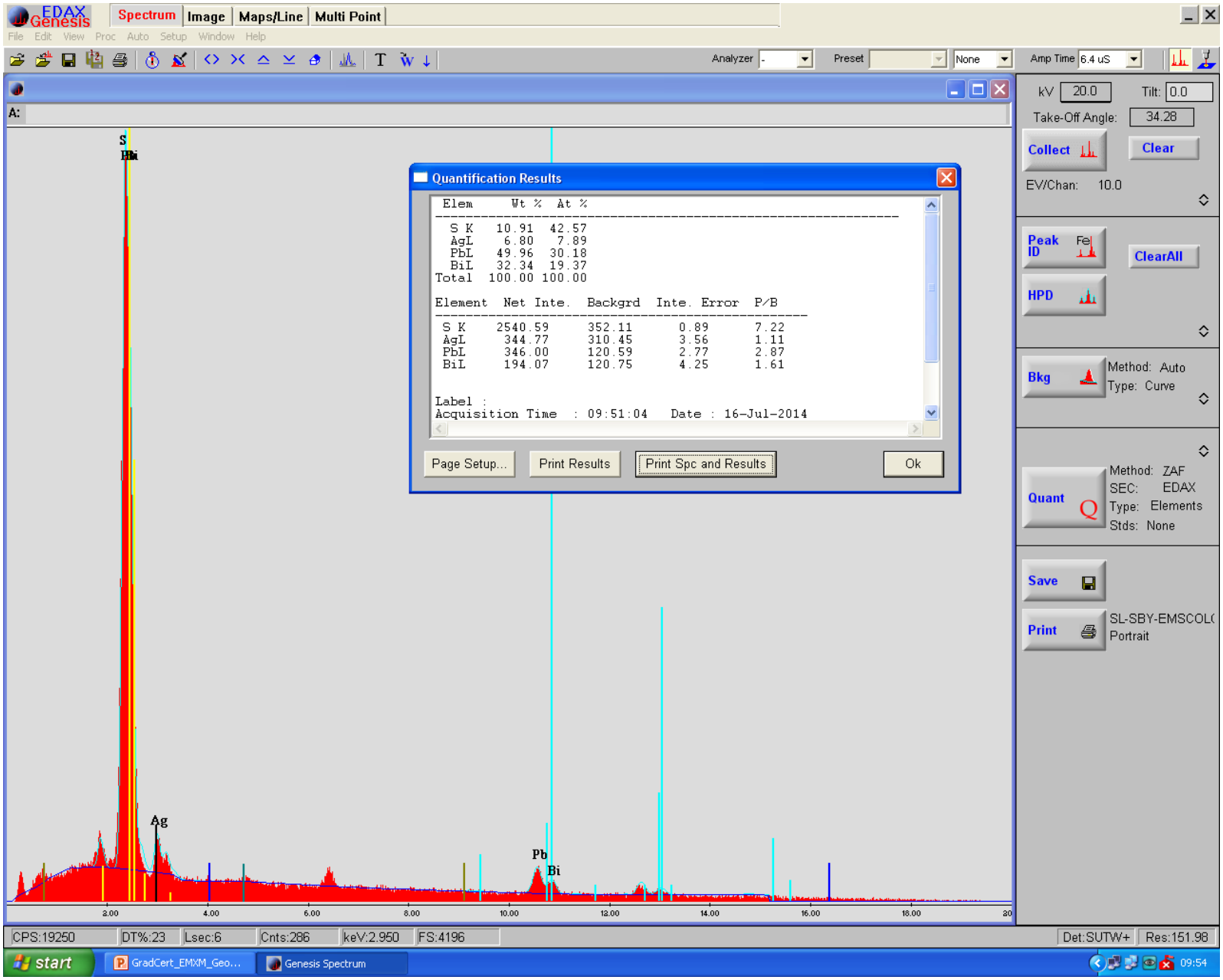
EDAX Genesis
Spectrum
Image
Maps/Line
Multi Point
File Edit View Proc Auto Setup Window Help
Analyzer
Preset
None
Amp Time 6.4 uS
kV 20.0
Tilt: 0.0
Take-Off Angle: 34.28
Collect
Clear
EV/Chan: 10.0
Peak ID
ClearAll
HPD
Bkg
Method: Auto
Type: Curve
Quant
Method: ZAF
SEC: EDAX
Type: Elements
Stds: None
Save
Print
SL-SBY-EMSCOL(
Portrait
Quantification Results
Elem Wt % At %
S K 10.91 42.57
AgL 6.80 7.89
PbL 49.96 30.18
BiL 32.34 19.37
Total 100.00 100.00
Element Net Inte. Backgrd Inte. Error P/B
S K 2540.59 352.11 0.89 7.22
AgL 344.77 310.45 3.56 1.11
PbL 346.00 120.59 2.77 2.87
BiL 194.07 120.75 4.25 1.61
Label :
Acquisition Time : 09:51:04 Date : 16-Jul-2014
Page Setup...
Print Results
Print Spc and Results
Ok
S
Ag
Pb
Bi
2.00
4.00
6.00
8.00
10.00
12.00
14.00
16.00
18.00
20
CPS:19250
DT%:23
Lsec:6
Cnts:286
keV:2.950
FS:4196
Det:SUTW+
Res:151.98
start
GradCert_EMXM_Geo...
Genesis Spectrum
09:54

Calcite +/-Fe,Mn

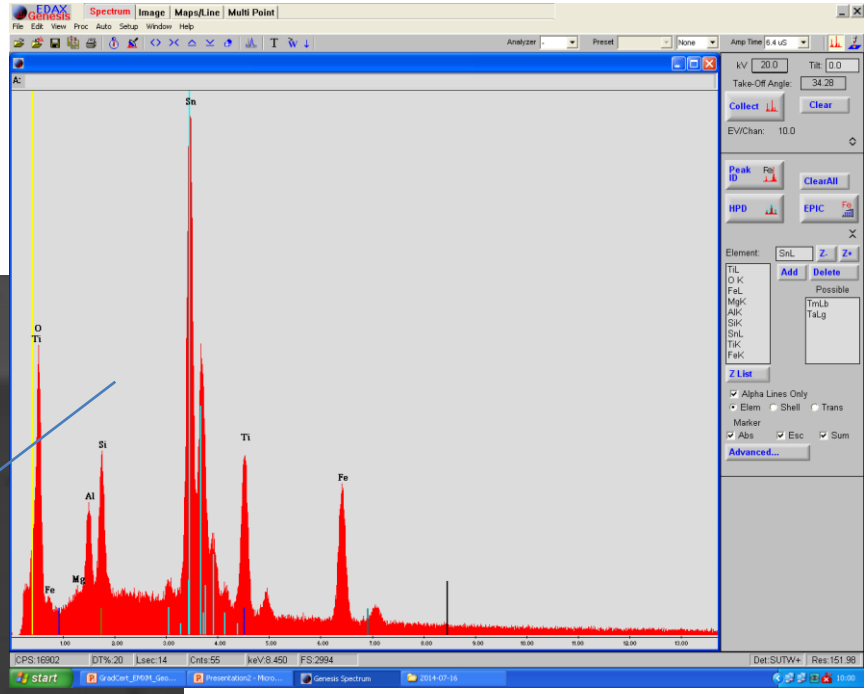

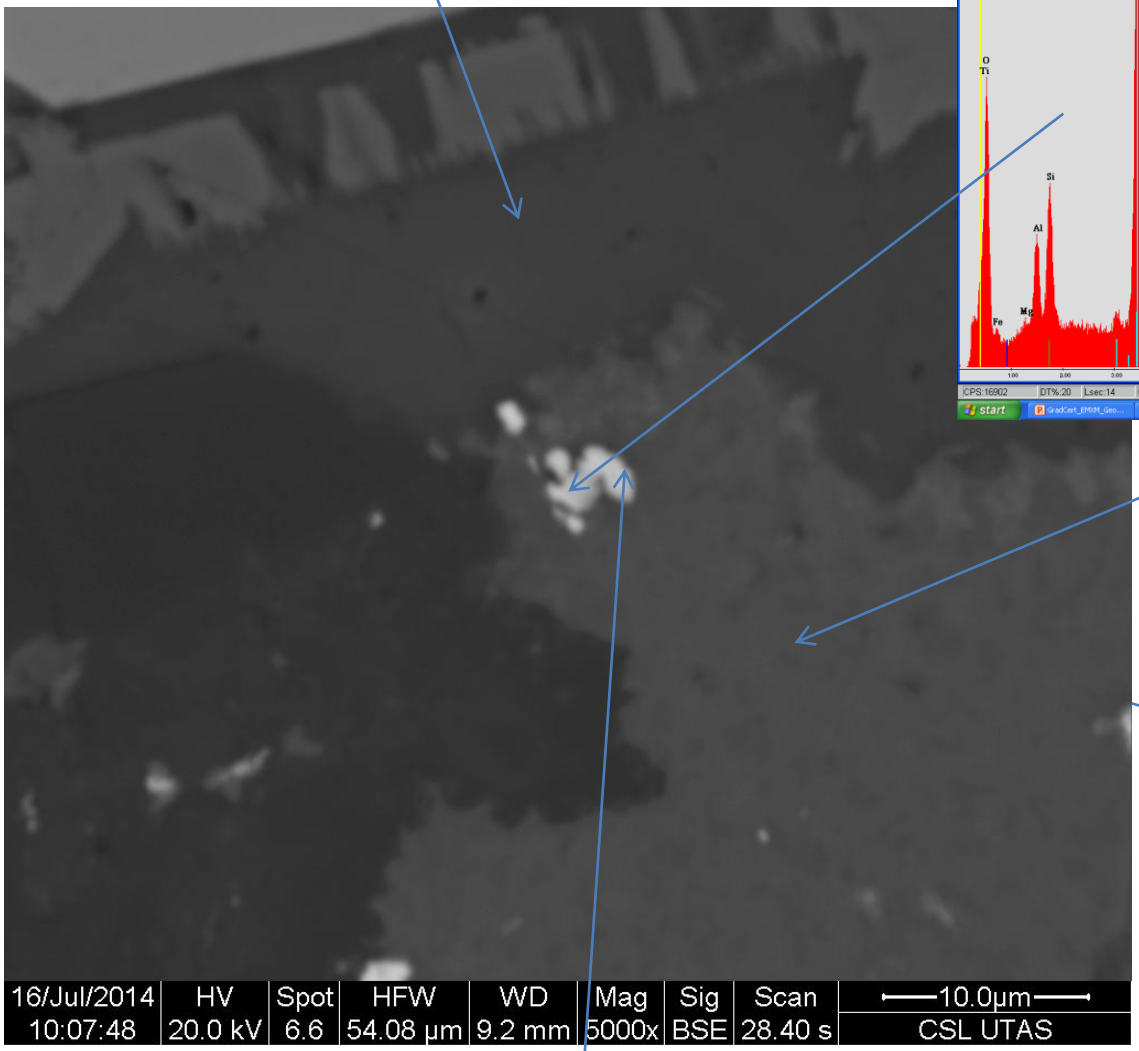

Chlorite, Fe-rich

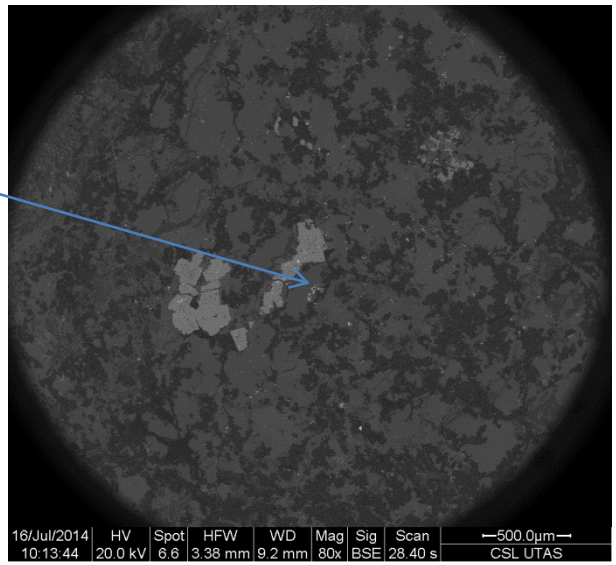

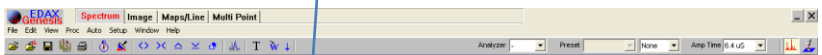

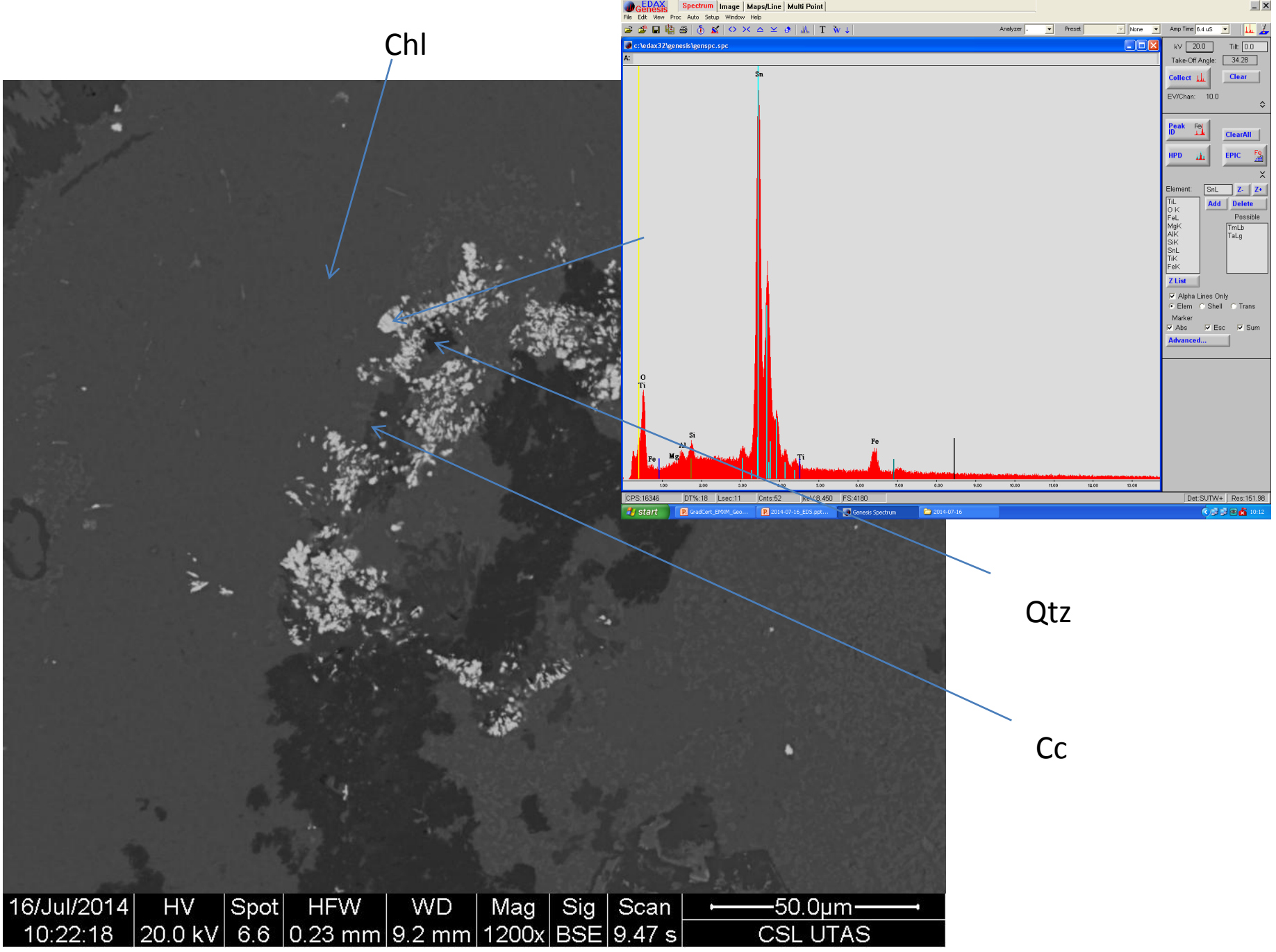
Chl
Qtz
Cc
Sn
O
Ti
Si
Al
Mg
Fe
Ti
Fe
16/Jul/2014
10:22:18
HV
20.0 kV
Spot
6.6
HFW
0.23 mm
WD
9.2 mm
Mag
1200x
Sig
BSE
Scan
9.47 s
50.0µm
CSL UTAS

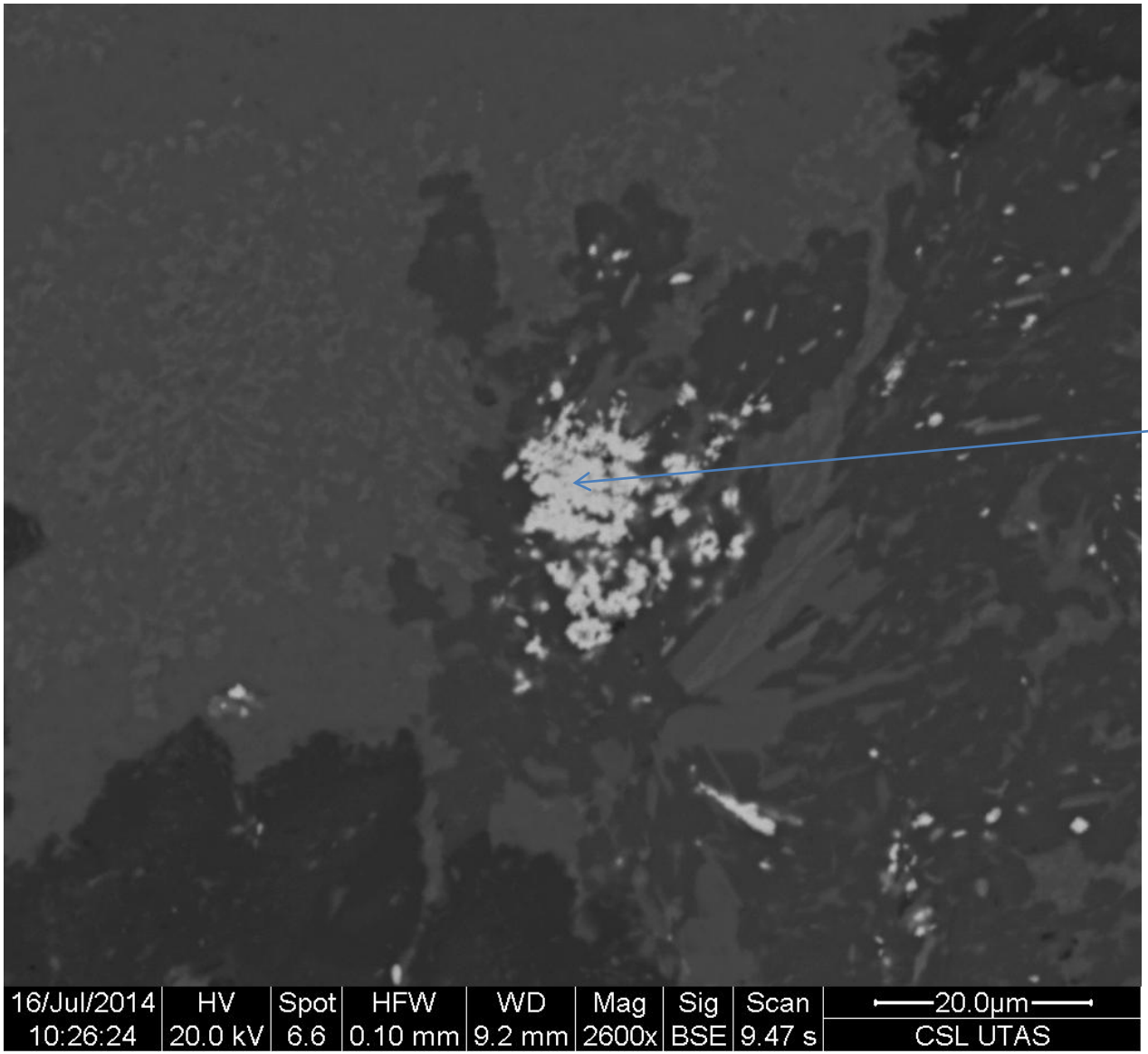
16/Jul/2014
10:26:24
HV
20.0 kV
Spot
6.6
HFW
0.10 mm
WD
9.2 mm
Mag
2600x
Sig
BSE
Scan
9.47 s
20.0µm
CSL UTAS

Cass

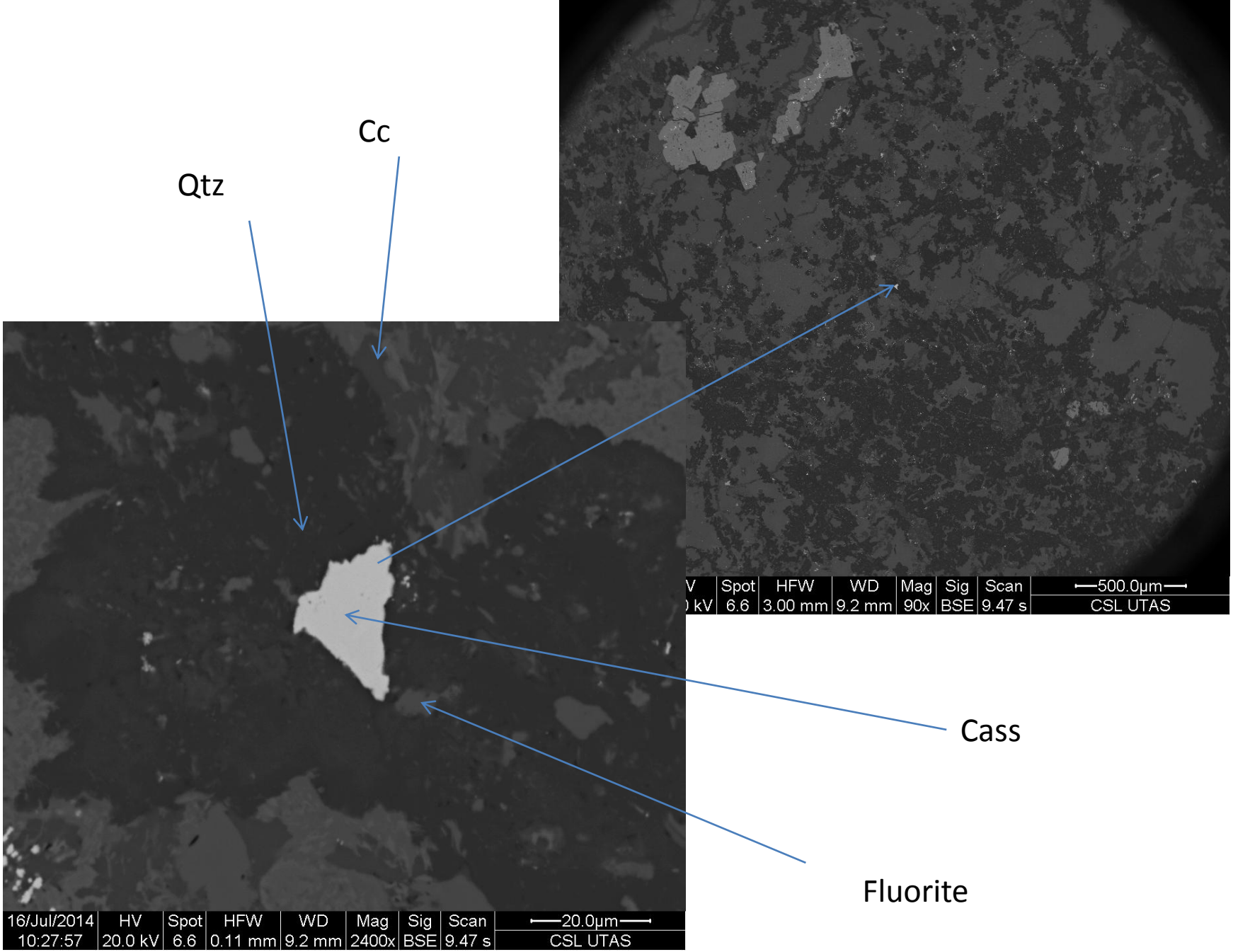
Cc
Qtz
Cass
Fluorite
V Spot HFW WD Mag Sig Scan 500.0µm
) kV 6.6 3.00 mm 9.2 mm 90x BSE 9.47 s CSL UTAS
16/Jul/2014 HV Spot HFW WD Mag Sig Scan 20.0µm
10:27:57 20.0 kV 6.6 0.11 mm 9.2 mm 2400x BSE 9.47 s CSL UTAS

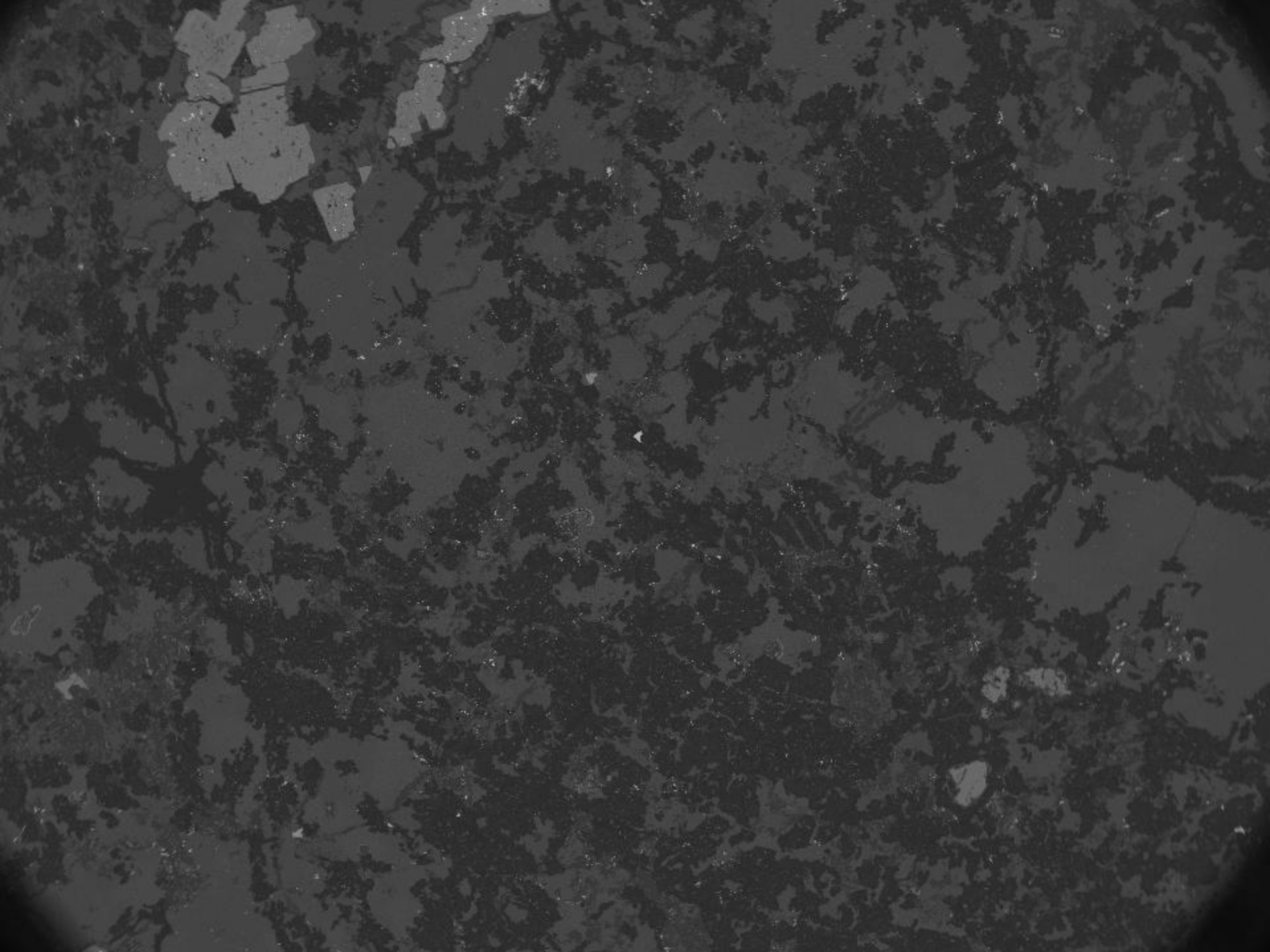

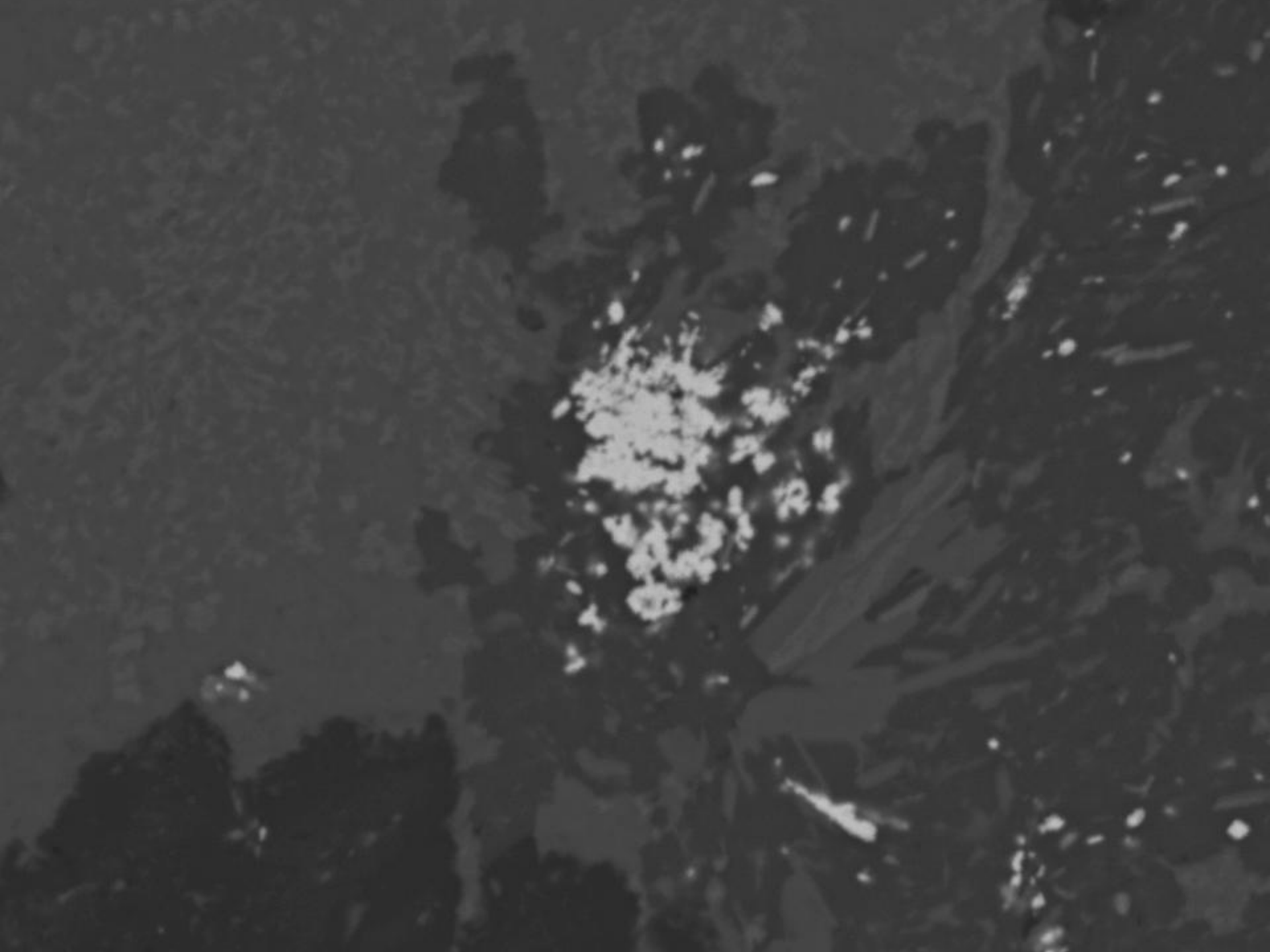

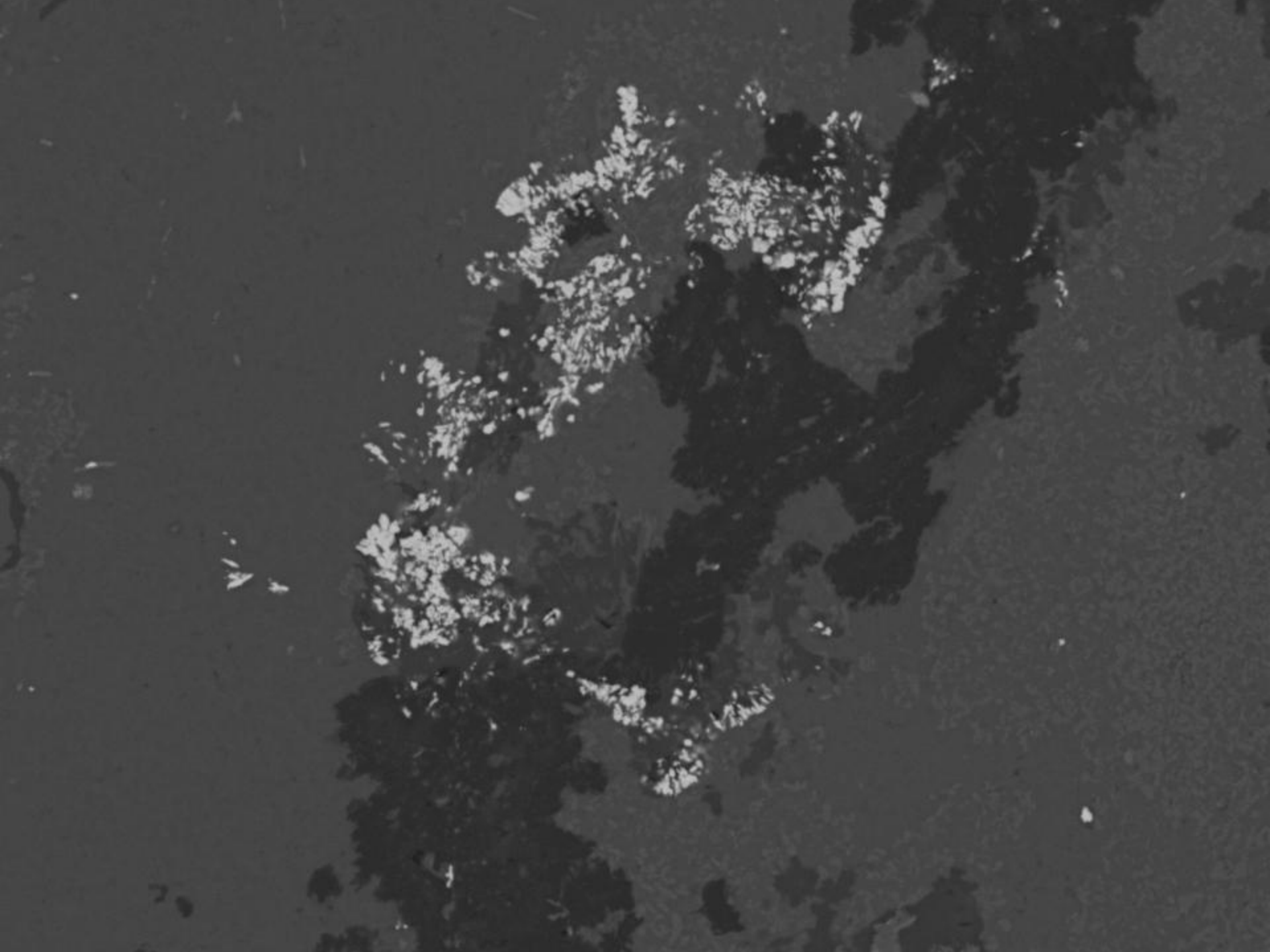

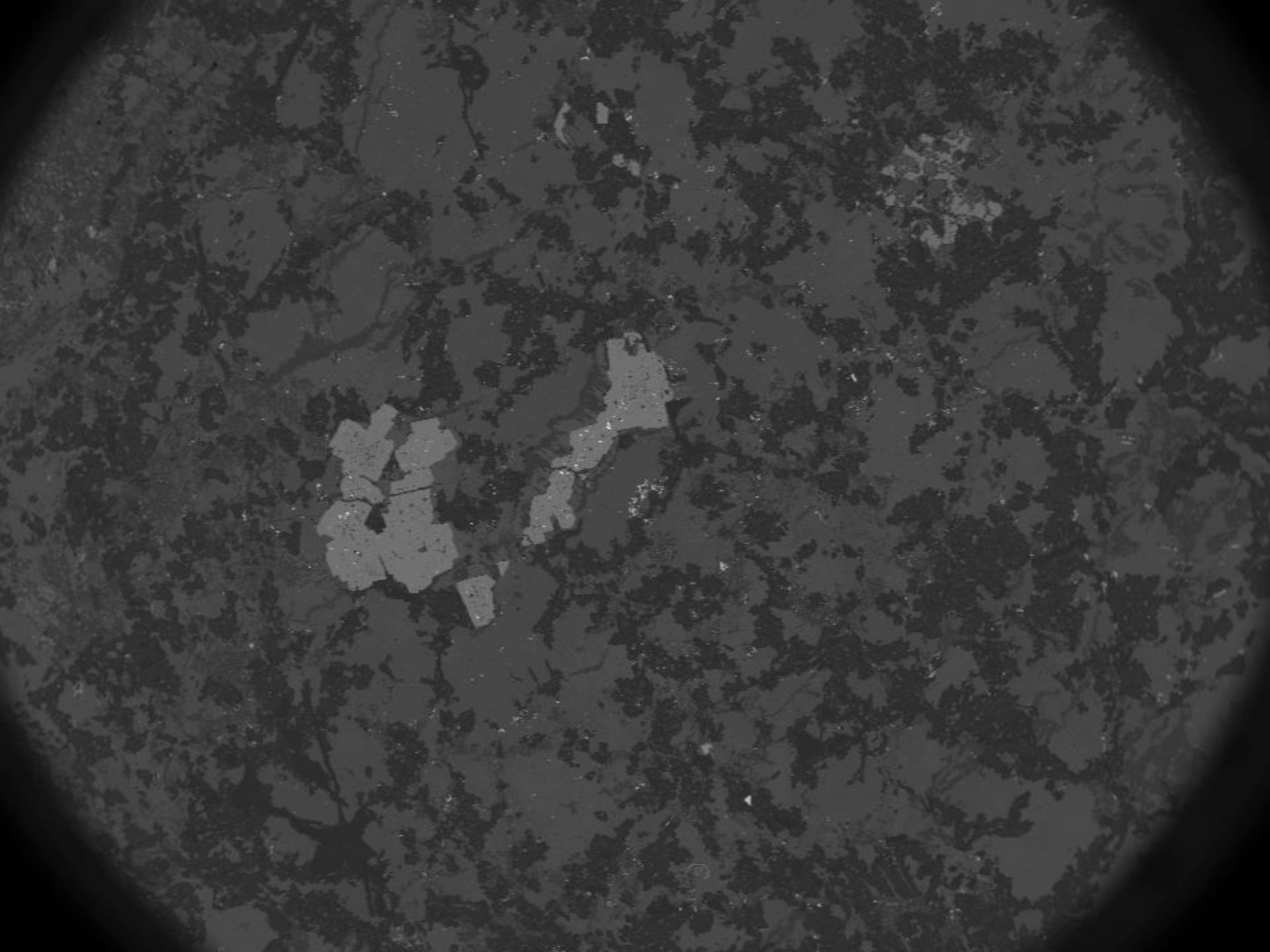

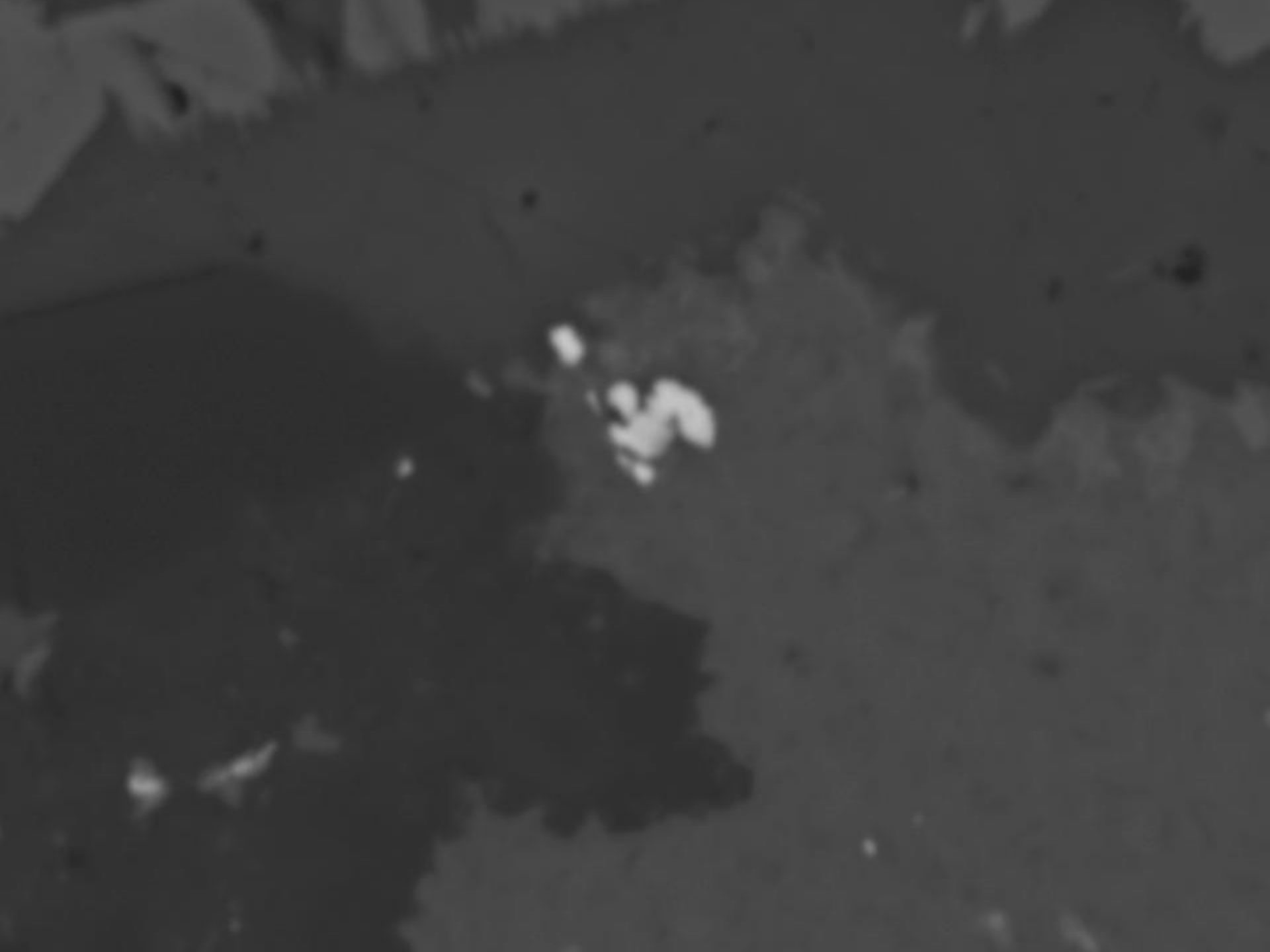

Appendix 6: Laser Raman Results

Laser RAMAN spectra for Vonsenite

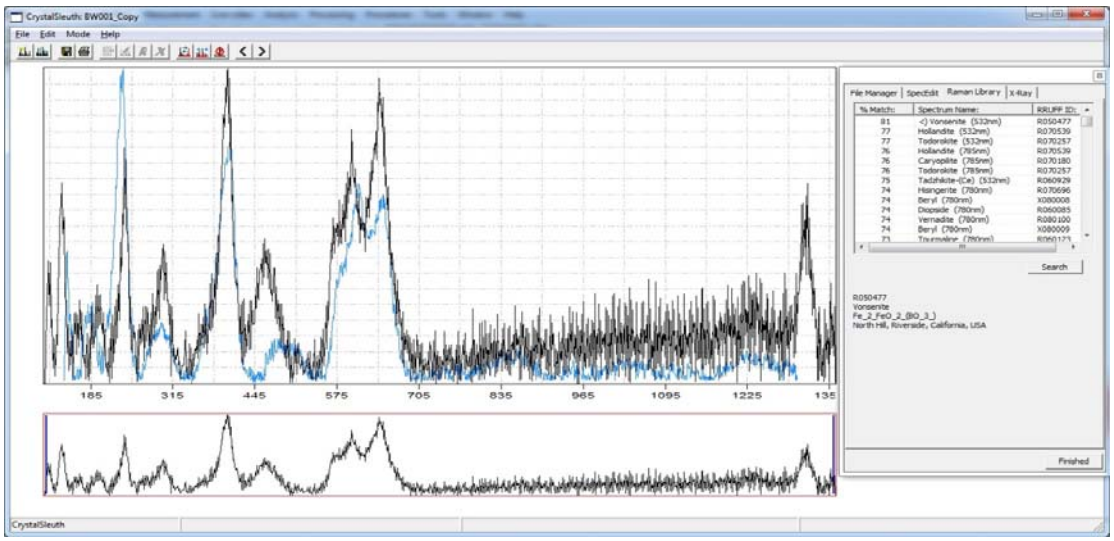

BW001 206

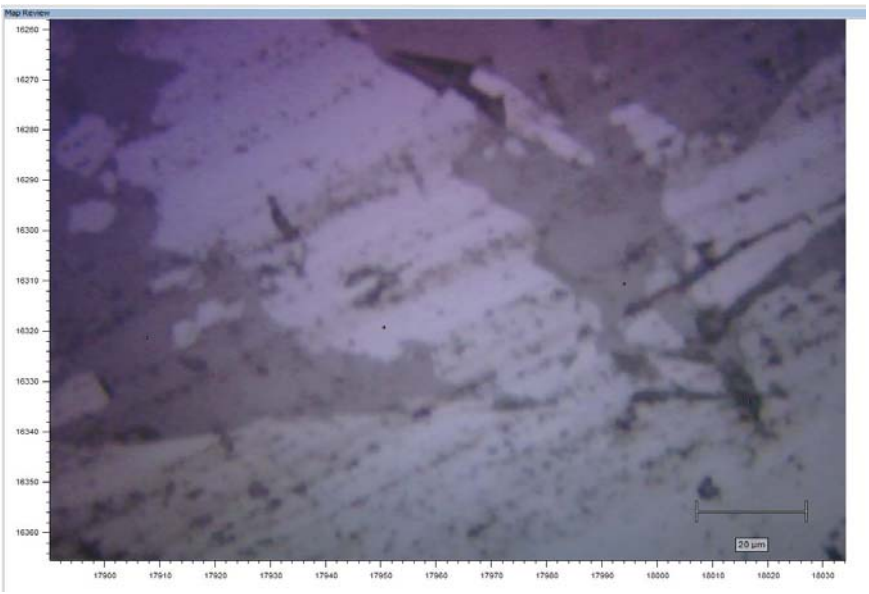

BW001vo

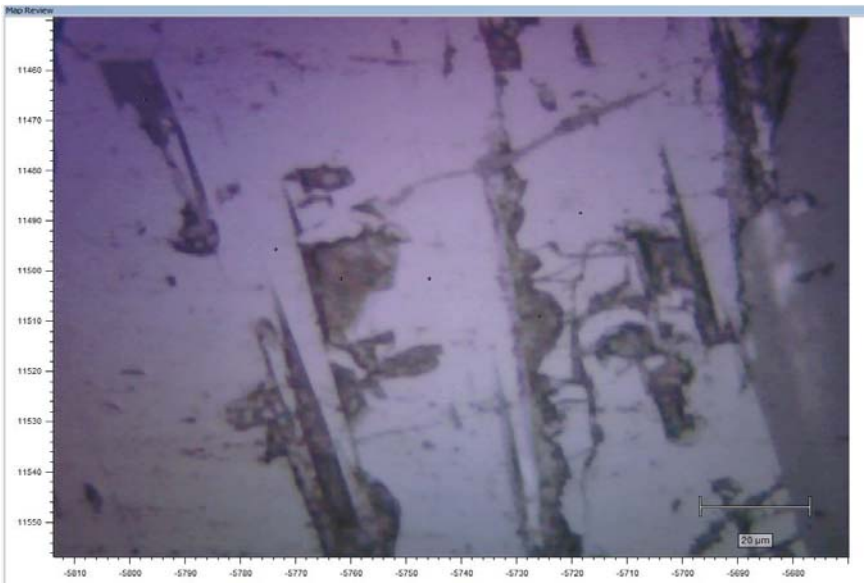

BW001 208.9

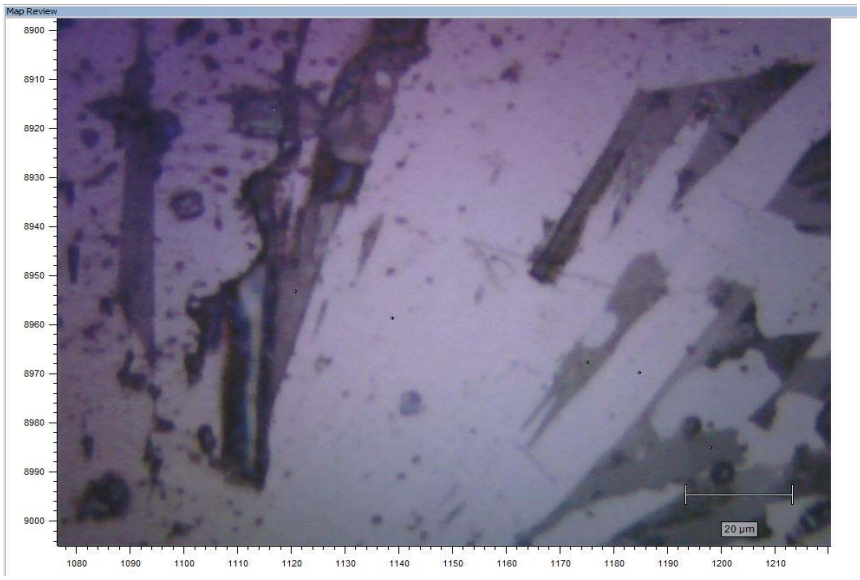
Map Review
8900
8910
8920
8930
8940
8950
8960
8970
8980
8990
9000
1080
1090
1100
1110
1120
1130
1140
1150
1160
1170
1180
1190
1200
1210
20 µm

Appendix 7: Tourmaline investigation results

Major and trace element data for Tourmaline analysed by Microprobe. Boron is added stochiometrically									
Sample	BW001-257.9	BW001-257.9	BW001-257.9	BW001-257.9	BW001-257.9	BW001-257.9	BW001-257.9	BW001-257.9	BW001-257.9
Analysis No.	257.9 C1 S1	257.9 C1 S1	257.9 C1 S3	257.9 C1 S4	257.9 C1 S5	257.9 C1 S6	257.9 C1 S7	257.9 C2 S1	257.9 C2 S2
Group	1	1							
SiO2	33.5254	33.5254	33.6395	33.6214	34.2914	33.3769	33.1466	34.1101	33.4712
TiO2	0.442482	0.442482	0.880298	0.430466	0.27592	0.381773	0.824536	0.425382	0.093889
Al2O3	32.261	30.1058	30.2934	32.5835	32.2688	32.453	30.4277	32.115	29.8793
V2O3	-0.00645	-0.00383	0.209284	-0.02691	-0.08282	-0.05855	-0.03148	-0.02638	0.077583
Cr2O3	-0.01509	0.018995	0.023871	0.007517	0.006846	-0.00216	-0.02721	-0.00287	-0.01002
Fe2O3									
FeO	14.5885	16.9021	15.6861	15.0422	14.5709	14.8553	17.3557	14.8557	17.4548
MgO	1.3061	1.22174	1.97415	1.16752	1.27991	1.17209	0.95656	1.45792	0.904367
CaO	0.39463	0.474645	0.444892	0.21517	0.125971	0.315717	0.409075	0.257403	0.437616
MnO	0.077316	0.091032	0.096016	0.087482	0.078939	0.084875	0.107862	0.077751	0.112468
ZnO									
BaO									
Na2O	2.11146	2.0764	2.18146	2.08803	1.82973	2.23516	2.1247	1.95402	2.14991
K2O	0.055688	0.059504	0.06726	0.053584	0.028569	0.044207	0.053613	0.043575	0.0414
Rb2O									
Cs2O									
F	0.920972	1.11315	1.11871	0.585243	0.630159	0.890085	1.06519	0.722057	1.23396
Cl	0.009701	-0.00132	-0.00574	-0.00531	0.004431	-0.00354	-0.00706	-0.01373	0.015899
H2O									
B2O3	10.0804	9.90923	9.95924	10.1232	10.1713	10.0756	9.90129	10.1208	9.87817
Li2O									
H2O*	3.033449698	2.881916897	2.924934399	3.210308666	3.188214585	3.049617271	2.918052477	3.15328376	2.806902545
B2O3*	-	-	-	-	-	-	-	-	-
Li2O*	0.195740066	0.020081355	0.015404995	0.120376519	0.154752203	0.176747803	0	0.107696949	0.023795288
Total	98.98129876	98.75330925	99.50878039	99.30377718	98.82302179	99.04682207	99.22512848	99.35770871	98.57123983
O=F	0.387795738	0.468716558	0.471057719	0.246429578	0.265342458	0.37479008	0.448521933	0.304038154	0.519586294
Total*	98.59350303	98.28459269	99.03772267	99.05734761	98.55767933	98.67203199	98.77660654	99.05367055	98.05165354
Structural formula based on 31 anions (O, OH, F)									
T: Si	5.789367356	5.810617479	5.840498854	5.782851071	5.895255518	5.766780538	5.809744824	5.857326452	5.910342954
AlT	0.210632644	0.189382521	0.159501146	0.217148929	0.104744482	0.233219462	0.190255176	0.142673548	0.089657046
B	3.004713835	3.008460151	2.984659692	3.00546893	3.018297836	3.004876004	2.995560273	2.999849666	3.010829111
Z: AlZ	6	6	6	6	6	6	6	6	6
Mg	0	0	0	0	0	0	0	0	0
Cr	0	0	0	0	0	0	0	0	0
Fe3+	0	0	0	0	0	0	0	0	0
Y: AlY	0.355213286	0.051442961	0.039249308	0.387955216	0.433421704	0.375206048	0.095289515	0.356828518	0.128583822
Ti	0.057461042	0.112159178	0.114934623	0.055678281	0.035671498	0.049603622	0.108679703	0.054930847	0.012467428
V	-0.000893019	-0.000540106	0.029132669	-0.003710938	-0.011415541	-0.008110697	-0.004423812	-0.00363191	0.01098378
Cr	-0.002060259	0.002641501	0.003276774	0.001022224	0.000930529	-0.000295064	-0.0037707	-0.000389649	-0.001398893
Fe3+	0	0	0	0	0	0	0	0	0
Mg	0.336234377	0.320349081	0.51096259	0.299363666	0.32802383	0.301895704	0.249941765	0.373214644	0.238064507
Mn	0.011308689	0.013561757	0.014119839	0.012744731	0.011494624	0.012420897	0.016012984	0.011308582	0.016821167
Fe2+	2.10680225	2.486181349	2.277568168	2.163682672	2.094883079	2.14647012	2.54399468	2.133366895	2.577580694
Zn	0	0	0	0	0	0	0	0	0
Li*	0.135933634	0.014204278	0.010756029	0.083264149	0.106990277	0.122809371	0	0.074372073	0.016897498
∑Y	3.000000001	3.000000001	3.000000001	3.000000001	3.000000001	3.000000001	3.005724135	3.000000001	3.000000001
X: Ca	0.073013789	0.089446366	0.082758508	0.039652044	0.02320308	0.058444418	0.07682077	0.047357382	0.082792737
Ba	0	0	0	0	0	0	0	0	0
Na	0.706946999	0.708099065	0.734335497	0.696321501	0.609889678	0.748760457	0.722042141	0.650567403	0.736052066
K	0.0122681	0.013351832	0.014897583	0.011757633	0.00626572	0.009743994	0.011988	0.009545801	0.009326105
Rb	0	0	0	0	0	0	0	0	0
Cs	0	0	0	0	0	0	0	0	0
r	0.207771112	0.189102738	0.168008411	0.252268822	0.360641522	0.183051131	0.189149089	0.292529414	0.171829093
OH	3.494184646	3.381189489	3.387415377	3.683196752	3.656089976	3.514671005	3.411639089	3.61186413	3.306135486
F	0.502976248	0.619203987	0.614273587	0.318351098	0.342619022	0.486365565	0.590458068	0.392131589	0.689106571
Cl	0.002839106	-0.000393476	-0.001688964	-0.00154785	0.001291003	-0.00103657	-0.002097156	-0.003995719	0.004757943
F content	Fluor-	Fluor-	Fluor-				Fluor-		Fluor-
Mineral Name	Schorl	Schorl	Schorl	Schorl	Schorl	Schorl	Schorl	Schorl	Schorl
CatSum	18.79694272	18.81935741	18.81665128	18.75320011	18.65765632	18.82182487	18.81213532	18.70732025	18.83900002
Si excess	0	0	0	0	0	0	0	0	0
X+B+Si excess	3.796942723	3.819357414	3.816651281	3.753200108	3.657656315	3.821824873	3.806411183	3.707320252	3.839000018
Li*	***0.135933633***	***0.014204277***	***0.010756028***	***0.083264148***	***0.106990276***	***0.12280937***	***-0.005724135***	***0.074372072***	***0.016897497***
T+Z+Y	15	15	15	15	15	15	15.00572413	15	15
Ideal T+Z+Y	15	15	15	15	15	15	15.00572413	15	15

Major and trace e								
Sample	BW001-239.5	BW001-239.5	BW001-239.5	BW001-239.5	BW001-239.5	BW001-239.5	BW001-239.5	BW001-239.5
Analysis No.	239.5_C1_S1	239.5_C1_S2	239.5_C1_S3	239.5_C2_S1	239.5_C2_S2	239.5_C2_S3	239.5_C2_S4	239.5_C3_S1
Group	Green	Green	Green	Green	Green	Green	Green	Green
SiO2	30.8751	25.7682	30.8732	33.2489	32.9557	33.053	33.2899	32.9719
TiO2	0.05483	-0.00679	0.011127	0.052501	0.071776	0.227334	0.029114	0.0166
Al2O3	25.386	17.9059	24.2307	29.2792	27.8556	27.3427	25.7605	27.0229
V2O3	-0.17741	0.069121	0.11372	-0.03776	-0.07881	-0.038	0.093686	-0.01271
Cr2O3	0	0.011091	0.017817	-0.02145	-0.01998	0.002654	-0.02563	-0.00927
Fe2O3								
FeO	20.4016	25.4241	21.5137	19.4896	21.1524	21.8153	22.7267	22.0866
MgO	0.0674	1.60445	0.031422	0.130408	0.107647	0.136279	0.065831	0.105632
CaO	0.141203	0.784381	0.157323	0.337135	0.358991	0.342274	0.199908	0.191387
MnO	0.074223	0.574942	0.048826	0.052895	0.050079	0.073792	0.051218	0.065304
ZnO								
BaO								
Na2O	2.31244	0.030228	2.07474	2.13498	2.14077	2.24753	2.22121	2.26159
K2O	0.04678	4.29681	0.049786	0.055692	0.064741	0.113017	0.054377	0.061684
Rb2O								
Cs2O								
F	0.076244	0.261089	0.064568	0.310445	0.302005	0.532498	0.063699	0.104125
Cl	0.005973	0.025872	-0.00922	-0.00706	-0.00484	0.001982	0.00944	0.006281
H2O								
B2O3	9.8879	9.169	9.82849	9.93396	9.83803	9.75134	9.78777	9.81539
Li2O	0.002							
H2O*	3.108149299	2.656396477	3.086756859	3.225249922	3.187449426	3.07864267	3.25808076	3.262679708
B2O3*	-	-	-	-	-	-	-	-
Li2O*	0.191766052	0	0.073361336	0.006575151	0	0	0	0
Total	92.45219835	88.57479048	92.16631719	98.19127107	97.98155843	98.68034267	97.58580376	97.95009271
O=F	0.032104231	0.109937329	0.027187792	0.13071977	0.12716592	0.224220123	0.02682188	0.043844146
Total*	92.42009412	88.46485315	92.1391294	98.0605513	97.85439251	98.45612255	97.55898188	97.90624856
Structural formula								
T: Si	5.885496908	5.544888817	5.943302433	5.915238568	5.9356961	5.949274065	6.066453325	5.966865421
AlT	0.114503092	0.455111183	0.056697567	0.084761432	0.0643039	0.050725935	0	0.033134579
B	3.253471748	3.405641613	3.265887312	3.050602356	3.058563283	3.029602168	3.078749375	3.06604158
Z: AlZ	5.588777798	4.085984336	5.440835718	6	5.848716222	5.749570807	5.5326396	5.730413833
Mg	0.019153282	0.514687348	0.00901755	0	0.028903577	0.036567105	0.017883864	0.028497471
Cr	0	0	0	0	0	0	0	0
Fe3+	0	0	0	0	0.122380201	0	0.449476536	0.241088697
Y: AlY	0	0	0	0.054412136	0	0	0	0
Ti	0.007859841	-0.001098751	0.001610813	0.007023981	0.009721675	0.030770761	0.003989744	0.002259077
V	-0.027114194	0.011925116	0.017552011	-0.005386055	-0.011380629	-0.005483786	0.013688029	-0.001844131
Cr	0	0.001886926	0.002711791	-0.003017156	-0.002845195	0.000377685	-0.00369272	-0.001326348
Fe3+	0	0	0	0	-0.122380201	0	-0.449476536	-0.241088697
Mg	0	0	0	0.034586591	0	0	0	0
Mn	0.011983923	0.104789685	0.007961283	0.007970679	0.007639809	0.011249886	0.007905525	0.010009855
Fe2+	3.252332848	4.575202721	3.463516704	2.899705571	3.186080623	3.283751439	3.46349642	3.342620933
Zn	0	0	0	0	0	0	0	0
Li*	0.147006503	0	0.056794132	0.004704252	0	0	0	0
∑Y	3.39206892	4.692705697	3.550146733	3.000000001	3.066836083	3.320665984	3.035910462	3.110630691
X: Ca	0.028838743	0.180839573	0.032448607	0.064262331	0.069275924	0.066006188	0.039031046	0.03710841
Ba	0	0	0	0	0	0	0	0
Na	0.854657471	0.01261145	0.774384624	0.736437087	0.747580533	0.784341956	0.784799734	0.793529362
K	0.011376103	1.179542111	0.012226776	0.012639979	0.014875756	0.025951078	0.012641429	0.014240766
Rb	0	0	0	0	0	0	0	0
Cs	0	0	0	0	0	0	0	0
r	0.105127683	0	0.180939993	0.186660604	0.168267787	0.123700778	0.163527791	0.155121462
OH	3.952105673	3.81288379	3.963697654	3.827456558	3.82944938	3.696275132	3.960373345	3.938479817
F	0.045964691	0.177681104	0.039310397	0.174672108	0.172028008	0.303120273	0.036711227	0.059593816
Cl	0.001929636	0.009435106	-0.00300805	-0.002128667	-0.001477388	0.000604595	0.002915428	0.001926367
F content								
Mineral Name	Schorl	Feruvite	Schorl	Schorl	Schorl	Schorl	Schorl	Schorl
CatSum	19.14834407	20.07201213	19.08494732	18.86394175	18.95713158	19.01270529	19.01758537	19.02155081
Si excess	0	0	0	0	0	0	0.066453325	0
X+B+Si excess	4.148344066	4.778634747	4.084947319	3.863941752	3.890295496	3.90590139	3.981674909	3.910920118
Li*	***0.147006502***	***-0.293377381***	***0.056794131***	***0.004704251***	***-0.066836083***	***-0.106803896***	***-0.035910462***	***-0.110630691***
T+Z+Y	15	15.29337738	15	15	15.06683608	15.1068039	15.10236379	15.11063069
Ideal T+Z+Y	15	15.29337738	15	15	15.06683608	15.1068039	15.03591046	15.11063069

Major and trace e							
Sample	BW001-239.5	BW001-239.5	BW001-239.5	BW001-239.5	BW001-239.5	BW002_234.9	BW002_234.9
Analysis No.	239.5_C3_S2	239.5_C3_S3	239.5_C3_S4	239.5_C4_S1	239.5_C4_S2	BW002_234.9_C1S1	BW002_234.9_C1S2
Group	Green	Green	Green	Green	Green		
SiO2	27.614	7.54494	33.1324	32.89	33.0345	98.4806	34.1386
TiO2	0.004847	0.01065	0.008297	0.003082	0.014523	0.00151	0.419613
Al2O3	25.1899	5.54796	26.9877	26.1842	27.7544	0.472374	32.305
V2O3	-0.04887	0.05129	0.052935	0.136509	0.000653	-0.09701	0.137227
Cr2O3	-0.01222	-0.00476	-0.00214	-0.02281	0.001334	0.018404	0.00273
Fe2O3							
FeO	15.4137	45.5988	22.1079	22.2908	20.3661	0.490113	15.5059
MgO	0.738447	2.35208	0.042482	0.084008	0.30877	-0.00925	0.805185
CaO	7.62942	1.45442	0.171786	0.201506	0.358951	0.006547	0.125649
MnO	0.189329	1.32079	0.039941	0.035029	0.079216	-0.00224	0.096874
ZnO							
BaO							
Na2O	1.31451	0.078476	2.67562	2.47977	2.25784	-0.0099	2.06201
K2O	0.048672	0.846434	0.044347	0.079325	0.083857	0.107163	0.042928
Rb2O							
Cs2O							
F	0.031029	0.11642	0.086473	0.078947	0.456649	-0.02661	0.342352
Cl	0.003615	0.036722	0.001296	0.010525	0.008154	0.005517	0.003305
H2O							
B2O3	9.83792	7.44063	9.80117	9.78972	9.84345	11.7469	10.1468
Li2O							
H2O*	3.13868952	1.77929625	3.284068321	3.248241326	3.107106228	5.595040301	3.335109056
B2O3*	-	-	-	-	-	-	-
Li2O*	1.863416414	0	0	0	0	20.6179516	0.153119859
Total	92.95640493	74.17414825	98.43427532	97.48885233	97.67550323	137.3971099	99.62240191
O=F	0.01306545	0.04902123	0.036411379	0.03324239	0.192282215	-0.011204732	0.144154922
Total*	92.94333948	74.12512702	98.39786394	97.45560994	97.48322101	137.4083146	99.47824699
Structural formula							
T: Si	5.249666396	2.453829899	5.974719688	5.997833836	5.956546637	10.5761334	5.851954561
AlT	0.750333604	3.546170101	0.025280312	0.002166164	0.043453363	0	0.148045439
B	3.228299979	4.177020279	3.050779167	3.081548719	3.063672649	2.177547901	3.002289378
Z: AlZ	4.893634509	-1.419609774	5.710417143	5.625464517	5.854677096	0.059788539	6
Mg	0.209281221	1.140379228	0.011420316	0.022838088	0.08299854	-0.001480903	0
Cr	0	0	0	0	0	0	0
Fe3+	0.89708427	6.279230546	0.278162541	0.351697395	0	0	0
Y: AlY	0	0	0	0	0	0	0.378460029
Ti	0.000692941	0.002604708	0.00112514	0.000422653	0.001969264	0.000121948	0.054090989
V	-0.007448839	0.01337412	0.007653347	0.019958858	9.44026E-05	-0.008352886	0.018859868
Cr	-0.001836746	-0.001223971	-0.000305108	-0.003288753	0.000190177	0.001562658	0.000369993
Fe3+	-0.89708427	-6.279230546	-0.278162541	-0.351697395	0	0	0
Mg	0	0	0	0	0	0	0.205759293
Mn	0.030486338	0.3638381	0.006100555	0.005410583	0.012098331	-0.000203756	0.014065274
Fe2+	2.450559667	12.40218117	3.334019413	3.399477771	3.071076781	0.044017812	2.22284004
Zn	0	0	0	0	0	0	0
Li*	1.424630908	0	0	0	0	8.904546588	0.105554515
∑Y	3	6.501543581	3.070430805	3.070283716	3.085428955	8.941692363	3.000000001
X: Ca	1.554001939	0.506799466	0.033190214	0.039370976	0.069345714	0.000753314	0.023076605
Ba	0	0	0	0	0	0	0
Na	0.484521593	0.049484864	0.935483064	0.876776327	0.789344938	-0.002061381	0.685319142
K	0.011804297	0.351188515	0.010202049	0.018454368	0.019289664	0.014681811	0.009387597
Rb	0	0	0	0	0	0	0
Cs	0	0	0	0	0	0	0
r	0	0.092527155	0.021124672	0.065398329	0.122019683	0.986626255	0.282216656
OH	3.980179479	3.860013651	3.950287785	3.95121587	3.737100899	4.008033724	3.813442404
F	0.018655808	0.119745767	0.04931614	0.045531305	0.260407345	-0.009037848	0.185597455
Cl	0.001164712	0.020240582	0.000396075	0.003252825	0.002491756	0.001004124	0.00096014
F content							
Mineral Name	Feruvite	Feruvite	Schorl	Schorl	Schorl	Rossmanite	Schorl
CatSum	20.27862781	23.5860367	19.1000853	19.08643411	18.96475756	21.76705505	18.72007272
Si excess	0	0	0	0	0	4.576133405	0
X+B+Si excess	5.278627808	5.084493123	4.029654494	4.01615039	3.941652966	6.767055051	3.720072722
Li*	***1.424630907***	***-3.501543581***	***-0.070430805***	***-0.070283716***	***-0.023104591***	***8.904546588***	***0.105554513***
T+Z+Y	15	18.50154358	15.0704308	15.07028372	15.02310459	19.5761334	15
Ideal T+Z+Y	15	18.50154358	15.0704308	15.07028372	15.02310459	15	15

Major and trace e						
Sample	BW002_234.9	BW002_234.9	BW002_234.9	BW002_234.9	BW002_234.9	BW002_234.9
Analysis No.	BW002_234.9_C1S3	BW002_234.9_C1S4	BW002_234.9_C1S5	BW002_234.9_C1S6	BW002_234.9_C2S1	BW002_234.9_C2S2
Group						
SiO2	33.8223	34.0432	33.7682	33.9933	33.3289	33.8868
TiO2	0.587054	0.462122	0.405172	0.387305	0.635482	0.306708
Al2O3	31.2077	31.9344	31.9511	31.987	31.0896	32.4112
V2O3	-0.01213	0.044113	0.038853	0.027706	0.021972	0.101835
Cr2O3	-0.01652	0.002055	-0.01654	0.013689	-0.01005	-0.01438
Fe2O3						
FeO	15.3675	14.5303	14.3226	14.7733	15.8176	14.3806
MgO	1.15191	1.26204	1.36609	1.40794	0.965865	0.993959
CaO	0.225147	0.179895	0.230001	0.128862	0.226326	0.149897
MnO	0.07919	0.070597	0.077538	0.06842	0.115468	0.087405
ZnO						
BaO						
Na2O	2.0896	1.93315	1.80989	2.16472	1.94285	1.64435
K2O	0.049714	0.043253	0.085719	0.030853	0.044341	0.035092
Rb2O						
Cs2O						
F	0.78629	0.637897	0.835713	0.592554	0.975052	0.343013
Cl	0.003248	0.001957	0.008848	0.003713	0.001634	0.009335
H2O						
B2O3	10.074	10.1569	10.1325	10.1387	10.0193	10.2252
Li2O						
H2O*	3.080810042	3.175074644	3.063239736	3.202346827	2.963459476	3.307141676
B2O3*	-	-	-	-	-	-
Li2O*	0.186944013	0.209291487	0.189938362	0.155789443	0.119041082	0.219688506
Total	98.68275705	98.68624513	98.2688621	99.07619827	98.25684056	98.08784418
O=F	0.331084887	0.268600715	0.35189554	0.249508037	0.410567324	0.14443325
Total*	98.35167217	98.41764442	97.91696656	98.82669023	97.84627323	97.94341093
Structural formula						
T: Si	5.871300126	5.869581038	5.849572487	5.850514374	5.833378058	5.852492744
AlT	0.128699874	0.130418962	0.150427513	0.149485626	0.166621942	0.147507256
B	3.018570347	3.022777039	3.029709853	3.011973923	3.026946432	3.048248348
Z: AlZ	6	6	6	6	6	6
Mg	0	0	0	0	0	0
Cr	0	0	0	0	0	0
Fe3+	0	0	0	0	0	0
Y: AlY	0.256119694	0.358781796	0.372728308	0.338799949	0.246507424	0.449715645
Ti	0.076635491	0.05991756	0.052780851	0.05012733	0.083641757	0.039834207
V	-0.001688246	0.006097996	0.005396157	0.003823124	0.003083277	0.014101043
Cr	-0.00226734	0.000280133	-0.002265307	0.001862721	-0.001390723	-0.001963562
Fe3+	0	0	0	0	0	0
Mg	0.298097434	0.324383229	0.352780096	0.36123799	0.252013681	0.255910049
Mn	0.011643599	0.010309764	0.011376706	0.009974004	0.017117744	0.012785931
Fe2+	2.230952684	2.095112278	2.0748852	2.12634747	2.31523845	2.077032657
Zn	0	0	0	0	0	0
Li*	0.130506686	0.145117151	0.132318001	0.10782735	0.083788553	0.152583825
∑Y	3.000000001	2.999999907	3.000000012	2.999999938	3.000000162	2.999999795
X: Ca	0.041875013	0.03323177	0.042687782	0.023762014	0.04244155	0.027737091
Ba	0	0	0	0	0	0
Na	0.703300879	0.646233009	0.607876359	0.722352717	0.659303335	0.550619318
K	0.01100952	0.009513745	0.018943135	0.006774179	0.009900638	0.007731735
Rb	0	0	0	0	0	0
Cs	0	0	0	0	0	0
r	0.243814587	0.311021476	0.330492725	0.247111091	0.288354478	0.413911855
OH	3.567368543	3.651594827	3.539558674	3.676385167	3.459792433	3.809912877
F	0.431675903	0.347833332	0.457843743	0.32253182	0.539722882	0.187354796
Cl	0.000955554	0.000571841	0.002597582	0.001083013	0.000484685	0.002732327
F content					Fluor-	
Mineral Name	Schorl	Schorl	Schorl	Schorl	Schorl	Schorl
CatSum	18.77475576	18.71175552	18.69921713	18.76486282	18.73859205	18.63433639
Si excess	0	0	0	0	0	0
X+B+Si excess	3.77475576	3.711755553	3.699217129	3.764862829	3.738591973	3.634336473
Li*	***0.130506685***	***0.145117282***	***0.132317986***	***0.107827423***	***0.083788316***	***0.152584109***
T+Z+Y	15	14.99999996	15	14.99999999	15.00000007	14.99999992
Ideal T+Z+Y	15	14.99999996	15	14.99999999	15.00000007	14.99999992

Major and trace e						
Sample	BW002_234.9	BW002_234.9	BW002_234.9	BW002_234.9	BW002_234.9	BW002_234.9
Analysis No.	BW002_234.9_C2S3	BW002_234.9_C2S4	BW002_234.9_C2S5	BW002_234.9_C2S6	BW002_234.9_C3S1	BW002_234.9_C3S2
Group						
SiO2	33.5089	33.5526	33.4282	34.2962	33.8244	33.2275
TiO2	0.626409	0.330898	0.550548	0.444052	0.270153	0.704721
Al2O3	30.9219	32.2738	31.3105	32.0218	33.5653	32.2382
V2O3	-0.04935	0.03537	-0.07434	-0.03517	-0.04819	-0.08299
Cr2O3	-0.00287	0.0048	-0.02009	0.016432	-0.00072	0.019085
Fe2O3						
FeO	16.1279	14.1092	16.0836	14.6729	14.2506	15.7952
MgO	1.21689	1.46698	0.680966	1.26077	1.37028	0.969275
CaO	0.220105	0.200505	0.193922	0.079798	0.152454	0.295977
MnO	0.063458	0.051411	0.107219	0.06682	0.064488	0.070284
ZnO						
BaO						
Na2O	2.15175	1.63015	1.94879	2.00673	1.99676	2.13369
K2O	0.032746	0.039643	0.047677	0.025215	0.024309	0.042913
Rb2O						
Cs2O						
F	1.03438	0.802557	0.749761	0.337056	0.793928	0.909662
Cl	-0.00177	0.005711	0.002743	0.006744	0.006236	0
H2O						
B2O3	9.98599	10.161	10.0498	10.2024	10.1432	10.0204
Li2O						
H2O*	2.947565558	3.074197548	3.074898105	3.331482923	3.134791074	3.035437152
B2O3*	-	-	-	-	-	-
Li2O*	0.062027987	0.137267126	0.149207052	0.201966266	0.076253058	0.075083015
Total	98.84603155	97.87608967	98.28340116	98.93519619	99.62424213	99.45443717
O=F	0.435548698	0.337934469	0.315703539	0.141924923	0.334301037	0.383033411
Total*	98.41048285	97.5381552	97.96769762	98.79327127	99.28994109	99.07140376
Structural formula						
T: Si	5.845483754	5.821573729	5.842394657	5.887828458	5.774112915	5.747589673
AlT	0.154516246	0.178426271	0.157605343	0.112171542	0.225887085	0.252410327
B	3.006904427	3.043118648	3.031820805	3.023289273	2.988810436	2.991860629
Z: AlZ	6	6	6	6	6	6
Mg	0	0	0	0	0	0
Cr	0	0	0	0	0	0
Fe3+	0	0	0	0	0	0
Y: AlY	0.20292244	0.42121073	0.291858677	0.366867673	0.527185641	0.319847572
Ti	0.08217487	0.043174679	0.072359213	0.057327595	0.034680529	0.091669751
V	-0.00690226	0.004920317	-0.010417039	-0.004840892	-0.006595625	-0.011509533
Cr	-0.000395838	0.000658462	-0.002776088	0.00223036	-9.71769E-05	0.002610091
Fe3+	0	0	0	0	0	0
Mg	0.316460969	0.379443363	0.177423798	0.322666261	0.348716932	0.249944535
Mn	0.00937632	0.007555375	0.015872137	0.00971631	0.009324377	0.010297464
Fe2+	2.35284925	2.047258139	2.35080798	2.106595232	2.034437325	2.2849106
Zn	0	0	0	0	0	0
Li*	0.043514484	0.095778991	0.104871365	0.139437255	0.052348069	0.052229669
∑Y	3.000000236	3.000000056	3.000000043	2.999999795	3.00000007	3.000000151
X: Ca	0.041138442	0.037273234	0.036313042	0.014677727	0.02788378	0.054853419
Ba	0	0	0	0	0	0
Na	0.727778054	0.548388891	0.660373745	0.667951525	0.660888045	0.715593304
K	0.007287475	0.008774841	0.010630296	0.005522385	0.005293962	0.009469684
Rb	0	0	0	0	0	0
Cs	0	0	0	0	0	0
r	0.223796029	0.405563034	0.292682918	0.311848364	0.305934213	0.220083593
OH	3.42985425	3.557934154	3.584763754	3.815036141	3.569568198	3.5023637
F	0.570669039	0.440386523	0.414423768	0.183001697	0.428627666	0.4976363
Cl	-0.000523289	0.001679324	0.000812478	0.001962161	0.001804136	0
F content	Fluor-					
Mineral Name	Schorl	Schorl	Schorl	Schorl	Schorl	Schorl
CatSum	18.78310854	18.63755566	18.73913792	18.71144082	18.6828763	18.77177714
Si excess	0	0	0	0	0	0
X+B+Si excess	3.783108427	3.637555622	3.739137894	3.711440891	3.682876237	3.771777057
Li*	***0.043514132***	***0.095778901***	***0.104871297***	***0.139437534***	***0.05234794***	***0.052229434***
T+Z+Y	15.00000012	15.00000003	15.00000003	14.99999993	15.00000006	15.00000008
Ideal T+Z+Y	15.00000012	15.00000003	15.00000003	14.99999993	15.00000006	15.00000008

Major and trace e						
Sample	BW002_234.9	BW002_234.9	BW004_231.0	BW004_231.0	BW004_231.0	BW004_231.0
Analysis No.	BW002_234.9_C3S3	BW002_234.9_C3S4	BW004_231.0_C1S1	BW004_231.0_C1S2	BW004_231.0_C1S3	BW004_231.0_C1S4
Group						
SiO2	33.7496	33.771	33.905	31.1731	33.5187	33.4676
TiO2	0.331302	0.303458	0.809533	0.417232	0.476615	0.584131
Al2O3	33.2902	33.4766	30.7828	29.5827	31.8959	31.3631
V2O3	0.005751	0.089251	-0.05918	0.03266	0.065943	0.064972
Cr2O3	-0.00863	-0.01295	0.008208	0	-0.00288	-0.00072
Fe2O3						
FeO	14.6336	14.2394	15.0538	11.0818	14.939	15.1942
MgO	1.14143	1.22011	1.65816	1.42186	1.22035	1.53968
CaO	0.161925	0.13112	0.379845	0.25771	0.246508	0.401404
MnO	0.082668	0.04005	0.050931	0.039363	0.048107	0.0738
ZnO						
BaO						
Na2O	1.98712	1.82085	2.02894	1.9736	2.01144	2.05674
K2O	0.045751	0.04536	0.050584	0.022568	0.037783	0.050461
Rb2O						
Cs2O						
F	0.527073	0.395903	1.07326	0.987544	0.896392	1.08038
Cl	0.006871	0.009242	0.011474	0.016131	0.013876	-0.00133
H2O						
B2O3	10.1618	10.2145	10.0348	10.279	10.078	10.0202
Li2O						
H2O*	3.253606078	3.318030532	2.945345852	2.781205754	3.029060466	2.941271022
B2O3*	-	-	-	-	-	-
Li2O*	0.109263773	0.118148604	0.154043566	0.891375129	0.153048816	0.097218901
Total	99.47933085	99.18007314	98.88754442	90.95784888	98.62784328	98.93310792
O=F	0.221935806	0.166703761	0.451919986	0.415827359	0.377445782	0.454918021
Total*	99.25739504	99.01336938	98.43562443	90.54202152	98.2503975	98.4781899
Structural formula						
T: Si	5.773746785	5.772737218	5.881084829	5.745584741	5.813291923	5.811858587
AlT	0.226253215	0.227262782	0.118915171	0.254415259	0.186708077	0.188141413
B	3.000737169	3.013860812	3.004489063	3.270192506	3.017015428	3.003551412
Z: AlZ	6	6	6	6	6	6
Mg	0	0	0	0	0	0
Cr	0	0	0	0	0	0
Fe3+	0	0	0	0	0	0
Y: AlY	0.485890249	0.517006983	0.174082026	0.171689094	0.332960954	0.230826051
Ti	0.042622008	0.039008317	0.105596373	0.057829921	0.062161777	0.076281895
V	0.000788817	0.012231925	-0.00823024	0.004826299	0.009169539	0.009046083
Cr	-0.001167281	-0.001750181	0.001125658	0	-0.000394914	-9.88549E-05
Fe3+	0	0	0	0	0	0
Mg	0.291103168	0.310917667	0.428774229	0.390678601	0.315520744	0.398592831
Mn	0.011978771	0.00579864	0.007482757	0.006145089	0.007066901	0.010855069
Fe2+	2.093612377	2.035567703	2.183714364	1.708128519	2.166768369	2.206603494
Zn	0	0	0	0	0	0
Li*	0.075171834	0.081218833	0.107454972	0.660702009	0.106746706	0.067893635
∑Y	2.999999944	2.999999885	3.00000014	2.999999532	3.000000075	3.000000203
X: Ca	0.029679779	0.024013997	0.070592369	0.050891255	0.045806133	0.074684386
Ba	0	0	0	0	0	0
Na	0.659113269	0.603474461	0.682354023	0.705277835	0.676377115	0.692495125
K	0.009985004	0.009891666	0.011193487	0.005306472	0.008359686	0.011179049
Rb	0	0	0	0	0	0
Cs	0	0	0	0	0	0
r	0.301221948	0.362619876	0.235860121	0.238524438	0.269457066	0.22164144
OH	3.712837907	3.78329462	3.407861234	3.419316414	3.504247884	3.40704147
F	0.285169965	0.214027989	0.588765764	0.575644827	0.491673552	0.593349957
Cl	0.001992127	0.002677391	0.003373002	0.005038759	0.004078564	-0.000391426
F content			Fluor-	Fluor-		Fluor-
Mineral Name	Schorl	Schorl	Schorl	Schorl	Schorl	Schorl
CatSum	18.69951523	18.65124091	18.76862901	19.03166766	18.74755841	18.78191009
Si excess	0	0	0	0	0	0
X+B+Si excess	3.699515222	3.651240932	3.768628956	4.031667979	3.747558371	3.781909995
Li*	***0.075171885***	***0.081218965***	***0.107454775***	***0.660702793***	***0.106746595***	***0.067893338***
T+Z+Y	15.00000001	14.99999998	15.00000006	14.99999968	15.00000004	15.00000009
Ideal T+Z+Y	15.00000001	14.99999998	15.00000006	14.99999968	15.00000004	15.00000009

Major and trace e						
Sample	BW004_231.0	BW004_231.0	BW004_231.0	BW004_231.0	BW004_231.0	BW004_231.0
Analysis No.	BW004_231.0_C1S5	BW004_231.0_C1S6	BW004_231.0_C1S7	BW004_231.0_C1S8	BW004_231.0_C1S9	BW004_231.0_C1S10
Group						
SiO2	33.1705	33.7384	99.3898	99.572	-0.02102	33.3928
TiO2	0.889253	0.428982	0.012865	-0.00177	-0.00973	1.05918
Al2O3	30.4897	31.8407	0.058668	0.027791	-0.00034	29.8359
V2O3	-0.07885	-0.03146	-0.16867	-0.00829	-0.06488	0.004707
Cr2O3	0.002041	0.003415	-0.00665	0.023618	0.008167	0.012977
Fe2O3						
FeO	16.1497	15.2512	0.0426	0.07294	1.20568	15.2995
MgO	1.31225	1.48614	-0.01916	0.004395	0.259876	1.79713
CaO	0.334441	0.210439	0.001597	0.013701	57.5248	0.202314
MnO	0.115327	0.058447	-0.02269	0.00743	0.216653	0.081924
ZnO						
BaO						
Na2O	1.92058	1.90565	0.008485	0.004984	-0.00607	2.11322
K2O	0.051457	0.076091	0.009466	0.007284	-0.00228	0.0486
Rb2O						
Cs2O						
F	1.07791	0.959392	-0.01261	-0.03471	0.015882	1.23385
Cl	0.006499	0.024526	0.001143	-0.0023	0.005472	-0.00841
H2O						
B2O3	9.9732	10.0548	11.7916	11.78	7.50722	9.98466
Li2O						
H2O*	2.903604124	3.004680743	5.617150543	5.64037842	2.271592483	2.830529237
B2O3*	-	-	-	-	-	-
Li2O*	0.045795265	0.027034854	20.96046706	20.95726028	13.81066292	0.117422058
Total	98.36340739	99.0384376	137.6640616	138.0647117	82.7216854	98.00630329
O=F	0.453877972	0.403973333	-0.005309721	-0.014615417	0.006687469	0.519539976
Total*	97.90952942	98.63446426	137.6693713	138.0793271	82.71499793	97.48676332
Structural formula						
T: Si	5.82239632	5.837557995	10.62120642	10.61820684	-0.005527239	5.866444286
AlT	0.17760368	0.162442005	0	0	6.005527239	0.133555714
B	3.021707937	3.00295188	2.175068718	2.168340353	3.407398418	3.027775052
Z: AlZ	6	6	0.007389057	0.003492801	-6.005632608	6
Mg	0	0	-0.003052362	0.000698685	0.101870933	0
Cr	0	0	0	0	0.001697906	0
Fe3+	0	0	5.995663305	0	0	0
Y: AlY	0.129916078	0.330552792	0	0	0	0.044004392
Ti	0.117380467	0.055817007	0.001033862	-0.000141941	-0.001924018	0.13993058
V	-0.011096737	-0.004364247	-0.014451526	-0.000708781	-0.013678241	0.000662995
Cr	0.000283249	0.000467168	-0.000561861	0.001991281	0	0.001802486
Fe3+	0	0	-5.995663305	0	0	0
Mg	0.343379902	0.383331929	0	0	0	0.470663103
Mn	0.017146145	0.008565539	-0.002053772	0.000671102	0.048253188	0.012190429
Fe2+	2.37066506	2.206819108	0.003807129	0.006504826	0.265132895	2.247787988
Zn	0	0	0	0	0	0
Li*	0.032326126	0.01881093	9.007889473	8.987492028	14.60427995	0.082958297
∑Y	3.00000029	3.000000226	3	8.995808514	14.90206377	3.00000027
X: Ca	0.062896562	0.039011316	0.00018285	0.001565395	16.2064662	0.038080768
Ba	0	0	0	0	0	0
Na	0.653625527	0.639288249	0.001758048	0.001030478	-0.003094647	0.719803052
K	0.01152266	0.016795717	0.001290497	0.000990929	-0.000764837	0.010892233
Rb	0	0	0	0	0	0
Cs	0	0	0	0	0	0
r	0.271955251	0.304904717	0.996768605	0.996413198	0	0.231223947
OH	3.399687935	3.467823338	4.004054772	4.012121778	3.984353838	3.316970915
F	0.598378743	0.524984798	-0.00426178	-0.011706107	0.013207623	0.685533038
Cl	0.001933322	0.007191864	0.000207008	-0.000415671	0.002438539	-0.002503953
F content	Fluor-	Fluor-				Fluor-
Mineral Name	Schorl	Schorl	Rossmanite	Rossmanite		Schorl
CatSum	18.74975286	18.69804732	21.79950653	21.79013399	34.61000513	18.79655124
Si excess	0	0	4.62120642	4.618206838	0	0
X+B+Si excess	3.749752721	3.698047194	6.799506533	6.790133993	19.61000513	3.796551133
Li*	***0.032325696***	***0.018810579***	***9.007889473***	***8.987492028***	***14.60427995***	***0.082957915***
T+Z+Y	15.00000014	15.00000012	19.62120642	19.61820684	15	15.00000011
Ideal T+Z+Y	15.00000014	15.00000012	15	15	15	15.00000011

Major and trace e						
Sample	BW001_286.3	BW001_286.3	BW001_286.3	BW001_286.3	BW001_286.3	BW001_286.3
Analysis No.	BW001_286.3_C1S1	BW001_286.3_C1S2	BW001_286.3_C1S3	BW001_286.3_C1S4	BW001_286.3_C2S1	BW001_286.3_C2S2
Group						
SiO2	33.8548	33.7259	33.7796	33.6186	33.665	33.8524
TiO2	0.831151	0.982438	1.0652	0.850085	0.661992	0.328514
Al2O3	30.5722	29.5494	29.6236	29.8439	30.751	32.775
V2O3	0.10702	0.001696	0.03917	0.046984	0.117057	-0.10873
Cr2O3	0.016498	0.004115	0.005492	0.014407	0.001362	0.009584
Fe2O3						
FeO	14.097	14.6505	14.5341	14.457	16.0967	14.7016
MgO	2.69944	2.79386	2.78055	2.76856	1.50352	1.19903
CaO	0.55949	0.642911	0.685267	0.541052	0.315916	0.236709
MnO	0.072955	0.083081	0.088644	0.066344	0.077469	0.077787
ZnO						
BaO						
Na2O	2.24119	2.26507	2.20316	2.25128	2.13314	1.92582
K2O	0.054425	0.06978	0.053735	0.053456	0.03247	0.031758
Rb2O						
Cs2O						
F	1.07487	1.09352	1.09325	1.05954	1.03189	0.81956
Cl	0.011229	0.011552	0.013714	0.020937	0.00222	0
H2O						
B2O3	10.0447	10.0032	10.0084	10.0222	9.97833	10.1206
Li2O						
H2O*	2.962841136	2.925986498	2.931836445	2.936664638	2.961141838	3.101081826
B2O3*	-	-	-	-	-	-
Li2O*	0.110953594	0.111934221	0.120593003	0.10018796	0.013326778	0.122987811
Total	99.31076273	98.91494372	99.02631145	98.6511976	99.34253462	99.19370164
O=F	0.452597913	0.46045091	0.46033722	0.446142875	0.434500228	0.34509396
Total*	98.85816482	98.45449281	98.56597423	98.20505472	98.90803439	98.84860768
Structural formula						
T: Si	5.841630133	5.866536249	5.865207661	5.853046871	5.849894965	5.817214221
AlT	0.158369867	0.133463751	0.134792339	0.146953129	0.150105035	0.182785779
B	2.9917065	3.003484353	2.999589026	3.011852189	2.992922861	3.001926571
Z: AlZ	6	5.924443226	5.927298616	5.976743633	6	6
Mg	0	0.075556774	0.072701384	0.023256367	0	0
Cr	0	0	0	0	0	0
Fe3+	0	0	0	0	0	0
Y: AlY	0.058849884	0	0	0	0.147630448	0.455011982
Ti	0.107848593	0.128512127	0.139085161	0.111297518	0.086505344	0.042452202
V	0.014805483	0.000236531	0.005452885	0.006558374	0.016308375	-0.014980242
Cr	0.002250715	0.000565931	0.000753937	0.001983131	0.000187121	0.00130211
Fe3+	0	0	0	0	0	0
Mg	0.69437812	0.648931559	0.647026196	0.695306654	0.389481832	0.307159667
Mn	0.010662391	0.012240683	0.013036589	0.009783399	0.011402055	0.011321875
Fe2+	2.034213336	2.131211993	2.110440092	2.104924646	2.339172737	2.112740656
Zn	0	0	0	0	0	0
Li*	0.076991648	0.078301376	0.084205326	0.070146481	0.009312364	0.084991799
∑Y	3.000000171	3.000000199	3.000000185	3.000000203	3.000000277	3.00000005
X: Ca	0.103434109	0.119819282	0.127481263	0.100925064	0.058816438	0.043581082
Ba	0	0	0	0	0	0
Na	0.749789469	0.763917916	0.741688911	0.759939027	0.718680177	0.641635143
K	0.011980385	0.015484875	0.011902678	0.011872915	0.007197974	0.006962052
Rb	0	0	0	0	0	0
Cs	0	0	0	0	0	0
r	0.134796036	0.100777926	0.118927149	0.127262994	0.215305411	0.307821722
OH	3.410154668	3.395020767	3.395631369	3.410426062	3.432263045	3.554599954
F	0.586561637	0.601573714	0.600333096	0.583396266	0.567083176	0.445400046
Cl	0.003283696	0.00340552	0.004035534	0.006177672	0.000653778	0
F content	Fluor-	Fluor-	Fluor-	Fluor-	Fluor-	
Mineral Name	Schorl	Schorl	Schorl	Schorl	Schorl	Schorl
CatSum	18.85691056	18.90270654	18.88066198	18.88458931	18.77761763	18.69410489
Si excess	0	0	0	0	0	0
X+B+Si excess	3.856910484	3.902706451	3.880661899	3.88458922	3.777617487	3.694104858
Li*	***0.076991398***	***0.078301087***	***0.084205058***	***0.070146184***	***0.009311941***	***0.084991713***
T+Z+Y	15.00000008	15.00000009	15.00000008	15.00000009	15.00000015	15.00000004
Ideal T+Z+Y	15.00000008	15.00000009	15.00000008	15.00000009	15.00000015	15.00000004

Major and trace e							
Sample	BW001_286.3	BW001_286.3	BW001_286.3	THBW017	THBW017	THBW017	THBW017
Analysis No.	BW001_286.3_C2S3	BW001_286.3_C2S4	BW001_286.3_C2S5	THBW017_C1S1	THBW017_C1S2	THBW017_C1S3	THBW017_C1S4
Group							
SiO2	34.5248	33.5574	33.9011	33.7881	33.4284	33.8683	33.3022
TiO2	0.403256	0.82886	0.2358	0.622277	0.681445	0.280776	0.86339
Al2O3	32.8087	30.8145	33.5166	31.0441	30.5562	32.8578	30.4199
V2O3	0.040481	-0.05656	-0.02491	-0.01511	0.010024	-0.11208	-0.02267
Cr2O3	0.010287	0.014976	0	-0.01652	0.000678	-0.00216	0.024392
Fe2O3							
FeO	14.5447	16.22	13.9269	15.8704	17.1985	15.4949	17.4602
MgO	1.06595	1.15582	1.03335	1.17011	0.765463	0.533411	0.611264
CaO	0.127215	0.343793	0.178182	0.261677	0.264724	0.125318	0.332765
MnO	0.075636	0.083796	0.09157	0.083756	0.12689	0.051964	0.091977
ZnO							
BaO							
Na2O	1.82814	1.95872	1.69412	2.20874	2.17071	1.76506	2.1151
K2O	0.054887	0.0368	0.031134	0.060866	0.036653	0.025555	0.067119
Rb2O							
Cs2O							
F	0.368012	1.01055	0.425565	0.882939	0.836645	0.317312	0.854267
Cl	-0.00089	-0.00088	0.001957	-0.00133	0.003926	0.00466	0.006294
H2O							
B2O3	10.2103	9.98828	10.2401	10.022	9.95517	10.1814	9.93524
Li2O							
H2O*	3.34669436	2.962497341	3.30083654	3.037436137	3.031157679	3.331290588	3.017023247
B2O3*	-	-	-	-	-	-	-
Li2O*	0.179127587	0.064723467	0.199321379	0.133116129	0.04355438	0.151990634	0.060600468
Total	99.58729595	98.98327581	98.75162592	99.15255727	99.11014006	98.87549722	99.13906172
O=F	0.154959635	0.425514546	0.179193605	0.371781098	0.352287979	0.133611273	0.359708114
Total*	99.43233631	98.55776126	98.57243231	98.78077617	98.75785208	98.74188595	98.7793536
Structural formula							
T: Si	5.880025246	5.847379165	5.803216681	5.863179608	5.84625677	5.831200774	5.832994024
AlT	0.119974754	0.152620835	0.196783319	0.136820392	0.15374323	0.168799226	0.167005976
B	3.001613247	3.004220954	3.025710731	3.001871081	3.005240185	3.025800624	3.003759661
Z: AlZ	6	6	6	6	6	6	6
Mg	0	0	0	0	0	0	0
Cr	0	0	0	0	0	0	0
Fe3+	0	0	0	0	0	0	0
Y: AlY	0.465586057	0.175631662	0.565146758	0.212163479	0.144470033	0.498635939	0.112595913
Ti	0.051647536	0.108611268	0.030354253	0.081203346	0.08962184	0.036353425	0.113722493
V	0.005527683	-0.007901803	-0.003418791	-0.002102218	0.001405553	-0.015471647	-0.003183567
Cr	0.001385199	0.002063214	0	-0.002266496	9.37492E-05	-0.000294031	0.003377858
Fe3+	0	0	0	0	0	0	0
Mg	0.270640881	0.300242178	0.26370052	0.302694593	0.199569902	0.136909981	0.159608484
Mn	0.010910944	0.012367502	0.013276816	0.01231037	0.018796433	0.00757797	0.013645316
Fe2+	2.071613732	2.363631642	1.993725886	2.303102646	2.515410447	2.231050335	2.557548127
Zn	0	0	0	0	0	0	0
Li*	0.122687775	0.045354559	0.137214379	0.092894368	0.030632232	0.105237869	0.042685558
∑Y	2.999999806	3.000000221	2.999999821	3.000000089	3.000000188	2.999999841	3.000000182
X: Ca	0.02321368	0.064184126	0.032679581	0.048651096	0.049603607	0.023117225	0.062447333
Ba	0	0	0	0	0	0	0
Na	0.60367658	0.661747282	0.562271438	0.743123304	0.736056174	0.58921111	0.718284292
K	0.011925485	0.00818049	0.006799053	0.013474192	0.008177685	0.005613051	0.01499763
Rb	0	0	0	0	0	0	0
Cs	0	0	0	0	0	0	0
r	0.361184255	0.265888103	0.398249928	0.194751408	0.206162535	0.382058614	0.204270745
OH	3.802033951	3.443363145	3.769041626	3.515835068	3.536085291	3.825859642	3.524919238
F	0.198222938	0.55689673	0.230390628	0.484556069	0.462751064	0.17278061	0.473212433
Cl	-0.000256889	-0.000259874	0.000567746	-0.000391137	0.001163645	0.001359748	0.001868329
F content		Fluor-					
Mineral Name	Schorl	Schorl	Schorl	Schorl	Schorl	Schorl	Schorl
CatSum	18.64042891	18.73833299	18.62746072	18.80711973	18.79907778	18.64374196	18.79948904
Si excess	0	0	0	0	0	0	0
X+B+Si excess	3.640428977	3.738332879	3.627460788	3.807119685	3.799077678	3.643742	3.799488941
Li*	***0.122688031***	***0.045354227***	***0.137214621***	***0.092894233***	***0.030631937***	***0.105238072***	***0.042685277***
T+Z+Y	14.99999994	15.00000011	14.99999994	15.00000005	15.00000011	14.99999996	15.0000001
Ideal T+Z+Y	14.99999994	15.00000011	14.99999994	15.00000005	15.00000011	14.99999996	15.0000001

Major and trace e								
Sample	THBW017	THBW017	THBW017	THBW017	THBW017	THBW017	THBW017	THBW017
Analysis No.	THBW017_C2S1	THBW017_C2S2	THBW017_C2S3	THBW017_C2S4	THBW017_C2S5	THBW017_C2S6	THBW017_C2S7	THBW017_C2S8
Group								
SiO2	32.054	32.2129	32.7459	31.6662	32.2241	28.5887	32.5938	32.8246
TiO2	0.522315	0.525912	0.304273	0.436764	0.652503	0.134169	0.555017	0.670697
Al2O3	29.9125	29.4418	30.5372	30.3217	29.9268	30.1043	30.1418	30.2771
V2O3	-0.06426	-0.15236	0.013552	0.110681	0.081214	0.067736	0.047801	-0.15693
Cr2O3	-0.00863	-0.01365	-0.02085	-0.00648	0.00476	0.025406	0.027298	0.01021
Fe2O3								
FeO	14.8461	16.4361	14.849	13.9495	16.0156	19.0679	15.2978	16.0004
MgO	1.00871	0.723447	0.606594	1.4547	0.809221	0.694724	1.41456	1.05933
CaO	0.368887	0.284411	0.099597	0.382636	0.313129	0.205401	0.343086	0.285556
MnO	0.072495	0.074323	0.081243	0.059842	0.089321	0.077863	0.119539	0.100032
ZnO								
BaO								
Na2O	1.69599	1.97521	1.62667	1.77897	1.73638	1.14788	2.01583	2.01758
K2O	0.071699	0.05282	0.040739	0.0336	0.043642	0.026191	0.067701	0.036031
Rb2O								
Cs2O								
F	0.905739	0.837733	0.377325	0.761739	0.89593	0.480576	0.927054	1.01219
Cl	0.004635	0.017508	0.012931	0.00989	-0.00265	0.066035	-0.00752	0.00261
H2O								
B2O3	10.0861	10.0048	10.2018	10.1415	10.0172	9.89696	10.0316	9.99612
Li2O								
H2O*	2.890019845	2.919652923	3.172198715	2.960096525	2.915394303	2.954953348	2.935581808	2.90121217
B2O3*	-	-	-	-	-	-	-	-
Li2O*	0.357833847	0.252969749	0.386929204	0.358347009	0.19996076	0	0.193646096	0.162131051
Total	94.72413369	95.59357667	95.03510192	94.41968553	95.92250506	93.53879435	96.7045939	97.19886922
O=F	0.381381544	0.352746106	0.158881081	0.320747143	0.377251247	0.20235721	0.390356699	0.426205105
Total*	94.34275215	95.24083057	94.87622084	94.09893839	95.54525382	93.33643714	96.31423721	96.77266412
Structural formula								
T: Si	5.788550233	5.816088816	5.853995113	5.713119559	5.78638121	5.358077877	5.794283281	5.820527037
AlT	0.211449767	0.183911184	0.146004887	0.286880441	0.21361879	0.641922123	0.205716719	0.179472963
B	3.143974789	3.118012329	3.148041441	3.15825919	3.10485127	3.201729522	3.078244737	3.059585124
Z: AlZ	6	6	6	6	6	6	6	6
Mg	0	0	0	0	0	0	0	0
Cr	0	0	0	0	0	0	0	0
Fe3+	0	0	0	0	0	0	0	0
Y: AlY	0.154980818	0.08109186	0.287984801	0.160549497	0.119858959	0.007729147	0.10952	0.148037417
Ti	0.070931774	0.071406054	0.040905301	0.059257721	0.088110874	0.018909827	0.074197925	0.089435509
V	-0.009304052	-0.022055454	0.001942418	0.016010109	0.011692328	0.010178365	0.006813112	-0.022310674
Cr	-0.001232179	-0.00194854	-0.002946978	-0.000924332	0.000675785	0.003764665	0.003836816	0.00143141
Fe3+	0	0	0	0	0	0	0	0
Mg	0.271557903	0.19472265	0.161659816	0.391254501	0.216621688	0.194104437	0.37488205	0.280028791
Mn	0.011088719	0.011366066	0.012301756	0.009144694	0.013585185	0.01236037	0.017999485	0.015024069
Fe2+	2.242105012	2.48173825	2.21997777	2.104708706	2.405057438	2.988639099	2.274310207	2.372737545
Zn	0	0	0	0	0	0	0	0
Li*	0.259871975	0.183679169	0.278174847	0.259999019	0.144397859	0	0.13844051	0.1156161
∑Y	2.999999969	3.000000055	2.99999973	2.999999916	3.000000115	3.23568591	3.000000106	3.000000167
X: Ca	0.071373759	0.055018056	0.019076528	0.073964076	0.060243082	0.041245333	0.065346957	0.054251507
Ba	0	0	0	0	0	0	0	0
Na	0.593823962	0.691450887	0.563821638	0.622290031	0.604530027	0.417117067	0.694809086	0.693650158
K	0.016518067	0.012166289	0.00929104	0.007733484	0.009997454	0.006262176	0.015353887	0.008150753
Rb	0	0	0	0	0	0	0	0
Cs	0	0	0	0	0	0	0	0
r	0.318284212	0.241364767	0.407810795	0.296012409	0.325229436	0.535375424	0.224490069	0.243947582
OH	3.481290889	3.516287239	3.782750796	3.562338231	3.492009815	3.694172377	3.481054522	3.431581098
F	0.517290559	0.478355464	0.213331465	0.43463777	0.50879664	0.284852872	0.521211116	0.567634549
Cl	0.001418552	0.005357297	0.003917739	0.003023999	-0.000806455	0.020974751	-0.002265638	0.000784353
F content	Fluor-				Fluor-		Fluor-	Fluor-
Mineral Name	Schorl	Schorl	Schorl	Schorl	Schorl	Foitite	Schorl	Schorl
CatSum	18.8256905	18.87664756	18.74023046	18.86224668	18.77962188	18.90204001	18.85375471	18.81563762
Si excess	0	0	0	0	0	0	0	0
X+B+Si excess	3.825690562	3.876647561	3.740230609	3.862246761	3.779621843	3.666354098	3.853754677	3.815637558
Li*	***0.259872065***	***0.183679116***	***0.278175265***	***0.259999181***	***0.144397709***	***-0.23568591***	***0.138440371***	***0.115615871***
T+Z+Y	14.99999994	15	14.99999985	14.99999992	15.00000003	15.23568591	15.00000003	15.00000006
Ideal T+Z+Y	14.99999994	15	14.99999985	14.99999992	15.00000003	15.23568591	15.00000003	15.00000006

Major and trace e						
Sample	BW001_239.5	BW001_239.5	BW001_239.5	BW001_239.5	BW001_239.5	BW001_239.5
Analysis No.	BW001_239.5_C1S1	BW001_239.5_C1S2	BW001_239.5_C1S3	BW001_239.5_C2S1	BW001_239.5_C2S2	BW001_239.5_C2S3
Group						
SiO2	33.7949	33.5445	33.6458	33.4854	33.2098	33.2488
TiO2	0.695064	0.624436	0.966643	0.538661	0.951253	0.545318
Al2O3	26.3402	26.9395	26.9681	30.7337	29.198	30.9668
V2O3	-0.06442	-0.05822	0.010978	-0.00699	0.099164	-0.14068
Cr2O3	-0.0036	0.004086	0.007462	0.006833	-0.01723	-0.01294
Fe2O3						
FeO	15.7002	16.614	17.608	15.3034	16.2581	15.2739
MgO	4.07544	3.30626	2.58441	1.37787	1.47929	1.51248
CaO	1.81924	1.55409	1.17321	0.267767	0.395389	0.301049
MnO	0.030992	0.077047	0.047412	0.064314	0.111278	0.106776
ZnO						
BaO						
Na2O	1.57159	1.75399	1.94957	2.07422	2.13405	2.01652
K2O	0.059246	0.064789	0.042752	0.082011	0.043528	0.04632
Rb2O						
Cs2O						
F	0.56017	0.450316	0.386058	1.10272	1.29659	0.926733
Cl	0.00098	0.003506	0.004108	0.012454	0.001666	0.001941
H2O						
B2O3	10.0016	9.97829	9.94447	10.0164	9.91081	10.0493
Li2O						
H2O*	3.122620139	3.172006885	3.207194163	2.898922363	2.77347637	2.983712067
B2O3*	-	-	-	-	-	-
Li2O*	0.054800144	0.024507437	0.009925182	0.16214006	0.115535827	0.121030931
Total	97.75902228	98.05310432	98.55609235	98.11982242	97.9607002	97.94706
O=F	0.235872034	0.189615564	0.162558305	0.464324774	0.545958048	0.390221535
Total*	97.52315025	97.86348876	98.39353404	97.65549765	97.41474215	97.55683846
Structural formula						
T: Si	5.9807684	5.940058515	5.949433837	5.86292142	5.876901065	5.823741654
AlT	0.0192316	0.059941485	0.050566163	0.13707858	0.123098935	0.176258346
B	3.055227203	3.049957118	3.035251157	3.027181447	3.027328023	3.038296463
Z: AlZ	5.47466663	5.562366781	5.569621958	6	5.966531629	6
Mg	0.52533337	0.437633219	0.430378042	0	0.033468371	0
Cr	0	0	0	0	0	0
Fe3+	0	0	0	0	0	0
Y: AlY	0	0	0	0.204963986	0	0.216351176
Ti	0.092502051	0.083153031	0.12853803	0.070924268	0.126589857	0.071828485
V	-0.009140509	-0.00826581	0.001556366	-0.00098125	0.014069543	-0.01975615
Cr	-0.000503714	0.000572062	0.001043219	0.0009459	-0.002410698	-0.001791991
Fe3+	0	0	0	0	0	0
Mg	0.549865672	0.435167205	0.250884857	0.359646114	0.356782594	0.394933807
Mn	0.004645593	0.011556089	0.007100988	0.009537836	0.016679275	0.015841106
Fe2+	2.323630124	2.460365341	2.603819072	2.240796958	2.406068038	2.237340387
Zn	0	0	0	0	0	0
Li*	0.039000884	0.017452175	0.007057546	0.114166355	0.08222171	0.085253324
∑Y	3.000000102	3.000000093	3.000000078	3.000000168	3.000000319	3.000000144
X: Ca	0.344947867	0.294851413	0.222268636	0.050231169	0.074966002	0.056496424
Ba	0	0	0	0	0	0
Na	0.539252209	0.602203632	0.668390811	0.704142012	0.732206478	0.684818551
K	0.013375912	0.01463623	0.009644057	0.018318471	0.009826738	0.010350307
Rb	0	0	0	0	0	0
Cs	0	0	0	0	0	0
r	0.102424012	0.088308725	0.099696497	0.227308348	0.183000782	0.248334718
OH	3.68618295	3.74675618	3.782874594	3.385689094	3.273847848	3.486060701
F	0.313523123	0.252191641	0.215894335	0.610615387	0.725652502	0.513363117
Cl	0.000293927	0.001052178	0.001231071	0.003695519	0.000499649	0.000576182
F content				Fluor-	Fluor-	Fluor-
Mineral Name	Schorl	Schorl	Schorl	Schorl	Schorl	Schorl
CatSum	18.95280328	18.9616485	18.93555476	18.79987318	18.8443274	18.78996183
Si excess	0	0	0	0	0	0
X+B+Si excess	3.95280321	3.961648415	3.935554682	3.799873115	3.844327274	3.789961762
Li*	***0.039000708***	***0.017452001***	***0.007057385***	***0.114166124***	***0.082221264***	***0.085253112***
T+Z+Y	15.00000007	15.00000008	15.00000008	15.00000006	15.00000013	15.00000007
Ideal T+Z+Y	15.00000007	15.00000008	15.00000008	15.00000006	15.00000013	15.00000007

Major and trace e						
Sample	BW001_239.5	BW001_239.5	BW001_239.5	BW001_239.5	BW001_239.5	BW001_239.5
Analysis No.	BW001_239.5_C3S1	BW001_239.5_C3S2	BW001_239.5_C3S3	BW001_239.5_C3S4	BW001_239.5_C4S1	BW001_239.5_C4S2
Group						
SiO2	33.5928	33.024	32.9268	33.3868	33.3076	33.4028
TiO2	0.182462	0.010951	0.018458	0.061572	1.09466	1.00259
Al2O3	28.2884	27.4858	29.0965	28.529	28.7572	28.3749
V2O3	-0.06218	0.084444	0.005294	0.05984	-0.07275	-0.10256
Cr2O3	0.01602	-0.01215	0.03444	-0.01002	0.016348	-0.01006
Fe2O3						
FeO	20.7461	20.8431	17.6175	19.9922	16.1079	16.0015
MgO	0.262984	0.380327	0.802323	0.438731	1.71493	1.81357
CaO	0.248815	0.364539	0.188664	0.283644	0.436826	0.423943
MnO	0.027108	0.072113	0.050037	0.062009	0.071745	0.104579
ZnO						
BaO						
Na2O	2.49534	2.04834	1.70304	2.22905	2.13879	2.28806
K2O	0.081861	0.065553	0.258684	0.049215	0.05855	0.054954
Rb2O						
Cs2O						
F	0.450701	0.359503	0.28518	0.580288	1.10521	1.13845
Cl	0.014589	0.0197	0.002167	0.01553	0.005644	-0.00044
H2O						
B2O3	9.82598	9.83527	10.0357	9.85228	9.94803	9.94305
Li2O						
H2O*	3.160528299	3.147195699	3.203471438	3.087163904	2.861214843	2.838696132
B2O3*	-	-	-	-	-	-
Li2O*	0	0	0.072452337	0	0.161096354	0.204804774
Total	99.3315083	97.7286857	96.30071077	98.6173029	97.7129942	97.47883691
O=F	0.189777677	0.151376731	0.12008138	0.244343165	0.465373244	0.479369685
Total*	99.14173062	97.57730897	96.18062939	98.37295974	97.24762095	96.99946722
Structural formula						
T: Si	5.963545247	5.960094779	5.913041375	5.947549113	5.897669149	5.929064871
AlT	0.036454753	0.039905221	0.086958625	0.052450887	0.102330851	0.070935129
B	3.010942081	3.063924	3.110837129	3.029480759	3.040481482	3.046429719
Z: AlZ	5.882192013	5.806482252	6	5.937255212	5.898886907	5.865058021
Mg	0.069597908	0.102326753	0	0.062744788	0.101113093	0.134941979
Cr	0	0	0	0	0	0
Fe3+	0	0.091190995	0	0	0	0
Y: AlY	0	0	0.071299179	0	0	0
Ti	0.024358553	0.001486271	0.002492681	0.008248353	0.145759565	0.133828141
V	-0.008850196	0.012219013	0.000762235	0.008546704	-0.010327945	-0.014595708
Cr	0.002248517	-0.001733705	0.0048899	-0.001411258	0.002288638	-0.001411812
Fe3+	0	-0.091190995	0	0	0	0
Mg	0	0	0.214792533	0.053767065	0.351567638	0.344952991
Mn	0.004076069	0.011023583	0.007610942	0.009356291	0.010760054	0.015722933
Fe2+	3.080000417	3.145877423	2.645828354	2.978378054	2.385239452	2.375308477
Zn	0	0	0	0	0	0
Li*	0	0	0.052324191	0	0.114712798	0.146195148
∑Y	3.101833361	3.077681591	3.000000016	3.056885209	3.000000199	3.00000017
X: Ca	0.047325207	0.070489615	0.036300121	0.054137038	0.082871117	0.080624762
Ba	0	0	0	0	0	0
Na	0.858884766	0.716757744	0.592970513	0.769892181	0.734263715	0.787440222
K	0.018539324	0.015092966	0.059263801	0.011184569	0.013225817	0.012444034
Rb	0	0	0	0	0	0
Cs	0	0	0	0	0	0
r	0.075250703	0.197659676	0.311465564	0.164786212	0.169639351	0.119490982
OH	3.742569821	3.78877795	3.837374289	3.668384441	3.379398767	3.361043571
F	0.253040913	0.205196486	0.16196619	0.326926964	0.61890755	0.639088791
Cl	0.004389266	0.006025564	0.000659521	0.004688595	0.001693683	-0.000132362
F content					Fluor-	Fluor-
Mineral Name	Schorl	Schorl	Schorl	Schorl	Schorl	Schorl
CatSum	18.98931466	18.94394591	18.79937161	18.92157976	18.87084222	18.9269388
Si excess	0	0	0	0	0	0
X+B+Si excess	3.935691378	3.866264324	3.799371574	3.864694548	3.87084215	3.926938751
Li*	***-0.053623282***	***-0.077681591***	***0.052324135***	***-0.056885209***	***0.114712525***	***0.146194926***
T+Z+Y	15.05362328	15.07768159	15.00000004	15.05688521	15.00000007	15.00000005
Ideal T+Z+Y	15.05362328	15.07768159	15.00000004	15.05688521	15.00000007	15.00000005

Major and trace e							
Sample	BW001_239.5	BW001_239.5	BW010_83.4	BW010_83.4	BW010_83.4	BW010_83.4	BW010_83.4
Analysis No.	BW001_239.5_C4S3	BW001_239.5_C4S4	BW010_83.4_C1S1	BW010_83.4_C1S2	BW010_83.4_C1S4	BW010_83.4_C1S4	BW010_83.4_C2S1
Group							
SiO2	33.6695	32.9436	30.5639	30.7183	31.2613	30.6119	32.9717
TiO2	0.641705	0.930764	0.446306	0.263565	0.397074	0.299016	0.939897
Al2O3	32.063	29.0222	28.082	29.0423	28.0378	28.8937	28.9549
V2O3	-0.05763	-0.21475	0.010854	0.044223	0.031011	-0.10208	0.104696
Cr2O3	-0.00935	0.004078	0.015772	0.026787	0.000683	0.007527	-0.01367
Fe2O3							
FeO	15.6553	16.4673	13.4459	13.1602	14.3712	13.8574	14.8518
MgO	1.2246	1.47836	1.80615	1.55876	1.16937	1.14049	2.36657
CaO	0.302012	0.376026	0.339844	0.245391	0.118533	0.157998	0.563216
MnO	0.139152	0.090775	0.056879	0.072169	0.046844	0.105693	0.074878
ZnO							
BaO							
Na2O	2.0778	2.05052	2.05546	1.65159	1.76365	1.67704	1.86739
K2O	0.026527	0.043124	0.029998	0.03262	0.029218	0.046176	0.041231
Rb2O							
Cs2O							
F	0.964519	1.13178	1.00469	0.794123	0.346957	0.317337	1.1288
Cl	-0.0062	0.002039	0	0.005662	0.014375	0.00236	0.009634
H2O							
B2O3	10.0228	9.93928	10.1057	10.1898	10.2106	10.2425	10.0056
Li2O							
H2O*	3.024734622	2.828801444	2.731184703	2.84693004	3.056164929	3.063862286	2.839122214
B2O3*	-	-	-	-	-	-	-
Li2O*	0.034186379	0.115313561	0.554648212	0.515986803	0.552490946	0.5533579	0.143594288
Total	99.772656	97.209211	91.24928592	91.16840684	91.40727088	90.87427719	96.8493585
O=F	0.40613217	0.476561133	0.423047063	0.334383146	0.146093959	0.1336218	0.475306338
Total*	99.36652383	96.73264987	90.82623885	90.8340237	91.26117692	90.74065539	96.37405216
Structural formula							
T: Si	5.801068228	5.869145612	5.71407309	5.712043429	5.814029768	5.709897567	5.855299008
AlT	0.198931772	0.130854388	0.28592691	0.287956571	0.185970232	0.290102433	0.144700992
B	2.980770791	3.05651805	3.261156449	3.270605739	3.277854646	3.297708132	3.067037501
Z: AlZ	6	5.962969256	5.901652403	6	5.959708775	6	5.915479097
Mg	0	0.037030744	0.098347597	0	0.040291225	0	0.084520903
Cr	0	0	0	0	0	0	0
Fe3+	0	0	0	0	0	0	0
Y: AlY	0.311820692	0	0	0.076789084	0	0.061699004	0
Ti	0.083143342	0.12469934	0.062746643	0.036855543	0.055534443	0.041942393	0.125518792
V	-0.007960929	-0.030674736	0.001626937	0.00659305	0.004624128	-0.015265904	0.014906705
Cr	-0.001273674	0.000574416	0.002331306	0.003938164	0.000100431	0.001110032	-0.001919339
Fe3+	0	0	0	0	0	0	0
Mg	0.314538714	0.35560748	0.405036373	0.432097866	0.283921988	0.317130534	0.542000105
Mn	0.020307034	0.013697958	0.009006887	0.011366605	0.007379211	0.016698213	0.011262835
Fe2+	2.255738202	2.453478292	2.102242889	2.046504984	2.235214696	2.161602224	2.205681621
Zn	0	0	0	0	0	0	0
Li*	0.02368682	0.082617527	0.417008844	0.385854539	0.413224749	0.415083143	0.102549517
∑Y	3.000000202	3.000000276	2.999999879	2.999999835	2.999999645	2.999999638	3.000000236
X: Ca	0.055751063	0.071776016	0.068072904	0.048888938	0.023619306	0.031575284	0.107161891
Ba	0	0	0	0	0	0	0
Na	0.694099778	0.708295846	0.745062848	0.59544743	0.635959526	0.606496515	0.642968392
K	0.005830664	0.009801249	0.007154641	0.007738144	0.00693233	0.010987854	0.009340931
Rb	0	0	0	0	0	0	0
Cs	0	0	0	0	0	0	0
r	0.244318496	0.210126889	0.179709608	0.347925488	0.333488838	0.350940347	0.240528786
OH	3.476245908	3.361694141	3.405963664	3.531205867	3.791394095	3.812055343	3.36313059
F	0.525564477	0.637690216	0.594036336	0.467009815	0.204074989	0.187198624	0.633969915
Cl	-0.001810385	0.000615643	0	0.001784318	0.004530917	0.000746033	0.002899495
F content	Fluor-	Fluor-	Fluor-				Fluor-
Mineral Name	Schorl	Schorl	Schorl	Schorl	Schorl	Schorl	Schorl
CatSum	18.73645244	18.8463913	19.08144667	18.92268007	18.94436553	18.9467675	18.82650883
Si excess	0	0	0	0	0	0	0
X+B+Si excess	3.736452324	3.84639119	4.081446804	3.922680213	3.944365749	3.946767725	3.826508739
Li*	***0.023686504***	***0.082617137***	***0.417009101***	***0.385854848***	***0.413225323***	***0.415083728***	***0.102549189***
T+Z+Y	15.00000011	15.00000011	14.99999986	14.99999986	14.99999978	14.99999978	15.00000009
Ideal T+Z+Y	15.00000011	15.00000011	14.99999986	14.99999986	14.99999978	14.99999978	15.00000009

Major and trace e			
Sample	BW010_83.4	BW010_83.4	BW010_83.4
Analysis No.	BW010_83.4_C2S2	BW010_83.4_C2S3	BW010_83.4_C2S4
Group			
SiO2	33.1925	33.3653	33.4237
TiO2	0.408272	0.574302	1.16452
Al2O3	31.2044	30.0411	28.8984
V2O3	-0.05659	0.081038	0.10378
Cr2O3	0.015125	0.000685	0.008897
Fe2O3			
FeO	13.8495	14.6859	15.191
MgO	2.07619	1.99547	2.157
CaO	0.301958	0.43452	0.368208
MnO	0.047858	0.056998	0.086939
ZnO			
BaO			
Na2O	2.14664	2.10058	2.01961
K2O	0.061747	0.052605	0.056596
Rb2O			
Cs2O			
F	0.827927	0.966976	1.17111
Cl	0.005283	0.011896	0.002524
H2O			
B2O3	10.1256	10.0523	9.98442
Li2O			
H2O*	3.037092898	2.951902971	2.842239456
B2O3*	-	-	-
Li2O*	0.214321428	0.201326882	0.139036841
Total	97.45782433	97.57289985	97.6179803
O=F	0.348617072	0.407166745	0.493121904
Total*	97.10920725	97.16573311	97.12485839
Structural formula			
T: Si	5.80136852	5.861610394	5.898238687
AlT	0.19863148	0.138389606	0.101761313
B	3.054776693	3.048284985	3.041297266
Z: AlZ	6	6	5.908555148
Mg	0	0	0.091444852
Cr	0	0	0
Fe3+	0	0	0
Y: AlY	0.229163988	0.081654556	0
Ti	0.053661256	0.075872255	0.154538083
V	-0.007930015	0.011414436	0.014683356
Cr	0.002090072	9.51454E-05	0.001241329
Fe3+	0	0	0
Mg	0.540961217	0.52260753	0.476003723
Mn	0.007084852	0.008481395	0.012994758
Fe2+	2.024326585	2.157637468	2.241868715
Zn	0	0	0
Li*	0.150642051	0.1422373	0.098670274
∑Y	3.000000006	3.000000085	3.000000238
X: Ca	0.056545061	0.081787952	0.069617542
Ba	0	0	0
Na	0.727438973	0.715497298	0.691006589
K	0.013767811	0.011789828	0.012741252
Rb	0	0	0
Cs	0	0	0
r	0.202248155	0.190924922	0.226634617
OH	3.540792525	3.459201841	3.345649093
F	0.457642602	0.537256304	0.653596049
Cl	0.001564873	0.003541856	0.000754858
F content		Fluor-	Fluor-
Mineral Name	Schorl	Schorl	Schorl
CatSum	18.85252853	18.85736009	18.81466277
Si excess	0	0	0
X+B+Si excess	3.852528536	3.85736007	3.814662673
Li*	***0.15064205***	***0.14223719***	***0.098669943***
T+Z+Y	14.99999999	15.00000002	15.00000009
Ideal T+Z+Y	14.99999999	15.00000002	15.00000009

Appendix 8: Sample photographs

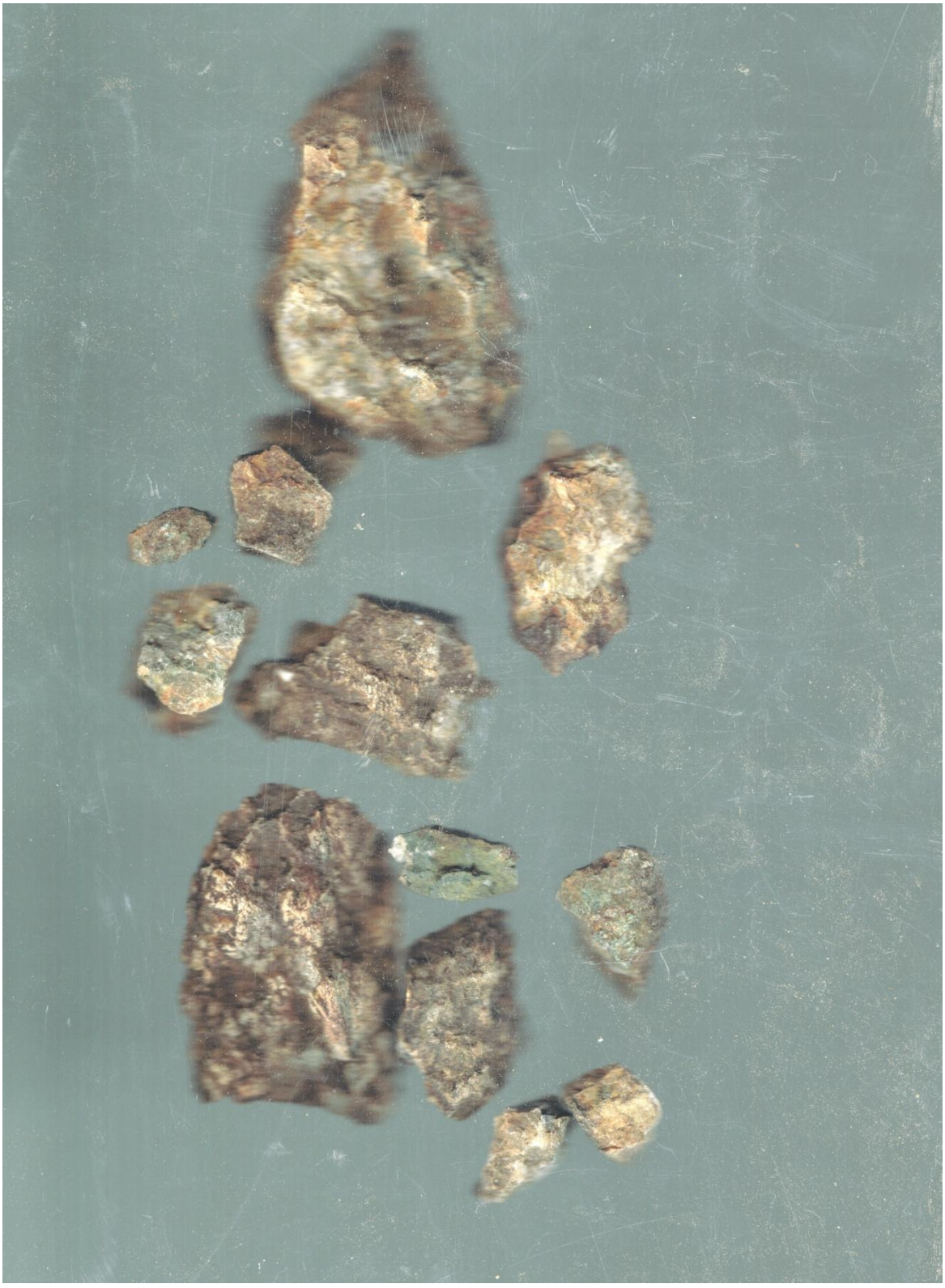

Figure 1 THBW031

Figure 2 THBW030

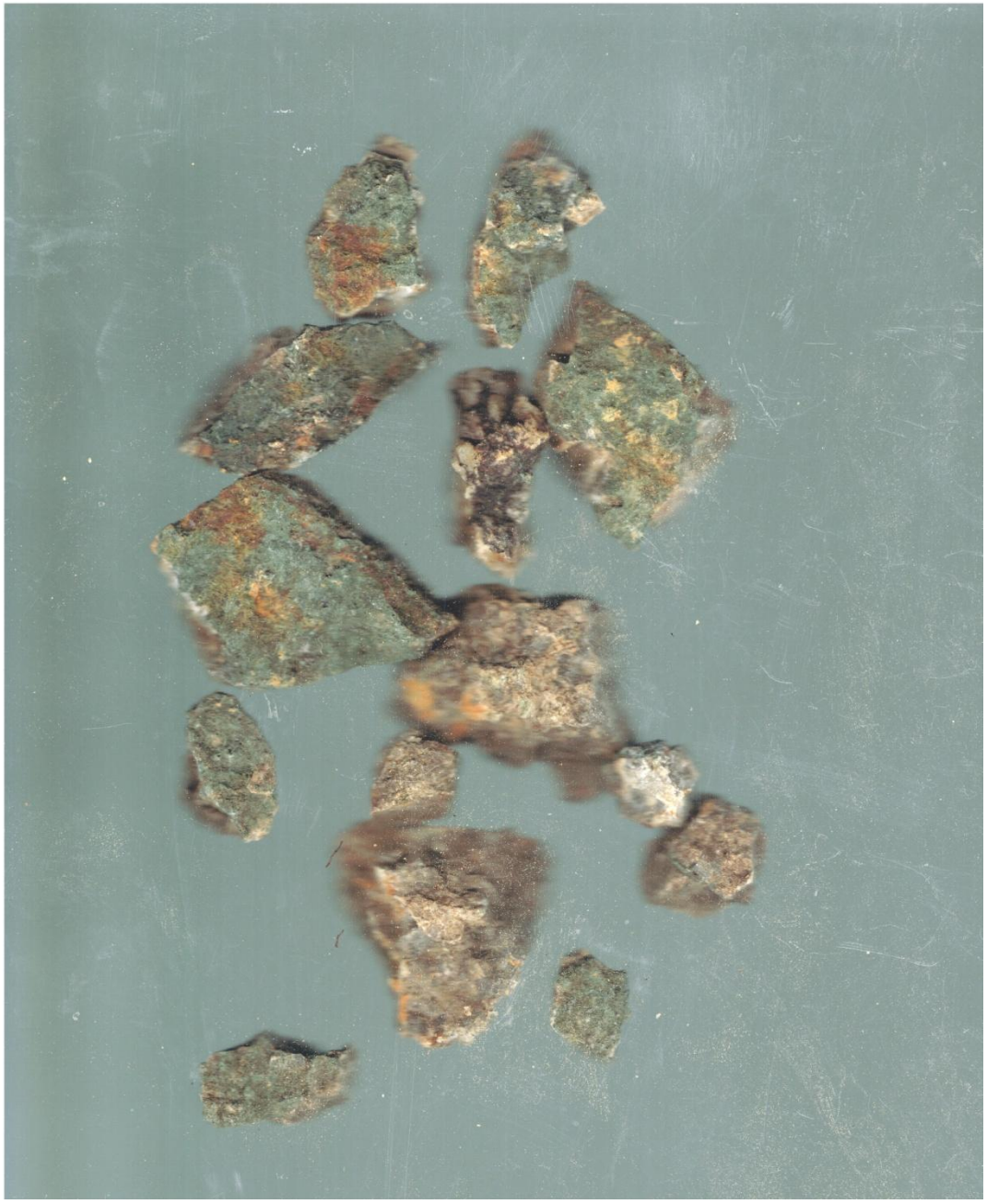

Figure 3 THBW025

Figure 4 THBW024

Figure 5 THBW021

Figure 6 THBW020

Figure 7 THBW019B

Figure 8 THBW019A

Figure 9 THBW018

Figure 10 THBW018

Figure 11 THBW 017

Figure 12 THBW 017

Figure 13 THBW 017

Figure 14 THBW 015

Figure 15 THBW 014

Appendix 9: Geochronology results

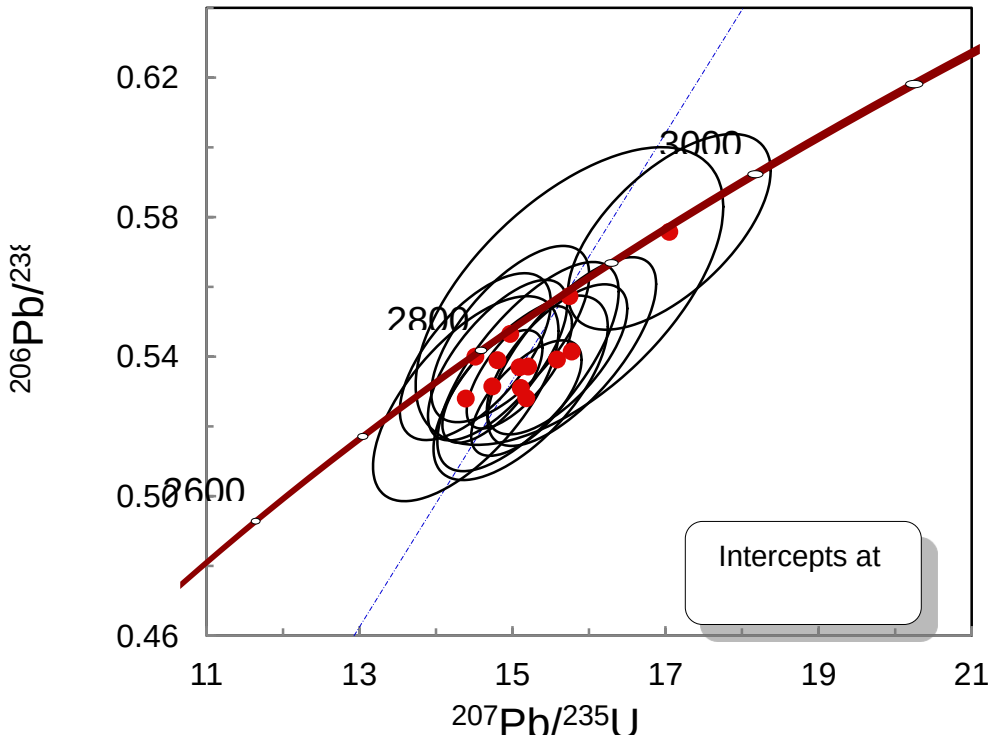

Mt Francisco Pilbara

		207 cor 206Pb/238U age	+/-1 ster	206Pb/238U ratio	+/-1 RSE	207Pb/206Pb ratio	+/-1 RSE	Pb204 ppm	Pb206 ppm	Pb207 ppm	Pb208 ppm	Th232 ppm	U238 ppm	Ti49 ppm	Fe56 ppm	Zr90 ppm
SE10C022	ok	**2666**	**64**	0.5281	2.1%	0.2085	2.3%	0.00	3.6	0.7	0.0	0	6.9	1449	6041	1770
SE10C020	ok	**2690**	**103**	0.5310	3.3%	0.2063	3.7%	0.00	1.5	0.3	0.0	0	3.0	1059	2484	1094
SE10C027	ok	**2703**	**116**	0.5280	3.7%	0.1977	4.2%	0.01	1.3	0.3	0.0	0	2.6	970	1958	1022
SE10C025	ok	**2711**	**63**	0.5314	2.0%	0.2011	2.1%	0.01	4.2	0.8	0.0	0	8.1	1459	5960	1724
SE10C029	ok	**2726**	**84**	0.5392	2.6%	0.2096	2.9%	0.01	3.0	0.6	0.0	0	5.8	1307	4359	1409
SE10C019	ok	**2729**	**117**	0.5372	3.7%	0.2053	3.6%	0.00	1.4	0.3	0.0	0	2.8	984	2210	1053
SE10C018	ok	**2733**	**105**	0.5415	3.3%	0.2113	3.2%	0.00	1.5	0.3	0.0	0	3.0	1026	2497	1081
SE10C021	ok	**2733**	**69**	0.5369	2.2%	0.2038	2.1%	0.00	4.3	0.9	0.0	0	8.2	1565	5692	1667
SE10C016	ok	**2762**	**92**	0.5390	2.8%	0.1992	2.9%	0.00	2.1	0.4	0.0	0	4.0	1214	3416	1222
SE10C026	ok	**2783**	**98**	0.5400	2.9%	0.1950	3.4%	0.00	1.6	0.3	0.0	0	3.2	1078	2431	1089
SE10C017	ok	**2808**	**103**	0.5465	3.0%	0.1987	3.4%	0.00	1.8	0.3	0.0	0	3.4	1133	3059	1190
SE10C030	pb loss? Ir	**2851**	**180**	0.5574	5.1%	0.2049	6.7%	0.00	1.0	0.2	0.0	0	1.9	2032	2181	571
SE10C028	Common F	**2926**	**121**	0.5758	3.2%	0.2148	4.0%	0.01	3.1	0.7	0.1	0	6.0	1394	4828	1610
SE10C031	discordant	**2838**	**253**	0.5858	7.2%	0.2519	7.7%	0.00	0.7	0.2	0.0	0	1.3	1321	1907	608

Pb/U Age:
Mean = 2736±49 [1.8%] 95% conf.
Wtd by data-pt errs only, 0 of 14 rej.
MSWD = 0.42, probability = 0.96

207Pb/206Pb age:
Mean = 2862±47 [1.6%] 95% conf.
Wtd by data-pt errs only, 0 of 14 rej.
MSWD = 0.36, probability = 0.98

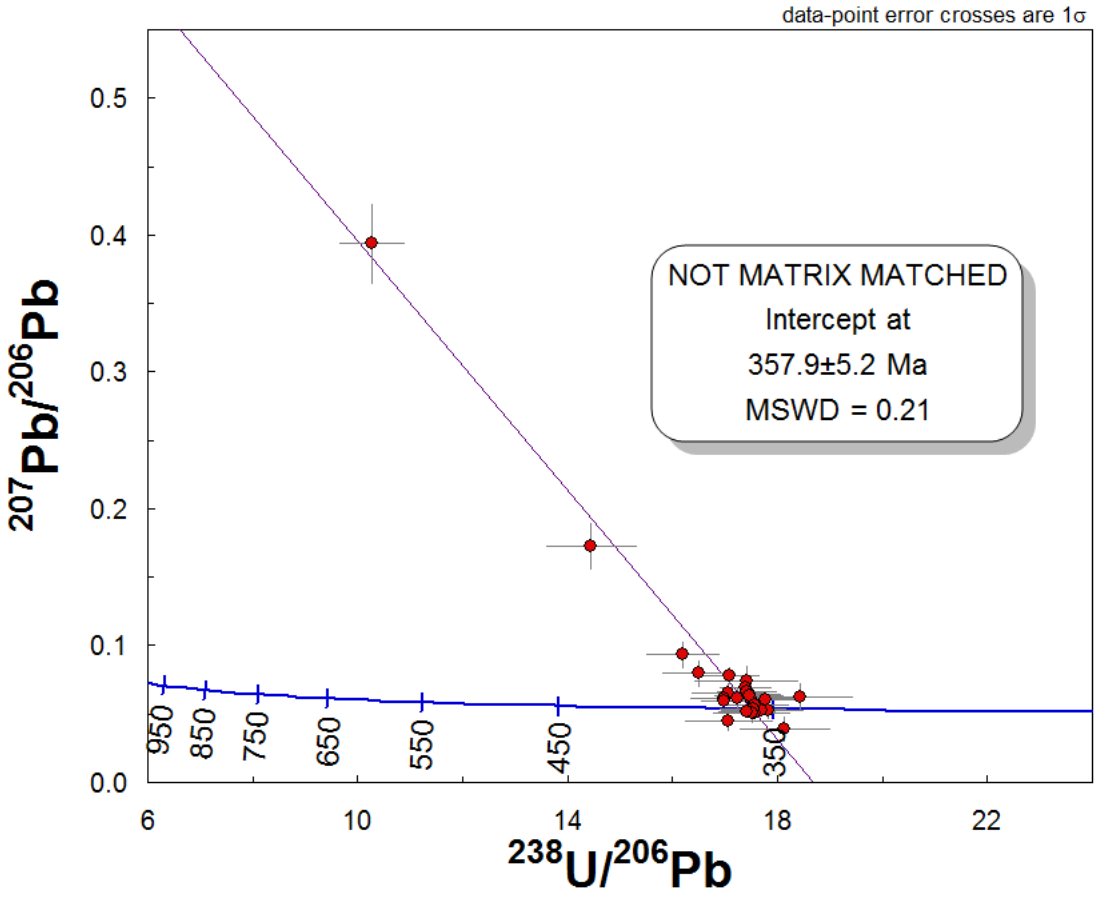

BW001-215.7

			207 cor	206Pb	206Pb/238U		208Pb/232Th		207Pb/206Pb		Pb204	Pb206	Pb207	Pb208	Th232	U238	Ti49	Fe56	Zr
			age	+/-1 st	ratio	+/-1 RS	ratio	+/-1 RSE	ratio	+/-1 RSE	ppm	ppm	ppm	ppm	ppm	ppm	ppm	ppm	ppm
BW00	AU27A	ok	337	19	0.0542	5.6%			0.0627	16.9%	0.00	1	0	0	0	13	974	1609	75
BW00	AU27A	ok	352	17	0.0551	4.8%			0.0392	25.3%	0.00	0	0	0	0	7	989	1265	113
BW00	AU27A	ok	350	11	0.0563	3.1%			0.0603	11.5%	0.00	1	0	0	0	13	981	1007	82
BW00	AU27A	ok	351	21	0.0575	5.8%			0.0741	15.2%	0.00	0	0	0	0	5	1300	2638	163
BW00	AU27A	ok	352	14	0.0561	3.9%			0.0524	12.5%	0.00	1	0	0	0	10	1664	4353	84
BW00	AU27A	ok	354	10	0.0575	2.9%			0.0689	8.4%	0.00	1	0	0	0	17	1157	1063	50
BW00	AU27A	ok	354	12	0.0573	3.5%			0.0647	8.7%	0.00	1	0	0	0	12	1038	1422	75
BW00	AU27A	ok	354	12	0.0574	3.4%			0.0667	8.9%	0.00	1	0	0	0	12	1147	2481	81
BW00	AU27A	ok	355	12	0.0565	3.4%			0.0524	9.5%	0.00	1	0	0	0	14	970	2384	57
BW00	AU27A	ok	355	19	0.0571	5.2%			0.0617	18.1%	0.00	0	0	0	0	5	1157	2340	99
BW00	AU27A	ok	355	14	0.0573	3.9%			0.0637	9.4%	0.00	1	0	0	0	12	1925	2366	122
BW00	AU27A	ok	356	13	0.0569	3.7%			0.0564	12.7%	0.00	1	0	0	0	10	1108	1652	99
BW00	AU27A	ok	356	12	0.0585	3.4%			0.0778	9.0%	0.00	1	0	0	0	12	1436	638	82
BW00	AU27A	ok	358	10	0.0569	2.8%			0.0508	8.1%	0.00	1	0	0	0	18	1199	927	102
BW00	AU27A	ok	358	13	0.0570	3.7%			0.0531	12.0%	0.00	1	0	0	0	11	2570	6485	93
BW00	AU27A	ok	358	13	0.0570	3.7%			0.0534	10.9%	0.00	1	0	0	0	11	1961	3395	116
BW00	AU27A	ok	359	16	0.0571	4.3%			0.0511	15.7%	0.02	0	0	0	0	7	1309	5668	55
BW00	AU27A	ok	350	31	0.0974	6.1%			0.3938	7.5%	0.00	0	0	0	0	3	561	10389	42
BW00	AU27A	ok	361	11	0.0574	3.2%			0.0517	7.7%	0.00	1	0	0	0	18	1184	1715	75
BW00	AU27A	ok	360	15	0.0580	4.2%			0.0611	13.1%	0.00	0	0	0	0	8	1519	5432	72
BW00	AU27A	ok	362	15	0.0586	4.1%			0.0655	12.1%	0.00	0	0	0	0	9	2164	4839	120
BW00	AU27A	ok	365	15	0.0588	4.0%			0.0617	10.7%	0.00	1	0	0	0	11	939	3464	78
BW00	AU27A	ok	367	9	0.0589	2.6%			0.0590	5.7%	0.00	1	0	0	0	23	2706	2612	134
BW00	AU27A	ok	371	19	0.0586	5.0%			0.0450	18.6%	0.00	0	0	0	0	6	1059	1960	98
BW00	AU27A	ok	367	16	0.0606	4.3%			0.0798	12.7%	0.00	0	0	0	0	8	1349	3685	70
BW00	AU27A	ok	368	16	0.0618	4.4%			0.0933	10.9%	0.00	0	0	0	0	8	1173	17433	75
BW00	AU27A	ok	369	24	0.0692	6.1%			0.1725	10.2%	0.00	0	0	0	0	6	906	4929	97

Appendix 10: ID-TIMS method

Analytical Methodology

U-Pb dating of cassiterite by thermal ionization mass spectrometry (TIMS) methods was first reported by Gulson and Jones (1992). More recently, several groups in China (e.g., Yuan et al., 2008; 2011; Zhang et al., 2014, 2015) have also reported U-Pb TIMS ages for cassiterites from several tin-bearing deposits (together with LA-ICP U-Pb ages, Re-Os molybenite ages, and $^{40}Ar/^{39}Ar$ muscovite ages).

Cassiterite is extremely difficult to dissolve, and this has greatly hampered previous attempts to date the mineral using U-Pb TIMS methods. It is critical that the individual sample aliquots be fully dissolved prior to the separation and purification of U and Pb for isotopic analysis. The current study is being carried out at the Pacific Centre for Isotopic and Geochemical Research at the University of British Columbia. Our initial attempts to dissolve cassiterite using concentrated HCl encountered the same problems with dissolution that had been encountered by previous workers. We are currently investigating the use of concentrated hydroiodic acid (HI) instead of HCl for cassiterite dissolution, a method described by Yamazaki et al. (2013) in a tin isotope study. Initial results look very favorable, indicating a significantly more rapid dissolution rate than that obtained using concentrate HCl. The HI has been purified by sub-boiling distillation of commercially available concentrated HI stock.

The methodology that will be employed for separation and purification of U and Pb after dissolution of the individual cassiterite aliquots will generally follow that described for U-Pb TIMS dating of rutiles by Scoates and Friedman (2008), with the following modifications. Clean, hand-picked cassiterite grains are first ground in an agate mortar and sieved to separate the 50-100 micron size fraction, which were first cleaned in an ultrasonic bath in 1N HNO_3 for ten minutes, then washed in warm 1N HNO_3 for ten minutes to remove any possible surface contamination, and finally rinsed in ultra-pure acetone and dried. Individual sample aliquots (5-15 individual grains per aliquot) are weighed into a series of PFA mini-crucibles together with a few drops of concentrated HI together with a carefully weighed drop of $^{233–235}U$-^{205}Pb isotopic tracer. A number of these mini-crucibles are then placed inside a high-pressure dissolution bomb and several milliliters of concentrated HI are added. Dissolution is done at 210° for approximate 72 hours. Each sample is carefully examined to ensure that the samples have been completely dissolved. Any sample in which undissolved cassiterite remains is dried down on a hotplate and the bomb dissolution step is repeated until complete dissolution has been achieved.

The dissolved samples are dried down, re-dissolved in 3.1 HCL, and loaded onto pre-cleaned anion exchange columns. U and Pb are separated and purified using first 0.5N HBr and then 7N HNO_3, as described by Scoates and Friedman (2008).

Purified Pb and U from each sample aliquot are loaded onto single zone-refined Re filaments with 5 μL of silicic acid activator (Gerstenberger and Haase, 1997). Isotopic ratios are measured using a modified single collector VG-54R thermal ionization mass spectrometer equipped with a Daly photomultiplier. Measurements are done in peak-switching mode on the Daly detector. U fractionation is determined directly on individual runs using the $^{233–235}U$ tracer. Pb isotope ratios are corrected for a fractionation of 0.23 to 0.32%/amu based on replicate analyses of the NBS-981 and NBS-982 Pb reference materials and the values recommended by Thirwall (2000). All analytical errors

are numerically propagated through the entire age calculation using the technique of Roddick (1987). Final plotting and regression of the final isotopic compositions are calculated with Isoplot 3.00 (Ludwig, 2000); all errors are quoted at the 2σ level.

References

Gerstenberger, H., and Haase, G., 1997, A highly effective emitter substance for mass spectrometric Pb isotope ratio determinations: Chemical Geology, v. 136, p. 309–312.

Gulson, B.L. and Jones, M.T., 1992, Cassiterite: Potential for direct dating of mineral deposits and a precise age for the Bushveld Complex granites; Geology, v. 20, p. 355-358.

Ludwig, K.R., 2000, Isoplot/Ex 3.00, a geochronological toolkit for Microsoft Excel: Berkeley Geochronology Center.

Roddick, J.C., 1987, Generalized numerical error analysis with application to geochronology and thermodynamics: Geochimica et Cosmochimica Acta, v. 51, p. 2129–2135.

Scoates, J.S. and Friedman, R.M., 2008, Precise age of the Platiniferous Merensky Reef, Bushveld Complex, South Africa, by the U-Pb zircon chemical abrasion ID-TIMS technique – digital supplement; Economic Geology, v. 103, pp. 465-471.

Thirwall, M.F., 2000, Inter-laboratory and other errors in Pb isotope analyses investigated using a 207Pb-204Pb double spike: Chemical Geology, v. 163, p. 299–322.

Yamazaki, E., Nakai, S., Yokoyama, T., Ishihara, S and Tang, H., 2013, Tin isotope analysis of cassiterites from Southeastern and Eastern Asia; Geochemical Journal, v. 47, pp. 21-35.

Yuan, S., Peng, J., Hu, R., Li, H., Shen, N. and Zhang, D., 2008, A precise U–Pb age on cassiterite from the Xianghualing tin-polymetallic deposit (Hunan, South China); Mineralium Deposita, v. 43, pp. 375-382.

Yuan, S., Peng, J., Hao, S., Li, H., Geng, J. and Zhang, D., 2011, *In situ* LA-MC-ICP-MS and ID-TIMS U–Pb geochronology of cassiterite in the giant Furong tin deposit, Hunan Province, South China: New constraints on the timing of tin–polymetallic mineralization; Ore Geology Reviews, v. 43, pp. 235-242.

Zhang, R.-Q., Lua, J.-J., Wang, R.-C., Yang, P., Zhu, J.-C., Yao, Y., Gao, J.-F., Li, C., Lei, Z.-H., Zhang, W.-L. and Guo, W.-M., 2015, Constraints of *in situ* zircon and cassiterite U–Pb, molybdenite Re–Os and muscovite ^{40}Ar–^{39}Ar ages on multiple generations of granitic magmatism and related W–Sn mineralization in the Wangxianling area, Nanling Range, South China; Ore Geology Reviews, v. 65, pp. 1021-1042.

Appendix 11: Hylogger

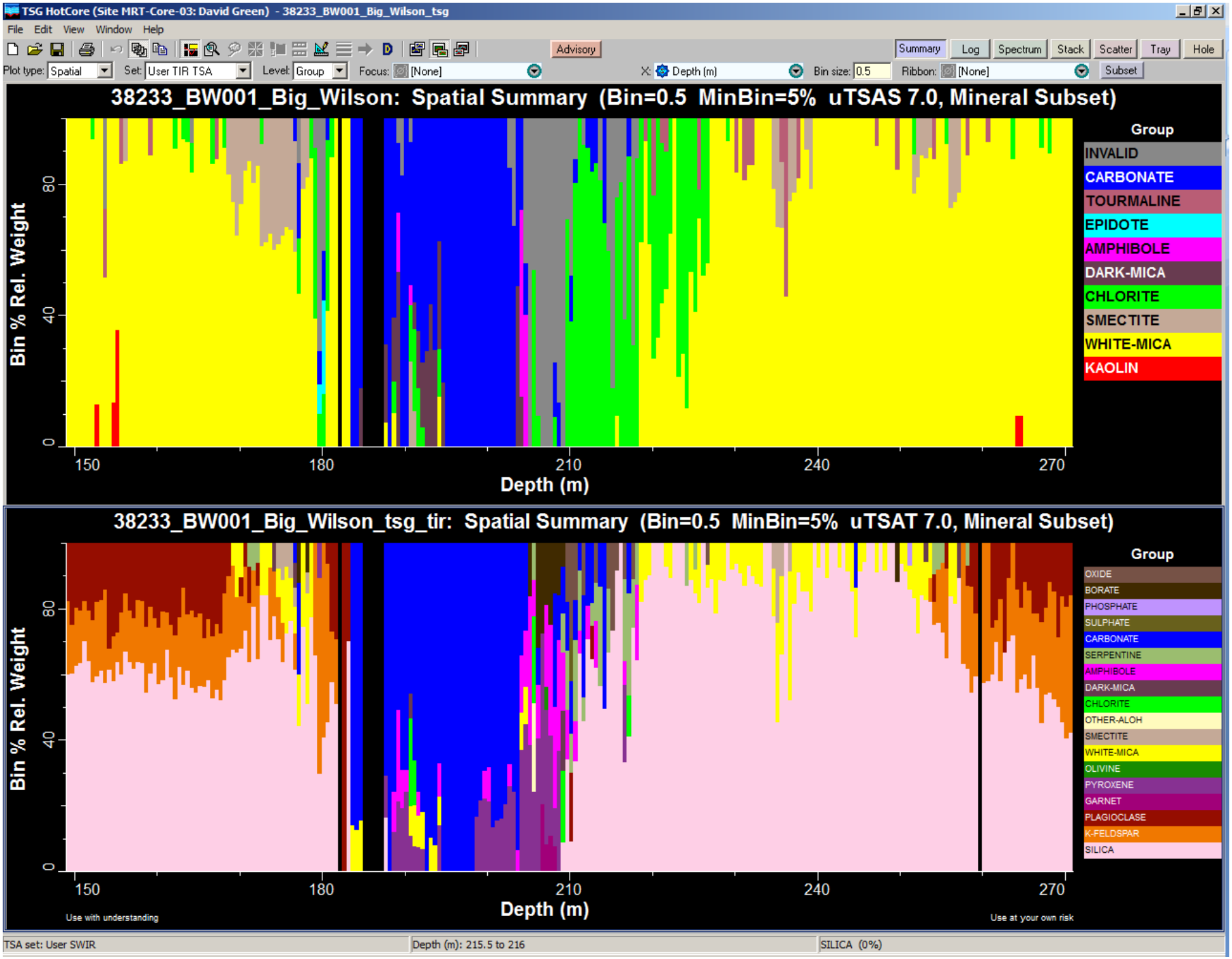
TSG HotCore (Site MRT-Core-03: David Green) - 38233_BW001_Big_Wilson_tsg
File Edit View Window Help
Advisory
Summary Log Spectrum Stack Scatter Tray Hole
Plot type: Spatial Set: User TIR TSA Level: Group Focus: [None] X: Depth (m) Bin size: 0.5 Ribbon: [None] Subset
38233_BW001_Big_Wilson: Spatial Summary (Bin=0.5 MinBin=5% uTSAS 7.0, Mineral Subset)
Bin % Rel. Weight
0
40
80
150
180
210
240
270
Depth (m)
Group
INVALID
CARBONATE
TOURMALINE
EPIDOTE
AMPHIBOLE
DARK-MICA
CHLORITE
SMECTITE
WHITE-MICA
KAOLIN
38233_BW001_Big_Wilson_tsg_tir: Spatial Summary (Bin=0.5 MinBin=5% uTSAT 7.0, Mineral Subset)
Bin % Rel. Weight
0
40
80
150
180
210
240
270
Depth (m)
Use with understanding
Use at your own risk
Group
OXIDE
BORATE
PHOSPHATE
SULPHATE
CARBONATE
SERPENTINE
AMPHIBOLE
DARK-MICA
CHLORITE
OTHER-ALOH
SMECTITE
WHITE-MICA
OLIVINE
PYROXENE
GARNET
PLAGIOCLASE
K-FELDSPAR
SILICA
TSA set: User SWIR
Depth (m): 215.5 to 216
SILICA (0%)

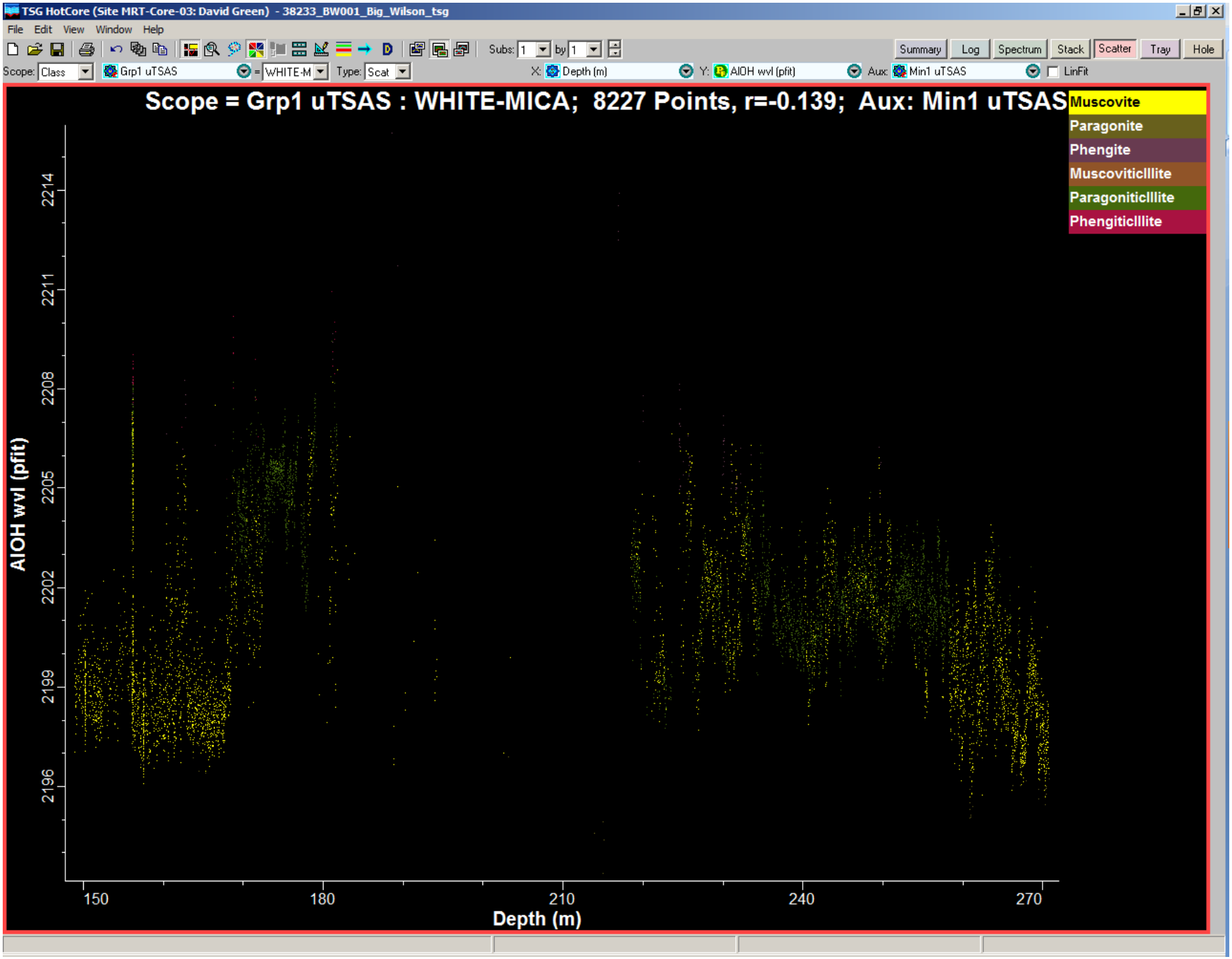
TSG HotCore (Site MRT-Core-03: David Green) - 38233_BW001_Big_Wilson_tsg
File Edit View Window Help
Summary Log Spectrum Stack Scatter Tray Hole
Scope: Class Grp1 uTSAS = WHITE-M Type: Scat X: Depth (m) Y: AlOH wvl (pfit) Aux: Min1 uTSAS LinFit
Scope = Grp1 uTSAS : WHITE-MICA; 8227 Points, r=-0.139; Aux: Min1 uTSAS
Muscovite
Paragonite
Phengite
MuscoviticIllite
ParagoniticIllite
PhengiticIllite
AlOH wvl (pfit)
2214
2211
2208
2205
2202
2199
2196
150
180
210
240
270
Depth (m)

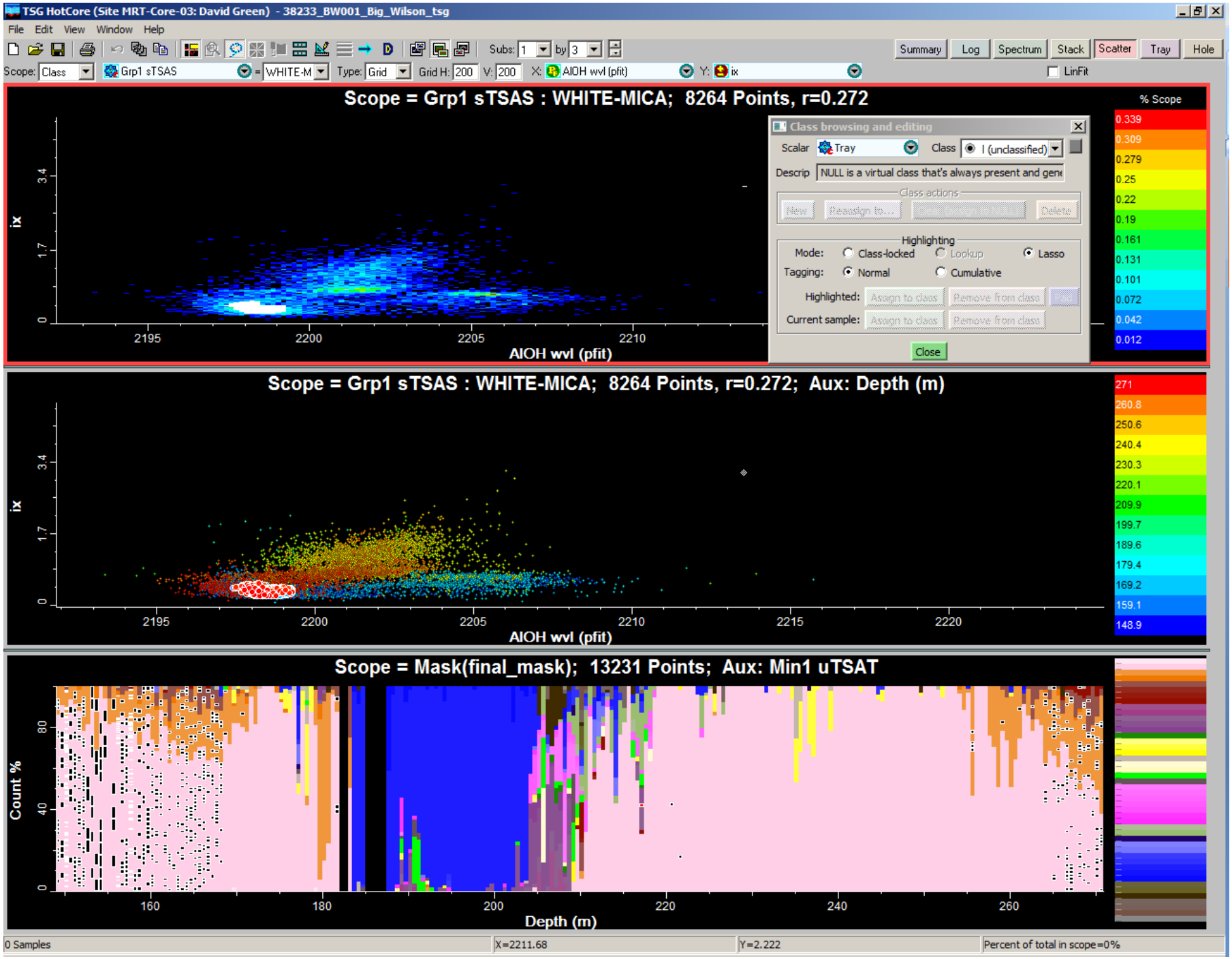
TSG HotCore (Site MRT-Core-03: David Green) - 38233_BW001_Big_Wilson_tsg
File Edit View Window Help
Summary Log Spectrum Stack Scatter Tray Hole
Scope: Class Grp1 sTSAS = WHITE-M Type: Grid Grid H: 200 V: 200 X: AlOH wvl (pfit) Y: ix LinFit
Scope = Grp1 sTSAS : WHITE-MICA; 8264 Points, r=0.272
% Scope
0.339
0.309
0.279
0.25
0.22
0.19
0.161
0.131
0.101
0.072
0.042
0.012
Class browsing and editing
Scalar Tray Class 1 (unclassified)
Descrip NULL is a virtual class that's always present and gene
Class actions
New Reassign to... Delete
Highlighting
Mode: Class-locked Lookup Lasso
Tagging: Normal Cumulative
Highlighted: Assign to class Remove from class
Current sample: Assign to class Remove from class
Close
ix
AlOH wvl (pfit)
Scope = Grp1 sTSAS : WHITE-MICA; 8264 Points, r=0.272; Aux: Depth (m)
271
260.8
250.6
240.4
230.3
220.1
209.9
199.7
189.6
179.4
169.2
159.1
148.9
Scope = Mask(final_mask); 13231 Points; Aux: Min1 uTSAT
Count %
Depth (m)
0 Samples
X=2211.68
Y=2.222
Percent of total in scope=0%

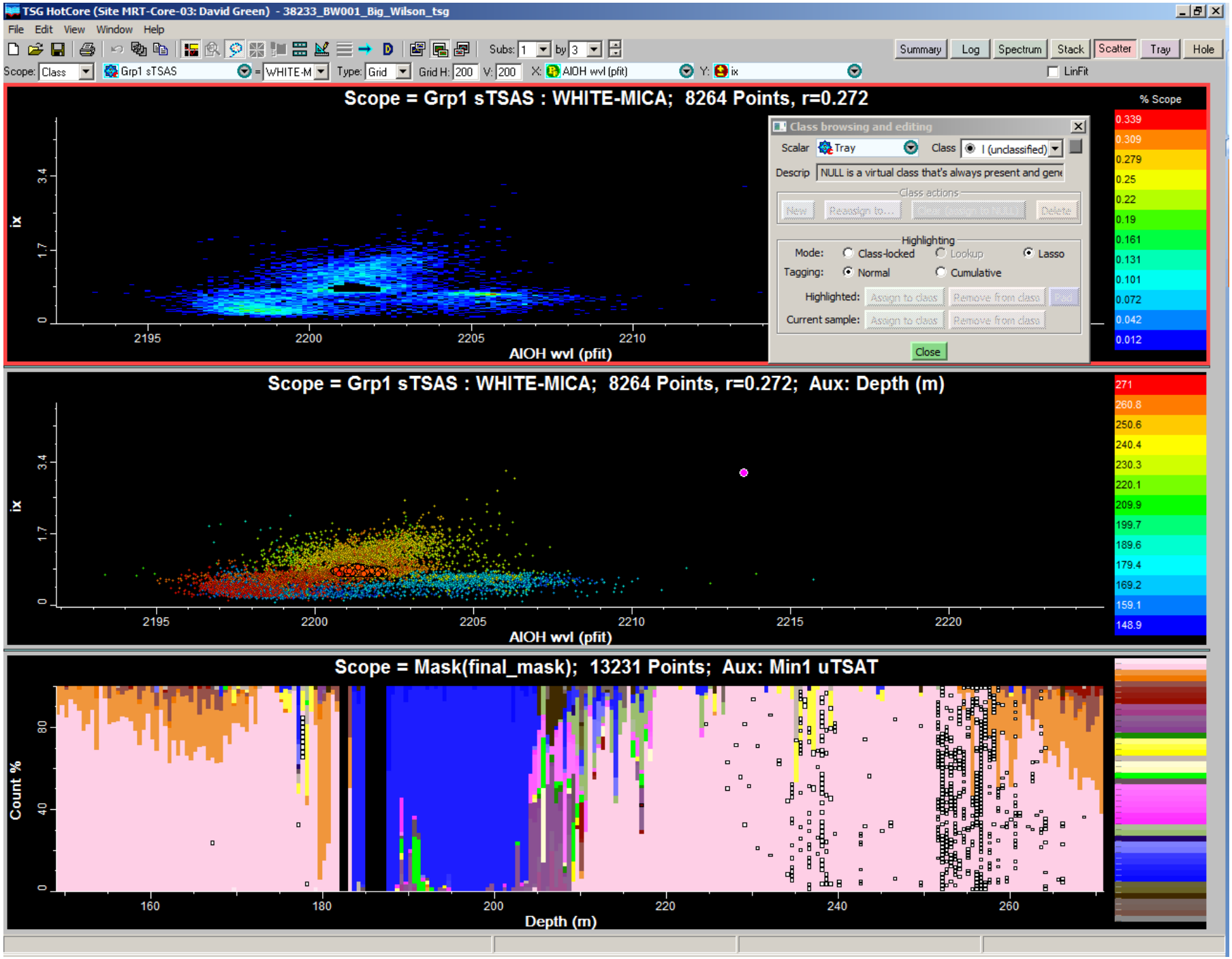
TSG HotCore (Site MRT-Core-03: David Green) - 38233_BW001_Big_Wilson_tsg
File Edit View Window Help
Summary Log Spectrum Stack Scatter Tray Hole
Scope = Grp1 sTSAS : WHITE-MICA; 8264 Points, r=0.272
% Scope
0.339
0.309
0.279
0.25
0.22
0.19
0.161
0.131
0.101
0.072
0.042
0.012
Class browsing and editing
Scalar Tray
Class 1 (unclassified)
Descrip NULL is a virtual class that's always present and gene
Class actions
New
Reassign to...
Delete
Highlighting
Mode: Class-locked Lookup Lasso
Tagging: Normal Cumulative
Highlighted:
Assign to class
Remove from class
Current sample:
Close
ix
AlOH wvl (pfit)
Scope = Grp1 sTSAS : WHITE-MICA; 8264 Points, r=0.272; Aux: Depth (m)
271
260.8
250.6
240.4
230.3
220.1
209.9
199.7
189.6
179.4
169.2
159.1
148.9
Scope = Mask(final_mask); 13231 Points; Aux: Min1 uTSAT
Count %
Depth (m)

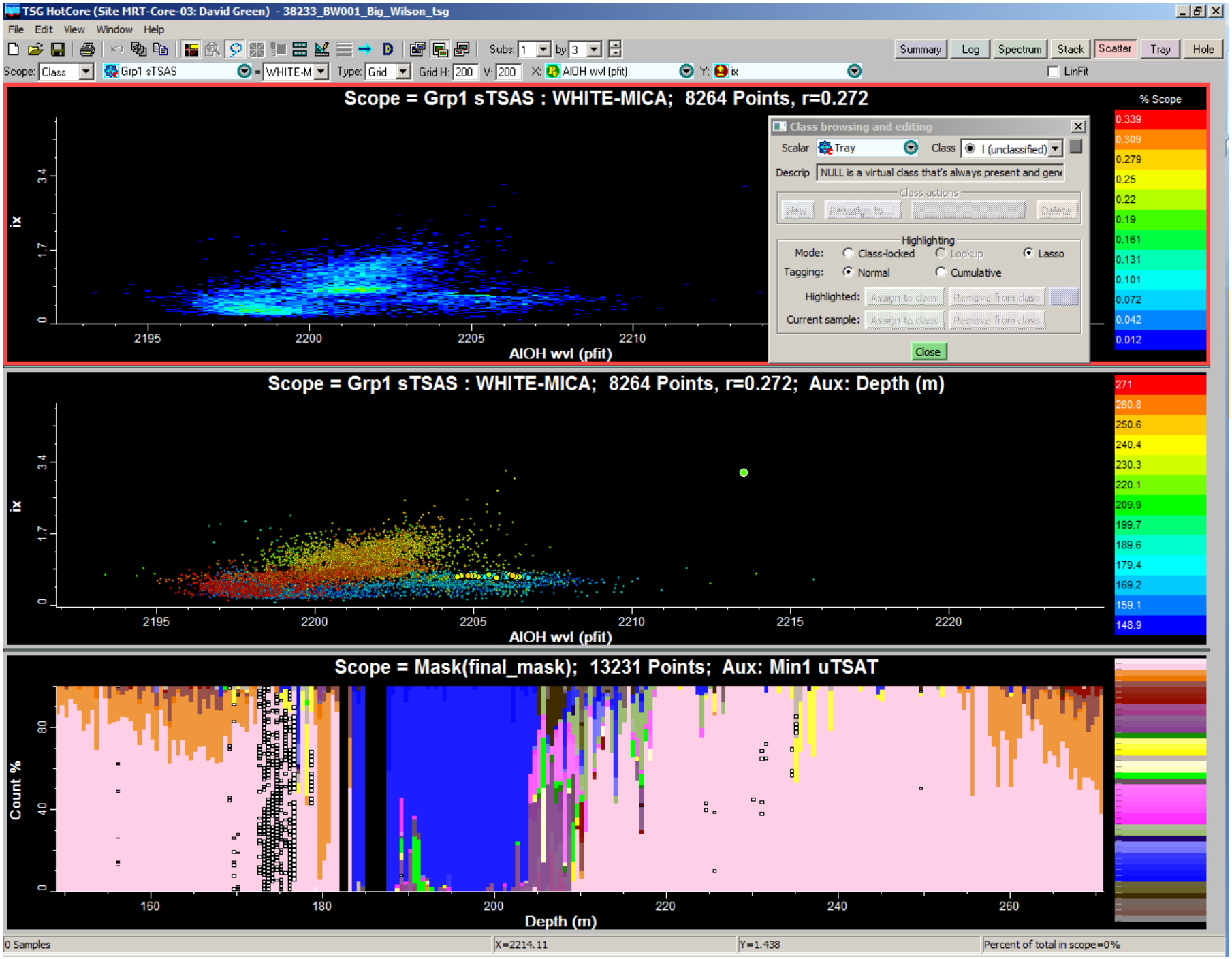
TSG HotCore (Site MRT-Core-03: David Green) - 38233_BW001_Big_Wilson_tsg
File Edit View Window Help
Summary Log Spectrum Stack Scatter Tray Hole
Scope: Class Grp1 sTSAS = WHITE-M Type: Grid Grid H: 200 V: 200 X: AlOH wvl (pfit) Y: ix LinFit
Scope = Grp1 sTSAS : WHITE-MICA; 8264 Points, r=0.272
% Scope
0.339
0.309
0.279
0.25
0.22
0.19
0.161
0.131
0.101
0.072
0.042
0.012
ix
AlOH wvl (pfit)
Class browsing and editing
Scalar Tray Class I (unclassified)
Descrip NULL is a virtual class that's always present and gene
Class actions
New Reassign to... Delete
Highlighting
Mode: Class-locked Lookup Lasso
Tagging: Normal Cumulative
Highlighted: Assign to class Remove from class
Current sample: Assign to class Remove from class
Close
Scope = Grp1 sTSAS : WHITE-MICA; 8264 Points, r=0.272; Aux: Depth (m)
271
260.8
250.6
240.4
230.3
220.1
209.9
199.7
189.6
179.4
169.2
159.1
148.9
Scope = Mask(final_mask); 13231 Points; Aux: Min1 uTSAT
Count %
Depth (m)
0 Samples
X=2214.11
Y=1.438
Percent of total in scope=0%

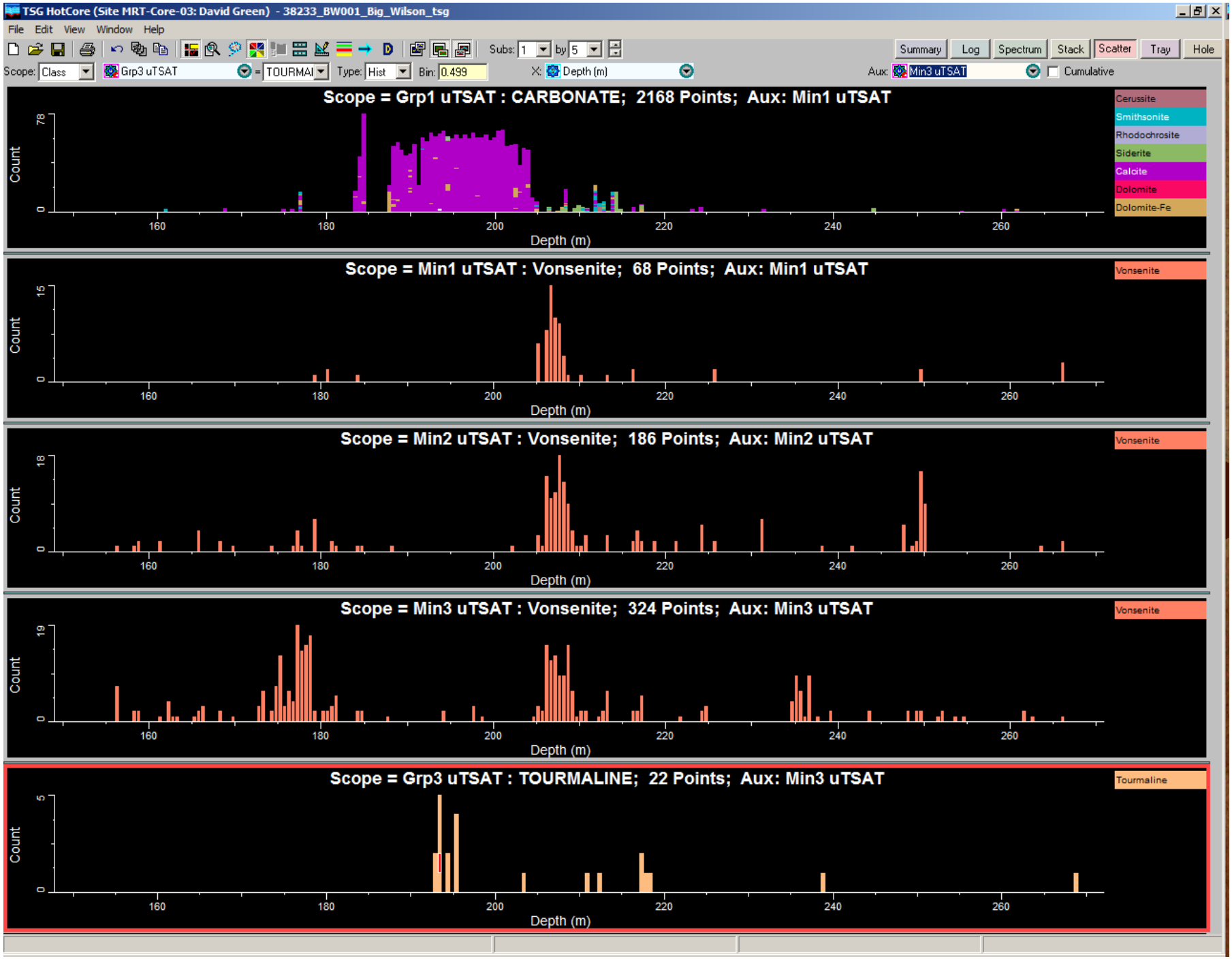
TSG HotCore (Site MRT-Core-03: David Green) - 38233_BW001_Big_Wilson_tsg
File Edit View Window Help
Subs: 1 by 5
Summary Log Spectrum Stack Scatter Tray Hole
Scope: Class Grp3 uTSAT = TOURMAI Type: Hist Bin: 0.499 X: Depth (m) Aux: Min3 uTSAT Cumulative
Scope = Grp1 uTSAT : CARBONATE; 2168 Points; Aux: Min1 uTSAT
Cerussite
Smithsonite
Rhodochrosite
Siderite
Calcite
Dolomite
Dolomite-Fe
Count
Depth (m)
Scope = Min1 uTSAT : Vonsenite; 68 Points; Aux: Min1 uTSAT
Vonsenite
Scope = Min2 uTSAT : Vonsenite; 186 Points; Aux: Min2 uTSAT
Vonsenite
Scope = Min3 uTSAT : Vonsenite; 324 Points; Aux: Min3 uTSAT
Vonsenite
Scope = Grp3 uTSAT : TOURMALINE; 22 Points; Aux: Min3 uTSAT
Tourmaline

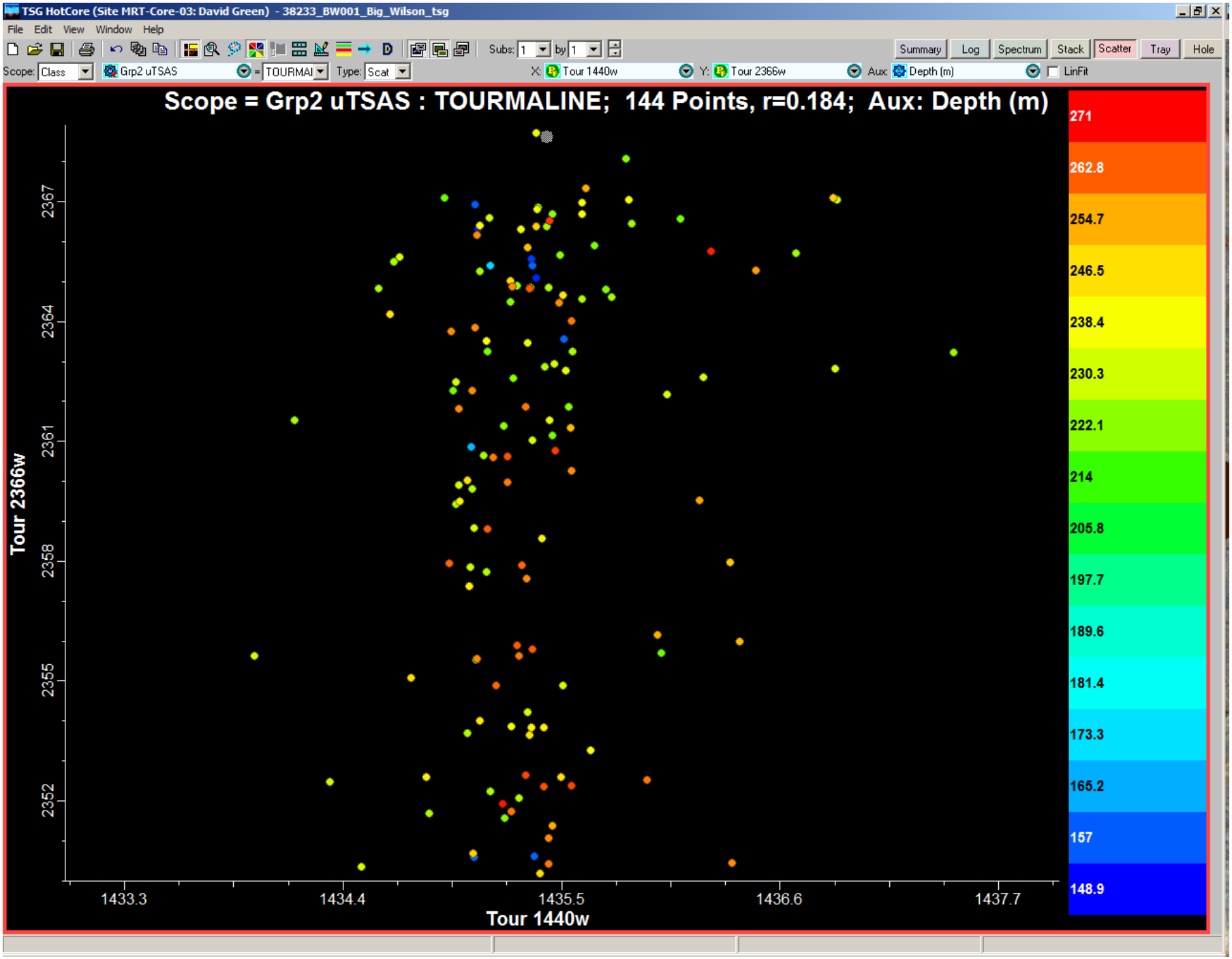
TSG HotCore (Site MRT-Core-03: David Green) - 38233_BW001_Big_Wilson_tsg
File Edit View Window Help
Summary Log Spectrum Stack Scatter Tray Hole
Scope: Class Grp2 uTSAS = TOURMAI Type: Scat X: Tour 1440w Y: Tour 2366w Aux: Depth (m) LinFit
Scope = Grp2 uTSAS : TOURMALINE; 144 Points, r=0.184; Aux: Depth (m)
271
262.8
254.7
246.5
238.4
230.3
222.1
214
205.8
197.7
189.6
181.4
173.3
165.2
157
148.9
Tour 2366w
2367
2364
2361
2358
2355
2352
1433.3
1434.4
1435.5
1436.6
1437.7
Tour 1440w

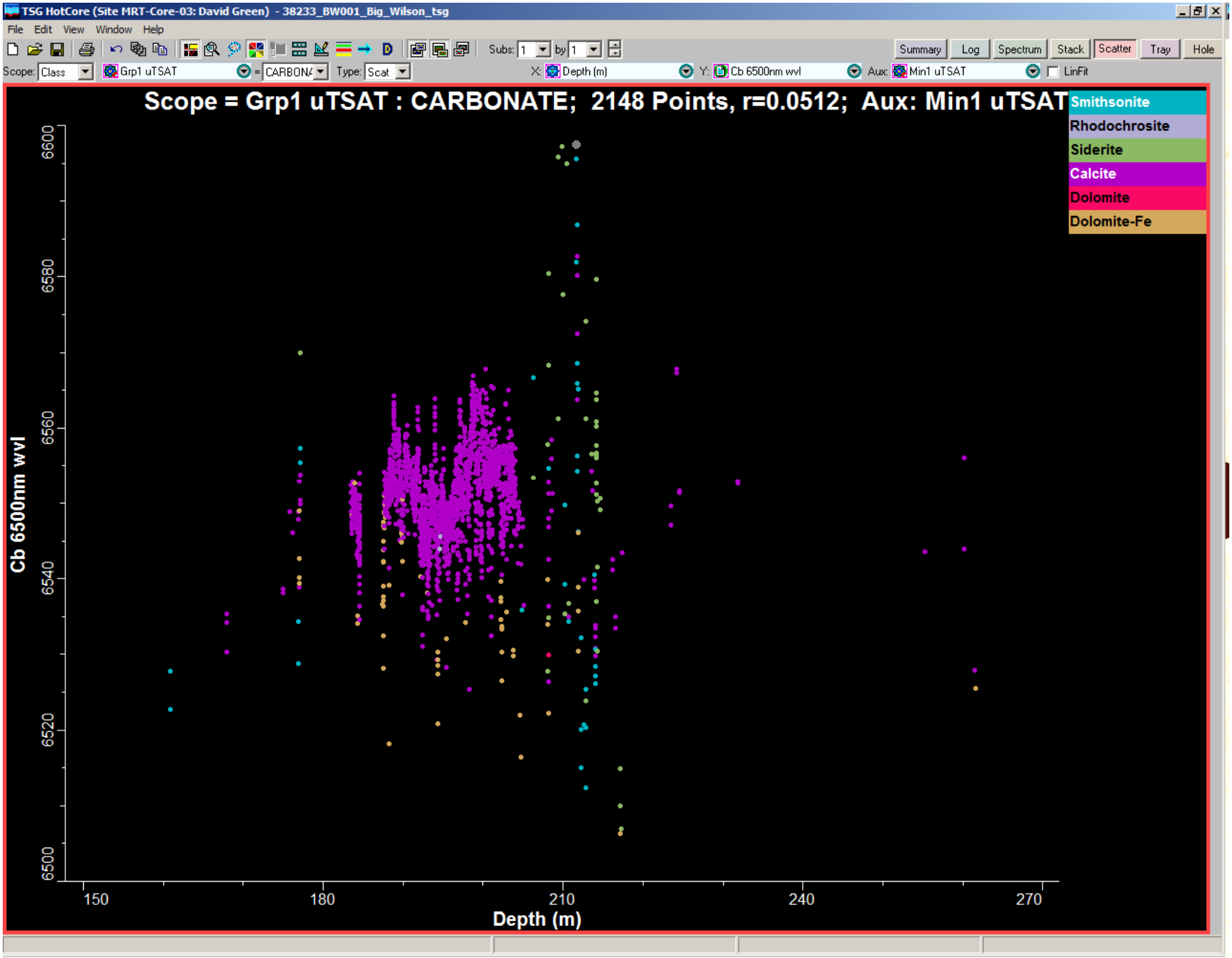
TSG HotCore (Site MRT-Core-03: David Green) - 38233_BW001_Big_Wilson_tsg
File Edit View Window Help
Summary Log Spectrum Stack Scatter Tray Hole
Scope: Class Grp1 uTSAT = CARBONA Type: Scat X: Depth (m) Y: Cb 6500nm wvl Aux: Min1 uTSAT LinFit
Scope = Grp1 uTSAT : CARBONATE; 2148 Points, r=0.0512; Aux: Min1 uTSAT
Smithsonite
Rhodochrosite
Siderite
Calcite
Dolomite
Dolomite-Fe
Cb 6500nm wvl
6600
6580
6560
6540
6520
6500
150
180
210
240
270
Depth (m)

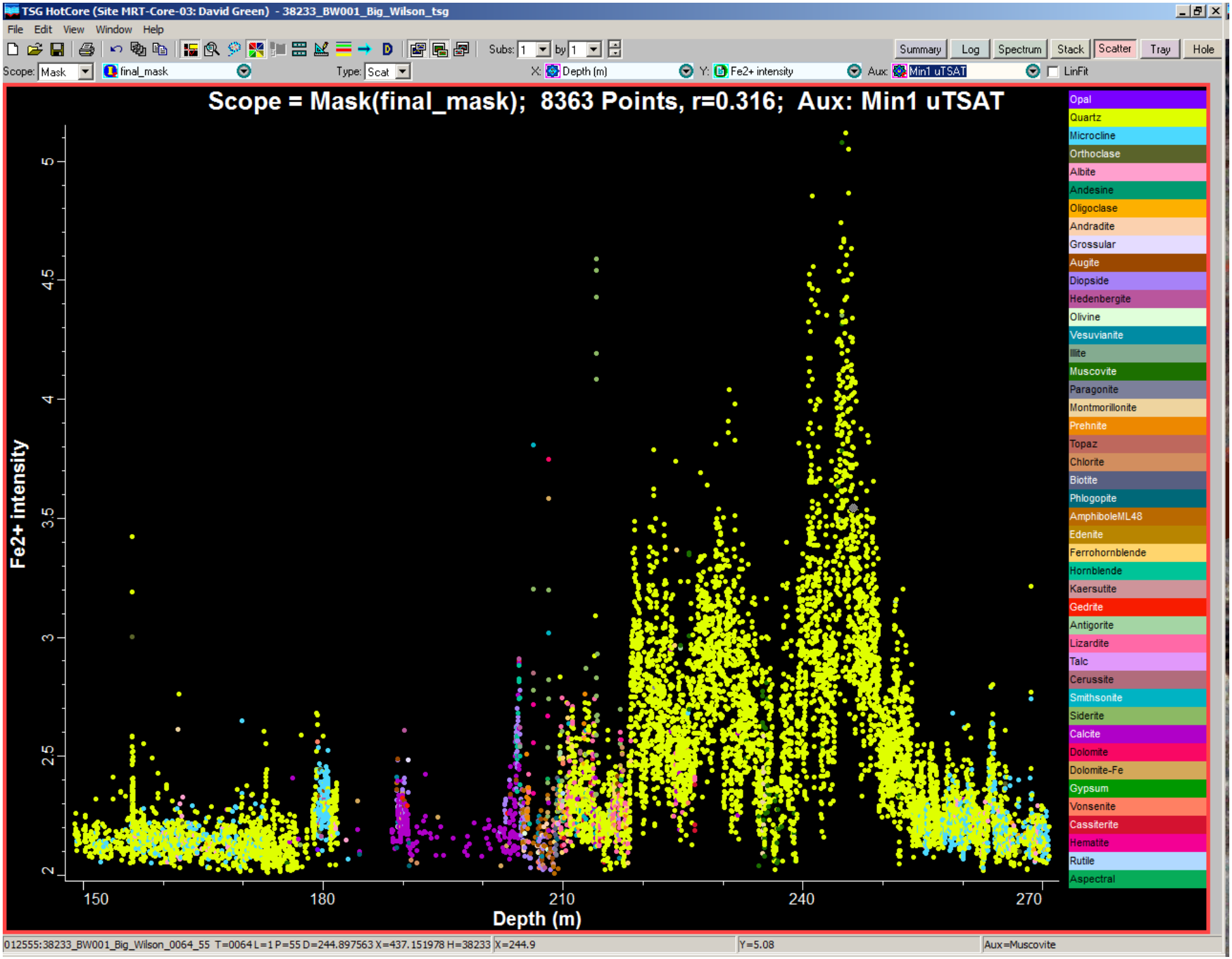
TSG HotCore (Site MRT-Core-03: David Green) - 38233_BW001_Big_Wilson_tsg
File Edit View Window Help
Summary Log Spectrum Stack Scatter Tray Hole
Scope: Mask final_mask Type: Scat X: Depth (m) Y: Fe2+ intensity Aux: Min1 uTSAT LinFit
Scope = Mask(final_mask); 8363 Points, r=0.316; Aux: Min1 uTSAT
Fe2+ intensity
Depth (m)
2
2.5
3
3.5
4
4.5
5
150
180
210
240
270
Opal
Quartz
Microcline
Orthoclase
Albite
Andesine
Oligoclase
Andradite
Grossular
Augite
Diopside
Hedenbergite
Olivine
Vesuvianite
Illite
Muscovite
Paragonite
Montmorillonite
Prehnite
Topaz
Chlorite
Biotite
Phlogopite
AmphiboleML48
Edenite
Ferrohornblende
Hornblende
Kaersutite
Gedrite
Antigorite
Lizardite
Talc
Cerussite
Smithsonite
Siderite
Calcite
Dolomite
Dolomite-Fe
Gypsum
Vonsenite
Cassiterite
Hematite
Rutile
Aspectral
012555:38233_BW001_Big_Wilson_0064_55 T=0064 L=1 P=55 D=244.897563 X=437.151978 H=38233
X=244.9
Y=5.08
Aux=Muscovite

Appendix 12: Terraspec results

H0002	Version	3									
H0003	Date_generated	14/05/2016									
H0004	Reporting_period_end_date	28/05/2016									
H0005	State	TAS									
H0100	Tenement	EL45/2010									
H0101	Tenement_holder	Venture Minerals Ltd									
H0102	Project_name	Big Wilson									
H0106	Tenement_operator	Venture Minerals Ltd									
H0150	250K_map_sheet	SK5503 Burnie									
H0151	100K_map_sheet	7914 Pieman									
H0152	50K_map_sheet	na									
H0153	25K_map_sheet	3637 Rosebury, 3638 Parsons									
H0200	Start_date_of_data_acquisition	28/05/2015									
H0201	End_date_of_data_acquisition	28/05/2016									
H0202	Data_format	SG3									
H0203	Number_of_data_records	310									
H0204	Date_of_metadata_update	28/05/2016									
H0500	Feature_Located	drill core SWIR spectral reading									
H0600	Sample_code	DRILL CORE									
H0601	Sample_type	drill core									
H0602	Sample_description	drill core									
H0702	Job_no	na									
H0800	Assay_code	SWIR									
H0801	Assay_company	UTAS									
H0900	Remarks:	SWIR spectra measured with Terraspec instrument and processed with TSG software									
H1000	Hole	From	To	Sample	Sample_name	Min1_sTSAS	Wt1_sTSAS	Min2_sTSAS	Wt2_sTSAS	Alunite_1480	H-K_Index
H1001		metres	metres								
D	BW001	0	1	BW001_000	FSFR.2112 Int=15.0 sec C/L	NULL	NULL	NULL	NULL	1476.46	1.563
D	BW001	1	2	BW001_001	FSFR.2112 Int=15.0 sec C/L	NULL	NULL	NULL	NULL	1472.37	1.631
D	BW001	2	3	BW001_002	FSFR.2112 Int=15.0 sec	NULL	NULL	NULL	NULL	1470.51	0.174
D	BW001	3	4	BW001_003	FSFR.2112 Int=15.0 sec	Diaspore	0.637	Muscovite	0.363	NULL	0.561
D	BW001	4	5	BW001_004	FSFR.2112 Int=15.0 sec	Diaspore	0.618	Muscovite	0.382	NULL	0.233
D	BW001	5	6	BW001_005	FSFR.2112 Int=15.0 sec	Diaspore	1	NULL	NULL	NULL	0.151
D	BW001	6	7	BW001_006	FSFR.2112 Int=15.0 sec	Diaspore	1	NULL	NULL	NULL	0.0454
D	BW001	7	8	BW001_007	FSFR.2112 Int=15.0 sec	Diaspore	0.77	Kaolinite-PX	0.23	NULL	0.326
D	BW001	8	9	BW001_008	FSFR.2112 Int=15.0 sec	Tourmaline	1	NULL	NULL	1471.85	0.573
D	BW001	9	10	BW001_009	FSFR.2112 Int=11.0 sec	Diaspore	1	NULL	NULL	NULL	0.157
D	BW001	10	11	BW001_010	FSFR.2112 Int=11.0 sec	Muscovite	1	NULL	NULL	NULL	0.464
D	BW001	11	12	BW001_011	FSFR.2112 Int=11.0 sec clay	Diaspore	1	NULL	NULL	NULL	0.262
D	BW001	12	13	BW001_012	FSFR.2112 Int=11.0 sec clay	Diaspore	1	NULL	NULL	NULL	0.285
D	BW001	13	14	BW001_013	FSFR.2112 Int=11.0 sec clay	Aspectral	1	NULL	NULL	1470.64	0.113
D	BW001	14	15	BW001_014	FSFR.2112 Int=11.0 sec clay	Aspectral	1	NULL	NULL	1472.17	0.2
D	BW001	15	16	BW001_015	FSFR.2112 Int=11.0 sec clay	Aspectral	1	NULL	NULL	NULL	0.0829
D	BW001	16	17	BW001_016	FSFR.2112 Int=11.0 sec clay	Aspectral	1	NULL	NULL	NULL	0.236
D	BW001	17	18	BW001_017	FSFR.2112 Int=11.0 sec clay	Diaspore	1	NULL	NULL	NULL	0.141
D	BW001	18	19	BW001_018	FSFR.2112 Int=11.0 sec clay	Diaspore	1	NULL	NULL	NULL	0.335
D	BW001	19	20	BW001_019	FSFR.2112 Int=11.0 sec clay	Diaspore	0.627	Montmorillonite	0.373	NULL	0.298
D	BW001	20	21	BW001_020	FSFR.2112 Int=11.0 sec clay	Diaspore	0.729	Nontronite	0.271	NULL	0.245

H1000	Hole	From	To	Sample	Sample_name	Min1_sTSAS	Wt1_sTSAS	Min2_sTSAS	Wt2_sTSAS	Alunite_1480	H-K_Index
H1001		metres	metres								
D	BW001	21	22	BW001_021	FSFR.2112 Int=11.0 sec clay	Diaspore	1	NULL	NULL	NULL	0.208
D	BW001	22	23	BW001_022	FSFR.2112 Int=11.0 sec clay	Diaspore	0.794	Kaolinite-PX	0.206	NULL	0.267
D	BW001	23	24	BW001_023	FSFR.2112 Int=11.0 sec clay	Diaspore	1	NULL	NULL	NULL	0.229
D	BW001	24	25	BW001_024	FSFR.2112 Int=11.0 sec clay	Aspectral	1	NULL	NULL	NULL	0.116
D	BW001	25	26	BW001_025	FSFR.2112 Int=11.0 sec clay	Diaspore	1	NULL	NULL	NULL	0.101
D	BW001	26	27	BW001_026	FSFR.2112 Int=11.0 sec clay	Diaspore	0.727	Nontronite	0.273	NULL	0.0945
D	BW001	27	28	BW001_027	FSFR.2112 Int=11.0 sec clay	Diaspore	0.716	Nontronite	0.284	NULL	0.141
D	BW001	28	29	BW001_028	FSFR.2112 Int=11.0 sec clay	Diaspore	0.699	Muscovite	0.301	NULL	0.181
D	BW001	29	30	BW001_029	FSFR.2112 Int=11.0 sec clay	Aspectral	1	NULL	NULL	NULL	0.077
D	BW001	30	31	BW001_030	FSFR.2112 Int=11.0 sec	Aspectral	1	NULL	NULL	NULL	0.0664
D	BW001	31	32	BW001_031	FSFR.2112 Int=11.0 sec	Phlogopite	0.549	Calcite	0.451	1472.44	NULL
D	BW001	32	33	BW001_032	FSFR.2112 Int=11.0 sec	Diaspore	0.605	Calcite	0.395	NULL	NULL
D	BW001	33	34	BW001_033	FSFR.2112 Int=11.0 sec	Diaspore	0.545	Calcite	0.455	NULL	0.045
D	BW001	34	35	BW001_034	FSFR.2112 Int=11.0 sec	Diaspore	0.684	Calcite	0.316	NULL	0.024
D	BW001	35	36	BW001_035	FSFR.2112 Int=11.0 sec	Diaspore	0.79	Calcite	0.21	1471.79	1.36
D	BW001	36	37	BW001_036	FSFR.2112 Int=11.0 sec	Diaspore	0.762	Calcite	0.238	1470.76	1.287
D	BW001	37	38	BW001_037	FSFR.2112 Int=11.0 sec clay	Diaspore	0.578	Phlogopite	0.422	NULL	0.179
D	BW001	38	39	BW001_038	FSFR.2112 Int=11.0 sec clay	Diaspore	1	NULL	NULL	NULL	0.308
D	BW001	39	40	BW001_039	FSFR.2112 Int=11.0 sec c/l	NULL	NULL	NULL	NULL	1493.37	1.323
D	BW001	40	41	BW001_040	FSFR.2112 Int=11.0 sec c/l	NULL	NULL	NULL	NULL	1472.1	1.245
D	BW001	41	42	BW001_041	FSFR.2112 Int=11.0 sec clay	Diaspore	0.647	Kaolinite-PX	0.353	NULL	0.803
D	BW001	42	43	BW001_042	FSFR.2112 Int=11.0 sec clay	Diaspore	1	NULL	NULL	NULL	0.364
D	BW001	43	44	BW001_043	FSFR.2112 Int=11.0 sec clay	Diaspore	0.675	Kaolinite-PX	0.325	NULL	0.313
D	BW001	44	45	BW001_044	FSFR.2112 Int=11.0 sec clay	Aspectral	1	NULL	NULL	NULL	0.51
D	BW001	45	46	BW001_045	FSFR.2112 Int=11.0 sec clay	Diaspore	1	NULL	NULL	NULL	0.172
D	BW001	46	47	BW001_046	FSFR.2112 Int=11.0 sec clay	Diaspore	1	NULL	NULL	NULL	0.347
D	BW001	47	48	BW001_047	FSFR.2112 Int=11.0 sec clay	Diaspore	1	NULL	NULL	NULL	0.11
D	BW001	48	49	BW001_048	FSFR.2112 Int=11.0 sec clay	NULL	NULL	NULL	NULL	1471.03	1.67
D	BW001	49	50	BW001_049	FSFR.2112 Int=11.0 sec clay	Aspectral	1	NULL	NULL	NULL	0.143
D	BW001	50	51	BW001_050	FSFR.2112 Int=11.0 sec	Diaspore	0.832	Calcite	0.168	1496.38	0.817
D	BW001	51	52	BW001_051	FSFR.2112 Int=11.0 sec	Diaspore	0.564	Calcite	0.436	NULL	0.091
D	BW001	52	53	BW001_052	FSFR.2112 Int=11.0 sec	Calcite	1	NULL	NULL	NULL	0.653
D	BW001	53	54	BW001_053	FSFR.2112 Int=11.0 sec	Aspectral	1	NULL	NULL	1475.99	0.685
D	BW001	54	55	BW001_054	FSFR.2112 Int=11.0 sec	Siderite	1	NULL	NULL	1477.46	0.539
D	BW001	55	56	BW001_055	FSFR.2112 Int=11.0 sec	Calcite	1	NULL	NULL	1477.42	NULL
D	BW001	56	57	BW001_056	FSFR.2112 Int=11.0 sec	Calcite	1	NULL	NULL	1474.28	0.658
D	BW001	57	58	BW001_057	FSFR.2112 Int=11.0 sec	Phengite	1	NULL	NULL	1473.27	0.234
D	BW001	58	59	BW001_058	FSFR.2112 Int=11.0 sec	Tourmaline	1	NULL	NULL	NULL	0.878
D	BW001	59	60	BW001_059	FSFR.2112 Int=11.0 sec	Calcite	0.595	Phengite	0.405	1471.54	0.774
D	BW001	60	61	BW001_060	FSFR.2112 Int=11.0 sec	Calcite	0.563	Phengite	0.437	NULL	0.299
D	BW001	61	62	BW001_061	FSFR.2112 Int=11.0 sec	Calcite	0.622	Phengite	0.378	1473.29	0.163
D	BW001	62	63	BW001_062	FSFR.2112 Int=11.0 sec	Calcite	1	NULL	NULL	NULL	0.433
D	BW001	63	64	BW001_063	FSFR.2112 Int=11.0 sec	Calcite	1	NULL	NULL	1474.54	0.242
D	BW001	64	65	BW001_064	FSFR.2112 Int=11.0 sec	Aspectral	1	NULL	NULL	1471.94	1.291
D	BW001	65	66	BW001_065	FSFR.2112 Int=11.0 sec	Calcite	0.792	Actinolite	0.208	1473.86	NULL
D	BW001	66	67	BW001_066	FSFR.2112 Int=11.0 sec	Calcite	1	NULL	NULL	1474.17	NULL

H1000	Hole	From	To	Sample	Sample_name	Min1_sTSAS	Wt1_sTSAS	Min2_sTSAS	Wt2_sTSAS	Alunite_1480	H-K_Index
H1001		metres	metres								
D	BW001	67	68	BW001_067	FSFR.2112 Int=11.0 sec	Calcite	0.626	Phlogopite	0.374	1473.72	NULL
D	BW001	68	69	BW001_068	FSFR.2112 Int=11.0 sec	Chlorite-Mg	0.735	Phlogopite	0.265	1471.94	NULL
D	BW001	69	70	BW001_069	FSFR.2112 Int=11.0 sec	Saponite	0.552	Ankerite	0.448	NULL	0.0237
D	BW001	70	71	BW001_070	FSFR.2112 Int=11.0 sec	Saponite	0.6	Phlogopite	0.4	NULL	0.0234
D	BW001	71	72	BW001_071	FSFR.2112 Int=11.0 sec	Calcite	1	NULL	NULL	NULL	0.16
D	BW001	72	73	BW001_072	FSFR.2112 Int=11.0 sec	Calcite	0.57	Phlogopite	0.43	NULL	NULL
D	BW001	73	74	BW001_073	FSFR.2112 Int=11.0 sec	Calcite	0.512	Phlogopite	0.488	1471.55	NULL
D	BW001	74	75	BW001_074	FSFR.2112 Int=11.0 sec	Calcite	1	NULL	NULL	1474.32	1.052
D	BW001	75	76	BW001_075	FSFR.2112 Int=11.0 sec	Calcite	1	NULL	NULL	1476.27	1.667
D	BW001	76	77	BW001_076	FSFR.2112 Int=11.0 sec	Calcite	1	NULL	NULL	1475.88	0.683
D	BW001	77	78	BW001_077	FSFR.2112 Int=11.0 sec	Calcite	1	NULL	NULL	1476.31	0.836
D	BW001	78	79	BW001_078	FSFR.2112 Int=11.0 sec	Calcite	1	NULL	NULL	1474.84	0.722
D	BW001	79	80	BW001_079	FSFR.2112 Int=11.0 sec	Calcite	1	NULL	NULL	1477.07	0.622
D	BW001	80	81	BW001_080	FSFR.2112 Int=11.0 sec	Calcite	1	NULL	NULL	1472.05	0.563
D	BW001	81	82	BW001_081	FSFR.2112 Int=11.0 sec	Calcite	1	NULL	NULL	1473.75	1.096
D	BW001	82	83	BW001_082	FSFR.2112 Int=11.0 sec	Calcite	1	NULL	NULL	NULL	NULL
D	BW001	83	84	BW001_083	FSFR.2112 Int=11.0 sec	Calcite	1	NULL	NULL	1475.74	0.543
D	BW001	84	85	BW001_084	FSFR.2112 Int=11.0 sec	Calcite	1	NULL	NULL	1473.64	NULL
D	BW001	85	86	BW001_085	FSFR.2112 Int=11.0 sec	Calcite	0.823	Phengite	0.177	1473.34	0.445
D	BW001	86	87	BW001_086	FSFR.2112 Int=11.0 sec	Calcite	1	NULL	NULL	1474.74	0.749
D	BW001	87	88	BW001_087	FSFR.2112 Int=11.0 sec	Calcite	1	NULL	NULL	1476.3	0.533
D	BW001	88	89	BW001_088	FSFR.2112 Int=11.0 sec	Phlogopite	0.678	Calcite	0.322	NULL	NULL
D	BW001	89	90	BW001_089	FSFR.2112 Int=11.0 sec	Phlogopite	0.556	Calcite	0.444	1472.41	NULL
D	BW001	90	91	BW001_090	FSFR.2112 Int=11.0 sec	Calcite	1	NULL	NULL	1471.53	NULL
D	BW001	91	92	BW001_091	FSFR.2112 Int=11.0 sec	Aspectral	1	NULL	NULL	1475.67	0.148
D	BW001	92	93	BW001_092	FSFR.2112 Int=11.0 sec	Chlorite-Fe	0.753	Muscovite	0.247	1470.72	0.283
D	BW001	93	94	BW001_093	FSFR.2112 Int=11.0 sec	Chlorite-Fe	0.628	Muscovite	0.372	NULL	0.352
D	BW001	94	95	BW001_094	FSFR.2112 Int=11.0 sec	Chlorite-Fe	0.667	Muscovite	0.333	NULL	0.125
D	BW001	95	96	BW001_095	FSFR.2112 Int=11.0 sec	NULL	NULL	NULL	NULL	1475.5	0.174
D	BW001	96	97	BW001_096	FSFR.2112 Int=11.0 sec	Calcite	0.66	Montmorillonite	0.34	1473.2	0.597
D	BW001	97	98	BW001_097	FSFR.2112 Int=11.0 sec	Calcite	1	NULL	NULL	1476.02	NULL
D	BW001	98	99	BW001_098	FSFR.2112 Int=11.0 sec	Calcite	0.728	Muscovite	0.272	1471.12	0.81
D	BW001	99	100	BW001_099	FSFR.2112 Int=11.0 sec	Calcite	0.832	Hornblende	0.168	NULL	NULL
D	BW001	100	101	BW001_100	FSFR.2112 Int=11.0 sec	Calcite	0.679	Phlogopite	0.321	1473.92	NULL
D	BW001	101	102	BW001_101	FSFR.2112 Int=11.0 sec	Calcite	1	NULL	NULL	1476.39	NULL
D	BW001	102	103	BW001_102	FSFR.2112 Int=11.0 sec	Calcite	1	NULL	NULL	NULL	NULL
D	BW001	103	104	BW001_103	FSFR.2112 Int=11.0 sec	Calcite	1	NULL	NULL	NULL	0.155
D	BW001	104	105	BW001_104	FSFR.2112 Int=11.0 sec	Chlorite-Fe	1	NULL	NULL	1471.66	0.3
D	BW001	105	106	BW001_105	FSFR.2112 Int=11.0 sec	Muscovite	1	NULL	NULL	1471.82	0.259
D	BW001	106	107	BW001_106	FSFR.2112 Int=11.0 sec	Muscovite	1	NULL	NULL	NULL	0.209
D	BW001	107	108	BW001_107	FSFR.2112 Int=11.0 sec	Kaolinite-WX	0.565	Muscovite	0.435	NULL	0.407
D	BW001	108	109	BW001_108	FSFR.2112 Int=11.0 sec	ParagoniticIllite	0.615	Montmorillonite	0.385	NULL	0.487
D	BW001	109	110	BW001_109	FSFR.2112 Int=11.0 sec	Kaolinite-WX	0.562	Muscovite	0.438	NULL	0.664
D	BW001	110	111	BW001_110	FSFR.2112 Int=11.0 sec	Kaolinite-WX	0.645	Muscovite	0.355	NULL	0.553
D	BW001	111	112	BW001_111	FSFR.2112 Int=11.0 sec	Muscovite	1	NULL	NULL	1472.24	0.316
D	BW001	112	113	BW001_112	FSFR.2112 Int=11.0 sec	Muscovite	1	NULL	NULL	1473.89	0.521

H1000	Hole	From	To	Sample	Sample_name	Min1_sTSAS	Wt1_sTSAS	Min2_sTSAS	Wt2_sTSAS	Alunite_1480	H-K_Index
H1001		metres	metres								
D	BW001	113	114	BW001_113	FSFR.2112 Int=11.0 sec	Muscovite	0.699	Kaolinite-WX	0.301	NULL	0.476
D	BW001	114	115	BW001_114	FSFR.2112 Int=11.0 sec	Muscovite	1	NULL	NULL	NULL	0.369
D	BW001	115	116	BW001_115	FSFR.2112 Int=11.0 sec	Muscovite	1	NULL	NULL	NULL	0.358
D	BW001	116	117	BW001_116	FSFR.2112 Int=11.0 sec	Biotite	0.62	Muscovite	0.38	1472.95	0.33
D	BW001	117	118	BW001_117	FSFR.2112 Int=11.0 sec	Muscovite	1	NULL	NULL	NULL	0.302
D	BW001	118	119	BW001_118	FSFR.2112 Int=11.0 sec	Muscovite	1	NULL	NULL	1471.71	0.291
D	BW001	119	120	BW001_119	FSFR.2112 Int=11.0 sec	Muscovite	1	NULL	NULL	NULL	0.296
D	BW001	120	121	BW001_120	FSFR.2112 Int=11.0 sec	Muscovite	1	NULL	NULL	1472.04	0.284
D	BW001	121	122	BW001_121	FSFR.2112 Int=11.0 sec	Aspectral	1	NULL	NULL	1472.93	0.303
D	BW001	122	123	BW001_122	FSFR.2112 Int=11.0 sec	Calcite	1	NULL	NULL	1473.58	0.0342
D	BW001	123	124	BW001_123	FSFR.2112 Int=11.0 sec	Muscovite	1	NULL	NULL	1473.16	0.342
D	BW001	124	125	BW001_124	FSFR.2112 Int=11.0 sec	Muscovite	1	NULL	NULL	NULL	0.37
D	BW001	125	126	BW001_125	FSFR.2112 Int=11.0 sec	Muscovite	1	NULL	NULL	NULL	0.331
D	BW001	126	127	BW001_126	FSFR.2112 Int=11.0 sec	Chlorite-Fe	0.587	Muscovite	0.413	1471.03	0.428
D	BW001	127	128	BW001_127	FSFR.2112 Int=11.0 sec	Muscovite	1	NULL	NULL	NULL	0.342
D	BW001	128	129	BW001_128	FSFR.2112 Int=11.0 sec	Muscovite	1	NULL	NULL	NULL	0.464
D	BW001	129	130	BW001_129	FSFR.2112 Int=11.0 sec	Aspectral	1	NULL	NULL	NULL	0.244
D	BW001	130	131	BW001_130	FSFR.2112 Int=11.0 sec	Muscovite	1	NULL	NULL	NULL	0.246
D	BW001	131	132	BW001_131	FSFR.2112 Int=11.0 sec	Chlorite-FeMg	0.675	Muscovite	0.325	NULL	0.336
D	BW001	132	133	BW001_132	FSFR.2112 Int=11.0 sec	Aspectral	1	NULL	NULL	1472.79	0.217
D	BW001	133	134	BW001_133	FSFR.2112 Int=11.0 sec	Chlorite-FeMg	0.653	Muscovite	0.347	NULL	0.298
D	BW001	134	135	BW001_134	FSFR.2112 Int=11.0 sec	Muscovite	1	NULL	NULL	NULL	0.246
D	BW001	135	136	BW001_135	FSFR.2112 Int=11.0 sec	Aspectral	1	NULL	NULL	NULL	0.173
D	BW001	136	137	BW001_136	FSFR.2112 Int=11.0 sec	Aspectral	1	NULL	NULL	NULL	0.178
D	BW001	137	138	BW001_137	FSFR.2112 Int=11.0 sec	Aspectral	1	NULL	NULL	NULL	0.251
D	BW001	138	139	BW001_138	FSFR.2112 Int=11.0 sec	Aspectral	1	NULL	NULL	NULL	0.3
D	BW001	139	140	BW001_139	FSFR.2112 Int=11.0 sec	Muscovite	1	NULL	NULL	NULL	0.262
D	BW001	140	141	BW001_140	FSFR.2112 Int=11.0 sec	Muscovite	1	NULL	NULL	NULL	0.3
D	BW001	141	142	BW001_141	FSFR.2112 Int=11.0 sec	Aspectral	1	NULL	NULL	1470.73	0.268
D	BW001	142	143	BW001_142	FSFR.2112 Int=11.0 sec	Muscovite	1	NULL	NULL	NULL	0.303
D	BW001	143	144	BW001_143	FSFR.2112 Int=11.0 sec	Muscovite	1	NULL	NULL	NULL	0.158
D	BW001	144	145	BW001_144	FSFR.2112 Int=11.0 sec	Muscovite	1	NULL	NULL	NULL	0.175
D	BW001	145	146	BW001_145	FSFR.2112 Int=11.0 sec	Muscovite	1	NULL	NULL	NULL	0.329
D	BW001	146	147	BW001_146	FSFR.2112 Int=11.0 sec	Muscovite	1	NULL	NULL	NULL	0.629
D	BW001	147	148	BW001_147	FSFR.2112 Int=11.0 sec	Aspectral	1	NULL	NULL	1486.81	0.405
D	BW001	148	149	BW001_148	FSFR.2112 Int=11.0 sec	Muscovite	1	NULL	NULL	1473.21	0.36
D	BW001	149	150	BW001_149	FSFR.2112 Int=11.0 sec	Aspectral	1	NULL	NULL	NULL	0.319
D	BW001	150	151	BW001_150	FSFR.2112 Int=11.0 sec	Aspectral	1	NULL	NULL	NULL	0.249
D	BW001	151	152	BW001_151	FSFR.2112 Int=11.0 sec	Aspectral	1	NULL	NULL	NULL	0.259
D	BW001	152	153	BW001_152	FSFR.2112 Int=11.0 sec	Aspectral	1	NULL	NULL	NULL	0.231
D	BW001	153	154	BW001_153	FSFR.2112 Int=11.0 sec	Muscovite	1	NULL	NULL	NULL	0.287
D	BW001	154	155	BW001_154	FSFR.2112 Int=11.0 sec	Tourmaline-Fe	1	NULL	NULL	NULL	0.307
D	BW001	155	156	BW001_155	FSFR.2112 Int=11.0 sec	Muscovite	1	NULL	NULL	NULL	0.276
D	BW001	156	157	BW001_156	FSFR.2112 Int=11.0 sec	Muscovite	1	NULL	NULL	NULL	0.53
D	BW001	157	158	BW001_157	FSFR.2112 Int=11.0 sec	Muscovite	1	NULL	NULL	1470.28	0.427
D	BW001	158	159	BW001_158	FSFR.2112 Int=11.0 sec	Muscovite	1	NULL	NULL	NULL	0.235

H1000	Hole	From	To	Sample	Sample_name	Min1_sTSAS	Wt1_sTSAS	Min2_sTSAS	Wt2_sTSAS	Alunite_1480	H-K_Index
H1001		metres	metres								
D	BW001	159	160	BW001_159	FSFR.2112 Int=11.0 sec	Muscovite	1	NULL	NULL	NULL	0.497
D	BW001	160	161	BW001_160	FSFR.2112 Int=11.0 sec	Muscovite	1	NULL	NULL	NULL	0.183
D	BW001	161	162	BW001_161	FSFR.2112 Int=11.0 sec	Aspectral	1	NULL	NULL	NULL	0.286
D	BW001	162	163	BW001_162	FSFR.2112 Int=11.0 sec	Muscovite	1	NULL	NULL	NULL	0.546
D	BW001	163	164	BW001_163	FSFR.2112 Int=11.0 sec	Muscovite	1	NULL	NULL	NULL	0.494
D	BW001	164	165	BW001_164	FSFR.2112 Int=11.0 sec	Muscovite	1	NULL	NULL	NULL	0.308
D	BW001	165	166	BW001_165	FSFR.2112 Int=11.0 sec	Muscovite	1	NULL	NULL	NULL	0.179
D	BW001	166	167	BW001_166	FSFR.2112 Int=11.0 sec	Aspectral	1	NULL	NULL	1470.76	0.316
D	BW001	167	168	BW001_167	FSFR.2112 Int=11.0 sec	Muscovite	1	NULL	NULL	NULL	0.384
D	BW001	168	169	BW001_168	FSFR.2112 Int=11.0 sec	Muscovite	1	NULL	NULL	NULL	0.209
D	BW001	169	170	BW001_169	FSFR.2112 Int=11.0 sec	ParagoniticIllite	0.541	Montmorillonite	0.459	NULL	0.478
D	BW001	170	171	BW001_170	FSFR.2112 Int=11.0 sec	ParagoniticIllite	1	NULL	NULL	NULL	0.488
D	BW001	171	172	BW001_171	FSFR.2112 Int=11.0 sec	Phengite	1	NULL	NULL	1473.17	0.406
D	BW001	172	173	BW001_172	FSFR.2112 Int=11.0 sec	ParagoniticIllite	0.585	Montmorillonite	0.415	NULL	0.602
D	BW001	173	174	BW001_173	FSFR.2112 Int=11.0 sec	ParagoniticIllite	0.658	Montmorillonite	0.342	NULL	0.584
D	BW001	174	175	BW001_174	FSFR.2112 Int=11.0 sec	ParagoniticIllite	0.619	Montmorillonite	0.381	NULL	0.627
D	BW001	175	176	BW001_175	FSFR.2112 Int=11.0 sec	ParagoniticIllite	0.553	Montmorillonite	0.447	NULL	0.573
D	BW001	176	177	BW001_176	FSFR.2112 Int=11.0 sec	ParagoniticIllite	0.59	Montmorillonite	0.41	NULL	0.551
D	BW001	177	178	BW001_177	FSFR.2112 Int=11.0 sec	Chlorite-FeMg	1	NULL	NULL	1486.94	NULL
D	BW001	178	179	BW001_178	FSFR.2112 Int=11.0 sec	ParagoniticIllite	0.714	Montmorillonite	0.286	NULL	0.728
D	BW001	179	180	BW001_179	FSFR.2112 Int=11.0 sec	PhengiticIllite	0.595	Chlorite-FeMg	0.405	NULL	0.437
D	BW001	180	181	BW001_180	FSFR.2112 Int=11.0 sec	Aspectral	1	NULL	NULL	1470.12	0.0518
D	BW001	181	182	BW001_181	FSFR.2112 Int=11.0 sec	Muscovite	1	NULL	NULL	NULL	0.387
D	BW001	182	183	BW001_182	FSFR.2112 Int=11.0 sec l/c	NULL	NULL	NULL	NULL	1497.46	1.118
D	BW001	183	184	BW001_183	FSFR.2112 Int=11.0 sec l/c	NULL	NULL	NULL	NULL	1490.56	NULL
D	BW001	184	185	BW001_184	FSFR.2112 Int=11.0 sec l/c	NULL	NULL	NULL	NULL	NULL	1.303
D	BW001	185	186	BW001_185	FSFR.2112 Int=11.0 sec l/c	NULL	NULL	NULL	NULL	1480.31	1.282
D	BW001	186	187	BW001_186	FSFR.2112 Int=11.0 sec l/c	Aspectral	1	NULL	NULL	1473.57	0.219
D	BW001	187	188	BW001_187	FSFR.2112 Int=11.0 sec	Chlorite-Mg	1	NULL	NULL	1472.46	0.144
D	BW001	188	189	BW001_188	FSFR.2112 Int=11.0 sec	Phlogopite	0.635	Calcite	0.365	1472.61	NULL
D	BW001	189	190	BW001_189	FSFR.2112 Int=11.0 sec	Phengite	1	NULL	NULL	1486	1.058
D	BW001	190	191	BW001_190	FSFR.2112 Int=11.0 sec	Calcite	0.632	Prehnite	0.368	1472.57	NULL
D	BW001	191	192	BW001_191	FSFR.2112 Int=11.0 sec	Chlorite-Mg	0.665	Muscovite	0.335	NULL	0.682
D	BW001	192	193	BW001_192	FSFR.2112 Int=11.0 sec	Calcite	1	NULL	NULL	1472.39	0.138
D	BW001	193	194	BW001_193	FSFR.2112 Int=11.0 sec	Phlogopite	0.606	Calcite	0.394	NULL	0.129
D	BW001	194	195	BW001_194	FSFR.2112 Int=11.0 sec	Phlogopite	1	NULL	NULL	1490.36	NULL
D	BW001	195	196	BW001_195	FSFR.2112 Int=11.0 sec	Calcite	1	NULL	NULL	NULL	NULL
D	BW001	196	197	BW001_196	FSFR.2112 Int=11.0 sec	Calcite	1	NULL	NULL	NULL	0.118
D	BW001	197	198	BW001_197	FSFR.2112 Int=11.0 sec	Calcite	0.785	Wood	0.215	NULL	NULL
D	BW001	198	199	BW001_198	FSFR.2112 Int=11.0 sec	Calcite	1	NULL	NULL	1470.26	0.0542
D	BW001	199	200	BW001_199	FSFR.2112 Int=11.0 sec	Calcite	1	NULL	NULL	NULL	NULL
D	BW001	200	201	BW001_200	FSFR.2112 Int=11.0 sec	Calcite	0.746	Wood	0.254	NULL	NULL
D	BW001	201	202	BW001_201	FSFR.2112 Int=11.0 sec	Calcite	0.632	Phlogopite	0.368	NULL	NULL
D	BW001	202	203	BW001_202	FSFR.2112 Int=11.0 sec	Calcite	0.617	Muscovite	0.383	NULL	0.234
D	BW001	203	204	BW001_203	FSFR.2112 Int=11.0 sec	Aspectral	1	NULL	NULL	1471.53	0.251
D	BW001	204	205	BW001_204	FSFR.2112 Int=16.0 sec	NULL	NULL	NULL	NULL	1489.55	0.0463

H1000	Hole	From	To	Sample	Sample_name	Min1_sTSAS	Wt1_sTSAS	Min2_sTSAS	Wt2_sTSAS	Alunite_1480	H-K_Index
H1001		metres	metres								
D	BW001	205	206	BW001_205	FSFR.2112 Int=16.0 sec	NULL	NULL	NULL	NULL	1496.22	3.58
D	BW001	206	207	BW001_206	FSFR.2112 Int=16.0 sec	NULL	NULL	NULL	NULL	NULL	2.286
D	BW001	207	208	BW001_207	FSFR.2112 Int=16.0 sec	Diaspore	1	NULL	NULL	NULL	2.033
D	BW001	208	209	BW001_208	FSFR.2112 Int=16.0 sec	NULL	NULL	NULL	NULL	1497.36	3.109
D	BW001	209	210	BW001_209	FSFR.2112 Int=16.0 sec	NULL	NULL	NULL	NULL	1491.99	1.407
D	BW001	210	211	BW001_210	FSFR.2112 Int=16.0 sec	NULL	NULL	NULL	NULL	1483.77	0.793
D	BW001	211	212	BW001_211	FSFR.2112 Int=16.0 sec	Diaspore	0.549	Chlorite-FeMg	0.451	NULL	0.132
D	BW001	212	213	BW001_212	FSFR.2112 Int=16.0 sec	Chlorite-Fe	0.54	Diaspore	0.46	1471.1	NULL
D	BW001	213	214	BW001_213	FSFR.2112 Int=16.0 sec	Chlorite-Fe	0.593	Diaspore	0.407	1471.53	NULL
D	BW001	214	215	BW001_214	FSFR.2112 Int=16.0 sec	NULL	NULL	NULL	NULL	NULL	1.831
D	BW001	215	216	BW001_215	FSFR.2112 Int=16.0 sec	Diaspore	1	NULL	NULL	1496.43	3.16
D	BW001	216	217	BW001_216	FSFR.2112 Int=16.0 sec	NULL	NULL	NULL	NULL	1490.69	2.512
D	BW001	217	218	BW001_217	FSFR.2112 Int=16.0 sec	NULL	NULL	NULL	NULL	NULL	2.507
D	BW001	218	219	BW001_218	FSFR.2112 Int=16.0 sec	Muscovite	1	NULL	NULL	1470.26	1.766
D	BW001	219	220	BW001_219	FSFR.2112 Int=16.0 sec	Muscovite	1	NULL	NULL	NULL	1.067
D	BW001	220	221	BW001_220	FSFR.2112 Int=16.0 sec	Diaspore	0.61	Tourmaline-Fe	0.39	NULL	0.491
D	BW001	221	222	BW001_221	FSFR.2112 Int=16.0 sec	Chlorite-Fe	1	NULL	NULL	1472.02	NULL
D	BW001	222	223	BW001_222	FSFR.2112 Int=16.0 sec	Muscovite	1	NULL	NULL	NULL	1.145
D	BW001	223	224	BW001_223	FSFR.2112 Int=16.0 sec	Chlorite-Fe	0.611	Diaspore	0.389	NULL	NULL
D	BW001	224	225	BW001_224	FSFR.2112 Int=16.0 sec	Phengite	0.556	Diaspore	0.444	1473.13	2.172
D	BW001	225	226	BW001_225	FSFR.2112 Int=16.0 sec	ParagoniticIllite	1	NULL	NULL	NULL	1.337
D	BW001	226	227	BW001_226	FSFR.2112 Int=16.0 sec	Chlorite-Fe	0.668	Diaspore	0.332	1498.71	1.021
D	BW001	227	228	BW001_227	FSFR.2112 Int=16.0 sec	Muscovite	1	NULL	NULL	NULL	1.341
D	BW001	228	229	BW001_228	FSFR.2112 Int=16.0 sec	Muscovite	1	NULL	NULL	NULL	1.467
D	BW001	229	230	BW001_229	FSFR.2112 Int=16.0 sec	Muscovite	1	NULL	NULL	NULL	1.174
D	BW001	230	231	BW001_230	FSFR.2112 Int=16.0 sec	Diaspore	1	NULL	NULL	NULL	0.447
D	BW001	231	232	BW001_231	FSFR.2112 Int=16.0 sec	Diaspore	0.625	Muscovite	0.375	NULL	0.497
D	BW001	232	233	BW001_232	FSFR.2112 Int=16.0 sec	Muscovite	1	NULL	NULL	NULL	1.369
D	BW001	233	234	BW001_233	FSFR.2112 Int=16.0 sec	Muscovite	1	NULL	NULL	NULL	2.603
D	BW001	234	235	BW001_234	FSFR.2112 Int=16.0 sec	ParagoniticIllite	0.616	Diaspore	0.384	NULL	0.878
D	BW001	235	236	BW001_235	FSFR.2112 Int=16.0 sec	Tourmaline-Fe	0.555	Muscovite	0.445	1470.67	0.826
D	BW001	236	237	BW001_236	FSFR.2112 Int=16.0 sec	Tourmaline-Fe	0.592	Diaspore	0.408	1496.28	8.113
D	BW001	237	238	BW001_237	FSFR.2112 Int=16.0 sec	Diaspore	0.56	Muscovite	0.44	1471.28	2.288
D	BW001	238	239	BW001_238	FSFR.2112 Int=16.0 sec	ParagoniticIllite	1	NULL	NULL	NULL	0.837
D	BW001	239	240	BW001_239	FSFR.2112 Int=16.0 sec	ParagoniticIllite	0.637	Diaspore	0.363	NULL	1.08
D	BW001	240	241	BW001_240	FSFR.2112 Int=16.0 sec	Muscovite	0.589	Diaspore	0.411	NULL	1.383
D	BW001	241	242	BW001_241	FSFR.2112 Int=16.0 sec	ParagoniticIllite	1	NULL	NULL	NULL	1.182
D	BW001	242	243	BW001_242	FSFR.2112 Int=16.0 sec	Muscovite	1	NULL	NULL	NULL	1.554
D	BW001	243	244	BW001_243	FSFR.2112 Int=16.0 sec	Muscovite	1	NULL	NULL	NULL	1.588
D	BW001	244	245	BW001_244	FSFR.2112 Int=16.0 sec	Muscovite	1	NULL	NULL	NULL	1.54
D	BW001	245	246	BW001_245	FSFR.2112 Int=16.0 sec	Muscovite	1	NULL	NULL	NULL	1.29
D	BW001	246	247	BW001_246	FSFR.2112 Int=16.0 sec	Muscovite	1	NULL	NULL	NULL	1.09
D	BW001	247	248	BW001_247	FSFR.2112 Int=16.0 sec	Muscovite	1	NULL	NULL	NULL	1.365
D	BW001	248	249	BW001_248	FSFR.2112 Int=16.0 sec	Muscovite	1	NULL	NULL	NULL	1.234
D	BW001	249	250	BW001_249	FSFR.2112 Int=16.0 sec	ParagoniticIllite	1	NULL	NULL	NULL	1.136
D	BW001	250	251	BW001_250	FSFR.2112 Int=16.0 sec	Muscovite	0.566	Diaspore	0.434	NULL	1.131

H1000	Hole	From	To	Sample	Sample_name	Min1_sTSAS	Wt1_sTSAS	Min2_sTSAS	Wt2_sTSAS	Alunite_1480	H-K_Index
H1001		metres	metres								
D	BW001	251	252	BW001_251	FSFR.2112 Int=16.0 sec	ParagoniticIllite	1	NULL	NULL	NULL	1.411
D	BW001	252	253	BW001_252	FSFR.2112 Int=16.0 sec	Muscovite	0.604	Diaspore	0.396	NULL	0.517
D	BW001	253	254	BW001_253	FSFR.2112 Int=16.0 sec	ParagoniticIllite	1	NULL	NULL	NULL	0.827
D	BW001	254	255	BW001_254	FSFR.2112 Int=16.0 sec	ParagoniticIllite	0.53	Diaspore	0.47	NULL	0.753
D	BW001	255	256	BW001_255	FSFR.2112 Int=16.0 sec	ParagoniticIllite	0.601	Diaspore	0.399	NULL	0.909
D	BW001	256	257	BW001_256	FSFR.2112 Int=16.0 sec	ParagoniticIllite	0.524	Diaspore	0.476	NULL	1.032
D	BW001	257	258	BW001_257	FSFR.2112 Int=16.0 sec	ParagoniticIllite	0.504	Diaspore	0.496	NULL	0.98
D	BW001	258	259	BW001_258	FSFR.2112 Int=16.0 sec	ParagoniticIllite	0.544	Diaspore	0.456	NULL	0.757
D	BW001	259	260	BW001_259	FSFR.2112 Int=16.0 sec	Diaspore	0.613	Muscovite	0.387	NULL	0.607
D	BW001	260	261	BW001_260	FSFR.2112 Int=16.0 sec	Muscovite	1	NULL	NULL	NULL	0.803
D	BW001	261	262	BW001_261	FSFR.2112 Int=16.0 sec	Muscovite	0.69	Kaolinite-WX	0.31	NULL	0.654
D	BW001	262	263	BW001_262	FSFR.2112 Int=16.0 sec	Muscovite	1	NULL	NULL	NULL	0.642
D	BW001	263	264	BW001_263	FSFR.2112 Int=16.0 sec	ParagoniticIllite	1	NULL	NULL	NULL	0.638
D	BW001	264	265	BW001_264	FSFR.2112 Int=16.0 sec	ParagoniticIllite	1	NULL	NULL	NULL	0.685
D	BW001	265	266	BW001_265	FSFR.2112 Int=16.0 sec	Muscovite	1	NULL	NULL	NULL	0.186
D	BW001	266	267	BW001_266	FSFR.2112 Int=16.0 sec	Muscovite	1	NULL	NULL	1472.62	0.413
D	BW001	267	268	BW001_267	FSFR.2112 Int=16.0 sec	Muscovite	1	NULL	NULL	NULL	0.315
D	BW001	268	269	BW001_268	FSFR.2112 Int=16.0 sec	Muscovite	1	NULL	NULL	NULL	0.406
D	BW001	269	270	BW001_269	FSFR.2112 Int=16.0 sec	Muscovite	1	NULL	NULL	NULL	0.49
D	BW001	270	271	BW001_270	FSFR.2112 Int=16.0 sec	Muscovite	1	NULL	NULL	1470.74	0.348
D	BW001	271	272	BW001_271	FSFR.2112 Int=16.0 sec	Muscovite	1	NULL	NULL	1470.18	0.393
D	BW001	272	273	BW001_272	FSFR.2112 Int=16.0 sec	Muscovite	1	NULL	NULL	1474.44	0.708
D	BW001	273	274	BW001_273	FSFR.2112 Int=16.0 sec	Muscovite	1	NULL	NULL	1472.69	0.487
D	BW001	274	275	BW001_274	FSFR.2112 Int=16.0 sec	Muscovite	1	NULL	NULL	1474.16	0.46
D	BW001	275	276	BW001_275	FSFR.2112 Int=16.0 sec	Muscovite	1	NULL	NULL	1471.18	0.388
D	BW001	276	277	BW001_276	FSFR.2112 Int=16.0 sec	Tourmaline-Fe	0.651	Muscovite	0.349	1472.01	0.496
D	BW001	277	278	BW001_277	FSFR.2112 Int=16.0 sec	Tourmaline-Fe	0.617	Muscovite	0.383	1474.45	0.727
D	BW001	278	279	BW001_278	FSFR.2112 Int=16.0 sec	Muscovite	1	NULL	NULL	NULL	0.594
D	BW001	279	280	BW001_279	FSFR.2112 Int=16.0 sec	Tourmaline-Fe	1	NULL	NULL	1475.88	1.373
D	BW001	280	281	BW001_280	FSFR.2112 Int=16.0 sec	Muscovite	1	NULL	NULL	1473.72	0.628
D	BW001	281	282	BW001_281	FSFR.2112 Int=16.0 sec	Muscovite	1	NULL	NULL	NULL	0.272
D	BW001	282	283	BW001_282	FSFR.2112 Int=16.0 sec	Muscovite	1	NULL	NULL	NULL	0.457
D	BW001	283	284	BW001_283	FSFR.2112 Int=16.0 sec	Muscovite	0.608	Kaolinite-WX	0.392	NULL	0.393
D	BW001	284	285	BW001_284	FSFR.2112 Int=16.0 sec	Muscovite	1	NULL	NULL	NULL	0.378
D	BW001	285	286	BW001_285	FSFR.2112 Int=16.0 sec	Muscovite	1	NULL	NULL	NULL	0.734
D	BW001	286	287	BW001_286	FSFR.2112 Int=16.0 sec	Muscovite	1	NULL	NULL	NULL	0.68
D	BW001	287	288	BW001_287	FSFR.2112 Int=16.0 sec	ParagoniticIllite	0.706	Kaolinite-WX	0.294	NULL	0.982
D	BW001	288	289	BW001_288	FSFR.2112 Int=16.0 sec	Muscovite	1	NULL	NULL	NULL	0.508
D	BW001	289	290	BW001_289	FSFR.2112 Int=16.0 sec	Muscovite	1	NULL	NULL	NULL	0.356
D	BW001	290	291	BW001_290	FSFR.2112 Int=16.0 sec	Muscovite	1	NULL	NULL	1471.82	0.236
D	BW001	291	292	BW001_291	FSFR.2112 Int=10.0 sec	Muscovite	1	NULL	NULL	1471.11	0.34
D	BW001	292	293	BW001_292	FSFR.2112 Int=10.0 sec	Muscovite	1	NULL	NULL	1476	0.531
D	BW001	293	294	BW001_293	FSFR.2112 Int=10.0 sec	Muscovite	1	NULL	NULL	1471.79	0.407
D	BW001	294	295	BW001_294	FSFR.2112 Int=10.0 sec	Muscovite	1	NULL	NULL	1475.18	0.463
D	BW001	295	296	BW001_295	FSFR.2112 Int=10.0 sec	Muscovite	1	NULL	NULL	1474.28	0.351
D	BW001	296	297	BW001_296	FSFR.2112 Int=10.0 sec	Paragonite	1	NULL	NULL	1474.89	0.604

H1000	Hole	From	To	Sample	Sample_name	Min1_sTSAS	Wt1_sTSAS	Min2_sTSAS	Wt2_sTSAS	Alunite_1480	H-K_Index
H1001		metres	metres								
D	BW001	297	298	BW001_297	FSFR.2112 Int=10.0 sec	Muscovite	1	NULL	NULL	NULL	0.253
D	BW001	298	299	BW001_298	FSFR.2112 Int=10.0 sec	Tourmaline-Fe	1	NULL	NULL	NULL	0.266
D	BW001	299	300	BW001_299	FSFR.2112 Int=10.0 sec	Muscovite	1	NULL	NULL	1473.13	0.215
D	BW001	300	301	BW001_300	FSFR.2112 Int=10.0 sec	Muscovite	1	NULL	NULL	NULL	0.436
D	BW001	301	302	BW001_301	FSFR.2112 Int=10.0 sec	Muscovite	1	NULL	NULL	NULL	0.278
D	BW001	302	303	BW001_302	FSFR.2112 Int=10.0 sec	Muscovite	1	NULL	NULL	NULL	0.832
D	BW001	303	304	BW001_303	FSFR.2112 Int=10.0 sec	Muscovite	1	NULL	NULL	NULL	0.302
D	BW001	304	305	BW001_304	FSFR.2112 Int=10.0 sec	Muscovite	0.508	Chlorite-FeMg	0.492	1470.63	0.42
D	BW001	305	306	BW001_305	FSFR.2112 Int=10.0 sec	Muscovite	1	NULL	NULL	1472.23	0.277
D	BW001	306	307	BW001_306	FSFR.2112 Int=10.0 sec	Muscovite	1	NULL	NULL	NULL	0.424
D	BW001	307	308	BW001_307	FSFR.2112 Int=10.0 sec	ParagoniticIllite	1	NULL	NULL	1473.97	0.701
D	BW001	308	309	BW001_308	FSFR.2112 Int=10.0 sec	Muscovite	1	NULL	NULL	NULL	0.408
D	BW001	309	310	BW001_309	FSFR.2112 Int=10.0 sec	Chlorite-Fe	0.515	Muscovite	0.485	1473.35	0.527
EOF											

Version					
Date_generated					
Reporting_period_end_date					
State					
Tenement					
Tenement_holder					
Project_name					
Tenement_operator					
250K_map_sheet					
100K_map_sheet					
50K_map_sheet					
25K_map_sheet					
Start_date_of_data_acquisition					
End_date_of_data_acquisition					
Data_format					
Number_of_data_records					
Date_of_metadata_update					
Feature_Located					
Sample_code					
Sample_type					
Sample_description					
Job_no					
Assay_code					
Assay_company					
Remarks:					
Hole	White_Mica_Al-OH	White_Mica_Crys	Chlorite_Fe-OH	Depth_Water	Depth_Al-OH
BW001	2218.87	1.563	2245.77	0.185	0.289
BW001	2218.03	1.631	2254.8	0.131	0.214
BW001	2207.92	0.174	2248.05	0.122	0.0212
BW001	2206.78	0.561	2245.63	0.259	0.145
BW001	2206.87	0.233	NULL	0.526	0.123
BW001	2205.7	0.151	2259.7	0.428	0.0644
BW001	2207.39	0.0454	2256.6	0.293	0.0133
BW001	2207.08	0.326	2247.31	0.387	0.126
BW001	2202.37	0.573	2251.72	0.223	0.128
BW001	2205.07	0.157	NULL	0.561	0.088
BW001	2205.2	0.464	2246.41	0.531	0.246
BW001	2207.63	0.262	NULL	0.249	0.0654
BW001	2205.91	0.285	NULL	0.272	0.0775
BW001	2196.95	0.113	2248.57	0.394	0.0447
BW001	2205.84	0.2	2251.42	0.308	0.0616
BW001	2204.01	0.0829	2254.98	0.534	0.0443
BW001	2205.5	0.236	2247.22	0.666	0.157
BW001	2204.94	0.141	2245.55	0.638	0.0899
BW001	2205.56	0.335	NULL	0.278	0.093
BW001	2204.89	0.298	2246.04	0.819	0.244
BW001	2204.05	0.245	2249.59	0.519	0.127

Hole	White_Mica_Al-OH	White_Mica_Crys	Chlorite_Fe-OH	Depth_Water	Depth_Al-OH
BW001	2206.52	0.208	2247.05	0.564	0.118
BW001	2204.68	0.267	2245.24	0.47	0.126
BW001	2206.33	0.229	NULL	0.392	0.0897
BW001	2205.06	0.116	NULL	0.703	0.0816
BW001	2204.6	0.101	2251.29	0.66	0.0669
BW001	2204.84	0.0945	NULL	0.797	0.0754
BW001	2204.92	0.141	NULL	0.761	0.107
BW001	2203.72	0.181	NULL	0.837	0.152
BW001	2202.2	0.077	2256.26	0.527	0.0406
BW001	2207.43	0.0664	2246.3	0.493	0.0327
BW001	NULL	NULL	2246.74	0.255	NULL
BW001	NULL	NULL	NULL	0.0629	NULL
BW001	NULL	0.045	NULL	0.191	0.00858
BW001	2205.58	0.024	2262.43	0.414	0.00995
BW001	2218.37	1.36	2246.98	0.0381	0.0518
BW001	2219.78	1.287	2249.24	0.0346	0.0445
BW001	2205.48	0.179	NULL	0.179	0.032
BW001	2206.78	0.308	2248.43	0.293	0.0905
BW001	2218.12	1.323	2247.81	0.478	0.632
BW001	2218.6	1.245	2262.74	0.463	0.576
BW001	2206.65	0.803	NULL	0.229	0.184
BW001	2205.73	0.364	2247.2	0.16	0.0582
BW001	2206.08	0.313	NULL	0.409	0.128
BW001	2206.12	0.51	2262.11	0.247	0.126
BW001	2204.59	0.172	2252.56	0.571	0.098
BW001	2206.96	0.347	2245.21	0.17	0.0589
BW001	2203.49	0.11	2246.94	0.222	0.0244
BW001	2202.9	1.67	2251.45	0.0357	0.0595
BW001	2206.55	0.143	2247.91	0.536	0.0767
BW001	2207.83	0.817	2264.72	0.0421	0.0344
BW001	NULL	0.091	NULL	0.152	0.0138
BW001	2218.3	0.653	2260.16	0.0392	0.0256
BW001	2185.07	0.685	2248.07	0.0766	0.0525
BW001	2216.35	0.539	2247.01	0.0436	0.0235
BW001	NULL	NULL	NULL	0.0415	NULL
BW001	2215.03	0.658	2251.11	0.0451	0.0297
BW001	2214.86	0.234	2247.53	0.425	0.0996
BW001	2216	0.878	2247.13	0.155	0.136
BW001	2215.09	0.774	2245.06	0.155	0.12
BW001	2215.87	0.299	NULL	0.156	0.0467
BW001	2214.19	0.163	2264.25	0.221	0.0361
BW001	2216.02	0.433	2263.9	0.106	0.0459
BW001	2227.87	0.242	2248.65	0.157	0.0381
BW001	2214.47	1.291	2248.33	0.0564	0.0727
BW001	NULL	NULL	2263.66	0.0836	NULL
BW001	NULL	NULL	NULL	0.234	NULL

Hole	White_Mica_Al-OH	White_Mica_Crys	Chlorite_Fe-OH	Depth_Water	Depth_Al-OH
BW001	NULL	NULL	2247.83	0.119	NULL
BW001	NULL	NULL	2247.3	0.123	NULL
BW001	2227.05	0.0237	2248.25	0.559	0.0132
BW001	2227.8	0.0234	NULL	0.627	0.0147
BW001	NULL	0.16	2262.24	0.0963	0.0154
BW001	NULL	NULL	2247.37	0.23	NULL
BW001	NULL	NULL	2247.75	0.071	NULL
BW001	2213.91	1.052	2262.42	0.0305	0.0321
BW001	2216.51	1.667	2264.45	0.0303	0.0505
BW001	2201.46	0.683	2253.13	0.0367	0.0251
BW001	2197.91	0.836	2256.81	0.0414	0.0346
BW001	2213.07	0.722	2246.38	0.05	0.0361
BW001	2215.93	0.622	2261.35	0.0521	0.0324
BW001	2226.94	0.563	2249.95	0.0399	0.0225
BW001	2229.46	1.096	2261.12	0.0367	0.0402
BW001	NULL	NULL	2262.84	0.0845	NULL
BW001	NULL	0.543	NULL	0.0942	0.0512
BW001	NULL	NULL	NULL	0.197	NULL
BW001	2215.46	0.445	NULL	0.257	0.114
BW001	2214.06	0.749	2247.44	0.0586	0.0438
BW001	2216.2	0.533	2248.82	0.041	0.0219
BW001	NULL	NULL	2246.97	0.0488	NULL
BW001	NULL	NULL	2247.25	0.0953	NULL
BW001	NULL	NULL	NULL	0.145	NULL
BW001	NULL	0.148	2248.81	0.209	0.031
BW001	2197.32	0.283	2257.87	0.15	0.0424
BW001	2196.46	0.352	2254.76	0.216	0.076
BW001	2197.37	0.125	2259.88	0.31	0.0387
BW001	2215.7	0.174	NULL	0.32	0.0558
BW001	2206.64	0.597	2262.35	0.0664	0.0396
BW001	NULL	NULL	NULL	0.127	NULL
BW001	2205.16	0.81	2262.81	0.0814	0.066
BW001	NULL	NULL	NULL	0.0827	NULL
BW001	NULL	NULL	2249.88	0.0805	NULL
BW001	NULL	NULL	NULL	0.081	NULL
BW001	NULL	NULL	NULL	0.241	NULL
BW001	2215.52	0.155	NULL	0.29	0.045
BW001	2197.69	0.3	2254.69	0.119	0.0357
BW001	2203.47	0.259	2253.94	0.166	0.043
BW001	2207.18	0.209	2250.56	0.27	0.0565
BW001	2206.42	0.407	2255.79	0.245	0.0998
BW001	2209.27	0.487	NULL	0.369	0.18
BW001	2207.82	0.664	2248.63	0.309	0.205
BW001	2207.54	0.553	NULL	0.394	0.218
BW001	2202.5	0.316	2255.44	0.277	0.0875
BW001	2206.99	0.521	2248.46	0.173	0.0904

Hole	White_Mica_Al-OH	White_Mica_Crys	Chlorite_Fe-OH	Depth_Water	Depth_Al-OH
BW001	2207.22	0.476	2247.62	0.323	0.154
BW001	2205.8	0.369	2255.86	0.319	0.118
BW001	2200.44	0.358	2252.24	0.287	0.103
BW001	2198.54	0.33	2261.03	0.244	0.0805
BW001	2196.95	0.302	2252.79	0.333	0.1
BW001	2197.92	0.291	2255.59	0.269	0.0783
BW001	2197.21	0.296	2254.91	0.277	0.0818
BW001	2197.78	0.284	2253.76	0.174	0.0495
BW001	2215.84	0.303	2246.89	0.169	0.0512
BW001	2194.57	0.0342	2254.91	0.166	0.00569
BW001	2196.8	0.342	2259.13	0.21	0.0716
BW001	2196.93	0.37	2256.08	0.143	0.0528
BW001	2199.75	0.331	2252.38	0.224	0.0743
BW001	2197.24	0.428	2256	0.245	0.105
BW001	2197.63	0.342	2256.4	0.262	0.0897
BW001	2207.67	0.464	2247.59	0.309	0.143
BW001	2205.78	0.244	2247.56	0.214	0.0521
BW001	2198.05	0.246	2255.35	0.271	0.0667
BW001	2197.92	0.336	2256.79	0.267	0.0897
BW001	2198.23	0.217	2256.78	0.261	0.0567
BW001	2200.67	0.298	2258.04	0.254	0.0757
BW001	2197.55	0.246	NULL	0.308	0.0758
BW001	2198.95	0.173	2254.2	0.297	0.0514
BW001	2197.73	0.178	2255.13	0.295	0.0525
BW001	2196.93	0.251	NULL	0.189	0.0474
BW001	2199.37	0.3	2256.75	0.2	0.0599
BW001	2196.26	0.262	2252.92	0.302	0.0791
BW001	2198.51	0.3	2253.21	0.259	0.0778
BW001	2196.03	0.268	2250.89	0.219	0.0588
BW001	2196.23	0.303	2256.09	0.268	0.0812
BW001	2200.55	0.158	2247.08	0.32	0.0505
BW001	2205.36	0.175	2251.86	0.292	0.0512
BW001	2196.78	0.329	2248.39	0.216	0.0712
BW001	2197.81	0.629	2247.41	0.205	0.129
BW001	2196.19	0.405	2252.8	0.101	0.0409
BW001	2203.56	0.36	2250.11	0.132	0.0475
BW001	2207.31	0.319	2254.45	0.156	0.0498
BW001	2198.05	0.249	2249.68	0.127	0.0315
BW001	2198.92	0.259	2251.33	0.112	0.0291
BW001	2208.46	0.231	2260.59	0.131	0.0302
BW001	2199.03	0.287	2253.27	0.224	0.0643
BW001	2204.05	0.307	2247.35	0.197	0.0605
BW001	2206.44	0.276	2250.65	0.168	0.0463
BW001	2199.38	0.53	2253.91	0.216	0.115
BW001	2201.62	0.427	2250.17	0.125	0.0533
BW001	2197.06	0.235	2256.08	0.204	0.0478

Hole	White_Mica_Al-OH	White_Mica_Crys	Chlorite_Fe-OH	Depth_Water	Depth_Al-OH
BW001	2196.57	0.497	2253.38	0.249	0.124
BW001	2196.62	0.183	2251.19	0.236	0.0432
BW001	2198.98	0.286	2249.58	0.188	0.0538
BW001	2202.97	0.546	2245.37	0.141	0.0772
BW001	2198.99	0.494	2253.21	0.222	0.11
BW001	2196.22	0.308	2256.7	0.196	0.0602
BW001	2200.19	0.179	2248.58	0.312	0.0559
BW001	2197.12	0.316	2248.54	0.158	0.0498
BW001	2199.39	0.384	2255.02	0.165	0.0632
BW001	2202.9	0.209	2246.96	0.255	0.0533
BW001	2206.45	0.478	2246.57	0.302	0.144
BW001	2204.49	0.488	NULL	0.31	0.151
BW001	2202.39	0.406	2250.24	0.209	0.085
BW001	2206.68	0.602	NULL	0.479	0.289
BW001	2207.55	0.584	NULL	0.413	0.241
BW001	2206.42	0.627	NULL	0.434	0.272
BW001	2207.96	0.573	NULL	0.441	0.253
BW001	2206.88	0.551	2248.45	0.481	0.265
BW001	NULL	NULL	2252.69	0.0784	NULL
BW001	2203.31	0.728	NULL	0.503	0.367
BW001	2208.84	0.437	NULL	0.448	0.196
BW001	2203.65	0.0518	2246.03	0.35	0.0181
BW001	2207.55	0.387	2246.48	0.409	0.158
BW001	2222.23	1.118	NULL	0.44	0.492
BW001	2216.42	NULL	2247.21	0.355	NULL
BW001	2211.11	1.303	NULL	0.294	0.384
BW001	2203.62	1.282	2254.67	0.305	0.391
BW001	2227.31	0.219	2246.57	0.179	0.0392
BW001	NULL	0.144	2248.4	0.185	0.0266
BW001	NULL	NULL	2246.88	0.295	NULL
BW001	2213.2	1.058	NULL	0.128	0.136
BW001	NULL	NULL	2261.6	0.52	NULL
BW001	2198.03	0.682	2247.73	0.0897	0.0612
BW001	2199.27	0.138	2261.5	0.0846	0.0117
BW001	NULL	0.129	2263.84	0.124	0.016
BW001	NULL	NULL	2246.42	0.054	NULL
BW001	NULL	NULL	NULL	0.163	NULL
BW001	NULL	0.118	NULL	0.101	0.0119
BW001	NULL	NULL	NULL	0.289	NULL
BW001	NULL	0.0542	2263.24	0.253	0.0137
BW001	NULL	NULL	2261.35	0.115	NULL
BW001	NULL	NULL	NULL	0.315	NULL
BW001	NULL	NULL	2261.28	0.312	NULL
BW001	2194.89	0.234	NULL	0.182	0.0427
BW001	2194.61	0.251	2257.16	0.366	0.0916
BW001	NULL	0.0463	2258.4	0.132	0.00611

Hole	White_Mica_Al-OH	White_Mica_Crys	Chlorite_Fe-OH	Depth_Water	Depth_Al-OH
BW001	2211.03	3.58	2256.59	0.0245	0.0878
BW001	2215.07	2.286	2257.04	0.0411	0.0939
BW001	2203.96	2.033	2256.66	0.0301	0.0612
BW001	2202.59	3.109	2261.02	0.0261	0.0811
BW001	2229.85	1.407	2256.83	0.0305	0.0429
BW001	2201.9	0.793	2258.24	0.0405	0.0321
BW001	NULL	0.132	2258.83	0.12	0.0158
BW001	NULL	NULL	2256.86	0.163	NULL
BW001	NULL	NULL	2257.75	0.179	NULL
BW001	2201.91	1.831	2251.61	0.0292	0.0535
BW001	2202.88	3.16	2255.65	0.0322	0.102
BW001	2205.21	2.512	2252.76	0.0248	0.0623
BW001	2209.33	2.507	2255.05	0.0278	0.0698
BW001	2207.59	1.766	2249.66	0.175	0.308
BW001	2205.62	1.067	NULL	0.246	0.262
BW001	2205.64	0.491	2248.91	0.242	0.119
BW001	NULL	NULL	2256.39	0.167	NULL
BW001	2200.74	1.145	2246.45	0.207	0.237
BW001	NULL	NULL	2256.44	0.185	NULL
BW001	2207.87	2.172	NULL	0.112	0.243
BW001	2205.49	1.337	NULL	0.304	0.407
BW001	2207.26	1.021	2258.31	0.109	0.111
BW001	2203.67	1.341	2245.09	0.232	0.311
BW001	2207.46	1.467	NULL	0.212	0.311
BW001	2203.5	1.174	2245.07	0.257	0.302
BW001	2207	0.447	2246.86	0.219	0.0978
BW001	2200.9	0.497	2248.47	0.27	0.134
BW001	2206.81	1.369	NULL	0.234	0.32
BW001	2206.77	2.603	2248.68	0.127	0.33
BW001	2203.5	0.878	NULL	0.457	0.401
BW001	2205.23	0.826	2247.68	0.429	0.355
BW001	2205.21	8.113	2245.1	0.0275	0.223
BW001	2205.4	2.288	NULL	0.104	0.239
BW001	2204.08	0.837	NULL	0.346	0.29
BW001	2203.53	1.08	NULL	0.352	0.381
BW001	2205.44	1.383	NULL	0.219	0.302
BW001	2203.23	1.182	NULL	0.433	0.511
BW001	2204.02	1.554	NULL	0.269	0.418
BW001	2205.71	1.588	NULL	0.261	0.414
BW001	2205.03	1.54	2245.1	0.195	0.3
BW001	2203.68	1.29	NULL	0.253	0.326
BW001	2202.92	1.09	2245.74	0.32	0.349
BW001	2203.84	1.365	NULL	0.259	0.353
BW001	2204.08	1.234	NULL	0.305	0.376
BW001	2205.09	1.136	NULL	0.316	0.359
BW001	2203.35	1.131	NULL	0.278	0.315

Hole	White_Mica_Al-OH	White_Mica_Crys	Chlorite_Fe-OH	Depth_Water	Depth_Al-OH
BW001	2205.91	1.411	2248.92	0.251	0.354
BW001	2202.09	0.517	NULL	0.694	0.359
BW001	2204.13	0.827	NULL	0.455	0.376
BW001	2204.6	0.753	2246.72	0.398	0.299
BW001	2202.89	0.909	2247.52	0.443	0.403
BW001	2201.91	1.032	NULL	0.26	0.269
BW001	2203.38	0.98	2248.02	0.33	0.324
BW001	2199.59	0.757	NULL	0.398	0.301
BW001	2198.32	0.607	2246.62	0.333	0.202
BW001	2199.67	0.803	2248.48	0.375	0.301
BW001	2206.05	0.654	2254.49	0.275	0.18
BW001	2199.72	0.642	2247.56	0.217	0.139
BW001	2201.52	0.638	NULL	0.421	0.269
BW001	2205.18	0.685	NULL	0.418	0.287
BW001	2197.45	0.186	2256.82	0.312	0.0581
BW001	2201.7	0.413	2248.57	0.205	0.0846
BW001	2197.87	0.315	2251.01	0.278	0.0878
BW001	2199.47	0.406	2247.15	0.241	0.098
BW001	2197.63	0.49	2248.19	0.3	0.147
BW001	2197.9	0.348	2253.54	0.314	0.109
BW001	2196.45	0.393	2252.66	0.376	0.148
BW001	2197.36	0.708	NULL	0.339	0.24
BW001	2198.24	0.487	2251.29	0.247	0.12
BW001	2200.58	0.46	2264.4	0.218	0.1
BW001	2199.51	0.388	2260.52	0.261	0.101
BW001	2203.55	0.496	2246.21	0.236	0.117
BW001	2203.71	0.727	2247.23	0.145	0.106
BW001	2205.09	0.594	2246.86	0.367	0.218
BW001	2205.95	1.373	2245.71	0.0947	0.13
BW001	2202.81	0.628	NULL	0.314	0.197
BW001	2199.52	0.272	2248.07	0.273	0.0741
BW001	2202.84	0.457	NULL	0.283	0.129
BW001	2205.37	0.393	2249.15	0.324	0.127
BW001	2202.92	0.378	2250.23	0.321	0.121
BW001	2203.44	0.734	2245.62	0.266	0.195
BW001	2201.04	0.68	NULL	0.292	0.199
BW001	2206.48	0.982	NULL	0.354	0.347
BW001	2203.33	0.508	NULL	0.296	0.15
BW001	2197.07	0.356	2250.62	0.171	0.0609
BW001	2195.53	0.236	2253.24	0.245	0.0579
BW001	2197.18	0.34	2254.34	0.276	0.0936
BW001	2196.64	0.531	2253.15	0.251	0.133
BW001	2196.97	0.407	2249.45	0.23	0.0938
BW001	2198.5	0.463	NULL	0.239	0.111
BW001	2199.65	0.351	2257.18	0.349	0.123
BW001	2197.22	0.604	NULL	0.312	0.188

Hole	White_Mica_Al-OH	White_Mica_Crys	Chlorite_Fe-OH	Depth_Water	Depth_Al-OH
BW001	2199.45	0.253	2249.98	0.318	0.0803
BW001	2204.81	0.266	2245.7	0.259	0.0688
BW001	2199.05	0.215	2253.83	0.239	0.0513
BW001	2199.77	0.436	2253.37	0.239	0.104
BW001	2198.12	0.278	2260.46	0.304	0.0845
BW001	2198.51	0.832	2246.59	0.267	0.222
BW001	2198.26	0.302	2254.61	0.235	0.0708
BW001	2204.76	0.42	2251.13	0.288	0.121
BW001	2198.45	0.277	2258.27	0.266	0.0736
BW001	2201.2	0.424	2246.62	0.327	0.139
BW001	2204.27	0.701	NULL	0.406	0.284
BW001	2202.14	0.408	2247.1	0.304	0.124
BW001	2202.51	0.527	NULL	0.199	0.105

Appendix 13: Thin sections

Thin Section Log

Type: PTS **Origin: UTAS**

ID: BW001 56.1

Name: **Marble**

Phase	**%**	**Grainsize**
Calcite	90	Up to 1mm
FeTiO	10	5-300µm

Comments:

Bands of cc ranging between 10µm – 1mm being replaced by bands of 5-300µm opaque angular mineral.

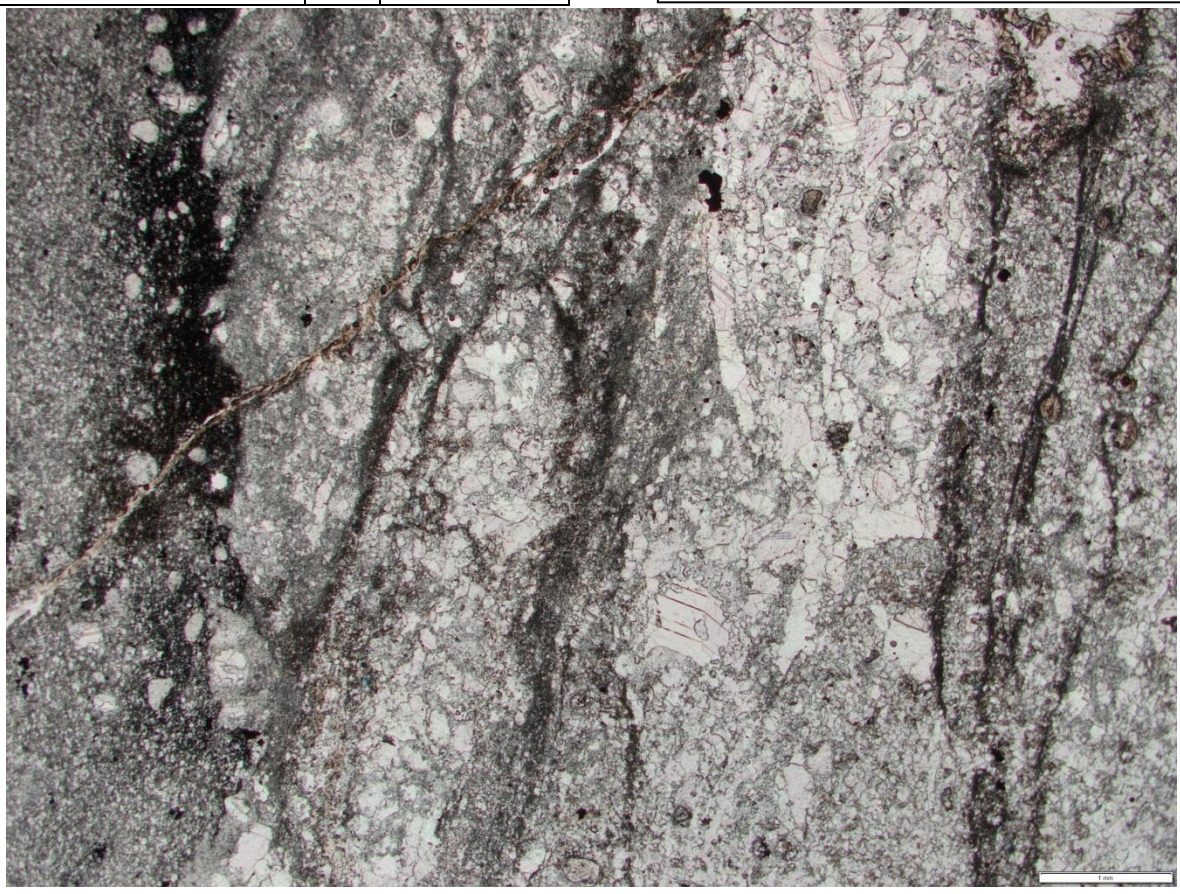

Thin Section Log

Type: PTS **Origin: UTAS**

ID: BW001 72.4

Name: ? rich Marble

Phase	**%**	**Grainsize**
calcite	95	2mm
FeTiO	Trace	100µm

Comments:

cc up to 2mm with glassy material in veins. Disseminated opaque angular mineral replacing cc

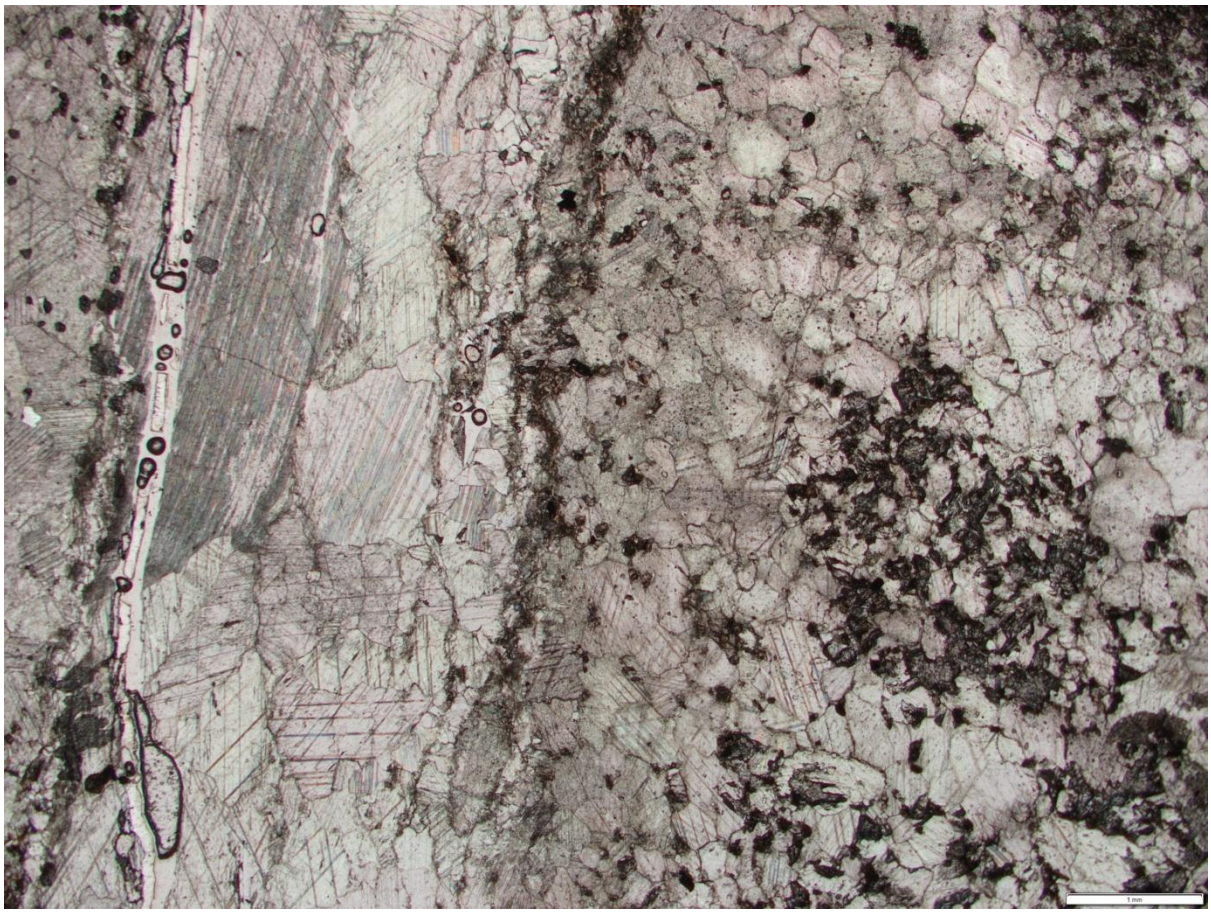

Thin Section Log

Type: PTS **Origin: UTAS**

ID: BW001 94.3

Name: **Biotite tourmaline granite**

Phase	%	Grainsize
Quartz	89	500µm
Biotite (phlogopite)	10	1mm
Tourmailne	1	3mm

Comments:

Euh qz with dis bt/phlogopite replacing qz. A single discontinouous blue-green tu vein crosscuts qz on one side of the slide

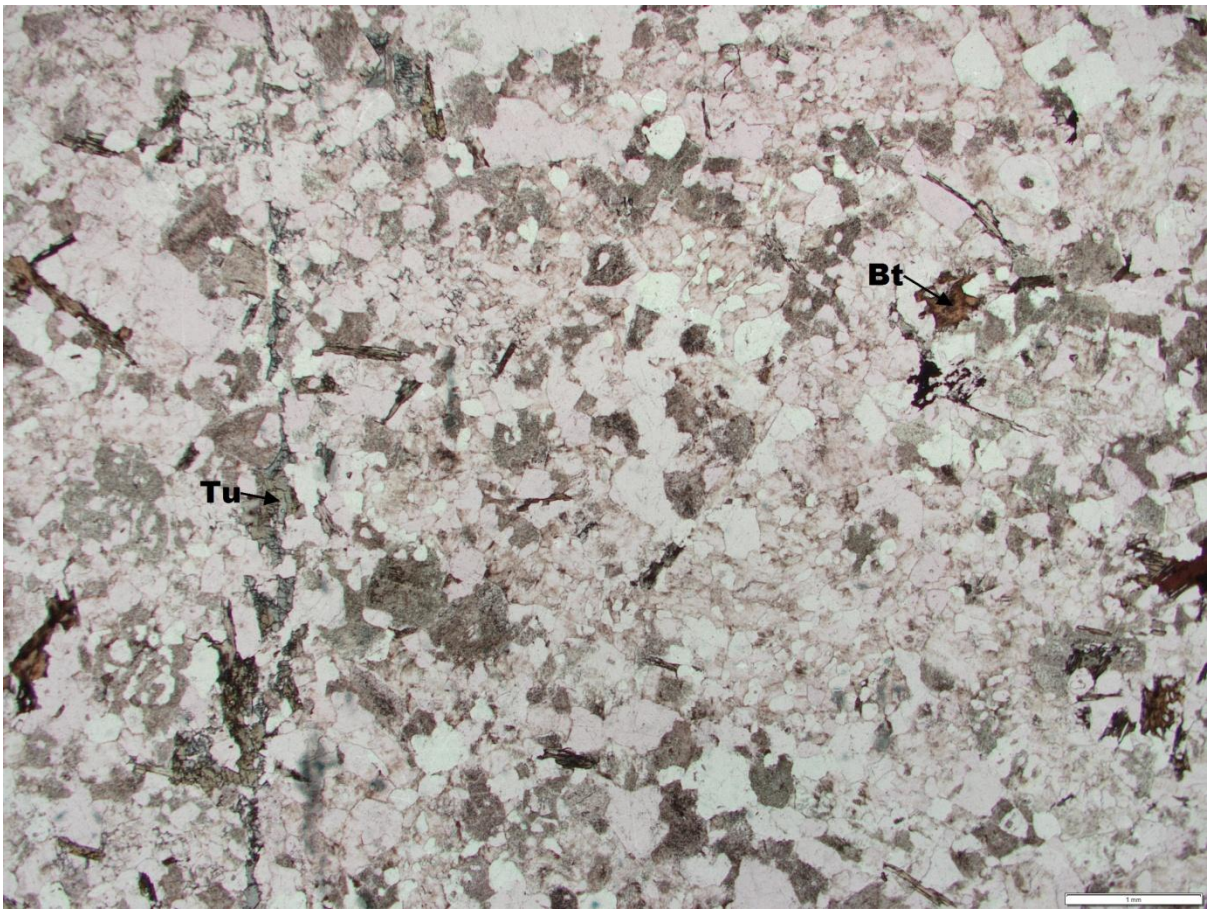

Thin Section Log

Type: PTS **Origin: UTAS**

ID: BW001 103.2

Name: **Garnett Marble**

Phase	%	Grainsize
Calcite	65	1mm
Garnet	25	100µm
Quartz	10	500 µm

Comments:

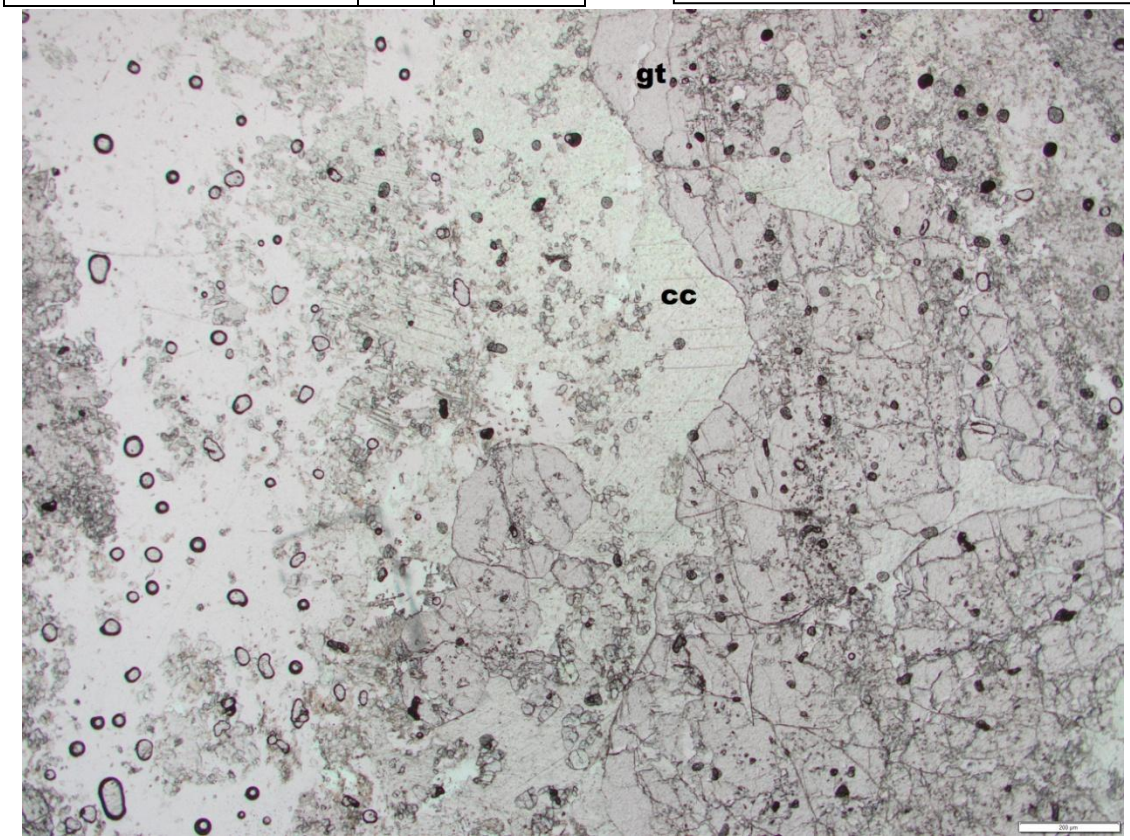

Thin Section Log

Type: PTS **Origin: UTAS**

ID: BW001 117.3

Name: Biotite rich Granite

Phase	%	Grainsize
Quartz	70	6mm
Biotite	20	2mm
Plagioclaise	10	1mm

Comments:

Biotite alteration on Granite. Plagioclase deteriorating to serecite?

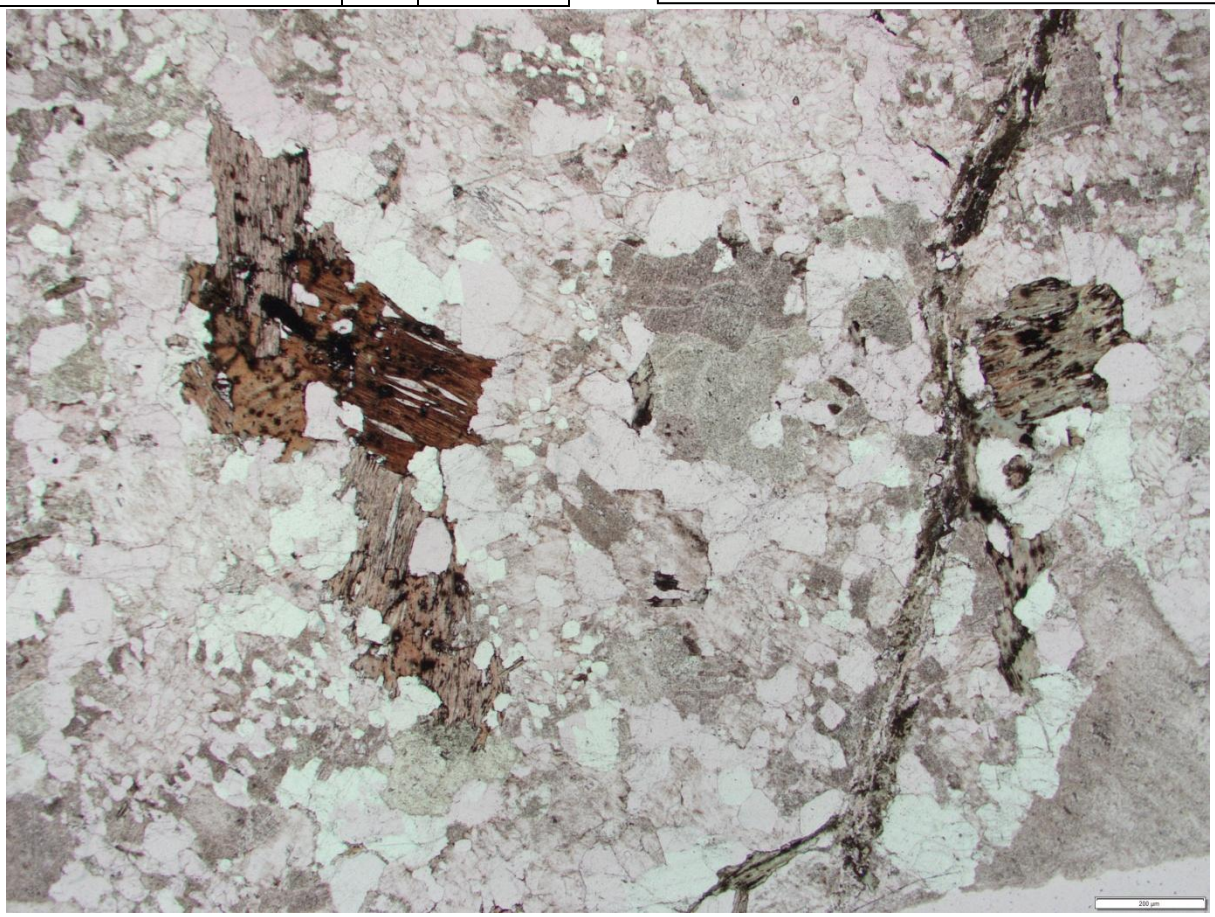

Thin Section Log

Type: PTS **Origin: UTAS**

ID: BW001 120.9

Name: **Garnet pyroxene skarn contact with garnet marble**

Phase	%	Grainsize
Garnet	45	
Calcite & other carbonate	15	
Vesuvianite	10	
Pyroxene	15	
Opaque	15	

Comments:

Contact between gtpxZMRB and gtveZXS

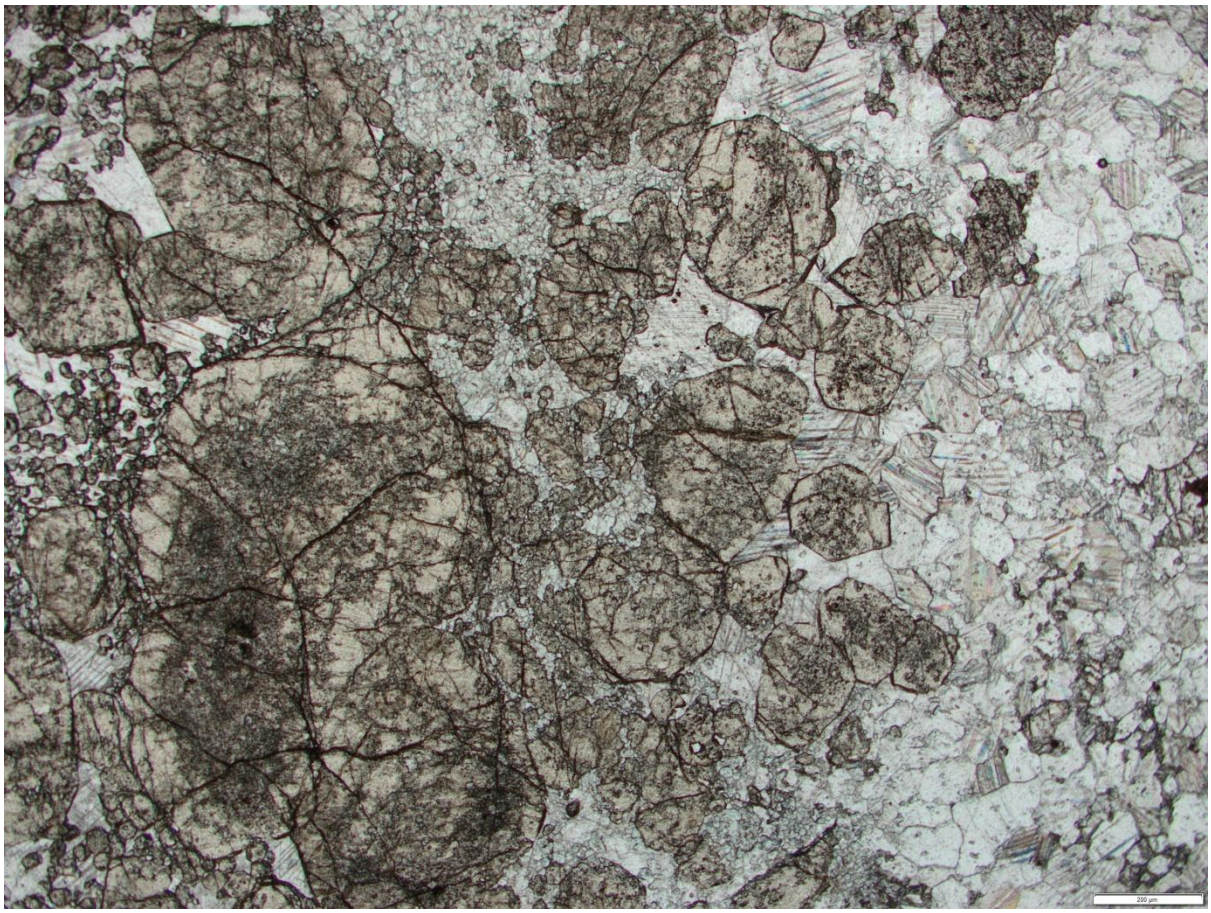

Thin Section Log

Type: PTS **Origin: UTAS**

ID: BW001 134.3

Name: Biotite rich granite

Phase	%	Grainsize
Quartz	35	1mm
Feldspar	45	1mm
Biotite	15	1mm
Serecite	5	10µm

Comments:

Occasional feldspar > serecite

Thin Section Log

Type: PTS **Origin: UTAS**

ID: BW001 140.4

Name: Biotite rich granite

Phase	%	Grainsize
Quartz	50	5mm
Feldspar	40	4mm
Biotite	10	3mm
Serecite	2	10µm
Tourmaline	?	0.5mm

Comments:

Occasional feldspar > srecite

Trace Tu?

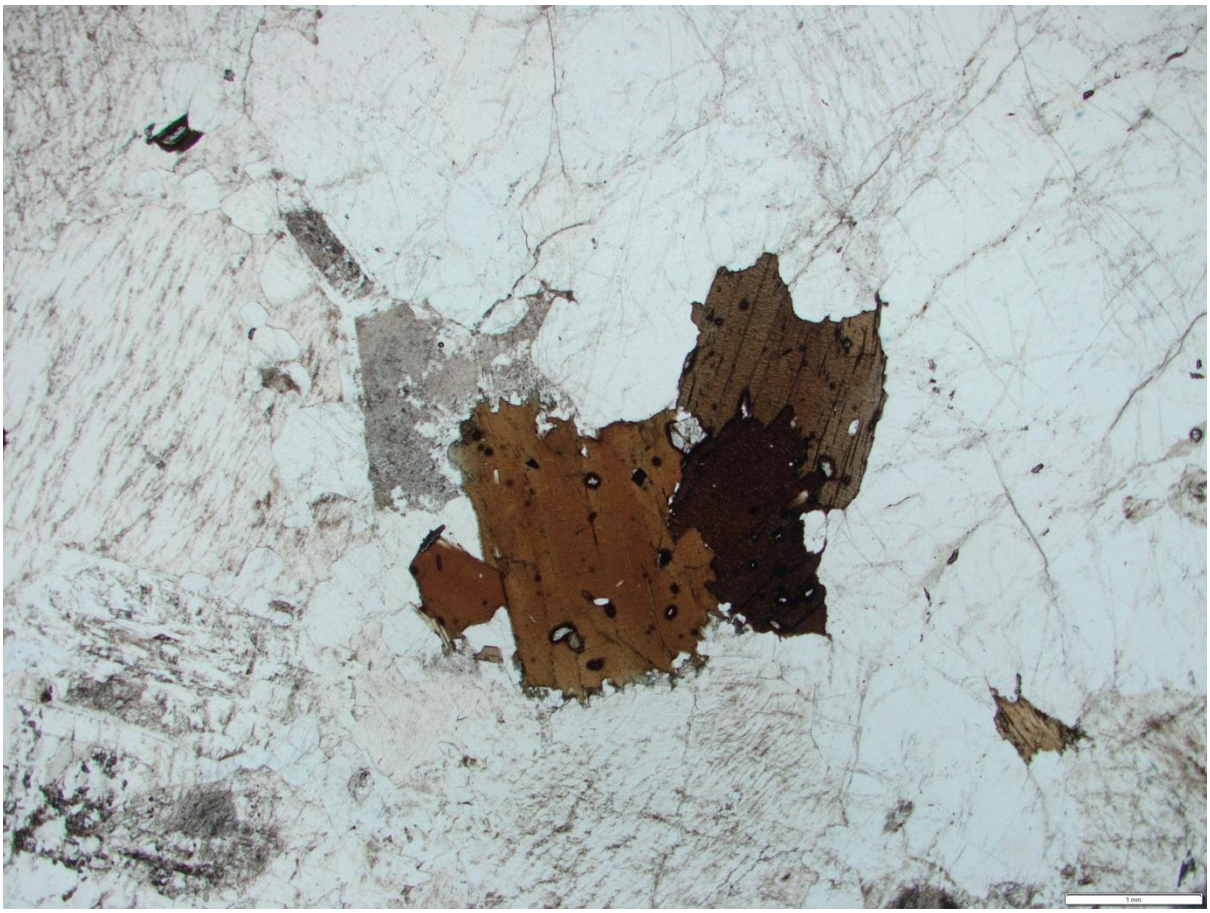

Thin Section Log

Type: PTS **Origin: UTAS**

ID: BW001 163.2

Name: Serecite altered biotite rich granite

Phase	%	Grainsize
Quartz	30	8mm
Feldspar	30	10mm
Biotite	15	3mm
Serecite	25	10µm

Comments:

Feldspars > serecite

Biotite > serecite

Thin Section Log

Type: PTS **Origin: UTAS**

ID: BW001 179.0

Name: Quartz amphibole skarn

Phase	%	Grainsize
Quartz	50	1mm
Amphibole	50	100µm

Comments:

Subrounded quartz

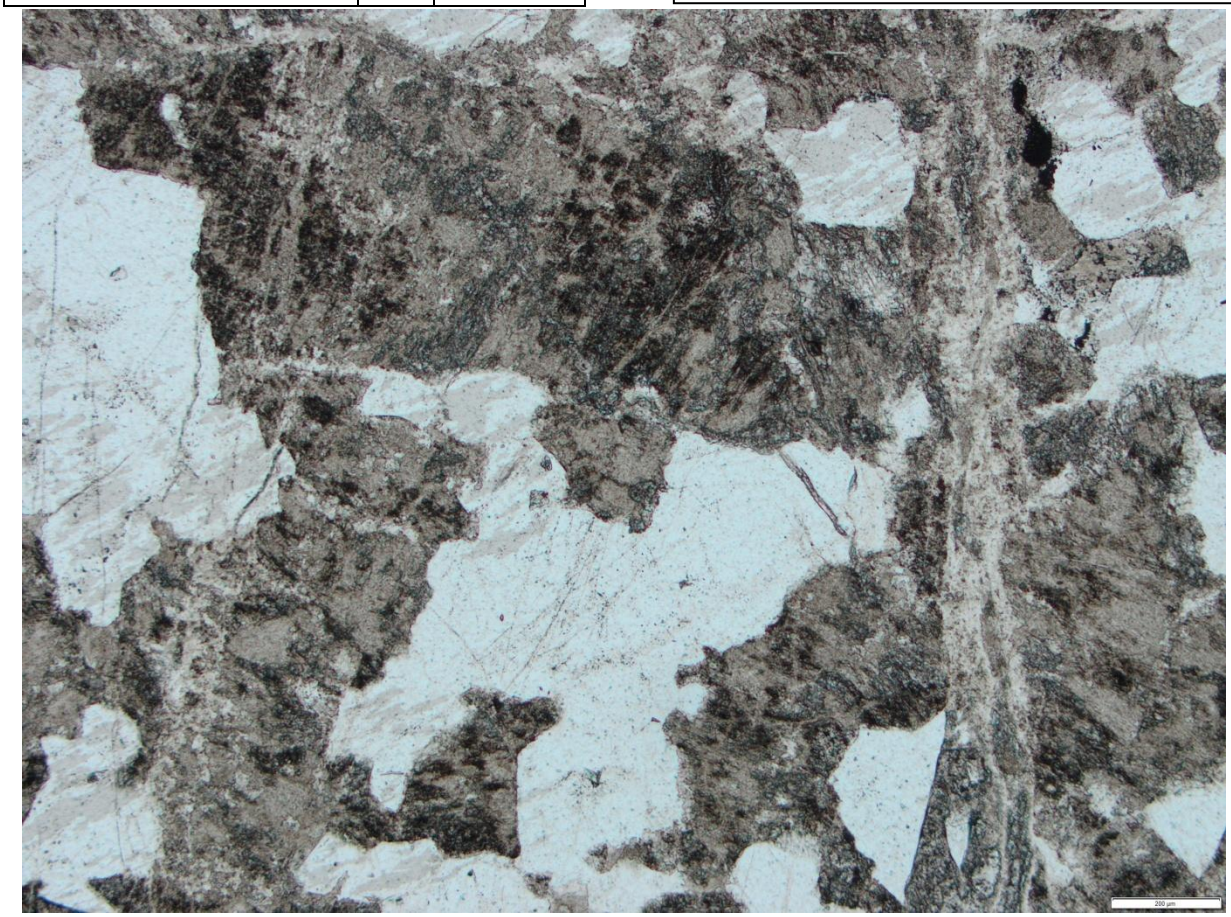

Thin Section Log

Type: PTS **Origin: UTAS**

ID: BW001 179.7

Name: Quartz-amphibole skarn

Phase	%	Grainsize
Quartz	75	2mm
Amphibole	25	.5mm

Comments:

Amphibole replacing feldspar?

Thin Section Log

Type: PTS **Origin: UTAS**

ID: BW001 200.9

Name: Vesuvianite marble

Phase	%	Grainsize
Calcite	85	200µm
Vesuvianite	5	150µm
FeTiO	10	200µm

Comments:

Fine grained ve replacing cc. Unknown opaque mineral

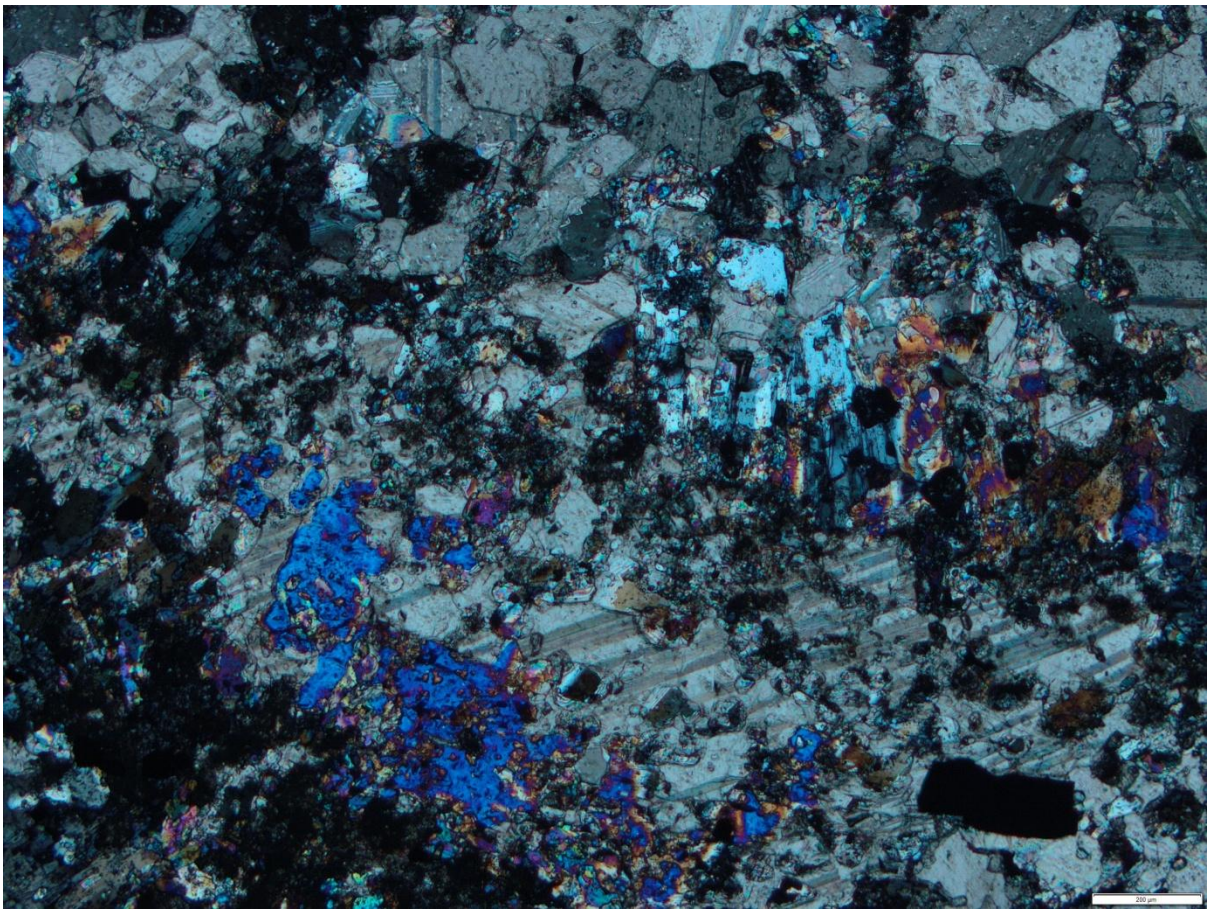

Thin Section Log

Type: TS **Origin: VMS**

ID: BW001 204.0

Name: Pyroxene, amphibole scarn

Phase	%	Grainsize
Pyroxene	70	
amphibole	10	
Cc / siderite	20	
Qz		
Titanate		
Minor sulphides	Trc	

Comments:

Cc pseudomorphing pyroxene, amphibole infilling cc vugs. Zoned amphiboles

Veins – cc + mnr qz

Thin Section Log

Type: PTS **Origin: UTAS**

ID: BW001 204.5

Name: Amphibole skarn

Phase	%	Grainsize
Amphibole	50	.5mm
calcite	45	1mm
FeTiO	5	

Comments:

Bladed amphibole infilling cc vugs

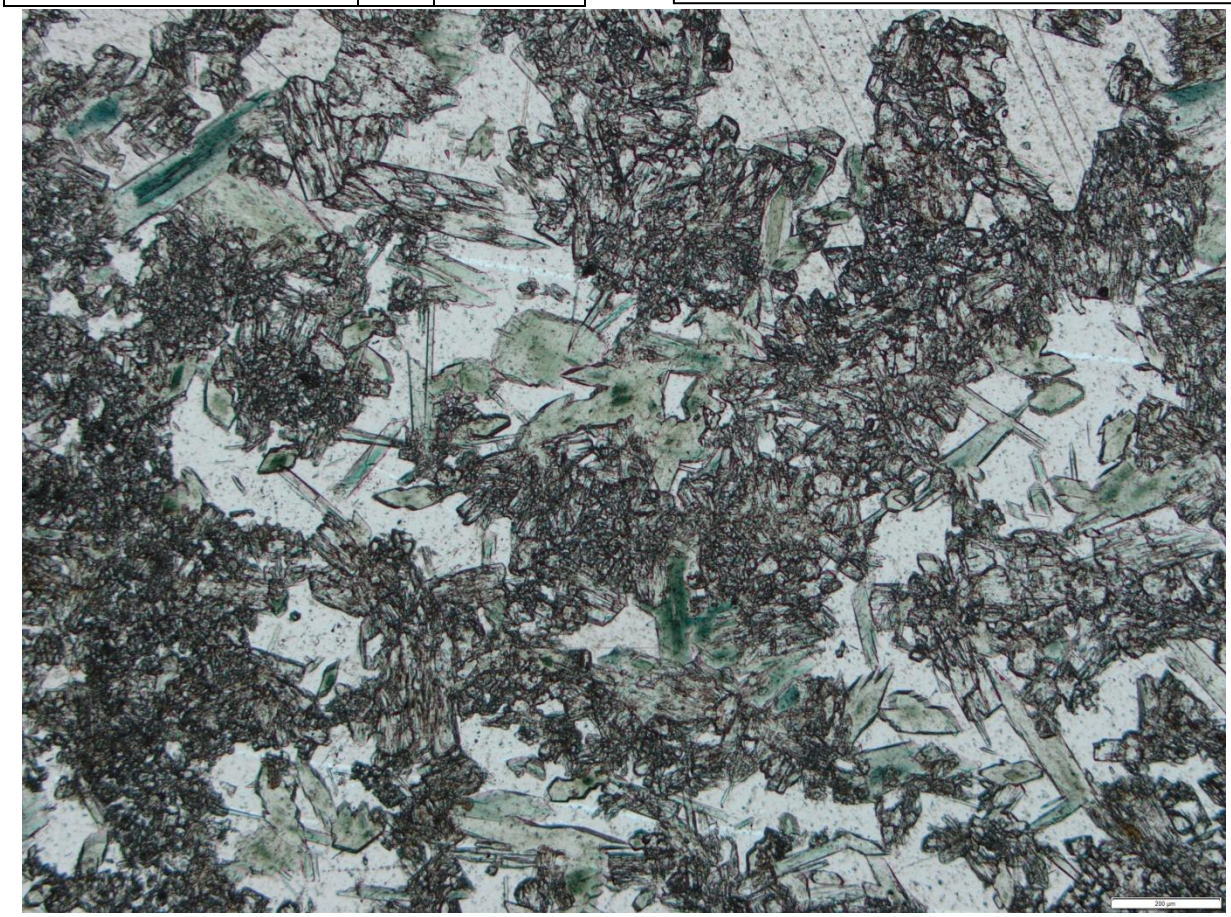

Thin Section Log

Type: TS **Origin: VMS**

ID: BW001 204.7

Name: Amphibole magnetite skarn

Phase	%	Grainsize
Magnetite	35	100µm
Amphibole	30	100µm
Pyroxene	25	100µm
Cc	5	250µm
Siderite	Tc	
sulphides	tc	

Comments:

Veins qz-cc

Granular magnetite

Magnetite replacing pyroxene?

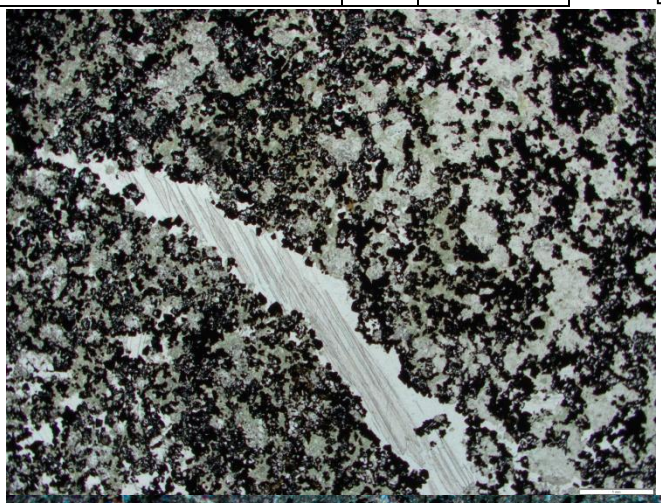

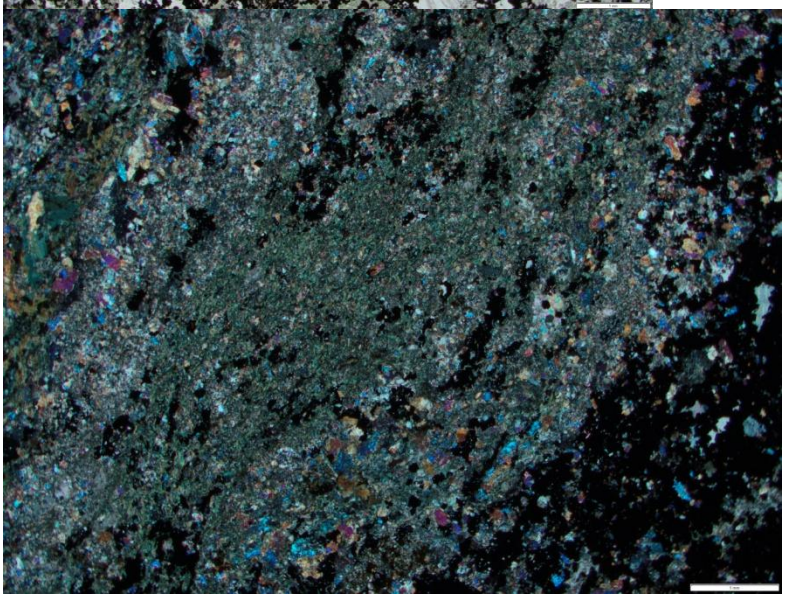

Thin Section Log

Type: TS **Origin: VMS**

ID: BW001 205.3

Name:

Phase	%	Grainsize
Magnetite	20	
Amphibole	30	
Pyroxene	30	
Vonsonite	20	
Carbonate	Tc	
Pyrite	tc	

Comments:

Zoned amphibole – magnetite + Pyroxene vonsonite

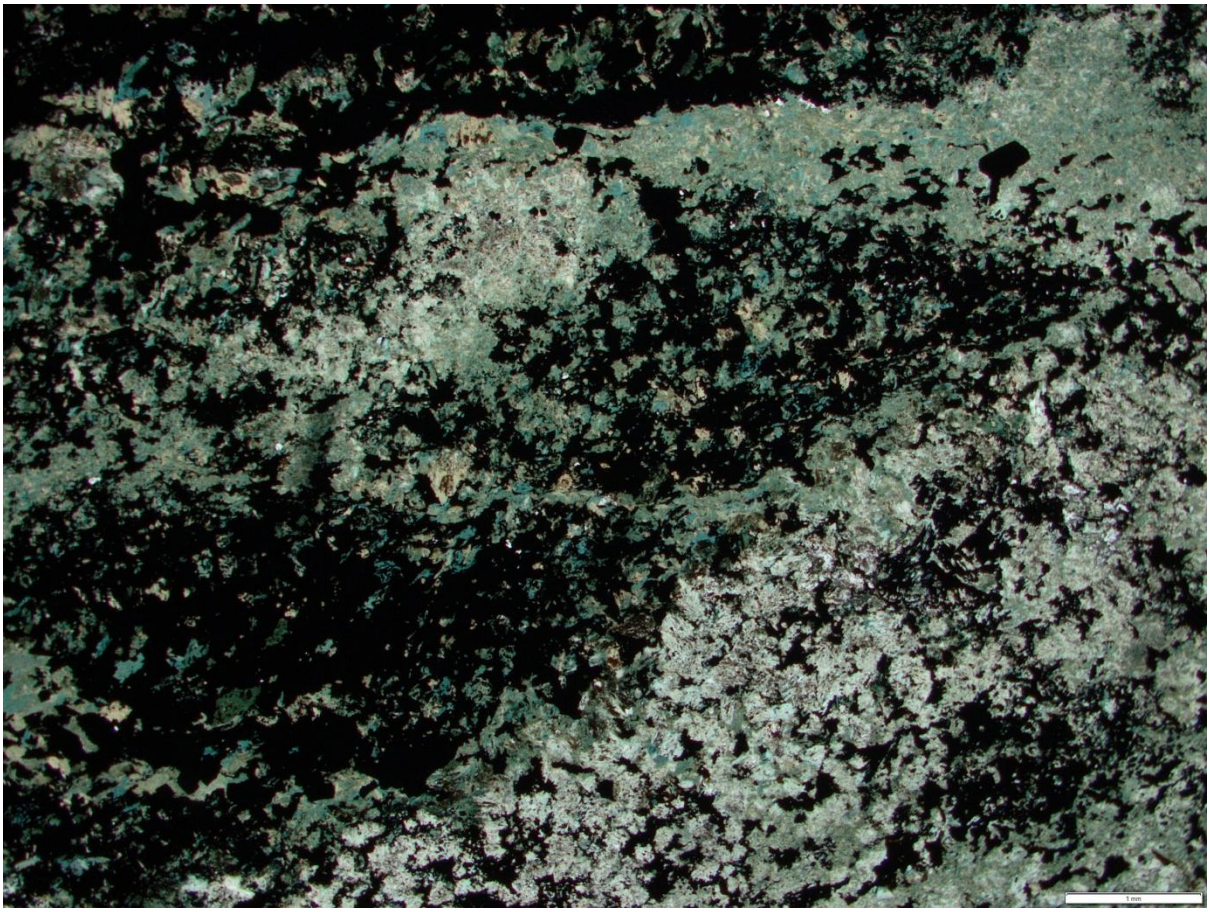

Thin Section Log

Type: TS **Origin: VMS**

ID: BW001 205.6

Name: Garnet amphibole sulphide skarn

Phase	%	Grainsize
Amphibole	50	
Suphides	30	
Garnett	20	
Cc	Tc	
Serecite	tc	

Comments:

Garnet overprinted by pyroxene - amphibole

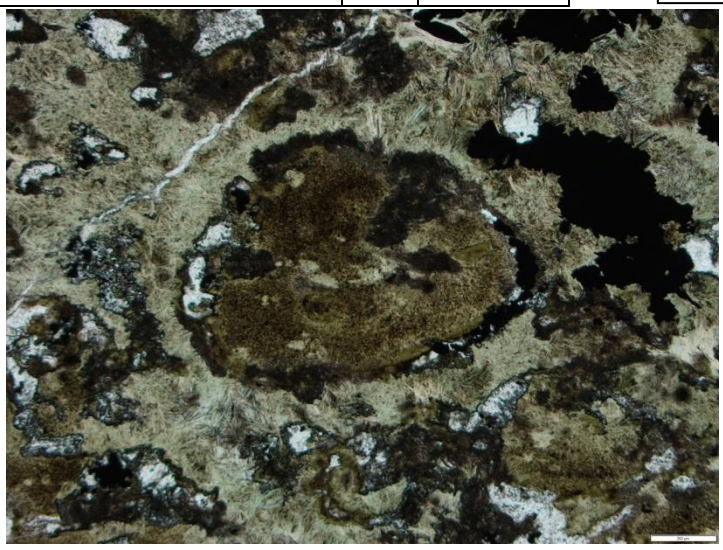

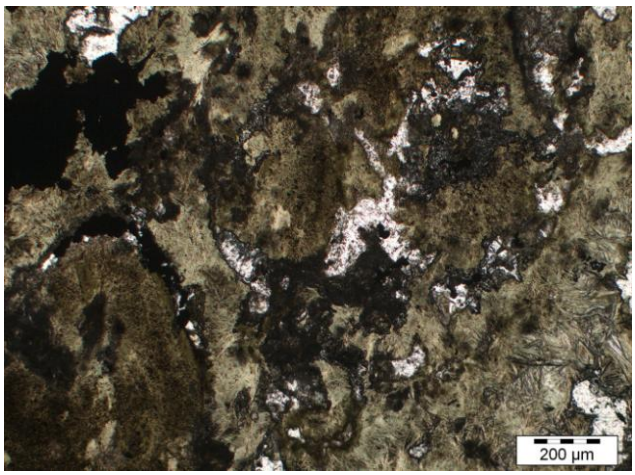

Thin Section Log

Type: TS **Origin: VMS**

ID: BW001 205.8

Name: Amphibole vonsonite scarn

Phase	%	Grainsize
Vonsonite	43	
Amphibole	55	
pyroxene	1	
Cc veins	1	
Garnet in veins	tc	

Comments:

Add comments here

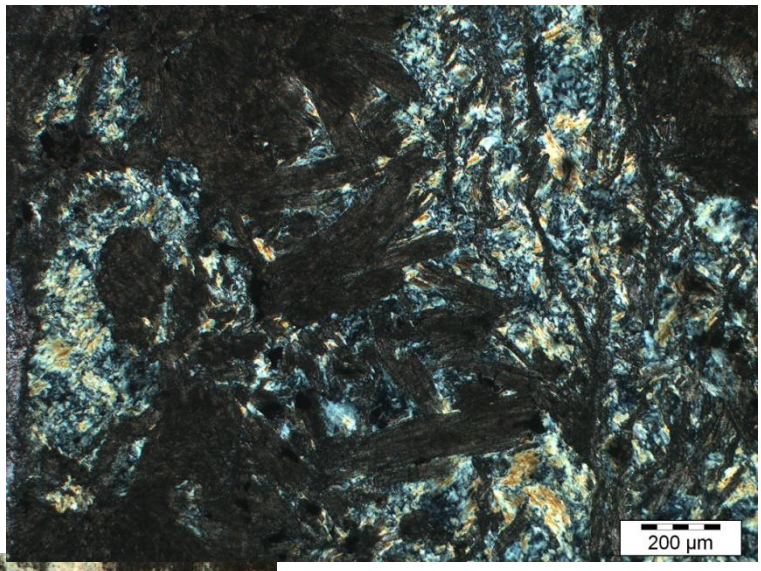

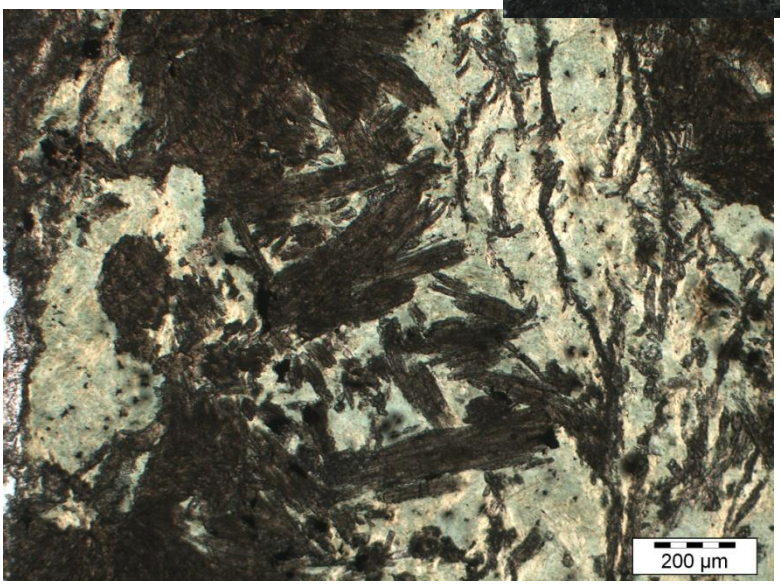

Thin Section Log

Type: PTS **Origin: UTAS**

ID: **BW001 206.3**

Name: CC vein in Amphibole magnetite vonsenite skarn

Phase	%	Grainsize
Amphiblole	60	
Magnetite	20	
Vonsenite	10	
Calcite	5	
pyroxene	5	

Comments:

Sd vein? mt replacing vo

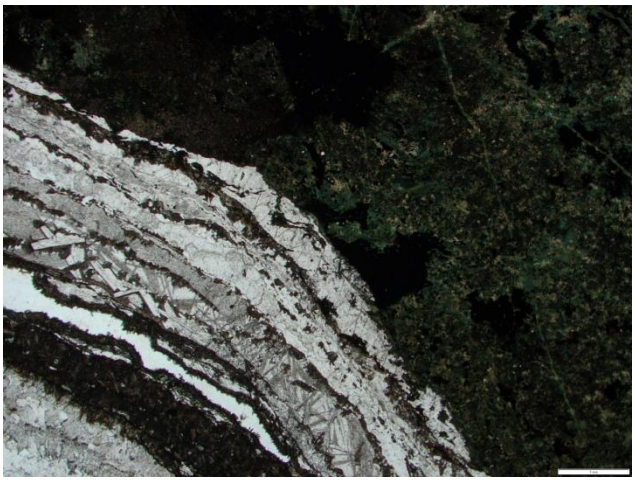

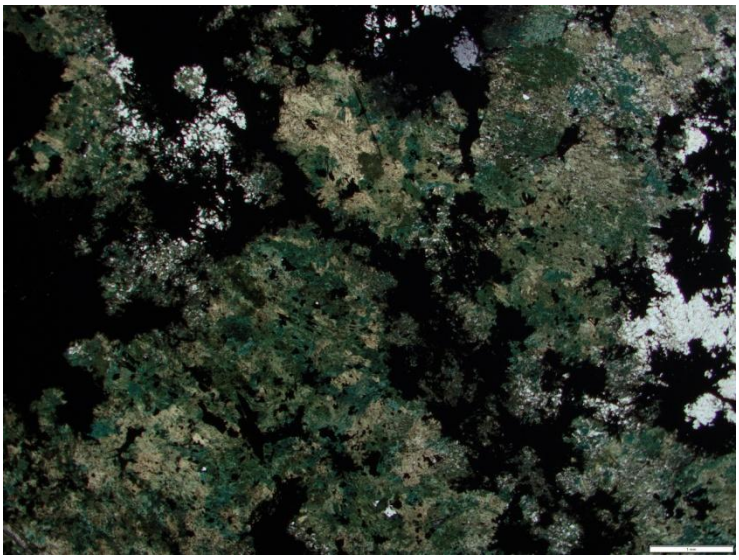

Thin Section Log

Type: TS **Origin: VMS**

ID: BW001 206.7

Name: Vonsenite amphibole skarn

Phase	%	Grainsize
Amphibole	15	
Vonsonite	40	
pyroxene	Trace	
garnet	4	
qz	1	
cc	Trace	

Comments:

Vonsonite > amphibole > garnet

Vonsonite + amphibole replacing garnet

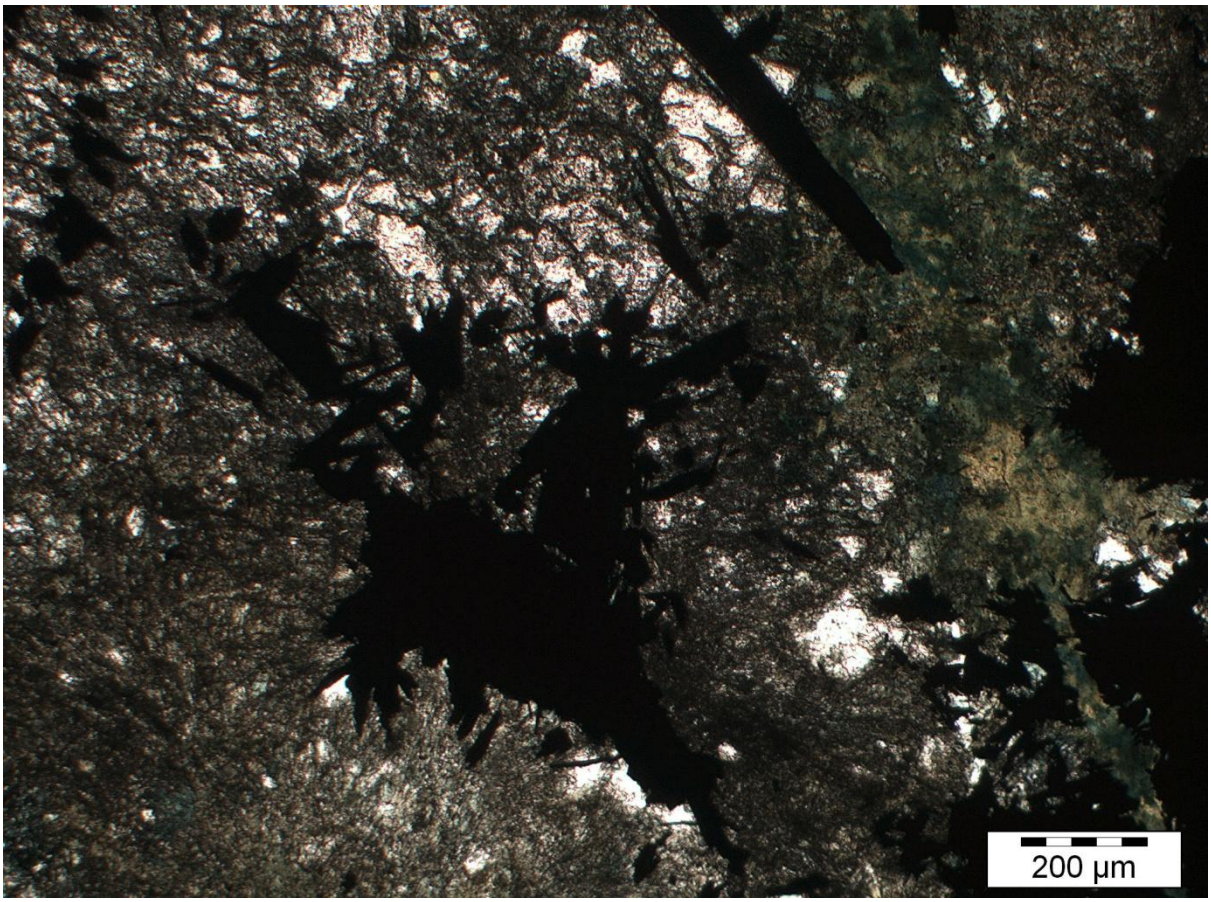

Thin Section Log

Type: PTS **Origin: UTAS**

ID: BW001 208.9

Name:

Phase	**%**	**Grainsize**
Actinolite		
Pyroxene		
Hematite (vonsonite?)		
Garnet		
Pyrrotite		
cpy		

Comments:

Thin Section Log

Type: PTS **Origin: UTAS**

ID: BW001 210.5

Name: Phyrrotite amphibole skarn

Phase	%	Grainsize
Pyrite	10	.25mm
Phyrrotite	20	.25mm
Garnett	15	.1mm
Amphibole	35	.2mm
Quartz	20	.4mm

Comments:

Gt vein separating phyrrotite from amphibole skarn – pyrite/amphibole oxidising in slide

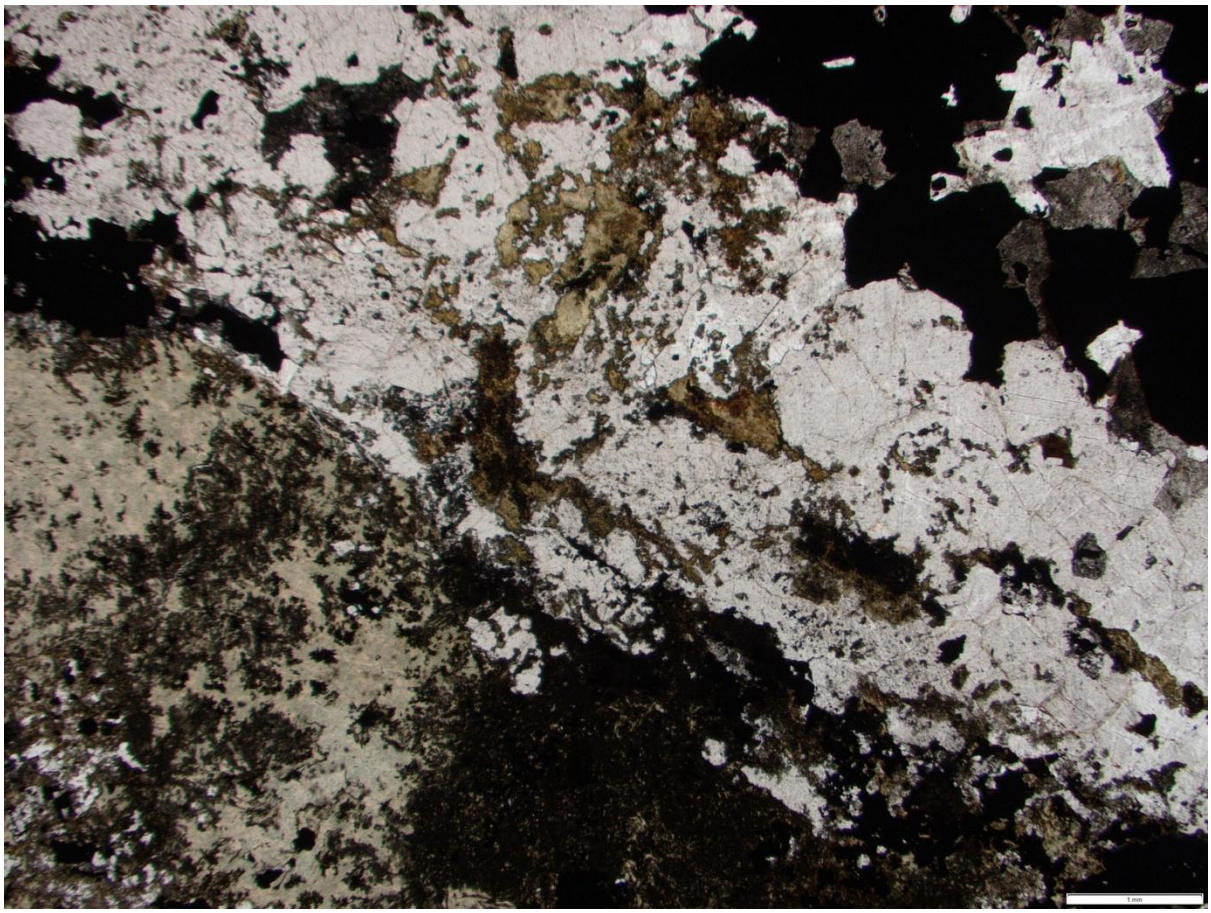

Thin Section Log

Type: TS **Origin: VMS**

ID: BW001 210.6

Name:

Phase	%	Grainsize
Qz	10	
Pyroxene	5	
Garnett	2	
Sulphides	25	
Amphibole	25	
Siderite	20	
Cassiterite	5/10	

Comments:

Qz veins – Mystery yellow – cassiterite?

Siderite?

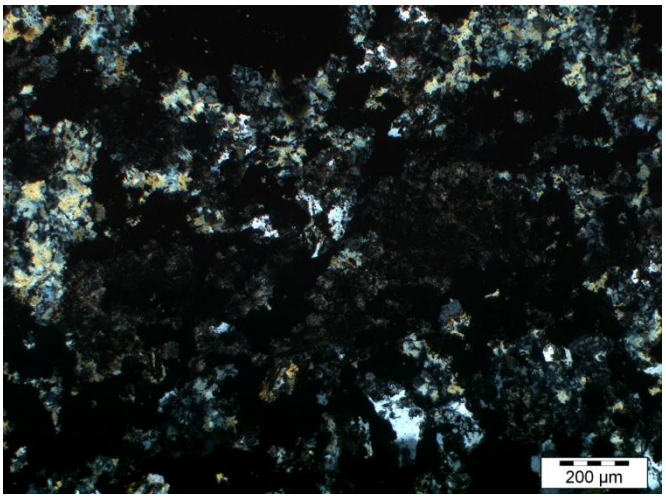

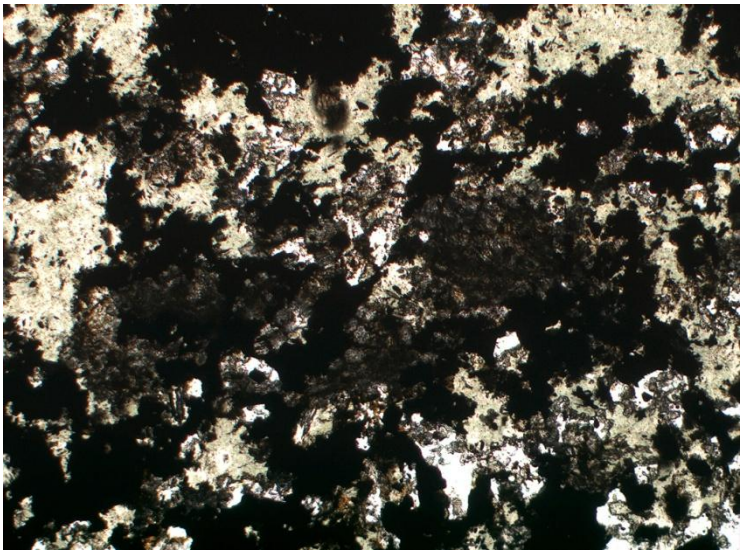

Thin Section Log

Type: TS **Origin: VMS**

ID: BW001 212.2

Name: Quartz carbonate amphibole pyrite scarn

Phase	%	Grainsize
Pyrite	20	4mm
Quartz	20	
Amphibole	30	
Pyroxene	5	
carbonate	25	

Comments:

Cc veins crosscutting amphibole – amphibole overprinting quartz

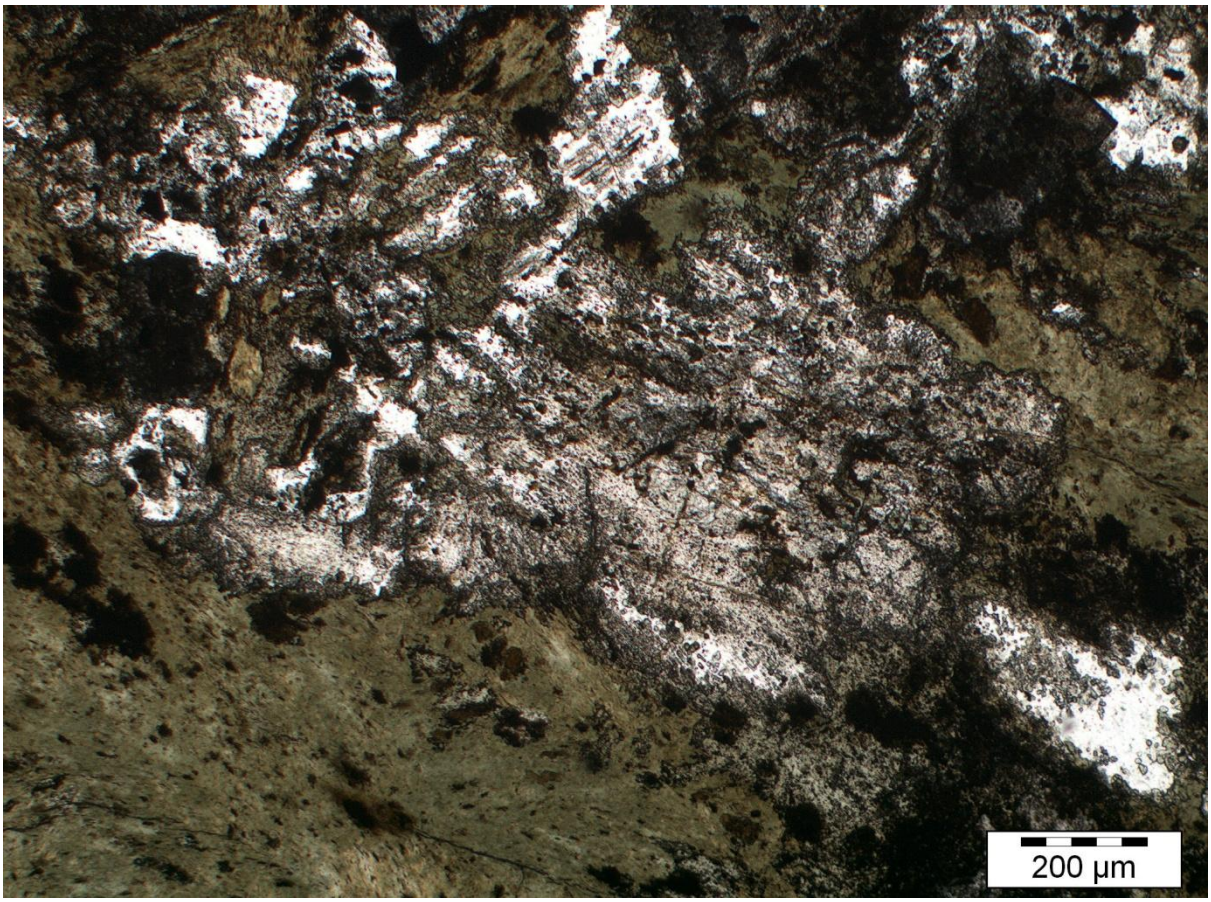

Thin Section Log

Type: TS **Origin: VMS**

ID: BW001 212.9

Name:

Phase	%	Grainsize
Pyrite	40	2mm
Calcite	20	2mm
UM	40	

Comments:

Add comments here

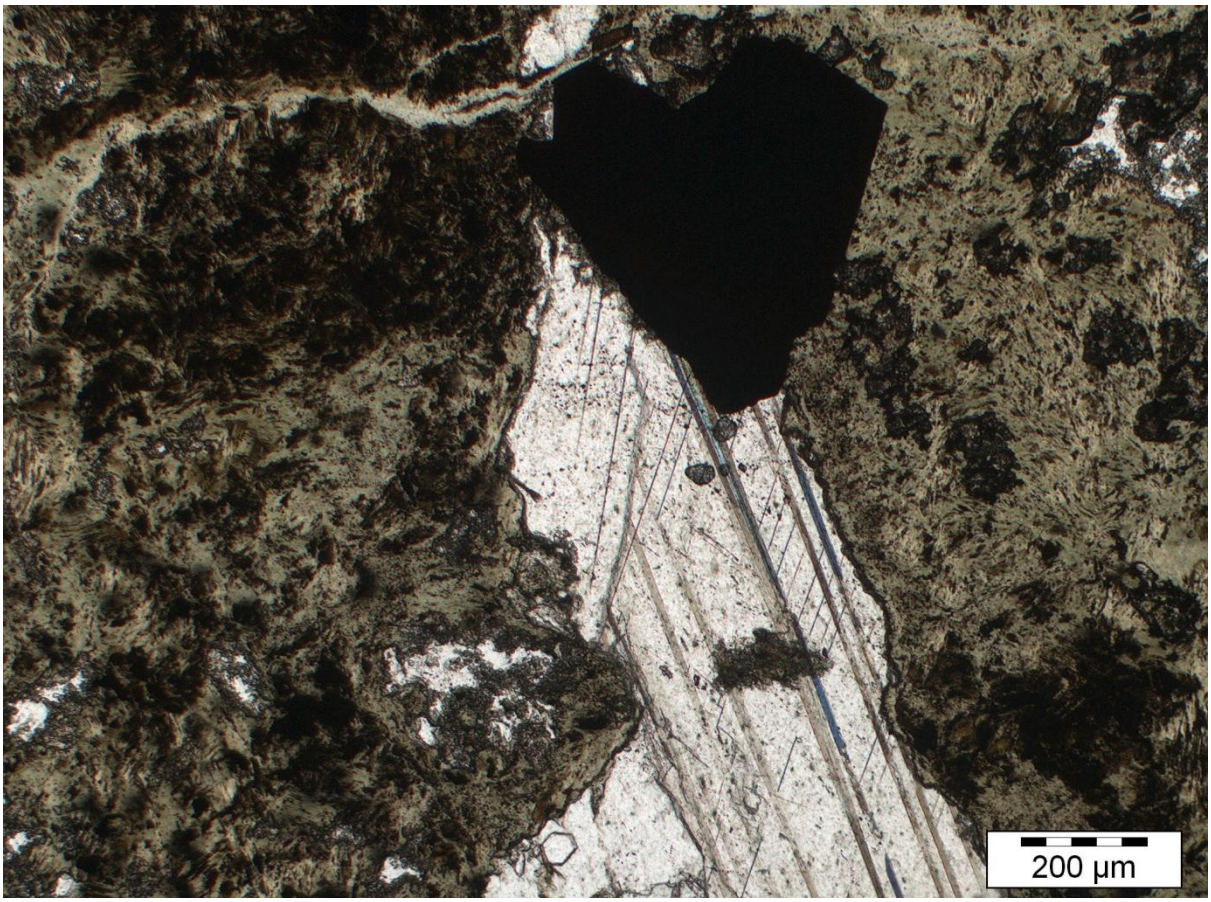

Thin Section Log

Type: TS **Origin: VMS**

ID: BW001 213.2

Name: quartz carbonate vein crosscutting amphibole Vonsenite skarn

Phase	%	Grainsize
Quartz	30	2mm
Calcite	5	1mm
amphibole	39	.5mm
Pyrite	1	
Vonsenite	25	

Comments:

Qz – vein crosscutting am-vo skarn

Thin Section Log

Type: TS **Origin: VMS**

ID: BW001 214.3

Name: quartz-carbonate-garnet skarn

Phase	%	Grainsize
Quartz	40	2mm
Calcite	35	3mm
Garnet	8	5mm
Pyrite	15	5mm
FeO? Bt?	2	.1mm

Comments:

FeO? Bt? replacing cc –

Py infilling cracks in cc – between cc crystals

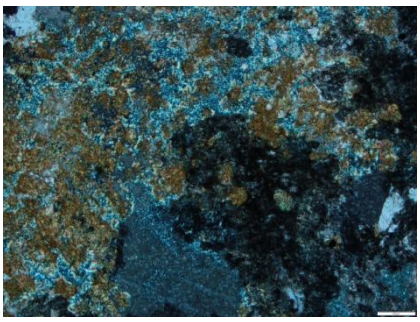

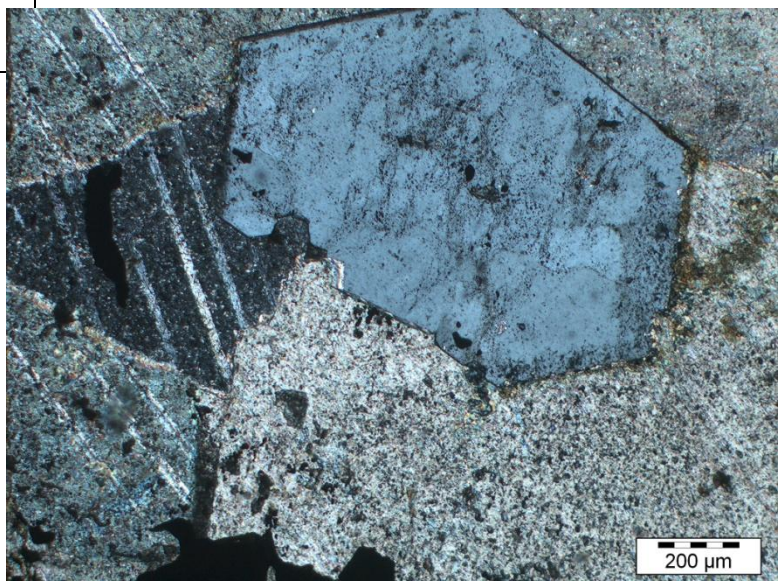

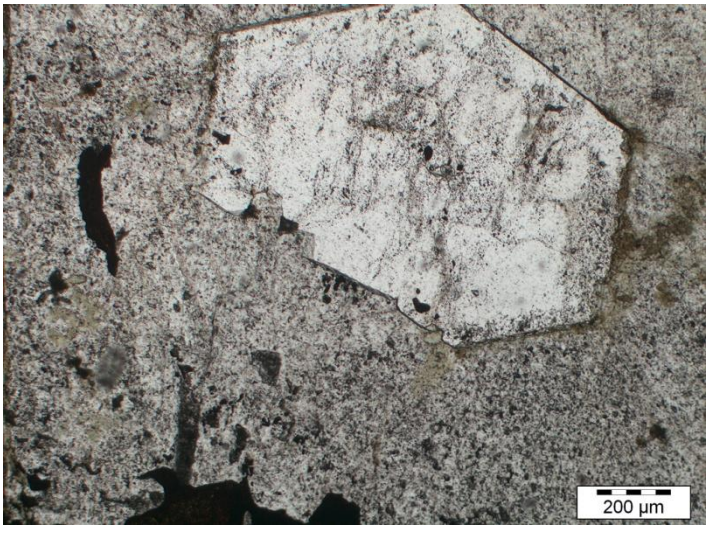

Thin Section Log

Type: TS **Origin: VMS**

ID: BW001 215.4

Name:

Phase	%	Grainsize

Comments:

Add comments here

Thin Section Log

Type: PTS **Origin: UTAS**

ID: BW001 215.7

Name:

Phase	%	Grainsize
Quartz		
Plag - albite		
Epidote?		
Augite		
Chalcopyrite		
Cassiterite		
Vonsenite		
Pink sulphide		
Pyrite		
Phyrrotite		
Calcite		
Serecite		

Comments:

Vonsenite, abundant cassiterite, euh qz, feldspars going to serecite.

Amphibole replacing vonsenite

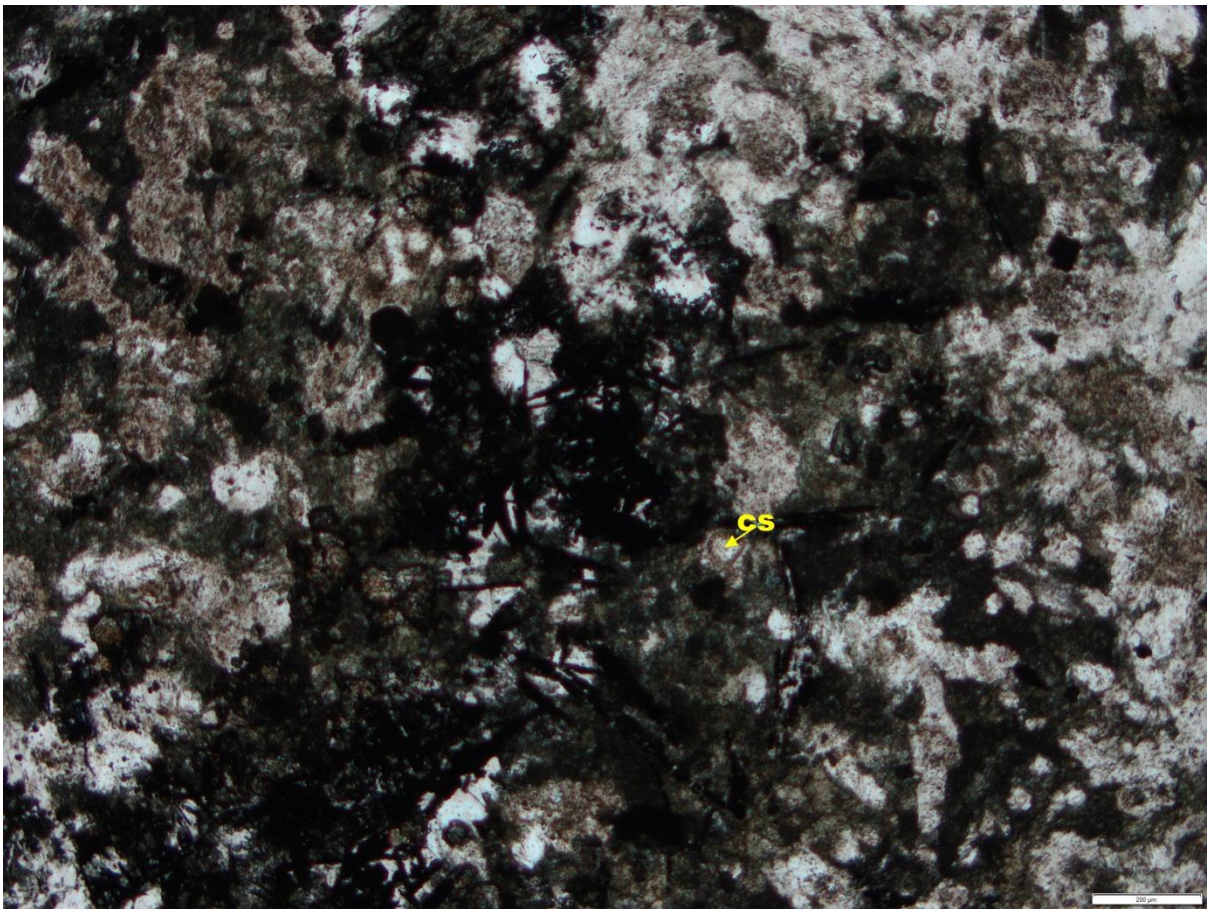

Thin Section Log

Type: TS **Origin: VMS**

ID: BW001 216.6

Name: Amphibole magnetite skarn

Phase	%	Grainsize
Amphibloe	42	1mm
Magnetite	38	1mm
Calcite	20	1mm

Comments:

Cc veining in ammtZXS

Not sure if am is replacing mt or mt replacing am

Thin Section Log

Type: TS **Origin: VMS**

ID: BW001 216.8

Name:

Phase	%	Grainsize
Amphibole	15	.1mm
Pyroxene	45	.1mm
Garnet	15	.1mm
Calcite	5	.1mm
Quartz	10	.1mm
Pyrite	5	1mm
Pyrrhotite	5	.2mm

Comments:

Sulphides replacing calc-silicates?

.1mm qzccV

Am replacing px

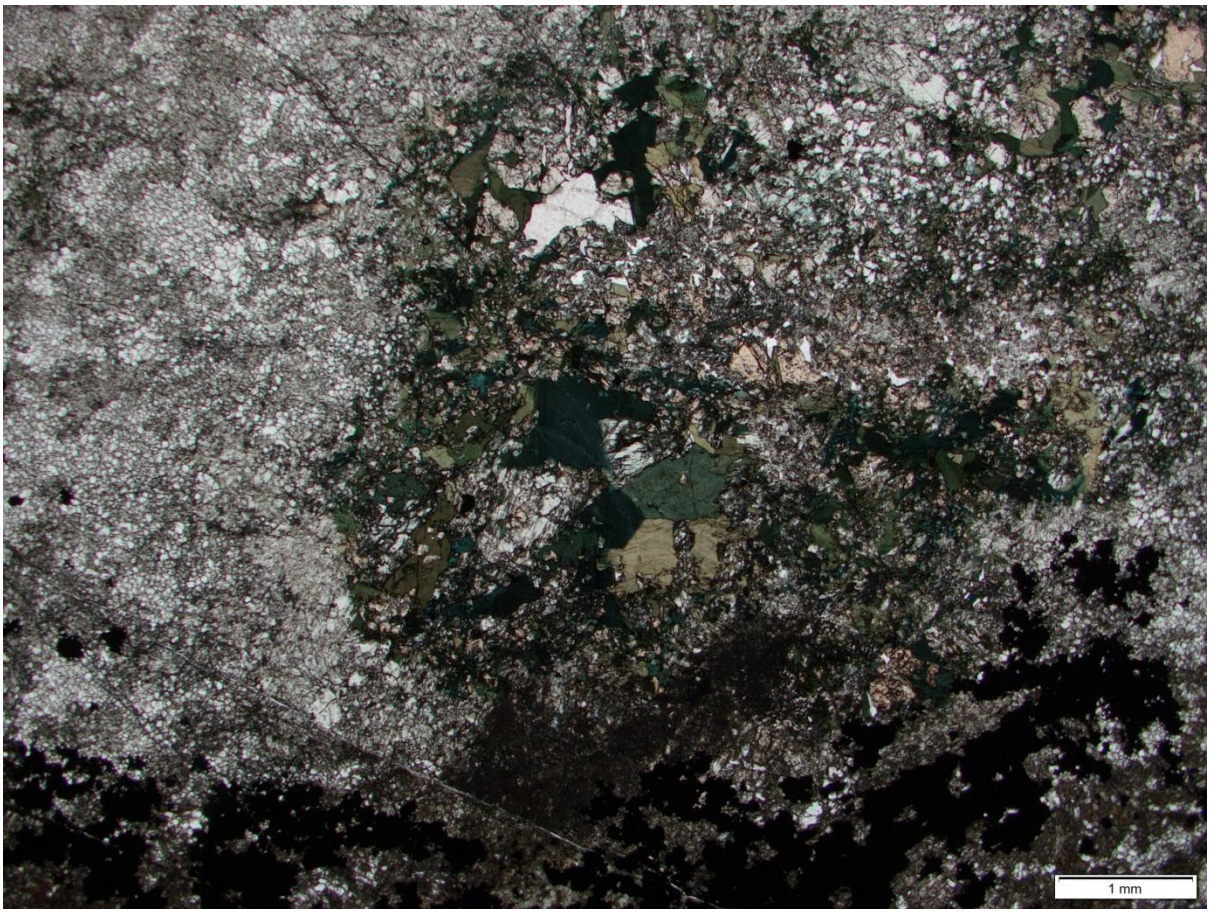

Thin Section Log

Type: TS **Origin: VMS**

ID: BW001 217.1

Name: amphibole magnetite cassiterite skarn

Phase	%	Grainsize
Amphibole	60	.1mm
Magnetite	32	.2mm
Cassiterite	2	.01mm
Calcite	1	.2mm
quartz	5	10µm

Comments:

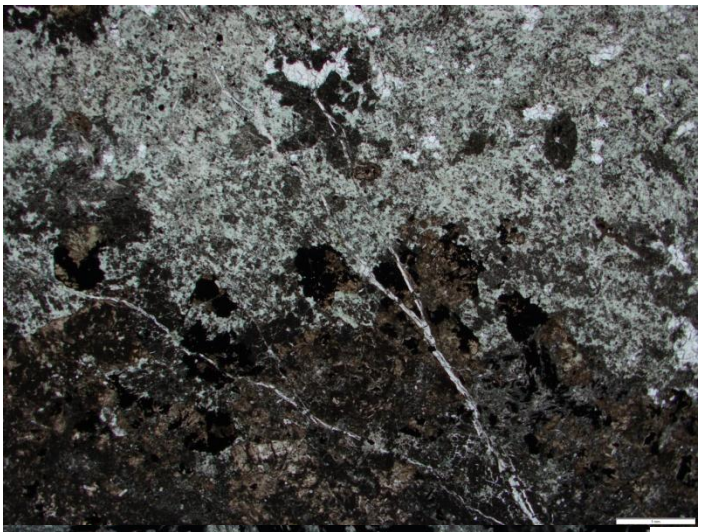

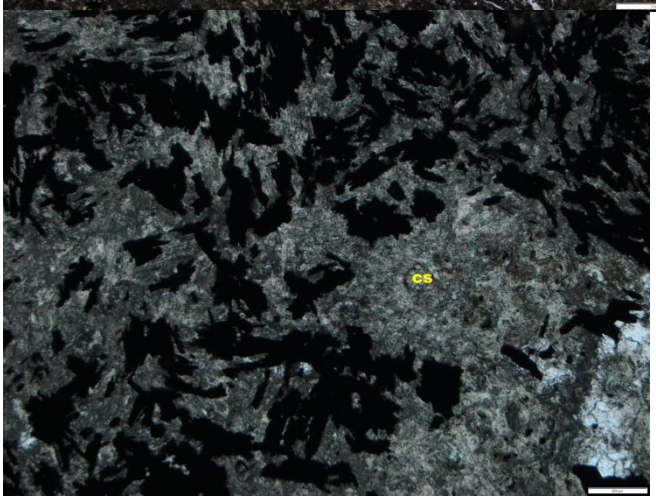

Thin Section Log

Type: TS **Origin: VMS**

ID: BW001 218.9

Name: serecite chlorite altered granite

Phase	%	Grainsize
Quartz	50	4mm
Serecite	30	.1mm
Tourmaline	4	.5mm
Chlorite	15	1mm
Garnet	1	1mm

Comments: serecite overprinting qz – Serecite-chlorite completely replacing feldspar

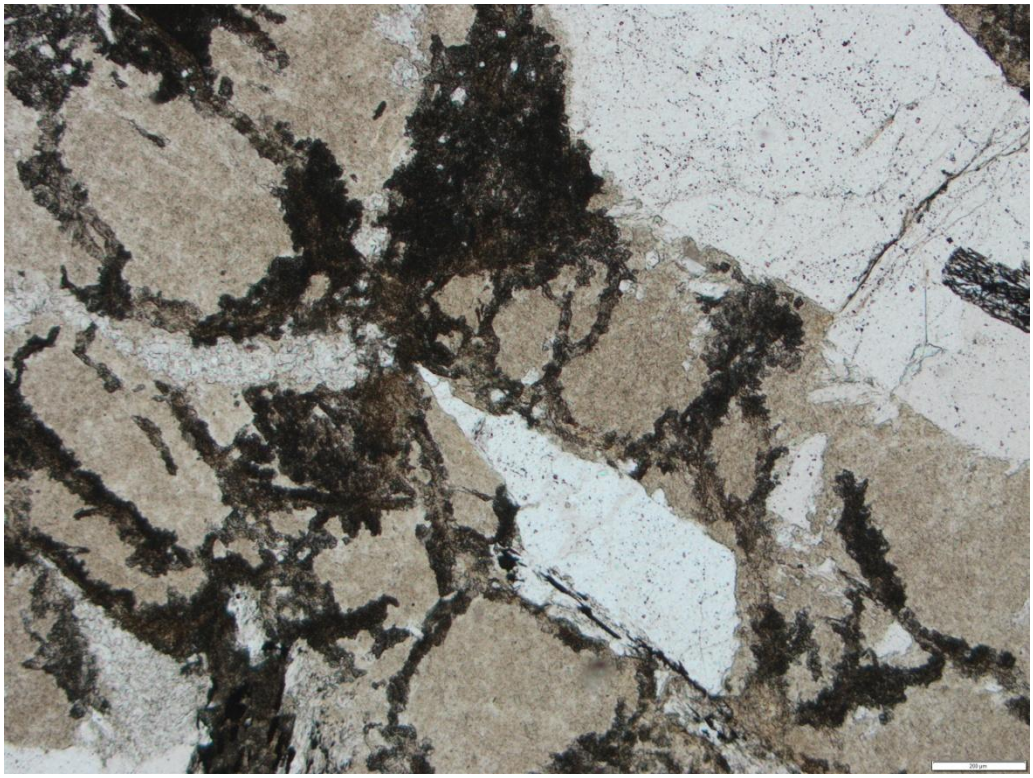

Thin Section Log

Type: TS **Origin: VMS**

ID: BW001 221.7

Name: chlorite siderite carbonate altered granite

Phase	%	Grainsize
Quartz	40	2mm
Calcite	10	1mm
Chlorite	25	.5mm
serecite	25	1mm

Comments:

Se replacing qz – fsp? Chlorite replacing se?

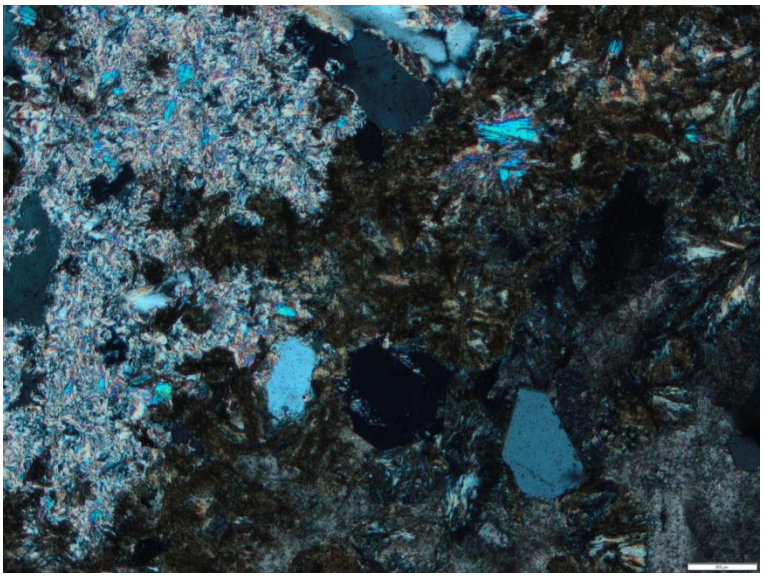

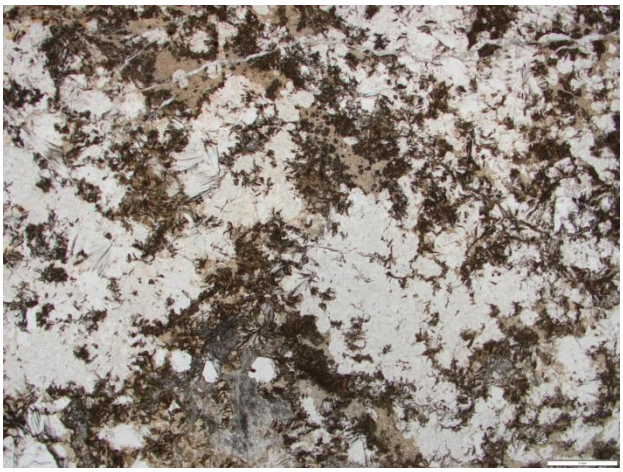

Thin Section Log

Type: PTS **Origin: UTAS**

ID: BW001 231.0

Name:

Phase	%	Grainsize

Comments:

Add comments here

Thin Section Log

Type: TS **Origin: VMS**

ID: BW001 231.3

Name: serecite chlorite altered granite

Phase	%	Grainsize
Serecite	25	.1mm
Quartz	65	5mm
chlorite	10	.25mm

Comments:

Quartz replaced by serecite/chlorite

No feldspar – perhaps completely replaced by se

Thin Section Log

Type: TS **Origin: VMS**

ID: BW001 233.4

Name: serecite altered quartzite

Phase	%	Grainsize
Quartz	50	5mm
Serecite	39	.1mm
Biotite	10	2mm
Chlorite	1	.2mm
tourmaline	.1	

Comments:

Se replacing quartz & biotite. No original feldspar

Cl replacing biotite

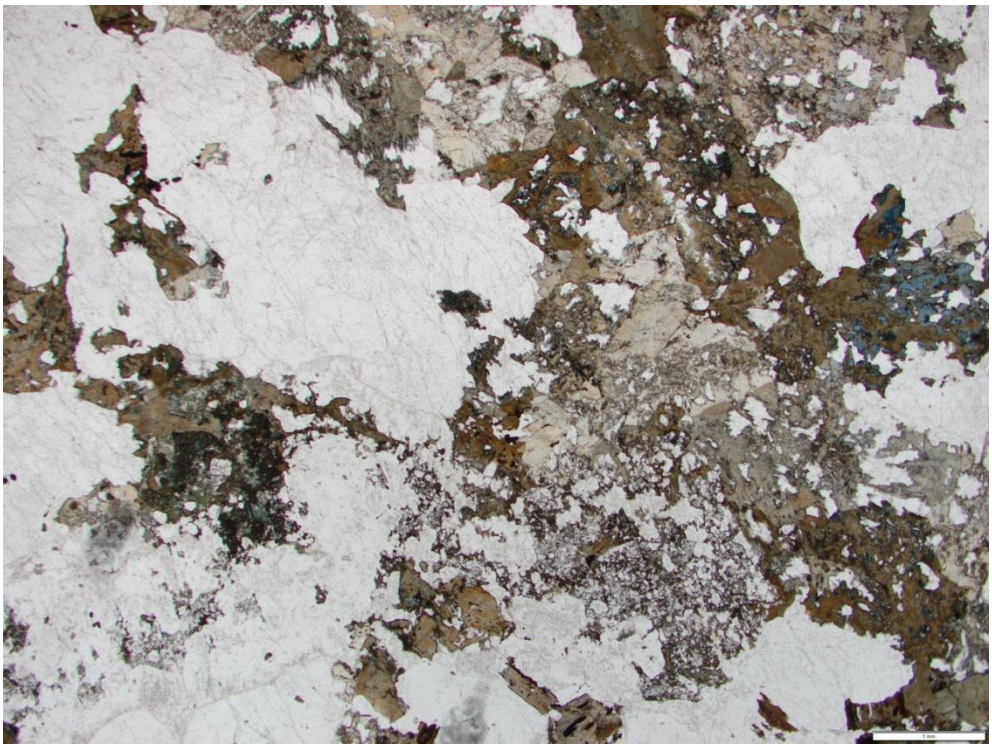

Thin Section Log

Type: TS **Origin: VMS**

ID: BW001 234.4

Name:

Phase	%	Grainsize
Quartz	60	5mm
Serecite	35	.1mm
Garnet?	?	2mm
FeTiO	5	.2mm

Comments:

Se replacing quartz. No original feldspar

Garnet? Or isotropic qz?

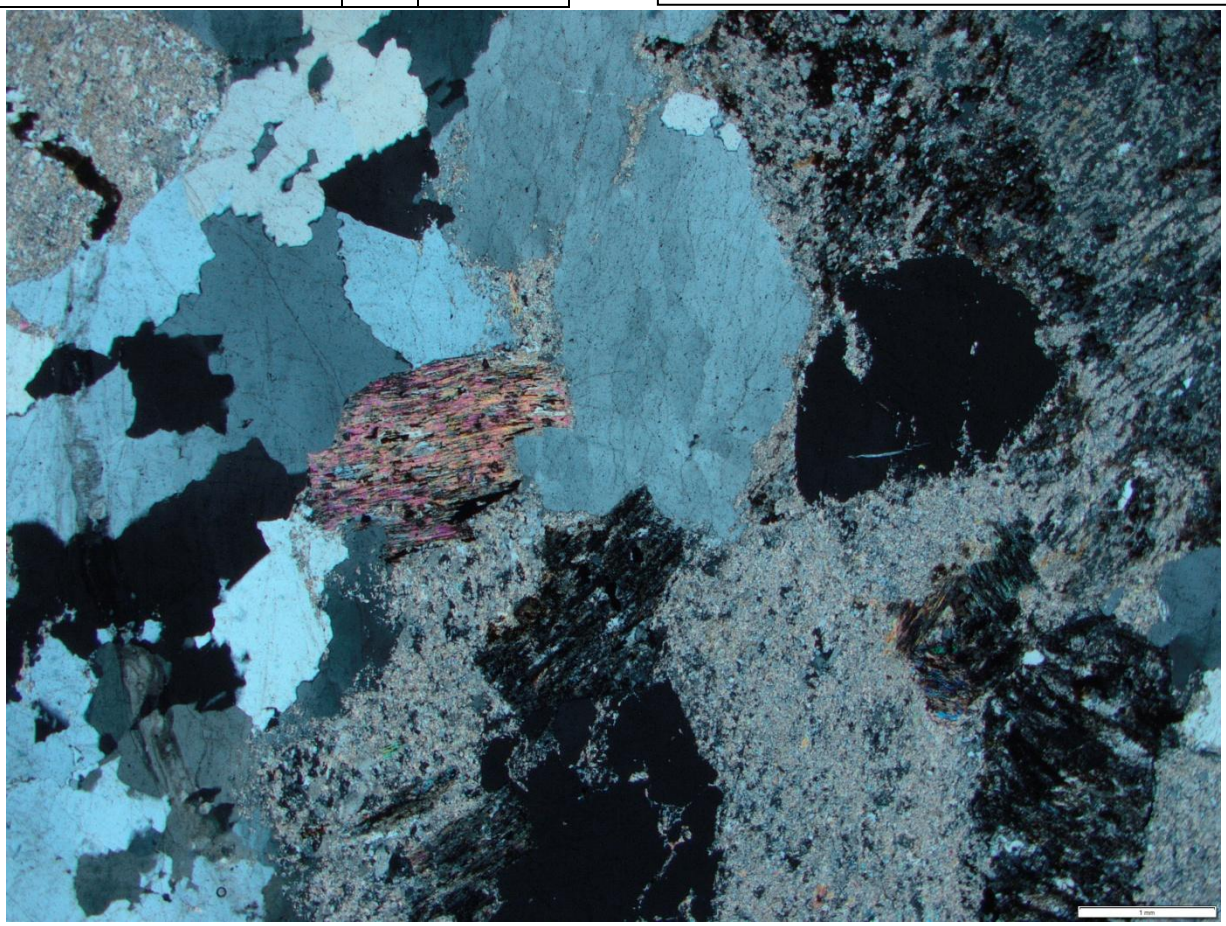

Thin Section Log

Type: PTS **Origin: UTAS**

ID: BW001 239.5

Name: Green tourmaline vein in granite

Phase	%	Grainsize
Quartz	60	
Serecite	15	
Tourmaline	15	
Chlorite	5	
biotite	5	

Comments:

Biotite rich granite with green tourmaline

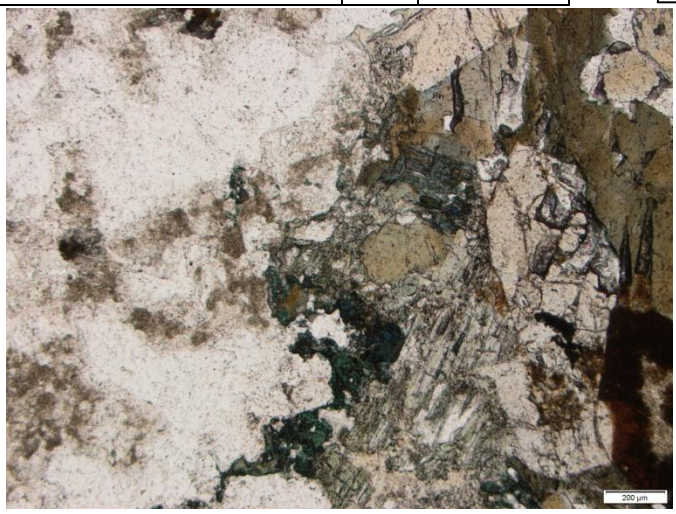

Thin Section Log

Type: TS **Origin: VMS**

ID: BW001 239.9

Name: Biotite rich granite with green tourmaline

Phase	**%**	**Grainsize**
Quartz Serecite Biotite Tourmaline		

Comments:

Quartz (& feldspar?) replaced by serecite

Green tourmaline

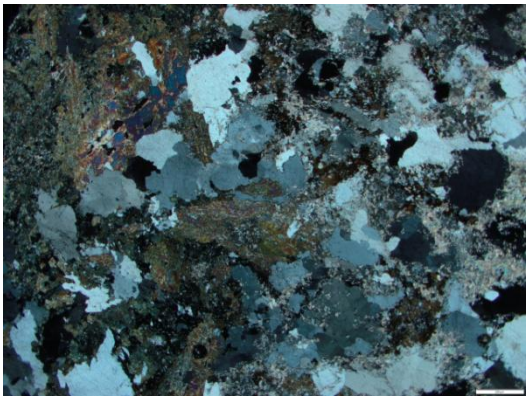

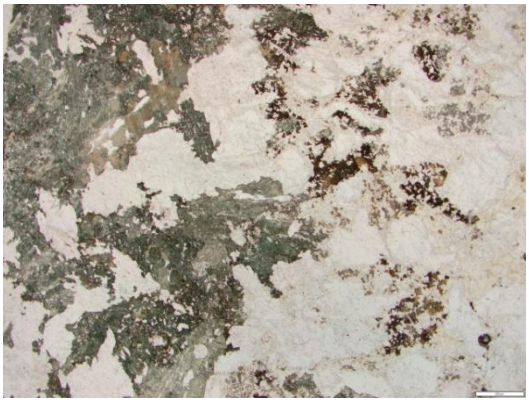

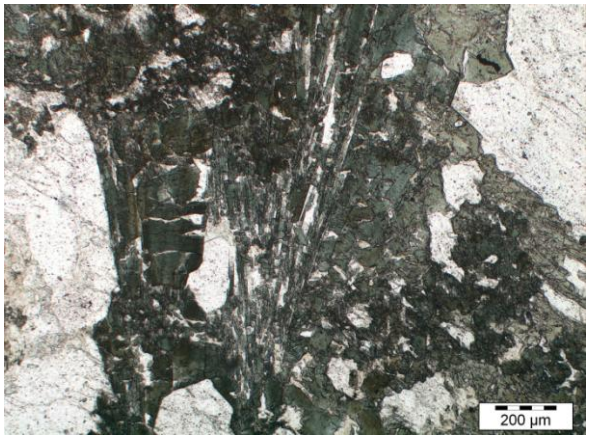

Thin Section Log

Type: TS **Origin:VMS**

ID: BW001 241.1

Name: Serecite altered granite

Phase	%	Grainsize
Quartz	40	4mm
Serecite	55	
Chlorite	5	

Comments:

Heavily se altered granite-qz replaced by se

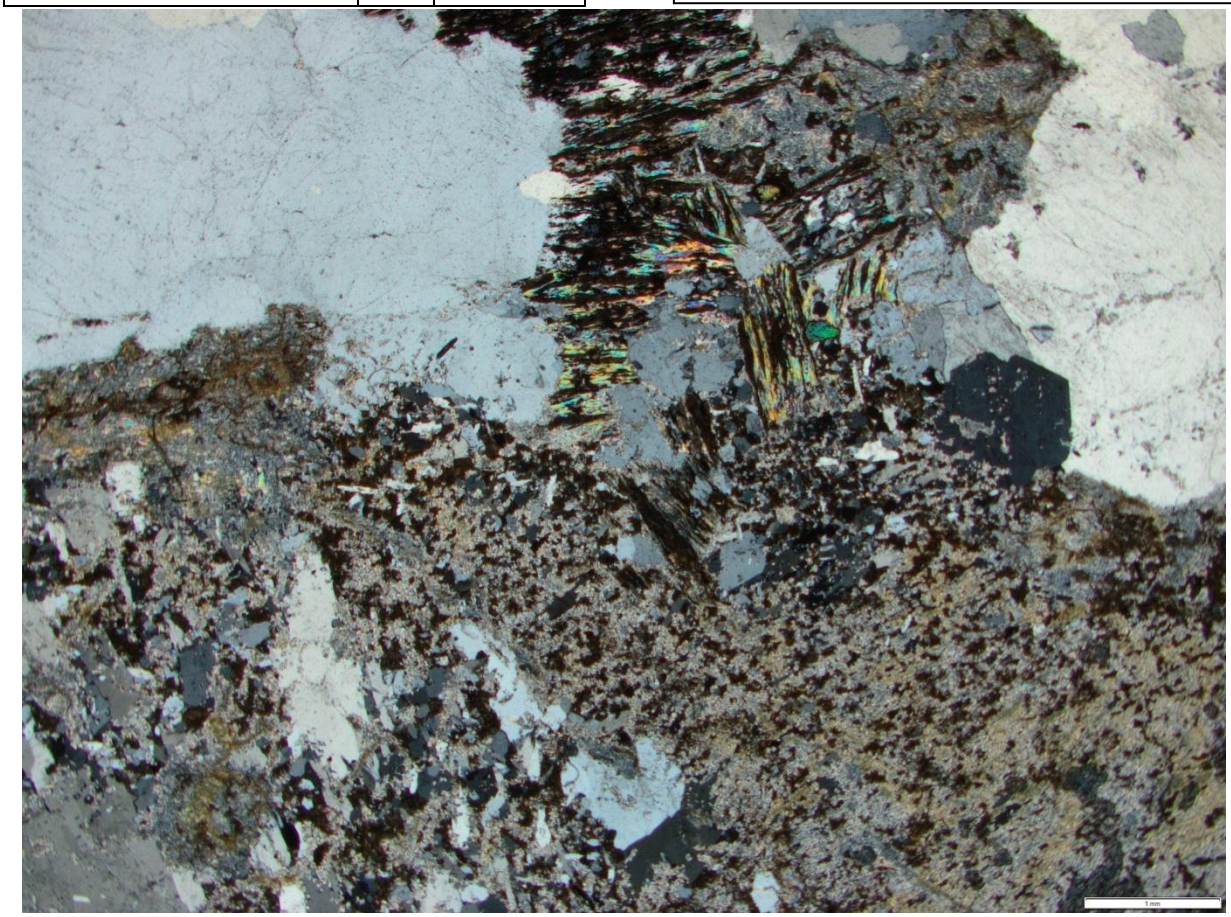

Thin Section Log

Type: PTS **Origin: UTAS**

ID: BW001 243.0

Name: serecite altered granite with tourmaline veins

Phase	%	Grainsize
Quartz	40	5mm
Serecite	59	
tourmaline	2	2mm

Comments:

Serecite replacing quartz – feldspar? No original feldspar present

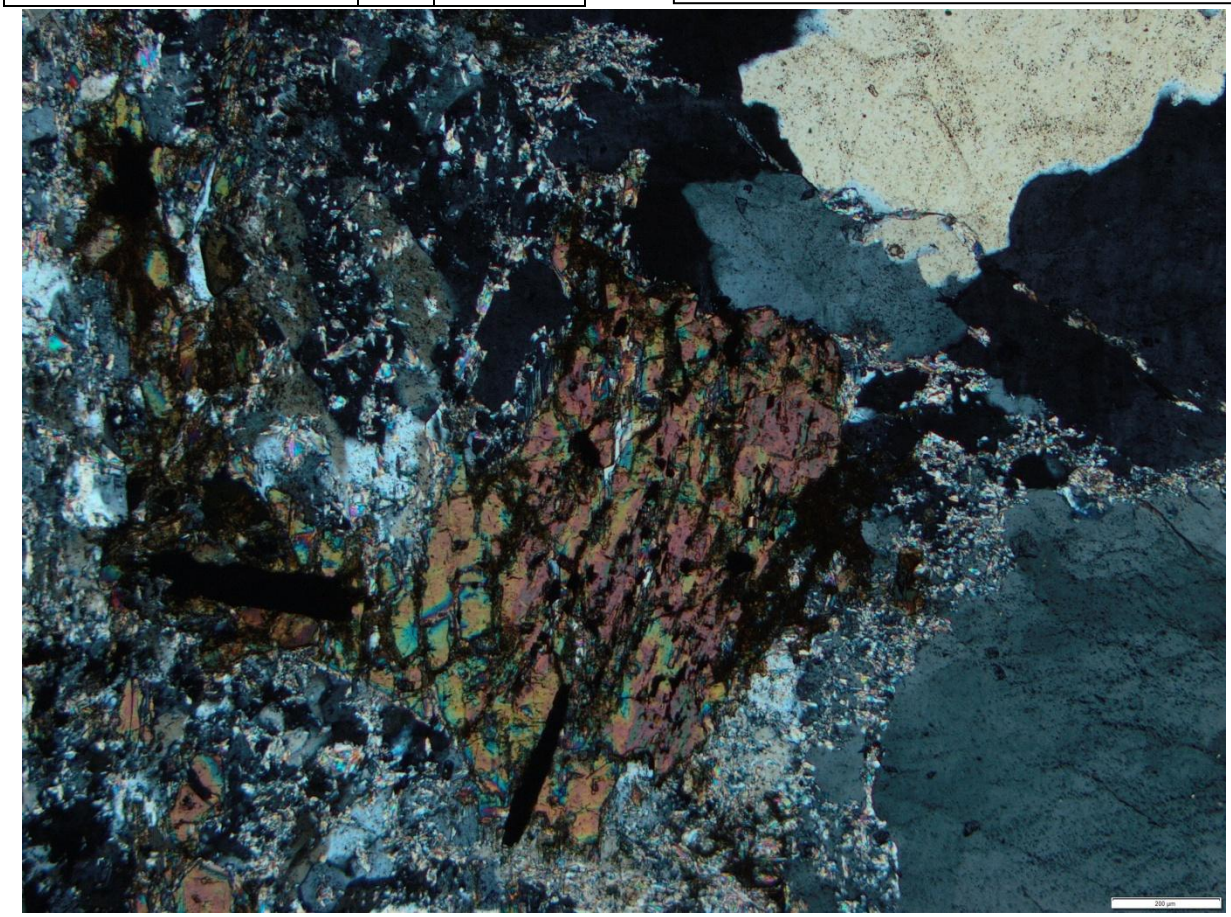

Thin Section Log

Type: TS **Origin: VMS**

ID: BW001 247.6

Name: Serecite altered granite

Phase	**%**	**Grainsize**
Quartz	50	5mm
Serecite	50	

Comments:

Heavily se altered qz – possibly full replacement of feldspar.

Occasional isotropic quartz

Thin Section Log

Type: TS **Origin: VMS**

ID: BW001 249.3

Name: Serecite altered granite

Phase	%	Grainsize
Quartz	40	
Serecite	50	
biotite	10	

Comments:

Strong se alteration of qz – no feldspar present but feldspar may be totally replaced by serecite

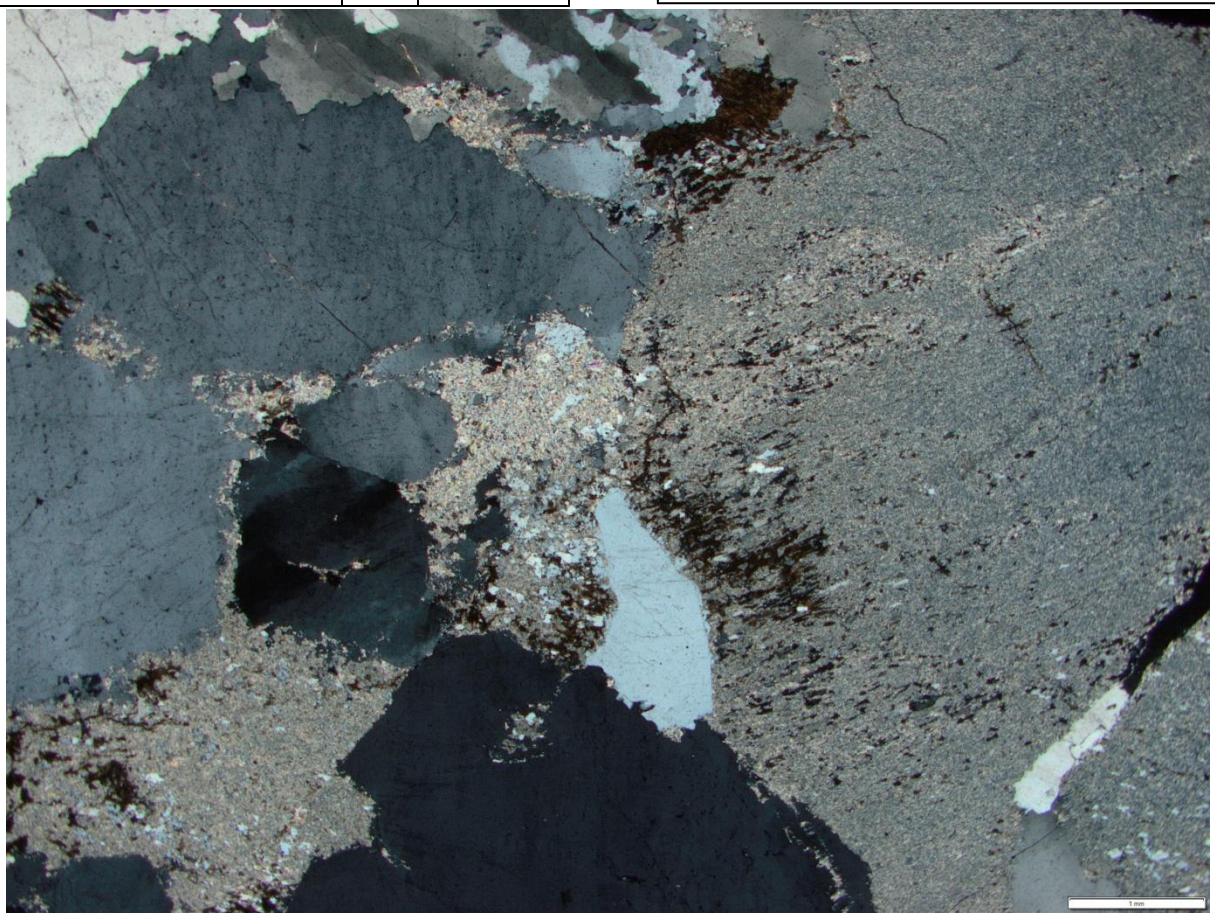

Thin Section Log

Type: PTS **Origin: UTAS**

ID: BW001 249.5

Name: Granite with green tourmaline

Phase	%	Grainsize
Quartz	45	
Serecite	30	
Tourmaline	15	
Biotite	2	
chlorite	5	
pyrite	5	

Comments: QZ-fsp? Altered to Se
Green tourmaline
Py oxidising

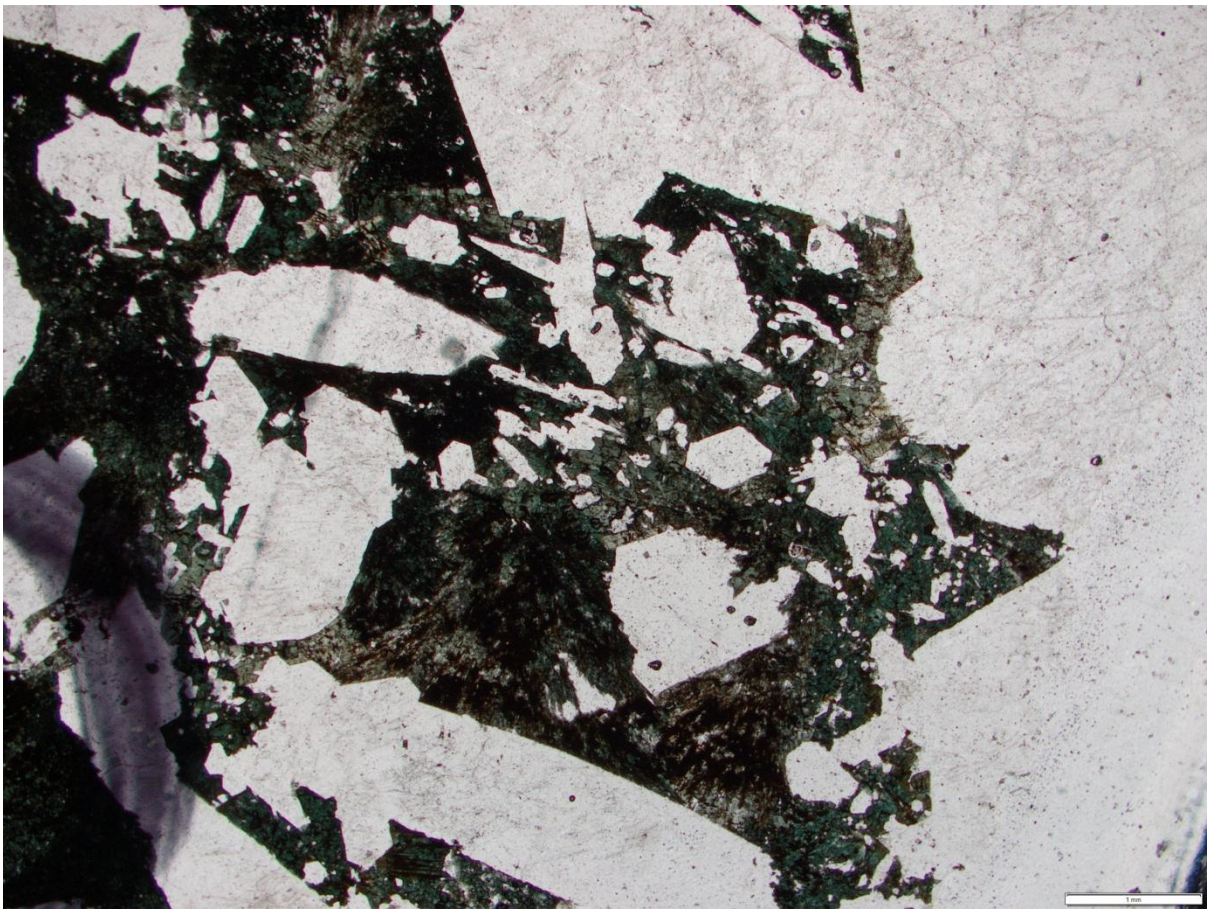

Thin Section Log

Type: TS **Origin:VMS**

ID: BW001 249.8

Name: Tourmaline pyrite granite

Phase	%	Grainsize
Quartz	30	2mm
Tourmaline	30	5mm
Pyrite	30	1mm
serecite	10	

Comments:

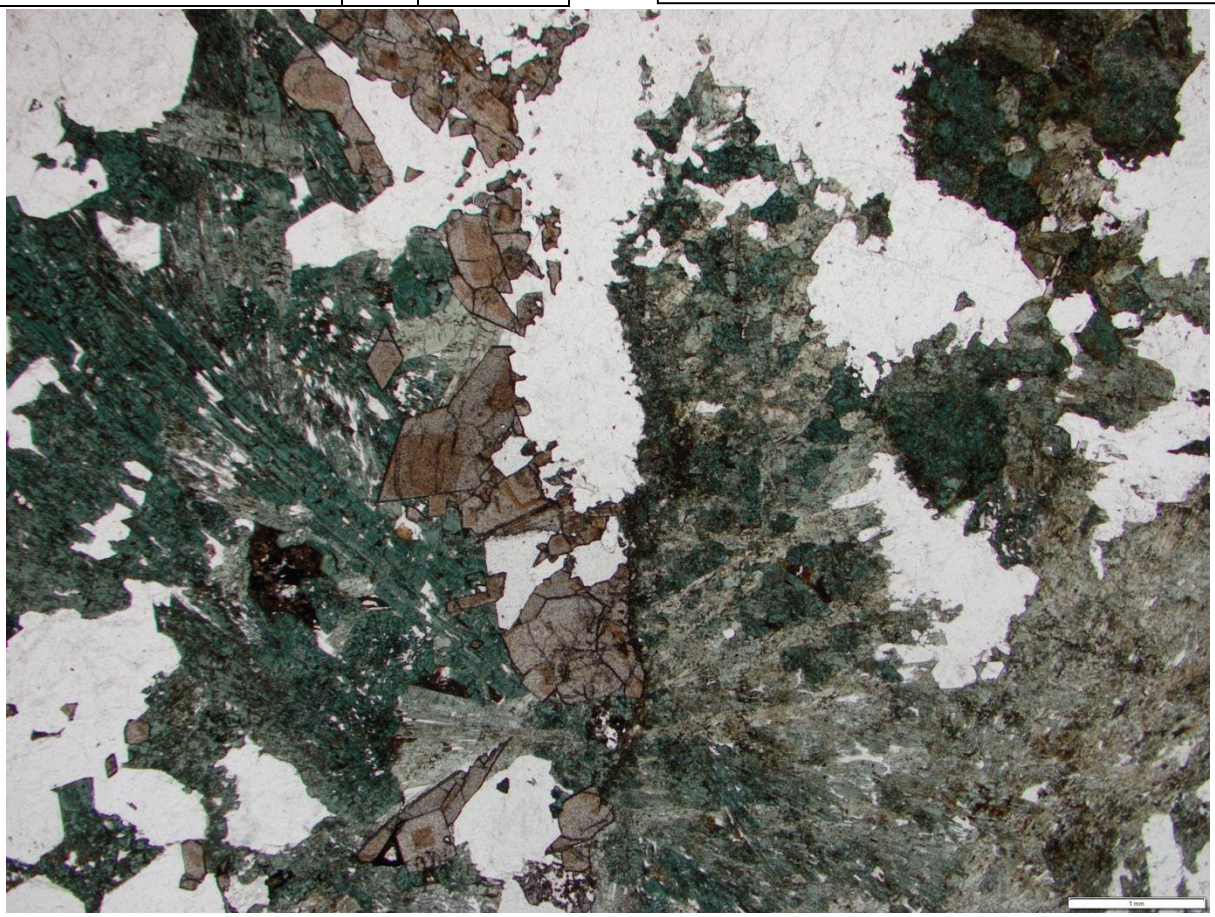

Thin Section Log

Type: PTS **Origin: UTAS**

ID: BW001 251.8

Name: serecite tourmaline granite

Phase	%	Grainsize
Quartz	40	5mm
Serecite	55	
tourmaline	5	1mm

Comments:

Se replacing qz – fsp?

Black tourmaline in thin veins

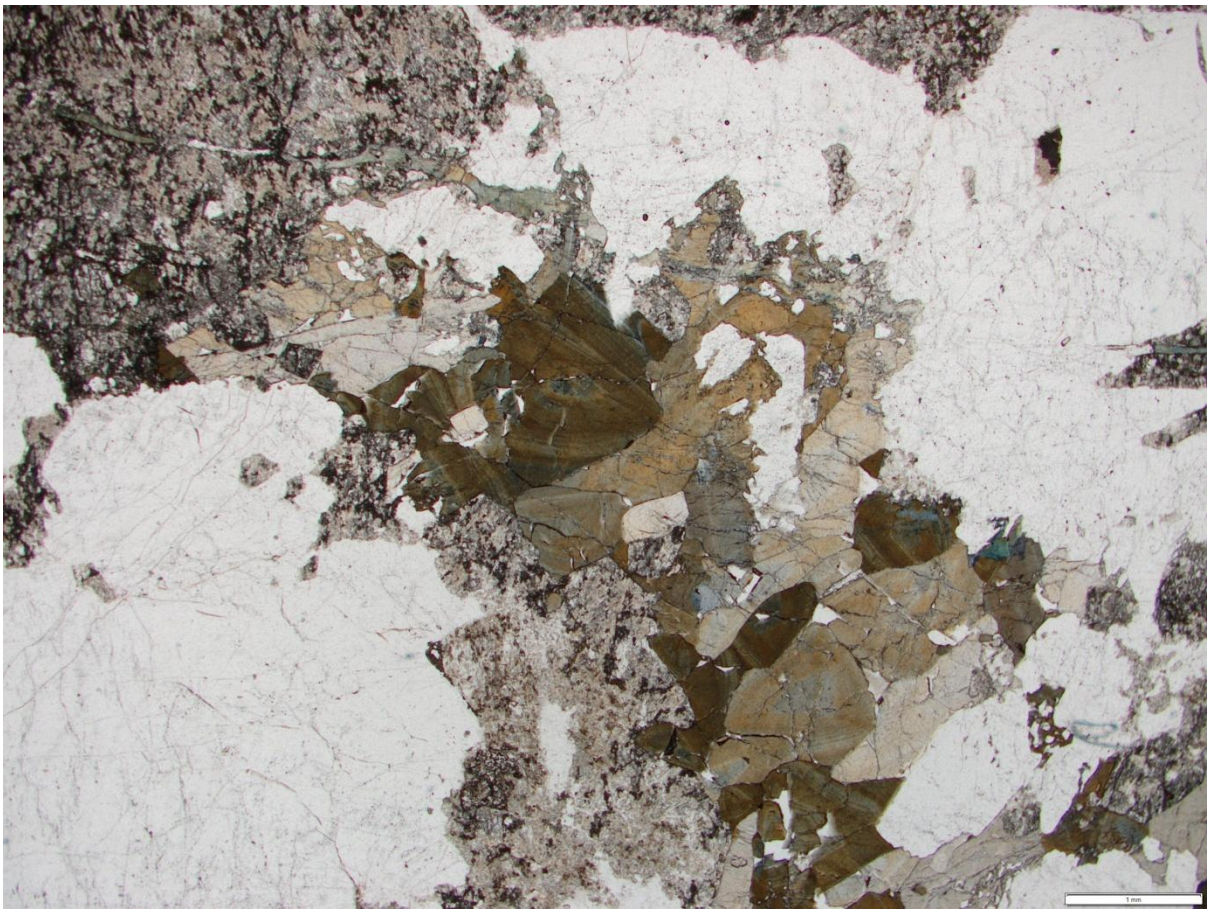

Thin Section Log

Type: PTS **Origin: UTAS**

ID: BW001 257.9

Name: tourmaline vein in serecite altered granite

Phase	%	Grainsize
Quartz	48	.5mm
Serecite	50	
tourmaline	2	5mm

Comments:

1mm wide black tu vein in heavily se altered qz. No fsp

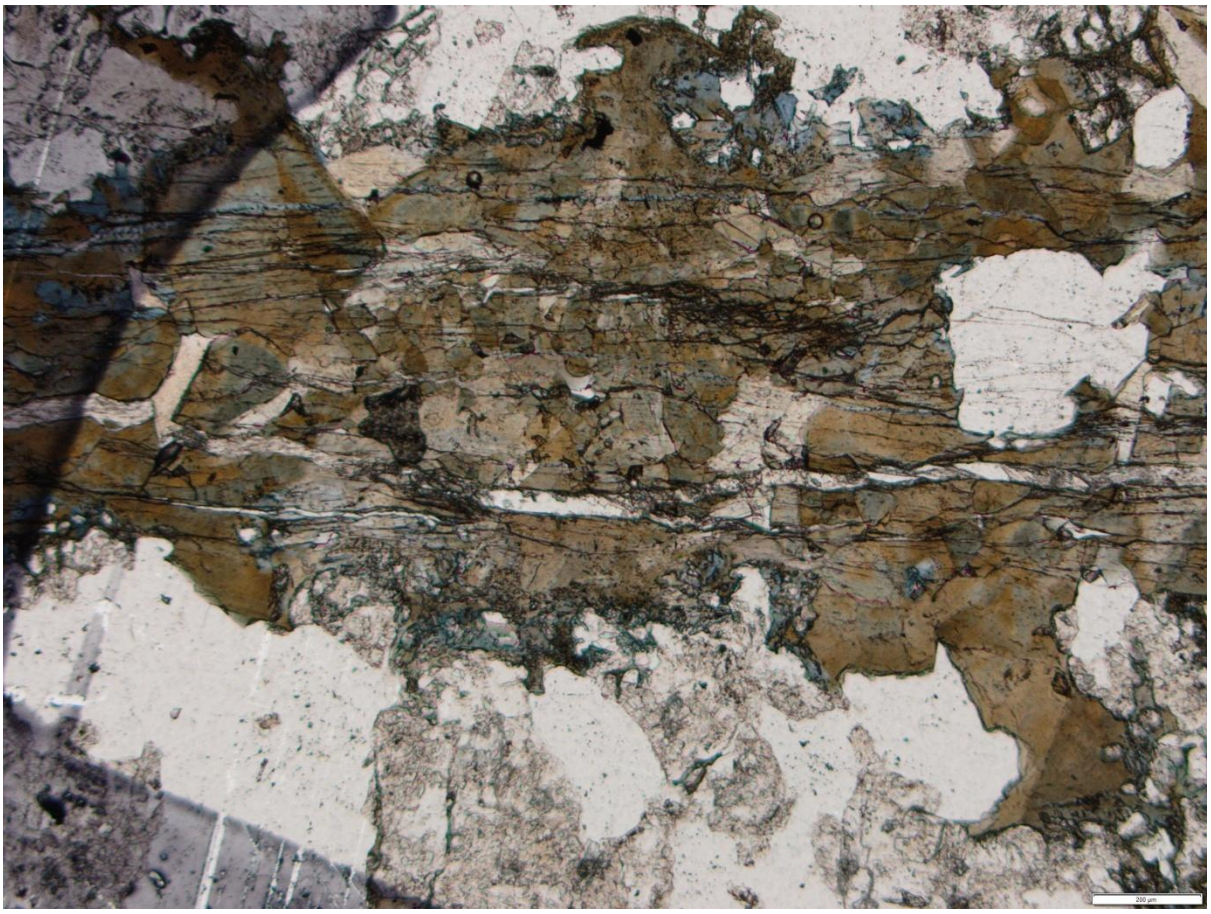

Thin Section Log

Type: PTS **Origin: UTAS**

ID: BW001 286.3

Name: se altered granite with tuV

Phase	%	Grainsize
Quartz	48	2mm
Serecite	48	
tourmaline	4	5mm

Comments:

3mm wide tuV in se altered granite. Qz>se, no Fsp

Thin Section Log

Type: PTS **Origin: UTAS**

ID: BW001 294.7

Name: Biotite rich granite

Phase	%	Grainsize
Quartz	60	5
Serecite	30	
biotite	10	2

Comments:

Quartz replaced by serecite. No feldspar, probably completely replaced by serecite

Thin Section Log

Type: PTS **Origin: UTAS**

ID: THBW017

Name: TuV in granite

Phase	%	Grainsize
Tu	20	
Qz	45	
Se	30	
chlorite	5	

Comments:
Green and black tourmaline concentrated in vein with quartz.
Heavy se alteration of qz in wallrock

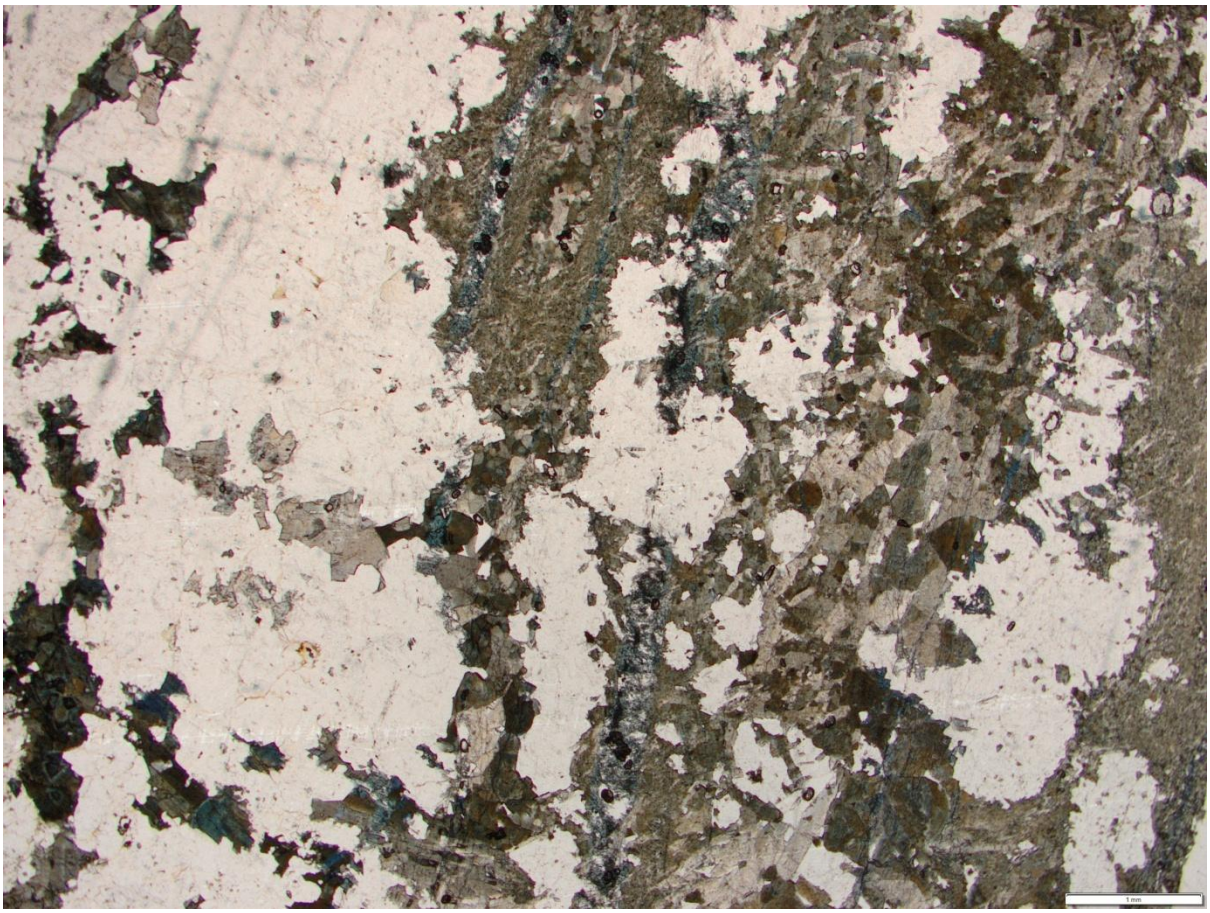

Thin Section Log

Type: PTS **Origin: UTAS**

ID: THLV001a

Name: Quartz-tourmaline

Phase	%	Grainsize
Quartz	60	10mm
Tourmaline	40	10mm

Comments:

Coarse grained quartz-tourmaline

Tu replacing qz?

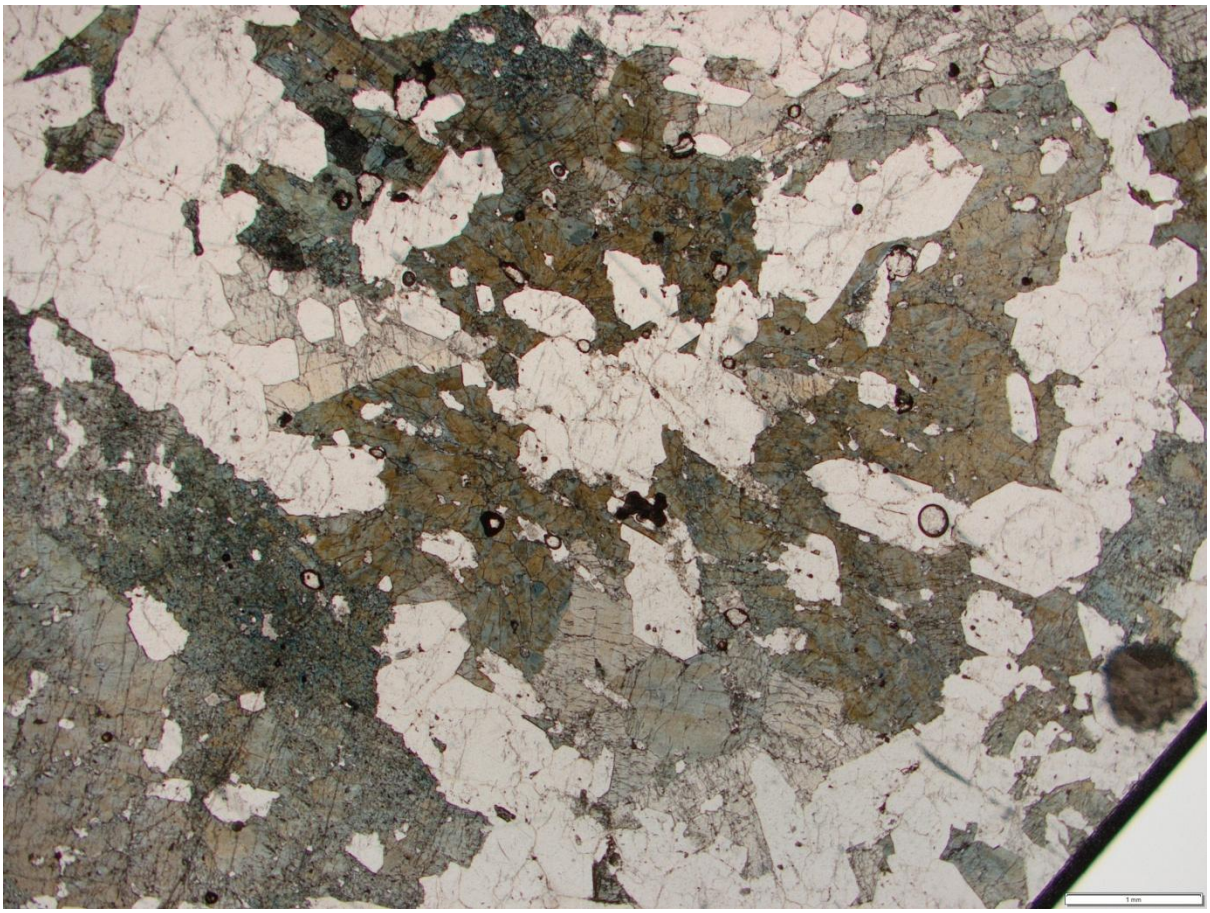

Thin Section Log

Type: PTS **Origin: UTAS**

ID: BW012 120.1

Name: Garnet vonsenite skarn

Phase	%	Grainsize
Garnet	30	.2mm
Vesuvianite	15	.2mm
Amphibole	20	.3mm
Vonsenite	25	1.5mm
Pyroxene	5	.1mm
Chlorite	5	.2mm
calcite	1	1mm

Comments:

Acicular vo

Am replacing gt

Am infilling gt

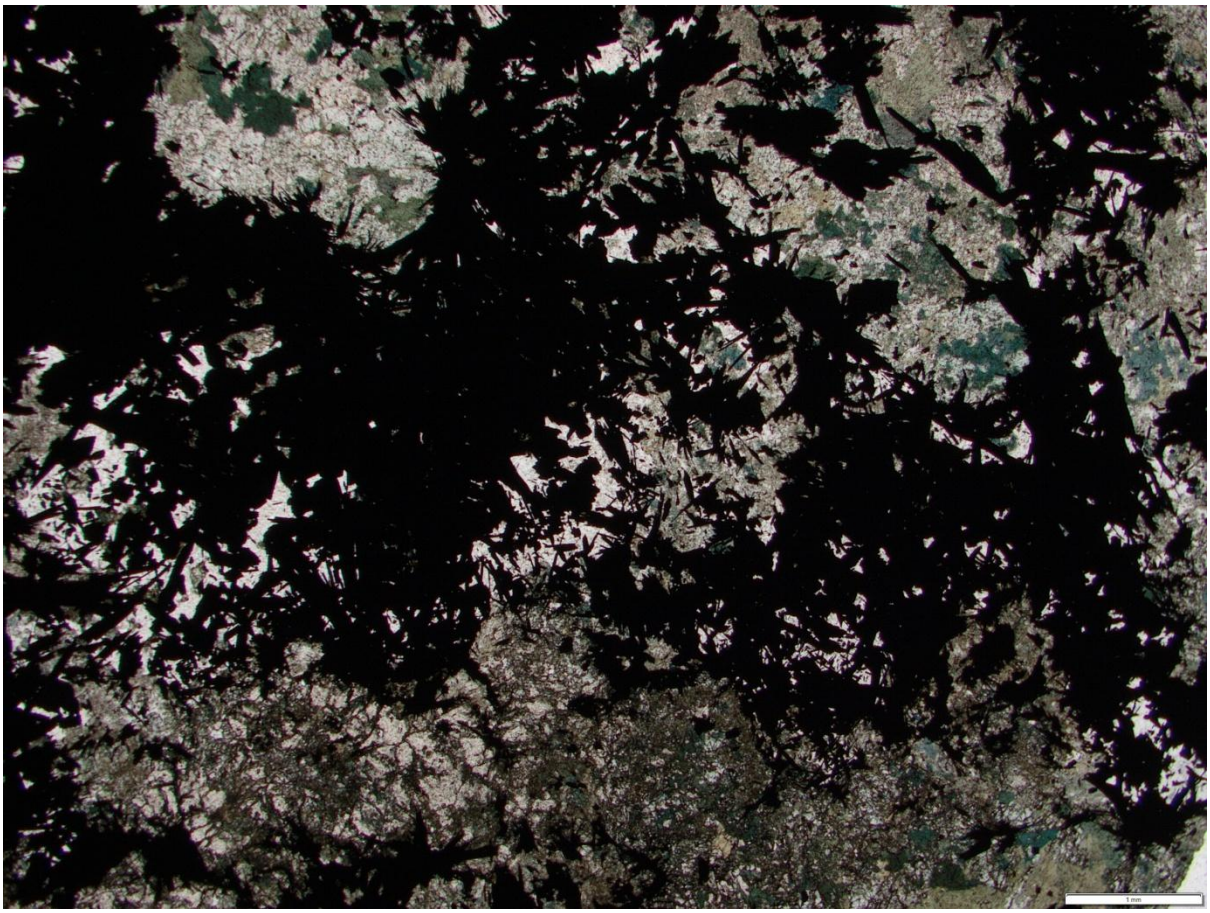

Thin Section Log

Type: PTS **Origin: UTAS**

ID: BW003A 210.1

Name: pyroxene marble

Phase	%	Grainsize
Pyroxene	50	.1mm
Calcite	40	.5mm
Garnet	10	.5mm

Comments:

Pyroxene replacing calcite

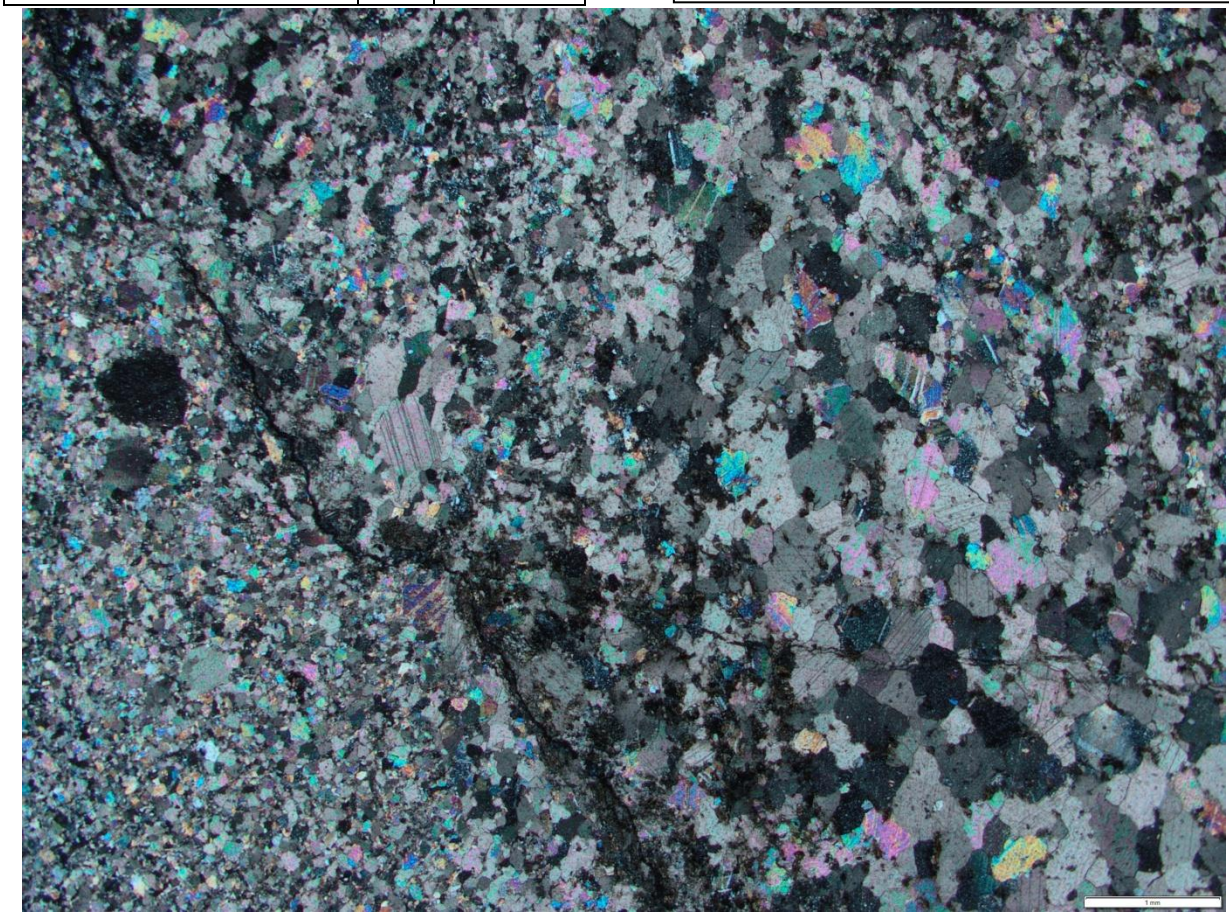

Thin Section Log

Type: PTS **Origin: UTAS**

ID: BW003A 248.0

Name: Biotite serecite chlorite altered granite

Phase	%	Grainsize
Quartz	40	10mm
Serecite	35	.1mm
Biotite	20	.5mm
Chlorite	4	.3mm
Feldspar	1	.3mm

Comments:

Biotite –serecite replacing feldspar and quartz.

Minor chlorite infill. Feldspar almost totally replaced

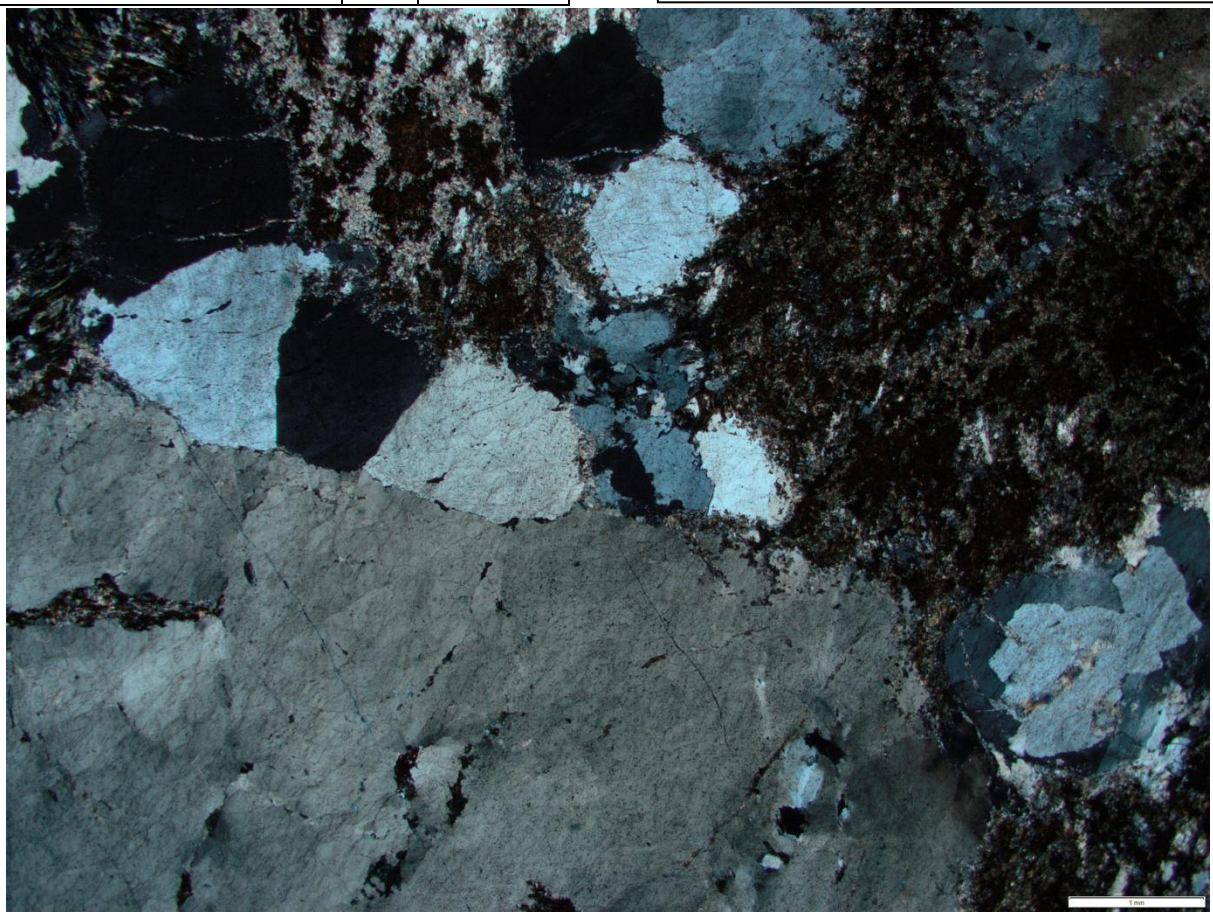

Thin Section Log

Type: TS **Origin: VMS**

ID: BW013_224.3

Name: Ultramafic - serpentenite

Phase	%	Grainsize
Serpentine	60	1mm
Pyroxene?	?	
Magnetite?	10	.5mm

Comments:

Granular magnetite?

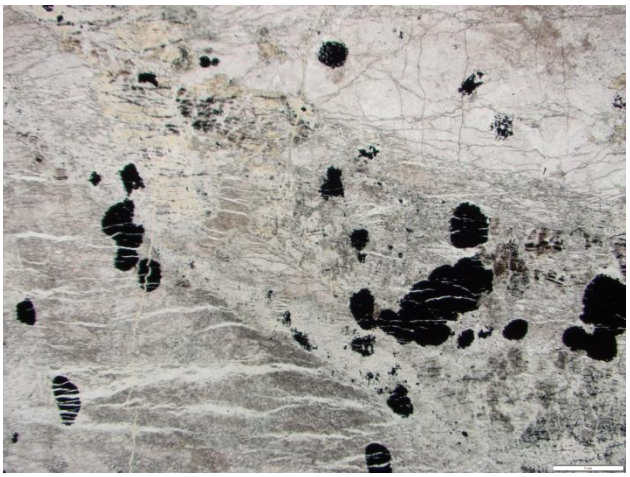

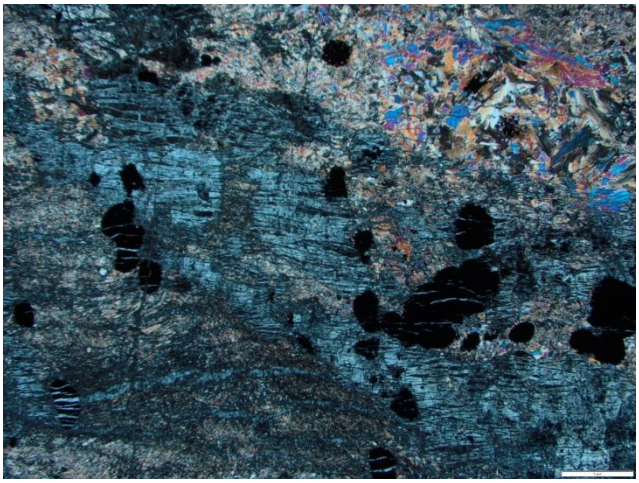

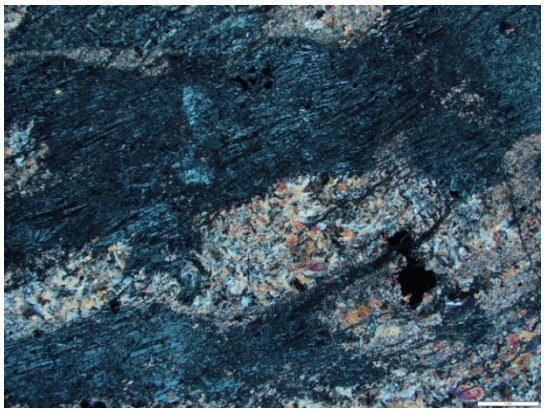

Thin Section Log

Type: TS **Origin: VMS**

ID: BW013 245.65

Name:

Phase	%	Grainsize

Comments:

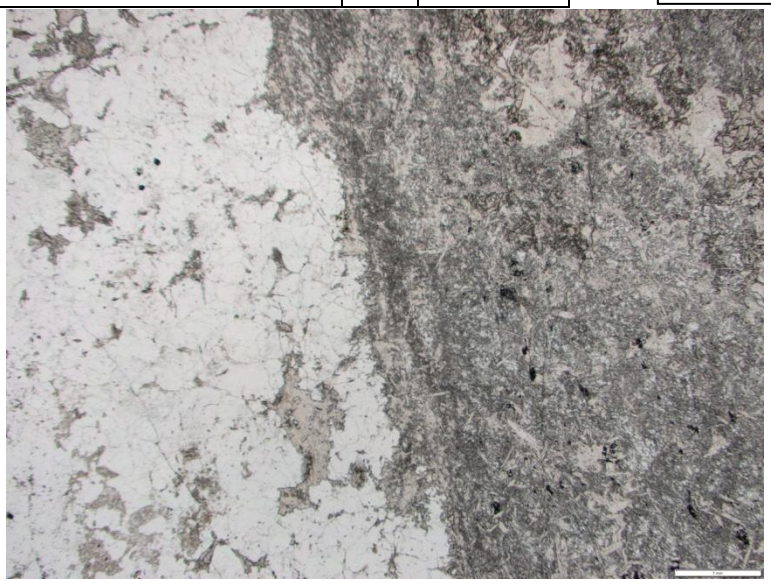

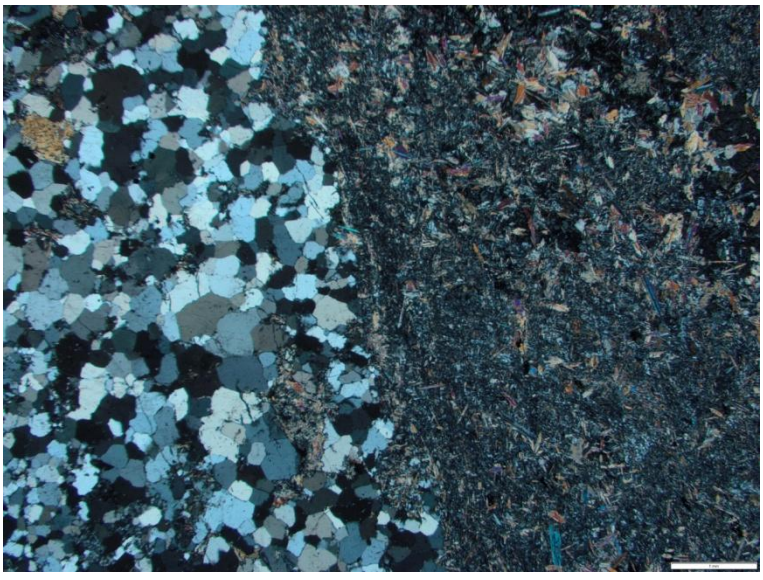

Thin Section Log

Type: TS **Origin: VMS**

ID: BW009A 138.3

Name:

Phase	%	Grainsize

Comments:

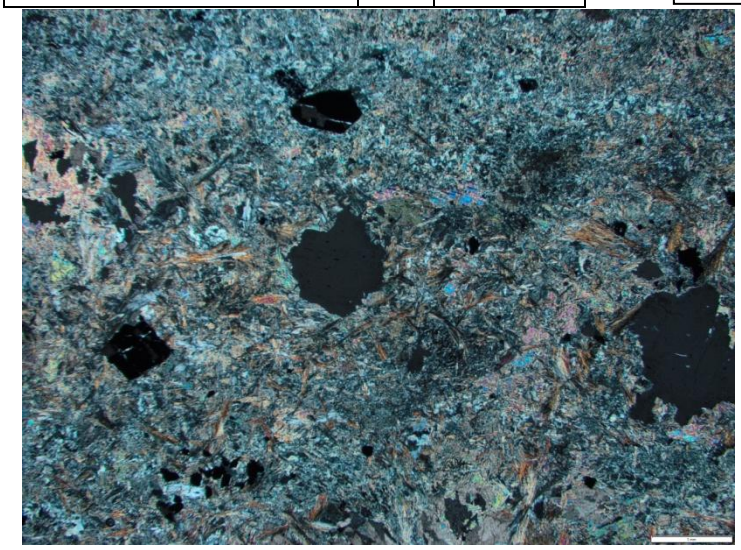

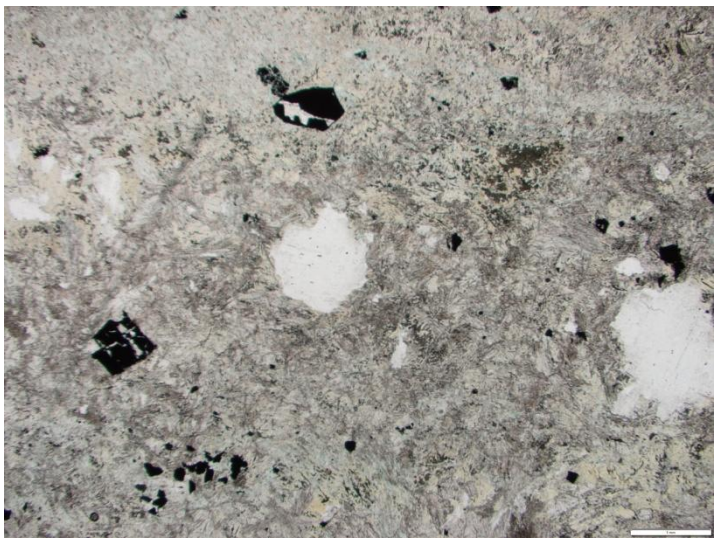

Thin Section Log

Type: TS **Origin: VMS**

ID: BW009A 157.2

Name:

Phase	%	Grainsize

Comments:

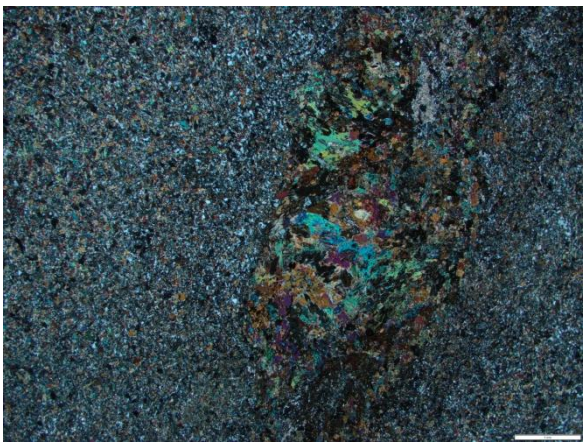

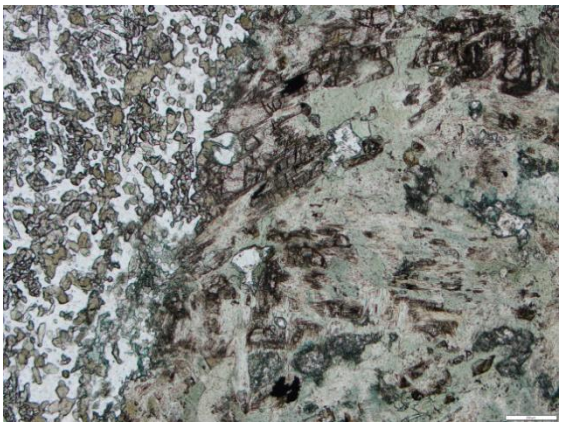

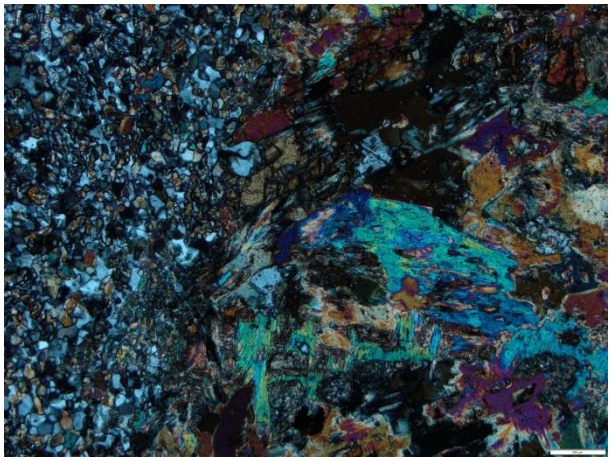

Thin Section Log

Type: TS **Origin: VMS**

ID: BW009A 158.9

Name: Amphibole hornsfels

Phase	%	Grainsize
Amphibole	80	200µm
Serpentine	15	2mm

Comments:

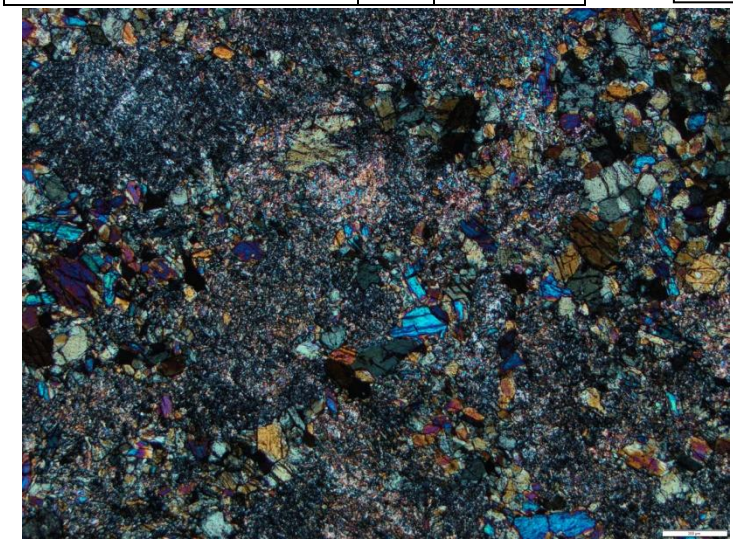

Thin Section Log

Type: TS **Origin:VMS**

ID: BW002 210.9

Name: Vonsenite vesuvianite amphibole skarn

Phase	%	Grainsize
Vonsenite	50	1mm
Vesuvianite	25	.2mm
Amphibole	15	.5mm
Pyroxene	5	.1mm
garnet	5	.2mm

Comments:

Acicular vonsenite

Amphibole replacing vesuvianite

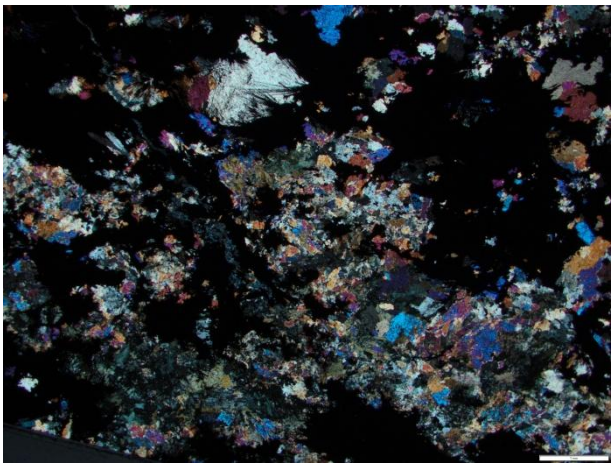

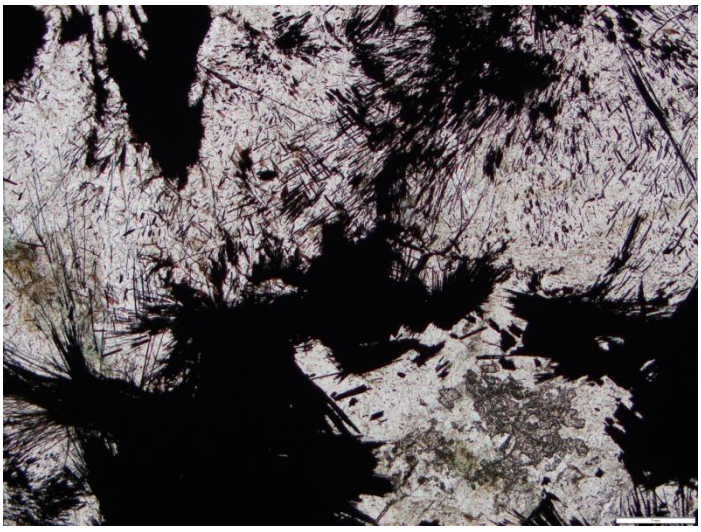

Thin Section Log

Type: TS **Origin: VMS**

ID: BW002 212.8

Name: Magnetite garnet skarn

Phase	%	Grainsize
Magnetite	40	1mm
Garnet	45	2mm
Amphibole	5	1mm
vesuvianite	10	1mm

Comments:

Pbl gt

Granular magnetite

Am replacing gt

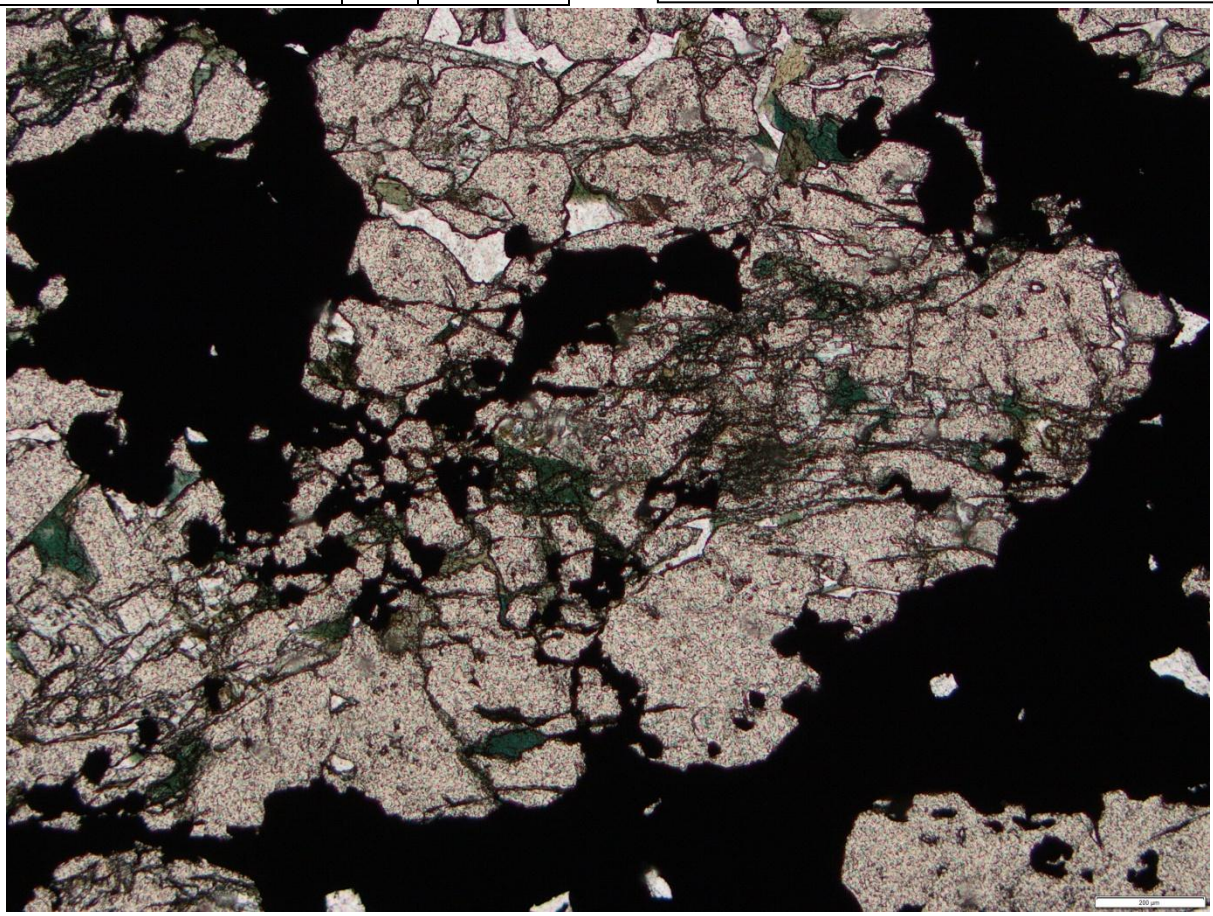

Thin Section Log

Type: TS **Origin: VMS**

ID: BW002 214.1

Name: amphibole vonsenite skarn

Phase	%	Grainsize
Orthopyroxene	19	
Amphibole	35	
Vonsenite	45	
serpentine	1	

Comments:

Acicular vonsenite

Amphibole replacing pyroxene

Amphibole replacing seprpentine

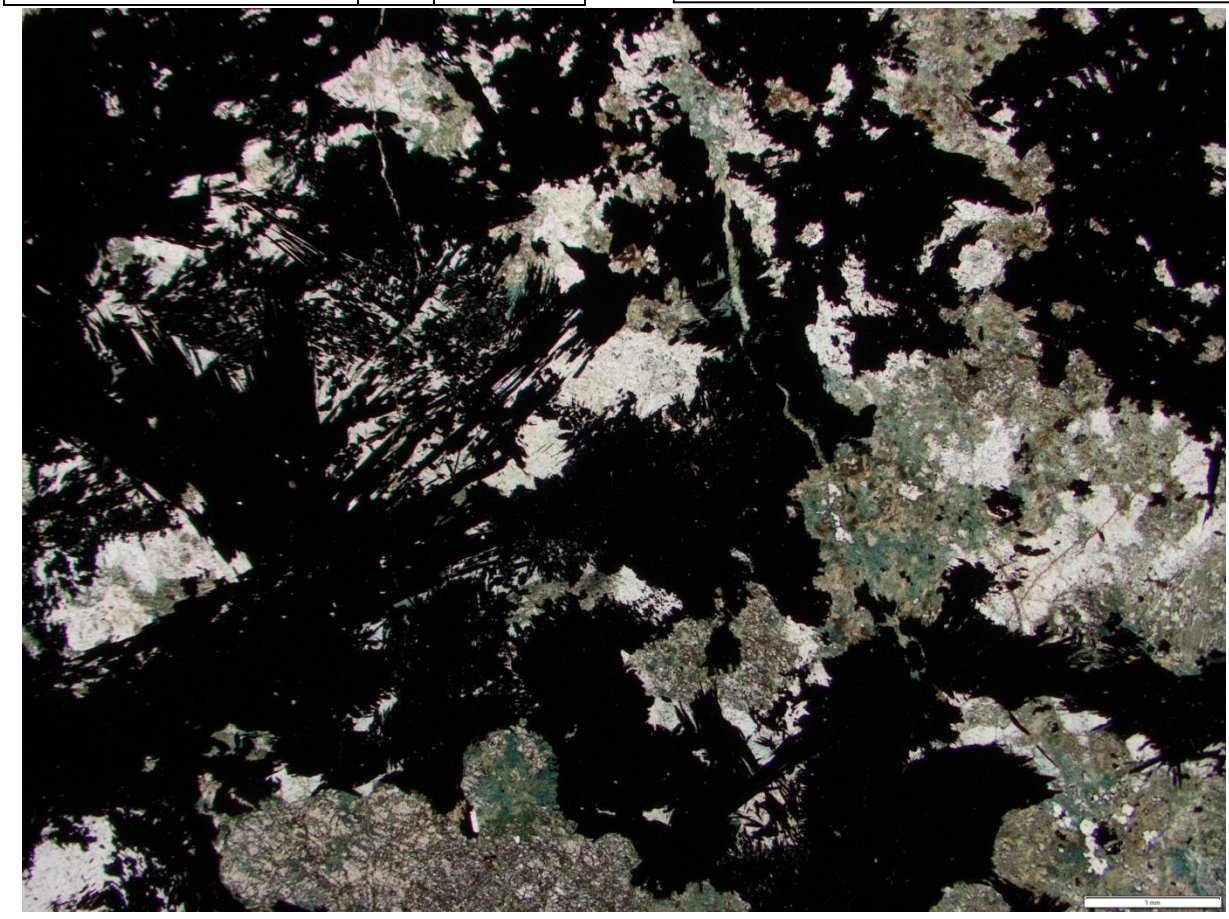

Thin Section Log

Type: TS **Origin: VMS**

ID: BW002 217.9

Name: Garnet amphibole skarn

Phase	%	Grainsize
Amphibole	29	.2mm
Garnet	50	.2mm
pyroxene	20	.1mm
Vonsenite? FeTio?	1	.5mm

Comments:

Am infilling cracks in gt

Am preplacing pyroxene

Thin Section Log

Type: TS **Origin: VMS**

ID: BW002 220.2

Name: vonsenite amphibole pyroxene skarn

Phase	%	Grainsize
Vonsenite	30	.7mm
Amphibole	40	.5mm
pyroxene	30	.2mm

Comments:

Amphibole replacing pyroxene

Acicular vonsenite

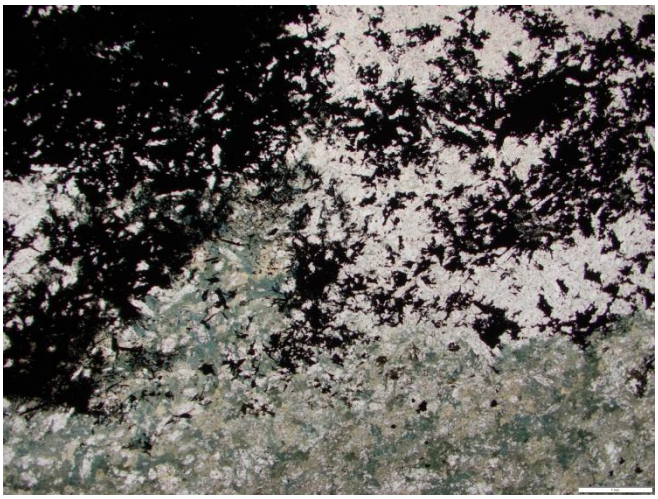

Thin Section Log

Type: TS **Origin:VMS**

ID: BW002 222.5

Name: Pyroxene magnetite skarn

Phase	%	Grainsize
Pyroxene	50	100µm
magnetite	50	100µm

Comments:

Granular magnetite

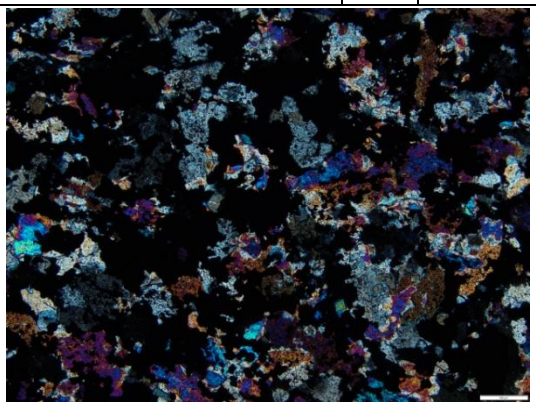

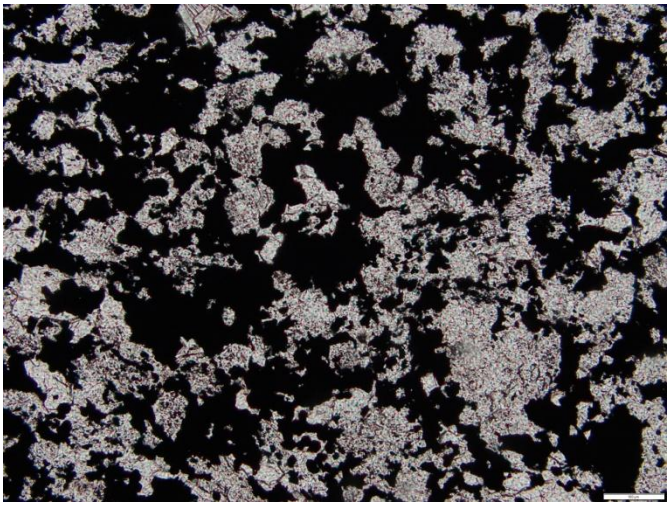

Thin Section Log

Type: TS **Origin: VMS**

ID: BW002 224.4

Name: Ultramafic

Phase	%	Grainsize
Serpentine	60	1mm
Magnetite	5	.5mm
Pyroxene	34	.2mm
olivine	1	.4mm

Comments:

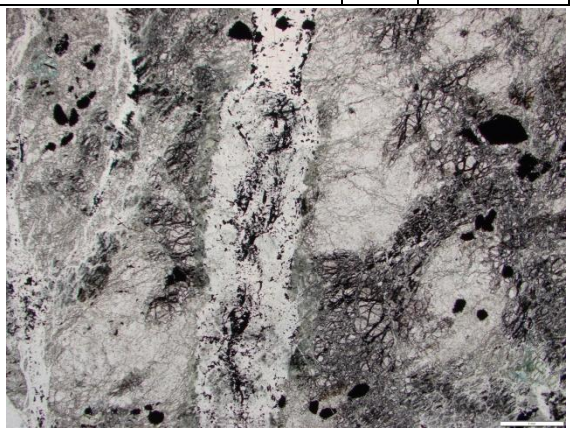

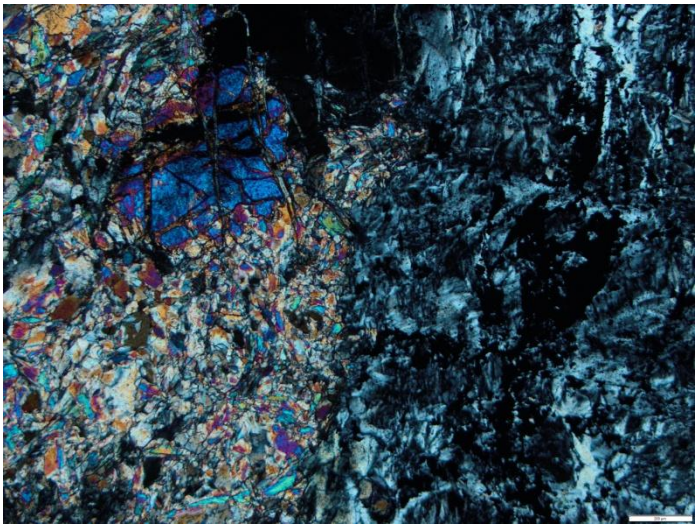

Thin Section Log

Type: TS **Origin:VMS**

ID: BW002 225.9

Name: Ultramafic

Phase	%	Grainsize
Serpentine	60	2mm
Pyroxene	30	.5mm
FeTiO	10	.3mm

Comments:

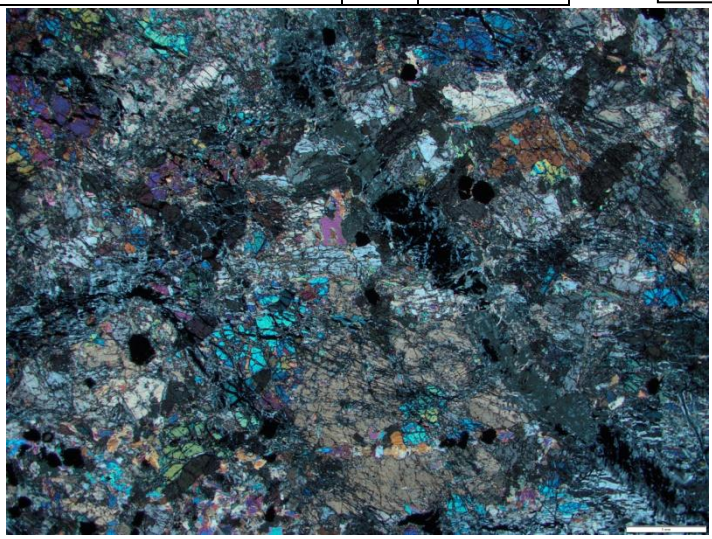

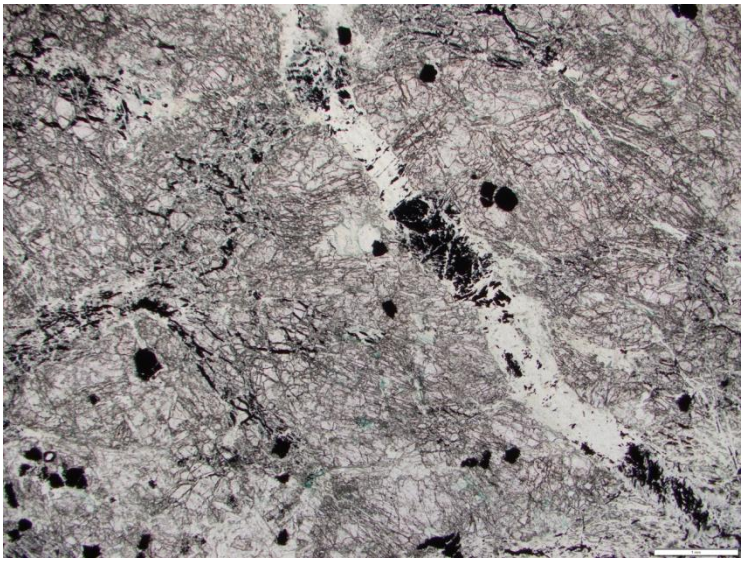

Thin Section Log

Type: TS **Origin: VMS**

ID: BW002 228.0

Name: serecite, pyroxene rich granite

Phase	%	Grainsize
Quartz	20	
Serecite	30	
Pyroxene	30	
FeTiO?	2	
Serpentine?	18	

Comments:

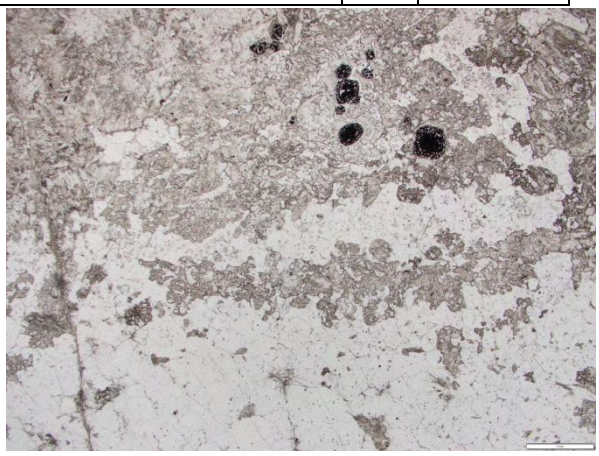

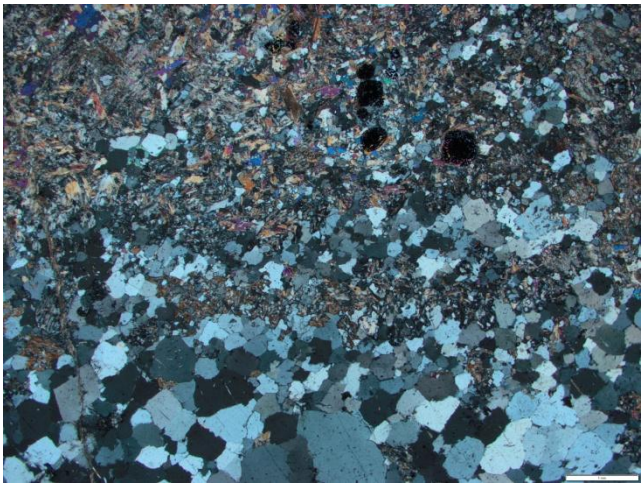

Thin Section Log

Type: TS **Origin: VMS**

ID: BW002 229.0

Name: Biotite rich granite

Phase	%	Grainsize
Quartz	48	1.5mm
Biotite	25	1.5mm
serecite	25	
Tourmlaine	2	1mm

Comments:

Feldspar replaced by biotite and serecite. No original feldspar remaining

Quartz replaced by serecite

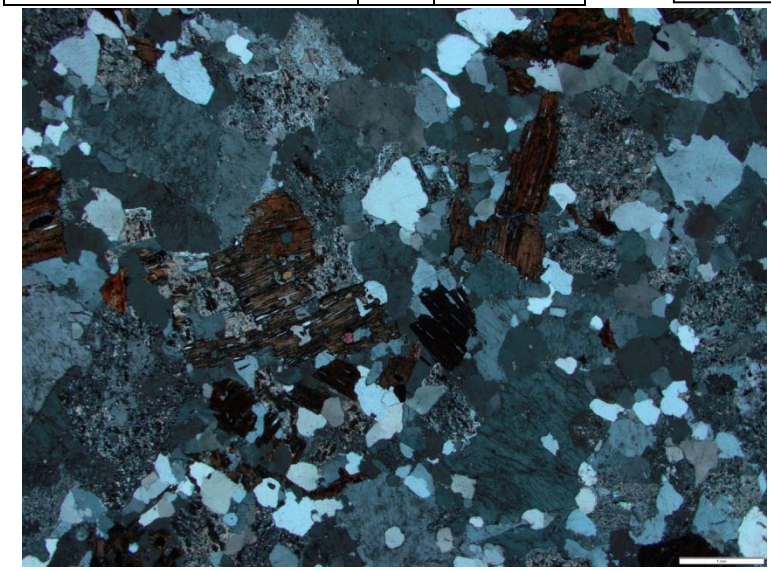

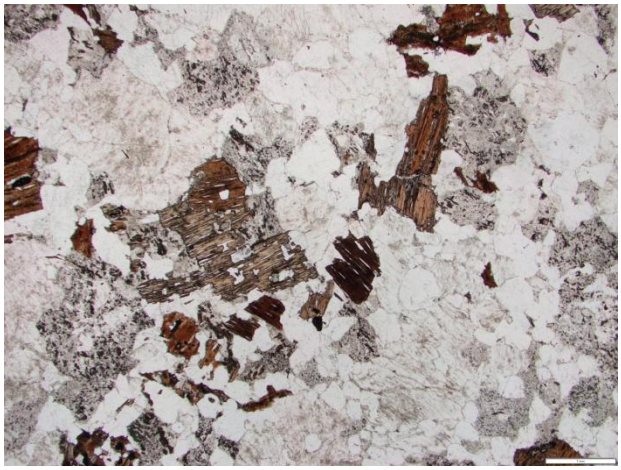

Thin Section Log

Type: TS **Origin:VMS**

ID: BW002 233.1

Name: serecite altered granite

Phase	%	Grainsize
Quartz	40	3mm
Serecite	59	
biotite	1	.5mm

Comments:
No original fsp remaining. Fsp replaced by serecite. Quartz replaced by serecite